RICE UNIVERSITY

$K^*(892)^0\Lambda$ and $K^+\Sigma^*(1385)^-$ Photoproduction on the Deuteron

by

Paul Mattione

A Thesis Submitted
in Partial Fulfillment of the
Requirements for the Degree

Doctor of Philosophy

Approved, Thesis Committee:

B. Paul Padley, Co-Chair
Rice University
Professor, Physics and Astronomy

Daniel Carman, Director
Thomas Jefferson National Accelerator Facility
Staff Scientist

Marjorie Corcoran
Rice University
Professor, Physics and Astronomy

David Scott
Rice University
Noah Harding Professor, Statistics and ECE

Gordon Mutchler, Co-Chair (deceased)
Rice University
Professor, Physics and Astronomy

Houston, Texas

May, 2011

ABSTRACT

$K^*(892)^0\Lambda$ and $K^+\Sigma^*(1385)^-$ Photoproduction on the Deuteron

by

Paul Mattione

Thirteen N^* states have been well-established according to the Particle Data Group, but some relativized quark models predict that many more N^* resonances exist. Diquark models predict that the N^* spectrum is limited by a correlated quark-pair in the nucleon, but there is strong evidence for the existence of the $N\frac{3}{2}^+(1900)^{**}$ resonance, which is absent in diquark models. Measuring the spectrum of N^* states will provide valuable information on the relevant degrees of freedom within the nucleons.

Most of the experimental searches for the N^* states have been conducted in the πN channel. Some models of baryon decays predict that most of the unobserved N^* states couple somewhat weakly to the πN channel, and that some couple non-negligibly to the KY, K^*Y, and KY^* channels. Measurements of the cross sections and polarization observables of strangeness photoproduction reactions can provide additional information on the spectrum of N^* states.

These measurements can be used in coupled-channel partial-wave analyses that can provide simultaneous constraints on the N^* resonance parameters from several channels. These analyses can also take into account hadronic rescattering, which is predicted to have a large effect on the measured cross sections. However, to determine the isospin decomposition of the photo-transition amplitudes to these channels, photoproduction measurements are necessary on both the proton and the neutron.

Measurements of the differential cross sections of the $\gamma n \to K^*(892)^0\Lambda$ and $\gamma n \to K^+\Sigma^*(1385)^-$ reactions have been performed using data from the Jefferson Lab Hall B CLAS g13 experiment.

No experimental cross section data have yet been published on the $\gamma n \rightarrow K^*(892)^0\Lambda$ reaction, and the only published cross section data on the $\gamma n \rightarrow K^+\Sigma^*(1385)^-$ reaction are limited to forward angles, where t-channel K^+ and K^{*+} exchanges are predicted to dominate. These cross sections are compared against theoretical models to study the channel interactions that give rise to their distributions. These reactions also have the same final state particles ($K^+\pi^-p\pi^-$), so studies of their potential interference were performed as well. A measurement of the $\gamma n \rightarrow p\pi^-$ cross section was also performed, and the agreement with published results within the uncertainties validated the integrity of the data and procedures used in this analysis.

Acknowledgments

I would first like to thank Gordon Mutchler for taking me on as his graduate student, and for introducing me to nuclear physics at Jefferson Lab. After I moved to Virginia I didn't get to see him in person very often, but I enjoyed our frequent phone conversations. While he certainly helped me a lot with my physics research, we also spent a lot of time talking about baseball, and whether the Houston Astros would ever figure out how to compete again. When he passed away I felt like my world had been turned upside down, and I didn't even know if I would continue doing physics anymore. I wish Gordon was still here to see how far I've come along; it's sad how much emptier the hallways are at the Bonner Lab with him gone.

I would truly like to thank Daniel Carman and Paul Padley for volunteering to take me on as their graduate student after Gordon passed away. Both Dan and Paul were always available for advice, whether about my writing, my research, or about preparing for life beyond graduate school. I would especially like to thank Daniel for pushing me to be better, to be more thorough in both my research and my writing. Also, this dissertation would not be anywhere near as polished without the great amount of time and effort that Paul, and especially Dan, volunteered to help me.

Of course, this work would not have been possible without the help and support of many different members of the CLAS collaboration. From preparing and running the g13 experiment, to detector calibrations and data cooking, a lot of different people contributed to this research. Also, many different members of the collaboration gave me valuable input on my analysis. I would especially like to thank Pawel Nadel-Turonski and Eugene Pasyuk for all of the help and advice that they gave me. Data analyses at CLAS are extremely complicated, and without their help and direction I would probably still have a long a way to go.

I would also like to thank my friends Ryan Bodenstein and Nicholas Zachariou for helping to

keep me grounded throughout the writing of my dissertation. They were an anchor for me while I was running on "Mattione Time," and helped remind me that there was more to life than just research. I especially enjoyed my chess games and discussions with Ryan; Ryan, if you're reading this, Qf2 is indeed the clinching move. That trap in the Albin Countergambit was truly devastating.

Finally, I would like to thank all of my friends and family for all of the love and support they have given me. It is inspiring to see all of the good in this world manifested in those that I love and care about. Life is a lot more fun when you can share it with the people that you love.

Table of Contents

Abstract ii

Acknowledgments iv

List of Tables xi

List of Figures xiii

1 Introduction to Hadrons 1

1.1 The Standard Model 1

1.2 Quantum Chromodynamics 3

1.3 Hadrons in SU(6) Spin-Flavor Symmetry 5

1.4 Hadron Structure 9

2 Excited Nucleons 11

2.1 Relativized Quark Model of the Baryons 12

2.1.1 Model Details 12

2.1.2 Mass Predictions 14

2.2 Diquark Models 15

2.3 The $^3P_0$ Strong Decay Model 18

2.3.1 Model Details 21

2.3.2 Decay Amplitude Predictions 23

2.3.3 Searching for N^* States 30

2.4 N^* Resonance Extraction 31

3 $\gamma n \to K^{*0}\Lambda$ & $\gamma n \to K^+\Sigma^{*-}$ Overview 38

3.1 $\gamma n \to K^{*0}\Lambda$ Overview 39
3.2 $\gamma n \to K^{+}\Sigma^{*-}$ Overview 45

4 CEBAF, CLAS, and the g13 Experiment 50
4.1 The CEBAF Accelerator 51
4.2 Hall B and the CLAS Detector 52
4.2.1 The Bremsstrahlung Photon Tagger 53
4.2.2 Beamline Detectors 54
4.2.3 The Torus Magnet 56
4.2.4 The Drift Chambers 57
4.2.5 The Time-of-Flight Scintillators 59
4.2.6 The Start Counter 60
4.2.7 The Cherenkov Counters 61
4.2.8 The Electromagnetic Calorimeters 62
4.3 The g13 Experiment 63
4.3.1 g13a: Circularly Polarized Photons 63
4.3.2 g13b: Linearly Polarized Photons 64
4.3.3 Liquid-Deuterium Target 66
4.3.4 Data Acquisition & Event Triggering 66

5 Momentum and Beam Energy Corrections 68
5.1 Standard Corrections 69
5.2 $\gamma D \to pp\pi^{-}$ Reaction Identification 70
5.2.1 Track Identification and Timing Cuts 71
5.2.2 Missing Mass and Missing Momentum Cuts 71
5.3 Additional Momentum Corrections 73
5.3.1 Kinematic Fitting 75
5.3.2 Determination of the Momentum Corrections 77
5.4 Beam Energy Corrections 81
5.5 Test of Additional Corrections 85

6 CLAS Acceptance and Flux Studies **89**

6.1 Monte Carlo Simulations in CLAS 90

6.2 Detector-Based Cuts 91

6.2.1 Data File Selection 93

6.2.2 Beam Trips 102

6.2.3 Tagger Counter Cuts 103

6.2.4 Fiducial Cuts 108

6.2.5 TOF Scintillator Paddle Cuts 114

6.2.6 Drift Chamber Hole Cuts 116

6.3 Trigger Efficiency Study 120

6.3.1 Triggering Efficiency Calculation 120

6.3.2 Trigger Simulation 126

6.4 Photon Flux Determination 126

6.4.1 Calculation of $N_{e^-}^T$ 127

6.4.2 Calculation of ϵ^T 128

6.4.3 Integrated Photon Flux 130

7 The $\gamma n \to p\pi^-$ Validation Reaction **134**

7.1 Experimental Yield 135

7.1.1 Physics Evaluation 136

7.1.2 Initial Cuts 136

7.1.3 Particle Identification 137

7.1.4 Final-State Identification Cuts 140

7.1.5 Yield Extraction 146

7.2 Simulated Detector Acceptance 147

7.3 Yield Correction Factor and Photon Flux 154

7.4 Differential Cross Section 157

8 $\gamma n \to K^{*0}\Lambda$ & $\gamma n \to K^+\Sigma^{*-}$ Analyses **166**

8.1 Experimental $\gamma n \to K^+\pi^-\Lambda$ Event Selection 167

8.1.1 Physics Evaluation 167

8.1.2 Initial Cuts . . . 169
8.1.3 Proton and π^- Identification . . . 170
8.1.4 Selecting Λ Events . . . 173
8.1.5 Final-State Identification Cuts . . . 173
8.2 Experimental Yield Extractions . . . 181
8.2.1 $\gamma n \to K^{*0}\Lambda$ Experimental Yields . . . 182
8.2.2 $\gamma n \to K^+\Sigma^{*-}$ Experimental Yields . . . 188
8.3 Monte Carlo Simulations . . . 193
8.4 Yield Correction Factors and Photon Flux . . . 203

9 $\gamma n \to K^{*0}\Lambda$ & $\gamma n \to K^+\Sigma^{*-}$ Cross Sections 205
9.1 $\gamma n \to K^{*0}\Lambda$ Differential Cross Section . . . 206
9.2 $\gamma n \to K^+\Sigma^{*-}$ Differential Cross Section . . . 211
9.3 Reaction Overlap Studies . . . 219
9.4 Systematic Uncertainty Studies . . . 221
9.4.1 γ & π^0 Background Scale Uncertainties . . . 226
9.4.2 $\gamma n \to K^+\Sigma^{*-}$ CLAS Acceptance Studies . . . 236
9.4.3 $\gamma n \to K^+\Sigma^{*-}$ Final-State Identification Studies . . . 241
9.4.4 $\gamma n \to K^+\Sigma^{*-}$ Yield Extraction Studies . . . 244
9.4.5 $\gamma n \to K^{*0}\Lambda$ Systematic Uncertainty Studies . . . 245
9.5 Summary . . . 252

Bibliography 254

A Momentum Correction Plots 259
A.1 Prior to Kinematic Fitting . . . 259
A.2 Momentum Correction Fits . . . 262
A.3 After Kinematic Fitting . . . 270

B Acceptance Study Plots 273
B.1 Fiducial Cuts . . . 273
B.2 Drift Chamber Hole Cuts . . . 285

C Yield Extraction Signal Fits **291**

C.1 $\gamma n \to p\pi^-$ Fits 291

C.2 $\gamma n \to K^{*0}\Lambda$ Fits 300

C.3 $\gamma n \to K^+\Sigma^{*-}$ Fits 306

D Cross Section Tables **319**

List of Tables

1.1 The masses and electrical charges of the quarks of the Standard Model [8]. 3

1.2 The valence quark content, electrical charges Q, spin-parities J^P, isospins I, isospin projections I_3, and masses of the hadrons featured in this analysis [8]. 8

2.1 Mass predictions for the ground-state baryons containing up, down, or strange quarks in the relativized quark model by Capstick and Isgur [34]. 14

2.2 The mass predictions of the relativized quark model [34] for the experimentally observed N^* spectrum [8]. 17

2.3 The PDG-assigned status of the experimental determination of the N^* states [8]. . . 20

6.1 The separate run ranges of the g13a dataset for which the CLAS detector acceptance was modeled. 90

6.2 Settings for the electron beam energy and current during the g13a experiment between runs 53333 and 53862. 94

6.3 The TOF scintillator paddles rejected for all of g13a. 115

6.4 The TOF scintillator paddles rejected for limited ranges of the g13a dataset. 116

7.1 Summary of the cuts used to extract the experimental yields of the $\gamma n \to p\pi^-$ reaction, in the order that they were performed in this analysis. 135

7.2 The liquid-deuterium target factors used in the differential cross section calculation of Equation 7.6. 158

8.1 Summary of the cuts used to extract the final-state events of the $\gamma n \to K^{*0}\Lambda$ and $\gamma n \to K^+\Sigma^{*-}$ reactions, in the order that they were performed in this analysis. . . . 168

8.2 Summary of the cuts used to extract the experimental yields of the $\gamma n \to K^{*0}\Lambda$ reaction from the $\gamma n \to K^+\pi^-\Lambda$ final-state events, in the order that they were performed in this analysis. 182

8.3 Summary of the cuts used to extract the experimental yields of the $\gamma n \to K^+\Sigma^{*-}$ reaction from the $\gamma n \to K^+\pi^-\Lambda$ final-state events, in the order that they were performed in this analysis. 182

9.1 The branching ratios of the K^{*0}, Λ, and Σ^{*-} to the decay channels that were studied in this analysis [8]. 206

9.2 The average differences between the $\gamma n \to K^{*0}\Lambda$ cross sections with different Σ^{*-} overlap cuts. 220

9.3 The average differences between the $\gamma n \to K^+\Sigma^{*-}$ cross sections with different K^{*0} overlap cuts. 222

9.4 Summary of the systematic uncertainties on the measurement of the $\gamma n \to K^+\Sigma^{*-}$ cross section. 224

9.5 Summary of the systematic uncertainties on the measurement of the $\gamma n \to K^{*0}\Lambda$ cross section. 225

9.6 Results from the studies used to determine the cross section scale uncertainties due to background events containing an additional photon or π^0 in the final state. 230

D.1 Cross section of the $\gamma n \to K^*(892)^0\Lambda$ reaction measured using the 2.655 GeV data from the CLAS g13a experiment. 319

D.2 Cross section of the $\gamma n \to K^+\Sigma^*(1385)^-$ reaction from 1.5 GeV to 1.9 GeV in photon energy, measured using the 2.655 GeV data from the CLAS g13a experiment. 320

D.3 Cross section of the $\gamma n \to K^+\Sigma^*(1385)^-$ reaction from 1.9 GeV to 2.5 GeV in photon energy, measured using the 2.655 GeV data from the CLAS g13a experiment. 321

List of Figures

1.1 The elementary particles of the Standard Model, excluding the Higgs boson [10]. . . 2

1.2 An example of hadronization due to color charge confinement [25]. 5

1.3 The valence quark content of the proton, neutron, and π^+ [30]. 6

1.4 The $n = 0$, $L = 0$, spin-0 pseudoscalar (A) and spin-1 vector (B) meson nonets of the SU(6) quark spin-flavor symmetry group [32]. 7

1.5 The $n = 0$, $L = 0$, spin-$\frac{1}{2}$ baryon octet (A) and spin-$\frac{3}{2}$ baryon decuplet (B) of the SU(6) quark spin-flavor symmetry group [33]. 8

1.6 An inexact portrayal of how the "sea" quarks may contribute to the structure of the proton [36]. 10

1.7 A depiction of how the valence quarks within the proton may be bound together to form a correlated quark-pair, or diquark [37]. 10

2.1 A Feynman diagram depicting quark-quark scattering via virtual gluon exchange. . . 13

2.2 The predicted N^* spectrum for resonances with mass less than 2200 MeV/c^2 in the relativized quark model of the baryons by Capstick and Isgur [34, 42]. 16

2.3 A comparison up to 2000 MeV/c^2 of the masses of the experimentally measured three- and four-star N^* and Δ^* states to those from the diquark model of Santopinto [38]. 19

2.4 $^3P_0$ and flux string-breaking quark-antiquark pair creation models of baryon decays [39]. 21

2.5 Hadrodynamic and elementary meson emission models of baryon decays [39]. 22

2.6 Comparison of the predicted and measured values of $|A_{N\pi}|$, the coupling amplitude between the N^* states and the $N\pi$ channel [39]. 24

2.7 The coupling amplitude predictions of the N^* model states with mass below 2200 MeV/c^2 into the $N\gamma$, $N\pi$, and ΛK channels [40]. 26

2.8 The coupling amplitude predictions of the N^* model states with mass below 2200 MeV/c^2 into the $N\gamma$, $N\pi$, and ΣK channels [40]. 27

2.9 The coupling amplitude predictions of the N^* model states with mass below 2200 MeV/c^2 into the $N\gamma$, $N\pi$, and ΛK^* channels [40]. 28

2.10 The coupling amplitude predictions of the N^* model states with mass below 2200 MeV/c^2 into the $N\gamma$, $N\pi$, and $\Sigma(1385)K$ channels [40]. 29

2.11 The different possible helicity flip combinations for the $\gamma p \rightarrow K^+\Lambda$ reaction [58]. . . 32

2.12 The combinations of beam and target polarizations necessary to measure the polarization observables of the $\gamma N \rightarrow K\Lambda$ reaction [59]. 33

2.13 Definitions of the axes used to define the polarization observables of the $\gamma p \rightarrow K^+\Lambda$ reaction in the center-of-mass frame [60]. 33

2.14 Fits to the beam-recoil polarization observables C_x and C_z of the $\gamma p \rightarrow K^+\Lambda$ reaction from CLAS [60] with and without the $N\frac{3}{2}^+(1900)$ state included in the fits [43]. 35

2.15 Fits to the differential cross sections of the $\gamma p \rightarrow K^+\Lambda$ and $\gamma p \rightarrow K^+\Sigma^0$ reactions from CLAS [70, 71], with and without the $N\frac{3}{2}^+(1900)$ state included in the fits [43]. 36

2.16 Fits to the beam asymmetries of the $\gamma p \rightarrow K^+\Lambda$ and $\gamma p \rightarrow K^+\Sigma^0$ reactions [72], with and without the $N\frac{3}{2}^+(1900)$ state included in the fits [43]. 37

3.1 Depictions of the t-channel, s-channel, and u-channel interactions considered in the model by Oh and Kim for the $\gamma n \rightarrow K^{*0}\Lambda$ reaction [68]. 40

3.2 The predictions and existing experimental data of the total cross sections σ of the $\gamma p \rightarrow K^{*+}\Lambda$ and $\gamma n \rightarrow K^{*0}\Lambda$ reactions as a function of photon energy [68]. 41

3.3 The prediction of the $\gamma n \rightarrow K^{*0}\Lambda$ differential cross section shown in bins of E_γ as a function of $\cos(\theta)$, where θ is the angle between the K^{*0} and the photon in the center-of-mass frame. 42

3.4 Quark flow diagram for the $\gamma n \to K^{*0}\Lambda$ reaction, showing the decays of the K^{*0} and Λ particles into the $p\pi^- K^+\pi^-$ final-state. 44
3.5 Comparison between the LEPS data [74] and model predictions by Oh, Ko, and Nakayama [69] of the differential cross section of the $\gamma n \to K^+\Sigma^{*-}$ reaction. 46
3.6 Depictions of the t-channel, s-channel, u-channel, and contact interactions considered in the model by Oh, Ko, and Nakayama for the $\gamma n \to K^+\Sigma^{*-}$ reaction [69]. 47
3.7 Comparison between the experimental data [75] and the total cross section predictions for the $\gamma p \to K^+\Sigma^{*0}$ reaction as a function of photon energy with and without resonance contributions [69]. 48
3.8 The prediction of the differential cross section of the $\gamma n \to K^+\Sigma^{*-}$ reaction at selected photon energies as a function of $\cos(\theta_{K^+})$, where θ_{K^+} is the angle between the photon and the K^+ in the center-of-mass frame [78]. 48
3.9 Quark flow diagram for the $\gamma n \to K^+\Sigma^{*-}$ reaction, showing the decays of the Σ^{*-} and Λ particles into the $p\pi^- K^+\pi^-$ final-state. 49

4.1 The Jefferson Lab CEBAF Accelerator [80]. 51
4.2 Experimental Hall B and the CLAS detector at Jefferson Lab [83]. 52
4.3 The Hall-B photon tagger [84]. 53
4.4 The CLAS detector, photon tagger, and beamline devices in experimental Hall B at Jefferson Lab [81]. 55
4.5 Cross sections of the CLAS detector along the beamline (A) and perpendicular to the beamline (B) [81]. 57
4.6 CLAS torus magnetic field [81]. 58
4.7 The two superlayers of the Region 3 drift chambers [81]. 59
4.8 The CLAS start counter surrounding the target cell [87]. 61
4.9 Time difference between the RF signal from the accelerator and the T-counters in the tagger, accounting for the electron propagation and cable times [84]. 62
4.10 A diagram of one of the Cherenkov counters spanning a sector in CLAS [81]. 62
4.11 Polarization transfer from longitudinally polarized electrons to circularly polarized photons as a function of E_γ/E_e in bremsstrahlung radiation [88]. 64

4.12 The data and Monte-Carlo-simulated photon energy distributions produced from an electron beam incident on a diamond radiator, after removing the $1/E_\gamma$ bremsstrahlung energy-dependence [89]. 65
4.13 Conical liquid-deuterium target used for the g13 experiment [92]. 66

5.1 For (A) protons and (B) π^-'s, the total momentum correction due to inelastic scattering in the target and various detector materials as a function of momentum. . 69
5.2 The photon energy correction multiplier due to the gravitational sag in the photon tagger as a function of tagger E-channel. 70
5.3 Time difference at the photoproduction vertex between the different particles in the $\gamma D \to pp\pi^-$ reaction. 72
5.4 The missing mass-squared of the $\gamma D \to pp\pi^-$ reaction. 73
5.5 The missing momentum in the direction of the beamline of the $\gamma D \to pp\pi^-$ reaction. 74
5.6 Initial missing energy distribution of the $\gamma D \to pp\pi^-$ reaction for runs 53630 through 53650 of g13a. 75
5.7 The confidence level distribution for the kinematic fit of the reaction $\gamma D \to pp\pi^-$ with the magnitudes of the track momenta treated as unknown. 77
5.8 Pull distributions of the track measurements from the kinematic fit of the reaction $\gamma D \to pp\pi^-$ with the magnitudes of the track momenta treated as unknown for the (A) photon, (B) protons, and (C) π^-. 78
5.9 The average difference between the fit and detected momentum after *eloss* corrections as a function of (A) p, (B) ϕ, and (C) θ for Sector 1 of CLAS for the proton and π^-. 80
5.10 The fit to the mean $\Delta(1/p)$ vs. $1/p$ for the 10 ϕ-bins in Sector 1 for the (A) protons and the (B) π^-. 82
5.11 The mean Δp vs. p distributions for the (A) proton and (B) π^- in Sector 1 of CLAS, updated with the ϕ-dependent corrections. 83
5.12 The fit to the mean $\Delta(1/p)$ as a function of θ in Sector 1 of CLAS for the (A) proton and (B) π^-. 83

5.13 The average difference between the fit and detected momentum after all momentum corrections as a function of (A) p, (B) ϕ, and (C) θ for Sector 1 of CLAS for the proton and π^-. 84

5.14 The calculated multiplicative energy correction factors to the photon energies as a function of run number for both the 1.990 GeV data (A) and the 2.655 GeV data (B). 86

5.15 The missing mass of the spectator proton in $\gamma n \to p\pi^-$ before (A) and after (B) the additional momentum and beam energy corrections. 88

6.1 The experimental difference between the photon time from the tagger and the electron RF beam bunch time. 92

6.2 Gaussian fits to the missing mass of the spectator proton in the $\gamma D \to p\pi^-(p)$ reaction from experiment (A) and simulation (B). 92

6.3 Gaussian fits to the time difference between the photon and the π^- in the $\gamma n \to p\pi^-$ reaction from experiment (A) and from simulation (B). 93

6.4 The rate of proton (A), π^+ (B), and π^- (C) track reconstruction for the run range of g13a used in this analysis. 95

6.5 The percentage of the average reconstruction rate of the protons (A), π^+'s (B), and π^-'s (C) in the six sectors of CLAS for the files in the 1.990 GeV, 40 nA data of g13a. 96

6.6 The percentage of the average reconstruction rate of the protons (A), π^+'s (B), and π^-'s (C) in the six sectors of CLAS for the files in the 1.990 GeV, 45 nA data of g13a. 97

6.7 The percentage of the average reconstruction rate of the protons (A), π^+'s (B), and π^-'s (C) in the six sectors of CLAS for the files in the 2.655 GeV, 40 nA data of g13a. 98

6.8 The percentage of the average reconstruction rate of the protons (A), π^+'s (B), and π^-'s (C) in the six sectors of CLAS for the files in the 2.655 GeV, 35 nA data of g13a. 99

6.9 The percentage of the average reconstruction rate of the protons (A), π^+'s (B), and π^-'s (C) in the six sectors of CLAS for the files in the 2.655 GeV, 33 nA data of g13a. 100

6.10 The percentage of the average reconstruction rate of the protons (A), π^+'s (B), and π^-'s (C) in the six sectors of CLAS for the files in the 2.655 GeV, 37 nA data of g13a. 101

6.11 Photon flux vs. first-hit T-counter (A) and E-bin (B) for a portion of the g13a experiment. 104

6.12 The number of charged particles corresponding to photons in the first-hit T-counters (A) and E-bins (B) for a portion of the g13a experiment. 106
6.13 Flux-normalized yields of charged particles vs. first-hit T-counter (A) and E-bin (B) for a portion of the g13a experiment. 107
6.14 Log-scale distributions of reconstructed pions in all sectors of CLAS as a function of θ and sector-normalized-ϕ with -40 cm < vertex-z < -30 cm. 110
6.15 For π^-'s with -40 cm < vertex-z < -30 cm and momentum < 400 MeV/c, the distribution of reconstructed tracks for all sectors in bins of θ as a function of sector-normalized-ϕ. 111
6.16 For π^+'s with -40 cm < vertex-z < -30 cm and momentum < 400 MeV/c, the distribution of reconstructed tracks for all sectors in bins of θ as a function of sector-normalized-ϕ. 112
6.17 The fit to the front edges of the fiducial cut functions for positively charged tracks as a function of momentum. 113
6.18 The difference between the measured and calculated times of the π^- in different scintillator paddles. 115
6.19 Track distributions of the protons (A) and π^-'s (B) in different vertex-z bins in Sector 3. 117
6.20 Track distributions of protons with -40 cm < vertex-z < -30 cm in the different sectors of CLAS. 118
6.21 Track distributions of π^-'s with -40 cm < vertex-z < -30 cm in the different sectors of CLAS. 119
6.22 The triggering efficiencies of protons as a function of sector-normalized-ϕ and SC paddle for each of the sectors of CLAS. 122
6.23 The proton triggering efficiencies as a function of momentum and SC paddle in one of the center bins of sector-normalized-ϕ for each of the sectors of CLAS. 123
6.24 The triggering efficiencies of π^-'s as a function of sector-normalized-ϕ and SC paddle. 124
6.25 The π^- triggering efficiencies as a function of momentum and SC paddle in one of the center bins of sector-normalized-ϕ for each of the sectors of CLAS. 125

6.26 The spectrum of photon times at the center of the target corresponding to "good" electron hits in one of the first-hit tagger T-counters [104]. 129
6.27 The calculated tagging ratios for the normalization runs of g13a. 131
6.28 Map showing the first-hit T-counter and E-bin matching of the tagger for g13a. . . . 132
6.29 The integrated photon flux of the 1.990 GeV (A) and 2.655 GeV (B) data files in this analysis. 133

7.1 For proton candidates, $\Delta\beta$ vs. p (A), and fits to the minimum (B) and maximum (C) $\Delta\beta$ cuts as a function of track momentum. 138
7.2 For π^- candidates, $\Delta\beta$ vs. p (A), and fits to the minimum (B) and maximum (C) $\Delta\beta$ cuts as a function of track momentum. 139
7.3 The vertex time difference between the proton and π^- as a function of proton momentum (A), and fits to the minimum (B) and maximum (C) time difference cuts as a function of proton momentum. 142
7.4 The vertex time difference between all of the detected photons and the π^- as a function of π^- momentum (A), and fits to the minimum (B) and maximum (C) time difference cuts as a function of π^- momentum. 143
7.5 The number of photons per event after 3σ cuts on $\Delta t_{\gamma,\pi^-}$. 144
7.6 The missing momentum of the spectator proton (A) shown vs. $\cos(\theta)$ of the missing momentum in the lab frame (B). 145
7.7 The distribution of the $\gamma n \to p\pi^-$ final-state events from several runs of the g13a experiment as a function of photon energy and $\cos(\theta_{\pi^-})$. 146
7.8 Fits to the missing mass of the spectator proton in the experimental data of the $\gamma D \to p\pi^-(p)$ reaction in the -0.04 $< \cos(\theta_{\pi^-}) <$ 0.04 bins. 148
7.9 The distribution of the generated Monte Carlo events of the $\gamma n \to p\pi^-$ reaction after running *gpp* as a function of photon energy and $\cos(\theta_{\pi^-})$. 149
7.10 The distribution of the reconstructed final-state Monte Carlo events of the $\gamma n \to p\pi^-$ reaction as a function of photon energy and $\cos(\theta_{\pi^-})$. 151
7.11 Fits to the missing mass of the spectator proton in the simulated data of the $\gamma D \to p\pi^-(p)$ reaction in the -0.04 $< \cos(\theta_{\pi^-}) <$ 0.04 bins. 152

7.12 Comparison between the experimental and simulated yields of the $\gamma n \to p\pi^-$ reaction in different photon energy bins as a function of $\cos(\theta_{\pi^-})$. 153
7.13 The calculated CLAS acceptance of the $\gamma n \to p\pi^-$ reaction in different photon energy bins as a function of $\cos(\theta_{\pi^-})$. 155
7.14 The missing mass of the $\gamma D \to p\pi^-(p)$ reaction for all photons, using inverse photon timing cuts and with the cut on the number of photons removed. 156
7.15 The integrated photon flux from runs 53850 through 53859, excluding run 53853, in the photon energy bins used in the cross section calculation. 158
7.16 The $\gamma n \to p\pi^-$ differential cross sections from the g13 experiment as a function of $\cos(\theta_{\pi^-})$, compared against the published results from the CLAS g10 experiment where available. 160
7.17 Comparison of the cross sections of the $\gamma n \to p\pi^-$ reaction for the different sectors in which the π^- was detected. 162
7.18 Systematic uncertainty percentages of the comparison of the differential cross section of the $\gamma n \to p\pi^-$ reaction for the different π^- sectors. 163
7.19 Systematic uncertainty percentages of the comparison of the differential cross section of the $\gamma n \to p\pi^-$ reaction for the different π^- sectors as a function of photon energy. 164
7.20 The comparison between the differential cross sections of the $\gamma n \to p\pi^-$ reaction calculated with and without the trigger simulation. 165

8.1 For proton candidates, $\Delta\beta$ vs. p (A), and fits to the minimum (B) and maximum (C) $\Delta\beta$ cuts as a function of track momentum. 171
8.2 For π^- candidates, $\Delta\beta$ vs. p (A), and fits to the minimum (B) and maximum (C) $\Delta\beta$ cuts as a function of track momentum. 172
8.3 The time difference between the proton and π^- at the Λ decay vertex as a function of proton momentum (A), and fits to the minimum (B) and maximum (C) time difference cuts as a function of proton momentum. 174
8.4 The $p\pi^-$ invariant mass fit to a Gaussian plus a linear function to select Λ events. . 175
8.5 The reaction vertex time difference between all of the detected photons and the π^- as a function of π^- momentum (A), and fits to the minimum (B) and maximum (C) time difference cuts as a function of π^- momentum. 176

8.6 For K^+ candidates, $\Delta\beta$ vs. p (A), and fits to the minimum (B) and maximum (C) $\Delta\beta$ cuts as a function of track momentum. 177

8.7 The reaction vertex time difference between the K^+ and π^- as a function of K^+ momentum (A), and fits to the minimum (B) and maximum (C) time difference cuts as a function of K^+ momentum. 178

8.8 The number of photons per event after $\pm 3\sigma$ cuts on the vertex time differences. . . . 179

8.9 The missing momentum of the spectator proton (A) shown vs. $\cos(\theta)$ of the missing momentum in the lab frame (B). 180

8.10 The invariant mass of $\pi^+\pi^-$, where the K^+ was assigned the π^+ mass. 181

8.11 The overlap of the invariant masses of the $K^{*0} \to K^+\pi^-$ and $\Sigma^{*-} \to \Lambda\pi^-$ decays in the photon energy bins used for yield extraction. 183

8.12 The distribution of the $\gamma n \to K^+\pi^-\Lambda$ final-state events from the 2.655 GeV data of the g13a experiment as a function of photon energy and $\cos(\theta_{K^{*0}})$. 184

8.13 Fits to the missing mass of the spectator proton of the $\gamma D \to K^+\pi^-\Lambda(p)$ reaction for the extraction of the $\gamma n \to K^{*0}\Lambda$ experimental yields. 185

8.14 Fits to the invariant mass of the Σ^{*-} in one $\cos(\theta_{K^{*0}})$ bin for each photon energy bin. 186

8.15 Fits to the invariant mass of the K^{*0} in one $\cos(\theta_{K^{*0}})$ bin for each photon energy bin. 187

8.16 The distribution of the $\gamma n \to K^+\pi^-\Lambda$ final-state events from the 2.655 GeV data of the g13a experiment as a function of photon energy and $\cos(\theta_{K^+})$. 188

8.17 Fits to the missing mass of the spectator proton of the $\gamma D \to K^+\pi^-\Lambda(p)$ reaction for the extraction of the $\gamma n \to K^+\Sigma^{*-}$ experimental yields. 190

8.18 The distribution of the $\gamma n \to K^+\pi^-\Lambda$ final-state events from the 2.655 GeV data of the g13a experiment as a function of photon energy and $\cos(\theta_{K^+})$. 191

8.19 Fits to the invariant mass of the Σ^{*-} in one merged $\cos(\theta_{K^+})$ bin of each photon energy bin above 1.9 GeV. 192

8.20 Fits to the invariant mass of the K^{*0} in one merged $\cos(\theta_{K^+})$ bin of each photon energy bin above 1.9 GeV. 193

8.21 Fits to the invariant mass of the Σ^{*-} in one $\cos(\theta_{K^+})$ bin for each photon energy bin. 194

8.22 The distributions of the generated Monte Carlo events of the $\gamma n \to K^{*0}\Lambda$ (A) and $\gamma n \to K^+\Sigma^{*-}$ (B) reactions after running *gpp*. 196

8.23 The missing mass of $\gamma D \to K^+\pi^-\Lambda(p)$ in the g13a experiment (A), $\gamma n \to K^{*0}\Lambda$ simulation (B), and $\gamma n \to K^+\Sigma^{*-}$ simulation (C). 197

8.24 The distributions of the reconstructed $\gamma n \to K^+\pi^-\Lambda$ final-state simulation events of the $\gamma n \to K^{*0}\Lambda$ (A) and $\gamma n \to K^+\Sigma^{*-}$ (B) reactions as a function of photon energy and $\cos(\theta)$ 198

8.25 Breit-Wigner fits to the simulated invariant mass distributions of the K^{*0} in one representative $\cos(\theta_{K^{*0}})$ bin for each photon energy bin. 199

8.26 Breit-Wigner fits to the simulated invariant mass distributions of the Σ^{*-} in one representative $\cos(\theta_{K^+})$ bin for each photon energy bin. 200

8.27 Comparison between the experimental and simulated yields of the $\gamma n \to K^{*0}\Lambda$ reaction in the different photon energy bins as a function of $\cos(\theta_{K^{*0}})$. 201

8.28 Comparison between the experimental and simulated yields of the $\gamma n \to K^+\Sigma^{*-}$ reaction in the different photon energy bins as a function of $\cos(\theta_{K^+})$. 201

8.29 The calculated CLAS acceptance of the $\gamma n \to K^{*0}\Lambda$ reaction in different photon energy bins as a function of $\cos(\theta_{K^{*0}})$. 202

8.30 The calculated CLAS acceptance of the $\gamma n \to K^+\Sigma^{*-}$ reaction in different photon energy bins as a function of $\cos(\theta_{K^+})$. 202

8.31 The integrated photon flux from the 2.655 GeV data in the photon energy bins used in the $\gamma n \to K^{*0}\Lambda$ and $\gamma n \to K^+\Sigma^{*-}$ cross section calculations. 204

9.1 The $\gamma n \to K^{*0}\Lambda$ differential cross section from the g13 experiment in different photon energy bins as a function of $\cos(\theta_{K^{*0}})$. 207

9.2 The statistical (A), systematic (B), and total (C) uncertainties of the $\gamma n \to K^{*0}\Lambda$ differential cross section from the g13 experiment. 209

9.3 A comparison of the g13 $\gamma n \to K^{*0}\Lambda$ cross section results with the published $\gamma p \to K^+\Lambda$ cross section data from the CLAS g11 experiment [118]. 210

9.4 The $\gamma n \to K^+\Sigma^{*-}$ differential cross section from the g13 experiment in different photon energy bins as a function of $\cos(\theta_{K^+})$. 213

9.5 The statistical (A) and systematic (B) uncertainties of the $\gamma n \to K^+\Sigma^{*-}$ differential cross section from the g13 experiment. 214

9.6 The total uncertainties of the $\gamma n \to K^+\Sigma^{*-}$ differential cross section from the g13 experiment. 215

9.7 A comparison of the g13 and LEPS [74] $\gamma n \to K^+\Sigma^{*-}$ cross section results with the published $\gamma n \to K^+\Sigma^-$ cross section data from the CLAS g10 experiment [121]. . . 218

9.8 Comparison of the $\gamma n \to K^+\Sigma^{*-}$ cross sections from the different portions of the g13a dataset. 219

9.9 Comparison between the $\gamma n \to K^{*0}\Lambda$ cross sections calculated with different Σ^{*-} overlap cuts. 220

9.10 Comparison between the $\gamma n \to K^+\Sigma^{*-}$ cross sections calculated with different K^{*0} overlap cuts. 222

9.11 Fits to the invariant mass of the K^{*0} in the high-mass sidebands of the $\gamma D \to K^+\pi^-\Lambda(p)$ missing mass distributions for each photon energy bin of the $\gamma n \to K^{*0}\Lambda$ analysis. 228

9.12 Fits to the invariant mass of the Σ^{*-} in the high-mass sidebands of the $\gamma D \to K^+\pi^-\Lambda(p)$ missing mass distributions for each photon energy bin of the $\gamma n \to K^+\Sigma^{*-}$ analysis. 229

9.13 Fits to the invariant mass of the K^{*0} in the high-mass sidebands of the simulated $\gamma D \to K^+\pi^-\Lambda(p)$ missing mass distributions for each photon energy bin of the $\gamma n \to K^{*0}\Lambda$ analysis. 231

9.14 Fits to the invariant mass of the Σ^{*-} in the high-mass sidebands of the simulated $\gamma D \to K^+\pi^-\Lambda(p)$ missing mass distributions for each photon energy bin of the $\gamma n \to K^+\Sigma^{*-}$ analysis. 232

9.15 Fits to the $\gamma D \to K^+\pi^-\Lambda(p)$ missing mass distributions of the $\gamma n \to K^{*0}\Lambda$ analysis to determine the ratios of the backgrounds in the signal and sideband regions. . . . 234

9.16 Fits to the $\gamma D \to K^+\pi^-\Lambda(p)$ missing mass distributions of the $\gamma n \to K^+\Sigma^{*-}$ analysis to determine the ratios of the backgrounds in the signal and sideband regions. 235

9.17 The systematic uncertainty percentages on the $\gamma n \to K^+\Sigma^{*-}$ cross section from changing the π^- minimum momentum cut from 100 MeV/c to 150 MeV/c. 237

9.18 The systematic uncertainty percentages on the $\gamma n \to K^+\Sigma^{*-}$ cross section from simultaneously changing the proton and K^+ minimum momentum cuts from 400 MeV/c to 450 MeV/c. 237

9.19 The systematic uncertainty percentages on the $\gamma n \to K^+\Sigma^{*-}$ cross section from tightening the fiducial cuts by 0.02 radians on all sides. 238

9.20 The systematic uncertainty percentages on the $\gamma n \to K^+\Sigma^{*-}$ cross section from the triggering efficiencies. 239

9.21 For the $\gamma n \to K^+\Sigma^{*-}$ reaction, a comparison of the experimental yields to those from the different simulation distributions. 240

9.22 The systematic uncertainty percentages on the $\gamma n \to K^+\Sigma^{*-}$ cross section from the simulation distribution used for calculating the CLAS acceptance. 241

9.23 The systematic uncertainty percentages on the $\gamma n \to K^+\Sigma^{*-}$ cross section from simultaneously tightening the proton, π^-, and K^+ particle identification cuts from $\pm 3\sigma$ to $\pm 2\sigma$. 242

9.24 The systematic uncertainty percentages on the $\gamma n \to K^+\Sigma^{*-}$ cross section from simultaneously tightening the $\Delta t_{p,\pi^-}$, $\Delta t_{\gamma,\pi^-}$, $\Delta t_{K^+,\pi^-}$ timing cuts from $\pm 3\sigma$ to $\pm 2\sigma$. 242

9.25 The systematic uncertainty percentages on the $\gamma n \to K^+\Sigma^{*-}$ cross section from tightening the Λ invariant mass cut from $\pm 3\sigma$ to $\pm 2\sigma$. 243

9.26 The systematic uncertainty percentages on the $\gamma n \to K^+\Sigma^{*-}$ cross section from changing the missing minimum cut from 200 MeV/c to 150 MeV/c. 243

9.27 The systematic uncertainty percentages on the $\gamma n \to K^+\Sigma^{*-}$ cross section from tightening the spectator proton missing mass cut from $\pm 3\sigma$ to $\pm 2\sigma$. 244

9.28 The systematic uncertainty percentages on the $\gamma n \to K^+\Sigma^{*-}$ cross section from changing the K^{*0} invariant mass overlap cuts from $\pm 1\Gamma$ to $\pm 2\Gamma$. 245

9.29 Fits to the invariant mass of the Σ^{*-} for the study of the systematic uncertainties of the background fits. 246

9.30 The systematic uncertainty percentages on the $\gamma n \to K^+\Sigma^{*-}$ cross section from the Σ^{*-} background fits. 247

9.31 The systematic uncertainty percentages on the $\gamma n \to K^+\Sigma^{*-}$ cross section from tightening the Σ^{*-} invariant mass cuts from $\pm 2\Gamma$ to $\pm 1\Gamma$. 247

9.32 For the $\gamma n \to K^{*0}\Lambda$ reaction, a comparison of the experimental yields to those from the different simulation distributions. 248

9.33 The systematic uncertainty percentages on the $\gamma n \to K^{*0}\Lambda$ cross section from the simulation distribution used for calculating the CLAS acceptance. 249

9.34 The systematic uncertainty percentages on the $\gamma n \to K^{*0}\Lambda$ cross section from changing the Σ^{*-} invariant mass overlap cuts from $\pm 1\Gamma$ to $\pm 1.5\Gamma$. 249

9.35 Fits to the invariant mass of the K^{*0} for the study of the systematic uncertainties of the background fits. 250

9.36 The systematic uncertainty percentages on the $\gamma n \to K^{*0}\Lambda$ cross section from changing the K^{*0} background fits from quadratic to linear functions. 251

9.37 The systematic uncertainty percentages on the $\gamma n \to K^{*0}\Lambda$ cross section from tightening the K^{*0} invariant mass cuts from $\pm 2\Gamma$ to $\pm 1\Gamma$. 251

A.1 The average difference between the fit and detected momentum after *eloss* corrections as a function of p in the six sectors of CLAS for the (A) proton and (B) π^-.259

A.2 The average difference between the fit and detected momentum after *eloss* corrections as a function of the sector-normalized ϕ in the six sectors of CLAS for the (A) proton and (B) π^-. 260

A.3 The average difference between the fit and detected momentum after *eloss* corrections as a function of θ in the six sectors of CLAS for the (A) proton and (B) π^-.261

A.4 The fit to the mean $\Delta(1/p)$ vs. $1/p$ for the 10 ϕ bins in Sector 1 for the (A) protons and the (B) π^-. 262

A.5 The fit to the mean $\Delta(1/p)$ vs. $1/p$ for the 10 ϕ bins in Sector 2 for the (A) protons and the (B) π^-. 263

A.6 The fit to the mean $\Delta(1/p)$ vs. $1/p$ for the 10 ϕ bins in Sector 3 for the (A) protons and the (B) π^-. 264

A.7 The fit to the mean $\Delta(1/p)$ vs. $1/p$ for the 10 ϕ bins in Sector 4 for the (A) protons and the (B) π^-. 265

A.8 The fit to the mean $\Delta(1/p)$ vs. $1/p$ for the 10 ϕ bins in Sector 5 for the (A) protons and the (B) π^-. 266

A.9 The fit to the mean $\Delta(1/p)$ vs. $1/p$ for the 10 ϕ bins in Sector 6 for the (A) protons and the (B) π^-. 267

A.10 The mean Δp vs. p, updated with the ϕ-dependent corrections, in the six sectors of CLAS for the (A) proton and (B) π^-. 268

A.11 The fit to the mean $\Delta(1/p)$ in $(\mathrm{GeV/c})^{-1}$ as a function of θ in the six sectors of CLAS for the (A) proton and (B) π^-. 269

A.12 The average difference between the fit and corrected momentum as a function of p in the six sectors of CLAS for the (A) proton and (B) π^-. 270

A.13 The average difference between the fit and corrected momentum as a function of the sector-normalized ϕ in the six sectors of CLAS for the (A) proton and (B) π^-. . . . 271

A.14 The average difference between the fit and corrected momentum as a function of θ in the six sectors of CLAS for the (A) proton and (B) π^-. 272

B.1 Log-scale distributions of reconstructed π^-'s in all sectors of CLAS as a function of θ and sector-normalized-ϕ. The two columns represent the vertex-z bins from -40 cm to -30 cm and from -30 cm to -20 cm. 273

B.2 Log-scale distributions of reconstructed π^-'s in all sectors of CLAS as a function of θ and sector-normalized-ϕ. The two columns represent the vertex-z bins from -20 cm to -10 cm and from -10 cm to 0 cm. 274

B.3 Log-scale distributions of reconstructed π^+'s in all sectors of CLAS as a function of θ and sector-normalized-ϕ. The two columns represent the vertex-z bins from -40 cm to -30 cm and from -30 cm to -20 cm. 275

B.4 Log-scale distributions of reconstructed π^+'s in all sectors of CLAS as a function of θ and sector-normalized-ϕ. The two columns represent the vertex-z bins from -20 cm to -10 cm and from -10 cm to 0 cm. 276

B.5 For π^-'s with -40 cm $<$ vertex-z $<$ -30 cm and momentum $<$ 400 MeV/c, the distribution of reconstructed tracks for all sectors in bins of θ as a function of sector-normalized-ϕ. 277

B.6 For π^-'s with -30 cm < vertex-z < -20 cm and momentum < 400 MeV/c, the distribution of reconstructed tracks for all sectors in bins of θ as a function of sector-normalized-ϕ. 278

B.7 For π^-'s with -20 cm < vertex-z < -10 cm and momentum < 400 MeV/c, the distribution of reconstructed tracks for all sectors in bins of θ as a function of sector-normalized-ϕ. 279

B.8 For π^-'s with -10 cm < vertex-z < 0 cm and momentum < 400 MeV/c, the distribution of reconstructed tracks for all sectors in bins of θ as a function of sector-normalized-ϕ. 280

B.9 For π^+'s with -40 cm < vertex-z < -30 cm and momentum < 400 MeV/c, the distribution of reconstructed tracks for all sectors in bins of θ as a function of sector-normalized-ϕ. 281

B.10 For π^+'s with -30 cm < vertex-z < -20 cm and momentum < 400 MeV/c, the distribution of reconstructed tracks for all sectors in bins of θ as a function of sector-normalized-ϕ. 282

B.11 For π^+'s with -20 cm < vertex-z < -10 cm and momentum < 400 MeV/c, the distribution of reconstructed tracks for all sectors in bins of θ as a function of sector-normalized-ϕ. 283

B.12 For π^+'s with -10 cm < vertex-z < 0 cm and momentum < 400 MeV/c, the distribution of reconstructed tracks for all sectors in bins of θ as a function of sector-normalized-ϕ. 284

B.13 Track distributions of the protons (A) and π^-'s (B) in different vertex-z bins in Sector 1. 285

B.14 Track distributions of the protons (A) and π^-'s (B) in different vertex-z bins in Sector 2. 286

B.15 Track distributions of the protons (A) and π^-'s (B) in different vertex-z bins in Sector 3. 287

B.16 Track distributions of the protons (A) and π^-'s (B) in different vertex-z bins in Sector 4. 288

B.17 Track distributions of the protons (A) and π^-'s (B) in different vertex-z bins in Sector 5. 289

B.18 Track distributions of the protons (A) and π^-'s (B) in different vertex-z bins in Sector 6. 290

C.1 Fits to the missing mass of the spectator proton in the experimental data of the $\gamma D \to p\pi^-(p)$ reaction in the 0.6 GeV $< E_\gamma <$ 0.8 GeV bin. 291

C.2 Fits to the missing mass of the spectator proton in the experimental data of the $\gamma D \to p\pi^-(p)$ reaction in the 0.8 GeV $< E_\gamma <$ 1.0 GeV bin. 292

C.3 Fits to the missing mass of the spectator proton in the experimental data of the $\gamma D \to p\pi^-(p)$ reaction in the 1.0 GeV $< E_\gamma <$ 1.2 GeV bin. 293

C.4 Fits to the missing mass of the spectator proton in the experimental data of the $\gamma D \to p\pi^-(p)$ reaction in the 1.2 GeV $< E_\gamma <$ 1.4 GeV bin. 294

C.5 Fits to the missing mass of the spectator proton in the experimental data of the $\gamma D \to p\pi^-(p)$ reaction in the 1.4 GeV $< E_\gamma <$ 1.6 GeV bin. 295

C.6 Fits to the missing mass of the spectator proton in the experimental data of the $\gamma D \to p\pi^-(p)$ reaction in the 1.6 GeV $< E_\gamma <$ 1.8 GeV bin. 296

C.7 Fits to the missing mass of the spectator proton in the experimental data of the $\gamma D \to p\pi^-(p)$ reaction in the 1.8 GeV $< E_\gamma <$ 2.0 GeV bin. 297

C.8 Fits to the missing mass of the spectator proton in the experimental data of the $\gamma D \to p\pi^-(p)$ reaction in the 2.0 GeV $< E_\gamma <$ 2.2 GeV bin. 298

C.9 Fits to the missing mass of the spectator proton in the experimental data of the $\gamma D \to p\pi^-(p)$ reaction in the 2.2 GeV $< E_\gamma <$ 2.4 GeV bin. 299

C.10 Fits to the missing mass of the spectator proton of the $\gamma D \to K^+\pi^-\Lambda(p)$ reaction for the $\gamma n \to K^{*0}\Lambda$ analysis in the 1.9 GeV to 2.1 GeV photon energy bin. 300

C.11 Fits to the missing mass of the spectator proton of the $\gamma D \to K^+\pi^-\Lambda(p)$ reaction for the $\gamma n \to K^{*0}\Lambda$ analysis in the 2.1 GeV to 2.3 GeV photon energy bin. 300

C.12 Fits to the missing mass of the spectator proton of the $\gamma D \to K^+\pi^-\Lambda(p)$ reaction for the $\gamma n \to K^{*0}\Lambda$ analysis in the 2.3 GeV to 2.5 GeV photon energy bin. 301

C.13 Fits to the invariant mass of the Σ^{*-} for the $\gamma n \to K^{*0}\Lambda$ analysis in the 1.9 GeV to 2.1 GeV photon energy bin. 302

C.14 Fits to the invariant mass of the Σ^{*-} for the $\gamma n \to K^{*0}\Lambda$ analysis in the 2.1 GeV to 2.3 GeV photon energy bin. 302

C.15 Fits to the invariant mass of the Σ^{*-} for the $\gamma n \to K^{*0}\Lambda$ analysis in the 2.3 GeV to 2.5 GeV photon energy bin. 303

C.16 Fits to the invariant mass of the K^{*0} for the $\gamma n \to K^{*0}\Lambda$ analysis in the 1.9 GeV to 2.1 GeV photon energy bin. 304

C.17 Fits to the invariant mass of the K^{*0} for the $\gamma n \to K^{*0}\Lambda$ analysis in the 2.1 GeV to 2.3 GeV photon energy bin. 304

C.18 Fits to the invariant mass of the K^{*0} for the $\gamma n \to K^{*0}\Lambda$ analysis in the 2.3 GeV to 2.5 GeV photon energy bin. 305

C.19 Fits to the missing mass of the spectator proton of the $\gamma D \to K^+\pi^-\Lambda(p)$ reaction for the $\gamma n \to K^+\Sigma^{*-}$ analysis in the 1.5 GeV to 1.7 GeV photon energy bin. 306

C.20 Fits to the missing mass of the spectator proton of the $\gamma D \to K^+\pi^-\Lambda(p)$ reaction for the $\gamma n \to K^+\Sigma^{*-}$ analysis in the 1.7 GeV to 1.9 GeV photon energy bin. 307

C.21 Fits to the missing mass of the spectator proton of the $\gamma D \to K^+\pi^-\Lambda(p)$ reaction for the $\gamma n \to K^+\Sigma^{*-}$ analysis in the 1.9 GeV to 2.1 GeV photon energy bin. 308

C.22 Fits to the missing mass of the spectator proton of the $\gamma D \to K^+\pi^-\Lambda(p)$ reaction for the $\gamma n \to K^+\Sigma^{*-}$ analysis in the 2.1 GeV to 2.3 GeV photon energy bin. 309

C.23 Fits to the missing mass of the spectator proton of the $\gamma D \to K^+\pi^-\Lambda(p)$ reaction for the $\gamma n \to K^+\Sigma^{*-}$ analysis in the 2.3 GeV to 2.5 GeV photon energy bin. 310

C.24 Fits to the invariant mass of the Σ^{*-} for the $\gamma n \to K^+\Sigma^{*-}$ analysis in the 1.9 GeV to 2.1 GeV photon energy bin. 311

C.25 Fits to the invariant mass of the Σ^{*-} for the $\gamma n \to K^+\Sigma^{*-}$ analysis in the 2.1 GeV to 2.3 GeV photon energy bin. 311

C.26 Fits to the invariant mass of the Σ^{*-} for the $\gamma n \to K^+\Sigma^{*-}$ analysis in the 2.3 GeV to 2.5 GeV photon energy bin. 312

C.27 Fits to the invariant mass of the K^{*0} for the $\gamma n \to K^+\Sigma^{*-}$ analysis in the 1.9 GeV to 2.1 GeV photon energy bin. 312

C.28 Fits to the invariant mass of the K^{*0} for the $\gamma n \to K^+\Sigma^{*-}$ analysis in the 2.1 GeV to 2.3 GeV photon energy bin. 313

C.29 Fits to the invariant mass of the K^{*0} for the $\gamma n \to K^+\Sigma^{*-}$ analysis in the 2.3 GeV to 2.5 GeV photon energy bin. 313

C.30 Fits to the invariant mass of the Σ^{*-} for the $\gamma n \to K^+\Sigma^{*-}$ analysis in the 1.5 GeV to 1.7 GeV photon energy bin. 314

C.31 Fits to the invariant mass of the Σ^{*-} for the $\gamma n \to K^+\Sigma^{*-}$ analysis in the 1.7 GeV to 1.9 GeV photon energy bin. 315

C.32 Fits to the invariant mass of the Σ^{*-} for the $\gamma n \to K^+\Sigma^{*-}$ analysis in the 1.9 GeV to 2.1 GeV photon energy bin. 316

C.33 Fits to the invariant mass of the Σ^{*-} for the $\gamma n \to K^+\Sigma^{*-}$ analysis in the 2.1 GeV to 2.3 GeV photon energy bin. 317

C.34 Fits to the invariant mass of the Σ^{*-} for the $\gamma n \to K^+\Sigma^{*-}$ analysis in the 2.3 GeV to 2.5 GeV photon energy bin. 318

Chapter 1

Introduction to Hadrons

The goals of nuclear and particle physics are to identify the fundamental particles and forces of the universe, and to determine the structure of matter. The Standard Model of particle physics [1] includes a description of many of these phenomena, but a quantum theory of gravity has yet to be discovered. However the Standard Model has had much success, including the development of Quantum Electrodynamics (QED) and Quantum Chromodynamics (QCD) [2], as well as the unification of the electromagnetic and weak nuclear forces.

QCD is a theory describing the interactions of the strong nuclear force, and is an integral component of the Standard Model. It explains how quarks are bound together by gluons to form hadrons, such as the proton and neutron. Many of the particles predicted from QCD-inspired models have been observed, but many of the excited states of the hadrons are still "missing." While observation of these excited states is difficult, this problem of the "missing" resonances may be due to correlations between the quarks within these particles. The determination of these excited state spectra will help determine the relevant degrees of freedom within the hadrons.

1.1 The Standard Model

While not complete, the Standard Model of particle physics provides a useful description of the elementary particles of the universe and their interactions [1]. It encompasses the electromagnetic force, the weak nuclear force, and the strong nuclear force, but does not include the gravitational force. A small extension to the Standard Model can be made to account for neutrino oscillations

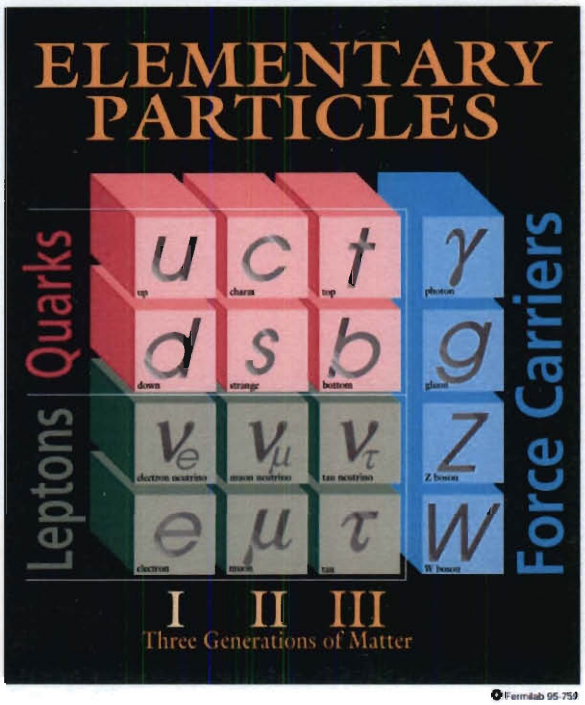

Figure 1.1 : The elementary particles of the Standard Model, excluding the Higgs boson [10]. The Higgs boson is the only elementary particle predicted by the Standard Model that has not yet been observed.

[3, 4, 5, 6, 7]. However, the Standard Model does not include the predicted dark matter and dark energy from the observed rotational velocities of the galaxies, gravitational lensing, and the rate of expansion of the universe [8]. Also, the Standard Model does not account for the matter-antimatter asymmetry of the universe [9], nor does it predict the masses of any of the fundamental particles. Despite these limitations the Standard Model successfully describes a broad range of physical phenomena, as introduced below.

The elementary particles of the Standard Model are shown in Figure 1.1, excluding the Higgs boson. They consist of six flavors, or types, of spin-$\frac{1}{2}$ quarks, six different spin-$\frac{1}{2}$ leptons, four types of spin-1 bosons, and the spin-0 Higgs boson. Each of the quarks and leptons has an antiparticle with opposite charge, although it has been theorized that neutrinos may be their own antiparticles [11]. The charges and masses of the six flavors of quarks are detailed in Table 1.1. The characteristics of the other elementary particles of the Standard Model are discussed in Reference [8].

The massless photon is the force carrier of the electromagnetic force, which is described by QED. This force characterizes the electromagnetic interaction between charged particles as the exchange

Quark	Electrical Charge (e)	Mass
u	$\frac{2}{3}$	1.5 to 3.0 MeV/c^2
d	$-\frac{1}{3}$	3 to 7 MeV/c^2
s	$-\frac{1}{3}$	95 ± 25 MeV/c^2
c	$\frac{2}{3}$	1.25 ± 0.09 GeV/c^2
b	$-\frac{1}{3}$	4.20 ± 0.07 GeV/c^2
t	$\frac{2}{3}$	172.0 ± 1.6 GeV/c^2

Table 1.1 : The masses and electrical charges of the quarks of the Standard Model [8]. Each quark has an antiquark with the same mass but the opposite charge.

of virtual photons. The ~80.4 GeV/c^2 $W^{\pm}$ and ~91.2 GeV/c^2 Z^0 bosons are the force carriers of the weak nuclear force [8]. The weak nuclear force mediates quark-flavor changing, such as in neutron beta decay $n \rightarrow pe^-\bar{\nu}_e$, along with other interactions such as muon decay $\mu^- \rightarrow e^-\bar{\nu}_e\nu_\mu$. The massless gluon is the force carrier of the strong nuclear force, which is described by the theory of QCD. The strong interaction binds the quarks together into hadrons such as the proton and neutron, and is discussed in more detail in Section 1.2 [1].

The interactions of the electromagnetic and weak nuclear forces are unified into what is known as the electroweak interaction [12, 13, 14, 15]. In this unification, the $W^{\pm}$ and Z^0 bosons are predicted to gain their masses through spontaneous electroweak symmetry breaking through the Higgs mechanism [16, 17, 18, 19]. The Higgs boson is predicted to exist as a consequence of this symmetry breaking, and is the only elementary particle predicted by the Standard Model that has not yet been detected. Many of the searches for the Higgs boson have been conducted by the CDF and D0 collaborations at the Fermilab Tevatron [20], and experiments are currently being performed with the Large Hadron Collider at CERN [21] as well. The masses of the elementary particles of the Standard Model are predicted to originate from their couplings to the Higgs potential field underlying the Higgs mechanism [22]. However the strength of these couplings, and therefore the masses of the elementary particles, are not predicted.

1.2 Quantum Chromodynamics

Quantum Chromodynamics is the accepted theory of the strong nuclear force in the Standard Model. Through this force, gluons bind quarks together to form particles known as hadrons. Unlike the elec-

tromagnetic interaction, which occurs between particles with electric charge, the strong interaction occurs between particles with color charge. The color charge is an abstract property of the quarks and gluons that characterizes their role in strong interactions. A quark's color charge can either be red, green, or blue, and an antiquark's anticolor charge can either be anti-red, anti-green, or anti-blue. The gluons have mixed combinations of color and anti-color charges and are self-interacting, unlike the electrically neutral photons of QED [23].

The three-state color charge degree of freedom of QCD is represented by the SU(3) special unitary group. The fundamental representation of the SU(n) special unitary group is the set of $n \times n$ unitary matrices with determinants equal to one. A unitary matrix U is a matrix whose inverse is equal to its conjugate transpose, such that $UU^\dagger = I$, the identity matrix. These matrices define the set of rotations that relate the members of the group, and in QCD are used to transform the quark fields between color charges. These matrices are constructed from the $N = n^2 - 1$ independent, traceless, Hermitian $n \times n$ matrices, known as the generators of the group. Hermitian matrices are equal to their conjugate transpose, and traceless matrices have the sum of their eigenvalues equal to zero. In SU(3), these generators are proportional to the Gell-Mann matrices [24], and are used to represent the gluons [2].

In QCD, a quark can combine with an antiquark with the opposite color charge to form a meson of neutral color. Also, three quarks (antiquarks) of different colors (anticolors) can combine to form a baryon (antibaryon) of neutral color. These are known as the valence quarks and antiquarks of the hadrons. Only combinations resulting in color-neutral hadrons are allowed by QCD, implying that unbound quarks and antiquarks cannot be isolated. This restriction is known as color charge confinement, also known as quark confinement [23].

Because gluons are self-interacting, the coupling of the strong force does not decrease with increasing distance between the quarks. If energy is supplied to a system of quarks in an attempt to separate them, the energy will instead create a quark-antiquark pair in the gluonic field between the quarks. This phenomenon is known as hadronization, an example of which is illustrated in Figure 1.2 [23].

The coupling of the strong force decreases with decreasing distance, such that the quarks behave freely at infinitely short distances. This "asymptotic freedom" is a consequence of the gluon self-interaction, and allows QCD predictions to be calculated perturbatively at high energies [26, 27, 28,

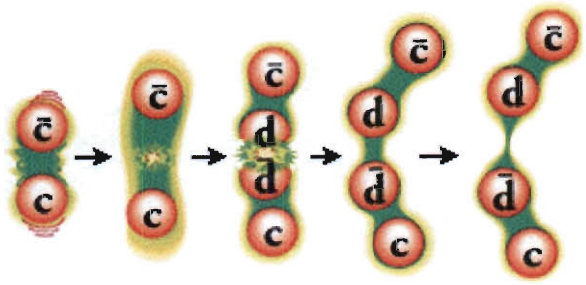

Figure 1.2 : An example of hadronization due to color charge confinement [25]. As energy is applied to the $c\bar{c}$ bound state, the quark-antiquark pair begins to separate. However, this causes the $d\bar{d}$ quark-antiquark pair to be produced in the gluonic field represented by the shaded region, preserving color charge confinement.

29]. This is because the calculation of the infinite series of QCD interaction terms converges quickly due to the smallness of the multiplicative coupling strength. At low energies the coupling strength of the strong force is too large for perturbative calculations to converge, so non-perturbative methods such as phenomenological quark models and lattice QCD may be employed to evaluate the strong interactions [23]. Phenomenological quark models are discussed in more detail in Section 2.1, where the QCD interactions within the nucleons were modeled to predict their spectrum of excited states.

1.3 Hadrons in SU(6) Spin-Flavor Symmetry

As discussed in Section 1.2, spin-$\frac{1}{2}$ quarks and antiquarks can be bound together by gluons to form mesons and baryons. Figure 1.3 shows the valence quark content of the proton, neutron, and π^+ particles. Protons and neutrons are baryons consisting of up and down valence quarks, and π^+'s are mesons consisting of an up valence quark and an anti-down valence quark. Protons and neutrons are also known as nucleons, due to their presence in the nucleus of atoms. Hadrons are characterized by both their valence quark content and how their valence quarks contribute to the total angular momentum of the particle [1].

The total angular momentum quantized vector **J** of a hadron is the quantum-mechanical combination of the total valence quark spin quantized vector **S** and the total orbital angular momentum quantized vector **L**. Mesons can either have their valence quark spins aligned ($\uparrow\uparrow$, $\downarrow\downarrow$) or anti-aligned ($\uparrow\downarrow$, $\downarrow\uparrow$), and when $L = 0$ are referred to as spin-1 or spin-0 mesons, respectively. Baryons can have their spins either aligned ($\uparrow\uparrow\uparrow$, $\downarrow\downarrow\downarrow$) or mixed (*e.g.* $\uparrow\downarrow\uparrow$), and when $L = 0$ are referred to as spin-$\frac{3}{2}$ or

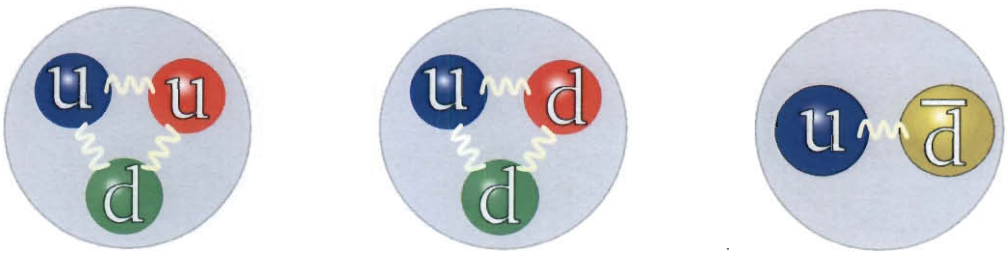

(A) (B) (C)

Figure 1.3 : The valence quark content of the proton (A), neutron (B), and π^+ (C) [30]. The colors of the quarks and antiquarks do not illustrate their specific color charges, but are for illustrative purposes only.

spin-$\frac{1}{2}$ baryons, respectively. Also, the valence quarks can orbit each other with a quantized orbital angular momentum L, whose quantum numbers (0, 1, 2, 3, etc.) correspond to the (S, P, D, F, etc.) orbitals. Finally, the valence quarks can have quantized distances from each other within the hadrons, which are represented by the principle quantum number n [1]. With the exception of some of the N^* states, all of the particles in this analysis have $n = 0$, or no radial excitation.

The hadrons with the minimum total angular momentum and no radial excitation are known as the ground state particles, and those with larger angular momentum are known as the excited states. The excited states have larger masses and are significantly more unstable than the ground states. The excited states typically decay through the strong force, and generally have lifetimes on the order of 10^{-23} seconds. The proton is the only hadron that has not been observed to decay, and has a lifetime of at least 10^{29} years [8].

The up, down, and strange quarks have comparably light masses and thus may be grouped together to form the SU(3) flavor symmetry group. Although not an exact symmetry due to the quark mass differences, this grouping is convenient for modeling the quark interactions within the hadrons [31]. When SU(3) flavor symmetry is combined with the SU(2) spin symmetry of the quarks, the SU(6) spin-flavor symmetry group is formed.

The ground state or spin-0 pseudoscalar mesons of SU(6) are shown in Figure 1.4, along with the excited spin-1 vector mesons. The ground state spin-$\frac{1}{2}$ baryons are shown in Figure 1.5, along with the excited spin-$\frac{3}{2}$ baryons. Not shown are the anti-baryons, which are instead made up of the $\bar{u}$, $\bar{d}$, and $\bar{s}$ antiquarks. These hadrons comprise each possible mesonic and baryonic combination of the up, down, and strange quarks and antiquarks with $n = 0$ and $L = 0$, and have all been

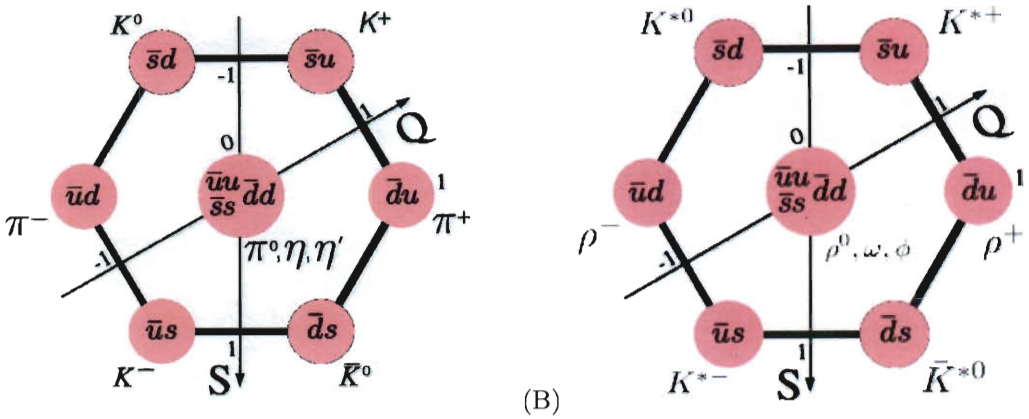

Figure 1.4 : The $n = 0$, $L = 0$, spin-0 pseudoscalar (A) and spin-1 vector (B) meson nonets of the SU(6) quark spin-flavor symmetry group [32]. The mesons are grouped along the electrical charge (Q) and strangeness (S) axes, and each of these particles has been experimentally observed [8]. A particle's strangeness is determined by its number of strange and anti-strange quarks.

experimentally observed [8]. The observation of these predicted hadrons is a major success of QCD and the Standard Model. Details on how the spin, flavor, and color components of the valence quark wavefunctions combine within hadrons are discussed in Reference [1].

While some of the resonances with $L > 0$ have been observed, such as some of the excited nucleons (N^*'s) [8], many of the excited states predicted by phenomenological models have not yet been experimentally observed. The observation of the "missing" nucleon resonances is a major remaining goal of nuclear and particle physics. This is because nucleons constitute the majority of atomic matter, and the spectrum of their excited states is dependent on their relevant internal degrees of freedom. These degrees of freedom are manifested in the non-perturbative region of QCD, and are not yet fully understood. The relativized quark model of the baryons by Capstick and Isgur [34] is discussed in Section 2.1, along with its predictions for the N^* resonance spectrum.

The hadrons featured in this analysis, such as the K^{*0} and Σ^{*-}, are detailed in Table 1.2. This table includes the valence quark content, electrical charges, spin-parities J^P, isospins I, isospin projections I_3, and masses of the particles. A particle's parity can either be +1 or -1, and reflects how its wavefunction behaves under spatial inversion [31].

Isospin I is a characteristic of the hadron multiplets containing up and down quarks. The hadrons within these multiplets, such as the π's and the N's, have similar masses due to the similarity in mass of the up and down quarks. Therefore, the members of these multiplets can be thought of as

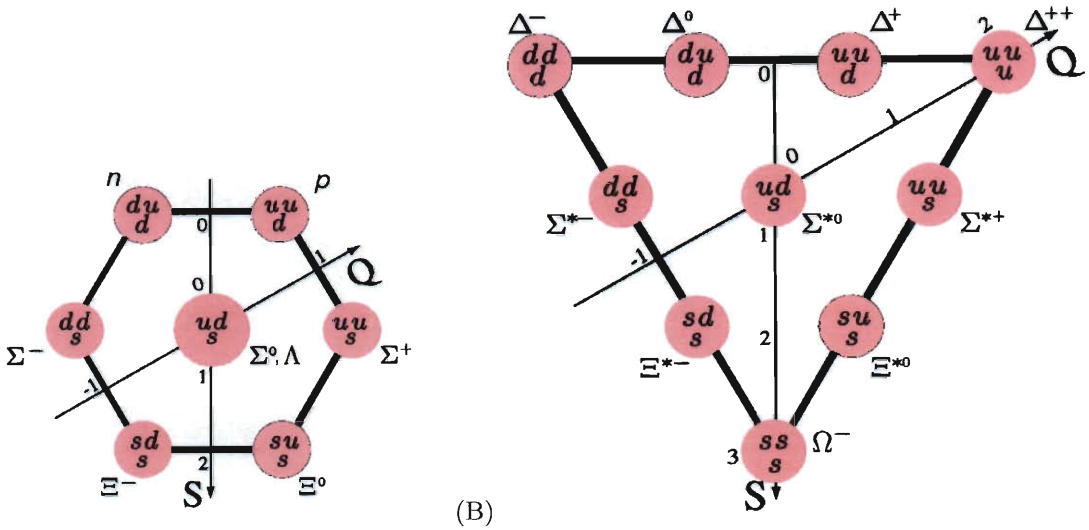

(A) (B)

Figure 1.5 : The $n = 0$, $L = 0$, spin-$\frac{1}{2}$ baryon octet (A) and spin-$\frac{3}{2}$ baryon decuplet (B) of the SU(6) quark spin-flavor symmetry group [33]. The baryons are grouped along the electrical charge (Q) and strangeness (S) axes, and each of these particles has been experimentally observed [8]. A particle's strangeness is determined by its number of strange and anti-strange quarks.

Particle	Valence Quark Content	Q (e)	J^P	I	I_3	Mass (MeV/c^2)
p	uud	1	$\frac{1}{2}^+$	$\frac{1}{2}$	$\frac{1}{2}$	$938.27203 \pm 8 \times 10^{-5}$
n	udd	0	$\frac{1}{2}^+$	$\frac{1}{2}$	$-\frac{1}{2}$	$939.56536 \pm 8 \times 10^{-5}$
π^-	$\bar{u}d$	-1	0^-	1	-1	$139.57018 \pm 3.5 \times 10^{-4}$
K^+	$u\bar{s}$	1	0^-	$\frac{1}{2}$	$\frac{1}{2}$	493.677 ± 0.016
Λ	uds	0	$\frac{1}{2}^+$	0	0	1115.683 ± 0.006
K^{*0}	$d\bar{s}$	0	1^-	$\frac{1}{2}$	$-\frac{1}{2}$	895.94 ± 0.22
Σ^{*-}	dds	-1	$\frac{3}{2}^+$	1	-1	1387.2 ± 0.5

Table 1.2 : The valence quark content, electrical charges Q, spin-parities J^P, isospins I, isospin projections I_3, and masses of the hadrons featured in this analysis [8].

differently charged projections of the same particle. Each hadron multiplet has an isospin magnitude I, with member particles of different isospin projections I_3. The isospin projection $I_3 = \frac{1}{2}$ is assigned to the up quark, and $I_3 = -\frac{1}{2}$ is assigned to the down quark. The $\bar{u}$ and $\bar{d}$ antiquarks are assigned the opposite isospin projections, and the isospin projections of the hadrons are the sum of the isospin projections of their valence quarks [1].

1.4 Hadron Structure

In hadrons, the energy in the gluonic fields surrounding the quarks frequently fluctuates into virtual quark-antiquark pairs. These "sea" quarks, along with the energy in the gluonic fields, make up the majority of the mass of the proton. This can be seen from Tables 1.1 and 1.2, where the masses of the valence quarks are shown to make up only ~1% of the proton's total mass. Additionally, the valence quarks only account for about one third of the total angular momentum of the proton [35]. A depiction of the quark "sea" within the proton is shown in Figure 1.6, but this inexact portrayal is for illustrative purposes only. The quark-antiquark pairs within the "sea" are not stable, as they rapidly fluctuate into and out-of existence from the gluonic fields. In many phenomenological models the quarks have significantly larger masses, around 300 MeV/c^2 for the up and down quarks in the nucleons, which are intended to encapsulate some of these gluonic effects.

It is not fully understood how the quarks can contribute to the underlying structure of the baryons. For example, it is unknown whether the valence quarks within a baryon can form a correlated pair known as a diquark, as illustrated in Figure 1.7. If they do, then this phenomenon limits the spectrum of available excited states of the baryons [38]. As discussed in Chapter 2, measurement of the spectrum of the excited states of the nucleons will provide insight into their structure and internal degrees of freedom.

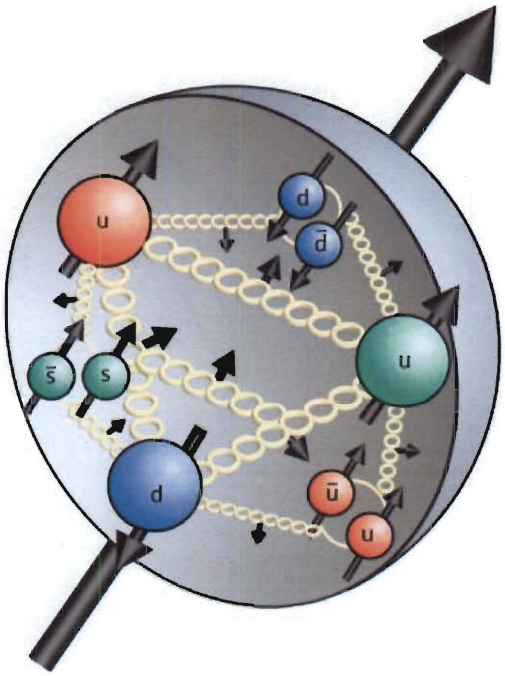

Figure 1.6 : An inexact portrayal of how the "sea" quarks may contribute to the structure of the proton [36]. The large, individual quarks indicate the proton's valence quarks, and the smaller quark-antiquark pairs indicate the "sea" quarks. The arrows illustrate spin and angular momentum axes, and how the individual components of the proton may contribute to its total angular momentum. The quark-antiquark pairs are not stable, as they rapidly fluctuate into and out-of existence from the gluonic fields. The colors of the quarks and antiquarks do not illustrate their specific color charges, but are for illustrative purposes only.

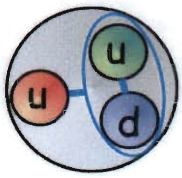

Figure 1.7 : A depiction of how the valence quarks within the proton may be bound together to form a correlated quark-pair, or diquark [37]. The colors of the quarks and antiquarks do not illustrate their specific color charges, but are for illustrative purposes only.

Chapter 2

Excited Nucleons

According to the Particle Data Group (PDG) 13 different N^* states have been well-established, with masses ranging from 1440 MeV/c^2 to 2600 MeV/c^2 [8]. While some relativized quark models predict that many more N^* states exist [34], diquark models predict that a correlated quark-pair inside of the nucleon would preclude the existence of many of these resonances [38]. Measuring the spectrum and properties of the N^* states will provide valuable information on the relevant degrees of freedom of the quark interactions within the nucleon.

A $^3P_0$ quark-antiquark pair creation model of the baryon decays [39] predicts that most of the unobserved N^* states couple somewhat weakly to the πN channels, where most of the experimental searches have been conducted [8]. However, many of the remaining, high-mass N^* states from 1750 MeV/c^2 to 2200 MeV/c^2 are predicted [40] to couple non-negligibly to hyperon (Y) channels, in which the baryons contain strange quarks. The higher-energy production thresholds for these channels restrict the couplings of the known lower-mass resonances, limiting their backgrounds for the extraction of the higher-mass resonances. Measuring the cross sections and polarization observables of the KY, K^*Y, and KY^* photoproduction reactions on both the proton and the neutron will contribute to disentangling the N^* states through coupled-channels analyses of their decays.

2.1 Relativized Quark Model of the Baryons

The relativized quark model of the baryons by Capstick and Isgur [34] provides predictions for the mass spectrum of the baryons. This is one of the first models to treat the quarks within the hadrons relativistically, and its predictions are similar to those of non-relativistic models. However by treating the motion and dynamics of the quarks relativistically, this model was able to explain the hyperfine mass-splitting between the baryons due to spin-orbit effects. This mass-splitting, such as the mass difference between the nucleon and Δ particles, was shown to be due to relativistic effects that were not included in previous models. For most of the ground-state baryons of SU(3) flavor symmetry, the mass predictions by this model agree with the experimentally measured values within the uncertainties. However the agreement is worse for the excited states, and moderate systematic shifts are needed to center the mass predictions on their measured values [34].

2.1.1 Model Details

The predictions for the spectrum of the baryons were obtained by solving the equation [34]:

$$H \mid \Psi\rangle = E \mid \Psi\rangle \tag{2.1}$$

for the energy eigenvalues E, where the baryons are represented as a system of three uncorrelated quarks by the energy eigenstates Ψ of the Hamiltonian energy operator H. In this model, the Hamiltonian H is defined as [34]:

$$H = H_0 + V_{oge} + V_{conf}, \tag{2.2}$$

where H_0 is the relativistic kinetic energy term, V_{oge} is a one-gluon-exchange potential, and V_{conf} is a confinement potential. The one-gluon-exchange potential contains terms for the Coulomb, hyperfine, and spin-orbit interactions between the quarks. The Coulomb term represents the distance-dependent strength of the strong interaction between the quarks, and the hyperfine interaction between the quarks simulates the magnetic dipole-magnetic dipole interaction of electrodynamics [41]. The confinement term includes string and spin-orbit terms that are functions of quark distance, momentum, and spin. Details of the potentials used in this model are discussed in Reference [34].

To obtain realistic predictions for the probability amplitudes of nuclear physics reactions, all

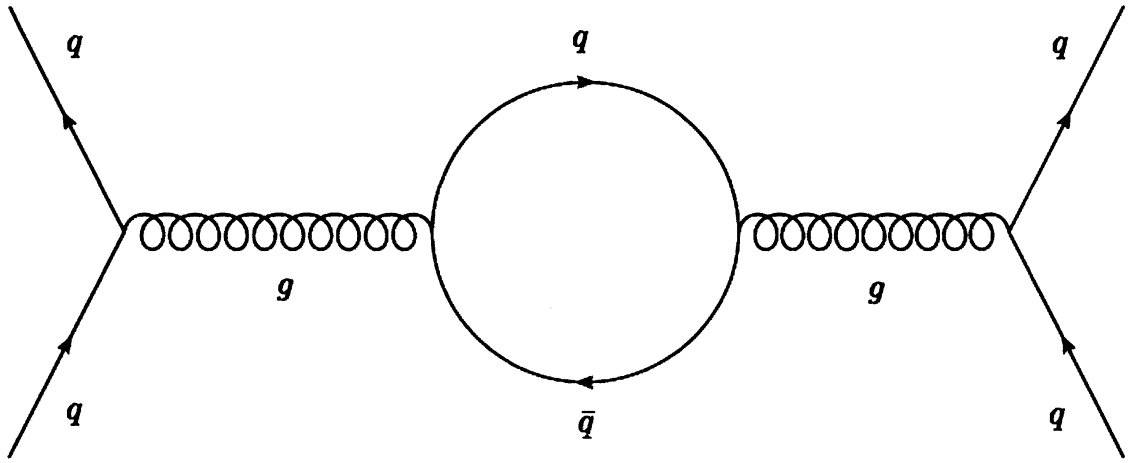

Figure 2.1 : A Feynman diagram depicting quark-quark scattering via virtual gluon exchange. The gluon briefly oscillates into a virtual quark-antiquark pair. The integral over the possible 4-momentum of this loop is infinite, because the virtual quark-antiquark pair is off-shell.

possible production mechanisms need to be considered. However, since the Heisenberg uncertainty principle allows four-momentum conservation to be violated over small distances and times, an infinite number of virtual particle loops contribute to the reactions. Figure 2.1 illustrates a Feynman diagram depicting quark-quark scattering, where the exchanged virtual gluon briefly oscillates into a virtual quark-antiquark pair. Because four-momentum conservation can be violated the virtual particles may be off-shell, having energy and momentum that violate the relativistic energy equation, such that $E^2 - p^2c^2 \neq m^2c^4$. Thus virtual particles can have an infinite number of possible four-momenta, causing the loop integrals necessary to calculate the loop probability amplitude to diverge. Since the coupling strength of the strong force is large at these energies, perturbation theory cannot be used to truncate the number of virtual particle loops necessary for convergence.

To solve this problem, a mass cutoff parameter Λ is introduced to regularize the divergence. Physics at higher energy scales than Λ are not treated directly and are instead represented by effective parameters, such as effective quark masses. To effectively describe hadrons, typical cutoffs are on the order of 0.2 fm, or $\Lambda = 200$ MeV/c^2. At this scale, bare quarks in hadronic models are replaced by constituent quarks. These constituent quarks include a representation of the surrounding gluonic field, and thus have effective masses on the order of several hundred MeV/c^2. In this model the cutoff $\Lambda = 200$ MeV/c^2 was used, along with constituent quark masses of 220 MeV/c^2 for the

State, J^P	Measured Mass (MeV/c^2)	Predicted Mass (MeV/c^2)
$N\frac{1}{2}^+$	939	960
$\Delta\frac{3}{2}^+$	1232	1230
$\Lambda\frac{1}{2}^+$	1116	1115
$\Sigma\frac{1}{2}^+$	1193	1190
$\Sigma\frac{3}{2}^+$	1384	1370
$\Xi\frac{1}{2}^+$	1318	1305
$\Xi\frac{3}{2}^+$	1533	1505
$\Omega\frac{3}{2}^+$	1672	1635

Table 2.1 : Mass predictions for the ground-state baryons containing up, down, or strange quarks in the relativized quark model by Capstick and Isgur [34]. J^P is the spin-parity of the particles. The uncertainty on the extraction of the mass predictions is about 20 MeV/c^2.

up and down quarks and 419 MeV/c^2 for the strange quarks. Details on these and other effective parameters used in this model are discussed in Reference [34].

Because it was impossible to solve for the eigenvalues of the Hamiltonian in Equation 2.1 directly in this model, variational methods were used. The baryon wavefunctions were expanded in a large harmonic-oscillator basis to obtain trial wavefunctions for solving Equation 2.1. This basis is convenient for handling the combination of the spatially dependent potentials with the momentum-dependent terms in the Hamiltonian because wavefunctions in this basis are form-invariant under Fourier transformations. The specifics of the flavor, spin, orbital, and spatial wavefunctions of the constituent quarks of the baryons used in this model are detailed in Reference [34].

2.1.2 Mass Predictions

After diagonalizing the Hamiltonian defined in Equation 2.2 in the large harmonic-oscillator basis, Equation 2.1 was solved for the eigenvalues E. The masses of the baryons were then extracted from these eigenvalues. The mass predictions of this model for the ground-state baryons are shown in Table 2.1, where J^P is the spin-parity of the particles as discussed in Section 1.3. The uncertainty on the extraction of these masses was approximately 20 MeV/c^2, so the matching between the model and the experimental data is excellent. Although the mass predictions for the ground-state hyperons were systematically low, a slight increase in the effective masses of the strange quarks would have caused the the excited-state spectra predictions to worsen [34].

Figure 2.2 shows the spectrum of the predicted N^* states by the relativized quark model with masses less than 2200 MeV/c^2. Table 2.2 shows the matching between the model states and those that have experimental evidence for their existence, as recognized by the Particle Data Group [8]. A particle state is considered to be established by the PDG if it has been observed in at least two separate analyses, and if they consider the partial-wave amplitudes to be well-behaved with reasonable uncertainties. These states are assigned either a three- or four-star status, depending on how much information on the state is known. Otherwise, if the evidence for a state is poor it is either assigned a two- or one-star status [8].

The predictions of the positive parity N^* states masses were on average $\sim$50 MeV/c^2 too low, and for the negative parity states were on average $\sim$40 MeV/c^2 too high [34]. The accuracy of these predictions was limited by the many QCD effects that were not included in the model, such as the mixing with gluonic excitations and the physics masked by the mass cutoff parameter Λ. Mass predictions were also made for Δ^*'s, Λ^*'s, Σ^*'s, Ξ^*'s, and Ω^*'s, as well as for the charmed Λ_c^*'s and Σ_c^*'s and the bottom-quark-flavored Λ_b^*'s and Σ_b^*'s. Where experimental information is available, the quality of the mass predictions of these states is comparable to those of the N^*'s [34].

2.2 Diquark Models

In some competing models of the baryons, the three quarks are treated as a quark-diquark pair. Although the cause of this potential correlated quark-pairing in the diquarks is not fully understood, it is not prohibited by QCD. In the light-quark-mass spin-flavor-color symmetry group, $SU_s(2) \otimes SU_f(3) \otimes SU_c(3)$, the correlated quarks must be in an antisymmetric, non-excited state to form colorless baryons. This restriction on the degrees of freedom limits the spectrum of the nucleon's possible excited states, largely to those already experimentally observed [38].

With the non-relativistic diquark model by Santopinto [38], the masses of the non-strange baryons were determined by solving for the energy eigenvalues of the baryon wavefunction Hamiltonian, as shown in Equation 2.1. However, in this model the Hamiltonian H is [38]:

$$H = E_0 + T + V_{dir} + V_{ex} + E_{DS}, \tag{2.3}$$

where E_0 is a model fit-parameter, T is the kinetic energy of the baryon, V_{dir} is the direct interaction

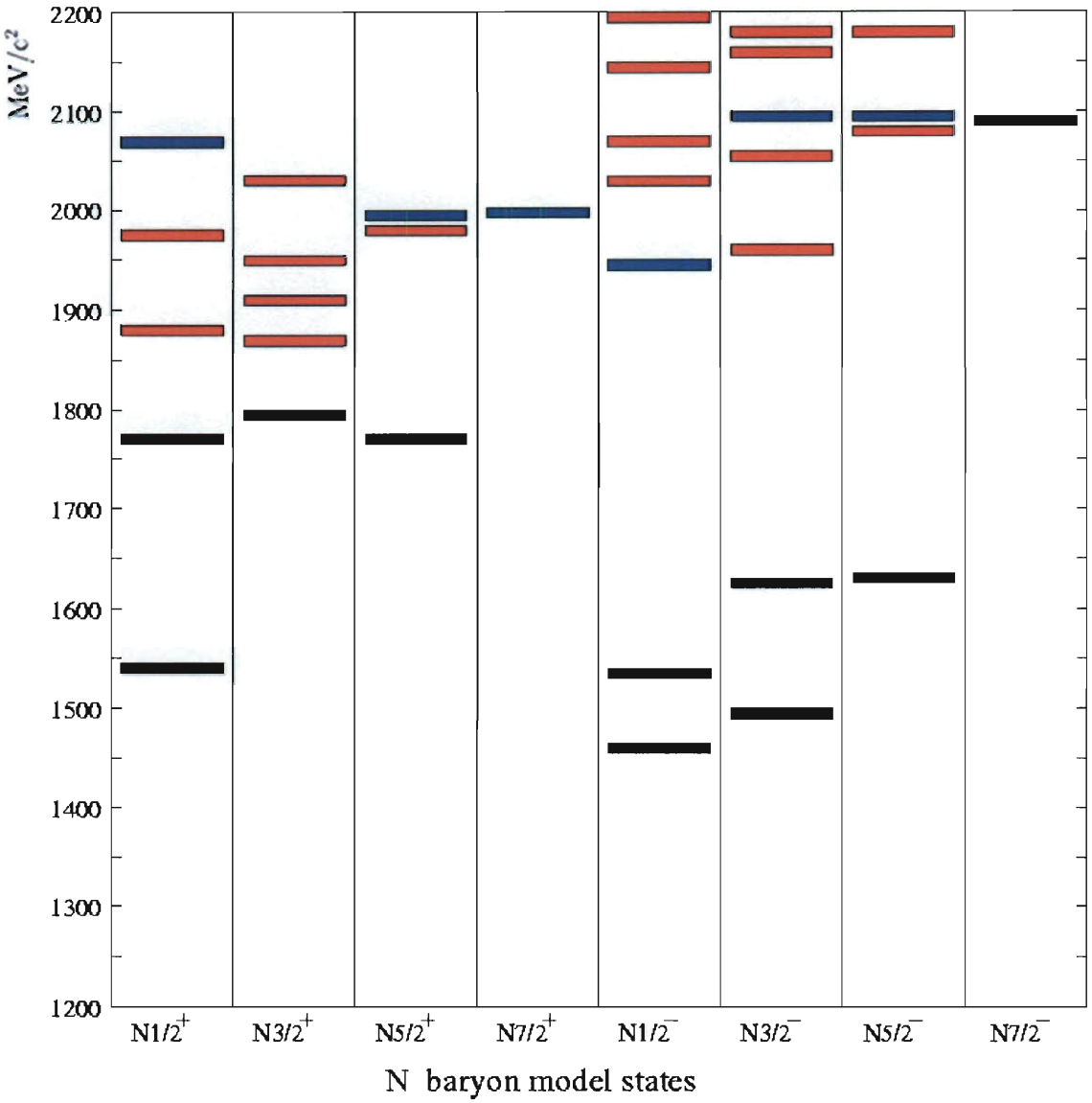

Figure 2.2 : The predicted N^* spectrum for resonances with mass less than 2200 MeV/c^2 in the relativized quark model of the baryons by Capstick and Isgur [34, 42]. The masses of the states are given in units of MeV/c^2, organized by spin-parity. The black resonances correspond to three- and four-star PDG N^* states, the blue resonances correspond to one- and two-star PDG N^* states, and the red resonances correspond to states with no experimental evidence [8, 34].

PDG State (J^P, Mass (MeV/c^2))	$L_{2I,2J}$	PDG Status	Predicted Mass (MeV/c^2)
$N\frac{1}{2}^+(1440)$	P_{11}	****	1540
$N\frac{3}{2}^-(1520)$	D_{13}	****	1495
$N\frac{1}{2}^-(1535)$	S_{11}	****	1460
$N\frac{1}{2}^-(1650)$	S_{11}	****	1535
$N\frac{5}{2}^-(1675)$	D_{15}	****	1630
$N\frac{5}{2}^+(1680)$	F_{15}	****	1770
$N\frac{3}{2}^-(1700)$	D_{13}	***	1625
$N\frac{1}{2}^+(1710)$	P_{11}	***	1770
$N\frac{3}{2}^+(1720)$	P_{13}	****	1795
$N\frac{3}{2}^+(1900)$	P_{13}	**	NA
$N\frac{7}{2}^+(1990)$	F_{17}	**	2000
$N\frac{5}{2}^+(2000)$	F_{15}	**	1980
$N\frac{3}{2}^-(2080)$	D_{13}	**	1960
$N\frac{1}{2}^-(2090)$	S_{11}	*	1945
$N\frac{1}{2}^+(2100)$	P_{11}	*	2065
$N\frac{7}{2}^-(2190)$	G_{17}	****	2090
$N\frac{5}{2}^-(2200)$	D_{15}	**	2095
$N\frac{9}{2}^+(2220)$	H_{19}	****	2345
$N\frac{9}{2}^-(2250)$	G_{19}	****	2215
$N\frac{11}{2}^-(2600)$	$I_{1,11}$	***	2600
$N\frac{13}{2}^+(2700)$	$K_{1,13}$	**	2820

Table 2.2 : The mass predictions of the relativized quark model [34] for the experimentally observed N^* spectrum [8]. $L_{2I,2J}$ represents the quantum numbers of the partial-wave of the N^* states, where L is the quark relative orbital angular momentum, I is the isospin, and J is the total spin. Isospin and the quark orbital angular momentum are discussed in Section 1.3, and partial-waves are discussed in Section 2.3.3.

potential, V_{ex} is an exchange interaction potential, and E_{DS} takes into account the energy splitting between the two possible diquark spin configurations. The direct interaction potential contains both a Coulomb-like term, which can be considered to represent one-gluon exchange, and a linear term that can be considered to represent quark confinement. The energy splitting arises from the scalar, spin-zero diquark spin configuration having a lower energy than the vector, spin-one configuration. Seven fit parameters, such as E_0, are included in this model of the Hamiltonian and were determined by comparing with experimental data. The total baryon wavefunctions contained the spin-flavor wavefunctions of the quarks and diquarks, as well as the radial and orbital spatial wavefunctions [38].

The predictions of the masses of the N^* and Δ^* states are shown in Figure 2.3, compared to the experimentally measured values of the three- and four-star states. Although this model is non-relativistic, the predicted masses match those of the excited spectrum fairly well. Also the many additional, unobserved states predicted by uncorrelated quark models were not predicted to exist due to the correlated quark-pair [38]. If only a few of these prohibited states are conclusively established, then the potential role of diquarks within the nucleon will be diminished. As discussed in Section 2.4, recently strong evidence was found for the existence of the $N\frac{3}{2}^+(1900)$ resonance, which is absent in diquark models [43]. However, there may also be mixing between states with correlated and uncorrelated quarks.

2.3 The $^3P_0$ Strong Decay Model

The N^* states decay too quickly to be detected directly, so they must be observed through their decay products. As seen in Table 2.3, most of the N^* resonance studies were conducted by searching through their couplings to the $N\pi$, $\Delta\pi$, and $N\gamma$ channels [8]. Although 13 N^* states have been well-established through these channels according to the PDG, the relativized quark model of the baryons discussed in Section 2.1 predicts that there are many more resonances that have not been observed.

The $^3P_0$ quark-antiquark pair creation decay model of the baryons by Capstick and Roberts [39] predicts that it may be easier to search for some of the unobserved N^* states through their decays to strangeness channels. For example, the $N\frac{3}{2}^-(1960)$ model state is predicted to be easier to extract in the ΛK^* channel than in the $N\pi$ channel. This is because the nearby $N\frac{3}{2}^-(2055)$ model state is

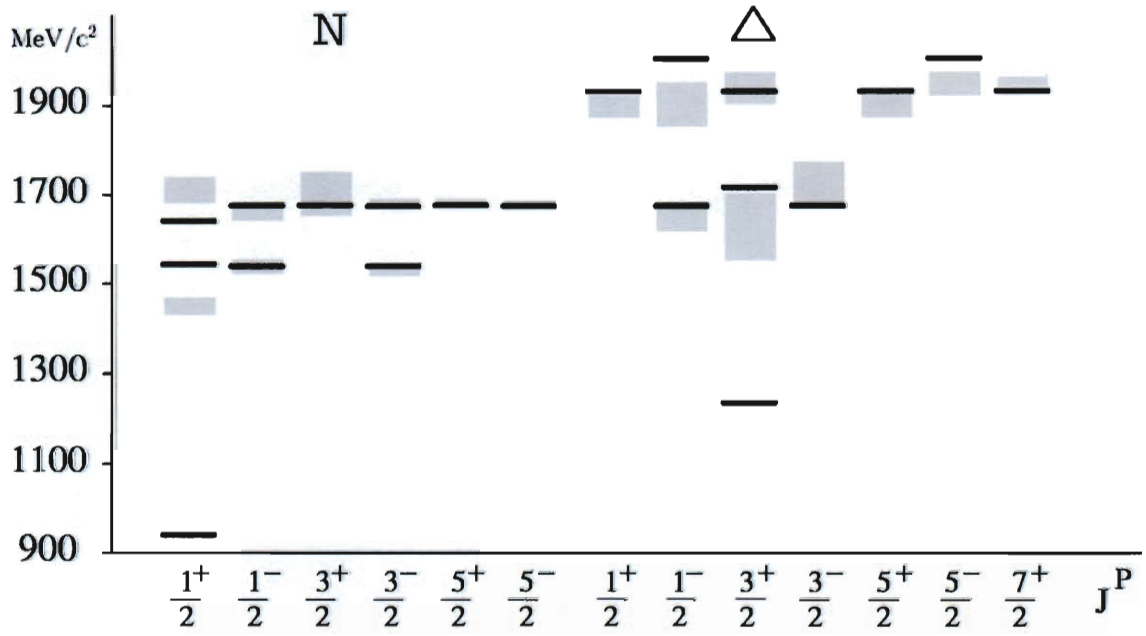

Figure 2.3 : A comparison up to 2000 MeV/c^2 of the masses of the experimentally measured three- and four-star N^* and Δ^* states, shown in grey, to those from the diquark model of Santopinto, shown in black [38]. The size of the grey bands represent the width of the particle resonances, as explained in Section 2.3.1.

PDG State (J^P, MeV/c^2)	L_{2I-2J}	Overall Status	Status in Channel						
			$N\pi$	$N\eta$	ΛK	ΣK	$\Delta\pi$	$N\rho$	$N\gamma$
$N\frac{1}{2}^+(1440)$	P_{11}	****	****	*			***	*	***
$N\frac{3}{2}^-(1520)$	D_{13}	****	****	***			****	****	****
$N\frac{1}{2}^-(1535)$	S_{11}	****	****	****			*	**	***
$N\frac{1}{2}^-(1650)$	S_{11}	****	****	*	***	**	***	**	***
$N\frac{5}{2}^-(1675)$	D_{15}	****	****	*	*		****	*	****
$N\frac{5}{2}^+(1680)$	F_{15}	****	****	*			****	****	****
$N\frac{3}{2}^-(1700)$	D_{13}	***	***	*	**	*	**	*	**
$N\frac{1}{2}^+(1710)$	P_{11}	***	***	**	**	*	**	*	***
$N\frac{3}{2}^+(1720)$	P_{13}	****	****	*	**	*	*	**	**
$N\frac{3}{2}^+(1900)$	P_{13}	**	**					*	
$N\frac{7}{2}^+(1990)$	F_{17}	**	**	*	*	*			*
$N\frac{5}{2}^+(2000)$	F_{15}	**	**	*	*	*	*	**	
$N\frac{3}{2}^-(2080)$	D_{13}	**	**	*	*				*
$N\frac{1}{2}^-(2090)$	S_{11}	*	*						
$N\frac{1}{2}^+(2100)$	P_{11}	*	*	*					
$N\frac{7}{2}^-(2190)$	G_{17}	****	****	*	*	*		*	*
$N\frac{5}{2}^-(2200)$	D_{15}	**	**	*	*				
$N\frac{9}{2}^+(2220)$	H_{19}	****	****	*					
$N\frac{9}{2}^-(2250)$	G_{19}	****	****	*					
$N\frac{11}{2}^-(2600)$	$I_{1\,11}$	***	***						
$N\frac{13}{2}^+(2700)$	$K_{1\,13}$	**	**						

Table 2.3 : The PDG-assigned status of the experimental determination of the N^* states [8]. The overall status of each N^* state is shown, as well as their statuses through their individual channel couplings. There is no experimental information on the N^* couplings to the K^*Y or KY^* channels. An overview of the Particle Data Group status assignments is located in Section 2.1.2.

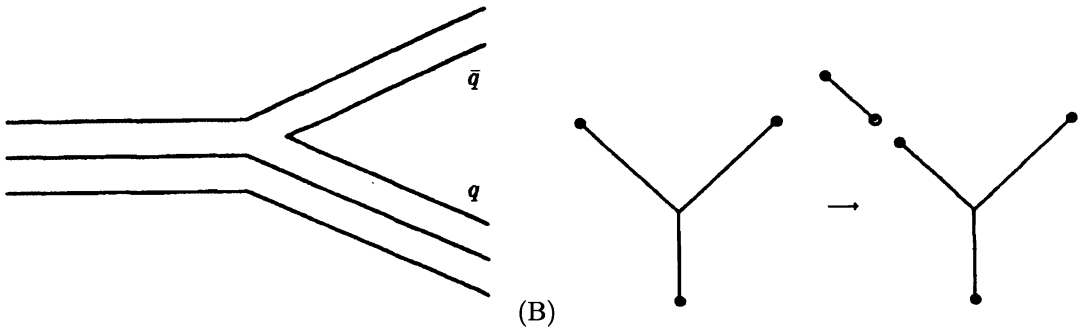

Figure 2.4 : $^3P_0$ (A) and flux string-breaking (B) quark-antiquark pair creation models of baryon decays [39].

predicted to have a strong coupling to the $N\pi$ channel, and their overlap will make extraction more difficult [40]. The observation of this or many of the other predicted high-mass N^* states would indicate fundamental problems with the diquark models [38] of the baryons.

2.3.1 Model Details

The $^3P_0$ strong decay model by Capstick and Roberts [39] models baryon decays as proceeding through the creation of a quark-antiquark pair anywhere in space. This process is diagrammed in Figure 2.4(A), where the antiquark forms a meson with one of the original quarks of the baryon, and the three remaining quarks form a new baryon. This quark-antiquark pair is created with the QCD vacuum quantum numbers, $J^{PC} = 0^{++}$, where C is the charge parity. The charge parity can be either $+1$ or -1, and is the eigenvalue of the charge conjugation operator, which replaces all charged particles with their antiparticles. In spectroscopic notation ($^{2S+1}L_J$) these quantum numbers correspond to $^3P_0$, where S is the total spin of the quark-antiquark system.

There may also be mixing with other decay mechanisms, such as one gluon exchange [44]. In this mechanism the quark-antiquark pair is created with the quantum numbers of the gluon, corresponding to $^3S_1$ in spectroscopic notation. Although $^3P_0$ decay models of light mesons have been shown to match experimental data fairly well, one gluon exchange has been shown to have sizable effects in some meson channels [45]. However, the contribution of one gluon exchange in baryon decays is not well understood, and was not included in the $^3P_0$ strong decay model by Capstick and Roberts [39].

Flux tube-breaking decay models [46, 47, 48, 49] are an alternative quark-antiquark pair creation

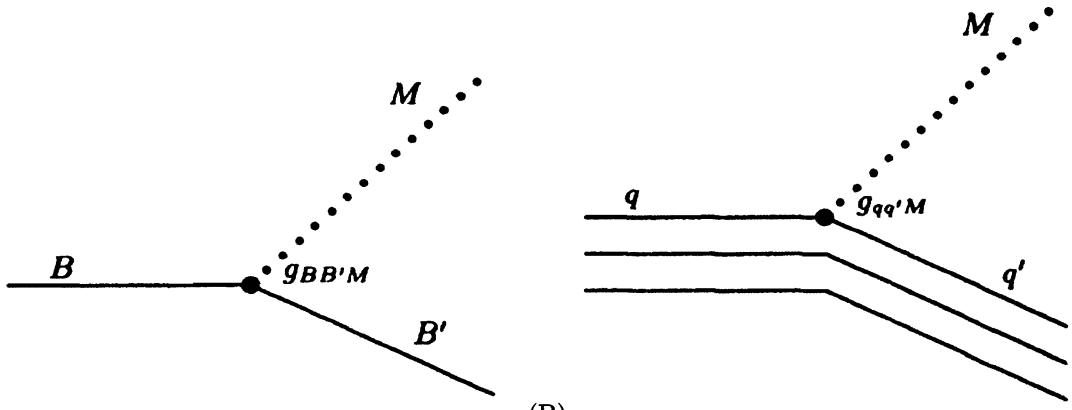

Figure 2.5 : Hadrodynamic (A) and elementary meson emission (B) models of baryon decays, where g is the decay coupling strength factor [39].

description of baryon decays. In these models the quark-pair is created within the flux tubes connecting the quarks in the baryon. Flux string-breaking models [50, 51], depicted in Figure 2.4(B), are similar to flux tube-breaking models except the flux tubes have zero width. In both of these models the quark-antiquark pair is produced with the QCD vacuum quantum numbers. These are in contrast to hadrodynamic models, in which hadrons are treated as structureless point-like particles, and elementary meson emission models [52], in which a structureless, point-like meson is emitted directly from one of the quarks of the baryon. The hadrodynamic and elementary meson emission models are illustrated in Figure 2.5.

In the $^3P_0$ strong decay model by Capstick and Roberts, the baryon decay transition amplitudes $\mathcal{M}$ were calculated as [39]:

$$\mathcal{M} = \langle BC \mid T \mid A \rangle \tag{2.4}$$

for the decay $A \rightarrow BC$, where A is the original baryon, B is the daughter baryon, C is the daughter meson, and T is the operator for the decay transition. Instead of using a Hamiltonian derived from QCD, the operator T was defined phenomenologically. T includes operators to create the quark-antiquark pair from the vacuum, as well as quark spin, color, flavor, and spatial wavefunctions. The wavefunctions of the A, B, and C hadrons also contain operators to create their constituent quarks from the vacuum, along with their spin, color, flavor, and spatial wavefunctions. The decay amplitude was solved by applying the decay transition operator T onto the original baryon A, and

integrating over all possible momenta of the quarks and particles in the system that could lead to the B and C decay products. This model also includes a phenomenological parameter for the $^3P_0$ coupling strength, γ [39]. This parameter was fit to the measured $N\pi$ amplitudes of the N^* and Δ^* resonances that have a PDG-assigned status [8] of two stars or higher.

Due to the Heisenberg uncertainty principle, decaying particles with short lifetimes have broad mass-probability distributions. The resonance (or total) width Γ of a state is the full-width at half-maximum of the state's mass-probability distribution. The N^* states, which have lifetimes on the order of 10^{-24} s, have resonance widths of several hundred MeV/c^2. This resonance width is also equal to the sum of the individual channel decay widths. In this $^3P_0$ strong decay model, the width $\Gamma_{A\to BC}$ of the $A \to BC$ decay was calculated as [39]:

$$\Gamma_{A\to BC} = |\mathcal{M}_{A\to BC}|^2 \Phi(ABC), \tag{2.5}$$

where $\Phi(ABC)$ is the four-momentum-dependent phase space for the decay. Finally, the decay amplitudes quoted by Capstick and Roberts were calculated as [40]:

$$|A_{A\to BC}| = \sqrt{\Gamma_{A\to BC}}, \tag{2.6}$$

which was evaluated in the rest frame of the decaying baryon. More details on the procedure for calculating the decay amplitudes and widths are discussed in References [39] and [53].

2.3.2 Decay Amplitude Predictions

Using this model, Capstick and Roberts calculated coupling amplitudes and decay widths for all of the predicted N^* and Δ^* states in the relativistic baryon model discussed in Section 2.1. The predicted amplitudes $|A_{N\pi}|$ for the N^* couplings to the $N\pi$ channel are shown in Figure 2.6 [39]. The experimental amplitudes are also shown, and were extracted from the measurements of the total widths of the N^* states and their branching ratios into the $N\pi$ channel. As seen in the figure, the N^* states that have not been observed have smaller coupling amplitudes to the $N\pi$ channel than the states with the same spin-parity that have been established. As discussed in Reference [39], the same holds true for the spectrum of Δ^* states as well.

Despite the significant overestimate of the $N\frac{3}{2}^+(1720)$ decay amplitude prediction, the predic-

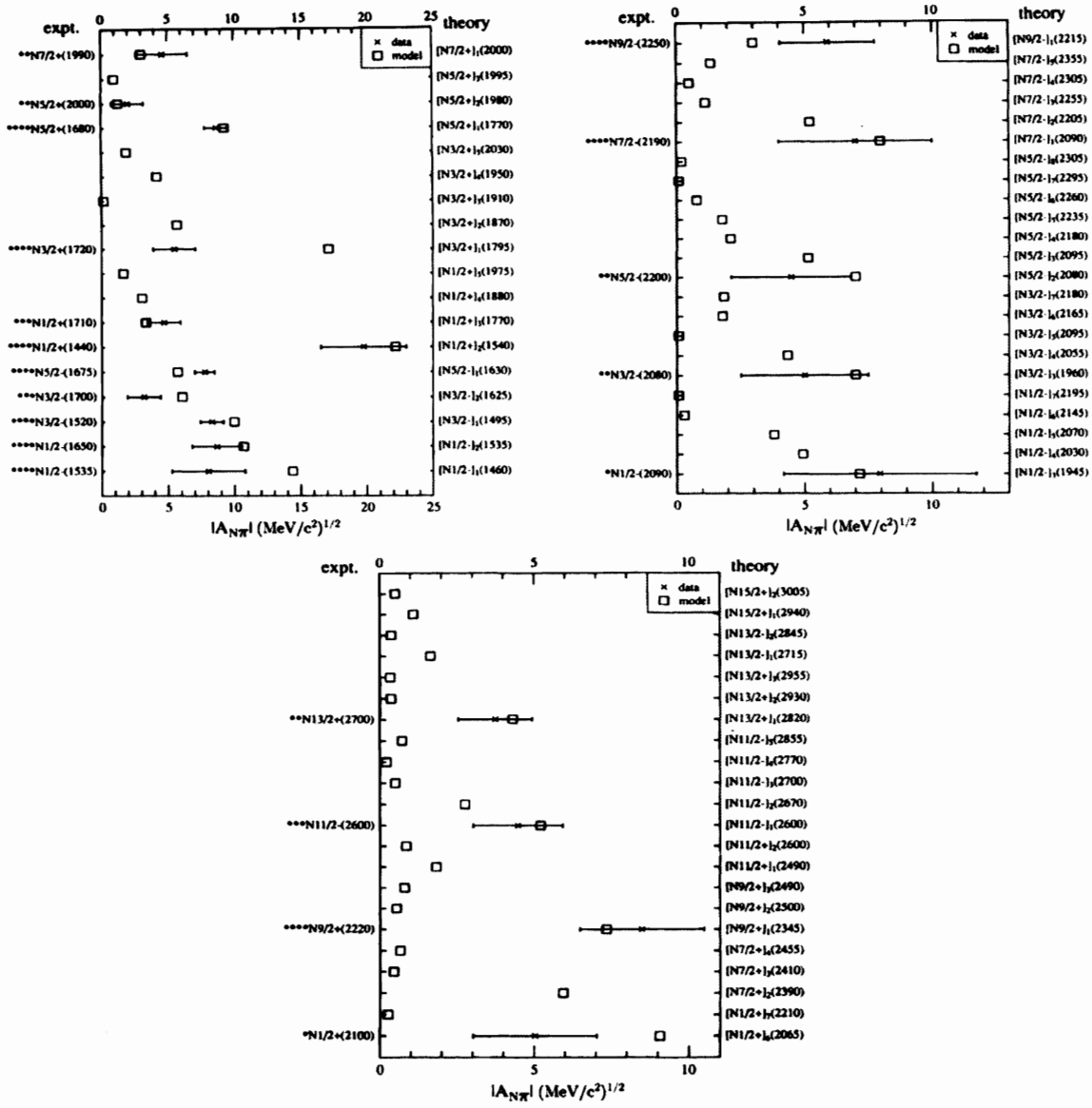

Figure 2.6 : Comparison of the predicted and measured values of $|A_{N\pi}|$, the coupling amplitude between the N^* states and the $N\pi$ channel. The experimentally measured N^* states on the left axes are matched with the relativized quark model N^* states on the right axes. The predicted amplitudes, shown with boxes, line up fairly well with the experimentally determined amplitudes, shown with crosses and error bars. The $N\frac{3}{2}^+(1720)$ resonance had the largest disparity between the predicted and experimental amplitudes, but was very sensitive to channel mixing [39].

tions for the other states match the extracted experimental values fairly well. The source of this disparity is not well understood, although the $N\frac{3}{2}^+(1720)$ amplitude was very sensitive to decay channel mixing. States that are close in mass, have the same spin-parity, and have similar couplings to $N\pi$ are likely to mix with the many decay channels available. This mixing may alter the individual channel couplings of the N^* states, and was not taken into account in these amplitude predictions.

The χ^2 per degree of freedom is a common measure of fit quality, and for normally distributed independent variables x_i is defined as [54]:

$$\frac{\chi^2}{N} = \frac{1}{N}\sum_{i=1}^{N}\frac{(x_i - \mu_i)^2}{\sigma_i^2}, \tag{2.7}$$

where the summation is over the N degrees of freedom, and the μ_i and σ_i are the means and standard deviations of the x_i variables. The expectation value of χ^2/N is equal to 1.0, and so the quality of a fit can be characterized by a comparison to this value [54]. For the lower-lying N^* states, the χ^2 per degree of freedom of the $|A_{N\pi}|$ amplitude predictions was $\sim$4.2. However with the $N\frac{3}{2}^+(1720)$ excluded, the χ^2 per degree of freedom reduced to $\sim$2.7 [39].

Capstick and Roberts also calculated the coupling amplitudes of the N^* and Δ^* states to several strangeness channels, including ΛK, ΣK, $\Lambda(1405)K$, $\Lambda(1520)K$, $\Sigma(1385)K$, ΛK^*, and ΣK^* [40]. These predictions are shown for the N^* model states with mass below 2200 MeV/c^2 in Figures 2.7 through 2.10 for the ΛK, ΣK, ΛK^*, and $\Sigma(1385)K$ channels, respectively. These figures illustrate the experimental status of these resonances in the $N\pi$ channel, along with the predictions of their coupling amplitudes to the $N\pi$, $N\gamma$, and strangeness channels. The $N\gamma$ transition amplitudes were calculated using an electromagnetic transition operator with relativized-quark-model wavefunctions, as detailed in References [55] and [56]. The predictions for the coupling amplitudes to the strangeness channels compare favorably to the experimental values that have been reliably determined, which are largely in the ΛK channel [40].

Although the coupling amplitudes to the strangeness channels are generally smaller than those to $N\pi$, the strangeness channels are still promising for N^* searches. Because the N^* resonance masses are several hundred MeV/c^2 wide, the lower-mass N^* states overlap with the unobserved high-mass states in the $N\pi$ channel. These effects are significantly reduced in the strangeness channels due to their higher-energy production thresholds. Therefore, some of the high-mass N^* states with small $N\pi$ coupling amplitudes may be easier to extract in the strangeness channels, where some of the

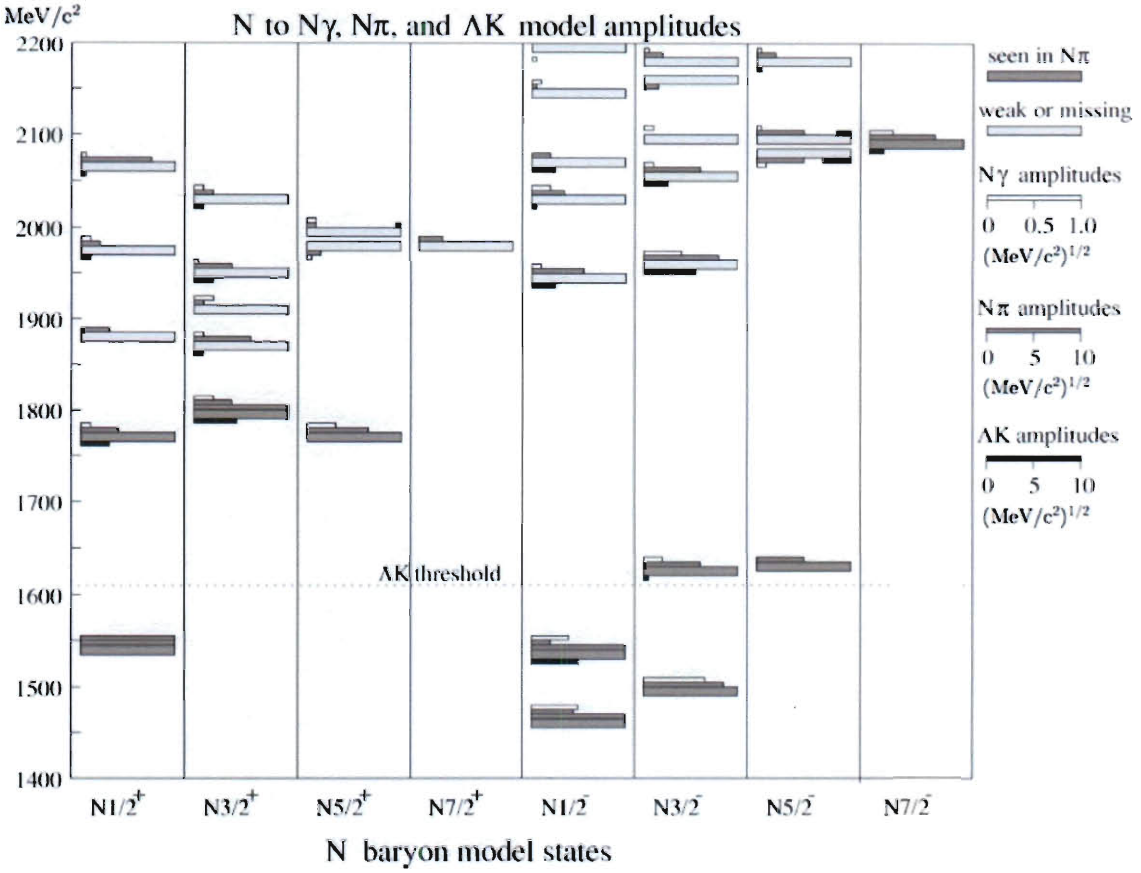

Figure 2.7 : The coupling amplitude predictions of the N^* model states with mass below 2200 MeV/c^2 into the $N\gamma$, $N\pi$, and ΛK channels [40]. The N^* states are sorted by their mass and spin-parity, and are shaded based on the experimental evidence for their existence. The $N\gamma$, $N\pi$, and ΛK amplitudes are represented by the length of the colored bars near the resonances. The $N\gamma$ and $N\pi$ amplitudes are shown to illustrate whether the $\gamma N \rightarrow N^* \rightarrow \Lambda K$ or the $\pi N \rightarrow N^* \rightarrow \Lambda K$ production reaction may be more favorable for the extraction of the given state.

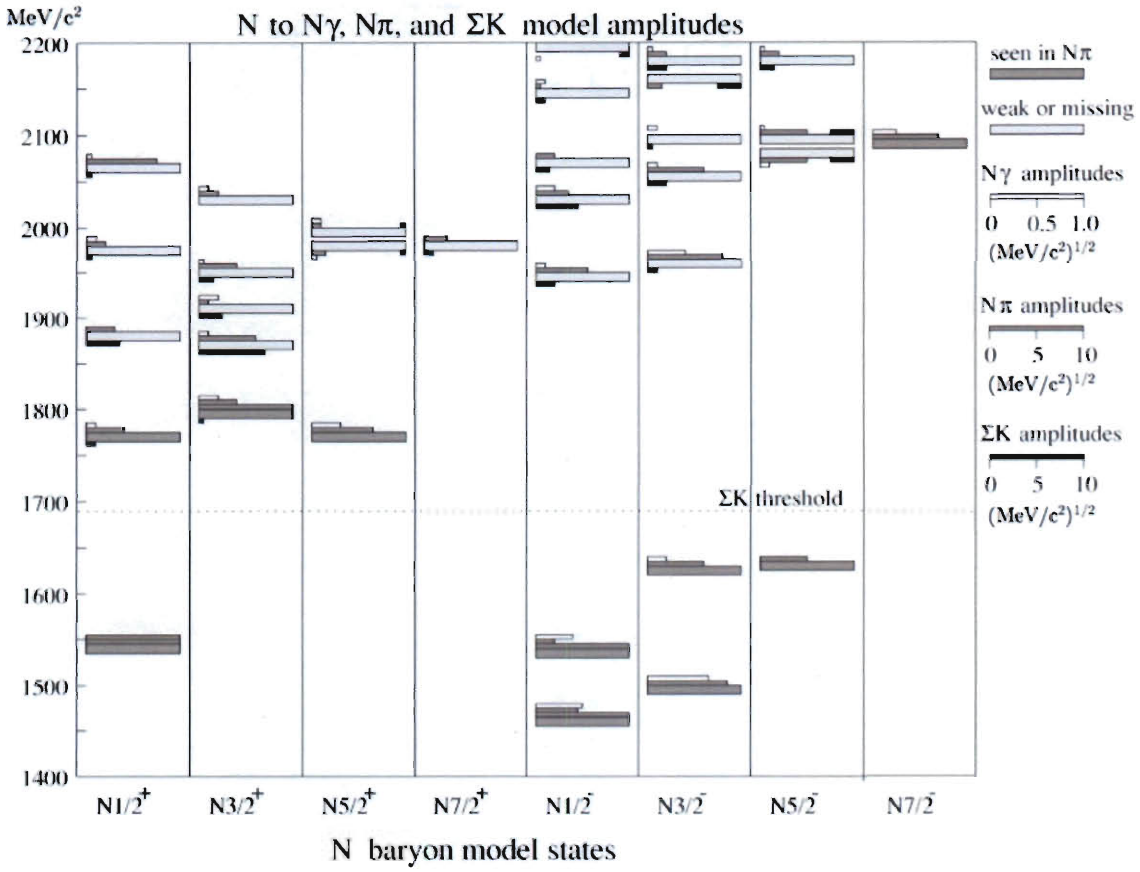

Figure 2.8 : The coupling amplitude predictions of the N^* model states with mass below 2200 MeV/c^2 into the $N\gamma$, $N\pi$, and ΣK channels [40]. The N^* states are sorted by their mass and spin-parity, and are shaded based on the experimental evidence for their existence. The $N\gamma$, $N\pi$, and ΣK amplitudes are represented by the length of the colored bars near the resonances. The $N\gamma$ and $N\pi$ amplitudes are shown to illustrate whether the $\gamma N \rightarrow N^* \rightarrow \Sigma K$ or the $\pi N \rightarrow N^* \rightarrow \Sigma K$ production reaction may be more favorable for the extraction of the given state.

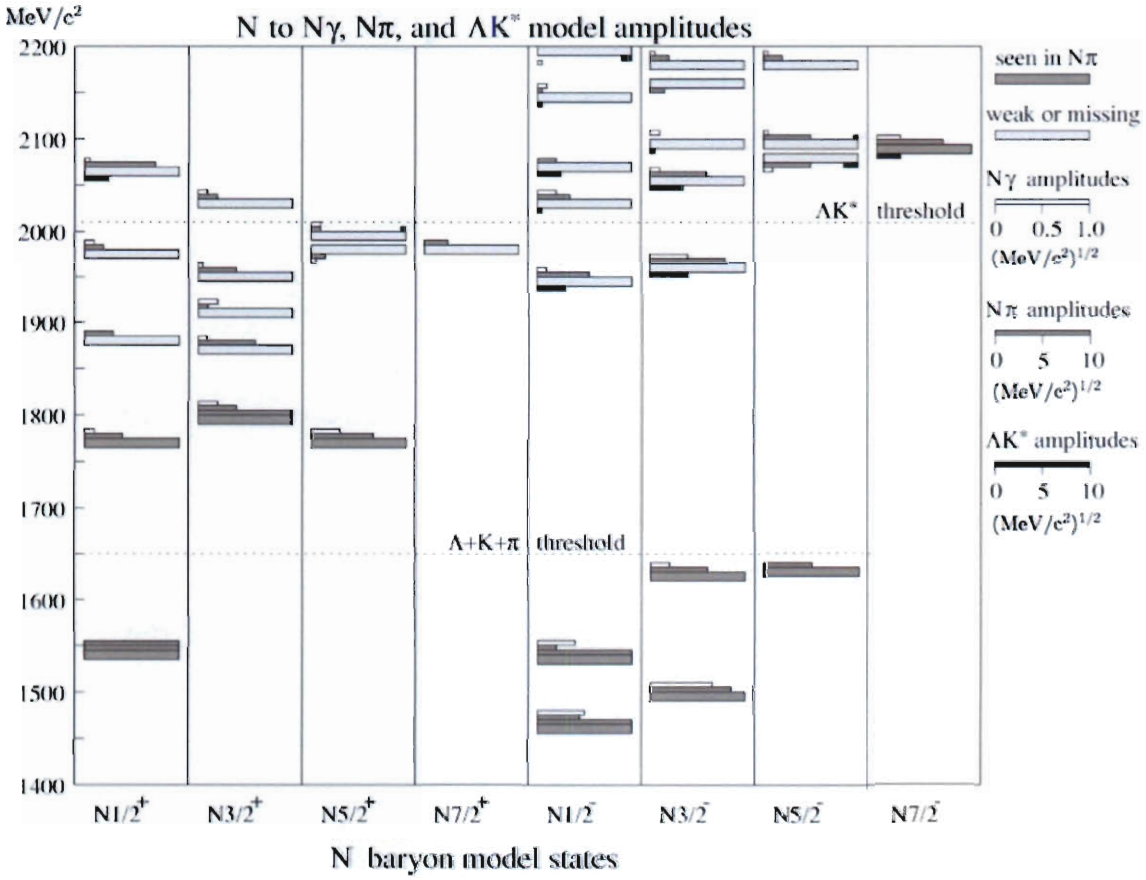

Figure 2.9 : The coupling amplitude predictions of the N^* model states with mass below 2200 MeV/c^2 into the $N\gamma$, $N\pi$, and ΛK^* channels [40]. The N^* states are sorted by their mass and spin-parity, and are shaded based on the experimental evidence for their existence. The $N\gamma$, $N\pi$, and ΛK^* amplitudes are represented by the length of the colored bars near the resonances. The $N\gamma$ and $N\pi$ amplitudes are shown to illustrate whether the $\gamma N \rightarrow N^* \rightarrow \Lambda K^*$ or the $\pi N \rightarrow N^* \rightarrow \Lambda K^*$ production reaction may be more favorable for the extraction of the given state.

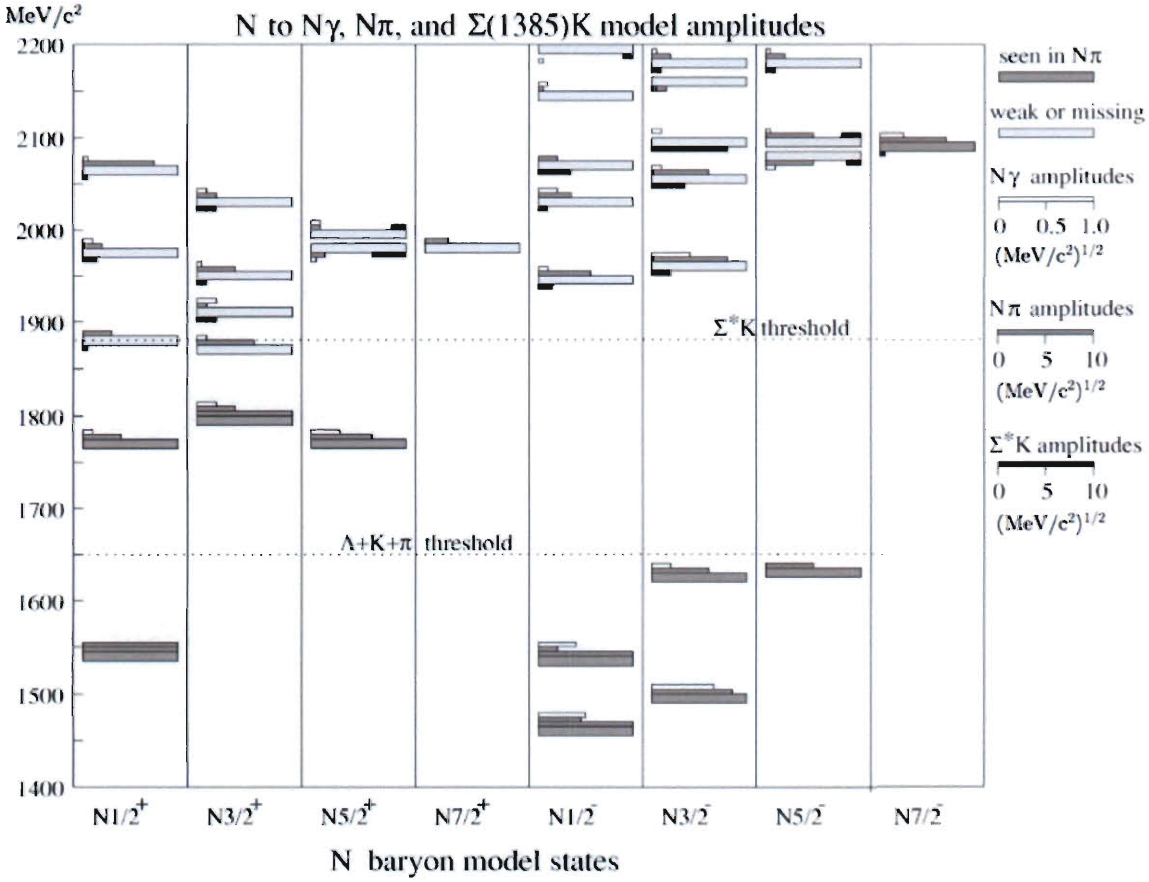

Figure 2.10 : The coupling amplitude predictions of the N^* model states with mass below 2200 MeV/c^2 into the $N\gamma$, $N\pi$, and $\Sigma(1385)K$ channels [40]. The N^* states are sorted by their mass and spin-parity, and are shaded based on the experimental evidence for their existence. The $N\gamma$, $N\pi$, and $\Sigma(1385)K$ amplitudes are represented by the length of the colored bars near the resonances. The $N\gamma$ and $N\pi$ amplitudes are shown to illustrate whether the $\gamma N \rightarrow N^* \rightarrow \Sigma(1385)K$ or the $\pi N \rightarrow N^* \rightarrow \Sigma(1385)K$ production reaction may be more favorable for the extraction of the given state.

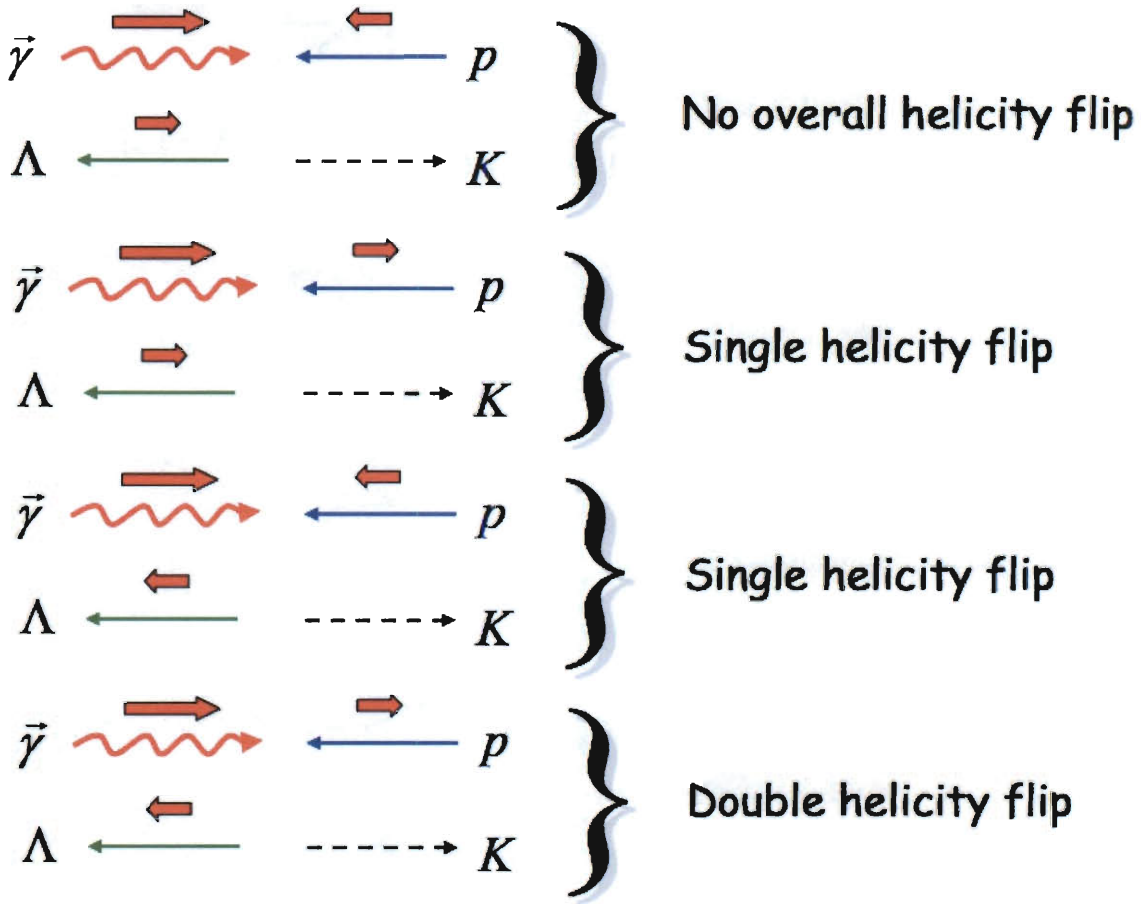

Figure 2.11 : The different possible helicity flip combinations for the $\gamma p \rightarrow K^{+}\Lambda$ reaction [58]. The particle arrows represent the direction of their momenta in the center-of-mass frame, and the red arrows the direction of their spin. Combinations of these helicity amplitudes yield 16 different polarization observables [57].

unobserved states are predicted to dominate over the others, such as the $N\frac{3}{2}^-(1960)$. However, one of the primary challenges in extracting the N^* states through the strangeness channels is that the reaction cross sections are significantly lower than those in the $N\pi$ channel.

2.3.3 Searching for N^* States

Due to the large experimental background and their large resonance widths, it is extremely unlikely that new N^* states will be directly observable through the invariant mass of their decay products. As discussed in Chapter 3 for the $\gamma n \to K^*(892)^0\Lambda$ and the $\gamma n \to K^+\Sigma^*(1385)^-$ reactions, the dominant photoproduction process leading to these strangeness final-states is not N^* decays but t-channel meson exchange. Instead, partial-wave analyses are necessary to extract the masses and widths of the contributing N^* states. In these analyses, the angular dependence of a given differential cross section is decomposed into a series of partial waves. Each N^* resonance contributes to the partial-wave corresponding to its spin and orbital angular momentum quantum numbers. However, if multiple N^* resonances contribute strongly to the same partial-wave they may be difficult to disentangle, especially if they overlap in mass.

By studying the amplitudes shown in Figures 2.7 through 2.10, predictions may be made as to which N^* resonances are most likely to be extracted in the given channels. In the ΛK channel the $N\frac{3}{2}^-(1960)$ model state, which corresponds to the PDG two-star $N\frac{3}{2}^-(2080)$ state, is predicted to be clearly observed. That is because it has a dominantly large coupling to ΛK compared to the other N^* states with the same spin-parity, or the same partial-wave. Also, while the predicted $N\frac{5}{2}^-(2080)$ and $N\frac{5}{2}^-(2095)$ states have similar couplings to ΛK and nearly the same mass, the $N\frac{5}{2}^-(2080)$ couples much more strongly to $N\gamma$ and thus is predicted to be separable in photoproduction experiments. Similarly, in the ΣK channel the $N\frac{1}{2}^+(1880)$ is predicted to be visible in the $\pi N \to \Sigma K$ reaction, and the $N\frac{3}{2}^+(1910)$ in photoproduction experiments [40].

Several of the high-mass N^* states are also predicted to couple strongly to the excited strangeness channels. The N^* states that are predicted to be observable in the ΛK channel are generally the same as those in the ΛK^* channel. Although the nearby $N\frac{3}{2}^-(2055)$ is also predicted to have a large coupling to ΛK^*, the $N\frac{3}{2}^-(1960)$ should still be extractable through its dominance in photoproduction. Also, the $N\frac{1}{2}^+(2065)$ may be observable because it is the only state with $J^P = \frac{1}{2}^+$ that has a large predicted coupling to ΛK^*. However, in the $\Sigma(1385)K$ channel there are fewer promising

Photon Beam	Target and/or Recoil Polarization																	
	Neither		Recoil			Target			Recoil & Target									
			x	y	z				x			y			z			
						x'	y'	z'	x'	y'	z'	x'	y'	z'	x'	y'	z'	
Unpolarized				P			T		T_x		L_x		Σ		T_z		L_z	
Linearly Polarized	σ	Σ	O_x	T	O_z	H	P	G	L_z	C_z	T_z	E		F	L_x	C_x	T_x	
Circularly Polarized			C_x		C_z	F		E		O_z		G		H		O_x		

Figure 2.12 : The combinations of beam and target polarizations necessary to measure the polarization observables of the $\gamma N \rightarrow K\Lambda$ reaction [59]. The axes used to define the recoil and target coordinates are illustrated in Figure 2.13. Details on the polarization observables and their extraction are discussed in Reference [57].

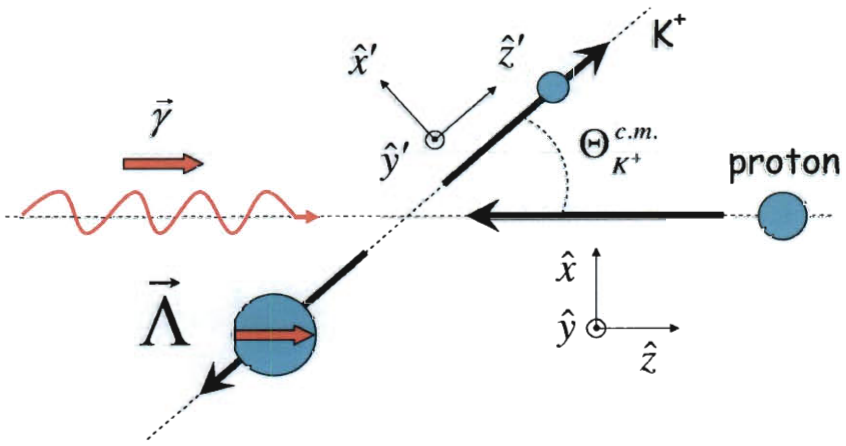

Figure 2.13 : Definitions of the axes used to define the polarization observables of the $\gamma p \rightarrow K^+\Lambda$ reaction in the center-of-mass frame [60]. The red arrows indicate an example of the possible polarization transfer in this reaction.

N^* states for extraction. Although several N^* states have large predicted couplings to $\Sigma(1385)K$, they may be difficult to distinguish due to their proximity in mass, such as the $N\frac{3}{2}^-(2055)$ and $N\frac{3}{2}^-(2095)$ resonances. Also, while the $N\frac{5}{2}^+(1980)$ has a much larger coupling to $\Sigma(1385)K$ than the $N\frac{5}{2}^+(1995)$, it has a smaller coupling to $N\gamma$ and thus may not be observable in photoproduction experiments. [40].

Due to isospin conservation in strong decays, the Δ^* resonances cannot decay into Λ channels. Since the K's have isospin $I = \frac{1}{2}$ and the Λ's have $I = 0$, the $I = \frac{3}{2}$ Δ^*'s cannot couple to the $K\Lambda$ channel, while the $I = \frac{1}{2}$ N^*'s can. It will likely be easier to extract N^* resonances from the Λ channels than from the $I = 1$ Σ and Σ^* channels since there are no Δ^* backgrounds in the Λ channels [40].

2.4 N^* Resonance Extraction

In many cases, the production cross sections do not contain enough information to unambiguously determine the contributing partial waves of the N^* states due to the spin of the particles [43]. Experimental measurements of the polarization observables of these reactions can provide the necessary spin-dependent information. For example, in pseudoscalar meson photoproduction there are 16 polarization observables [57]. These arise from the combinations of the four complex helicity amplitudes in the reaction, which are illustrated in Figure 2.11 for the $\gamma p \rightarrow K^+\Lambda$ reaction. The helicity of a particle is the projection of its spin in the direction of its momentum. These 16 observables are accessible through different combinations of polarized beams, polarized targets, and the Λ recoil polarization, as shown in Figure 2.12 [57]. The axes used to define these polarization observables are shown in Figure 2.13 for the $\gamma p \rightarrow K^+\Lambda$ reaction. Due to their constraint equations, a minimum of eight polarization observables need to be measured to determine the full set in pseudoscalar meson photoproduction reactions [61]. The polarization observables in vector meson photoproduction reactions are discussed in Reference [62].

However, rescattering effects can play a significant role in the extraction of N^* resonances in partial-wave analyses of the strangeness channels. Because the amplitudes for $\gamma N \rightarrow \pi N$ are generally much larger than those for $\gamma N \rightarrow KY$, rescattering off other nucleons in the target through $\gamma N \rightarrow \pi N \rightarrow KY$ can have up to a 20% effect on the total cross section [63]. Rescattering effects are predicted to not only alter the energy dependence of the $\gamma N \rightarrow \pi N$ and $\gamma N \rightarrow KY$ cross sec-

tions, but may also produce structures in these cross sections that resemble resonance contributions [64]. Because the photoproduction cross sections of the excited strangeness channels K^*Y and KY^* are sizable compared to those of the ground states, rescattering effects in these channels may be significant as well.

Coupled-channel partial-wave analyses can be used to take these rescattering effects into account, and to provide model parameter constraints on the N^* resonance contributions from several different channels simultaneously [65]. Several different models can be used to calculate these channel coupling effects, including the K-matrix scattering formalism [64, 43] and effective Lagrangian models of the interactions [66, 67]. These models calculate the transitions between the channels that are included in the calculations, which can be incorporated with their cross section data, polarization observables, and interaction vertex coupling strengths. Because the rescattering effects may be significant for the K^*Y and KY^* channels, they need to be included in coupled-channel analyses as well [68, 69].

Although it will be some time until all of the cross sections and polarization observables are measured for the strangeness channels, some coupled-channel analyses have already begun. Nikonov *et al.* [43] performed an analysis of the recently published beam-recoil polarization observables C_x and C_z of the $\gamma p \rightarrow K^+\Lambda$ and $\gamma p \rightarrow K^+\Sigma^0$ reactions from CLAS data [60]. For these and the $\gamma p \rightarrow K^0\Sigma^+$ reaction, the differential cross sections, recoil polarizations, and photon beam asymmetries were included in their analysis, in addition to measurements in several non-strange channels. It was found that the current spectrum of resonances could not reproduce the experimental data without including the partial-wave for the PDG $N\frac{3}{2}^+(1900)$ two-star state. Figures 2.14 through 2.16 show fits to the differential cross sections and polarization observables for the $\gamma p \rightarrow K^+\Lambda$ and $\gamma p \rightarrow K^+\Sigma^0$ reactions both with and without the resonance included in the fits. Although not a full coupled-channels analysis, these fits show strong evidence for the existence of the $N\frac{3}{2}^+(1900)$ state that is precluded in diquark models.

In pseudoscalar meson photoproduction reactions, measurements on both the proton and the neutron are necessary to resolve the isospin components of the photo-transition amplitudes. These isoscalar and isovector components arise from the fact that the electromagnetic interaction does not conserve isospin, as seen in $\Sigma^0 \rightarrow \Lambda\gamma$ decay. These amplitudes are needed to constrain phenomenological models of the nucleons and their photocouplings to the N^* resonances [73].

Finally, it is important to measure the properties of the excited states of both the proton and the

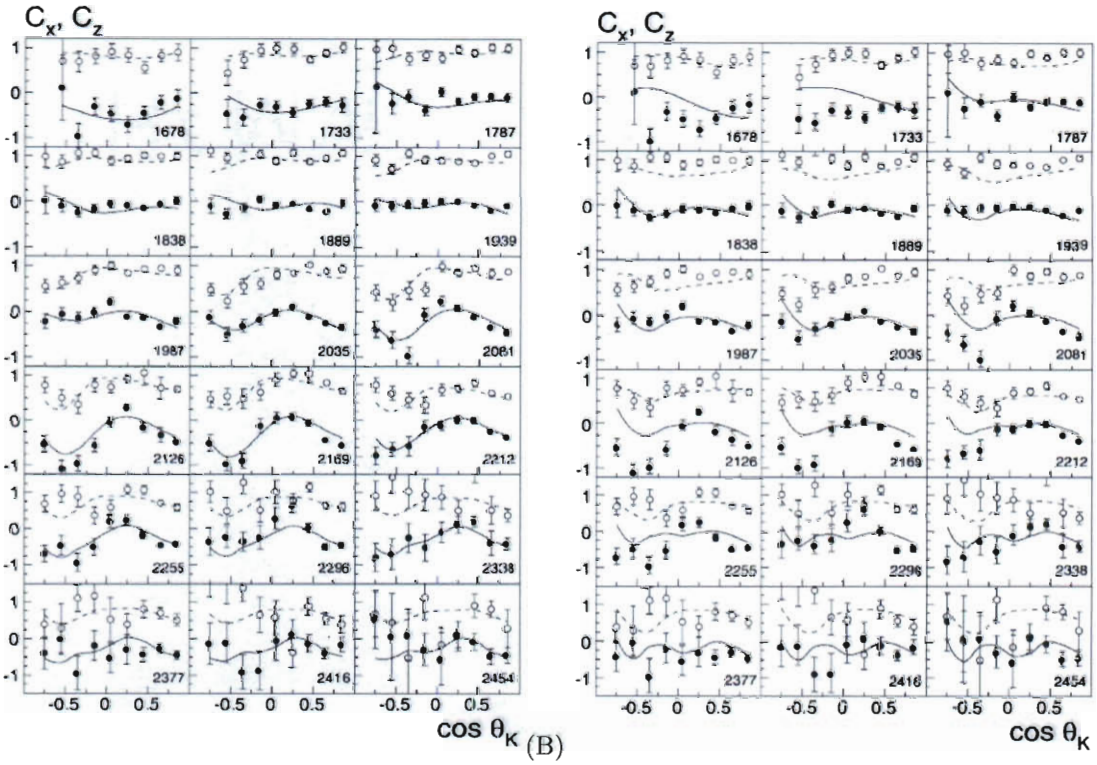

Figure 2.14 : Fits to the CLAS beam-recoil polarization observables C_x and C_z of the $\gamma p \rightarrow K^+\Lambda$ reaction from CLAS [60] with (A) and without (B) the $N\frac{3}{2}^+(1900)$ state included in the fits [43]. Each plot corresponds to a different bin in W, the energy of the system in the center of mass frame, given in units of MeV. The values of C_x (black points) and C_z (open points) are shown as a function of $\cos(\theta_K)$, where θ_K is the angle between the K^+ and the photon in the center-of-mass frame. The fits to C_x and C_z are shown by the solid and dashed curves, respectively.

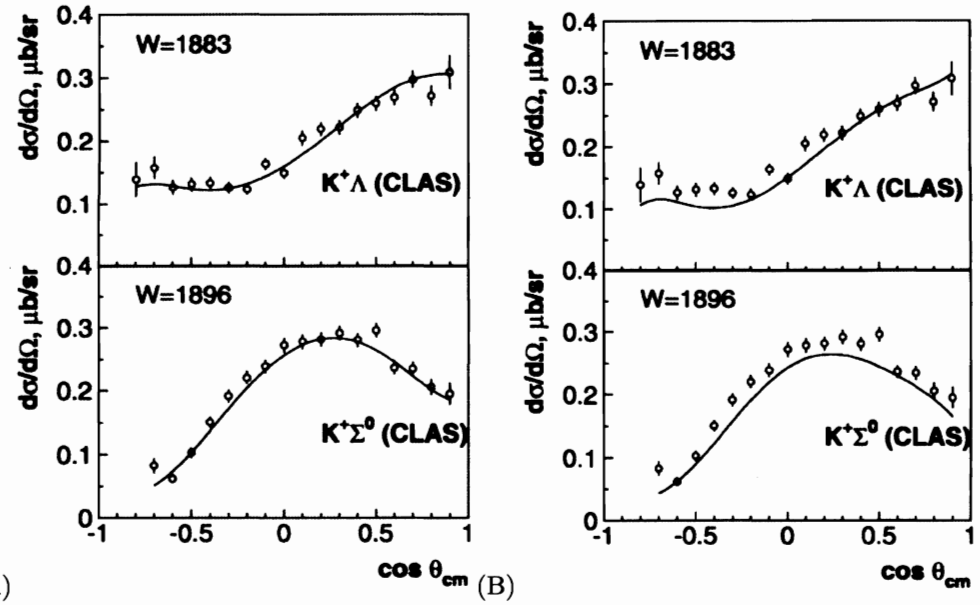

Figure 2.15 : Fits to the differential cross sections of the $\gamma p \rightarrow K^+\Lambda$ and $\gamma p \rightarrow K^+\Sigma^0$ reactions from CLAS [70, 71], with (A) and without (B) the $N\frac{3}{2}^+(1900)$ state included in the fits [43]. Each plot corresponds to a different bin in W, the energy of the system in the center of mass frame, given in units of MeV. The data are shown as a function of $\cos(\theta_{\rm cm})$, where $\theta_{\rm cm}$ is the angle between the K^+ and the photon in the center-of-mass frame.

neutron. Due to their valence quark content, these excited states may have different characteristics, as well as different couplings to the individual reaction channels. This information can be used to provide a greater understanding of how the differences between the up and down quarks affect the behavior of the nucleons.

This analysis of the cross sections of the $\gamma n \rightarrow K^{*0}\Lambda$ and $\gamma n \rightarrow K^+\Sigma^{*-}$ reactions is an important part of the search for the N^* states. Several of the missing, high-mass N^* states are predicted to be observable in these channels through partial-wave analyses. Measurement of the spectrum of the N^* states will help determine the role of diquarks within the nucleon.

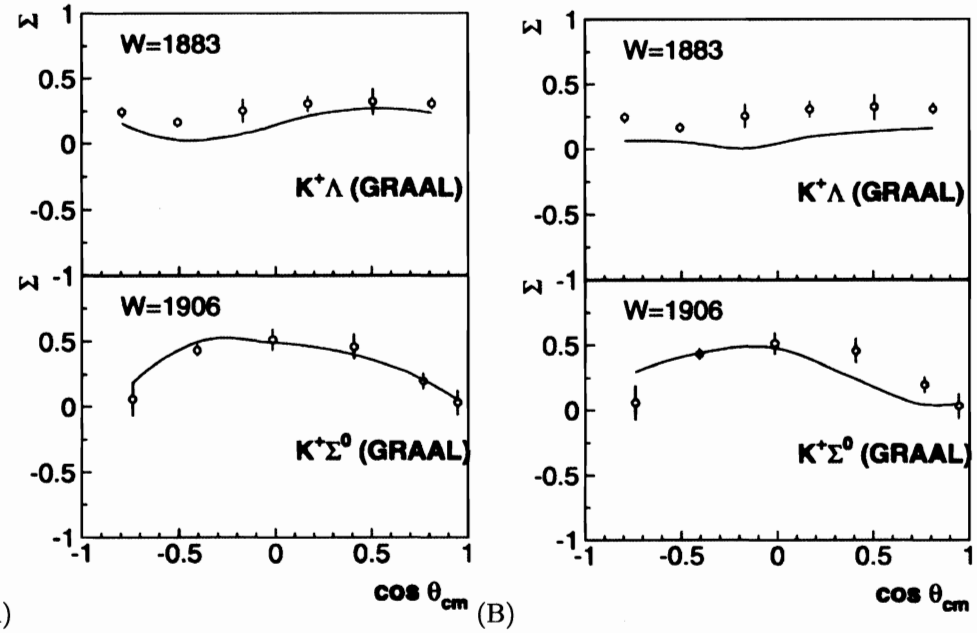

Figure 2.16 : Fits to the beam asymmetries of the $\gamma p \rightarrow K^+\Lambda$ and $\gamma p \rightarrow K^+\Sigma^0$ reactions [72], with (A) and without (B) the $N\frac{3}{2}^+(1900)$ state included in the fits [43]. Each plot corresponds to a different bin in W, the energy of the system in the center of mass frame, given in units of MeV. The data are shown as a function of $\cos(\theta_{\rm cm})$, where $\theta_{\rm cm}$ is the angle between the K^+ and the photon in the center-of-mass frame.

Chapter 3

$\gamma n \to K^{*0}\Lambda$ & $\gamma n \to K^{+}\Sigma^{*-}$ Overview

As discussed in Chapter 2, the excited strangeness channels are important for N^* searches due to the expected non-negligible couplings of some of the higher-mass resonances to these channels. In photoproduction reactions, it is necessary to study these channels on both the proton and the neutron to determine the isospin components of the photo-transition amplitudes. The cross sections for these excited channels, such as those for $\gamma n \to K^*(892)^0\Lambda$ and $\gamma n \to K^+\Sigma^*(1385)^-$, are sizable compared to those of the ground state reactions. Therefore, it is important to include these channels in the coupled-channel partial-wave analyses that can be used to extract the N^* resonances.

In this analysis, the $\gamma n \to K^*(892)^0\Lambda$ and $\gamma n \to K^+\Sigma^*(1385)^-$ cross sections were measured using data from the CLAS g13 experiment at Jefferson Lab. No data have been published on the $\gamma n \to K^*(892)^0\Lambda$ cross section, and the only $\gamma n \to K^+\Sigma^*(1385)^-$ cross section measurement [74] is limited to forward angles. On the proton, preliminary total cross section measurements of the $\gamma p \to K^*(892)^+\Lambda$ and $\gamma p \to K^+\Sigma^*(1385)^0$ analyses [75] have been performed. Also, the differential cross section of the $\gamma p \to K^*(892)^0\Sigma^+$ reaction has been published as well [76, 77]. Details of the g13 experiment, the CLAS detector, and the CEBAF accelerator at Jefferson Lab are located in Chapter 4.

The $K^*(892)^0$ (K^{*0}) and $\Sigma^*(1385)^-$ (Σ^{*-}) excited states decay too quickly to be detected, so in this analysis they were reconstructed through their decay products. Because these reactions have the same final-state particles they may interfere, so most of the region of their overlap was removed from this analysis. Model predictions for the cross sections of the $\gamma n \to K^{*0}\Lambda$ [68] and $\gamma n \to K^+\Sigma^{*-}$

[69, 78] reactions are given in the following sections, and were derived using the method of effective Lagrangians.

3.1 $\gamma n \rightarrow K^{*0}\Lambda$ Overview

As discussed in Section 2.3.2, the $N\frac{3}{2}^{-}(1960)$, $N\frac{1}{2}^{+}(2065)$, and $N\frac{5}{2}^{-}(2080)$ states show promise of being extracted through their coupling to the $\gamma n \rightarrow K^{*0}\Lambda$ reaction. However, there are no published data on either the cross section or polarization observables of this reaction. As such model predictions for these quantities are not well constrained, although the recently published preliminary total cross section of the $\gamma p \rightarrow K^{*+}\Lambda$ reaction [75] provides information on $\gamma n \rightarrow K^{*0}\Lambda$ through SU(3) flavor symmetry. Comparisons between the measured and predicted cross sections and polarization observables can provide insight into the processes contributing to this reaction.

Predictions for the cross section and some of the polarization observables of the $\gamma n \rightarrow K^{*0}\Lambda$ and $\gamma p \rightarrow K^{*+}\Lambda$ reactions by Oh and Kim [68] were determined by calculating the production amplitudes for these reactions using the method of effective Lagrangians. This method treats baryons as point-like particles, and models the strength of their interactions at each vertex with coupling constants. Although these predictions don't include coupled-channels effects, they are an important first attempt at modeling these reactions. As illustrated in Figure 3.1, this model included contributions from t-channel, s-channel, and u-channel interactions. A contact term, in which all of the particles couple to the same interaction vertex, was included for the $\gamma p \rightarrow K^{*+}\Lambda$ reaction but not for the $\gamma n \rightarrow K^{*0}\Lambda$ reaction [68].

In the predicted $\gamma n \rightarrow K^{*0}\Lambda$ t-channel interactions of this model, the photon couples directly to the K^{*0} by exchanging a virtual K^0 or κ with the target neutron to produce a Λ. Although the κ, or $K^{*}(800)^0$, is a controversial state that needs confirmation [8], its coupling to this channel is predicted to be suppressed. In the u-channel the photon instead couples to the produced Λ, and intermediate Λ, Σ^0, and Σ^{*0} virtual particles were included. In the s-channel only the ground state neutron was considered due to the lack of information on the N^* resonances [68]. Although not included, the $N\frac{1}{2}^{-}(1945)$, $N\frac{3}{2}^{-}(1960)$, $N\frac{1}{2}^{+}(2065)$, $N\frac{5}{2}^{-}(2080)$, and $N\frac{7}{2}^{-}(2090)$ model states are predicted by Capstick and Roberts to have strong couplings to this channel [40]. The Lorentz-invariant t, s, and u Mandelstam variables represent the reference-frame-invariant quantities that characterize the kinematics of these interactions, and their definitions are located in Reference [8].

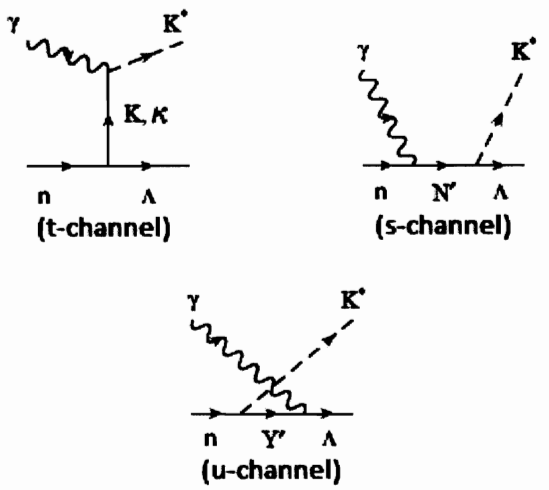

Figure 3.1 : Depictions of the t-channel, s-channel, and u-channel interactions considered in the model by Oh and Kim for the $\gamma n \to K^{*0}\Lambda$ reaction [68].

The effective Lagrangians for these reactions were constructed for each interaction vertex in the system, with the terms of the particles multiplied by the interaction coupling constants. The coupling constants used in this model, such as $g_{KN\Lambda}$, were determined from either phenomenology or quark model predictions when not available from experimental data. To calculate the production amplitudes, a non-point-like QCD substructure was modeled at each vertex by multiplying the interaction vertex terms with form factors. These vertices were then joined together by the propagators for the exchanged particles in the given channels. The cutoff parameters used in the calculation of the form factors were determined by matching to a preliminary total cross section measurement of the $\gamma p \to K^{*+}\Lambda$ reaction [75]. More details on the model calculations of the $\gamma n \to K^{*0}\Lambda$ and $\gamma p \to K^{*+}\Lambda$ reactions are discussed in Reference [68].

However, after the publication of these predictions a scaling error was discovered in the calculation of the preliminary $\gamma p \to K^{*+}\Lambda$ total cross section [79], and updated model predictions have not yet been performed [78]. Although the cross section predictions illustrated in Figures 3.2 and 3.3 need to be updated, the characteristics of their distributions can still be studied. The total cross sections of the $\gamma p \to K^{*+}\Lambda$ and $\gamma n \to K^{*0}\Lambda$ reactions are predicted to rise rapidly with photon energy from their production thresholds of just below 1.7 GeV, peak just above 2.0 GeV, then slowly decrease at higher energies. The differential cross section of the $\gamma n \to K^{*0}\Lambda$ reaction is plotted as a function

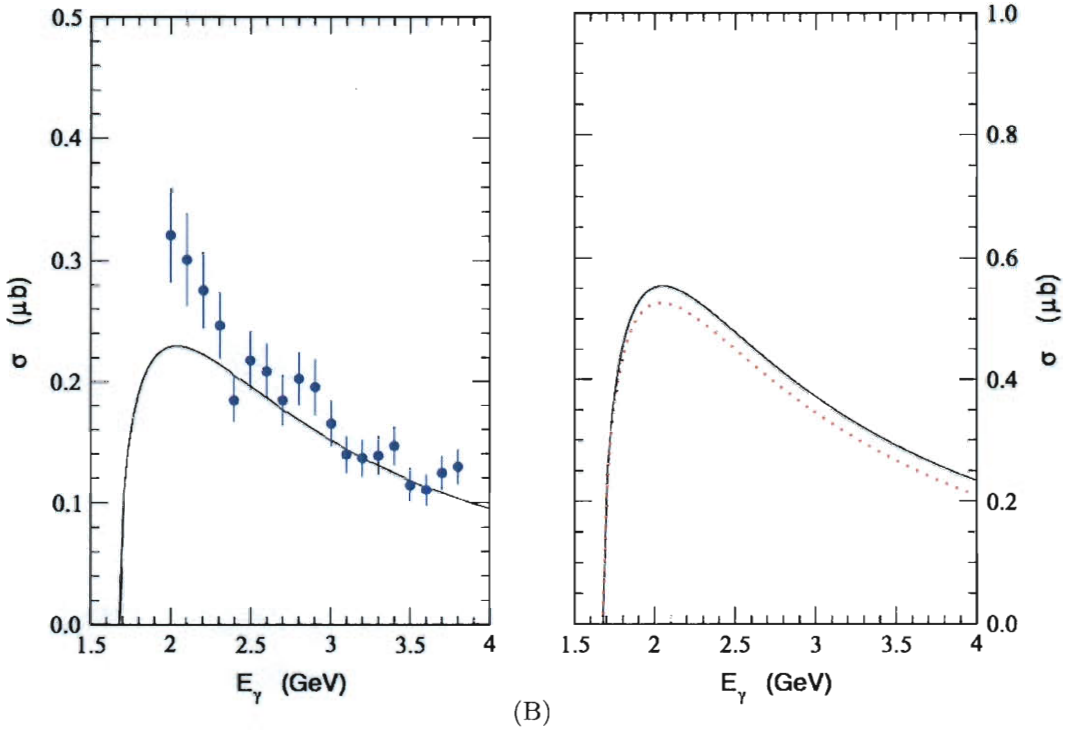

(A) (B)

Figure 3.2 : The $\gamma p \rightarrow K^{*+}\Lambda$ (A) and $\gamma n \rightarrow K^{*0}\Lambda$ (B) total cross section predictions as a function of photon energy, shown by the black curves [68]. The red, dotted curve indicates the predicted contributions from t-channel K exchange for the $\gamma n \rightarrow K^{*0}\Lambda$ reaction. The blue points are the CLAS preliminary total cross section data of the $\gamma p \rightarrow K^{*+}\Lambda$ reaction [75]. A scaling error was present in these preliminary CLAS data, which were too low by a factor of 1.5 [79].

of $\cos(\theta)$ in Figure 3.3, where θ is the angle between the K^{*0} and the photon in the center-of-mass frame. It is predicted to be strongly forward-peaked, with a slight rise at backward angles.

The preliminary $\gamma p \rightarrow K^{*+}\Lambda$ total cross section data are also shown in Figure 3.2(A), but are too low by a factor of 1.5 due to the scaling error [79]. The large difference between the experimental data and the predictions near 2.0 GeV was thought to partially be due to N^* resonance contributions, which were not included in the model predictions [68]. However until the model predictions are updated, it is difficult to interpret the differences between the preliminary $\gamma p \rightarrow K^{*+}\Lambda$ total cross section data and the model.

Due to their kinematics, the different interaction channels of Figure 3.1 will manifest themselves at different energy and angular regions of the $\gamma n \rightarrow K^{*0}\Lambda$ cross section. In the t-channel, since the photon couples to the produced meson, the contributions to the cross section are primarily at forward angles to the beamline. In the u-channel the photon couples to the produced baryon,

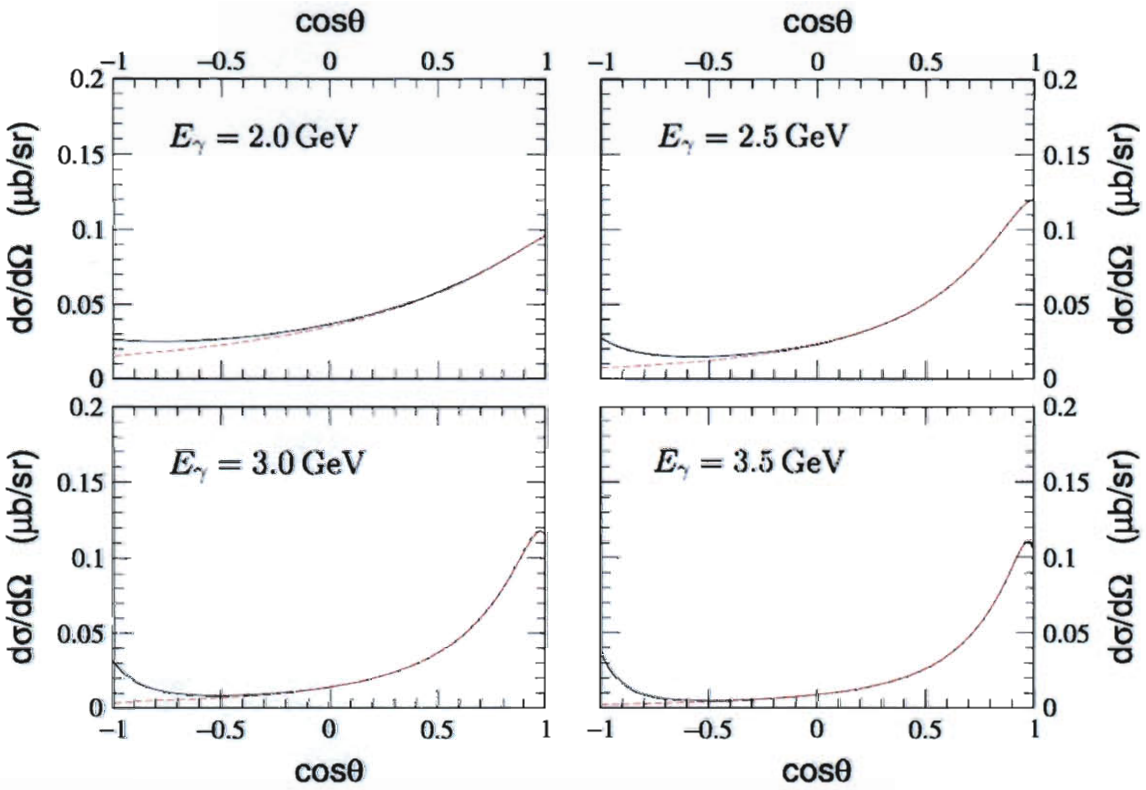

Figure 3.3 : The prediction of the $\gamma n \to K^{*0}\Lambda$ differential cross section shown in bins of E_γ as a function of $\cos(\theta)$, where θ is the angle between the K^{*0} and the photon in the center-of-mass frame. The black curves are the differential cross section predictions, and the red, dashed curves indicate the predicted contributions from t-channel K^0 exchange [68].

so the contributions to the cross section are primarily at backward angles. The regions of the s-channel contributions to the cross section depends on the masses of the individual states and their partial-waves. As shown by the red curve in Figures 3.2 and 3.3, the dominant process in these reactions is predicted to be t-channel K exchange. However, since the N^* resonance contributions were not included in this model, any significant deviations from these cross section predictions could potentially indicate N^* resonance effects.

With a resonance width, or decay rate, of 48.7 MeV/c^2, the mean lifetime of the K^{*0} particle is $\tau = \hbar/\Gamma = 1.35 \times 10^{-23}$ s, where $\hbar$ is the reduced Planck constant. This decay through the strong force occurs far too rapidly for the K^{*0} to be detected directly. Also, although the Λ lives significantly longer before it decays through the weak force, its average lifetime of 2.63×10^{-10} s means that it generally travels at most several centimeters before decaying. As shown in Chapter 4, there are no detector subsystems in CLAS capable of detecting the Λ several centimeters from the target.

Instead, these particles were reconstructed through their decay products. The Λ decays primarily into either $p\pi^-$ (~63.9%) or $n\pi^0$ (~35.8%), while the K^{*0} almost always decays into either $K^+\pi^-$ (~66.5%) or $K^0\pi^0$ (~33.3%) [8]. The K^{*0} branching ratio was quoted as ~99.8% to $K\pi$ in Reference [8], and was converted to $K^+\pi^-$ and $K^0\pi^0$ by multiplying by the squares of the corresponding Clebsch-Gordan coefficients, $\frac{2}{3}$ and $\frac{1}{3}$. The Clebsch-Gordan coefficients represent the expansion coefficients of quantized angular momentum. The coefficients corresponding to these decays were determined from the isospin magnitudes and projections of the individual particles, which are given in Table 1.2.

As discussed in Section 4.2.8, the electromagnetic calorimeters used to detect neutral particles in CLAS only span the forward 45° of the detector. Therefore, the best way to study the $\gamma n \rightarrow K^{*0}\Lambda$ reaction in CLAS is through the fully charged, $p\pi^-K^+\pi^-$ final-state. The K^+ and π^- lifetimes in their rest frames are 12.4 ns and 26.0 ns, respectively [8]. At relativistic speeds these particles can travel several meters in the lab before decaying, and are thus easily detectable. This decay chain is illustrated by the quark flow diagram in Figure 3.4.

Because free neutrons have a lifetime of about 15 minutes, fixed, free-neutron targets do not exist. Therefore, liquid-deuterium was used for the target material in the CLAS g13 experiment. Inside of a deuteron the proton and neutron are bound together, so when a photon strikes the neutron the

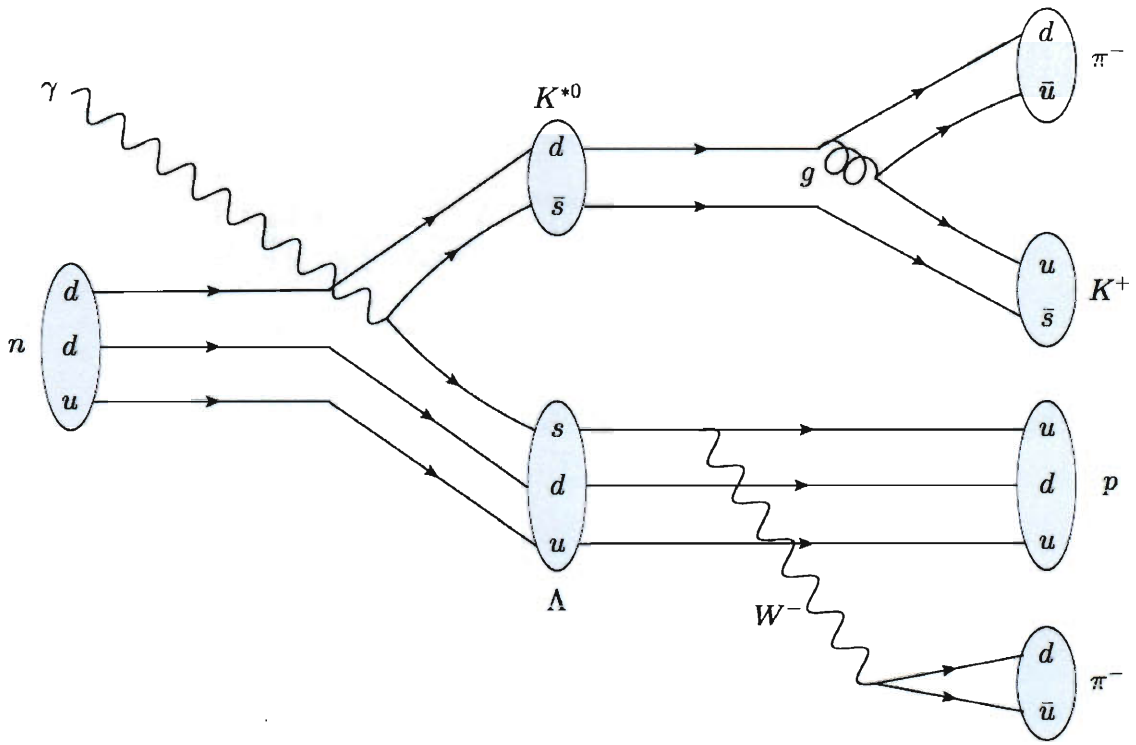

Figure 3.4 : Quark flow diagram for the $\gamma n \to K^{*0}\Lambda$ reaction, showing the decays of the K^{*0} and Λ particles into the $p\pi^{-}K^{+}\pi^{-}$ final-state.

proton is affected as well. Due to this binding the spectator proton can have non-zero momentum, known as Fermi motion. In quasi-free events where rescattering is minimal, the spectator protons typically have momenta less than 200 MeV/c.

As discussed in Section 6.2, spectator protons in quasi-free events are typically too slow to be detected in CLAS. However due to four-momentum conservation, one of the final-state particles does not need to be detected as the system will remain fully constrained. Therefore in this analysis the spectator proton remained unobserved, and its four-momentum was determined from the other four final-state particles. Although the spectator proton can be assumed to be at rest and a different particle chosen to remain unobserved to increase statistics, doing so would have introduced significant resolution smearing effects due to the Fermi motion of the nucleons.

3.2 $\gamma n \rightarrow K^{+}\Sigma^{*-}$ Overview

In Section 2.3.2 there are several N^* resonances that are predicted to couple strongly to the $\gamma n \rightarrow K^{+}\Sigma^{*-}$ reaction, including the $N\frac{3}{2}^{-}(1960)$, $N\frac{5}{2}^{+}(1980)$, $N\frac{5}{2}^{+}(1995)$, $N\frac{3}{2}^{-}(2055)$, and $N\frac{3}{2}^{-}(2095)$ states. The LEPS collaboration at SPring-8 in Japan recently published the first known data on this reaction, measurements of the differential cross section and beam asymmetry [74]. However as seen in Figure 3.5, these measurements were limited to the forward angles, where t-channel exchange is predicted to dominate. As shown in Chapter 9, the cross section from this analysis will cover a significantly larger angular range, providing a valuable contribution to N^* partial-wave analyses.

Oh, Ko, and Nakayama have made predictions for the cross section and some of the polarization observables of the $\gamma p \rightarrow K^{+}\Sigma^{*0}$ reaction [69]. These single-channel model predictions were derived using the method of effective Lagrangians, as introduced in Section 3.1. The $\gamma n \rightarrow K^{+}\Sigma^{*-}$ cross section predictions were then determined by employing SU(3) flavor symmetry to change the particles and the coupling constants used in the calculation [78].

As illustrated in Figure 3.6, this model included contact, t-channel, u-channel, and s-channel interactions for the $\gamma n \rightarrow K^{+}\Sigma^{*-}$ reaction. In the contact term, all of the particles couple to the same vertex. In the t-channel the photon couples directly to the K^{+} by exchanging a virtual K^{+} or K^{*+} with the target neutron to produce the Σ^{*-}. In the u-channel the photon couples to the produced Σ^{*-}, and intermediary Λ and Σ^{*-} virtual particles were included. The s-channel predictions incorporated the ground state neutron, along with the $N\frac{1}{2}^{-}(1945)$, $N\frac{3}{2}^{-}(1960)$, $N\frac{5}{2}^{+}(1980)$,

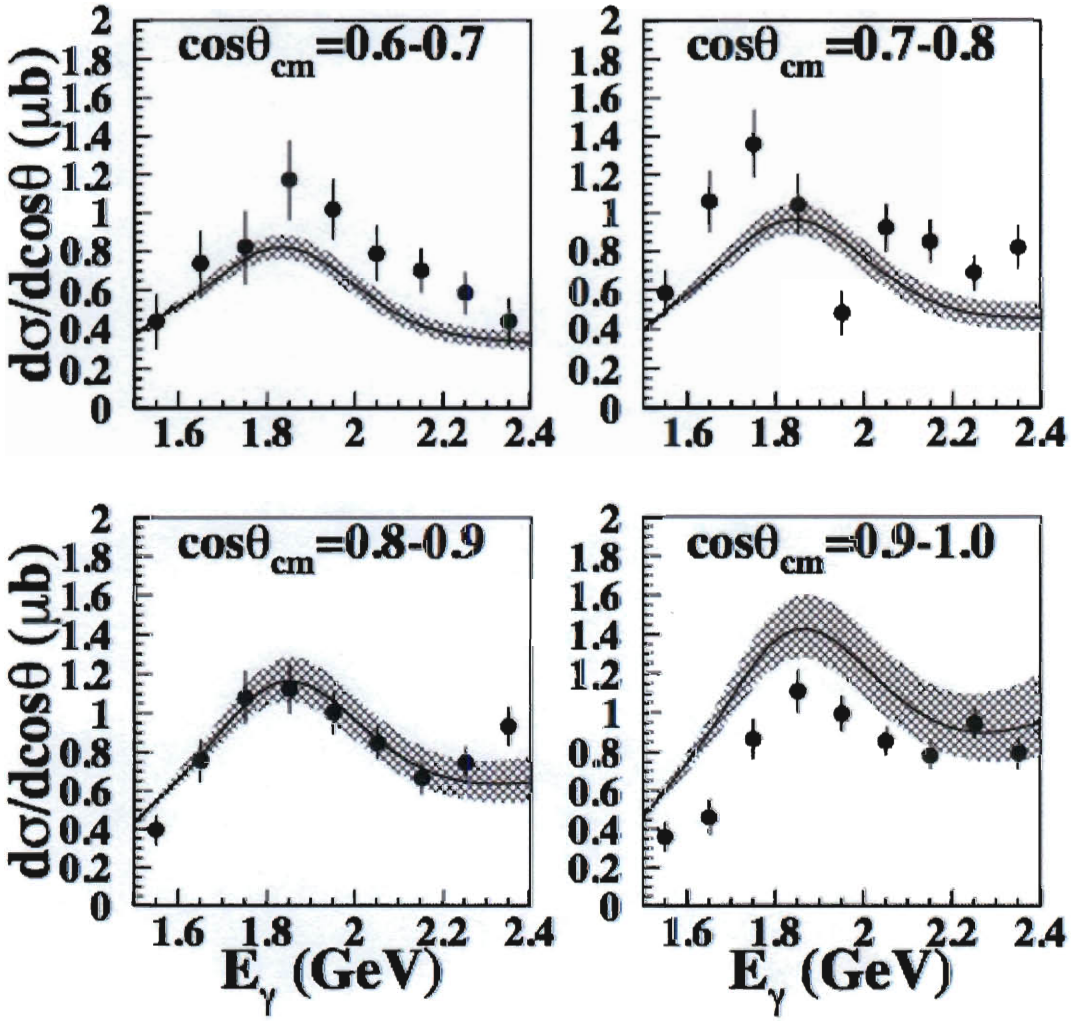

Figure 3.5 : Comparison between the LEPS data [74] (black points) and model predictions by Oh, Ko, and Nakayama [69] (black curves) of the differential cross section of the $\gamma n \to K^{+}\Sigma^{*-}$ reaction. The shaded bands represent the uncertainty of the model prediction [74].

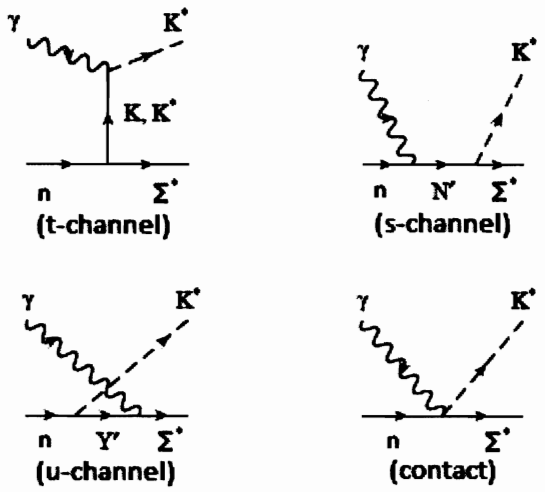

Figure 3.6 : Depictions of the t-channel, s-channel, u-channel, and contact interactions considered in the model by Oh, Ko, and Nakayama for the $\gamma n \to K^{+}\Sigma^{*-}$ reaction [69].

$N\frac{3}{2}^{-}(2095)$, $N\frac{5}{2}^{-}(2095)$, $\Delta\frac{5}{2}^{+}(1990)$, $\Delta\frac{3}{2}^{-}(2080)$, and $\Delta\frac{3}{2}^{-}(2145)$ resonances. These are the N^* and Δ^* resonances predicted by Capstick and Roberts to have the largest couplings to both the γN and $K\Sigma(1385)$ channels [40]. The mass widths of these resonances were assumed to be 300 MeV/c^2 when not experimentally available [69].

The cutoff parameters used in the calculation of the form factors were determined from a comparison to the preliminary total cross section measurement for the $\gamma p \to K^{+}\Sigma^{*0}$ reaction at CLAS [75]. The total cross section prediction for $\gamma p \to K^{+}\Sigma^{*0}$ is shown in Figure 3.7 along with the preliminary CLAS measurement. As seen in the figure, the preliminary total cross section distribution could not be described in this model without the inclusion of some of the N^* and Δ^* resonances that have not been well-established. More details on the model calculations of the $\gamma p \to K^{+}\Sigma^{*0}$ reaction are discussed in Reference [69].

Predictions for the differential cross section of the $\gamma n \to K^{+}\Sigma^{*-}$ reaction [78] are shown in Figure 3.8. The cross section is predicted to be strongly forward peaked due to the dominance of t-channel K^{+} exchange. The rise at backward angles is due to the contributions of the Λ and Σ^{*-} u-channel diagrams.

Due to the short lifetime of the Σ^{*-}, the $\gamma n \to K^{+}\Sigma^{*-}$ reaction was analyzed by reconstructing the Σ^{*-} through its decays. The Σ^{*-} decays strongly with a mean lifetime of 1.67×10^{-23} s, and

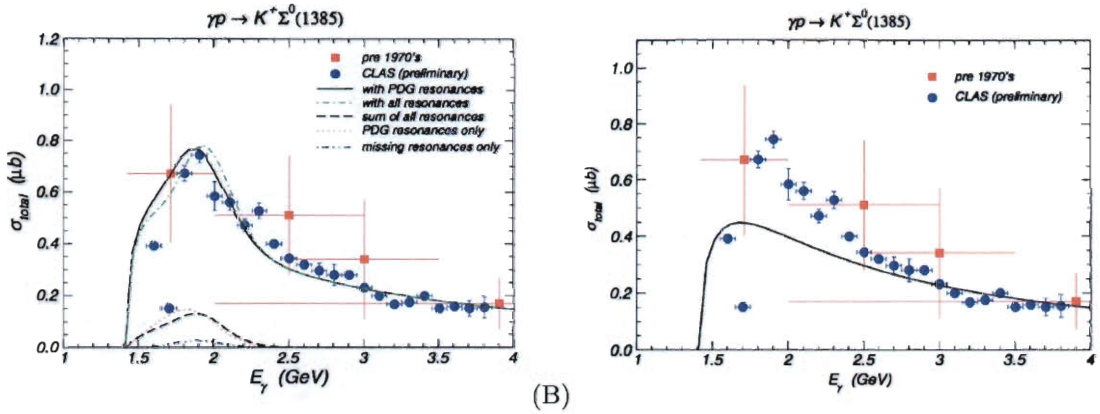

(A) (B)

Figure 3.7 : Comparison between the experimental data [75] and the total cross section predictions of the $\gamma p \to K^{+}\Sigma^{*0}$ reaction as a function of photon energy with (A) and without (B) resonance contributions. Here the "PDG" resonances are the included states with at least a one-star status, the $N\frac{1}{2}^{-}(1945)$, $N\frac{3}{2}^{-}(1960)$, $N\frac{5}{2}^{-}(2095)$, $\Delta\frac{5}{2}^{+}(1990)$, and $\Delta\frac{3}{2}^{-}(2080)$ resonances. The other resonances included in the calculation are the $N\frac{5}{2}^{+}(1980)$, $N\frac{3}{2}^{-}(2095)$, and $\Delta\frac{3}{2}^{-}(2145)$ model states [69].

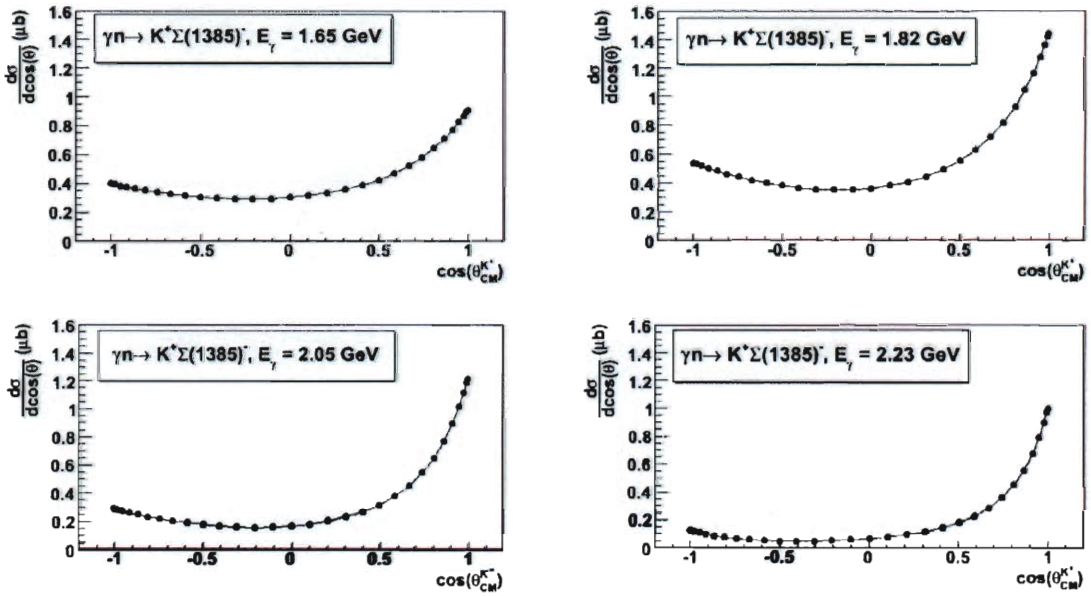

Figure 3.8 : The prediction of the differential cross section of the $\gamma n \to K^{+}\Sigma^{*-}$ reaction at selected photon energies as a function of $\cos(\theta_{K^{+}})$, where $\theta_{K^{+}}$ is the angle between the photon and the K^{+} in the center-of-mass frame [78]. The dominant process is t-channel K^{+} exchange, but the s-channel contributions due to the excited resonances are predicted to be non-negligible [69].

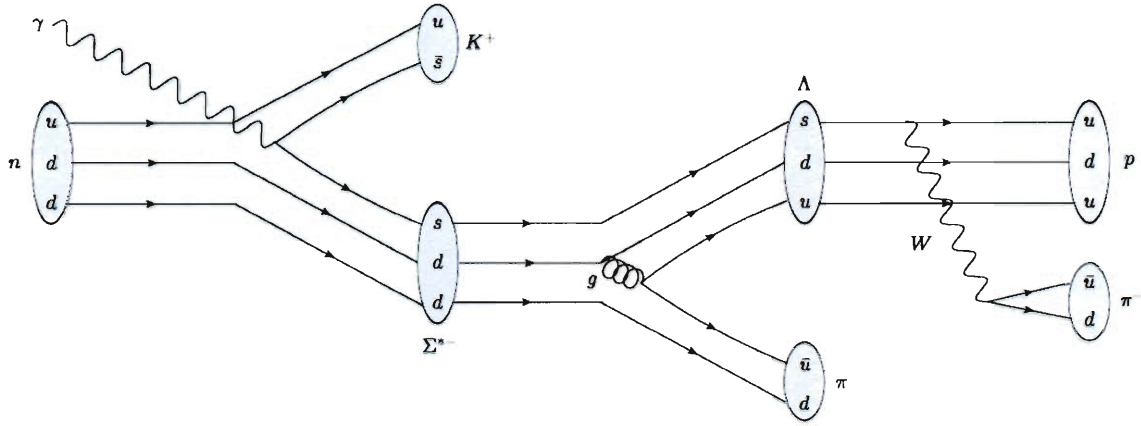

Figure 3.9 : Quark flow diagram for the $\gamma n \to K^{+}\Sigma^{*-}$ reaction, showing the decays of the Σ^{*-} and Λ particles into the $p\pi^{-}K^{+}\pi^{-}$ final-state. As shown in Figure 3.4, the $\gamma n \to K^{*0}\Lambda$ reaction has the same final-state particles and thus may quantum-mechanically interfere at the amplitude level.

a resonance width of 39.4 MeV/c^2. It decays primarily to $\Lambda\pi^{-}$ (87.0%), but also to $\Sigma^{0}\pi^{-}$ and $\Sigma^{-}\pi^{0}$ (~5.8% each) [8]. The contributions to the individual $\Sigma\pi$ channels were determined from the Clebsch-Gordan coefficients, as discussed in Section 3.1. The $\Sigma^{*-} \to \pi^{-}\Lambda \to \pi^{-}p\pi^{-}$ decay channel was the most dominant, so the $\gamma n \to K^{+}\Sigma^{*-}$ reaction was studied by detecting the $p\pi^{-}K^{+}\pi^{-}$ final-state. This decay chain is illustrated by the quark flow diagram in Figure 3.9.

In this analysis both the $\gamma n \to K^{+}\Sigma^{*-}$ and $\gamma n \to K^{*0}\Lambda$ reactions contain Λ's, and both have the same particles in the final state, $p\pi^{-}K^{+}\pi^{-}$. As such these reactions were analyzed in tandem, but due to their similarities there may be quantum-mechanical interference at the amplitude-level. Since there are no known model predictions for this potential interference, the majority of the overlap region between these reactions was cut out of the data. These overlap cuts are discussed in Section 8.2, and their effects on the cross section measurements are studied in Section 9.3.

Chapter 4

CEBAF, CLAS, and the g13 Experiment

The Continuous Electron Beam Accelerator Facility (CEBAF) at Jefferson Lab in Newport News, Virginia is capable of providing an electron beam to each of its three experimental halls at energies up to 6 GeV [80]. The CEBAF Large Acceptance Spectrometer (CLAS) in Hall B is used to study nuclear and hadronic interactions induced by both photon and electron beams. To study these interactions, CLAS was designed to efficiently detect both neutral and charged particles over a large portion of the solid angle [81].

The large angular acceptance and high luminosity capability of CLAS make it well suited for studying medium-energy reactions with multi-particle final-states. CEBAF and CLAS form an ideal environment for searching for the decays of excited nucleon states in the g13 experiment. The experiment ran from October 2006 to June 2007, collecting approximately 50 billion physics events. Circularly and linearly polarized photon beams were incident on a liquid-deuterium target near the center of CLAS [82]. The circularly polarized photon beam portion of the experiment, g13a, was used for this analysis.

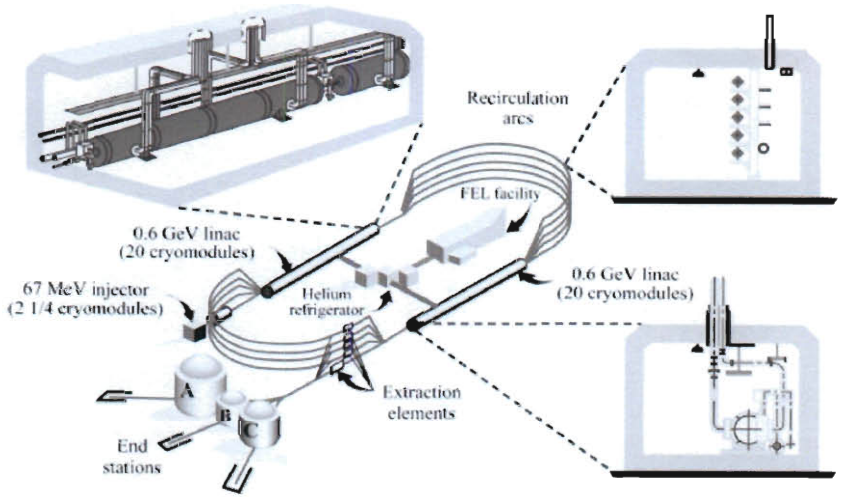

Figure 4.1 : The Jefferson Lab CEBAF Accelerator [80].

4.1 The CEBAF Accelerator

The superconducting radio frequency (RF) Continuous Electron Beam Accelerator Facility at Jefferson Lab is an underground, racetrack-shaped electron accelerator capable of producing a continuous-wave electron beam up to 6 GeV in energy. Beam currents supplied to experimental Halls A and C can range between 1 and 200 μA, and in experimental Hall B can range between 1 and 100 nA [80]. Additionally, the CEBAF polarized electron guns can provide up to 80 - 85% longitudinal beam polarization from their GaAs photocathodes [65]. The CEBAF accelerator is illustrated in Figure 4.1.

Electrons are initially produced in CEBAF at an energy of 100 keV using three independent RF-gain-switched lasers directed at a GaAs photocathode. The three resultant electron beams, one for each experimental hall, are each produced at 499 MHz with a relative 120° phase. These bunches are then interlaced into a 1497 MHz beam, accelerated to 67 MeV by a cryounit and two cryomodules, and injected into the accelerator. Each of the two linear accelerators (LINACs) shown in Figure 4.1 incorporate 160 accelerating cavities. The electron energies can increase by up to 600 MeV for each pass through the LINACs. The electrons can circulate through each of the LINACs up to five times, attaining a maximum energy of 6 GeV. Phased RF deflecting cavities are used to separate the electron bunches into the three experimental halls, including Hall B, which contains the CEBAF Large Acceptance Spectrometer [80].

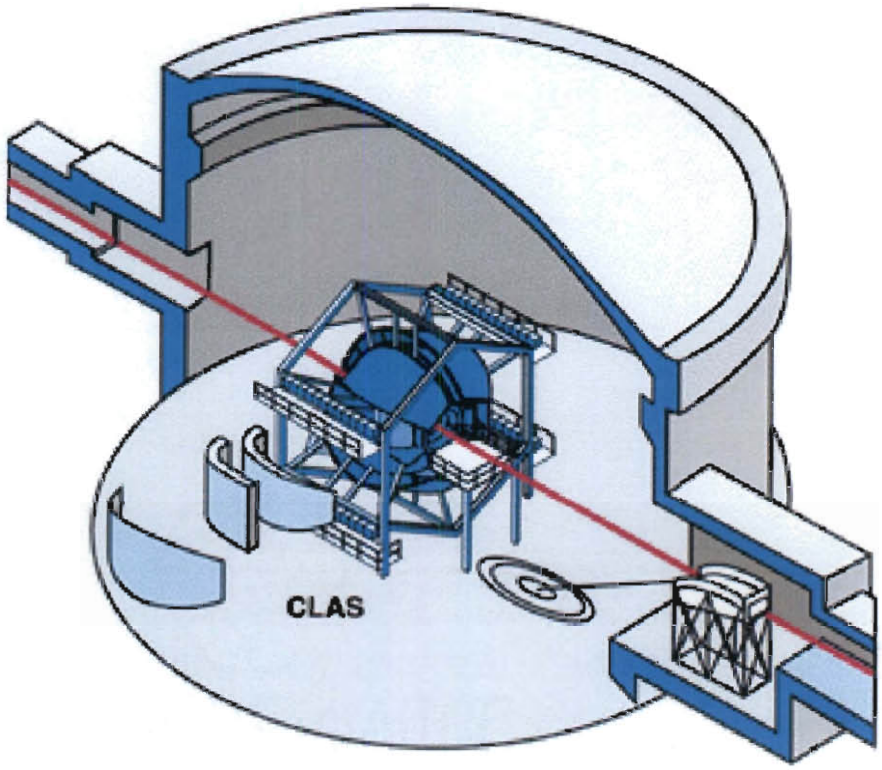

Figure 4.2 : Experimental Hall B and the CLAS detector at Jefferson Lab [83]. The electron beam enters at the bottom-right corner and passes through the photon tagger before reaching the CLAS detector.

4.2 Hall B and the CLAS Detector

The Hall B CLAS detector, shown in Figure 4.2, provides efficient detection of particles over a large fraction of the full 4π sr solid angle. Fast data acquisition and triggering rates allow experiments to typically achieve luminosities on the order of 10^{34} cm^{-2} s^{-1} [81]. The CLAS target can be changed for different experiments, and is ordinarily filled with either liquid-hydrogen or liquid-deuterium.

For the g13 experiment, a photon beam was produced from the electron beam via bremsstrahlung. These photons are not detected directly, but are tagged with the Hall B photon tagger. Surrounding the target, the start counter is used to determine the time at which physics reactions occur. Charged particles produced by the beam in the target are bent by a toroidal magnetic field, and are tracked in the drift chambers. The time-of-flight (TOF) scintillator paddles provide track timing information. At the forward angles, Cherenkov counters can be used to provide charged particle identification, and the electromagnetic calorimeters can be used to detect neutral particles.

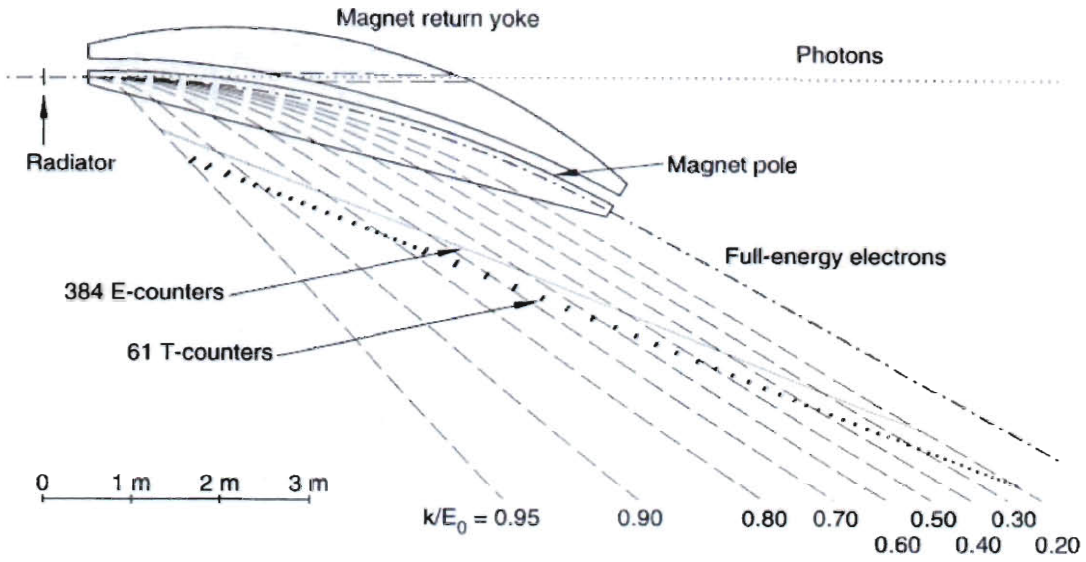

Figure 4.3 : The Hall-B photon tagger [84]. Typical electron trajectories are shown for different transfers of fractional energy to the photon.

4.2.1 The Bremsstrahlung Photon Tagger

A thin radiator can be placed in the beamline to generate photons from the electron beam via bremsstrahlung. In photon beam experiments, both the electrons and the radiated photons pass through a magnetic spectrometer known as the photon tagger, shown in Figure 4.3. Bremsstrahlung photons produced in the radiator continue down the beamline towards CLAS, whereas the electrons are deflected by the magnetic field in the tagger. The photons themselves are not detected, but instead are tagged from matching to the detected electrons. Photons that are produced with between $\sim$20% and $\sim$95% of the incident electron beam energy E_0 are capable of being tagged by the detector [84]. Also, a collimator is used to block photons that are produced at large angles from striking the CLAS detector [81].

The tagger magnet's field is tuned such that electrons with energies greater than $\sim$80% of E_0 strike a shielded beam dump below Hall B. Electrons that radiate more-energetic photons have lower energies, and strike the scintillator hodoscope. This hodoscope consists of a layer of E-counter scintillators that are used for determining the radiated photon's energy, and a layer of T-counter scintillators that are used for determining its timing [84].

The E-counters consist of 384 scintillators, each 20 cm long and 4 mm thick. The widths of these

counters vary from 6 to 18 mm, such that each spans a constant energy interval of $0.003E_0$. These scintillators overlap each other by $\frac{1}{3}$, so that the coincidence between counters provides 767 E-bins for energy measurements. From the overlapping scintillator paddles, the energy of the incident electron beam, and the applied magnetic field, the photon energy can be determined with a resolution of $0.001E_0$ [84]. A large vacuum chamber is used within the hodoscope to minimize the energy loss of the scattered electrons before hitting the E-counters. The E-counters are separated from this vacuum chamber by a strong, thin, woven Kevlar-mesh vacuum window with a thin layer of mylar [85].

The T-counters consist of 61 scintillator paddles, each 2 cm thick, and provide a timing resolution of 110 ps. The first 19 counters correspond to photon energies of $0.75E_0$ and greater, and are much narrower than the others. This allows experiments to run with a high photon flux while maintaining adequate electron-photon matching at high energies. Within each group, the T-counters vary in width to maintain the same counting rate, due to the $1/E_\gamma$ energy distribution of the bremsstrahlung photons. The T-counters overlap each other by about 10%, resulting in 121 T-bins. This overlap is primarily to ensure that there are no gaps between the counters [84].

4.2.2 Beamline Detectors

There are several detectors along the CLAS beamline shown in Figure 4.4 that are used for measuring the electron and photon beam characteristics. The beam position monitors (BPMs) measure the transverse position of the electron beam, as well as its intensity. There are two BPMs located upstream of the photon tagger, plus one between the tagger and CLAS that is not used during photon beam experiments. Each BPM consists of three RF cavities, with antennae that measure the induced electromagnetic fields within the cavities. These fields are produced by the electron beam, and vary with beam position and intensity. This information is used to center the electron beam on the CLAS target during electron beam experiments, and on the tagger radiator during photon beam experiments [81].

Three harps are used to measure the profile of the electron beam. Each harp consists of thin wires that are strung transverse to the beamline, along two perpendicular axes that are 45° to the floor of experimental Hall B. During harp scans these wires are moved horizontally across the electron beam, and the scattered electrons are detected by photomultiplier tubes (PMTs). These profile

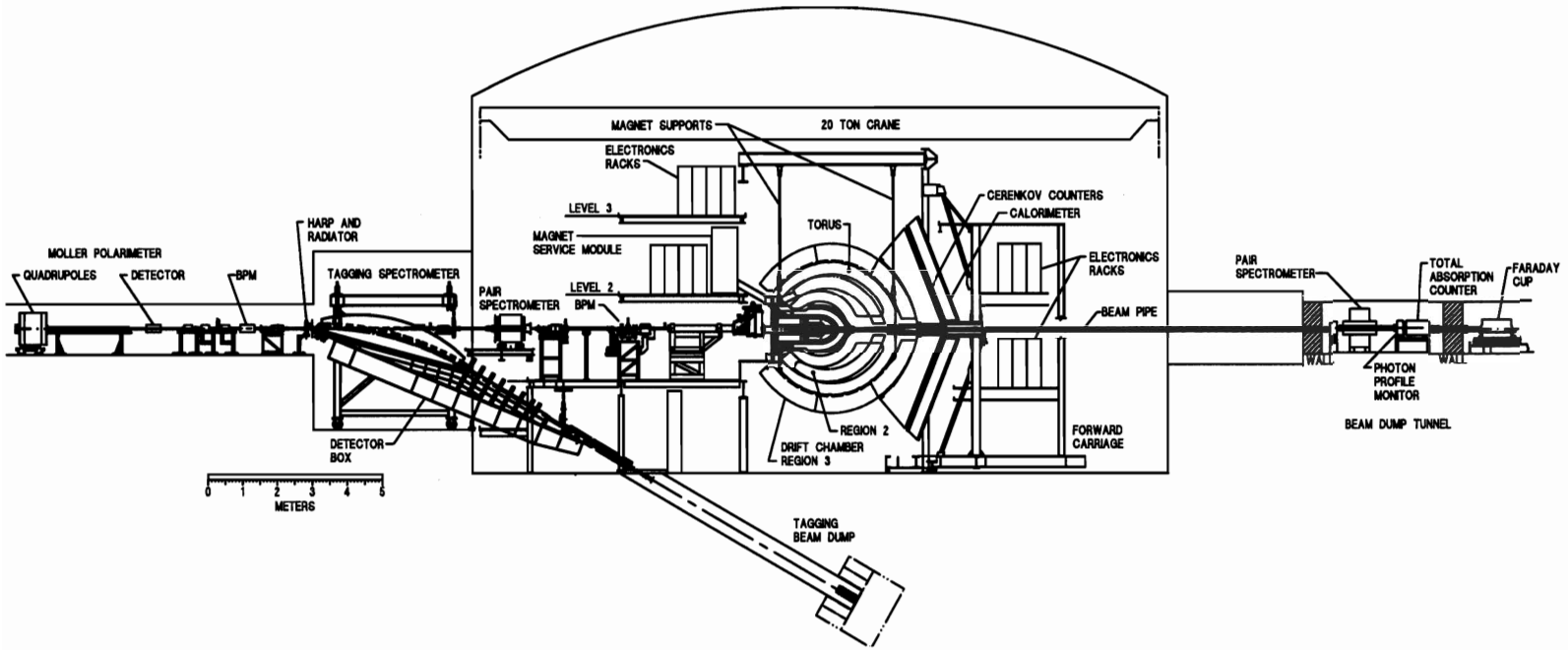

Figure 4.4 : The CLAS detector, photon tagger, and beamline devices in experimental Hall B at Jefferson Lab [81].

scans are generally performed after electron beam configuration changes, and are not performed while recording experimental data [81].

During electron beam experiments, the Faraday cup is used to measure the electron beam current. It is a metal cup that is located 29 m downstream of the CLAS target. The deposited charge on the Faraday cup is used to determine the incident electron flux for cross section measurements. During polarized electron beam experiments, the Faraday cup is also used to measure the helicity-correlated charge asymmetry of the electron beam [81].

During polarized beam experiments, the longitudinal polarization of the electron beam is measured by the Møller polarimeter every few days. For these measurements a magnetized, 25-μm-thick permendur foil is inserted into the beamline upstream of the photon tagger, tilted 20° from the beamline. The scattered electrons are bent by two quadrupole magnets into two detectors composed of lead and scintillating fibers, located on either side of the beamline. The asymmetry in the number of electrons incident on each detector yields the polarization of the electron beam [81]. The determination of the polarization of circularly and linearly polarized photon beams is discussed in Sections 4.3.1 and 4.3.2, respectively.

During photon beam experiments, the position and size of the photon beam are measured by the photon profile monitor. This monitor consists of an array of scintillator fibers located downstream from CLAS. These scintillators are used to detect the electron-positron pairs that are produced by the beam photons downstream of the photon tagger [81]. The Total Absorption Counter (TAC) was used for photon flux determination during 1 nA normalization runs, and is detailed in Section 6.4.2.

A pair spectrometer is located between the photon tagger and CLAS, and during photon beam experiments can be used to monitor variations in the photon flux. A thin foil converts less than 1% of the beam photons to electron-positron pairs, which are then detected after being swept away from the beamline using magnets [81]. This data is typically used to perform high-precision measurements, but in linearly polarized photon beam experiments is also used to monitor the ratio of photons that are polarized perpendicular and parallel to the floor of experimental Hall B.

4.2.3 The Torus Magnet

The CLAS detector is designed around six superconducting coils arranged in a toroidal configuration that produce an azimuthal magnetic field surrounding the beamline. This field bends charged

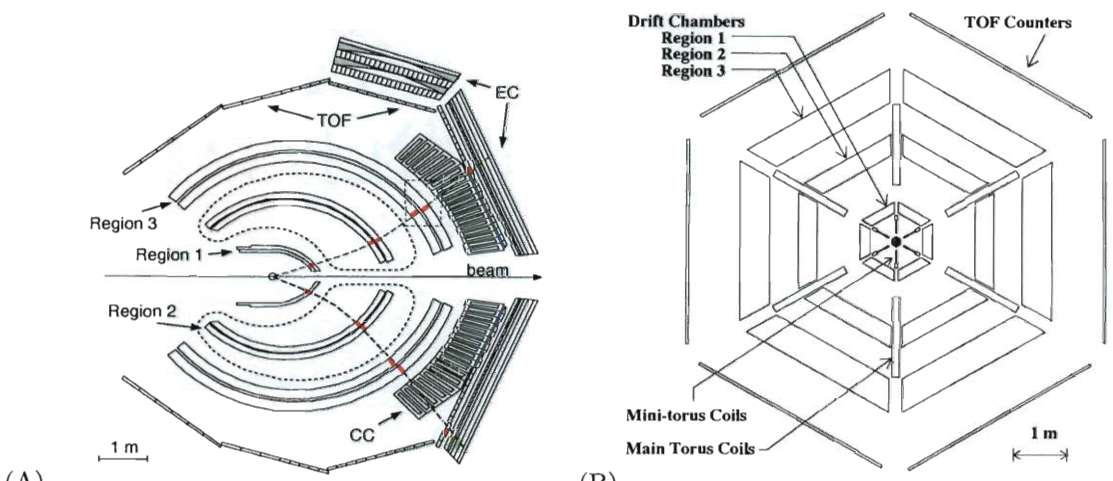

Figure 4.5 : (A) Cross section of the CLAS detector along the beamline. Typical charged particle tracks are shown with corresponding hits in the detector equipment. The torus magnet is outlined by the dotted line surrounding the Region 2 drift chambers. The Cherenkov counters (CC), time-of-flight scintillators (TOF), and electromagnetic calorimeters (EC) are also illustrated. (B) Cross section of the CLAS detector perpendicular to the beamline. The mini-torus shown in the middle is only used for electron runs [81].

particles through the drift chambers for momentum measurements. As illustrated in Figure 4.5, the torus coils are located between the Region 2 drift chambers of each sector. The magnetic field is concentrated around the Region 2 drift chambers, while Regions 1 and 3 of the drift chambers are relatively field-free [81].

As seen in Figure 4.6, the magnetic field from the superconducting torus coils is negligible in the region near the beamline, allowing the use of polarized targets. The coils are approximately five meters in length, and produce a field about five meters in diameter. At the maximum coil current of 3860 A, the integral magnetic field reaches 2.5 T · m in the forward region, and drops to 0.6 T · m at a 90° scattering angle [81]. All non-active parts of the detector, such as the photomultiplier tubes from the Cherenkov counters, electromagnetic calorimeters, and time-of-flight system, as well as the drift chamber support structures, are confined to the shadow of the torus coils to provide maximum angular acceptance.

4.2.4 The Drift Chambers

The six superconducting coils split the detector into six separate tracking sectors. In each sector the drift chambers are divided into three regions, each at a different distance from the beamline. The

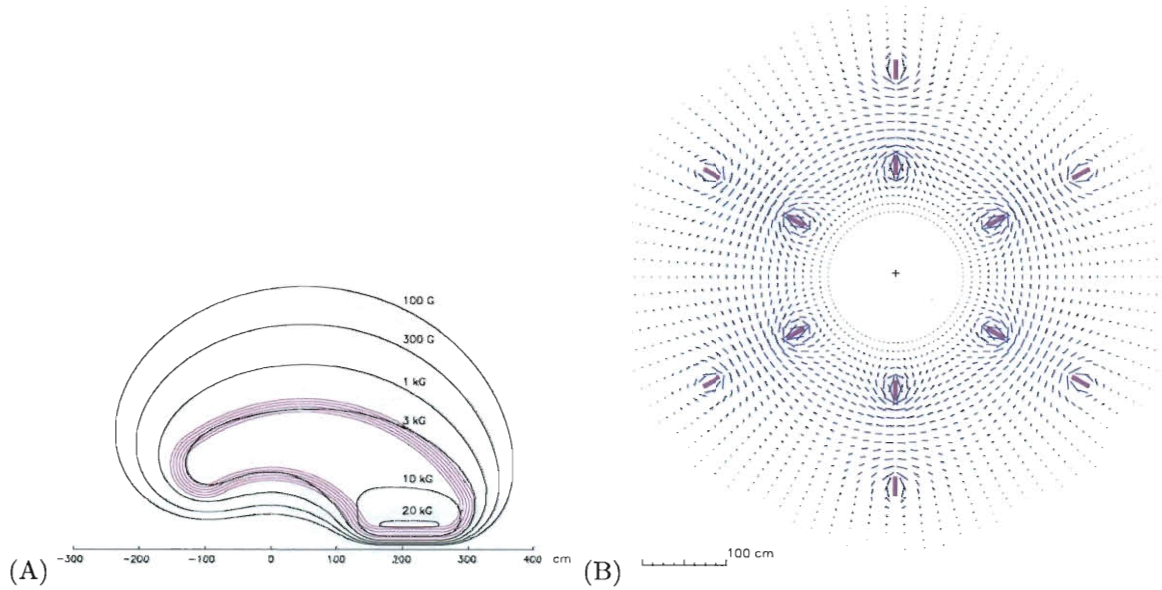

Figure 4.6 : (A) Magnetic field strength in the plane between two of the torus coils. The concentration of magenta lines is the projection of one of the coils onto the midplane. (B) Magnetic field vectors in the cross section of CLAS perpendicular to the beamline. The location of the six torus coils are shown in magenta [81].

chambers span from 8° to 142° in polar angle from the beamline and cover 80% of the azimuthal range [81]. Figure 4.5 illustrates the curved shape and location of the drift chamber regions within the CLAS detector.

In the drift chambers, wire layers are arranged such that the wires form a hexagonal cell pattern. In this arrangement there are six field wires surrounding each sense wire, as shown in Figure 4.7. For each region of the drift chambers, the wires are grouped into two superlayers, each consisting of six wire cell layers. The only exception is the second superlayer of Region 1, which consists of only four wire layers due to space constraints. The wires within the first superlayer of Regions 2 and 3 are aligned axially, perpendicular to the magnetic field's bend plane, to best measure the track curvature. The second superlayer for these regions is rotated by a 6° stereo angle with respect to the first, and provides some azimuthal tracking information while focusing on the axial direction. Region 1 has the opposite configuration, with stereo wires in the first superlayer and the axial wires in the second [81].

To detect the passage of a charged particle through the drift chambers, a strong electric field is created between the field and sense wires. A gas mixture of 90% argon and 10% CO_2 that

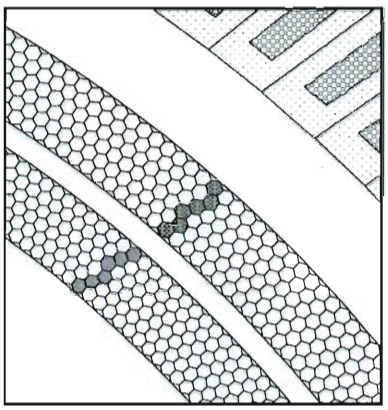

Figure 4.7 : The two superlayers of the Region 3 drift chambers [81]. The highlighted cells indicate where the sense wires have fired, which are located at the center of the hexagonal cells of field wires.

fills the drift chambers is ionized when a charged particle passes through. With this gas mixture, multiple scattering and flammability concerns are minimized while simultaneously allowing a fairly high saturated drift velocity of at least 4 cm/μs. A potential difference of ~2000 V between the field and sense wires causes the electrons freed during ionization to drift through the gas towards the sense wires. These electrons scatter in the gas, knocking more electrons free and causing a cascading avalanche that results in measurable signals on the sense wires [81].

The hexagonal cells of the CLAS drift chamber wires provide an average spatial resolution of 300 - 350 μm. With 10 - 12 wire layers per region, particles are tracked within a region at resolutions of 100 μm in the bend plane of the torus field and 1 mm in the azimuth. Overall, charged particles produced at a momentum of 1 GeV/c are measured with a momentum resolution of $\delta p/p \leq 0.5\%$, and at angular resolutions $\delta\theta$, $\delta\phi$ near 2 mrad [86].

4.2.5 The Time-of-Flight Scintillators

After passing through the drift chambers, particles hit the time-of-flight (TOF) scintillator paddles. These scintillators are located 3.5 to 5 meters from the center of CLAS, as shown in Figure 4.5. The TOF counters provide timing information that is used for charged particle identification. These plastic scintillators span the same solid angle as the drift chambers, between 8° and 142° in polar angle, and 80% of the azimuthal angle. Sectors 1, 2, and 4 contain 57 scintillator paddles, whereas sectors 3, 5, and 6 have one less scintillator paddle at the back due to space constraints. Each

scintillator is approximately 5 cm thick, and while the paddles at the forward angles are 15 cm wide, those at large angles are 22 cm wide. The paddles vary in length across the azimuth of the detector, from 32 cm at the forward angles up to 450 cm at large angles. Since there are fewer tracks in the back-angle paddles due to phase space, the last 18 scintillators in each sector are multiplexed into 9 logical paddles. Thus in the g13 experimental data, there were effectively 48 different TOF paddles in each sector [81].

When a charged particle passes through a scintillator its ionizing radiation excites the material, which in turn radiates photons. Some of these photons are internally reflected down the length of the scintillator, through the light guides, and into the PMTs at each end. The PMTs have diameters of either 2 or 3 in and provide a timing resolution between 150 ps - 250 ps, depending on the length of the scintillators [81]. Neutral particles produce significantly less radiation from their hadronic interactions in the scintillators, and are difficult to detect with the TOF.

4.2.6 The Start Counter

The start counter is a collection of 24 scintillator paddles in a hexagonal orientation surrounding the target, as seen in Figure 4.8. In photon beam experiments the start counter is used to determine the time at which physics reactions occur in CLAS. This information is used to synchronize the particles detected in CLAS with the tagged photons that produced them.

There are four 29-mm-wide paddles on each of the six sides of the start counter. Each paddle is 2.2 mm thick and has a PMT on the upstream end of the scintillator. These paddles are used to measure the time at which tracks pass through them by detecting the radiated photons induced from the ionization. The start counter can enclose targets up to 40 cm in length, and covers nearly the entire azimuth. It also covers the polar angle range from $7° \leq \theta \leq 145°$, essentially the same range as the TOF scintillators. Although the timing resolution in the start counter is only 260 ps due to their being only one PMT per scintillator, it is accurate enough to synchronize information with the photon tagger. In electron beam experiments the start counter is unnecessary and is thus removed [87].

The start time of a physics event in CLAS is determined by comparing the time of the 2 ns beam bunches from the accelerator to the times of the particles detected in the start counter. This bunched structure is seen in Figure 4.9 where the beam electrons, with 50 ps resolution, are matched

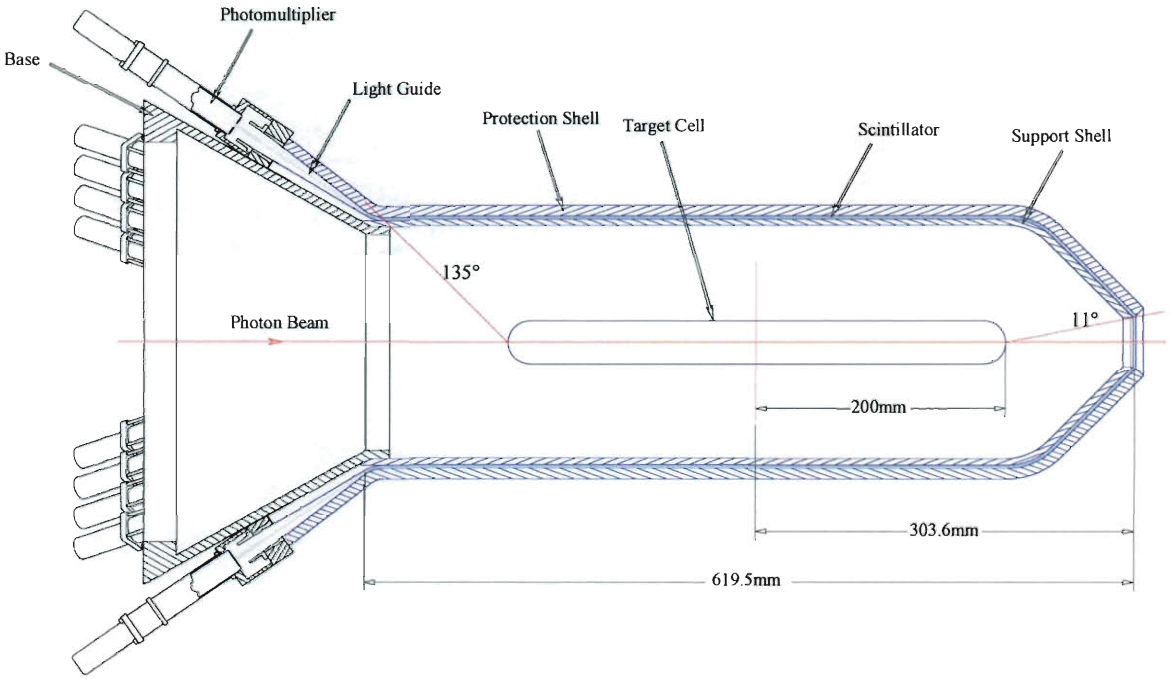

Figure 4.8 : The CLAS start counter surrounding the target cell [87].

with the 110-ps-resolution tagger T-counter hits. Once the correct event start time is determined, the photon matching the detected event can be determined by comparing the time of the photons measured in the tagger to the particle times measured in CLAS.

4.2.7 The Cherenkov Counters

The Cherenkov counters cover the forward angles of the CLAS detector up to 45°, and are located after the drift chambers but before the TOF scintillators as shown in Figure 4.5. The Cherenkov counters provide pion and electron differentiation while only minimally degrading the energy resolution. Charged particles that pass through the C_4F_{10} gas at sufficient velocity produce Cherenkov radiation, which is then detected by the PMTs [81].

The 216 Cherenkov counters are divided amongst the six sectors of the CLAS detector. Figure 4.10 illustrates how the Cherenkov radiation within the counters is collected by the light cones. These light cones and PMTs are located behind the torus magnetic coils where they will not obstruct particles passing through the detector [81]. Since the g13 experiment used a photon beam instead of an electron beam, the Cherenkov counters were disabled because electron-pion differentiation was

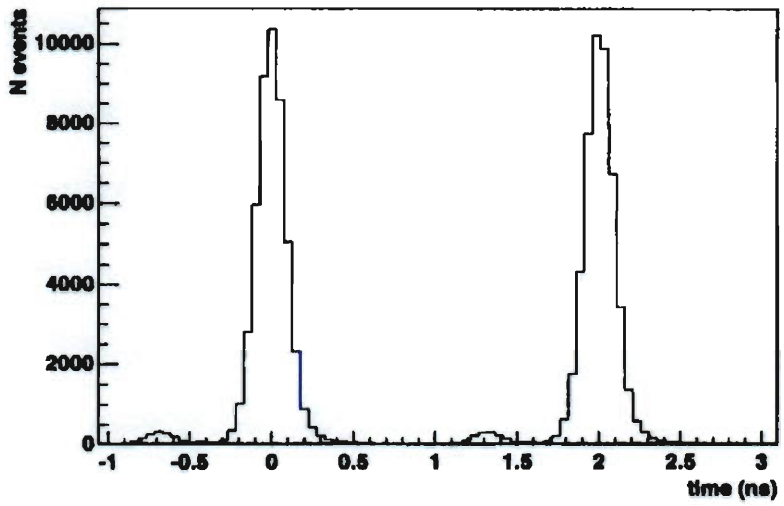

Figure 4.9 : Time difference between the RF signal from the accelerator and the T-counters in the tagger, accounting for the electron propagation and cable times [84]. The start counter is used to determine which electron bunch matches the detected event in CLAS.

not needed.

4.2.8 The Electromagnetic Calorimeters

The CLAS detector has electromagnetic calorimeters at both forward and large angles that are used to detect neutrons and photons. The calorimeters are located just beyond the TOF scintillator paddles, and the forward-angle calorimeters extend back to 45°. The forward-angle calorimeters consist of 39 alternating layers of scintillators and lead sheets, with a total thickness of 16 radiation

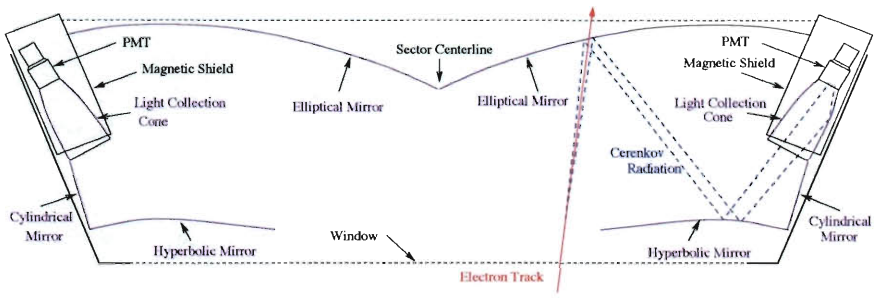

Figure 4.10 : A diagram of one of the Cherenkov counters spanning a sector in CLAS [81]. An electron track and its subsequent radiation is shown being reflected into the light cone and detected by the PMT.

lengths. The energy of the tracks passing through the calorimeters is determined by detecting the energy radiated in the lead sheets with the scintillators. Successive layers of scintillators are rotated 120° with respect to each other so that the hit locations along the different axes provide a more accurate measurement of the track position within the calorimeter.

Two of the six sectors of CLAS have large-angle calorimeters, each extending back to 75°. Their setup is similar to the forward angle calorimeters, but with only 33 layers and a total thickness of 12.9 radiation lengths. The energy resolutions of the forward- and large-angle calorimeters are, respectively, [81]:

$$\frac{\sigma}{E} = \frac{10.3\%}{\sqrt{E\ (\text{GeV})}}, \qquad \frac{\sigma}{E} = \frac{(7.5 \pm 0.2)\%}{\sqrt{E\ (\text{GeV})}}. \tag{4.1}$$

The electromagnetic calorimeters were not included in this analysis because the detection of neutral particles was not required, as discussed in Chapter 8.

4.3 The g13 Experiment

As mentioned previously, the g13 experiment was split into two parts: g13a, which used a circularly polarized photon beam, and g13b, which used a linearly polarized photon beam. A 40-cm-long unpolarized liquid-deuterium target was used for the experiment, and a current of −1500 A in the torus magnet was used to bend negatively charged particles away from the beamline. This setting was chosen to maximize the acceptance of low-momentum π^-'s from the decays of hyperons. Altogether, approximately 50 billion physics events were recorded during the experiment, taking up ∼130 TB of disk space [82]. Only data from g13a was used in this cross section analysis.

4.3.1 g13a: Circularly Polarized Photons

g13a ran from late October through December of 2006, with an additional week of running in March of 2007. It ran at two different beam energies, 1.990 and 2.655 GeV, for roughly an equal amount of time. A longitudinally polarized electron beam was supplied by CEBAF at currents between 33 and 45 nA, resulting in narrow beam bunches of between 412 and 562 electrons every 2 ns. As discussed in Section 4.3.4, a two-sector trigger was used to select events for data acquisition. With slightly more than two months of running, 20 billion physics events were recorded in the g13a dataset [82].

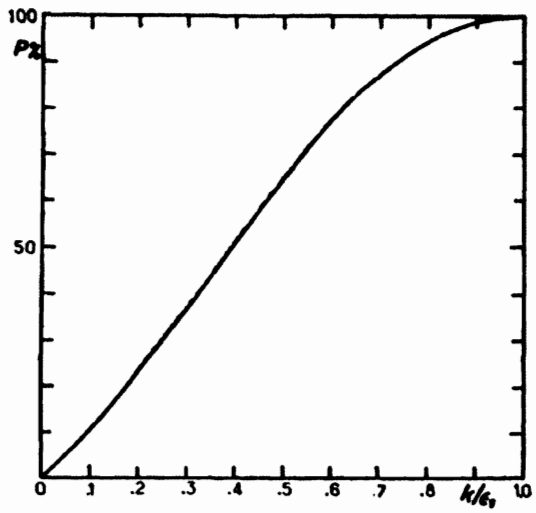

Figure 4.11 : Polarization transfer from longitudinally polarized electrons to circularly polarized photons as a function of E_γ/E_e in bremsstrahlung radiation [88].

The longitudinally polarized electron beam was incident on a 10^{-4} radiation-lengths-thick gold foil radiator and produced a circularly polarized photon beam [82]. As seen in Figure 4.11, the degree of polarization transfer to the photon beam was photon energy dependent. 100% polarization transfer from the electron to the photon occurred when the photons were produced at the incoming electron beam energy [88]. Due to this effect, the 1.990 GeV and 2.655 GeV beam energies were chosen to maximize the photon beam polarization in these N^* production regions. The electron beam polarization was ~84% for the 1.990 GeV data and ~78% for the 2.655 GeV data. A tungsten collimator 6.4 mm in diameter downstream of the radiator provided ~90% beam transmission to the liquid-deuterium target, resulting in a photon flux rate at the target on the order of 10^7 Hz [82].

4.3.2 g13b: Linearly Polarized Photons

g13b ran from mid-March through June of 2007. There were eight different electron beam energies between 3.3 GeV and 5.16 GeV during g13b. With the beam current ranging from 5 to 12 nA, the electrons arrived in bunches of between 62 and 150 electrons every 2 ns. A single-sector event trigger was used, and ~30 billion events were recorded over the 3.5 months of g13b [82]. Due to the method used for generating the linearly polarized photon beam, the photon beam flux incident on the target is difficult, if not impossible to calculate for g13b. Therefore, cross section measurements

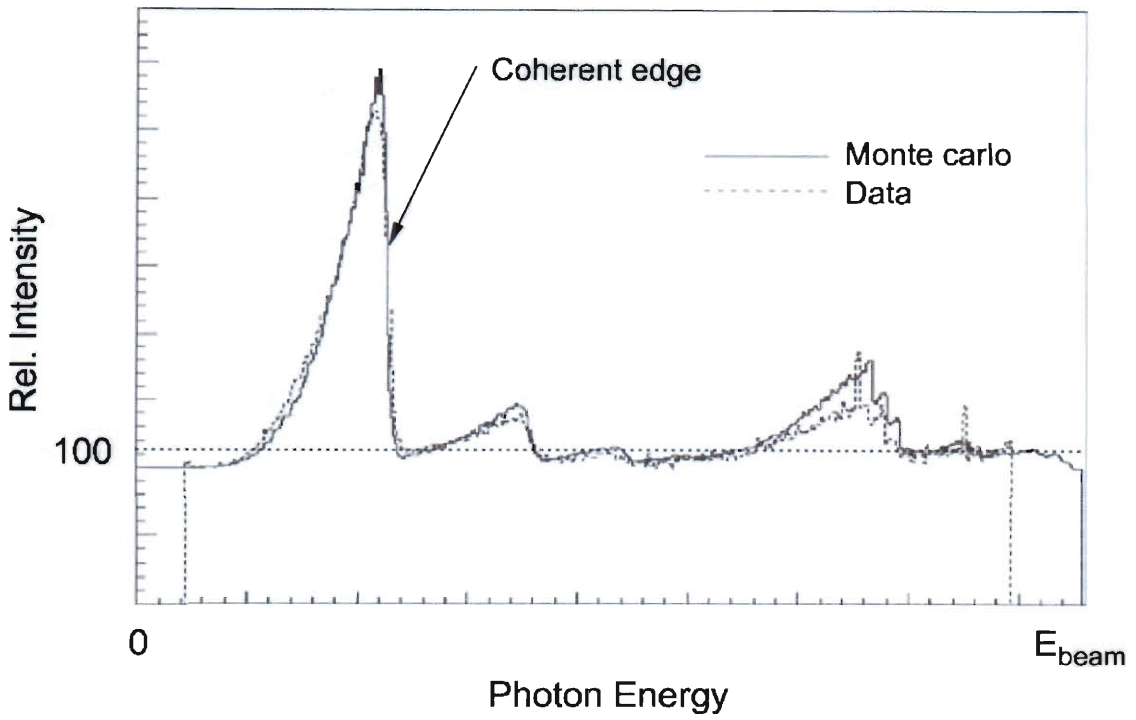

Figure 4.12 : The data and Monte-Carlo-simulated photon energy distributions produced from an electron beam incident on a diamond radiator, after removing the $1/E_\gamma$ bremsstrahlung energy-dependence [89].

are restricted to g13a.

A 50-μm-thick diamond radiator was used to produce the linearly polarized photons with ~200 MeV-wide coherent peaks at energies from 1.1 to 2.3 GeV [82]. When unpolarized electrons scattered off the diamond, the momentum transfer to the diamond was restricted to specific directions based on its orientation to the beam. This resulted in a large coherent peak in the radiated photon energy distribution, as shown in Figure 4.12. However scattering also occurred in higher-order planes, resulting in additional, smaller peaks at higher photon energies [90]. The energy of the coherent peak was tuned by adjusting the orientation of the diamond with respect to the beam. The polarization transfer to the radiated photons was larger for lower fractional beam energies, E_γ/E_e. The longitudinal polarization of the radiated photons in the coherent peak was between 70% and 90% [82], and was calculated from the energy of the incident electrons and the orientation of the diamond [91].

Figure 4.13 : Conical liquid-deuterium target used for the g13 experiment [92]. It was 40 cm long, and 4 cm in diameter at its widest point. The beamline ran through the center of the target.

4.3.3 Liquid-Deuterium Target

The liquid-deuterium target used in the g13 experiment is shown in Figure 4.13. It had a slightly conical shape and a rounded endcap with a thin aluminum window at the front. This window allowed the remnants of the photon beam to exit the target with minimal interactions. The target was 40 cm in length, and yielded a large event rate while maintaining an acceptable rate of photons in the tagger. The target was 4 cm in diameter at its widest, providing sufficient coverage of the beamline for the ~1 cm spread of the photon beam, as well as any slight beam position misalignments. The target was centered 20 cm upstream from the center of CLAS to maximize acceptance. The density of the liquid-deuterium in the target was 0.1625 g/cm^3 [65].

4.3.4 Data Acquisition & Event Triggering

Event triggering for the data acquisition (DAQ) system is essential for every experiment using the CLAS detector. Triggering on the signals from the different detector subsystems was used to allow physics events of interest to be selected for recording. During g13 physics events were recorded at a rate of about 10 kHz, with a dead-time of ~15%. The dead-time represents the percentage of the time that the DAQ system is too busy recording a physics event to accept trigger signals from other events. During g13a and g13b, approximately 20 billion and 30 billion physics events were recorded,

respectively [82]. These events were approximately 2.5 kB in size, resulting in a ~130 TB dataset.

There are two stages at which DAQ triggering occurs in CLAS. The Level-1 trigger acts on the prompt signals from the fast electronics of the various detector components, and the Level-2 trigger acts on the slower track reconstruction in the drift chambers. For the g13 experiment, only the Level-1 trigger was used. In g13a, it was set to record events with a coincidence between the start counter (ST) and TOF scintillators in at least two of the six CLAS sectors. In g13b, a coincidence between the ST and TOF was required in only one of the sectors. These trigger requirements were chosen to minimize the background from accidental detector hits, while maximizing the DAQ rate for charged-particle physics events. In photon beam experiments, the Level-1 trigger can be set to require an electron be detected within a given range of T-counters in the photon tagger, but this condition was not used for g13 [82].

When a signal is detected in any scintillator paddle of the ST that is greater than the pretrigger voltage threshold, a 28 ns pulse signal is sent to the Level-1 trigger for that sector. The same is true for the TOF scintillators, except that a 120 ns pulse signal is sent. In the Level-1 trigger, a coincidence between the ST and TOF within a sector was determined by sampling the ST and TOF channels for trigger pulses once every 15 ns. When this strobe found a coincidence that satisfied the triggering condition, the trigger notified the data acquisition system. A 20 ns latch then saved the sectors that were in coincidence, including the ones that had an ST and TOF coincidence 15 ns later during the next sampling. The lengths of these pulse signals were chosen such that trigger losses due to missed coincidences were negligible [93]. This triggering information was recorded, and was analyzed in Section 6.3 for the triggering efficiency studies.

Chapter 5

Momentum and Beam Energy Corrections

Several standard corrections were applied to the momentum and energy measurements of the CLAS g13a data. Corrections were performed to charged particles due to energy losses as they passed through the different materials of the detector, excluding the drift chambers. Also, energy corrections were applied to the beam photons due to a gravitational sag of the scintillator counters in the photon tagger.

However additional, experiment-specific corrections were made to the track momentum and beam energy. The measured track momentum was corrected due to differences between the actual toroidal magnetic field and the calculated one used for track reconstruction, energy losses in the drift chambers, and drift chamber misalignments. These corrections were determined by performing kinematic fits of the $\gamma D \rightarrow pp\pi^-$ reaction. Also, since the incoming electron beam energy from CEBAF was not measured by CLAS, it was assigned a nominal beam energy. Corrections to this value were determined by studying the missing energy of the $\gamma D \rightarrow pp\pi^-$ reaction. By making these small, additional corrections, the accuracy and resolution of the track measurements for final-state identification were optimized.

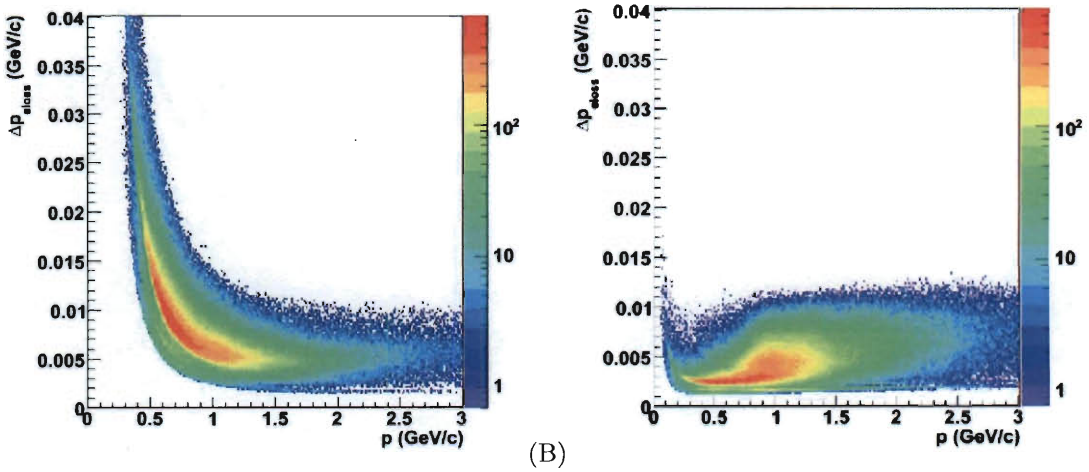

Figure 5.1 : For (A) protons and (B) π^-'s, the total momentum correction due to inelastic scattering in the target and various detector materials as a function of momentum. These corrections were derived from the Bethe-Bloch formula and performed by the CLAS *eloss* software package.

5.1 Standard Corrections

Before analyzing the physics events, the CLAS *eloss* software package performed an energy loss correction for charged particles [94]. As charged particles passed through the various target and detector components, their mean energy loss was described by the Bethe-Bloch equation [8]. The *eloss* package applied this correction separately for each of the different materials of the target and the start counter that the charged particles passed through. The momentum dependence of the total energy loss correction is shown in Figure 5.1 for both protons and π^-'s. This correction was large for low-momentum particles, resulting in minimum track momentum cut-offs that are discussed in Section 6.2.

Also, a correction to the measured photon energy was necessary because there was a slight gravitational sag in the tagger scintillator paddles [95]. This sag resulted in a mismatch between the energy of the detected electron and the scintillator paddle that it struck. This correction was a tagger E-counter-dependent multiplicative constant to the photon energy, and is thus scalable for

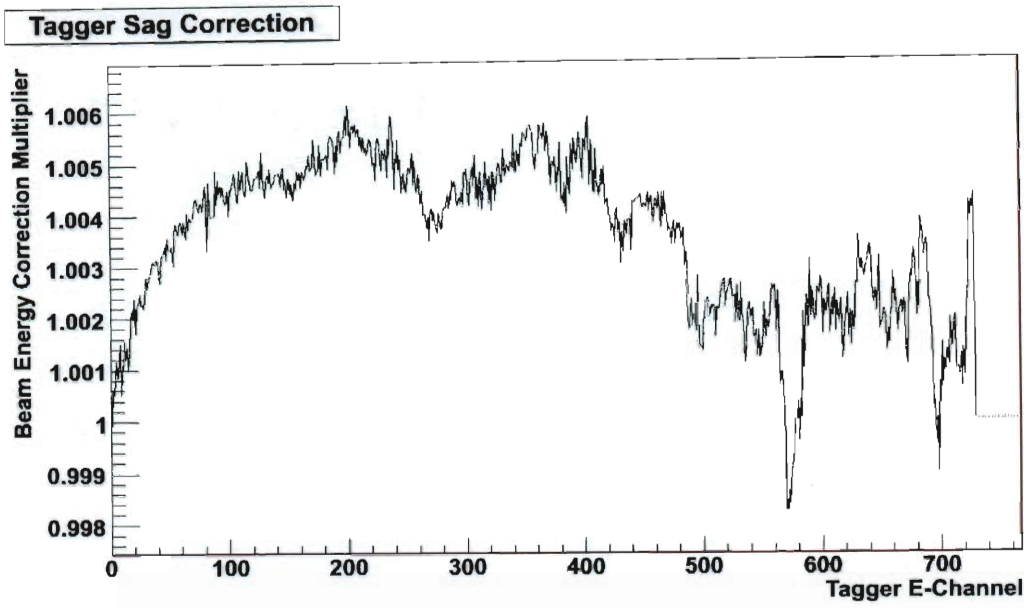

Figure 5.2 : The photon energy correction multiplier due to the gravitational sag in the photon tagger as a function of tagger E-channel. For a 2.655 GeV electron beam, this corresponded to a maximum correction of about 12 MeV near E-channel 200.

all electron beam energies. This correction was calculated in Reference [95], and is shown in Figure 5.2.

5.2 $\gamma D \rightarrow pp\pi^-$ Reaction Identification

To determine the additional, experiment-specific momentum corrections, the $\gamma D \rightarrow pp\pi^-$ reaction was studied. It is the simplest photoproduction reaction on the deuteron with a fully charged final-state. In this reaction, the photon strikes the neutron in the deuteron to produce a proton and a π^-. These particles often rescatter off the spectator proton in the deuteron, sometimes imparting the spectator proton with enough momentum to be detected in CLAS. This reaction was identified by placing a series of cuts on the g13a data, including particle identification, time difference, missing mass, and missing momentum cuts.

5.2.1 Track Identification and Timing Cuts

To select $\gamma D \rightarrow pp\pi^-$ events, all three final-state particles were required to be detected. $\Delta\beta$ cuts, where $\beta \equiv \frac{v}{c}$, were used to identify the proton and π^- tracks, and are discussed in Section 7.1.3. Also, the interaction vertex was determined to be the midpoint between the closest pair of detected particles at their distance of closest approach. The times of the particles at this vertex were calculated as discussed in Section 7.1.1.

Since multiple tagged photons were detected in most events, the one that was closest in time to the π^- was selected. The time difference between the particles at the interaction vertex is illustrated in Figure 5.3. The uncertainty in the calculated particle start time increased with decreasing β, so the time resolution of the typically slower protons was worse than that of the photons or pions. Cuts were placed on these distributions at ± 3 ns to remove the majority of the backgrounds from accidental tracks that originated from different events.

Events that contained more than one tagged photon within the timing cuts were not excluded from this momentum and energy correction analysis. As shown in Section 7.1.4, this phenomenon occurs for about 11% of all physics events. If the wrong photon was chosen for a given event, then the calculated correction for that event was skewed. However, the vast majority of the incorrect photons failed the cuts on the missing mass and missing momentum distributions in Section 5.2.2. Therefore, these events have a negligible effect on the momentum and beam energy corrections discussed in Sections 5.3 and 5.4, respectively.

5.2.2 Missing Mass and Missing Momentum Cuts

The missing mass-squared of the $\gamma D \rightarrow pp\pi^-$ reaction is illustrated in Figure 5.4. The asymmetric tail on the negative side of the signal peak was due to the resolution of the momentum measurements by the CLAS drift chambers. Thus when the missing momentum vector had a non-zero magnitude, the missing mass-squared was slightly less than zero. The background under this distribution is negligible, but cuts were placed at -0.002 $(\mathrm{GeV/c^2})^2$ and 0.001 $(\mathrm{GeV/c^2})^2$ to remove the majority of the background events while retaining the majority of the signal events. Although this cut accepted some $\gamma D \rightarrow pp\pi^-(\gamma)$ and $\gamma D \rightarrow pp\pi^-(\pi^0)$ events, cutting much tighter would have biased the study by removing too many events with large momentum-measurement errors. The majority of these remaining background events were removed by placing a cut on the confidence level of the

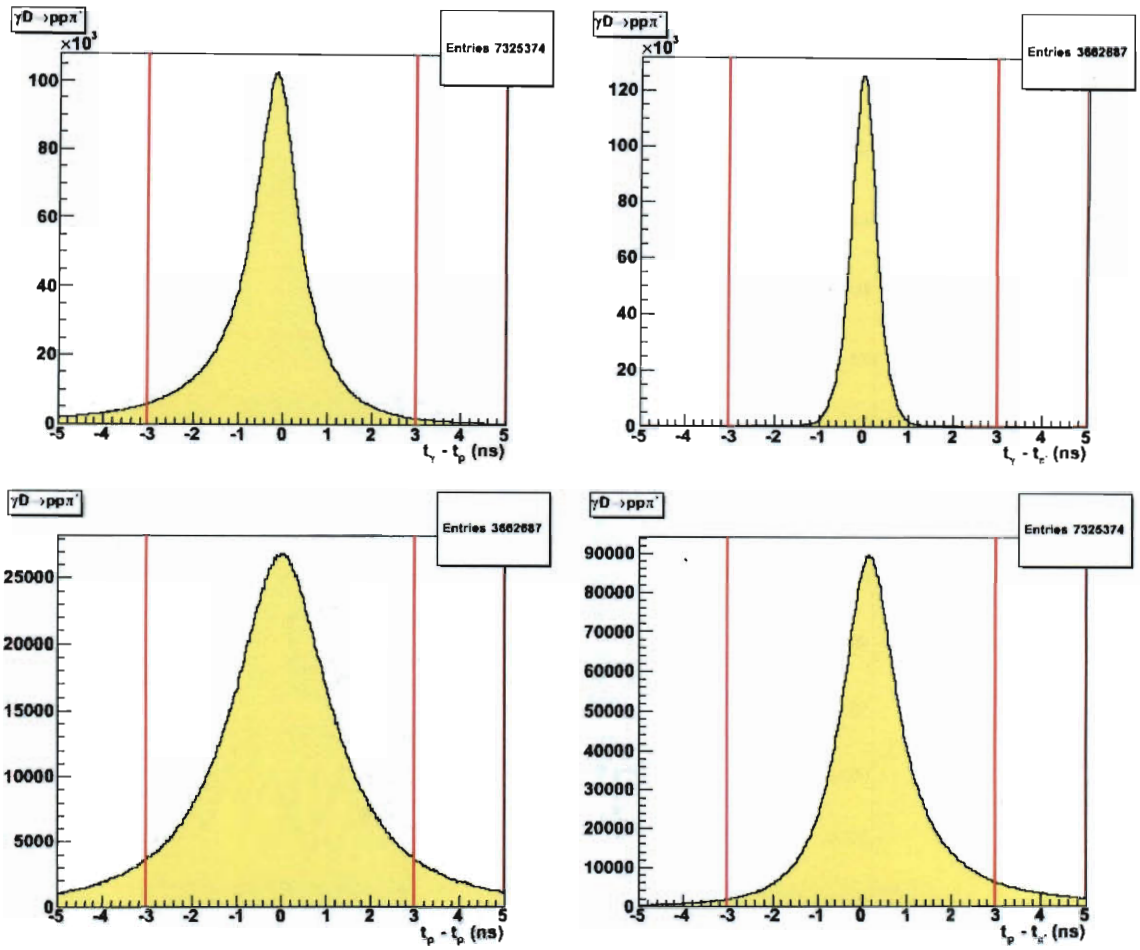

Figure 5.3 : Time difference at the photoproduction vertex between the different particles in the $\gamma D \rightarrow pp\pi^-$ reaction. The red lines indicate the ± 3 ns cuts placed on the distributions. The times of both protons are compared against those of the γ and π^-, doubling the number of entries in those histograms.

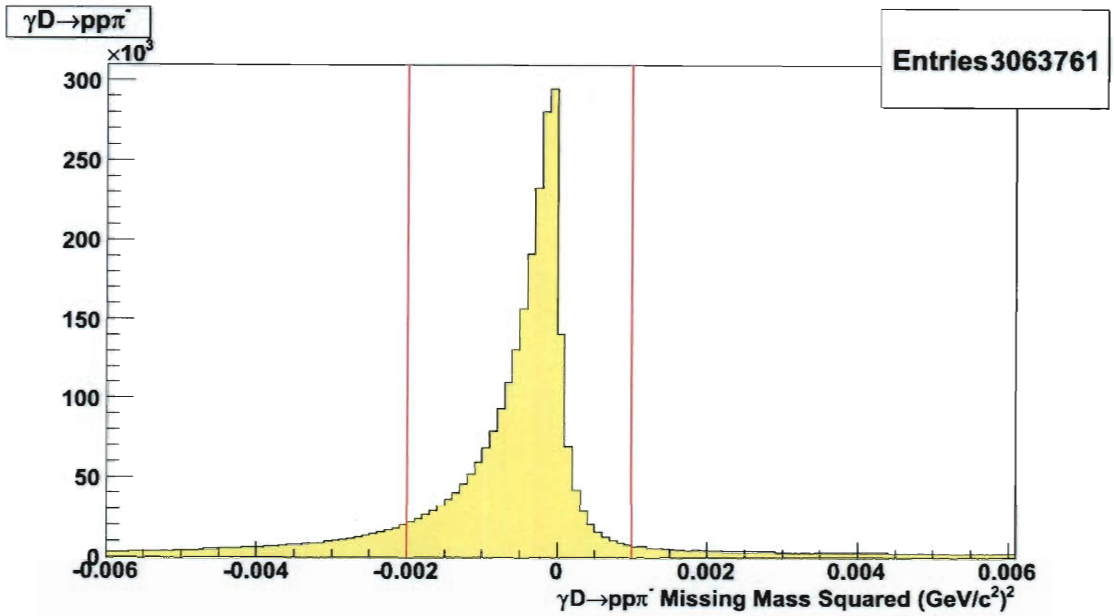

Figure 5.4 : The missing mass-squared of the $\gamma D \rightarrow pp\pi^-$ reaction. Cuts were placed requiring that the missing mass-squared be between -0.002 $(\mathrm{GeV/c^2})^2$ and 0.001 $(\mathrm{GeV/c^2})^2$, indicated by the red lines. The asymmetric tail is due to events with non-zero missing momentum, such as $\gamma D \rightarrow pp\pi^-\pi^0$ events.

kinematic fit, as detailed in Section 5.3.1.

Finally, the missing momentum in the direction of the beamline (momentum-z) is shown in Figure 5.5. This missing momentum-z distribution was cut at ± 0.06 GeV/c to ensure that events with a large missing momentum were excluded. These cuts removed the vast majority of the events in which the wrong photon was selected.

5.3 Additional Momentum Corrections

In addition to the *eloss* corrections, corrections to the measured track momenta were necessary due to energy losses in the drift chambers, drift chamber misalignments, and differences between the actual toroidal magnetic field and the calculated field map used for track reconstruction. To determine these additional corrections, kinematic fits of the $\gamma D \rightarrow pp\pi^-$ reaction were performed using data from runs 53630 through 53650 of g13a. The system was constrained by requiring four-momentum conservation, with the magnitudes of the track momenta treated as unknown. These measurements were treated as unknown to remove their bias from the kinematic fit.

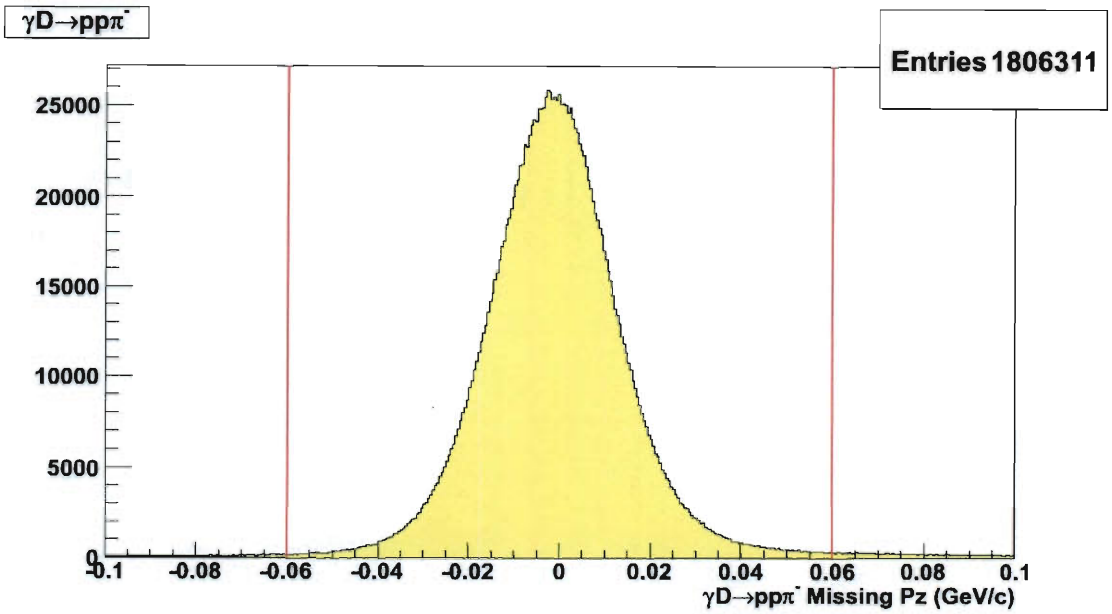

Figure 5.5 : The missing momentum in the direction of the beamline of the $\gamma D \rightarrow pp\pi^-$ reaction. The ± 0.06 GeV/c missing momentum-z cuts are indicated by the red lines.

Runs 53630 through 53650 were chosen due to the high stability of the incoming electron beam energy, as shown in Section 5.4. Additionally, for these runs the missing energy of the $\gamma D \rightarrow pp\pi^-$ reaction was centered around zero, as shown in Figure 5.6. This distribution was histogrammed after placing the cuts detailed in Section 5.2 to isolate the $\gamma D \rightarrow pp\pi^-$ events.

The momentum corrections were determined by studying the mean difference between the kinematically fit and measured momentum of the particles. Since particles of opposite charge were bent in opposite directions through the drift chambers, the errors on the track momentum measurements were fit separately for the protons and the π^-. These corrections were generally only a few MeV, and were largest for slow protons and tracks close to the torus magnets.

For a given magnetic field, the paths of the particles are dependent only on their charge and momentum. As such, the momentum-dependent corrections derived due to drift chamber misalignments and errors in the magnetic field map were applied to all particles of like charge. Therefore, these corrections for the proton were applied to both K^+'s and π^+'s as well. However, the corrections due to energy losses in the drift chambers were β-dependent. Particles with different masses had different momentum-dependence for these corrections, so for the π^+'s the π^- corrections were used. Since K^+'s have a similar momentum-dependent behavior as pions in CLAS, these π^- corrections

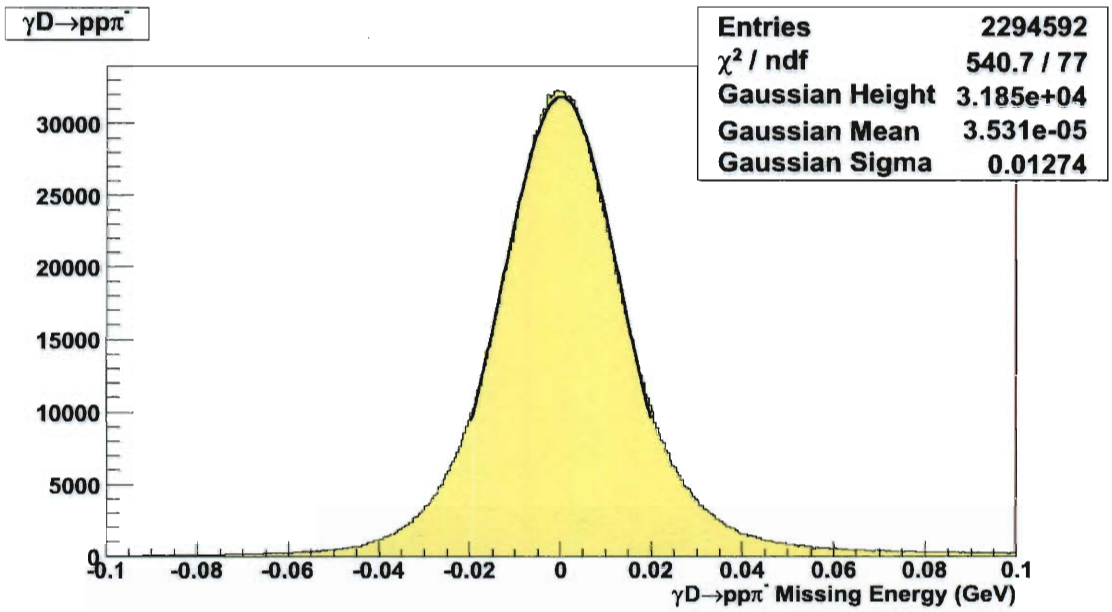

Figure 5.6 : Initial missing energy distribution of the $\gamma D \rightarrow pp\pi^-$ reaction for runs 53630 through 53650 of g13a. The Gaussian fit to the peak is centered around zero, indicating a suitable run range for determining momentum corrections.

were assigned to the K^+'s as well.

5.3.1 Kinematic Fitting

Kinematic fitting can be used as a method of testing whether a set of track measurements originated from a given physics reaction. For each event, the track measurements were fit such that they satisfied four-momentum conservation, and minimized the least-squares error of the measurements. In this analysis of the $\gamma D \rightarrow pp\pi^-$ reaction, the four-momentum constraint equations were:

$$\begin{pmatrix} E_\gamma + E_D - E_p - E_p - E_{\pi^-} \\ p_{x_p} + p_{x_p} + p_{x_{\pi^-}} \\ p_{y_p} + p_{y_p} + p_{y_{\pi^-}} \\ p_{z_\gamma} - p_{z_p} - p_{z_p} - p_{z_{\pi^-}} \end{pmatrix} = \mathbf{0}. \tag{5.1}$$

where E is the energy and the p_x, p_y, and p_z are the momentum components of the given particles. With the three track momentum magnitudes treated as unknown, this system was overdetermined with one degree of freedom. Since this system was overdetermined, these fits minimized the devia-

tions of the track parameters from their true values, relative to their uncertainties.

Because the track measurements were assumed to be Gaussian-distributed about their true values, the fit errors were assumed to follow a χ^2 distribution corresponding to the number of degrees of freedom in the fits. The confidence level of a fit is a measure of how well the measured track parameters fit the constraints. The confidence level (CL) is the integral of the χ^2 probability distribution function $f(\chi^2, N)$ [96]:

$$\mathrm{CL} = \int_{\chi^2}^{\infty} f(u, N)du, \tag{5.2}$$

where N is the number of degrees of freedom, and u has been substituted to represent χ^2. The confidence level corresponds to the probability of obtaining a larger χ^2 for the same system and similar measurements. For a large sampling of true events, normally distributed parameters yield a confidence level that is uniformly flat between 0 and 1. Background events in the data sample are evidenced by a steep rise near zero confidence [96]. The confidence level distribution for the kinematic fit used to determine the momentum corrections is shown in Figure 5.7. Events with a confidence level less than 0.1 were cut to remove the majority of the remaining background events before fitting the momentum corrections.

The effect that the individual track parameters have on a fit can be examined with pull distributions. The pull of a track parameter is defined as the deviation between its fit and measured values, normalized by the uncertainty in the deviation. In a normally distributed sample of true events, the pulls are Gaussian-distributed with a mean of zero and a standard deviation of one. If the center of a pull is shifted away from zero, then there is a systematic deviation in the track measurement. If the width of a pull is either too narrow or too wide, then the uncertainty on the track measurement has either been overestimated or underestimated, respectively. If large biases are found, then the track measurements and their uncertainties need to be corrected before any cuts may be placed on the confidence level of the fit [96].

The covariance matrix of the track measurements was used to constrain the variations of the track parameters in kinematic fitting. The procedures used to produce the covariance matrix used for kinematic fitting the g13 data are the same as those used for the CLAS eg3 experiment [97]. The corrections to the covariance matrix produced a flat confidence level (Figure 5.7), and Gaussian pulls (Figure 5.8) with means near zero and widths near one for the g13 data. More details on kinematic

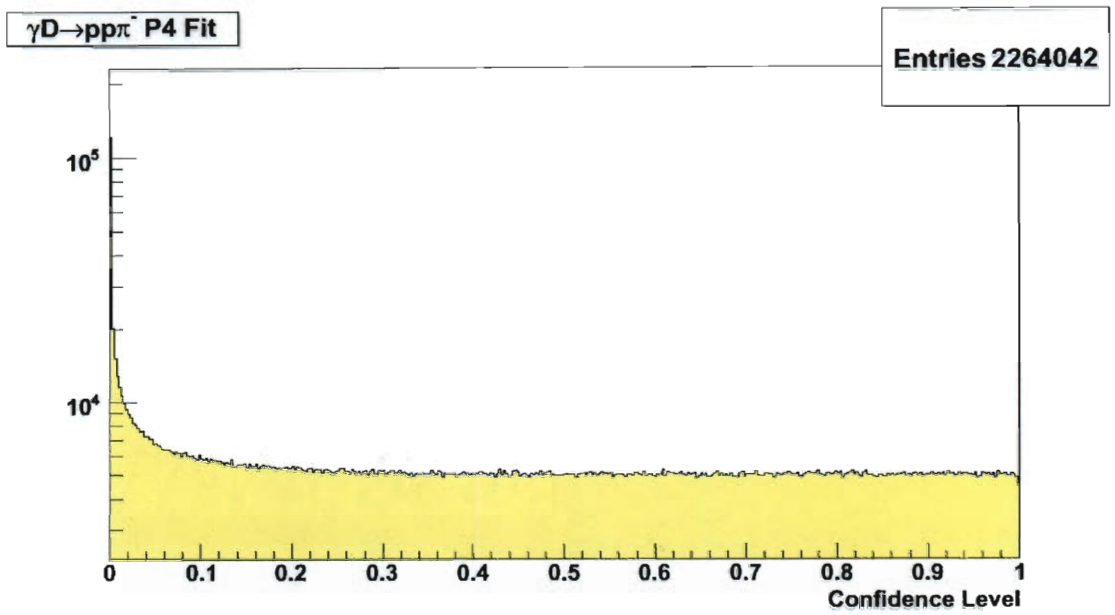

Figure 5.7 : The confidence level distribution for the kinematic fit of the reaction $\gamma D \rightarrow pp\pi^-$ with the magnitudes of the track momenta treated as unknown. The large spike near zero confidence corresponds to background events.

fitting, track measurement errors in CLAS, and the covariance matrix are discussed in Reference [97].

5.3.2 Determination of the Momentum Corrections

To fit the charged particle momentum corrections, the $\gamma D \rightarrow pp\pi^-$ reaction was kinematically fit requiring four-momentum conservation with the magnitudes of the track momenta of the protons and π^- treated as unknown. The average difference between the fit and detected momentum after performing known corrections, Δp, was studied for each particle in each sector of the detector. Since particles of opposite charge were bent in opposite directions through the drift chambers, the uncertainties on the track momentum measurements were fit separately for the protons and the π^-.

After *eloss* corrections, Δp is shown vs. p, ϕ, and θ for Sector 1 of the CLAS detector for the proton and π^- in Figure 5.9. In the lab coordinate system, ϕ is the azimuthal angle from the middle of Sector 1, and θ is the polar angle from the beamline. The full set of figures for all six sectors of CLAS is located in Appendix A.1. These skews in the charged particle momentum are sometimes as large as 10 MeV/c and were attributed to misalignments of the drift chambers, energy losses not

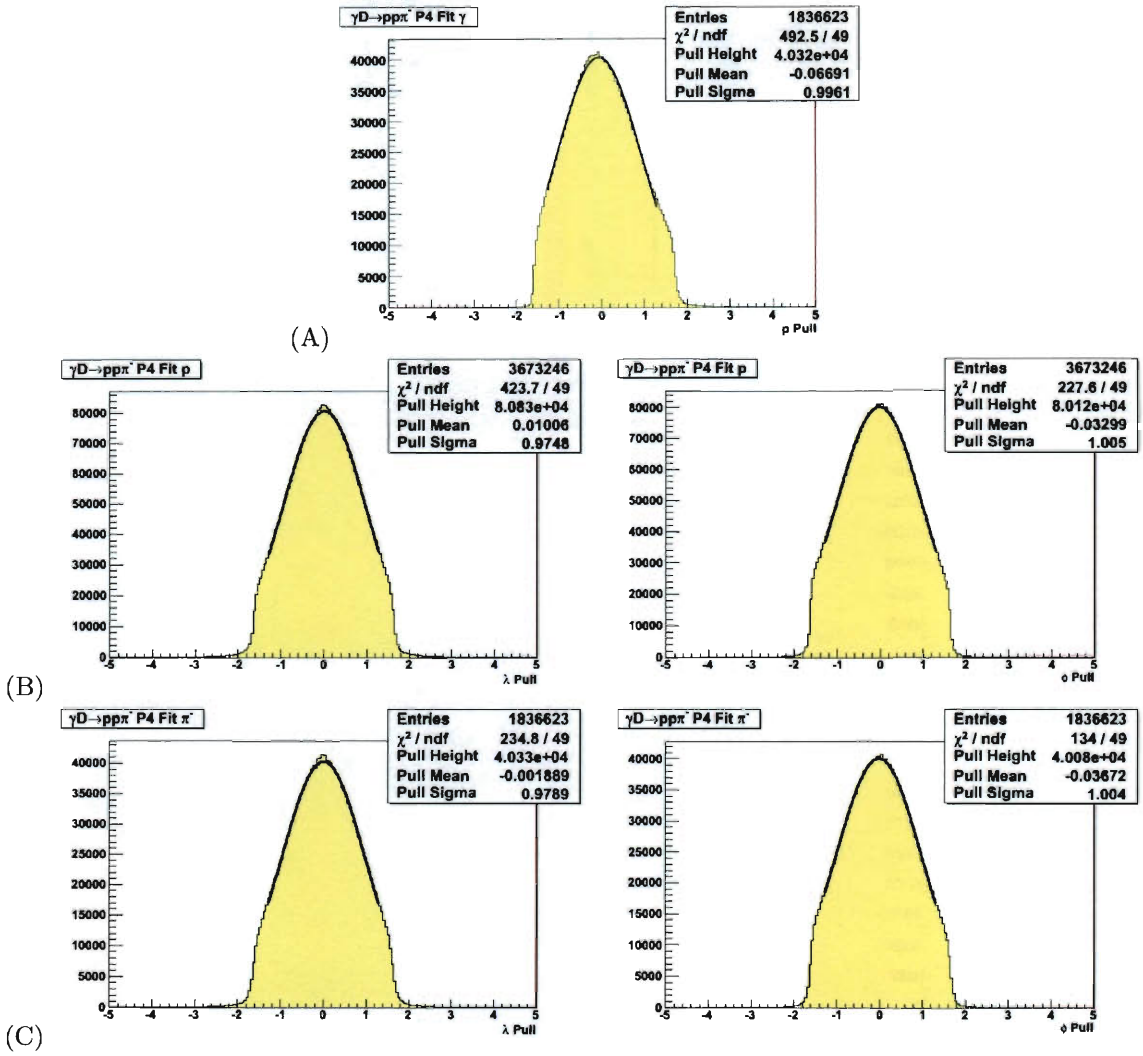

Figure 5.8 : Pull distributions of the track measurements from the kinematic fit of the reaction $\gamma D \rightarrow pp\pi^-$ with the magnitudes of the track momenta treated as unknown for the (A) photon, (B) protons, and (C) π^-. Events with a confidence level less than 10% were cut to remove background events, but this cut also removed the tails of the Gaussian distributions. The coordinate system used for the kinematic fit is defined in Reference [97].

taken into account by the *eloss* package, and differences between the actual and calculated magnetic fields. The error in the measurement of the track momentum was largest for low-momentum protons.

To determine the momentum of the charged particles, the path of the track traversing the drift chambers was measured. The path length of a charged particle in a magnetic field is proportional to:

$$x \sim \frac{\left| \int \vec{B} \times d\vec{l} \right|}{p}. \tag{5.3}$$

Therefore the errors in the momentum measurement were examined in terms of $\Delta(1/p)$, the difference between the inverse of the fit momentum and the inverse of the detected momentum after *eloss* corrections. Although $\int \vec{B} \times d\vec{l}$ varied with track direction and momentum, its value was not readily available for the kinematic fitting analysis. Therefore, during the fitting of the momentum corrections the p- and θ-dependence of $\int \vec{B} \times d\vec{l}$ were assumed to be absorbed to first-order in the fit parameters of Equations 5.4 and 5.6 detailed below [98]. The p, ϕ, and θ aspects of these corrections were fit in different stages because it was difficult to individually disentangle their contributions. These fits were iterated until the momentum corrections converged to a mean Δp of zero. This method of using kinematic fitting to determine momentum corrections was similar to the method detailed in Reference [95].

Starting with the ϕ-dependent measurement corrections, the following fits were iterated until the momentum corrections converged. The ϕ-dependent drift chamber misalignments and magnetic field map deviations were studied by splitting up the tracks in each sector into 10 bins in ϕ. These bins each spanned 5° of the sector azimuth, excluding the 5° region near the torus magnets at the edges of the sectors. This was because track reconstruction near the edges of the detector was problematic due to anomalies in the magnetic field near the surface of the magnets, and possible collisions with the magnet cryostats or the CLAS drift chamber detector frames. For each sector and ϕ-bin of the CLAS detector, these momentum measurement deviations were fit to:

$$\Delta\frac{1}{p} = A_0 + A_1\frac{1}{p}, \tag{5.4}$$

where the fit parameters A represent the contributions of the ϕ-dependent measurement deviations. The fits of the mean $\Delta(1/p)$ for the protons and π^- in the different ϕ-bins for Sector 1 are illustrated

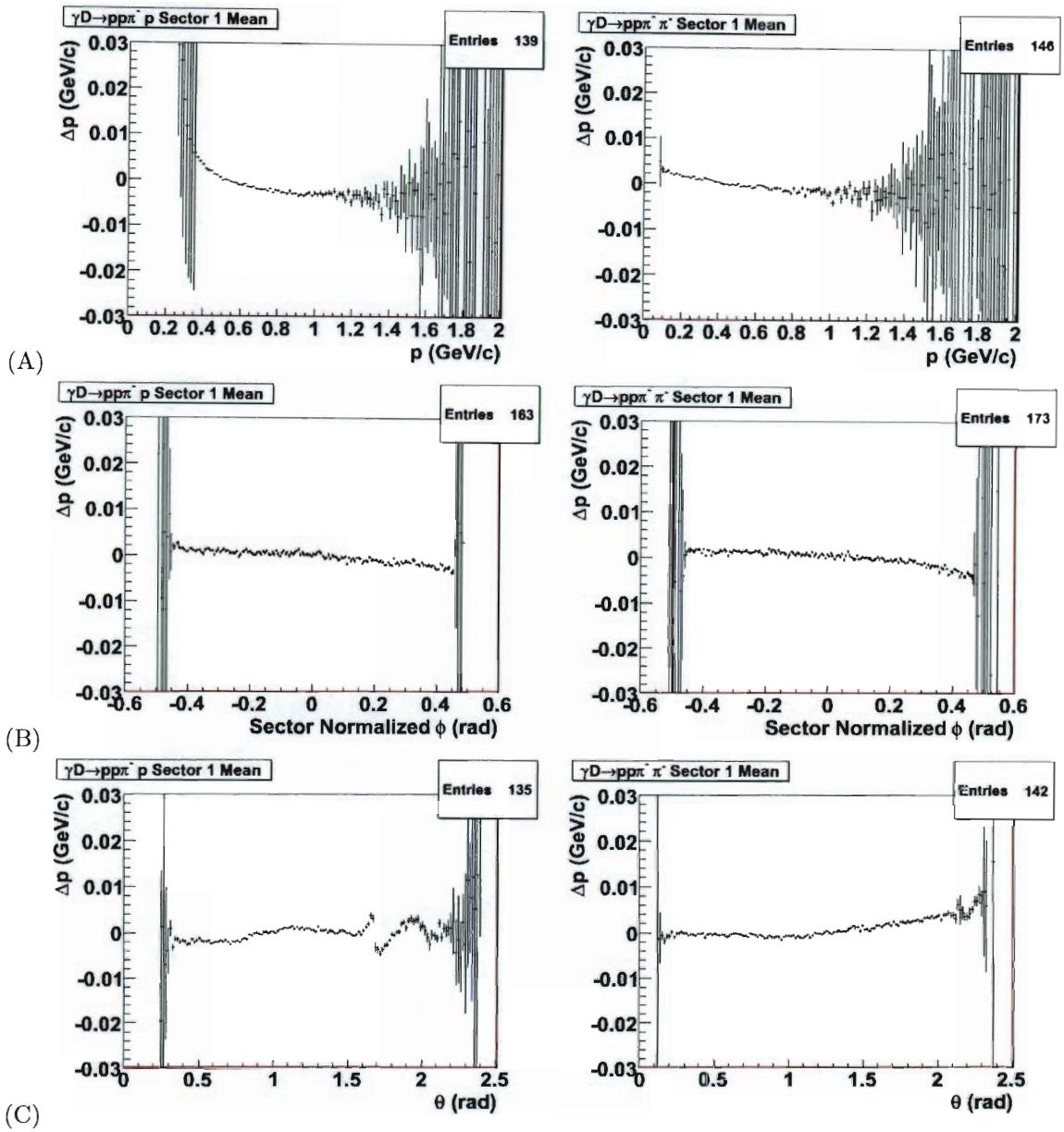

Figure 5.9 : The average difference between the fit and detected momentum after *eloss* corrections as a function of (A) p, (B) ϕ, and (C) θ for Sector 1 of CLAS for the proton and π^-. In (C), θ-dependent holes in the track reconstruction due to inefficient drift chambers and TOF scintillator paddles caused several regions of each sector to have dubious centroids.

in Figure 5.10.

Next, the deviations in the momentum due to energy losses not taken into account by *eloss* were studied as a function of momentum. As seen in Figure 5.11 for Sector 1, the Δp vs. p distributions were significantly improved by the ϕ-dependent corrections. The deviations in momentum were fit as:

$$\Delta p = B_0 e^{-B_1(p+B_2)}, \tag{5.5}$$

where the B's are the fit parameters. The functional form of this equation is an inexact but adequate representation of the Bethe-Bloch energy loss equation at low energies. This correction was not charge dependent but β-dependent, and as seen in Figure 5.11 was much larger for low-momentum protons than π^-'s. This additional energy loss correction was likely due to energy losses in the drift chambers, which were not modeled by the *eloss* software package.

Finally, the θ-dependent drift chamber measurement deviations were studied as a function of θ. Figure 5.12 shows the mean $\Delta(1/p)$ vs. θ in Sector 1 fit to the polynomial:

$$\Delta\frac{1}{p} = \sum_{i=0}^{7} C_i \theta^i, \tag{5.6}$$

where the C's are the fit constants. This fit was limited in θ-range, as the statistics at the backward angles were too low to yield reliable fits. Also, θ-dependent holes in the track reconstruction due to inefficient drift chambers and TOF scintillator paddles caused several regions of each sector to have low statistics, and thus large uncertainties.

After iterating these fits, the mean difference between the fit and corrected momentum is shown vs. p, ϕ, and θ for Sector 1 in Figure 5.13. All of the distributions are mostly flat, indicating that the momentum corrections have converged properly. A complete collection of the histograms for all of the CLAS sectors in this section is located in Appendix A.

5.4 Beam Energy Corrections

No component of the CLAS detector or beamline measured the energy of the incident electron beam. Instead, during track reconstruction it was assumed that the incoming electrons arrived with the nominal, requested beam energy. For g13a, this beam energy was 1.990 GeV for runs 53164 to 53537,

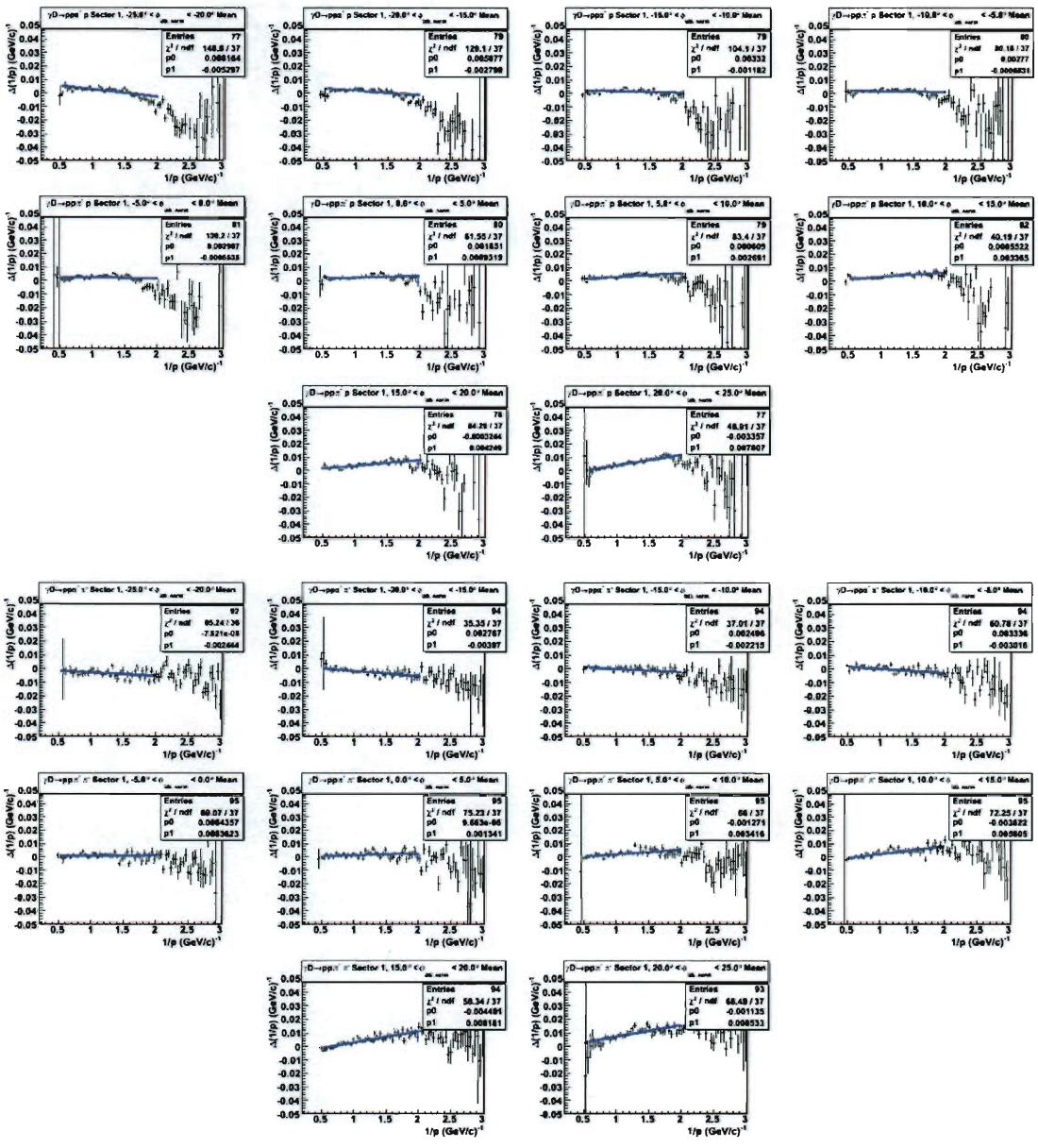

Figure 5.10 : The fit to the mean $\Delta(1/p)$ vs. $1/p$ for the 10 ϕ-bins in Sector 1 for the (A) protons and the (B) π^-. These deviations were due to the ϕ-dependent drift chamber misalignments, and differences between the actual magnetic field and the calculated magnetic field map used in track reconstruction.

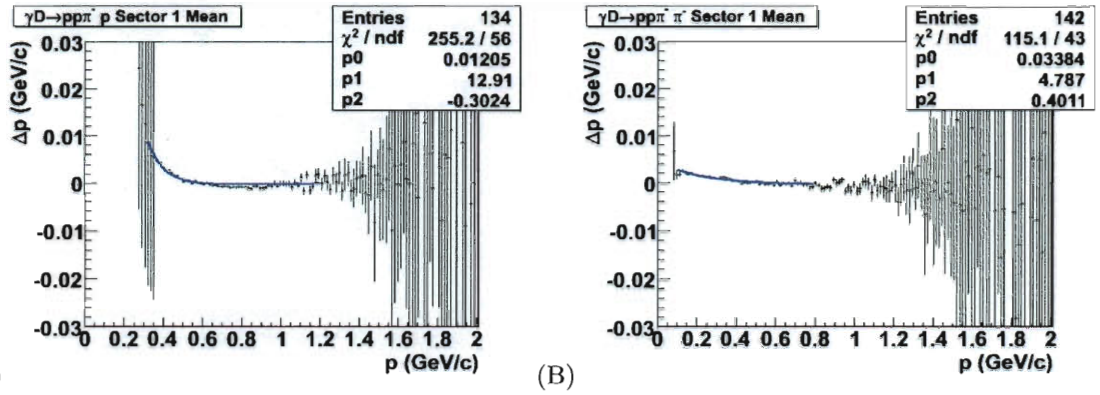

(A) (B)

Figure 5.11 : The mean Δp vs. p distributions for the (A) proton and (B) π^- in Sector 1 of CLAS, updated with the ϕ-dependent corrections. These deviations were likely due to energy losses of the particles as they traversed the drift chambers, which were not modeled by the *eloss* software package.

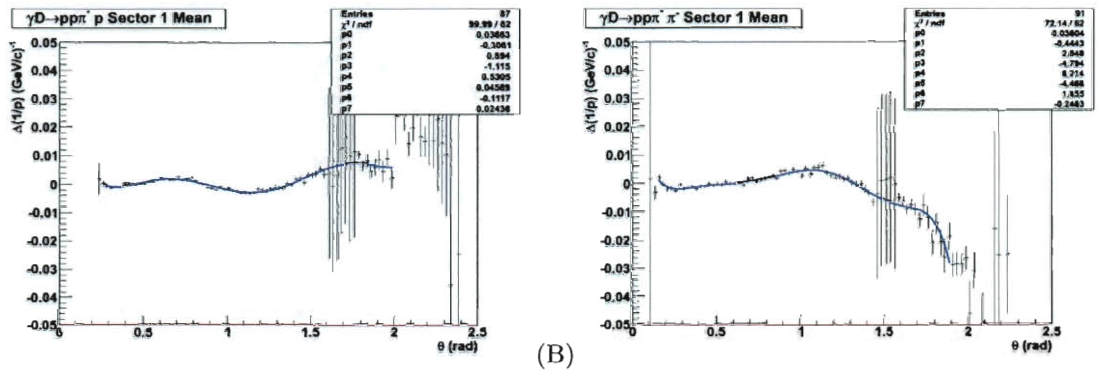

(A) (B)

Figure 5.12 : The fit to the mean $\Delta(1/p)$ as a function of θ in Sector 1 of CLAS for the (A) proton and (B) π^-. These corrections were not fit to the tracks that traversed the backward-most angles of the detector as the data was too sparse in these regions to be confident of the mean $\Delta(1/p)$. In these regions, no θ-dependent momentum corrections were performed.

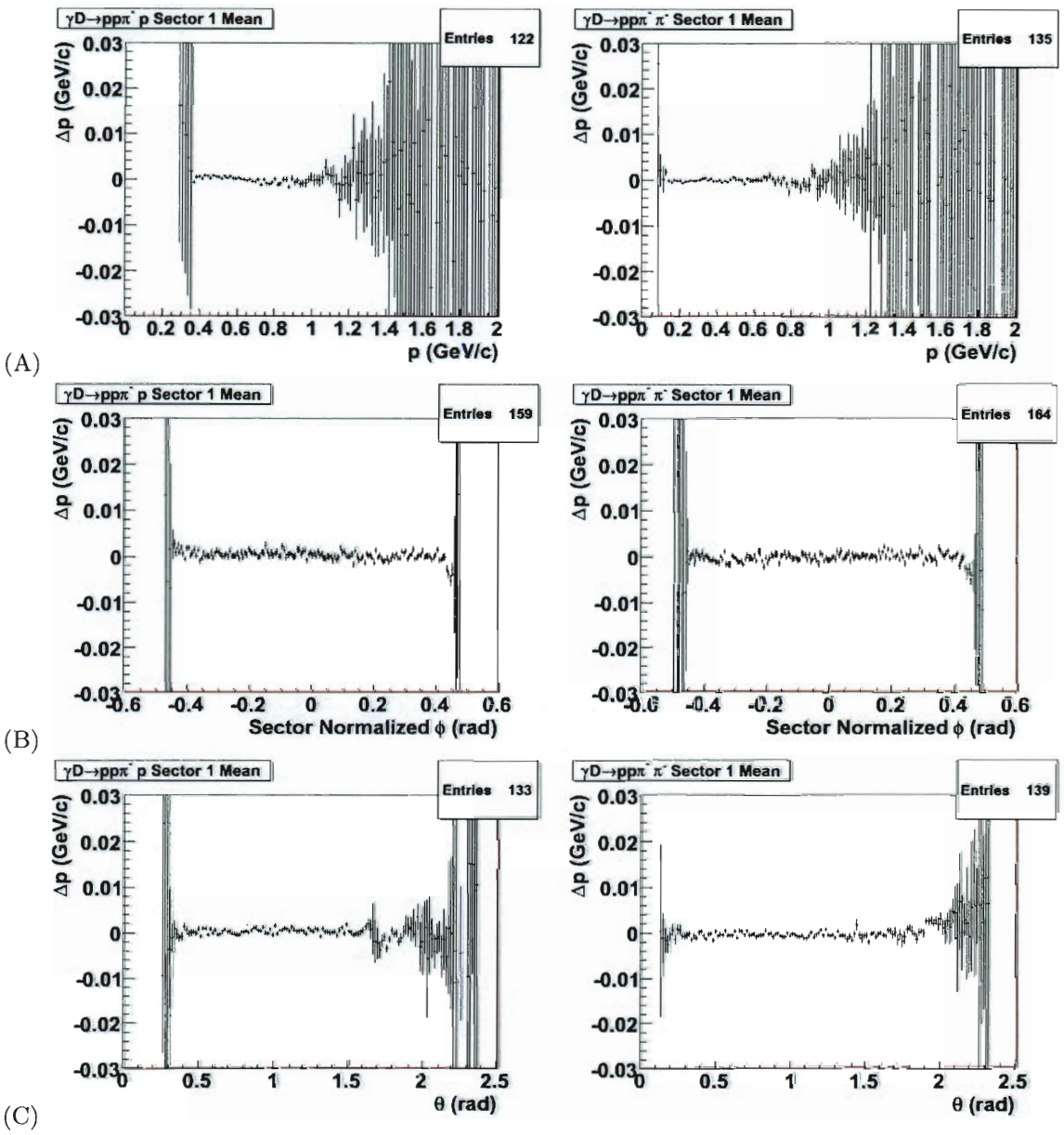

Figure 5.13 : The average difference between the fit and detected momentum after all momentum corrections as a function of (A) p, (B) ϕ, and (C) θ for Sector 1 of CLAS for the proton and π^-.

and 2.655 GeV for runs 53538 to 53862. Therefore, a run-dependent beam energy correction was required for when the electron beam deviated from the nominal energy. These drifts were typically only one or two MeV and had many different causes, including slight variations in cryogenic cooling, beam steering, and beam dispersion effects.

Typically beam energy measurements conducted by either Hall A or Hall C are used to determine the correct beam energy, but neither experimental Hall measured the beam energy during g13a. Instead, the correct beam energy was determined by studying the missing energy of the $\gamma D \to pp\pi^-$ reaction after applying the momentum corrections and tagger energy corrections. The photons produced from bremsstrahlung radiation had an E-bin dependent fraction of the incoming electron beam energy. Therefore instead of correcting the electron beam energy, the individual photon energies were corrected separately for each run by a single, energy-independent multiplicative factor. This correction factor is:

$$\mathrm{CF} = (E_\gamma - E_{\mathrm{Missing}})/E_\gamma, \tag{5.7}$$

where E_{Missing} is the average missing energy in the $\gamma D \to pp\pi^-$ reaction for the given run. This average was determined for each run by fitting the missing energy distributions to a Gaussian function, as done in Figure 5.6.

The calculated beam energy correction factor is shown in Figure 5.14 (A) for runs 53164 to 53537, and Figure 5.14 (B) for runs 53538 to 53862. "Junk" runs with little or no $\gamma D \to pp\pi^-$ events were assigned an energy correction factor of one. The beam energy corrections were quite small, and typically were less than 4 MeV for high-energy photons. Also, the beam energy was extremely stable for runs 53630 through 53650, the runs chosen to determine the additional track momentum corrections.

5.5 Test of Additional Corrections

The additional momentum and beam energy corrections determined in Sections 5.3 and 5.4 were tested by studying the missing mass of the spectator proton in the $\gamma n \to p\pi^-$ reaction. The cuts defined in Section 7.1 were used to select $\gamma n \to p\pi^-$ events from runs 53850 to 53859.

The missing mass of the spectator proton is shown in Figure 5.15 both before (A) and after (B)

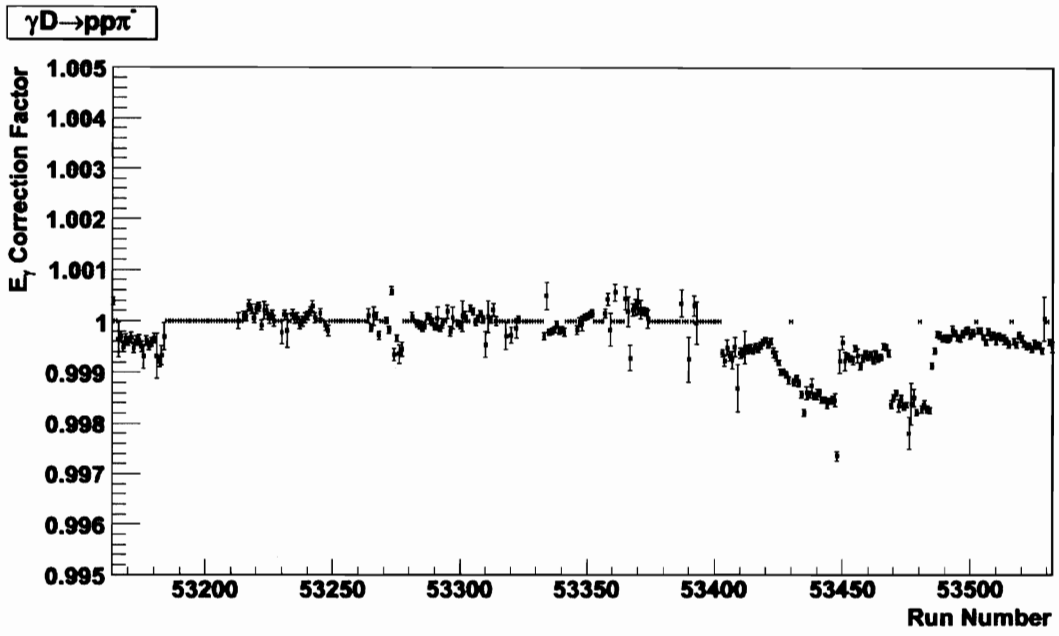

(A)

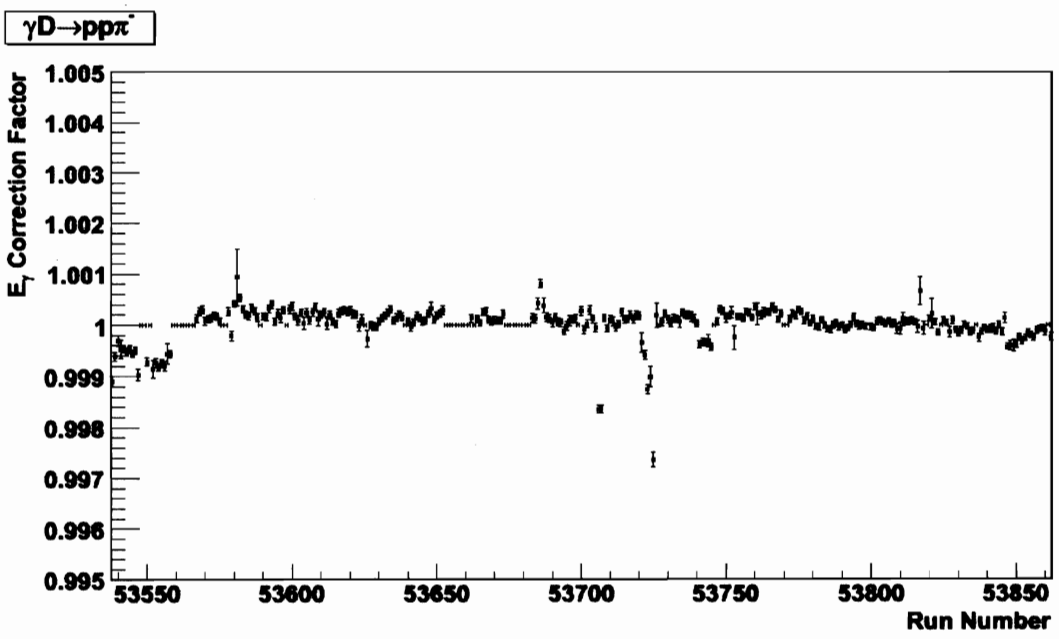

(B)

Figure 5.14 : The calculated multiplicative energy correction factors to the photon energies as a function of run number for both the 1.990 GeV data (A) and the 2.655 GeV data (B). These corrections were typically one to two MeV.

applying the additional momentum and beam energy corrections. By applying these corrections, the mean missing mass of the spectator proton improved from 936.3 MeV/c^2 to 938.0 MeV/c^2, very close to its actual 938.27 MeV/c^2 value. Also, the resolution of the missing mass peak improved from 10.65 MeV/c^2 to 10.05 MeV/c^2, a ~5.6% improvement. Therefore, these additional momentum and beam energy corrections slightly improved the accuracy and resolution of the event reconstruction in CLAS.

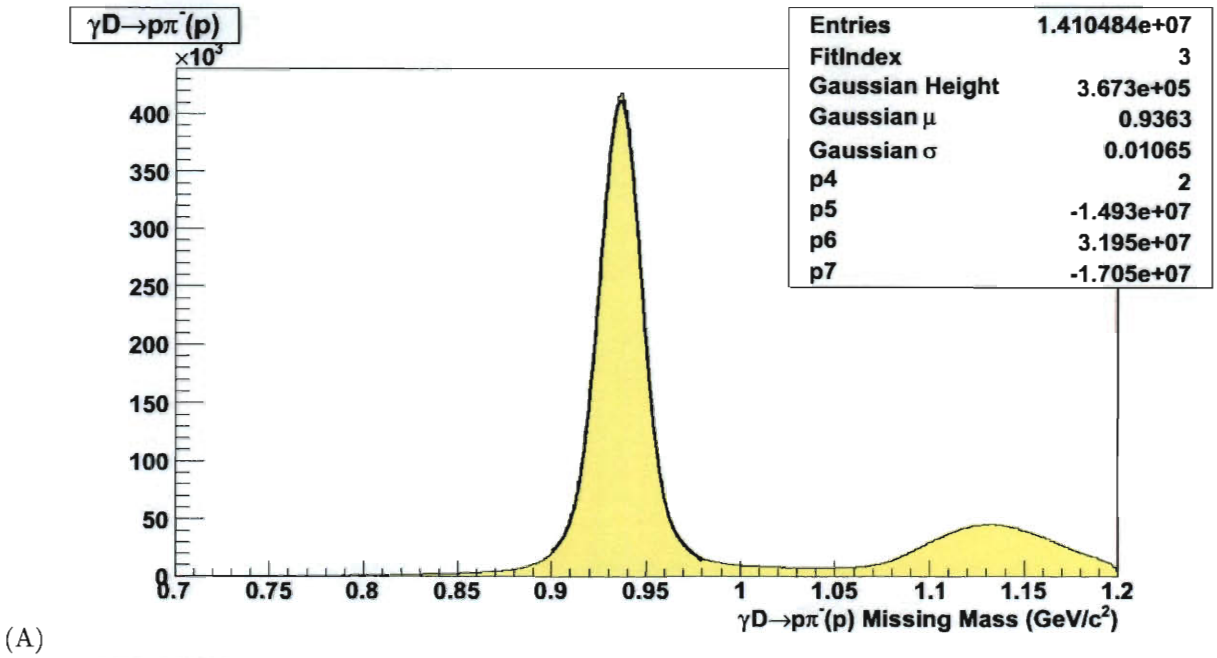

(A)

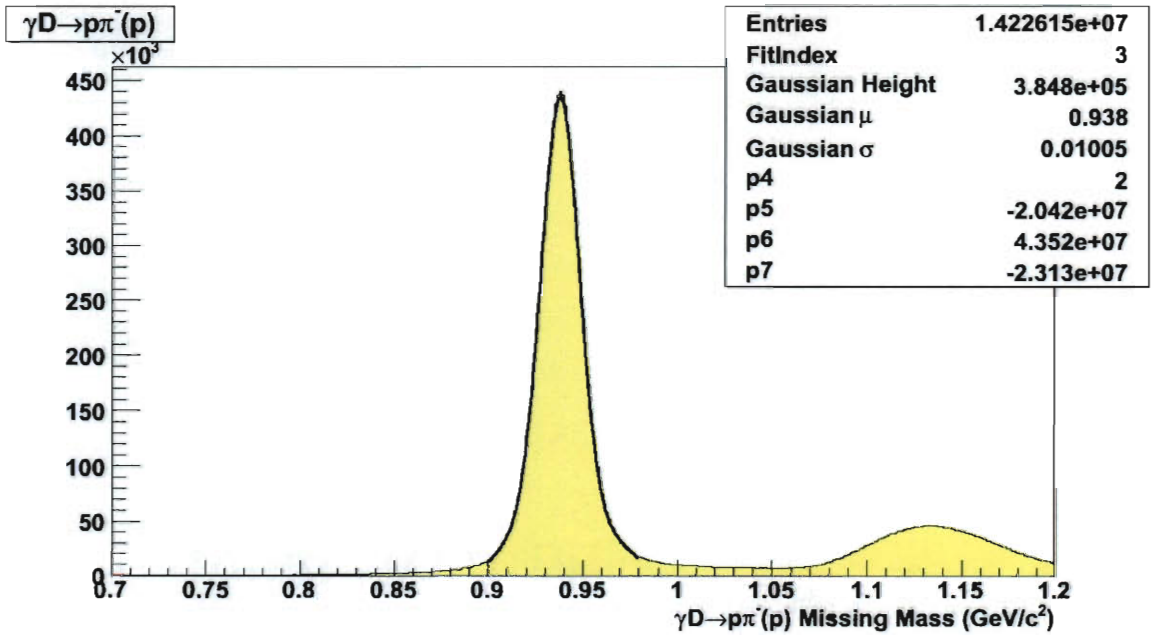

(B)

Figure 5.15 : The missing mass of the spectator proton in $\gamma n \rightarrow p\pi^-$ before (A) and after (B) the additional momentum and beam energy corrections. These distributions were fit to Gaussian functions plus polynomial backgrounds. With the additional corrections the mean missing proton mass improved from 936.3 MeV/c^2 to 938.0 MeV/c^2, and the missing mass resolution improved by ~5.6%.

Chapter 6

CLAS Acceptance and Flux Studies

To measure the cross sections in this analysis, acceptance corrections were needed to account for physics events that were not included in the experimental yield. These events were missing either due to incomplete geometric coverage of the detectors, detector inefficiencies, problems with the detector subsystems during the experiment, or analysis cuts used to reduce the background. These effects were taken into account by generating Monte Carlo data of the physics reactions being studied, simulating the detector response to these events, and applying the same analysis cuts to the simulated data. The fraction of the generated Monte Carlo events that survived these cuts was the acceptance correction for the analysis.

To ensure a proper simulation of the detector response, regions of the dataset that could not be properly modeled were rejected from the analysis. Acceptance studies were performed to determine these regions, which were typically due to dead or inefficient regions of the detectors. Junk data were excluded from the analysis, and regions without stable beam were removed to ensure a more accurate photon flux calculation. Also, an efficiency study was performed to model event losses due to inefficiencies in the DAQ triggering system. Due to both these studies and the different electron beam energies in g13a, the acceptance corrections were modeled separately for three different run ranges, as delineated in Table 6.1.

Run Range	Nominal Beam Energy (GeV)
53333 - 53429	1.990
53430 - 53537	1.990
53538 - 53862	2.655

Table 6.1 : The separate run ranges of the g13a dataset for which the CLAS detector acceptance was modeled.

6.1 Monte Carlo Simulations in CLAS

The *fsgen* software package [99] was used to generate the Monte Carlo data used for determining the CLAS acceptance corrections. For each physics event that was generated, *fsgen* randomly assigned the direction and momentum of the particles in the reaction. Rejection sampling was used to generate the Monte Carlo physics events according to the desired distributions. This was done by first randomly generating the characteristics of each event while preserving energy and momentum conservation. Next, for each event a random number was generated between zero and one for each of the desired probability distributions. If any of the random numbers were greater than the corresponding probability distributions, then the event was rejected.

The target nucleons in the deuteron were generated such that they matched the known Fermi motion distribution [100], and the photon energies such that they matched the bremsstrahlung distribution of the Hall B photon radiator. *fsgen* was capable of generating the reaction products either uniformly across the available phase space, with a specific t-slope, or with a custom distribution such as a cross section prediction. The t-slope is the value of b in the differential cross section formula:

$$\frac{d\sigma}{dt} = \sigma_0 e^{-bt}, \tag{6.1}$$

where σ_0 is the amplitude factor and t is defined in Section 3.1. *fsgen* was also capable of decaying these particles through many of their possible decay chains. The distributions used for each reaction in this analysis are discussed in Sections 7.2 and 8.3.

Based on CERN's detector simulation program suite *GEANT* [101], the *gsim* software package [102] was used to simulate the response of the Hall B photon tagger and the CLAS detector to the generated Monte Carlo events. It propagated the generated particles through a software simulation of CLAS, simulating their physics interactions with the target, detector materials, and the CLAS support frames. Where applicable, the generated particles were randomly decayed at their known

decay rates through their most common decay channels. *gsim* recorded detector hits based on the simulated particle interactions in the detector subsystems. Also, hits were generated in the tagger counters corresponding to the energy of the beam photon.

The *gpp* software package was used to improve the matching between the simulated detector response of *gsim* and that of CLAS. The resolutions of the simulated detector measurements were smaller than those of CLAS, so *gpp* was used to perform Gaussian smearing [102]. The simulated time measurements were smeared for the SC, tagger, and drift chamber subsystems. The tagger time smearing was determined by comparing the time difference between the photons and the RF electron beam bunches in g13a. This time difference was fit to a Gaussian, as shown in Figure 6.1.

The magnitude of the SC and drift chamber smearing in *gpp* was controlled by the use of smearing multipliers. The drift chamber smearing multipliers were determined by studying the missing mass of the $\gamma D \rightarrow p\pi^-(p)$ reaction, as shown in Figure 6.2. The multiplier for the SC time smearing was determined by studying the time difference between the photon and the π^- in the same reaction after smearing the tagger time, as seen in Figure 6.3. The standard smearing multiplier magnitudes of 1.0 provided the best resolution matching between the experimental data and the simulation for the DC and the SC. *gpp* was also used to reject dead photon tagger counters, as discussed in detail in Section 6.2.3.

The *user_ana* software package [103] was used to perform track reconstruction of the simulated data, the same package used for the g13 data. The simulated events were then evaluated in almost the exact same manner as the experimental data, as detailed throughout this analysis. However, neither the CLAS trigger nor particle rescattering off the spectator nucleon were simulated by these software packages, so these effects were taken into account separately. The trigger efficiency correction is discussed in Section 6.3, and rescattering events are discussed in Sections 7.1.4 and 8.1.5.

6.2 Detector-Based Cuts

To properly calculate the detector acceptance correction, dead and inefficient regions of the detector were either rejected from the analysis or modeled in simulation. Junk data were rejected from test runs, runs with critical equipment failure, and regions of data with unstable beam. Fiducial cuts were used to reject tracks passing near the edges of the CLAS drift chambers, where track reconstruction

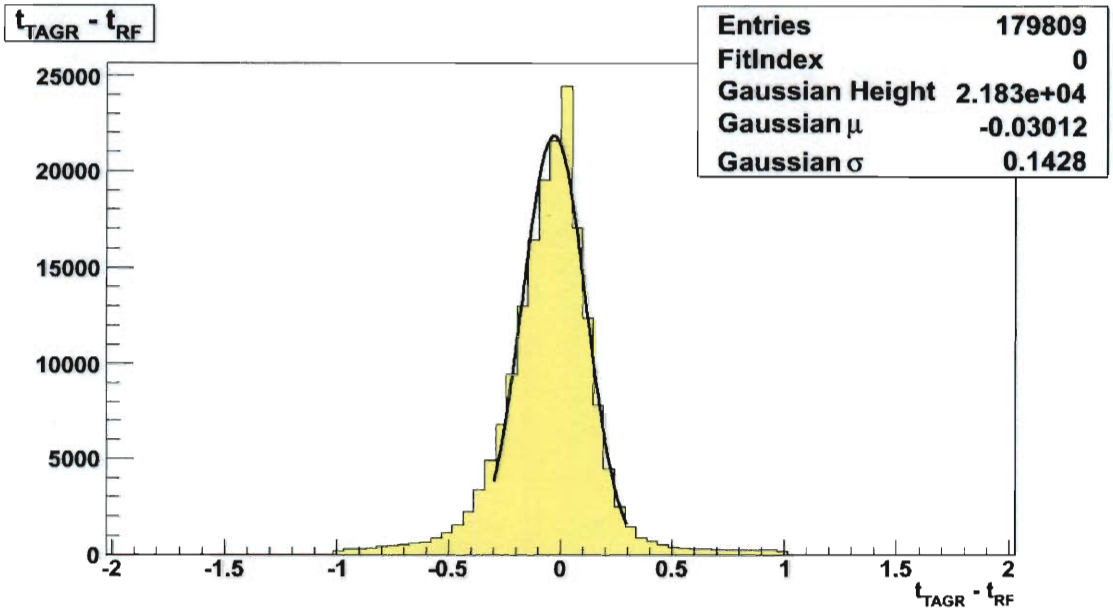

Figure 6.1 : The experimental difference between the photon time from the tagger and the electron RF beam bunch time. The standard deviation of this distribution was used to smear the tagger photon times in the *gpp* program.

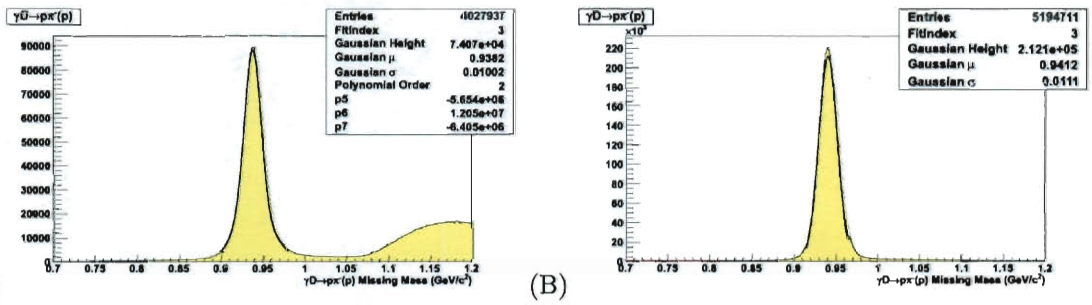

Figure 6.2 : Gaussian fits to the missing mass of the spectator proton in the $\gamma D \rightarrow p\pi^{-}(p)$ reaction from experiment (A) and simulation (B). The simulated drift chamber time measurements were Gaussian smeared using the standard magnitude multipliers, providing close resolution matching to the experimental data.

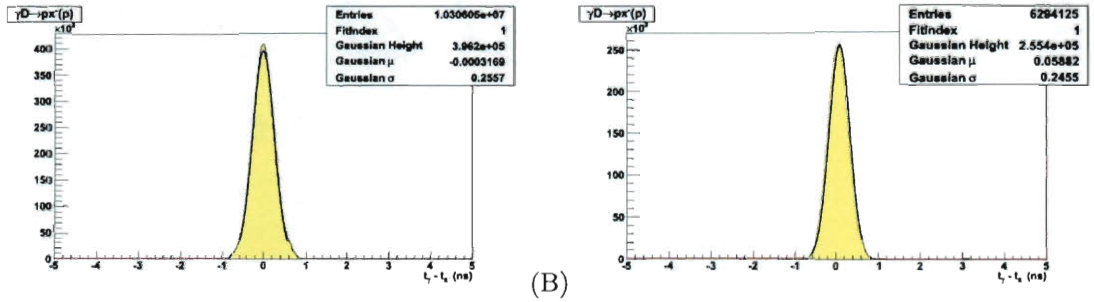

Figure 6.3 : Gaussian fits to the time difference between the photon and the π^- in the $\gamma n \rightarrow p\pi^-$ reaction from experiment (A) and from simulation (B). The simulated SC time measurements were Gaussian smeared using the standard magnitude multiplier, providing close resolution matching to the experimental data.

was not accurate. Also, data were discarded from malfunctioning or poorly calibrated regions of the detector, including bad scintillator paddles, drift chamber holes, and bad tagger counters.

In addition to these cuts, minimum momentum cuts were placed on the particles detected in this analysis. Low-momentum particles were difficult to detect because they lost a significant amount of energy traversing CLAS. Multiple scattering effects were sometimes quite large, and many of the particles were stopped before reaching the TOF scintillators. Therefore, a 100 MeV/c cut was used to remove low-momentum π^-'s, and a 400 MeV/c cut was used to reject low-momentum protons and K^+'s. The effects of these cuts were investigated during systematic uncertainty studies, as detailed in Section 9.4.2.

6.2.1 Data File Selection

The data taken during the g13a experiment evaluated for the acceptance corrections spans from runs 53333 to 53852, but some of these runs didn't contain usable physics events. About 15% of these runs were either system diagnostic runs or calibration runs and were not meant to be used for data analysis. These "junk" runs were indicated as such in both the electronic and hand-written logbooks, and data from these runs were ignored when performing this analysis. Also, runs for which the detector calibrations were significantly misaligned were rejected. Run 53853 had a significant misalignment of the tagger timing calibration and was rejected, but no other runs contained any problems.

There were also some files that contained data with critical system errors, such as high voltage supply losses and detector subsystem problems. Data files associated with these issues were disre-

Setting	E_e (GeV)	I_{beam} (nA)	Run Ranges
1	1.990	40	53333 - 53349, 53436, 53437, 53439 - 53449, 53505 - 53532
2	1.990	45	53350 - 53435, 53438, 53450 - 53504
3	2.655	40	53537, 53538
4	2.655	35	53539 - 53558, 53568 - 53634, 53664 - 53667, 53700, 53701
5	2.655	33	53635 - 53640
6	2.655	37	53567, 53641 - 53663, 53668 - 53698, 53702 - 53862

Table 6.2 : Settings for the electron beam energy and current during the g13a experiment between runs 53333 and 53862.

garded. These problems weren't always thoroughly logged when they occurred, so a study of the data was performed. Files containing these equipment failures were selected by doing a study of the number of reconstructed protons, π^+'s, and π^-'s per event in each sector of the detector.

For a given electron beam energy and current, the proton, π^+, and π^- reconstruction rates in each sector of the detector should have been relatively constant. These rates are shown as a function of run number in Figure 6.4. Table 6.1 shows the run ranges for the different beam energies, while Table 6.2 details the beam currents as well. Individual runs with rates lower than 80% of the rates of the adjacent runs were typically "junk" runs.

The reconstruction rates dropped significantly for runs 53436 - 53447 because a different event triggering condition was tested. For these runs, a pre-scaled single-sector trigger was added to the existing triggering condition. For a pre-scaled fraction of the time, events with a coincidence between the ST and TOF in at least one sector were accepted in addition to the two-sector triggers. These runs were rejected from the analysis because modeling the triggering efficiency for this small run range would have been impractical.

For each beam setting, data files where the reconstruction rates of either protons, π^+'s, or π^-'s in a given sector deviated by more than 5% from their average values were rejected. These cuts are illustrated for all sectors in Figures 6.5 through 6.10 for the six beam settings of Table 6.2, respectively. The files containing the pre-scaled single-sector trigger data are evidenced by the peak between 85% - 90% in Figure 6.5. The significant drop in the track reconstruction rate at run 53469 in Figure 6.4 corresponds to a trip of the central helium liquefier. Although this manifested as the double-peaked structures in both Figures 6.5 and 6.6, the difference in reconstruction rate was small enough that the vast majority of these files survived the 5% cuts.

Also, in run 53604 a low-voltage trip near the very front of the Region 2 drift chambers of Sector 5 caused a large hole to appear in track reconstruction that was unrepairable at the time. The

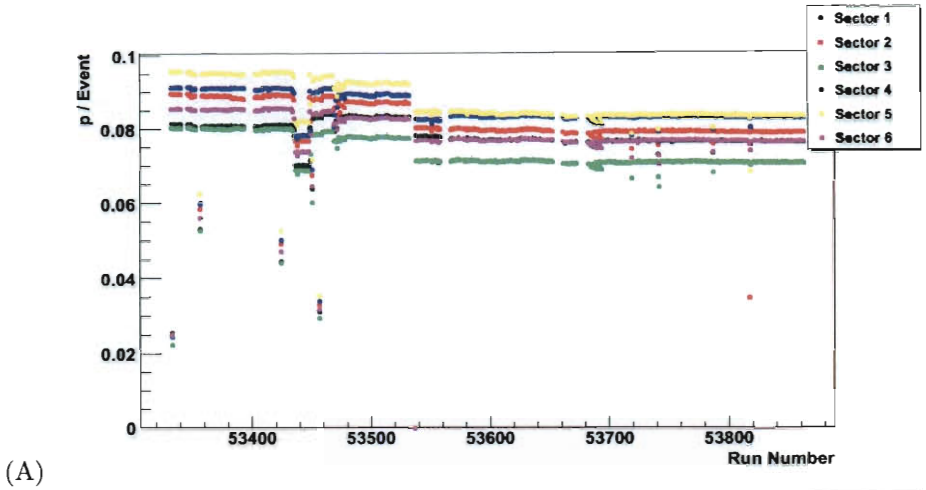

(A)

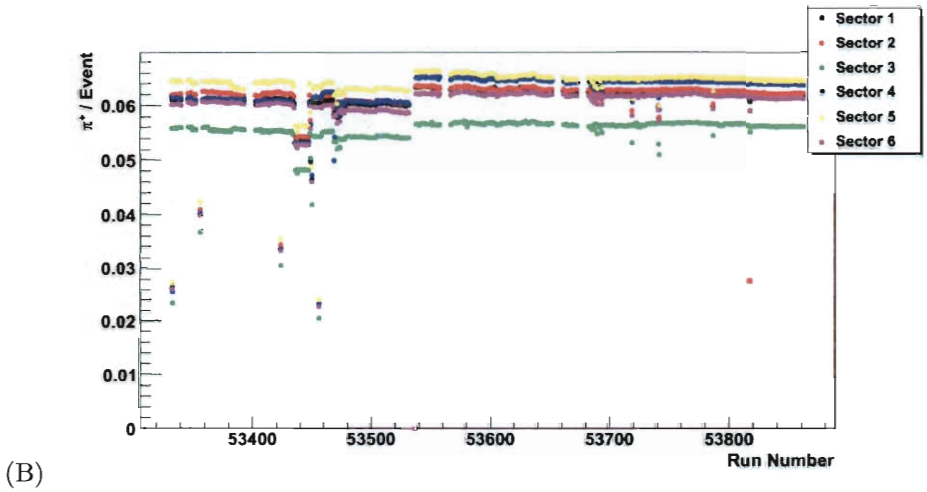

(B)

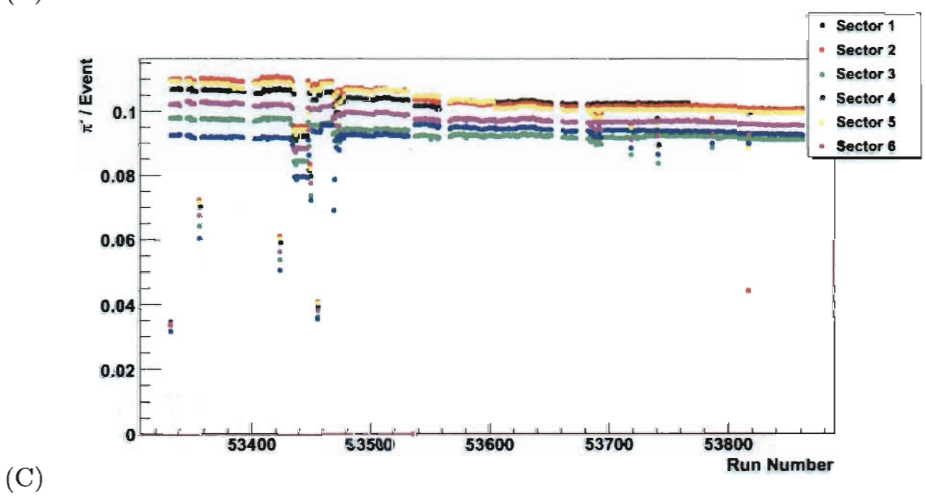

(C)

Figure 6.4 : The rate of proton (A), π^+ (B), and π^- (C) track reconstruction for the run range of g13a used in this analysis.

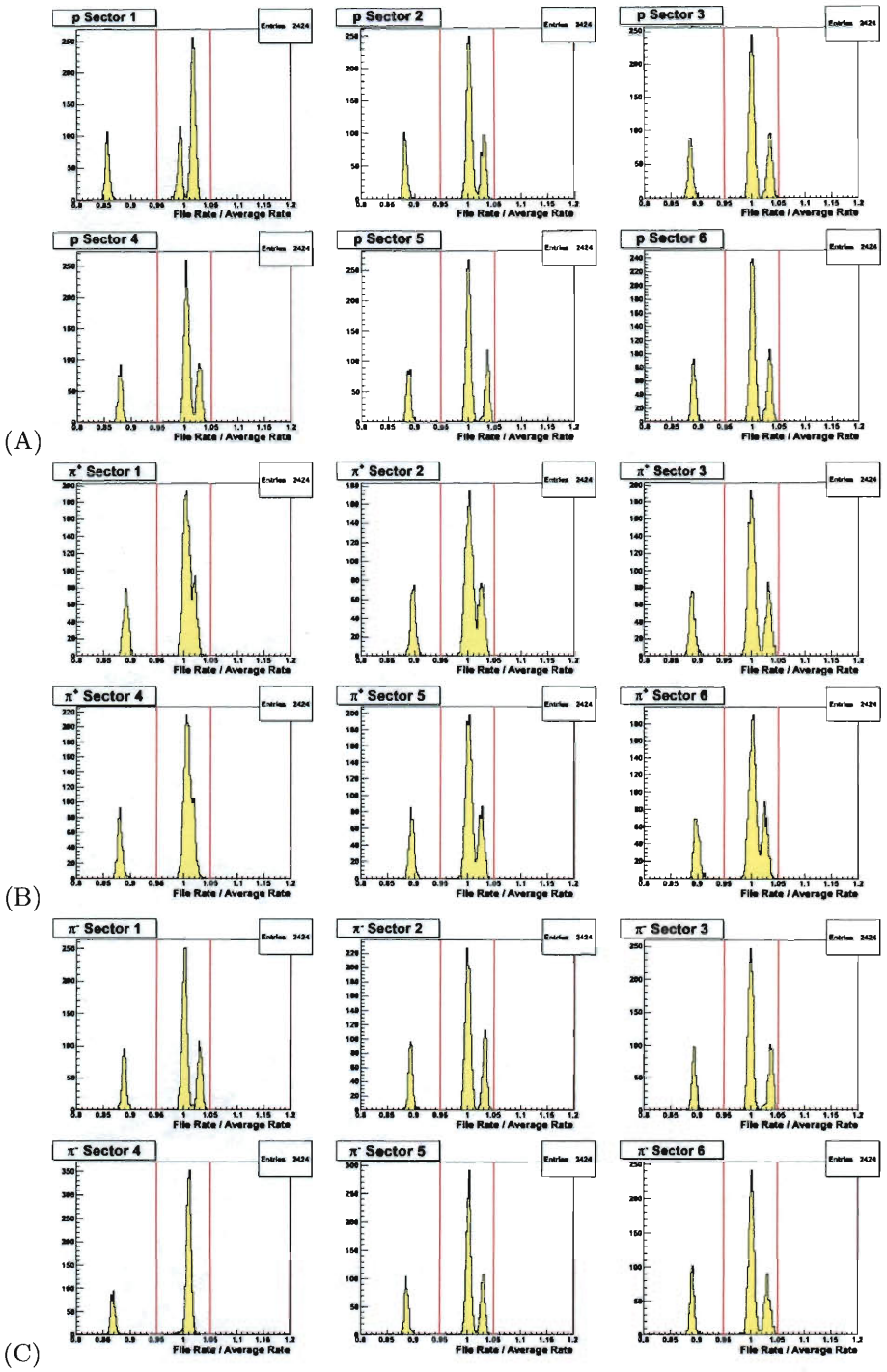

Figure 6.5 : The percentage of the average reconstruction rate of the protons (A), π^+'s (B), and π^-'s (C) in the six sectors of CLAS for the files in the 1.990 GeV, 40 nA data of g13a. Cuts were placed on these distributions at $\pm$ 5%, indicated by the red lines. These cuts removed data files containing temporary detector subsystem problems. The causes of the multiple-peaking are discussed in Section 6.2.1.

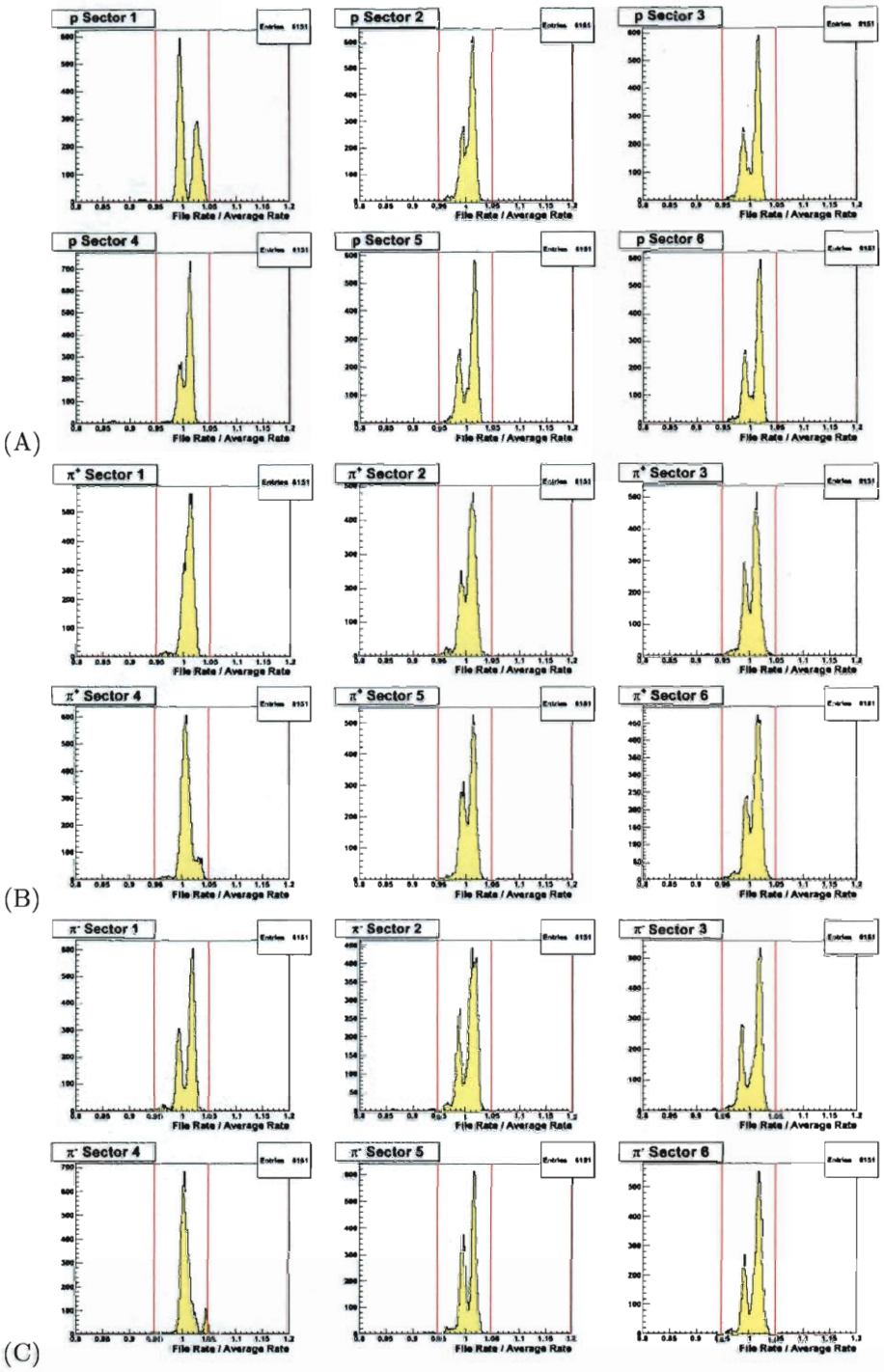

Figure 6.6 : The percentage of the average reconstruction rate of the protons (A), π^+'s (B), and π^-'s (C) in the six sectors of CLAS for the files in the 1.990 GeV, 45 nA data of g13a. Cuts were placed on these distributions at $\pm$ 5%, indicated by the red lines. These cuts removed data files containing temporary detector subsystem problems. The causes of the multiple-peaking are discussed in Section 6.2.1.

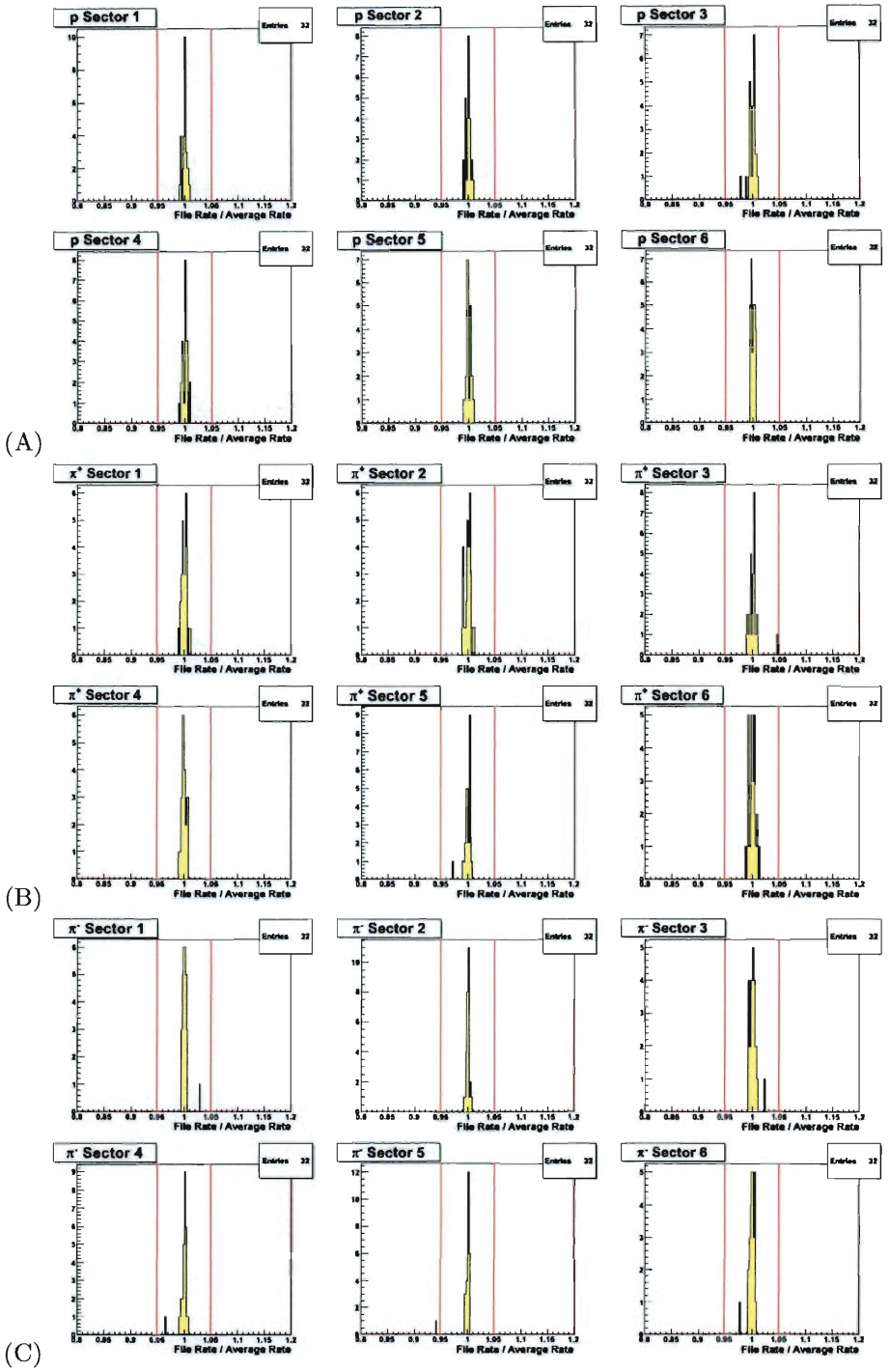

Figure 6.7 : The percentage of the average reconstruction rate of the protons (A), π^+'s (B), and π^-'s (C) in the six sectors of CLAS for the files in the 2.655 GeV, 40 nA data of g13a. Cuts were placed on these distributions at $\pm$ 5%, indicated by the red lines. These cuts removed data files containing temporary detector subsystem problems. The causes of the multiple-peaking are discussed in Section 6.2.1.

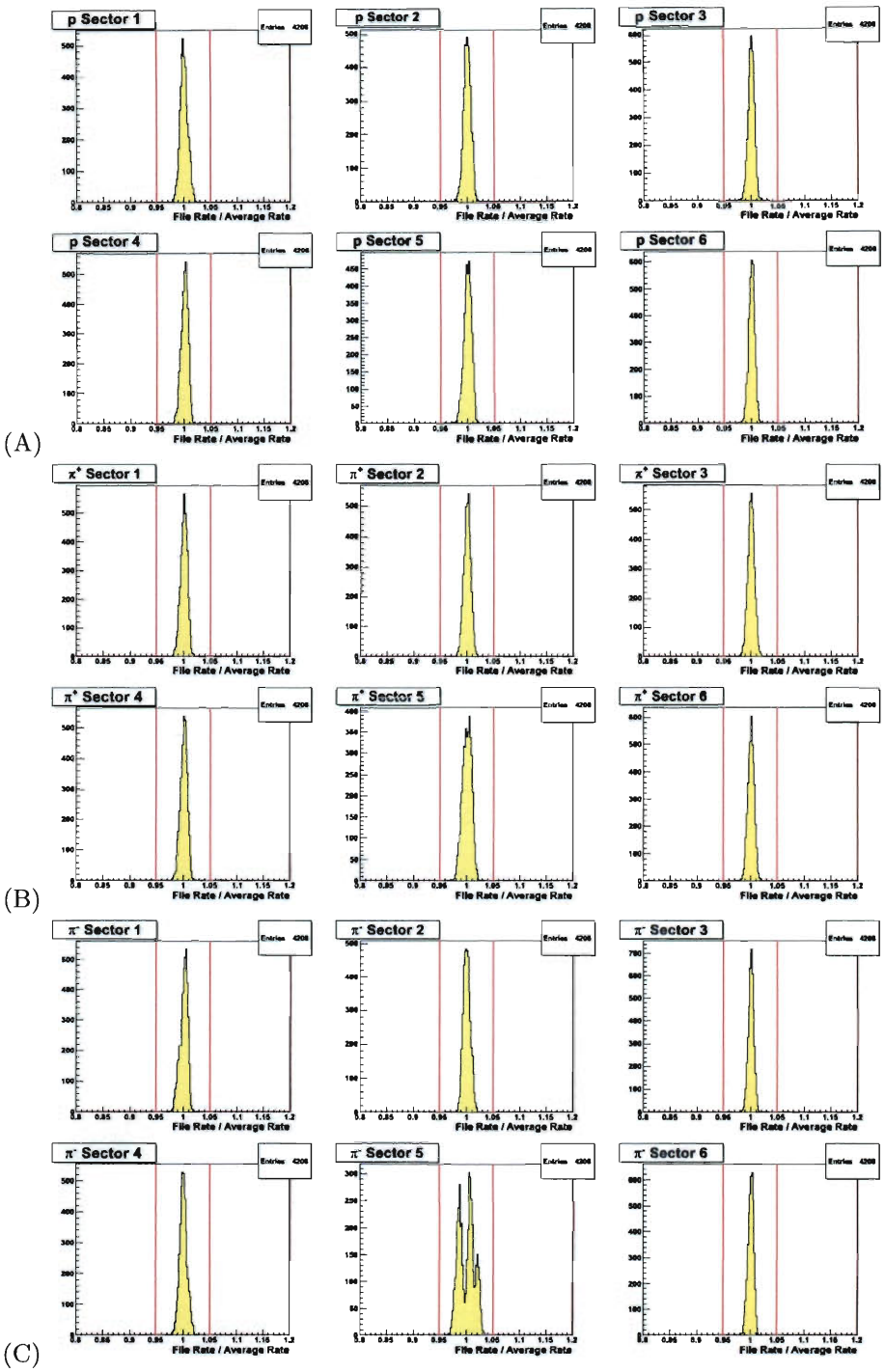

Figure 6.8 : The percentage of the average reconstruction rate of the protons (A), π^+'s (B), and π^-'s (C) in the six sectors of CLAS for the files in the 2.655 GeV, 35 nA data of g13a. Cuts were placed on these distributions at $\pm$ 5%, indicated by the red lines. These cuts removed data files containing temporary detector subsystem problems. The causes of the multiple-peaking are discussed in Section 6.2.1.

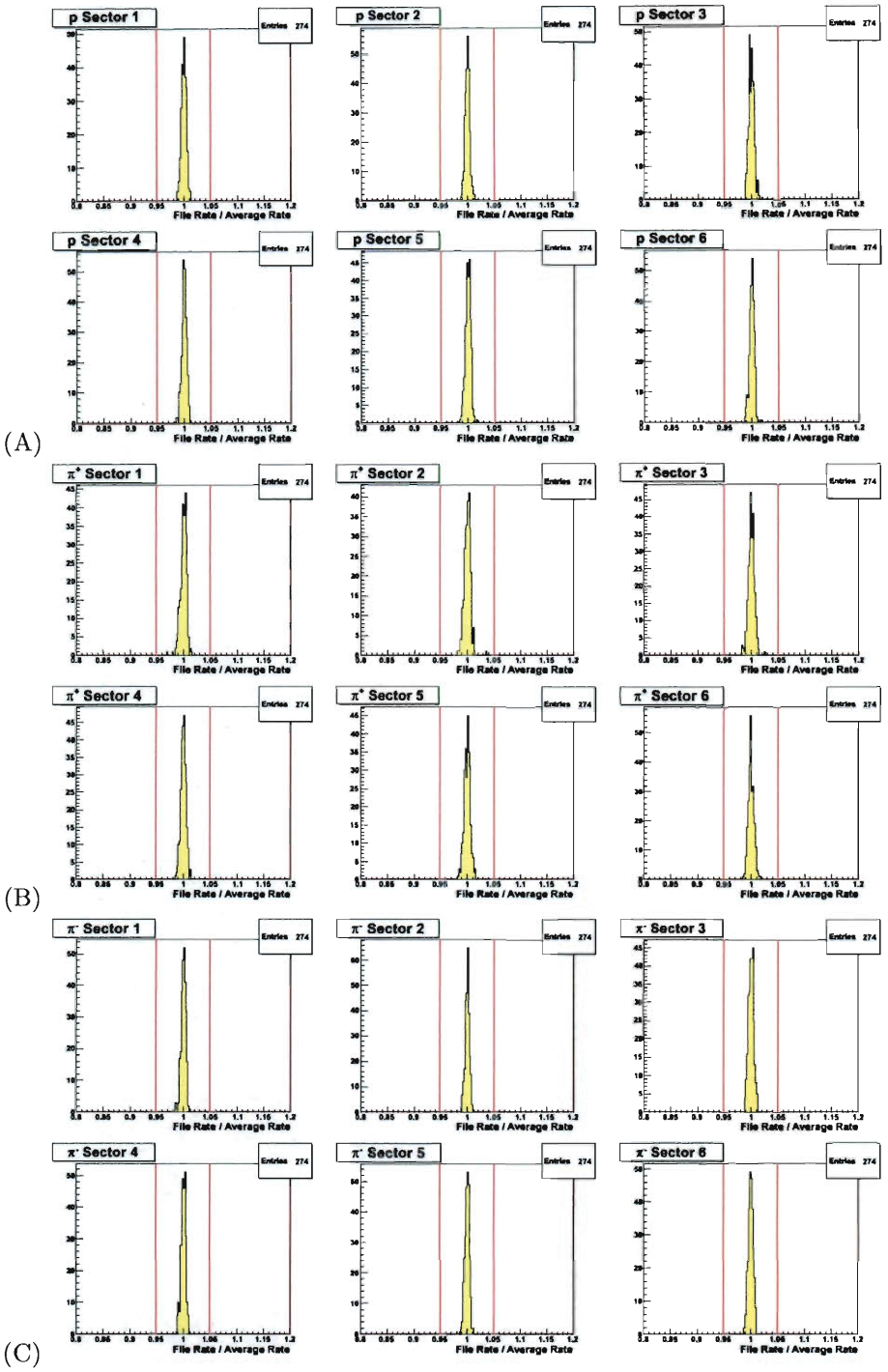

Figure 6.9 : The percentage of the average reconstruction rate of the protons (A), π^+'s (B), and π^-'s (C) in the six sectors of CLAS for the files in the 2.655 GeV, 33 nA data of g13a. Cuts were placed on these distributions at $\pm$ 5%, indicated by the red lines. These cuts removed data files containing temporary detector subsystem problems. The causes of the multiple-peaking are discussed in Section 6.2.1.

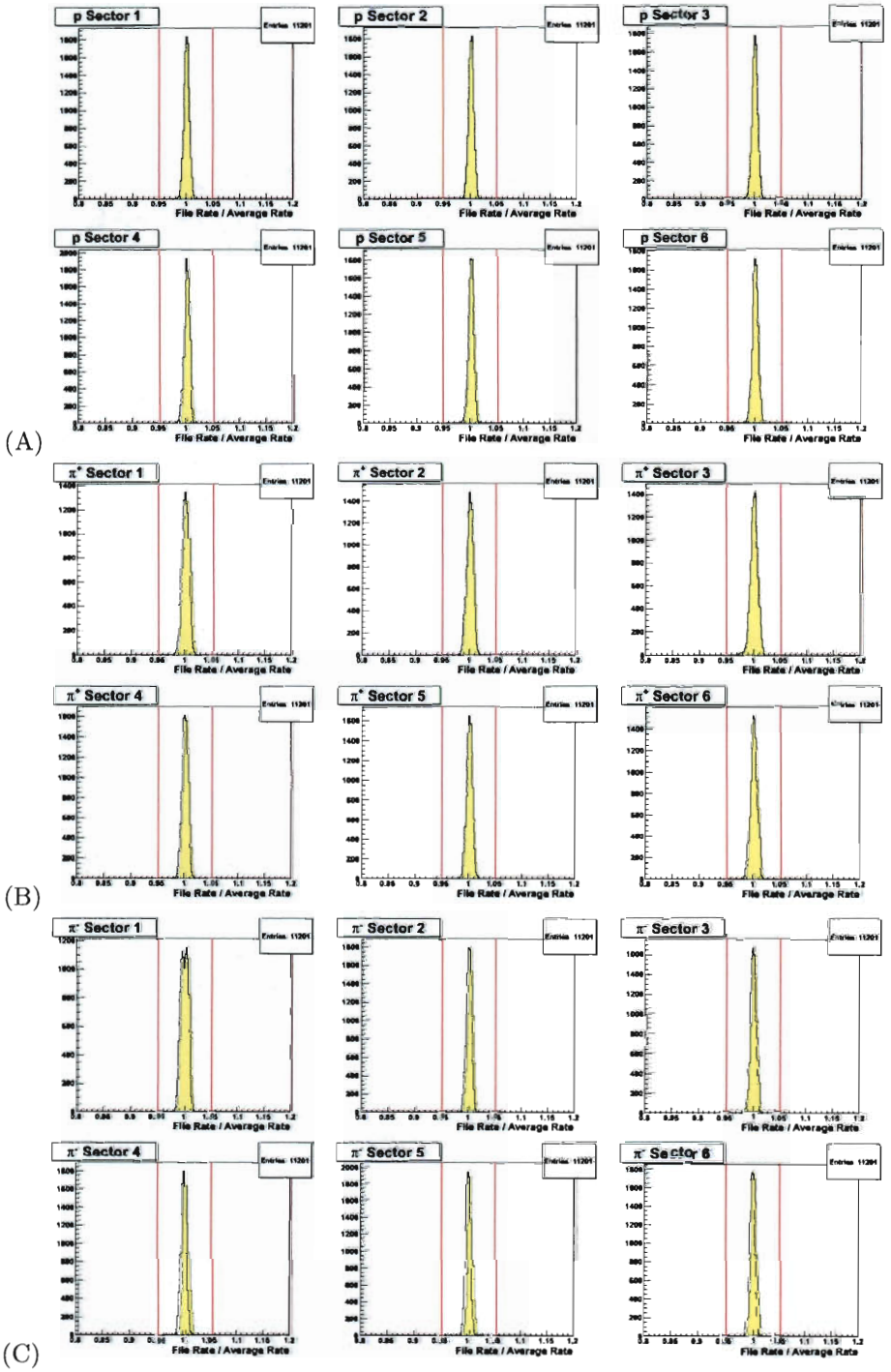

Figure 6.10 : The percentage of the average reconstruction rate of the protons (A), π^+'s (B), and π^-'s (C) in the six sectors of CLAS for the files in the 2.655 GeV, 37 nA data of g13a. Cuts were placed on these distributions at $\pm$ 5%, indicated by the red lines. These cuts removed data files containing temporary detector subsystem problems. The causes of the multiple-peaking are discussed in Section 6.2.1.

effects of this hole are visible primarily for the π^-'s in Figure 6.8(D), but not for the positively charged tracks. This is because the torus magnet was bending all but the fastest positively charged tracks in that region of the drift chambers forward enough that they missed either the Region 3 drift chambers or the TOF scintillator paddles. Overall, these cuts resulted in a loss of ~3.5% of the production data files, over half of which were the pre-scaled single-sector trigger data.

6.2.2 Beam Trips

During the g13 experiment, the electron beam supplied by the CEBAF accelerator frequently tripped off and wasn't delivered. This was usually due to beam steering migration from either natural causes or minor accelerator hardware problems such as magnet trips or vacuum leaks. It usually took from several seconds to several minutes for a stable beam to return; meanwhile the DAQ was usually still recording physics events. However as detailed in Section 6.4.1, the *gflux* software package [104] could not accurately calculate the flux for the 10 second scalar intervals containing beam trips. Therefore, these sections of the CLAS data were rejected from this analysis to ensure proper cross section calculations.

Scalar counts from different CLAS subsystems were recorded at the end of each interval and were used by the *sync* software package [104] to determine which intervals contained beam trips. The *sync* package assumed that the first whole scalar interval in each data file did not contain a beam trip, and compared the other scalar intervals to it. Scalar intervals containing a significantly different number of events than the first whole interval were flagged as containing beam trips. Information on these scalar intervals were then saved into *trip* files, including the beam trip flags. However, when a beam trip occurred in the first whole scalar interval of the data file, the *sync* routine incorrectly determined which scalar intervals contained the beam trips.

To fix this problem a new software program was written, the *tripfixer* routine [105], which looped over the existing *trip* files and re-determined which scalar intervals contained the beam trips. For each trip file, it first calculated the mean number of physics events per scalar interval. It then rejected the interval with the largest deviation from this average if it contained 90% or less of the physics events of the mean. This process was repeated until scalar regions stopped being rejected. These rejected scalar intervals were identified as containing beam trips. Using this procedure for g13a, 7.5% of all scalar intervals were re-identified as good data, and 1.3% of all scalar intervals were

re-identified as containing beam trips. Overall, ~15% of the scalar intervals were rejected due to beam trips. This routine was integrated into the *sync* software package for use in future experiments.

6.2.3 Tagger Counter Cuts

As detailed in Section 4.2.1, the Hall B photon tagger contains 61 barely overlapping T-counters and 384 partially overlapping E-counters. These counters detected deflected electrons to tag the photons that were incident on the CLAS target. Bins corresponding to dead and highly inefficient counters were rejected from the experimental data, simulation, and flux to calculate the cross sections in this analysis correctly. Bins corresponding to T-counters with less than 50% of the hits of the adjacent counters were rejected, along with bins corresponding to dead E-counters. These counters were identified by studying the photon flux and particle yields as a function of T-counter and E-counter.

Because the tagger counters partially overlap, 121 T-bins and 767 E-bins were used for determining the timing and energy of the radiated photons. For both sets of counters, the odd-numbered bins were assigned to electrons that were detected in only one of the partially overlapping counters, and the even-numbered bins were assigned when the electrons were detected in two counters. However when one of these counters was inefficient, electrons that would have been detected in two overlapping counters were instead detected in only one counter.

This bin migration caused these photons to be assigned the wrong energy, and was modeled in simulation by rejecting the dead and highly inefficient counters with *gpp*. *gpp* removed photons that were tagged in the non-overlapping bins of the rejected counters, and migrated photons that were tagged in their overlapping bins into the non-overlapping bins of the adjacent counters.

Shown in Figure 6.11 is the detected photon flux incident on the target for a portion of the g13a experiment. As seen in Figure 6.11(A), T-counters 30, 39, 45, and 55 were weak, having less than 50% of the counts of their adjacent counters, and T-counters 48 and 61 were either extremely weak or dead. These inefficiencies are evidenced by wide holes in the E-bin distribution of Figure 6.11(B). Additional holes in this distribution correspond to E-counters 60, 225, 240, 257, 281, and 364. The spikes in this distribution are from bin migration of the photons from the overlap bins of these dead E-counters. The calculation of the photon flux was performed by the *gflux* program as detailed in Section 6.4.

The sharp rise in flux near T-counter 19 was due to the expanded width of the T-counter

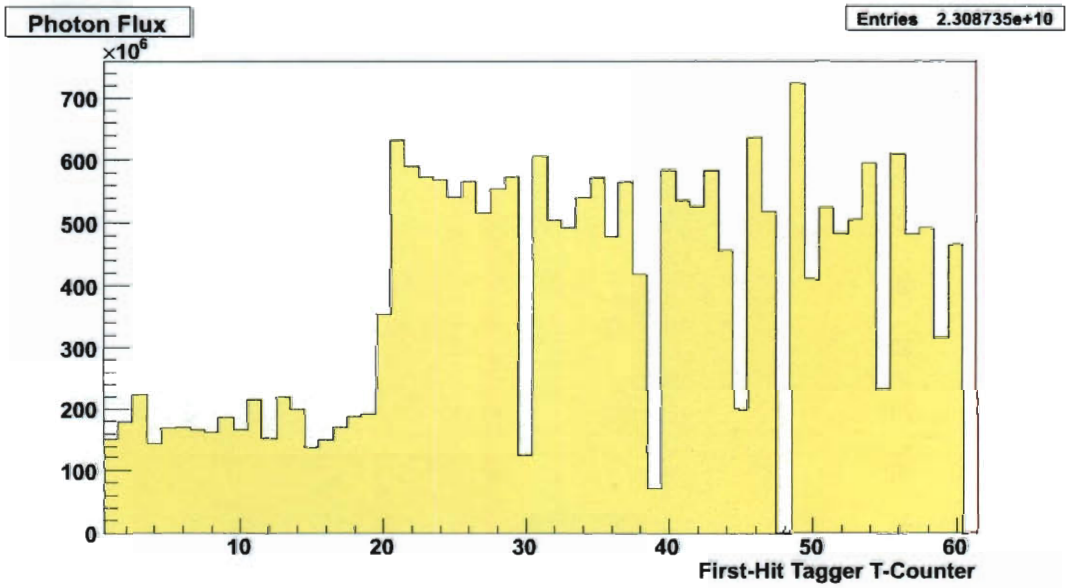

(A)

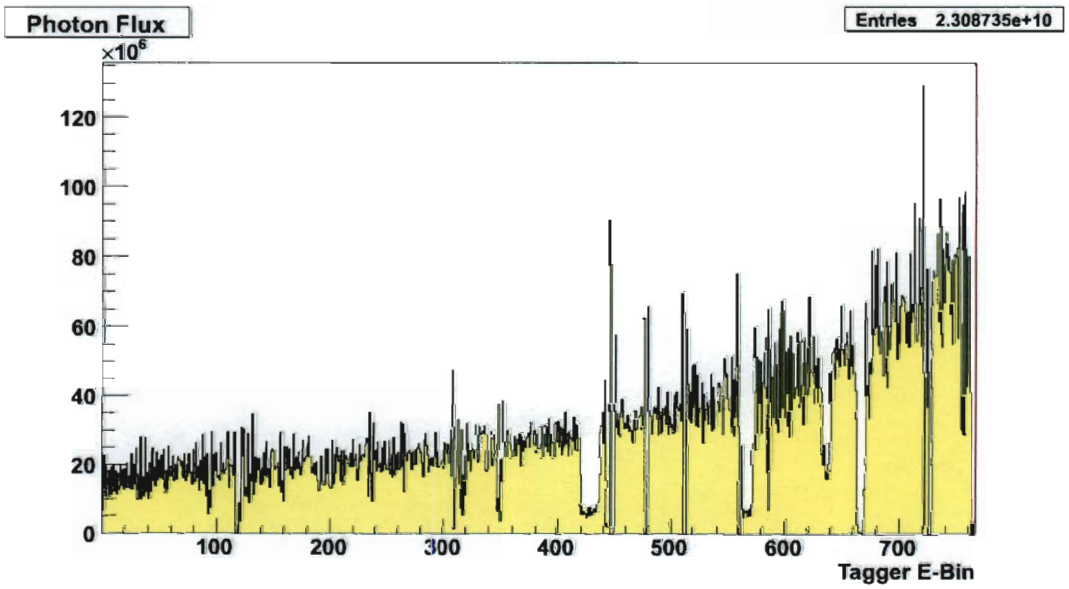

(B)

Figure 6.11 : Photon flux vs. first-hit T-counter (A) and E-bin (B) for a portion of the g13a experiment. Holes in the distribution correspond to either dead or inefficient T-counters or E-counters. Spikes in the distributions are due to bin migration from overlap bins containing dead or inefficient counters.

scintillators. T-counters 1 - 19 corresponded to photon energies from 75% to 95% of the electron beam energy. These T-counters are narrower than the others to allow for considerably higher tagged photon rates for high energy photons [84].

Figure 6.12 shows the charged particle yields for a portion of g13a as a function of the first-hit T-counters and E-bins that the photon with the closest time to the particles was tagged from. These distributions are very similar to those of the photon flux shown in Figure 6.11, and the same T-counters and E-counters appear to be dead or extremely inefficient. Although the other counters may not have been 100% efficient, their inefficiencies were taken into account in the photon flux calculation.

The effect of these inefficiencies was investigated by studying the flux-normalized yields of charged particles as a function of first-hit T-counters and E-bins, as shown in Figure 6.13. The flux-normalized yield was calculated as the yield of the charged particles divided by the photon flux. The general shapes of these distributions are from the contributions of many different photoproduction reactions. The bump from first-hit T-counters 49 to 58, is likely from photoproduction of the N(1440) or N(1520) resonances, which have relatively large cross sections [106]. The largest deviations from this distribution are T-counters 30, 39, 45, 55, and 61, the bad T-counters identified earlier. T-counter 48 does not appear to deviate much, but its uncertainty is large due to a lack of statistics. Inefficiencies in the other T-counters appear to cancel each other out to first-order.

However significant, periodic structures can be seen in the flux-normalized yields of charged particles as a function of E-bin, as shown in Figure 6.13(B). This phenomenon was determined to be caused by problems in the calibration of the photon tagger timing. Because there was a very high rate of deflected electrons incident on the tagger counters, accurate timing was essential to matching electron hits between the E-counters and the T-counters. Skews in the g13a timing calibration caused electrons hitting near the edges of the T-counters to be occasionally matched into the wrong T-bins. The maxima in Figure 6.13(B) correspond to E-bins for which an unphysically large number of T-counters were matched. The minima correspond to E-bins for which too few T-counter hits were matched because they were migrated into other E-bins.

This effect caused a small, periodic migration of the photon beam energies. However, the photon energy bins used for the cross section analyses detailed in Sections 7.1.5 and 8.2 were large compared to the period of the bin migration. This migration caused a slight decrease in the resolution of the

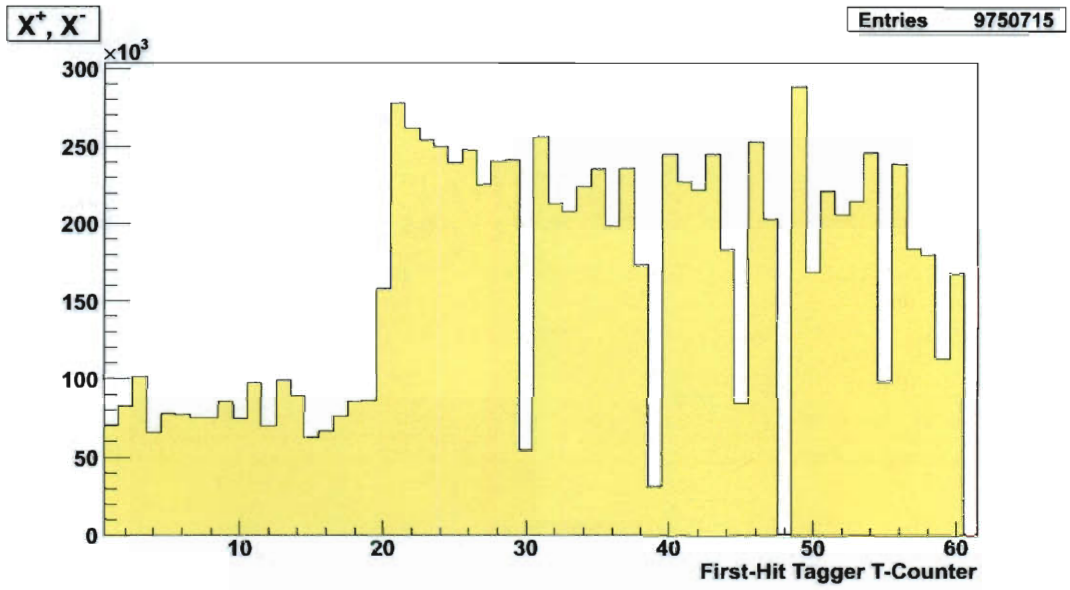

(A)

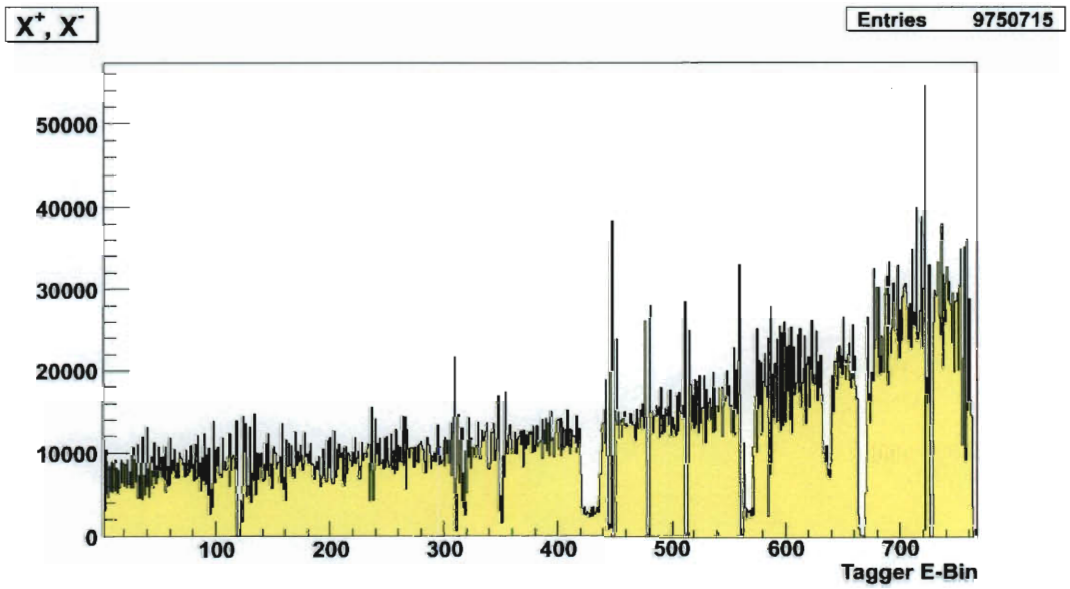

(B)

Figure 6.12 : The number of charged particles corresponding to photons in the first-hit T-counters (A) and E-bins (B) for a portion of the g13a experiment. Holes in the distribution correspond to either dead or inefficient T-counters or E-counters. Spikes in the distributions are due to bin migration from overlap bins containing dead or inefficient counters.

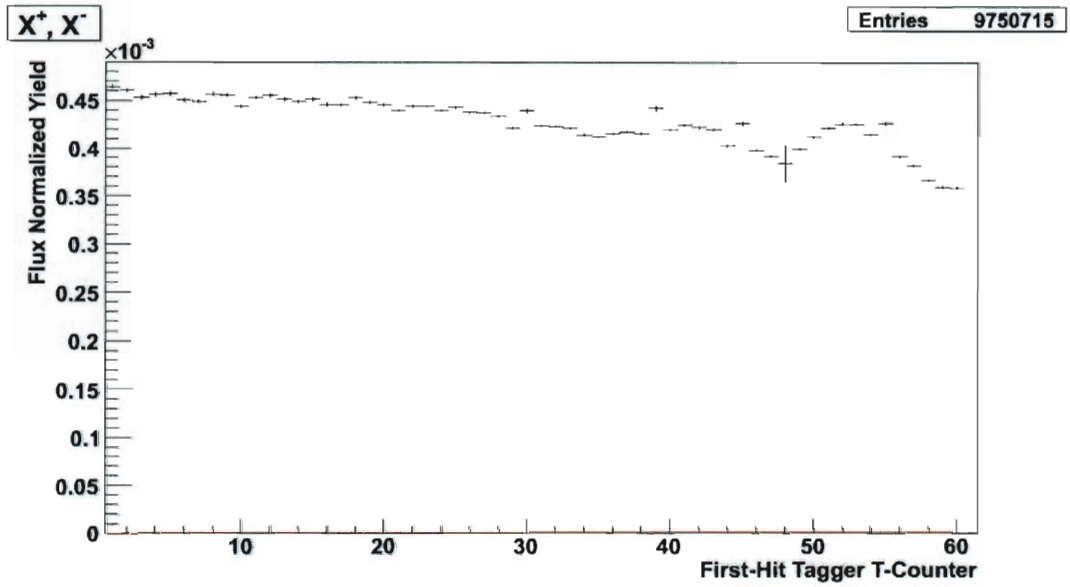

(A)

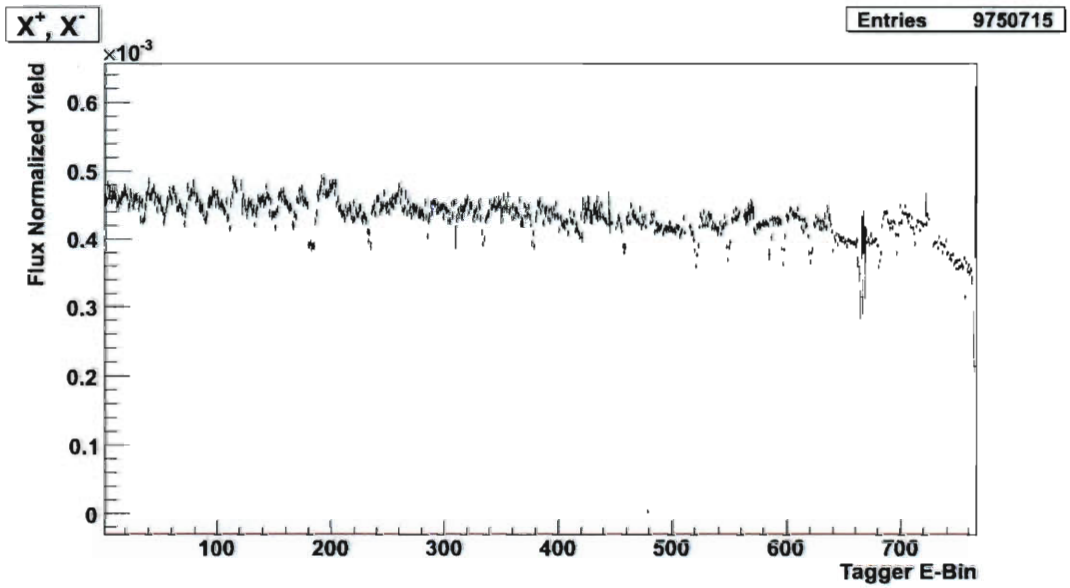

(B)

Figure 6.13 : Flux-normalized yields of charged particles vs. first-hit T-counter (A) and E-bin (B) for a portion of the g13a experiment. T-counters with large deviations were rejected. The periodic structure in the E-bin distribution is due to skews in the photon tagger timing calibration.

experimental data, which can be improved with a recalibration of the photon tagger timing. This recalibration was not finished in time for this analysis.

Several of the tagger counters were not bad for the entire run range, but were efficient at the beginning and got progressively worse throughout. Specifically, T-counters 30, 39, and 48 were working properly up to at least run 53430, and E-counters 60 and 281 didn't start failing until after run 53538. Therefore, these counters were only rejected for the later portions of the g13a run range.

Instead of rejecting all photons striking the bad counters, only photons striking the non-overlap bins were rejected. This was because photons striking the overlap region of the bad counters were migrated into the non-overlap region of the adjacent counters. Therefore, the non-overlap bins of T-counters 30, 39, 45, 48, 55, and 61 and E-counters 60, 225, 240, 257, 281, and 364 were rejected from this analysis. These bins were rejected in both the experimental data and the photon flux calculation so that the counter inefficiencies were properly cancelled in the cross section calculations. The rejection of these bins in the flux calculation is discussed in Section 6.4.3. The bad counters were rejected in simulation so that the acceptance calculations accurately reflected the bin migration from these counters. When the recalibration of the photon tagger is completed, the cross sections in this analysis will need to be recalculated.

6.2.4 Fiducial Cuts

Near the edges of the CLAS drift chambers, charged particles often escaped detection or failed track reconstruction. This occurred when the particles struck either the drift chamber support frames or the cryostats of the torus magnet. Additionally, the magnetic fields generated by the torus magnet were non-uniform near the cryostat surfaces, which sometimes caused tracks to fail reconstruction. The detector simulation package *gsim* was unable to completely model these regions of CLAS accurately. Therefore, the edges of the drift chambers were rejected from both the experimental data and simulation to properly calculate the detector acceptance.

These fiducial-cut regions of the detector were determined by studying the distribution of reconstructed tracks in the experimental data. Studied as a function of θ and sector-normalized-ϕ in bins of momentum and vertex position along the beamline (vertex-z), the edges where the number of reconstructed tracks rapidly decreased were rejected. Figure 6.14 shows the track distributions and fiducial cuts for the π^-'s and π^+'s with -40 cm $<$ vertex-z $<$ -30 cm. The plots were summed

over all sectors of the detector, as the geometry of CLAS was similar enough that the differences in the alignment of the sectors was negligible for this study. Four, 10-cm-wide vertex-z bins were used because the target was long enough to require slightly different cuts between these bins at the backward angles. Because the path of charged particles in a magnetic field is dependent only on their charge and momentum, these fiducial cuts were mass-independent. Comprehensive plots for all vertex-z bins are located in Appendix B.1.

The functional form of the fiducial cuts used for these distributions is:

$$\phi = C_1(1.0 - e^{C_1\theta + C_2}) + (\theta > C_3)(C_4 + C_5\theta + C_6\theta^2), \tag{6.2}$$

where the C's are the function parameters. The exponential portion of the function was used to describe the fiducial cuts at forward angles, and after the cutoff at C_3 the quadratic portion of the function was used to describe the backward angles. These function also had low- and high-θ bounds, outside of which all data were rejected. The sectors of the detector were assumed to be symmetric about their centers, such that the functions describing the cuts at low- and high-ϕ were mirror images. The parameters of these fiducial cut functions were manually adjusted until they removed almost all of the inefficient reconstruction regions at the edges of the drift chambers.

These cuts were checked by studying these track distributions in one-dimensional slices of θ as a function of sector-normalized-ϕ. These are illustrated for one of the momentum and vertex-z bins in Figures 6.15 and 6.16 for π^-'s and π^+'s, respectively. The plots in the figures represent different slices of θ from the front to the back of the sector, excluding the middle-θ bins where the fiducial cuts were relatively constant in sector-normalized-ϕ. The red lines indicate the location of the fiducial cuts in the given θ bins, and are almost all within or at the edge of the region of evenly reconstructed tracks. Plots for all of the vertex-z bins are located in Appendix B.1.

As seen in Figure 6.14 positively charged tracks had a momentum dependence to their low-θ bounds, whereas negatively charged tracks did not. This was because the torus magnet in CLAS was set to bend negatively charged particles outward from the beamline for the g13 experiment. As seen in Figures 4.5(A) and 4.6, this field was primarily present within Region 2 of the drift chambers. Therefore, the hit positions of the tracks in the Region 1 drift chambers were dependent only on the positions and angles that they were produced at and not their momentum. All low-θ negatively charged particles hitting Region 1 were bent outwards by the magnetic field and through the rest of

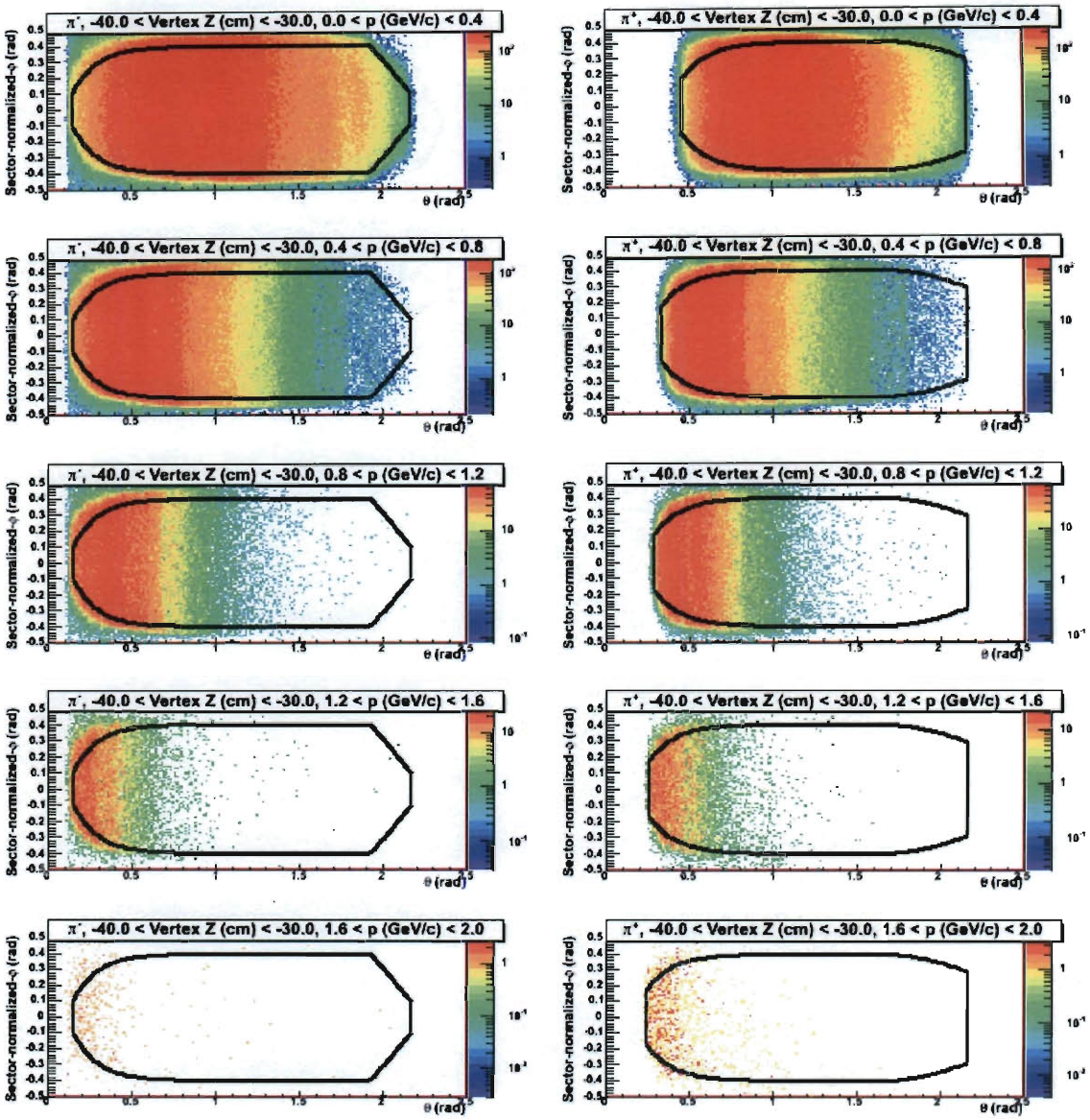

Figure 6.14 : Log-scale distributions of reconstructed pions in all sectors of CLAS as a function of θ and sector-normalized-ϕ with -40 cm < vertex-z < -30 cm. The left column contains π^-'s, and the right column contains π^+'s. The different rows represent 400 MeV wide momentum bins from 0 GeV/c to 2 GeV/c. The fiducial cuts are drawn in black. Positively charged tracks exhibit a momentum dependence to their fiducial cuts due to the CLAS torus magnetic field, whereas negatively charged tracks do not.

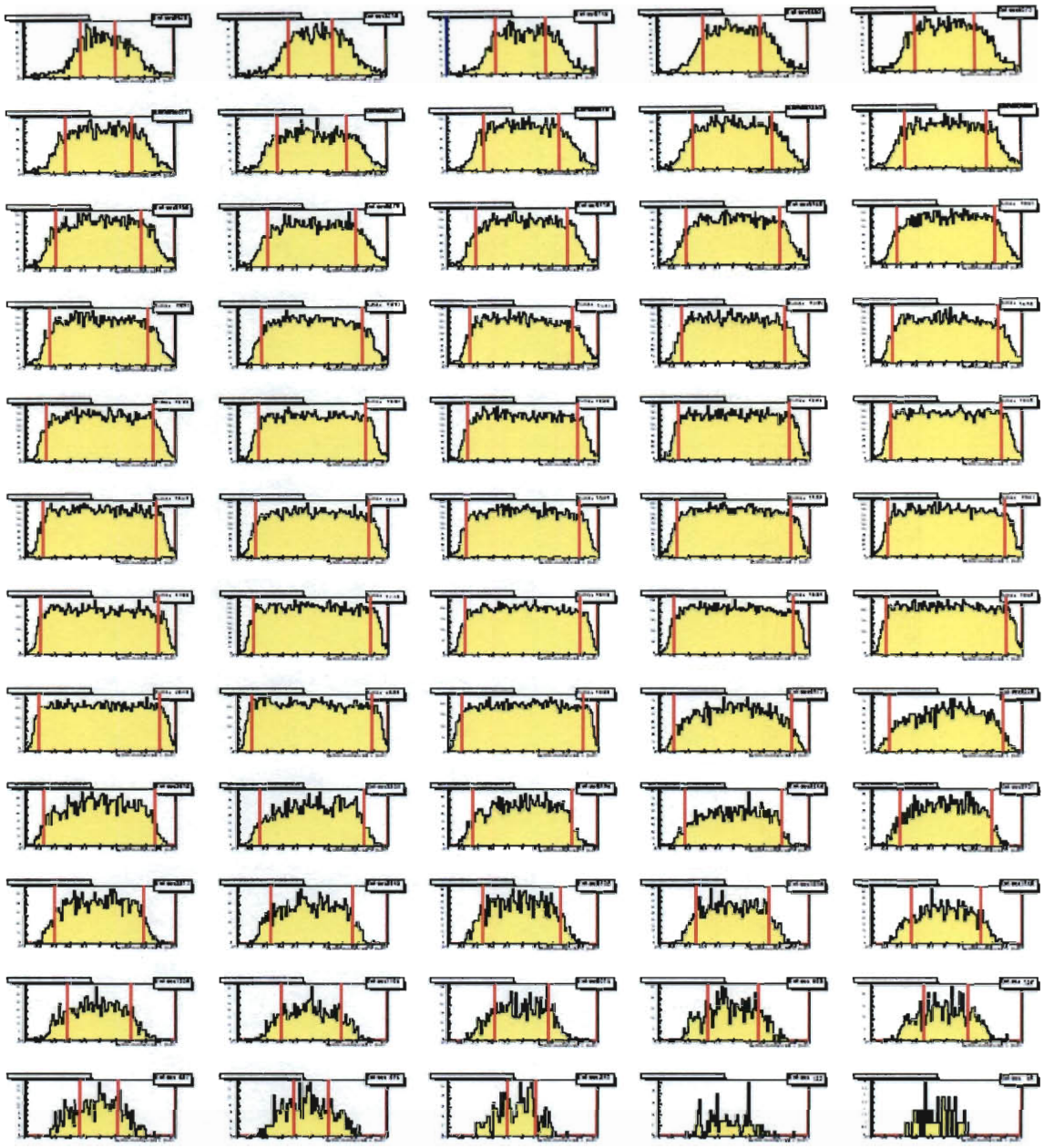

Figure 6.15 : For π^-'s with -40 cm < vertex-z < -30 cm and momentum < 400 MeV/c, the distribution of reconstructed tracks for all sectors in bins of θ as a function of sector-normalized-ϕ. The θ-bins are from the front to the back of CLAS, excluding the middle θ-bins where the cuts were relatively constant. The red lines indicate the location of the fiducial cuts.

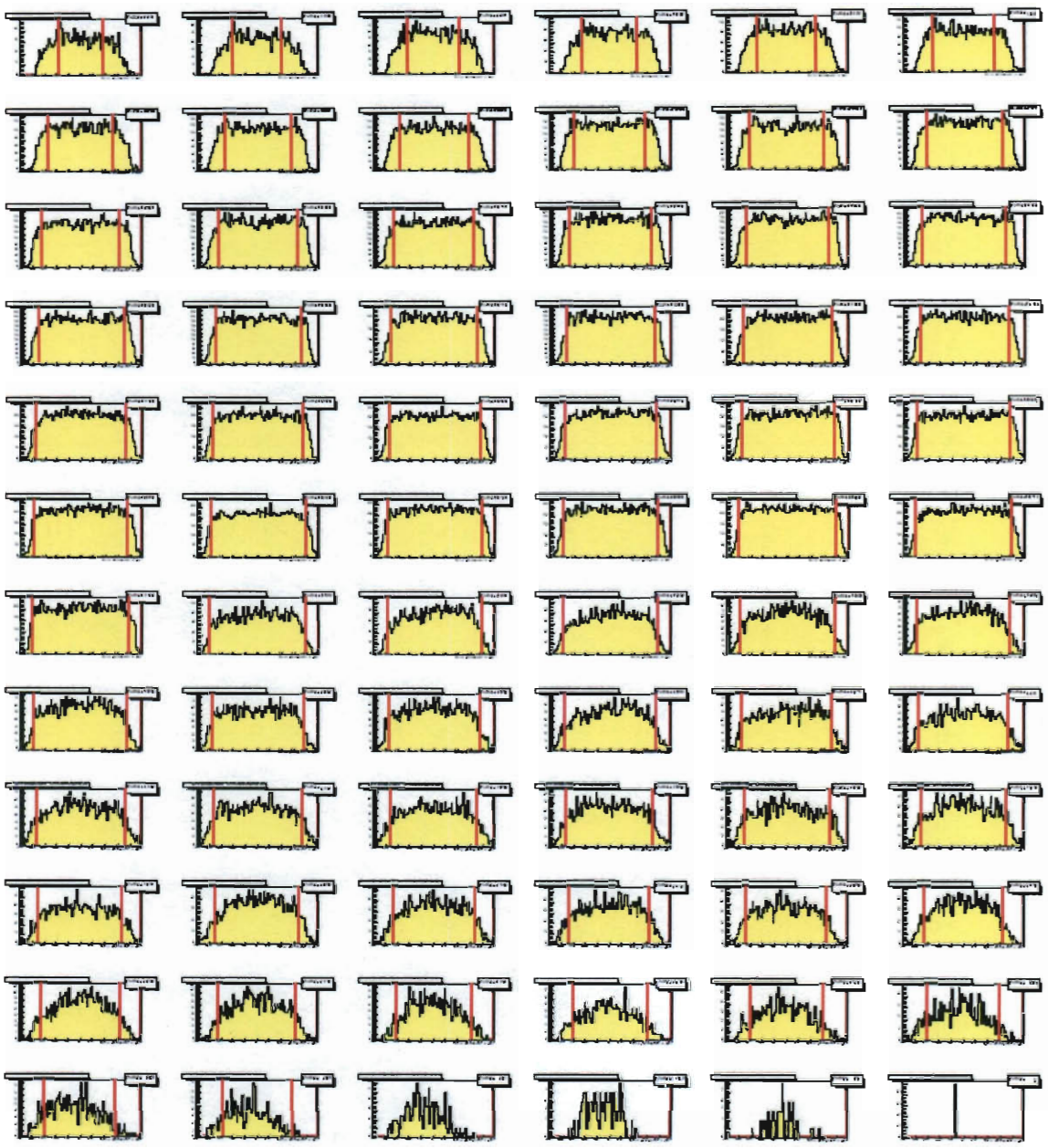

Figure 6.16 : For π^+'s with -40 cm < vertex-z < -30 cm and momentum < 400 MeV/c, the distribution of reconstructed tracks for all sectors in bins of θ as a function of sector-normalized-ϕ. The θ-bins are from the front to the back of CLAS, excluding the middle θ-bins where the cuts were relatively constant. The red lines indicate the location of the fiducial cuts.

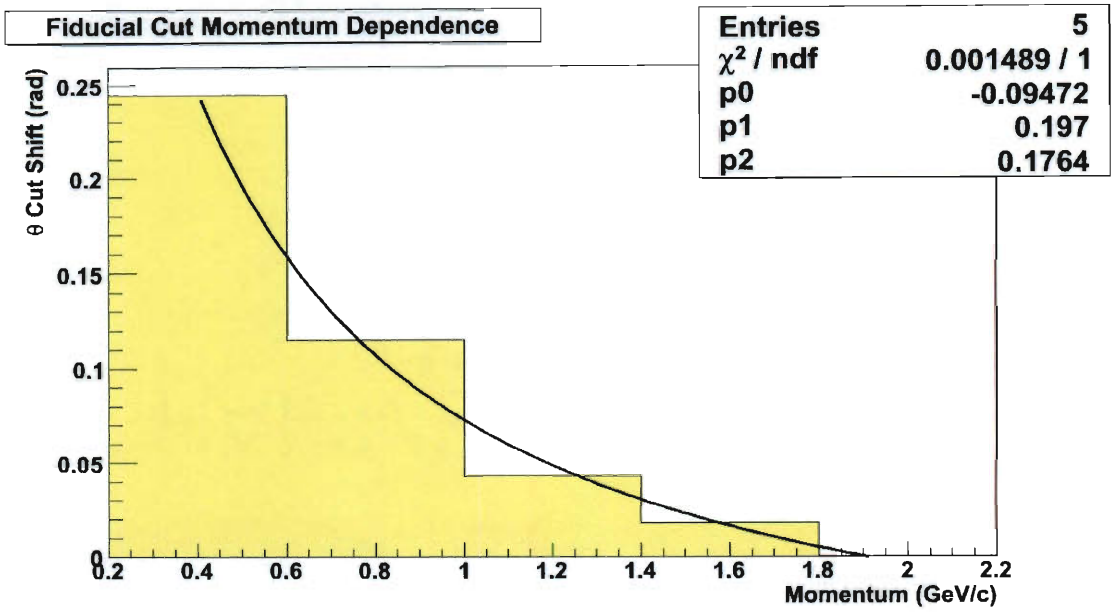

Figure 6.17 : The fit to the front edges of the fiducial cut functions for positively charged tracks as a function of momentum. This function was used as a momentum-dependent θ-shift to the fiducial cuts of positively charged tracks.

the drift chambers. However some slow, low-θ positively charged tracks bent inwards by this field missed either the Region 2 or Region 3 drift chambers and failed reconstruction. Therefore, there was no momentum dependence to the edges of the fiducial cuts for negatively charged tracks, but there was for positively charged tracks. The momentum-dependent θ-shift to the fiducial cuts of positively charged tracks was fit in Figure 6.17 to:

$$\theta_{\text{Shift}} = D_0 + D_1/(p + D_2), \tag{6.3}$$

where the D's are the function parameters. Thus for a given charge and z-vertex bin only a single cut function was used, and for positively charged tracks it was shifted along θ for different track momentum as determined by this fit. A momentum dependence for the high-θ cut bound was unnecessary due to the lack of high-momentum tracks traversing the backward region of the sectors.

6.2.5 TOF Scintillator Paddle Cuts

Inoperative, inefficient, and miscalibrated TOF scintillator paddles were cut from this analysis to obtain better matching between the experimental and simulated data. Inoperative paddles contained dead photomultiplier tubes (PMTs), many of which could not be replaced because access to them was blocked by the electromagnetic calorimeter. Paddles with timing miscalibrations had many tracks fail the particle identification cuts in this analysis, which were dependent on accurate timing information. Additionally, some aging PMTs did not amplify the signals from minimum-ionizing particles strongly enough to be recorded, causing tracking inefficiencies.

Figure 6.18 shows the comparison between the measured and calculated π^- times in the scintillator paddles. The calculated time was determined as:

$$t_{\text{Calculated}} = t_{\text{Start}} + \frac{x\sqrt{m^2c^4 + p^2c^2}}{pc^2}, \tag{6.4}$$

where t_{Start} is the event start time determined by the start counter and x is the path length of the particle from the reaction vertex to the TOF scintillator. Most of the paddles had their timing well calibrated except at the backward angles, in the region of paddles 40 to 48. There are significant secondary peaks in some of these paddles, resulting from these paddles actually being a logical multiplex of two physical scintillator paddles. When any of these PMTs were dead or inefficient it was extremely difficult to reproduce the effects correctly in simulation. Therefore, paddles 40 to 48 were rejected in all sectors from this analysis.

Four scintillator paddles were dead throughout the entire experiment, and paddle 8 in Sector 1 was dead for a significant portion of the run range. Also, twelve scintillator paddles were significantly inefficient and were rejected from the analysis to obtain matching with the detector simulation. Finally, three paddles were miscalibrated for limited run ranges and were rejected for these runs. Paddles that were rejected for the entire g13a experiment are listed in Table 6.3, and those that were rejected for only a portion of the run range are listed in Table 6.4.

In addition to these paddles, tracks striking scintillator paddle 23 were rejected from all sectors. This was because, as seen in Figure 4.5(A), there was a large overlap between the first and second planes of TOF counters. These planes overlap to ensure that particles were not lost between the scintillator planes, but the effects of this overlap on track reconstruction were not successfully modeled by *gsim*.

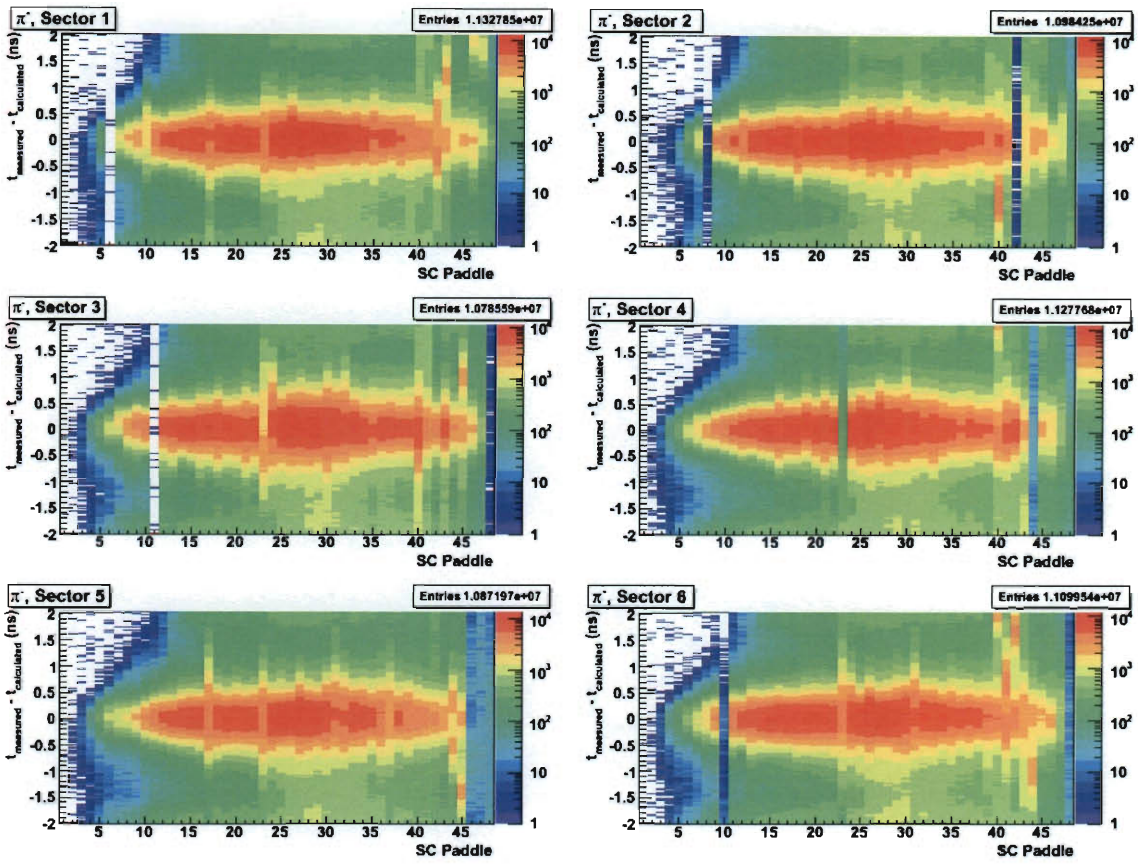

Figure 6.18 : The difference between the measured and calculated times of the π^- in different scintillator paddles. Dead, misaligned, and inefficient paddles were rejected from the experimental data and the detector simulation. Additionally, paddle 23 was rejected due to the panel overlap, and paddles 40 to 48 due to their multiplexing.

Rejected Scintillator Paddle	Reason
All Sectors - Paddle 23	Panel Overlap
All Sectors - Paddles 40 - 48	Multiplexed
Sector 1 - Paddle 6	Dead
Sector 1 - Paddles 10, 24	Inefficient
Sector 2 - Paddle 8	Dead
Sector 3 - Paddle 11	Dead
Sector 3 - Paddles 24, 35	Inefficient
Sector 5 - Paddles 24, 29, 30, 31, 37	Inefficient
Sector 6 - Paddle 10	Dead
Sector 6 - Paddles 24, 25, 31	Inefficient

Table 6.3 : The TOF scintillator paddles rejected for all of g13a.

Rejected Scintillator Paddle	Reason	Run Range
Sector 1 - Paddle 8	Dead	53333 - 53449
Sector 4 - Paddle 26	Misaligned	53430 - 53537
Sector 4 - Paddle 35	Misaligned	53449 - 53459
Sector 5 - Paddle 36	Misaligned	53449 - 53459

Table 6.4 : The TOF scintillator paddles rejected for limited ranges of the g13a dataset.

6.2.6 Drift Chamber Hole Cuts

Short-circuits on the drift chamber readout circuit boards in the CLAS drift chambers caused track reconstruction to fail in those regions due to loss of power to the signal amplifiers. To match the response of the drift chambers in experiment and simulation, these holes were cut from this analysis. Figure 6.19 shows the p, θ distribution of protons and π^-'s in Sector 3 in different bins of vertex-z. The large holes in these distributions correspond to either drift chamber holes, the SC panel overlap, or dead SC paddles. There is a vertex-z dependence to the location of the holes in these distributions due to the length of the 40-cm-long liquid-deuterium target. Figures 6.20 and 6.21 show the p, θ distributions for one of the vertex-z bins in all sectors for protons and π^-'s, respectively. p, θ distributions of each sector for all vertex-z bins are located in Appendix B.2.

The black lines indicate the cuts used to remove the seven different drift chamber holes from this analysis. The other large holes in the distributions correspond to scintillator paddles that were selected for cuts in Section 6.2.5, including the panel overlap at paddle 23 and many of the paddles from 40 - 48. Pions were more sensitive to scintillator inefficiencies than protons because many were minimum-ionizing due to their higher velocities. The p, θ distributions of some of the drift chamber holes were more sensitive to track momentum than the others because they were located in Region 3 of the drift chambers, which were traversed after the tracks were bent by the torus magnetic field.

While trigger inefficiencies also caused holes, cuts were placed to remove any effects they may have had on these distributions. Specifically, since g13a used a two-sector trigger only events with at least three charged particles were considered. Also, since pions had large trigger inefficiencies in some areas, events with three charged particles were required to have at most one pion. The trigger efficiency is discussed in more detail in Section 6.3.

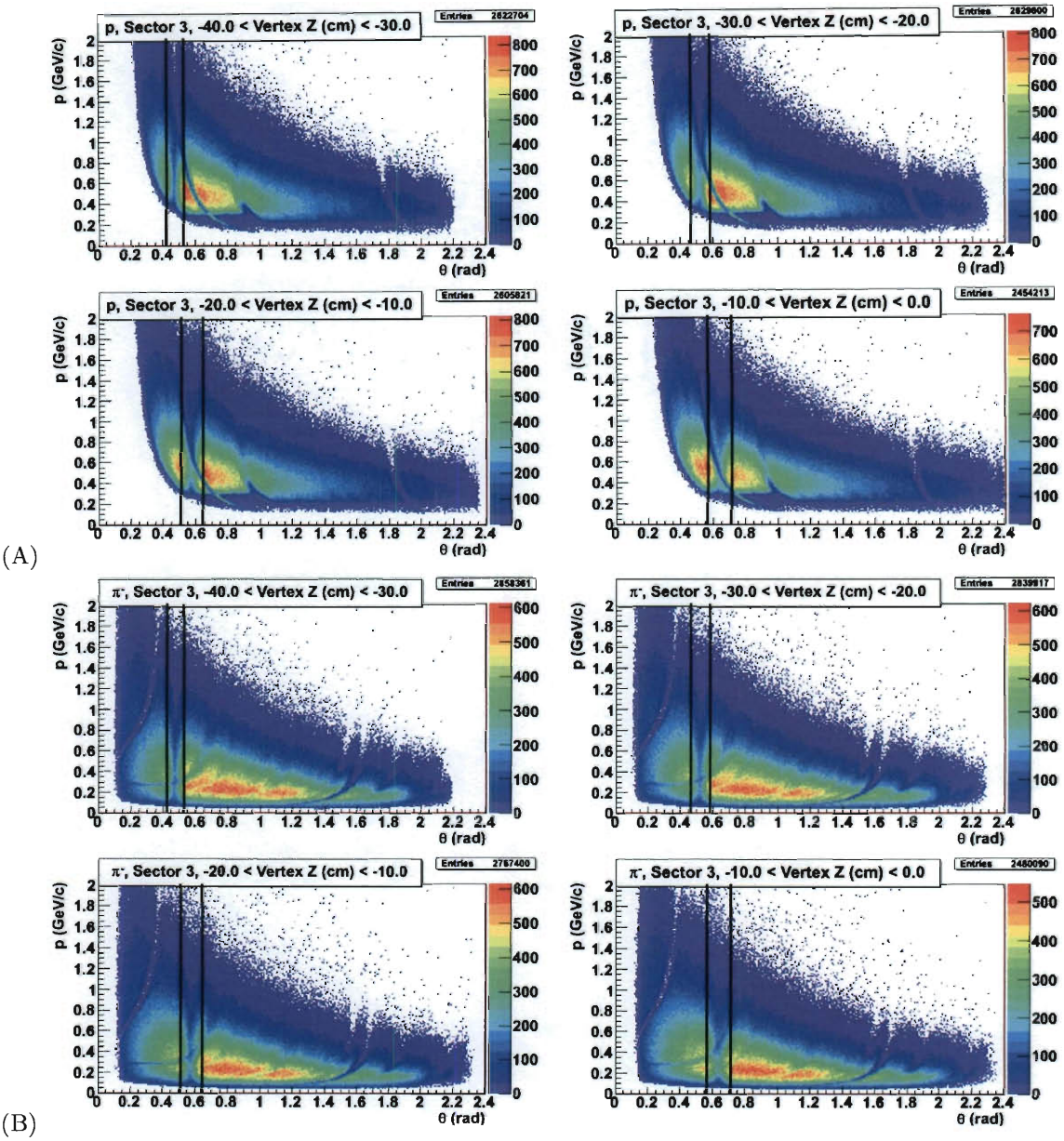

Figure 6.19 : Track distributions of the protons (A) and π^-'s (B) in different vertex-z bins in Sector 3. The black lines indicate the borders of the regions removed from the analysis due to holes in the drift chambers. The holes in the distributions without associated cuts correspond to either the panel overlap regions, or dead or inefficient scintillator paddles.

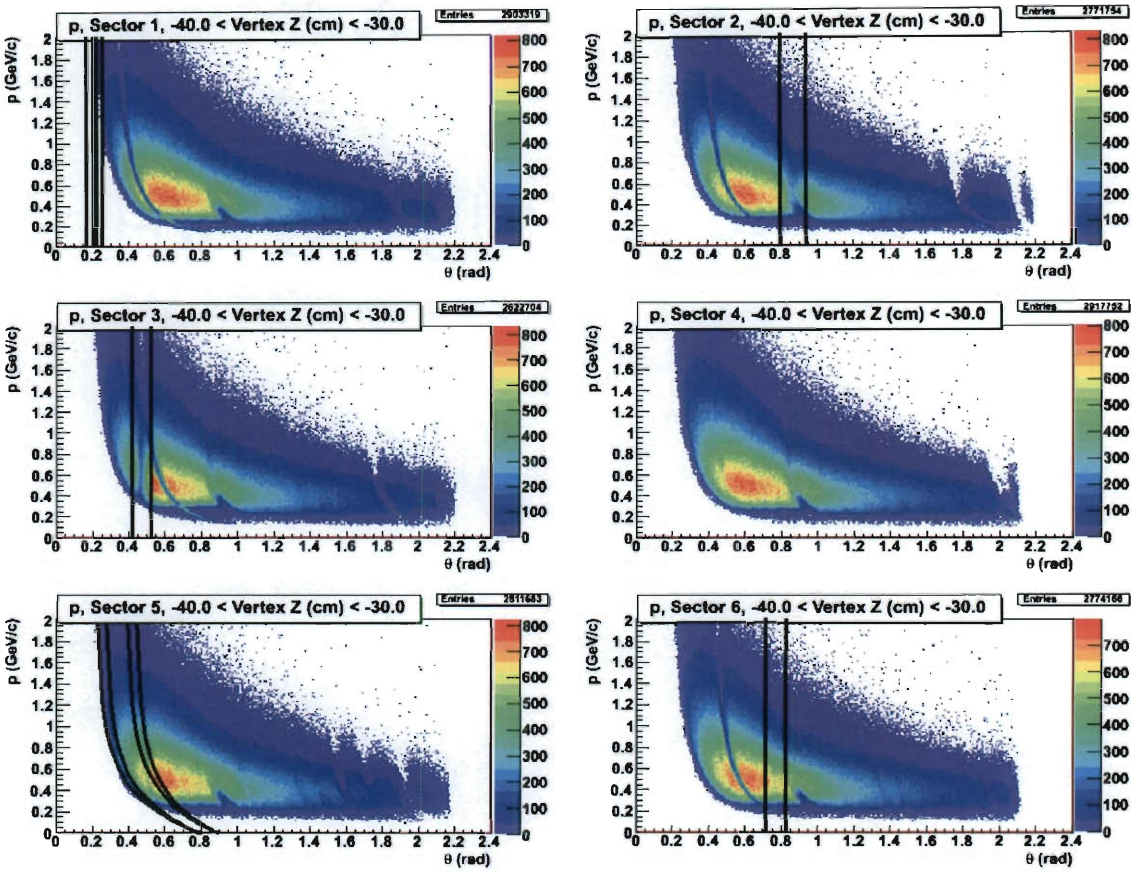

Figure 6.20 : Track distributions of protons with -40 cm < vertex-z < -30 cm in the different sectors of CLAS. The black lines indicate the borders of the regions removed from the analysis due holes in the drift chambers. The holes in the distributions without associated cuts correspond to either the panel overlap regions, or dead or inefficient scintillator paddles.

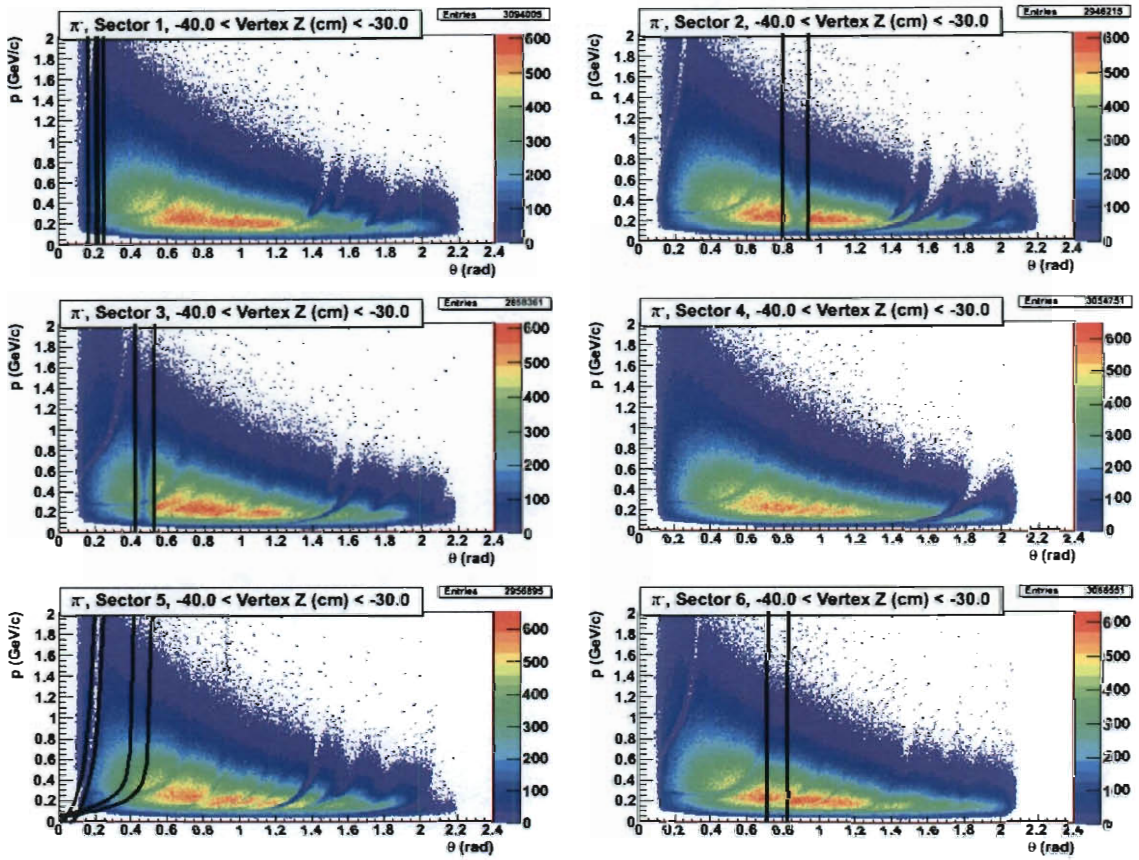

Figure 6.21 : Track distributions of π^-'s with -40 cm < vertex-z < -30 cm in the different sectors of CLAS. The black lines indicate the borders of the regions removed from the analysis due to holes in the drift chambers. The holes in the distributions without associated cuts correspond to either the panel overlap regions, or dead or inefficient scintillator paddles.

6.3 Trigger Efficiency Study

As discussed in Section 4.3.4, the g13a trigger was designed to record events with a ST and TOF coincidence in at least two sectors. However, charged particles hitting inefficient scintillator paddles in either the ST or TOF may not have produced signals large enough to pass the pretrigger voltage thresholds. Additionally, the decay products of the Λ did not contribute to the event trigger when the Λ decayed outside of the start counter. The triggering efficiency of these scintillators was studied to model in the Monte Carlo simulations event losses due to absent triggers.

Because there was no direct information recorded about events that failed to trigger, measured events were used to determine the trigger efficiency. Specifically, the $\gamma D \rightarrow pp\pi^-$ reaction was studied to determine whether the trigger bits were set for the protons and π^-'s as a function of momentum, ϕ, and SC paddle. The proton triggering efficiency was used for the K^+'s, and the systematic uncertainties associated with this assignment are studied in Section 9.4.2. The method used for this study was based on a similar analysis of the trigger efficiency for the CLAS g11a experiment [107].

6.3.1 Triggering Efficiency Calculation

As discussed in Section 4.3.4, a trigger bit was set in the recorded events for each sector that had a coincidence between the ST and TOF. Since g13a had a two-sector trigger, the trigger bits set in $\gamma D \rightarrow pp\pi^-$ events were studied because they had three particles in the final state. Since two of the particles were required to have trigger bits set for the event to be recorded, the triggering rate of the third particle was studied. The fact that the third particle was reconstructed did not influence the triggering efficiency calculation, as particles with a given direction and momentum had the same triggering efficiency whether or not their tracks were reconstructed.

The cuts detailed in Section 5.2 were used to select the $\gamma D \rightarrow pp\pi^-$ events. To perform the study, the trigger bits were checked for each of the three pairs of particles in the final state. If the trigger bits were set for both particles in a given pair, then the trigger bit of the sector of the third particle was examined. To remove ambiguities from determining which tracks set the sector-based trigger bits, each particle was required to be reconstructed in a different sector of the detector.

Figure 6.22 shows the sector-normalized-ϕ dependence of the proton triggering efficiencies for the different scintillator paddles. The proton triggering was highly efficient in general, but it was low

in a few of the scintillator paddles. In these paddles, the observed ϕ-dependence of the efficiency indicates that one of the PMTs on the edge of the scintillator was much more inefficient at amplifying the proton signal than the other. However, the efficiency generally increased slightly at the edges of the paddles near the highly inefficient PMTs due to the lower attenuation losses of the particle signals. The empty scintillator paddles were either dead or outside of the phase-space of this reaction at these energies.

Figure 6.23 shows the momentum-dependence of the proton triggering efficiency in one of the center ϕ-bins of each sector. At these energies, the protons deposited enough energy in the scintillator paddles such that the momentum dependence was negligible, except in the highly inefficient scintillator paddles. Slower protons deposited more energy in the scintillators than faster protons, and thus triggered more efficiently in these paddles. However, very slow protons had low triggering efficiencies because many did not reach the SC paddles before they lost all of their energy.

Figure 6.24 shows the triggering efficiencies of the π^- as a function of sector-normalized-ϕ and SC paddle. The π^- efficiencies were significantly lower than those of the proton in many of the scintillator paddles. This was because the π^-'s deposited much less energy than the protons in the paddles due to their higher velocities. As such, they were much more sensitive to PMT inefficiencies than protons. Many of these holes were not observed in the distributions of reconstructed π^-'s because the 20 mV detection threshold was much lower than the 100 mV pretrigger threshold. The large number of inefficient channels was due to the aging PMTs having low gain even though they were at their maximum voltage. Most of these PMTs have since been replaced with new, efficient PMTs.

The momentum dependence of the π^- trigger efficiencies is shown in Figure 6.25 for one of the center ϕ-bins. The π^- trigger efficiencies were significantly higher at low momentum for many of the inefficient paddles. The lack of statistics at the forward angles is from both the phase-space of the reaction and the CLAS magnetic field bending the π^-'s backwards.

The calculated trigger efficiencies were ignored for all bins with less than twenty reconstructed tracks due to low statistics. Instead, within each paddle the efficiencies were extrapolated into the regions without information by using the values in the closest momentum and sector-normalized-ϕ bins. For entire paddles without any information, the trigger efficiency was set to zero for the dead paddles and one for the operable paddles.

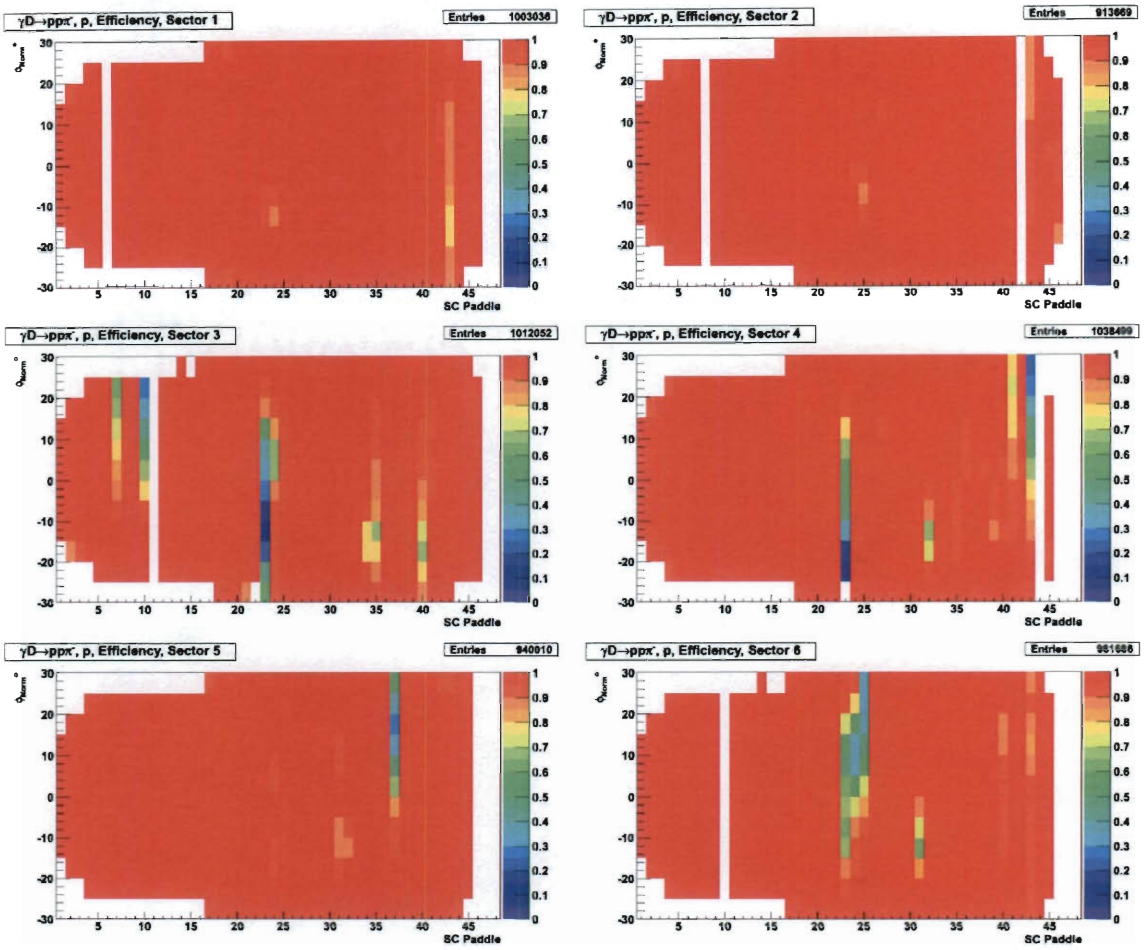

Figure 6.22 : The triggering efficiencies of protons as a function of sector-normalized-ϕ and SC paddle for each of the sectors of CLAS. The ϕ-dependence of the distributions is due to inefficient PMTs at the edges of the paddles. Bins with less than twenty events were excluded from the distributions. The triggering efficiencies were extrapolated into the regions without sufficient statistics for accurate efficiency calculations.

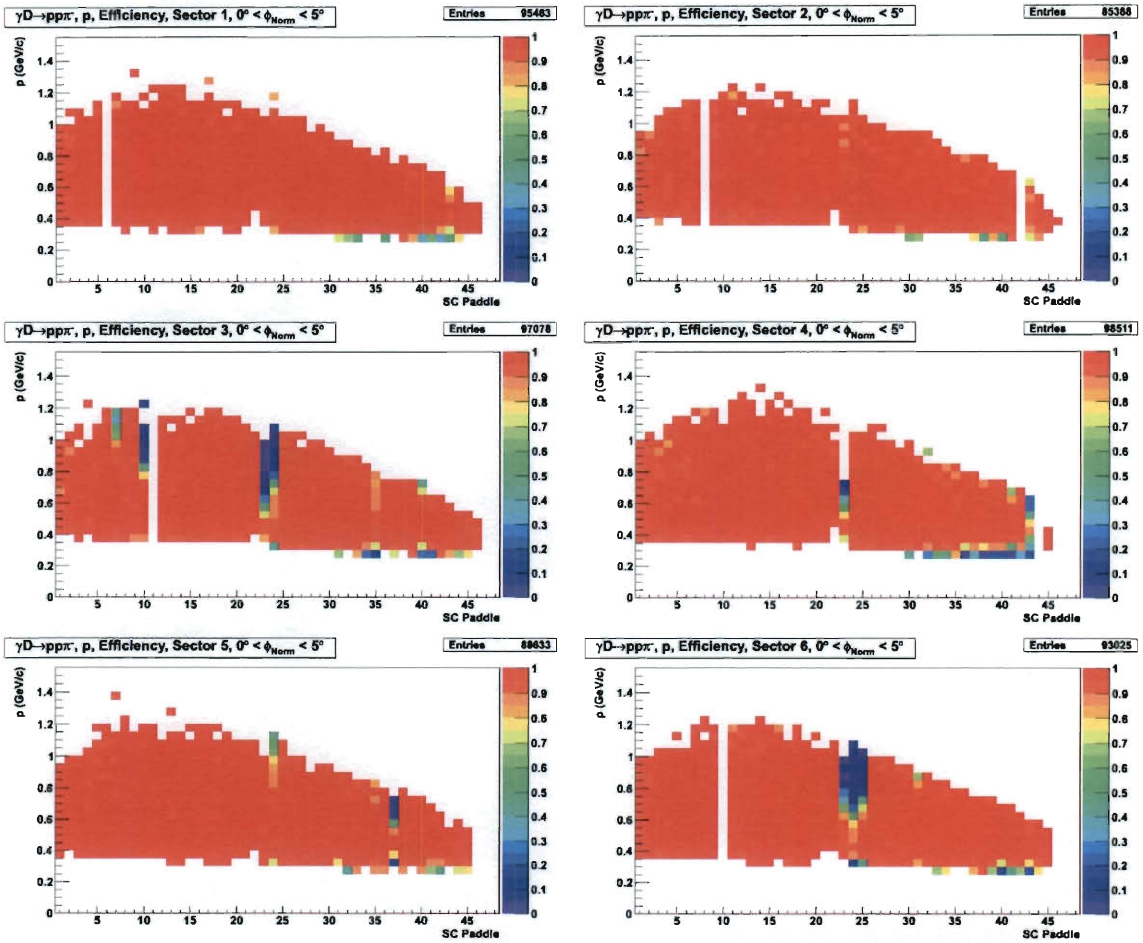

Figure 6.23 : The proton triggering efficiencies as a function of momentum and SC paddle in one of the center bins of sector-normalized-ϕ for each of the sectors of CLAS. In the inefficient paddles, low-momentum protons had higher triggering efficiencies because they deposited more energy in the TOF. Bins with less than twenty events were excluded from the distributions. The triggering efficiencies were extrapolated into the regions without sufficient statistics for accurate efficiency calculations.

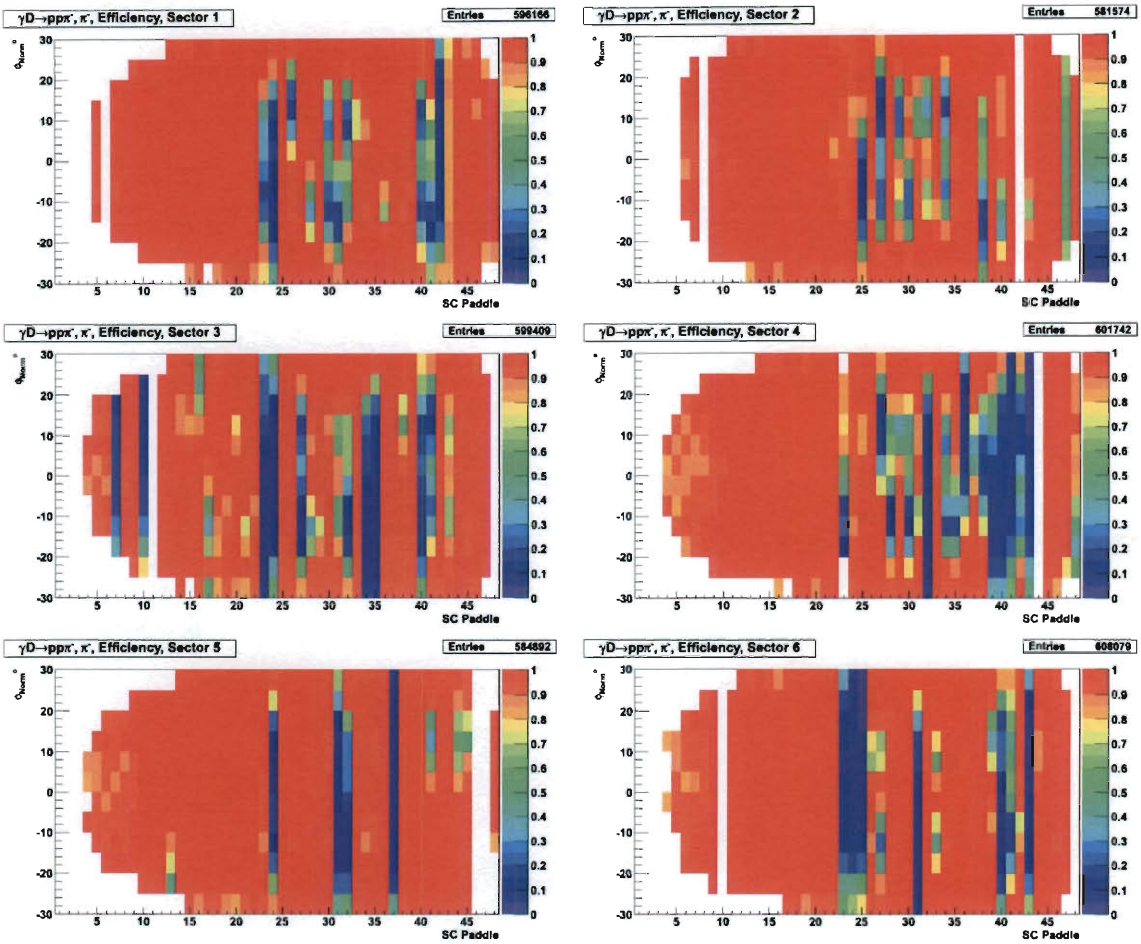

Figure 6.24 : The triggering efficiencies of π^-'s as a function of sector-normalized-ϕ and SC paddle. The ϕ-dependence of the distributions is due to inefficient PMTs at the edges of the paddles. The large number of inefficient paddles were due to low-gain PMTs, to which the fast π^-'s were more sensitive than the protons. Bins with less than twenty events were excluded from the distributions. The triggering efficiencies were extrapolated into the regions without sufficient statistics for accurate efficiency calculations.

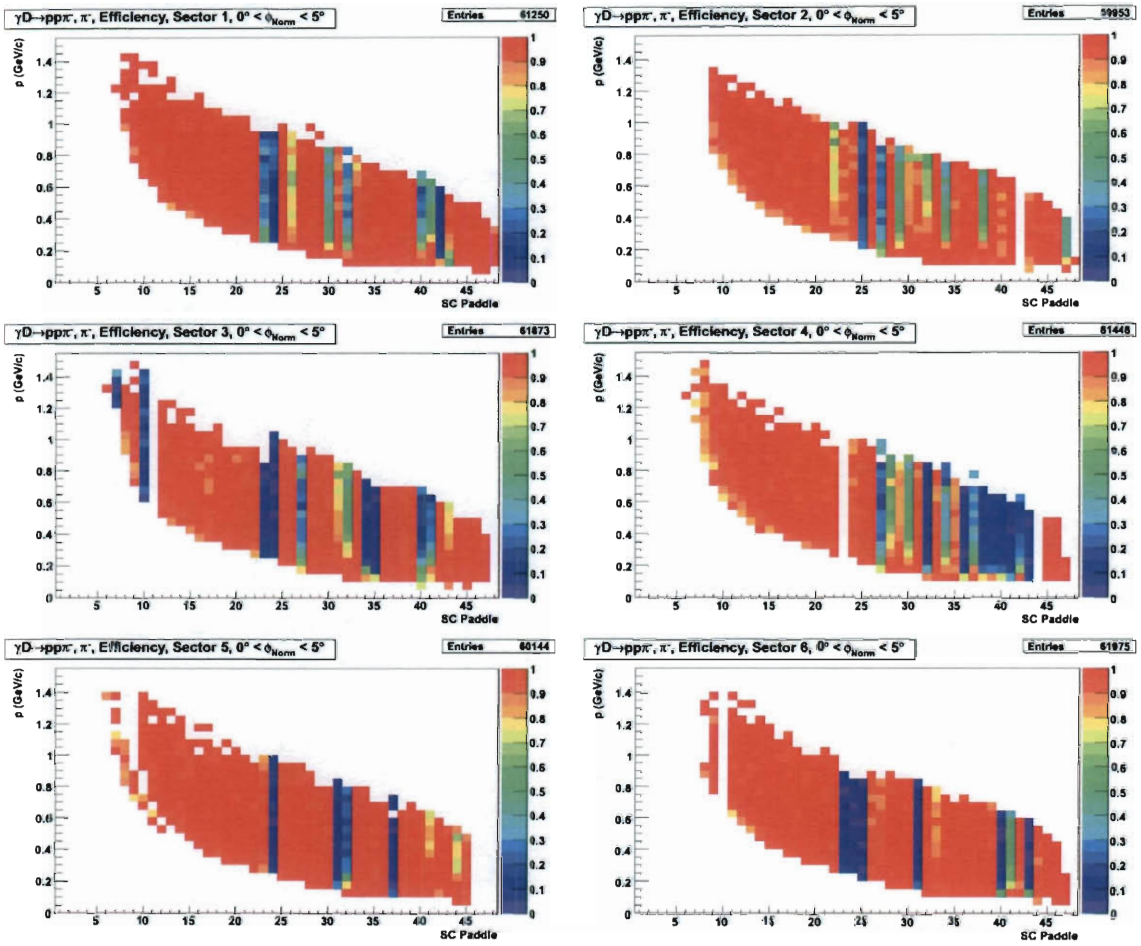

Figure 6.25 : The π^- triggering efficiencies as a function of momentum and SC paddle in one of the center bins of sector-normalized-ϕ for each of the sectors of CLAS. In the inefficient paddles, low-momentum π^-'s had higher triggering efficiencies because they deposited more energy in the TOF. The large number of inefficient paddles were due to low-gain PMTs, to which the fast π^-'s were more sensitive than the protons. Bins with less than twenty events were excluded from the distributions. The triggering efficiencies were extrapolated into the regions without sufficient statistics for accurate efficiency calculations.

6.3.2 Trigger Simulation

The CLAS trigger efficiency was simulated after performing track reconstruction in *user_ana*. However, the reconstructed tracks themselves weren't used to apply the triggering efficiency because they may have passed through regions of the detector with low acceptance. For example, during the experiment some of the particles that failed track reconstruction at the edges of the CLAS drift chambers still reached the TOF paddles and triggered. Therefore, the Monte Carlo generated particles were matched with their simulated hits in the start counter and TOF subsystems to model the CLAS trigger.

The triggering efficiency was assigned to each final-state charged particle generated by *fsgen*, using the efficiency maps calculated in Section 6.3.1. Final-state charged particles without matching simulated SC hits were excluded since they did not reach the TOF. Next, a random number was generated between zero and one for each particle and compared to its efficiency. If the random number was less than the efficiency then the SC signal was considered to be "strong" enough to trigger.

The sectors with these "strong" SC signals were then compared to the simulated hits in the start counter. If a coincidence between the ST and TOF in at least two different sectors occurred, then the event passed the simulated trigger. Events that failed this trigger were cut from the simulated data of this analysis. The scale of the effects of the simulated trigger on the acceptance vary for each reaction, and are studied in Sections 7.4 and 9.4.2.

6.4 Photon Flux Determination

The *gflux* software package was used to calculate the integrated photon flux per first-hit tagger T-counter on the target for each data file in the experiment [104]. This included only tagged photons that were incident on the target while the DAQ was ready to record events. This was because physics event losses during the DAQ dead-time or from inefficient tagger counters were not modeled in the acceptance corrections. Instead, these losses were taken into account by excluding these photons from the flux calculation.

For each first-hit T-counter, the number of tagged photons incident on the target while the DAQ was ready to record events N_γ^T was calculated as [104]:

$$N_{\gamma}^{T} = N_{e^-}^{T} \epsilon^{T}, \tag{6.5}$$

where $N_{e^-}^{T}$ is the number of "good" electron hits on a given first-hit T-counter while the DAQ was ready to record events and ϵ^{T} is the tagging ratio for a given first-hit T-counter. Electron hits were "good" when they produced signals that matched in time in the PMTs of both a T-counter and an E-counter. These electron hits were "good" regardless of whether these signals were recorded, as the experimental trigger condition may not have been satisfied. The tagging ratio is the fraction of the "good" electron hits in the first-hit T-counters that corresponded to photons that were incident on the target. Some of the tagged photons were lost before they reached the target due to beam dispersion, beam collimation, and Møller scattering [104]. A discussion on the calculation of the uncertainty of N_{γ}^{T} is located in Reference [104]. The determination of N_{γ}^{T} using *gflux* was performed by Charles Taylor of Idaho State University for the g13 experiment.

6.4.1 Calculation of $N_{e^-}^{T}$

To approximate an instantaneous flux rate calculation, the number of "good" electron hits for each first-hit T-counter while the DAQ was ready to record events were calculated separately for each 10 second scalar interval. The $N_{e^-}^{T}$ were calculated by summing over the scalar intervals introduced in Section 6.2.2 for each data file as [104]:

$$N_{e^-}^{T} = \sum_{S} R^{TS} \mathrm{Clock}^{S} \mathrm{LT}^{S}, \tag{6.6}$$

where R^{TS} is the rate of the number of "good" electron hits for a given first-hit T-counter in the scalar interval, Clock^{S} is the time length of the given scalar interval, and LT^{S} is the DAQ live-time during the given scalar interval. LT^{S} was calculated from the scalars as the fraction of the total number of triggers that were accepted by the DAQ to begin recording events. Scalar intervals containing beam trips were excluded from the flux calculation, as discussed in Section 6.2.2 [104].

The R^{TS} were determined by considering the probability distribution of x, the number of "good" electron hits for a given first-hit T-counter within a time interval τ. This probability was Poisson distributed since x was independent of previous events and the R^{TS} were assumed to be constant during the scalar interval. The Poisson distribution is defined as [104]:

$$P(x,\mu) = \frac{\mu^x}{x!}e^{-\mu}, \tag{6.7}$$

where μ is the expected value of x and is equal to τR^{TS}. Within the scalar interval S, the probability that there was at least one "good" electron hit on a given first-hit T-counter in the time interval τ is [104]:

$$P^{TS}(x \geq 1) = 1 - P^{TS}(x = 0) = 1 - e^{-\tau R^{TS}}. \tag{6.8}$$

Rearranging gives [104]:

$$R^{TS} = -\frac{1}{\tau}\ln(1 - P^{TS}(x \geq 1)). \tag{6.9}$$

Figure 6.26 illustrates the timing spectrum of the photons tagged from "good" electron hits in one of the first-hit T-counters. The hits corresponding to trigger signals are manifest at or near the spectrum peak, and the remaining, "out-of-time" hits correspond to electrons from subsequent electron beam bunches while the DAQ was recording the events. A timing window for τ was chosen similar to the one illustrated in the figure to ensure that the physics events causing the trigger did not bias the calculation of R^{TS}. $P^{TS}(x \geq 1)$ was then calculated as the fraction of the recorded events with "good" electron hits within the time window τ in the given first-hit T-counter for each scalar interval. Equations 6.9 and 6.6 were then used to calculate $N_{e^-}^T$ [104].

6.4.2 Calculation of ϵ^T

The fractions of the "good" electron hits in the first-hit T-counters that corresponded to photons that were incident on the target were energy-dependent due to beam collimation, which had a larger effect on low-energy photons due to beam dispersion. These ϵ^T were determined using several low-current normalization runs throughout the g13 experiment. During these runs, the total absorption counter (TAC) was inserted into the beamline to determine the number of photons incident on the target. The TAC was positioned about 25 meters downstream of CLAS, and consists of lead-glass blocks. PMTs attached to the lead-glass blocks were used to count the number of photons incident on the TAC, which was essentially 100% efficient [81]. A low beam current of 1 nA was necessary to prevent radiation damage to the TAC counters during these runs [104].

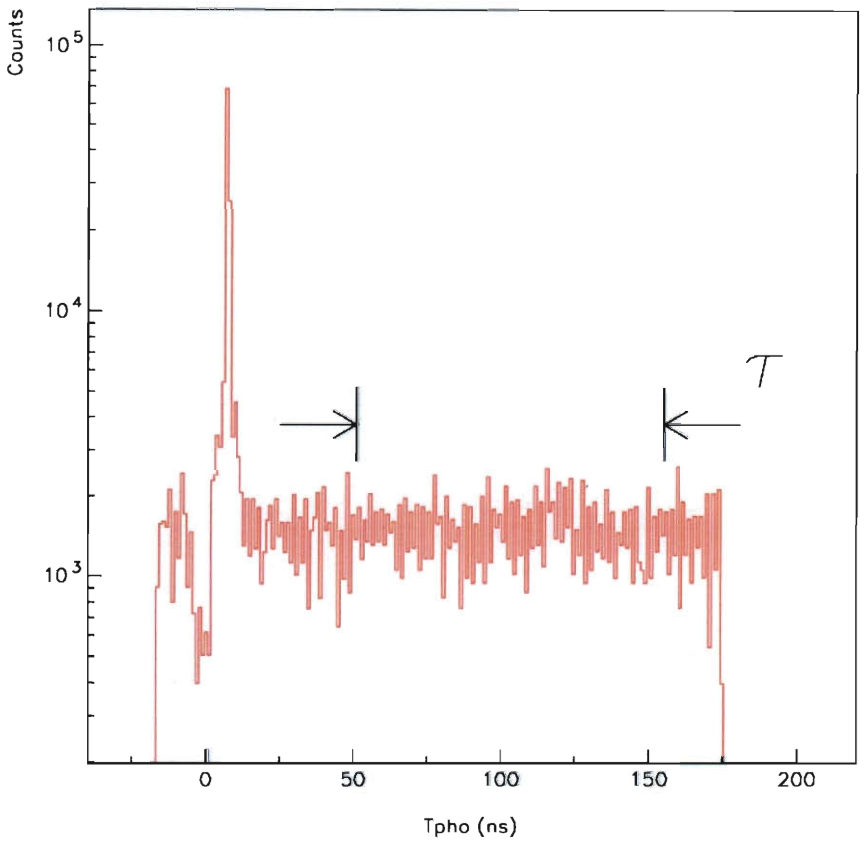

Figure 6.26 : The spectrum of photon times at the center of the target corresponding to "good" electron hits in one of the first-hit tagger T-counters [104]. The time window τ was chosen to sample "out-of-time" hits to calculate $P^{TS}(x \geq 1)$ such that the physics events causing the trigger did not bias the calculation.

The tagging ratios were assumed to be independent of photon intensity, and were calculated for each first-hit T-counter in each normalization run as [104]:

$$\epsilon^T = \frac{N^T_{\text{TAC}}}{N^T(1-\alpha)}, \tag{6.10}$$

where N^T is the total number of "good" electron hits in a given first-hit T-counter, N^T_{TAC} is the total number of these hits that match photon hits in the TAC for a given first-hit T-counter, and α is the photon attenuation factor. This factor takes into account the fraction of the photons incident on the target that did not reach the TAC. This photon attenuation factor was energy-independent for the g13a experiment, and was ~4% [108]. These losses were primarily due to electron-positron pair production and Compton scattering as the photons interacted with the target and the beamline components [108].

The tagging ratios calculated for the normalization runs of the g13a experiment are illustrated in Figure 6.27. The 2.655 GeV electron beam runs, 53589 and 53699, had larger tagging ratios than the 2.0 GeV runs due to the increased beam dispersion of the lower energy beam. The dips in the plot correspond with the dead or weak T-counters discussed in Section 6.2.3.

6.4.3 Integrated Photon Flux

After *gflux* calculated the integrated photon flux for each data file, the flux from the bad tagger counters was removed. First, *gflux* converted the photon flux from the first-hit tagger T-counters to E-bins. This conversion was performed by generating a map of the correspondence between the first-hit T-counters and the E-bins from each data file, such as the one shown in Figure 6.28. The fractions of the flux in each first-hit T-counter that were assigned to the E-bins were the same as the fractions of the hits that were in the map.

After running *gflux*, the flux was set to zero for the bad E-bins from Section 6.2.3. The flux was then mapped to T-bins, and the flux in the bad T-bins was set to zero. Finally, the flux was then mapped to photon energy. These conversion maps were generated for every run of the experiment because the mapping changed as the weak tagger counters degraded over time. The photon fluxes from the data files were combined together for the cross section calculations, and are shown in Figure 6.29.

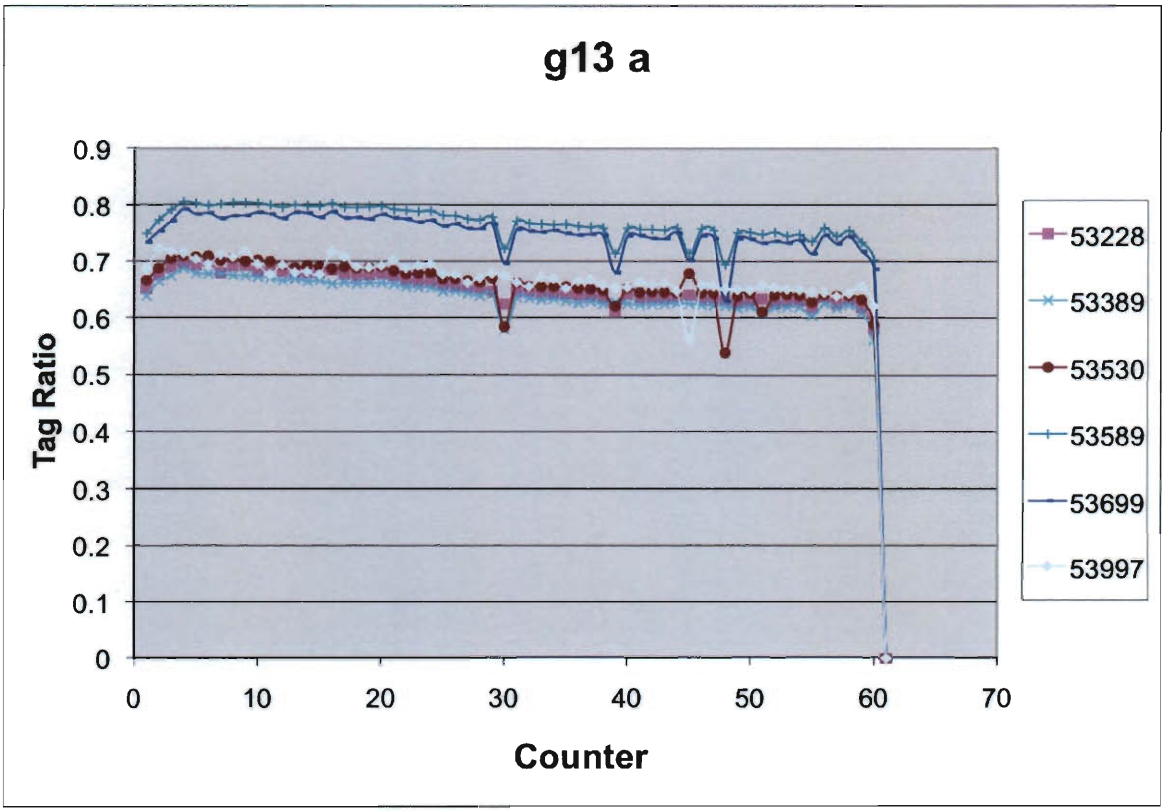

Figure 6.27 : The calculated tagging ratios for the normalization runs of g13a. Runs 53589 and 53699 had a 2.655 GeV electron beam and thus had larger tagging ratios than the other, 1.990 GeV runs. The dips in the distributions correspond to the dead or weak tagger T-counters, as discussed in Section 6.2.3.

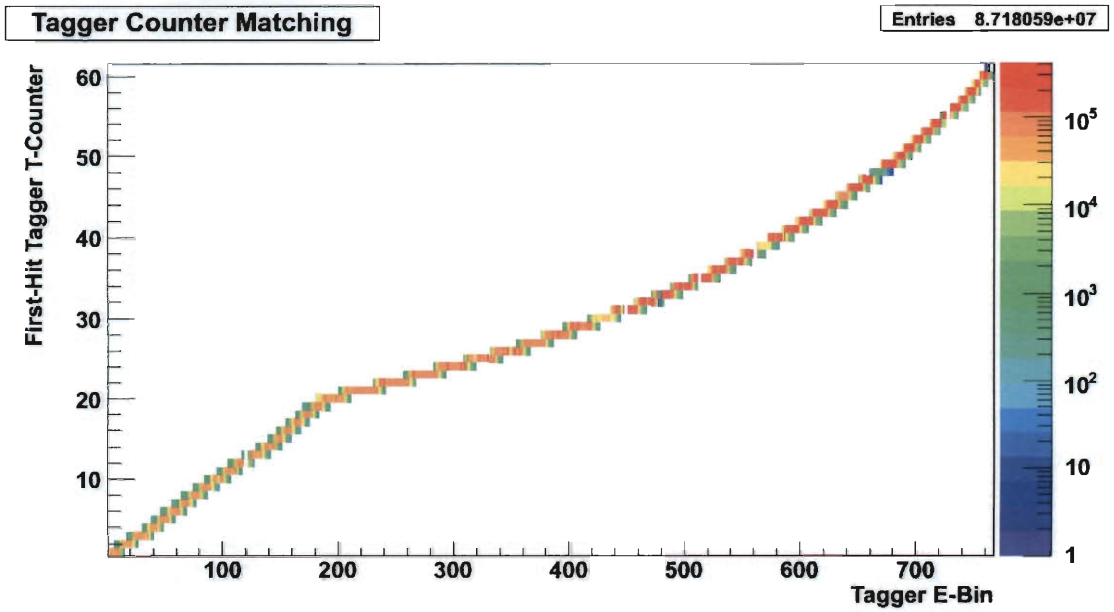

Figure 6.28 : Map showing the first-hit T-counter and E-bin matching of the tagger for g13a.

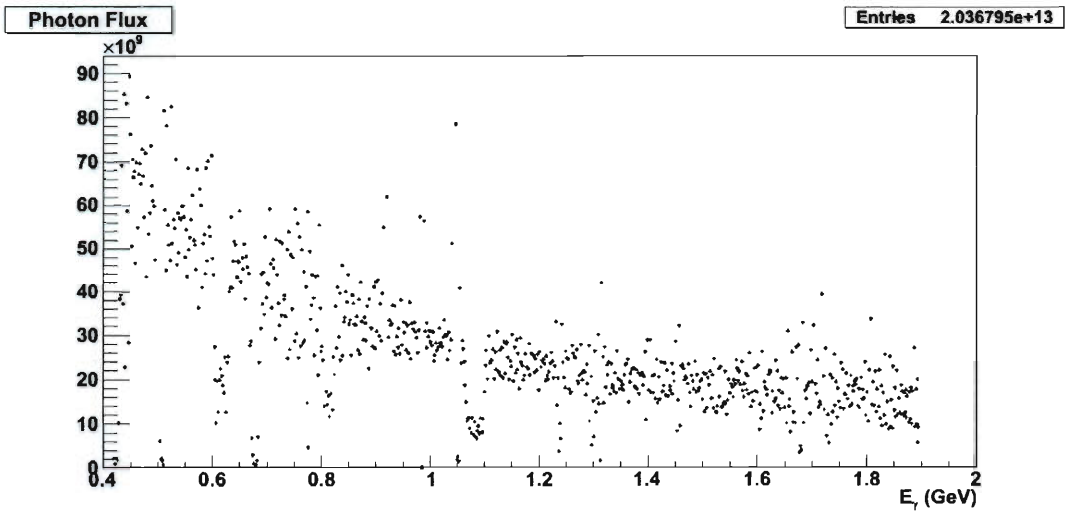

(A)

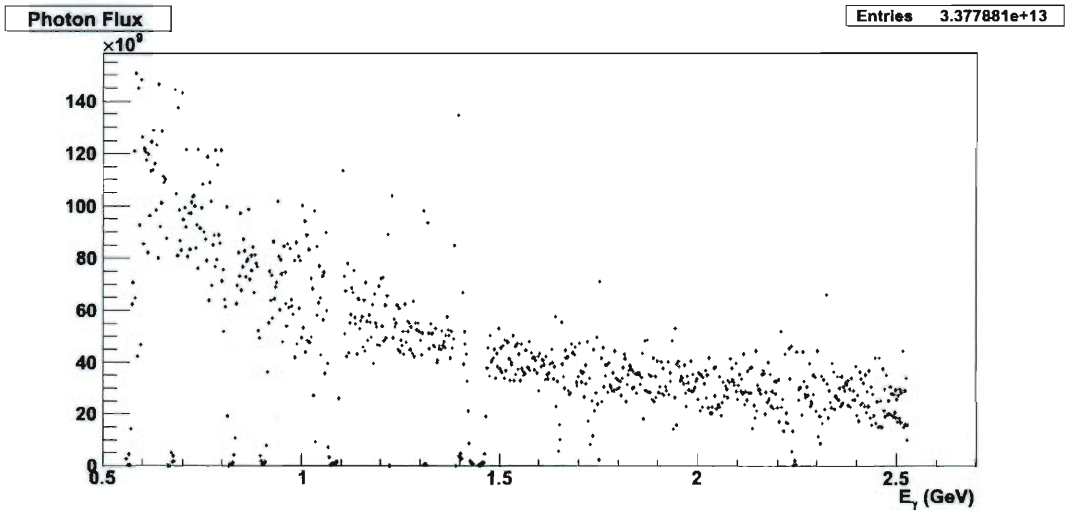

(B)

Figure 6.29 : The integrated photon flux of the 1.990 GeV (A) and 2.655 GeV (B) data files in this analysis. Dips in the distribution correspond to dead or inefficient tagger counters.

Chapter 7

The $\gamma n \to p\pi^-$ Validation Reaction

Before studying the $\gamma n \to K^{*0}\Lambda$ and $\gamma n \to K^+\Sigma^{*-}$ reactions, the differential cross section of the $\gamma n \to p\pi^-$ reaction was studied and compared to the published data from the CLAS g10 experiment [109]. This preliminary measurement was performed to ascertain whether the procedures used in this analysis would reproduce a known physics result. The cross sections largely agreed within the uncertainties, validating the integrity of the data and the procedures used in this analysis. This gives confidence in the similar approaches that were used to study the $\gamma n \to K^{*0}\Lambda$ and $\gamma n \to K^+\Sigma^{*-}$ reactions.

This preliminary $\gamma n \to p\pi^-$ differential cross section measurement employed the 2.655 GeV data from runs 53850 through 53859, excluding run 53853 due to significant photon timing calibration misalignments. This limited run range was chosen to increase the speed of the analysis by reducing the volume of the data to be analyzed. Although only ~3% of the 2.655 GeV data, these nine runs contained over five million $\gamma n \to p\pi^-$ events, significantly more than necessary for the comparison with the g10 data.

To extract the experimental yields, cuts were placed on the data to remove the background events. These yields were then acceptance-corrected and flux-normalized to calculate the differential cross section. When finalized, these results will provide a significant increase to the world statistics of this reaction. These data will provide better constraints on the N^* couplings to the neutron in the πN channel, as well as the photo-transition amplitudes of the γN interaction.

Cuts	Details
Data Range Cuts	Cut Junk Runs, Bad Files, Beam Trips
Minimum Momentum Cuts	π^- Momentum $\geq$ 100 MeV/c, p Momentum $\geq$ 400 MeV/c
Detector Region Cuts	Cut Inefficient SC Paddles, DC Holes, Fiducial Regions
Loose Skim Cuts	$\#X^+ \geq 1$, $\#X^- \geq 1$, $\lvert\Delta t_{p,\pi^-}\rvert \leq 8$ ns
	$0.7 < \gamma D \to p\pi^-(p)$ Missing Mass (GeV/c^2) < 1.2
Particle Identification	$\pm 3\sigma$ $\Delta\beta_{\pi^-}$ vs. π^- Momentum, $\pm 3\sigma$ $\Delta\beta_p$ vs. p Momentum
Vertex Time Differences	$\pm 3\sigma$ $\Delta t_{p,\pi^-}$ vs. p Momentum, $\pm 3\sigma$ $\Delta t_{\gamma,\pi^-}$ vs. π^- Momentum
Number of Photons	Cut Number of Photons > 1
Photon Tagger Cuts	Cut Bad Tagger Counters
Missing Momentum	$\gamma D \to p\pi^-(p)$ Missing Momentum $\leq$ 200 MeV/c
Track Combinations	Cut Number of Track Combinations > 1
Missing Mass	$\pm 3\sigma$ $\gamma D \to p\pi^-(p)$ Missing Mass

Table 7.1 : Summary of the cuts used to extract the experimental yields of the $\gamma n \to p\pi^-$ reaction, in the order that they were performed in this analysis.

7.1 Experimental Yield

The yields of the $\gamma n \to p\pi^-$ reaction were extracted by placing cuts on the data to remove background events while minimizing signal losses. Firstly the interaction vertex, particle times at the vertex, and missing four-momentum were calculated for the events. Next, skim cuts were placed to reduce the size of the dataset, along with cuts to remove the particles that were reconstructed in inefficient regions of the detector. Cuts on the particle types and timing were then performed to select events with the correct particles in the final state.

In addition, a cut was placed on the missing momentum of the reaction to remove the majority of the events with significant rescattering on the spectator proton. Finally, cuts were placed on the missing mass of $\gamma D \to p\pi^-(p)$ to eliminate events with additional particles in the final state. The yields were then calculated as the number of events that were above the background of this distribution in bins of photon energy and π^- angle. Table 7.1 shows a summary of the cuts detailed in the following subsections that were used to extract the experimental yields. This approach is very similar to the one used for the analysis of the $\gamma n \to K^{*0}\Lambda$ and $\gamma n \to K^+\Sigma^{*-}$ reactions, as discussed in Section 8.1.

7.1.1 Physics Evaluation

To test the hypothesis that the $\gamma n \rightarrow p\pi^-$ reaction occurred for a given event, preliminary particle identification was performed. Every positively charged track was labeled a proton candidate, and every negatively charged track was labeled a π^- candidate. The reaction was then evaluated separately for each possible combination of detected tracks.

The reaction vertex was determined to be the midpoint of the line bridging the proton and π^- paths at their distance of closest approach. The time of each particle at the reaction vertex was calculated as:

$$t_{\text{Vertex}} = t_{\text{TOF}} - \frac{x}{\beta c} = t_{\text{TOF}} - \frac{x\sqrt{m^2c^4 + p^2c^2}}{pc^2}, \tag{7.1}$$

where t_{TOF} is the track time measured at the TOF scintillators, x is the path length of the particles from the vertex to the TOF, $\beta \equiv \frac{v}{c} = \frac{pc}{E}$, and E and p are the energy and momentum of the particle. There were several tagged photons recorded for the majority of the events, so the photon with the closest vertex time to the π^- was selected. The π^- was chosen for the comparison because the uncertainty in the vertex time increased with σ_β/β, which was smaller for the π^-'s than for the protons. This uncertainty relation was derived from Equation 7.1, using the transformation of uncertainties.

The momentum and energy corrections determined in Chapter 5 were then applied to the reaction particles. Using four-momentum conservation, the missing mass of $\gamma D \rightarrow p\pi^-(p)$ was calculated along with the missing momentum. Histograms of these calculated quantities are shown in Section 7.1.4, along with the discussion of the final-state identification cuts.

7.1.2 Initial Cuts

First, cuts were placed to ignore the data in "junk" runs, data files containing critical system failures, and scalar intervals containing beam trips. Also, all particles that failed the minimum momentum, scintillator paddle, drift chamber hole, and fiducial cuts were rejected from the analysis. The studies of these cuts are located in Section 6.2.

Next, to increase the speed of the analysis of the $\gamma n \rightarrow p\pi^-$ reaction, loose skim cuts were placed to obtain a smaller subset of data for evaluation. First, only events with at least one positively charged track and one negatively charged track were considered. Next, the vertex time difference

between the proton and π^- candidates was required to be less than 8 ns. Also, the missing mass of $\gamma D \rightarrow p\pi^-(p)$ was required to be between 0.7 GeV/c^2 and 1.2 GeV/c^2 for at least one of the detected photons. Multiple photons were incident on the tagger counters during the DAQ recording window for the majority of the events, as discussed in Section 6.4. These cuts were designed to quickly reduce the size of the data sample without losing any signal events. Distributions of these quantities are located in Sections 7.1.4 and 7.1.5, where tighter cuts were applied to identify the final-state events and to extract the yields. Cuts restricting the number of detected particles were not implemented, because doing so would have removed signal events containing accidental tracks that originated from other events.

7.1.3 Particle Identification

Particles were identified by cutting on the $\Delta\beta$ vs. p distributions of the candidates for the given identity hypotheses. $\Delta\beta$ is defined as:

$$\Delta\beta = \beta_{\text{Hypothesis}} - \beta_{\text{Measured}} = \frac{pc}{\sqrt{m^2c^4 + p^2c^2}} - \frac{x}{c(t_{\text{TOF}} - t_{\text{Start}})}, \tag{7.2}$$

where p is the track momentum measured by the CLAS drift chambers, m is the mass of the hypothesized identity of the particle, x is the path length of the particle from the beamline to the TOF, t_{TOF} is the track time at the TOF scintillators, and t_{Start} is the event start time. The event start time was determined by the *user_ana* event reconstruction software by comparing the hit times in the start counter to the RF electron beam bunch times.

The $\Delta\beta$ vs. p distributions are shown in Figures 7.1(A) and 7.2(A) for protons and π^-'s, respectively. $\Delta\beta$ was centered around zero for particles of the hypothesized type. The extra bands of particles in the figures were either due to assigning an incorrect identity hypothesis, accidental tracks, or due to incorrect selections of the RF electron beam bunch for the reaction start time calculation. Accidental tracks were particles that originated from different physics events than the events that caused the trigger. These beam bunches arrived every 2.004 ns, resulting in extra bands of particles at regular intervals.

To determine the particle identification cuts, $\Delta\beta$ was fit to a Gaussian for different bins of track momentum. $\pm 3\sigma$ cuts were then fit to these results as a function of momentum by a linear polynomial for π^-'s, and by a piecewise exponential plus a linear polynomial for protons. These

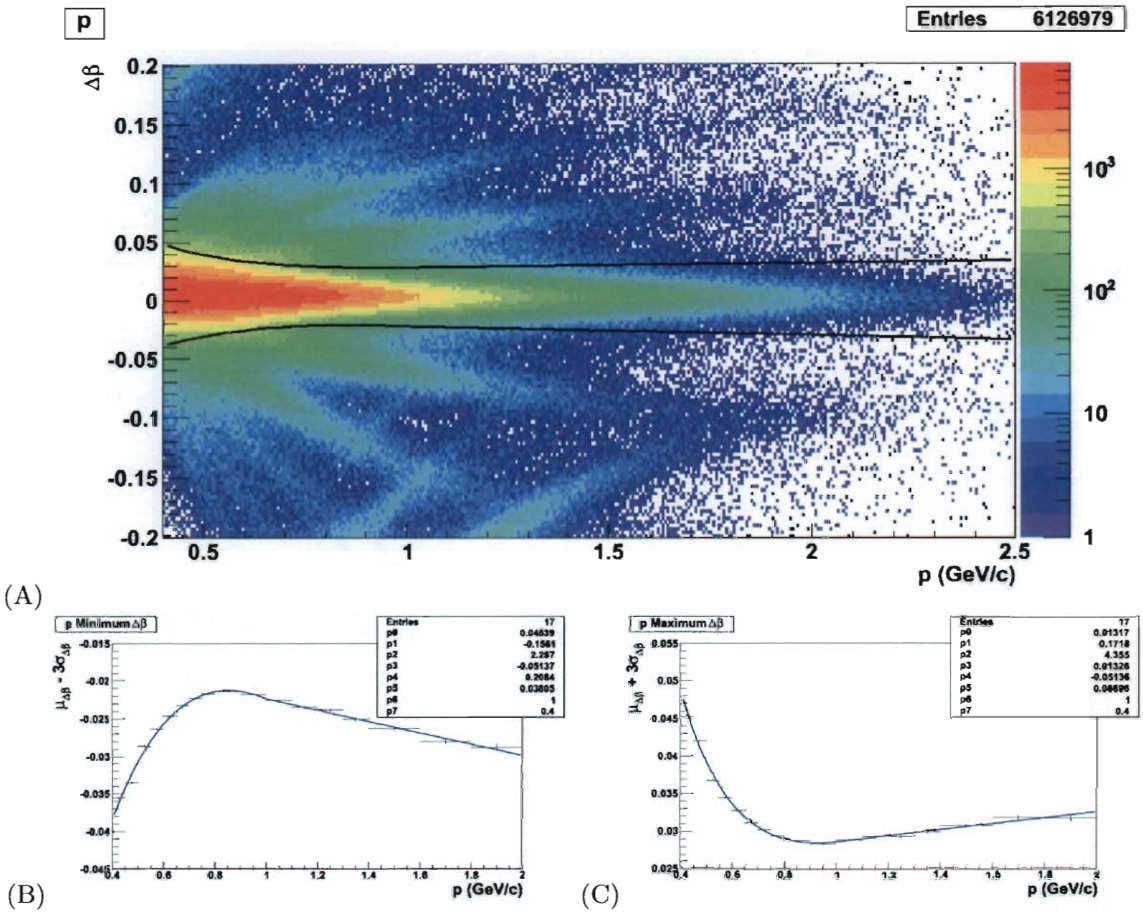

Figure 7.1 : For proton candidates, $\Delta\beta$ vs. p (A), and fits to the minimum (B) and maximum (C) $\Delta\beta$ cuts as a function of track momentum. The $\Delta\beta$ cuts were fit as a piecewise exponential plus linear function to the distributions of $\mu_{\Delta\beta} - 3\sigma_{\Delta\beta}$ (B) and $\mu_{\Delta\beta} + 3\sigma_{\Delta\beta}$ (C) derived from fitting a Gaussian to $\Delta\beta$ in each of the different momentum bins. These $\pm 3\sigma$ cuts for proton identification are illustrated by the black curves in (A). The width of $\Delta\beta$ varied with momentum due to the uncertainty in the β calculated from the track momentum. The extra bands of particles are either from accidental tracks, events with the reaction start time calculated incorrectly, or from particles with the incorrect identity hypothesis, such as K^+'s.

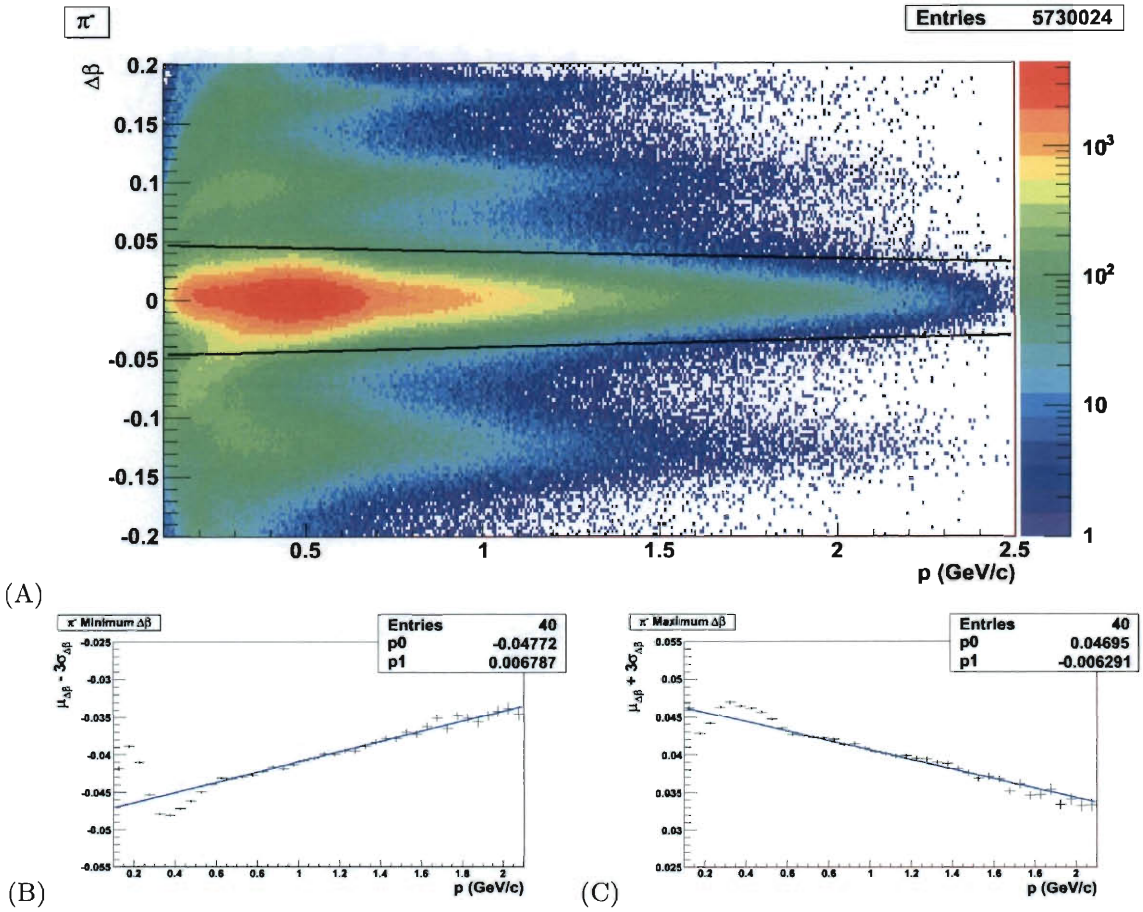

Figure 7.2 : For π^- candidates, $\Delta\beta$ vs. p (A), and fits to the minimum (B) and maximum (C) $\Delta\beta$ cuts as a function of track momentum. The $\Delta\beta$ cuts were fit as a linear function to the distributions of $\mu_{\Delta\beta} - 3\sigma_{\Delta\beta}$ (B) and $\mu_{\Delta\beta} + 3\sigma_{\Delta\beta}$ (C) derived from fitting a Gaussian to $\Delta\beta$ in each of the different momentum bins. These $\pm 3\sigma$ cuts for π^- identification are illustrated by the black lines in (A). The width of $\Delta\beta$ varied with momentum due to the uncertainty in the β calculated from the track momentum. The extra bands of particles are either from accidental tracks, events with the reaction start time calculated incorrectly, or from particles with the incorrect identity hypothesis, such as K^-'s. π^-'s with momentum less than 600 MeV/c were excluded from the fit due to their decays to μ^-'s, and the widening of the distribution from accidental tracks.

fits, along with the momentum binning, are shown in Figures 7.1 and 7.2 for protons and π^-'s, respectively. However, these cuts also rejected protons and π^-'s in events with the start time calculated incorrectly. A study of the yield correction for the loss of these events is detailed in Section 7.3.

A band of μ^-'s is visible in Figure 7.2(A) from -0.1 < $\Delta\beta$ < -0.03 at momenta less than 400 MeV/c. Above this momentum threshold the μ^-'s were largely indistinguishable from the π^-'s. This was acceptable because the μ^-'s were produced primarily from π^- decay, and their inclusion resulted in only a slight widening of the signal peak resolutions. Also, these decays were modeled by *gsim* in the Monte Carlo simulation to ensure accurate acceptance corrections. However, as seen in Figures 7.2(B) and 7.2(C), the change in the width of the π^- $\Delta\beta$ distribution was non-linear up to 600 MeV/c, partially due to a combination of accidental tracks and resolution effects. This effect is also studied for the $\gamma n \to K^{*0}\Lambda$ and $\gamma n \to K^+\Sigma^{*-}$ reactions in Section 8.1.3. Due to these complications, the π^- particle identification cut was extrapolated over this range.

The change in the width of the $\Delta\beta$ distribution with momentum was due primarily to the uncertainty of $\beta_{\text{Hypothesis}}$. This uncertainty is calculated as:

$$\sigma_{\beta_{\text{Hypothesis}}} = \frac{\sigma_p m^2 c^5}{(m^2c^4 + p^2c^2)^{3/2}}, \tag{7.3}$$

where σ_p is the uncertainty in the momentum measurement by the drift chambers. This equation was derived by transforming the uncertainty of σ_p using Equation 7.2. For high-momentum protons, the uncertainty in $\Delta\beta$ increased gradually with momentum because of the increasing σ_p. This was because higher momentum tracks were bent less in the drift chambers, and thus the uncertainties in their radius-of-curvature measurement were larger. However, the width of $\Delta\beta$ did not increase at high momentum for the π^-'s because the particle momentum was significantly larger than the mass, and thus the denominator of Equation 7.3 was increasing more rapidly than the numerator. The increase in the width of $\Delta\beta$ at low momentum for both particles is due to the denominator decreasing rapidly with particle momentum.

7.1.4 Final-State Identification Cuts

After performing the particle identification cuts, several additional cuts were used to identify the final state of the $\gamma n \to p\pi^-$ reaction. Firstly, $\pm 3\sigma$ cuts were placed on the vertex time difference between

the proton and the π^- as a function of proton momentum, as illustrated in Figure 7.3. These cuts were determined by fitting the distribution to a Gaussian in each of the different momentum bins, and then fitting the $\pm 3\sigma$ distributions to an exponential plus a linear function. The width of this distribution is much larger at low momentum because the uncertainty in the vertex times increased with σ_β/β. This time difference was studied vs. proton momentum because the slower protons had a much larger vertex time uncertainty than the π^-'s.

Next, the vertex time difference between all of the photons and the π^- was cut at $\pm 3\sigma$ as a function of π^- momentum, as illustrated in Figure 7.4. This cut was determined in the same manner as the cut on the proton and π^- time difference. The width of the cut varied with π^- momentum because the uncertainty in the π^- time increased with σ_β/β. The extra bands are either from photons originating in other beam bunches, from π^-'s that originated from other events, or from events where the wrong electron bunch was matched for the reaction start time calculation. Due to the interference from these bands, the fits were extrapolated below 200 MeV/c. Yield corrections for the event losses due to incorrect start time calculations are discussed in Section 7.3.

After performing these timing cuts, Figure 7.5 shows the distribution of the number of photons per event. In events with more than one photon it was difficult to unambiguously determine which photon caused the interaction. If the wrong photon were to be selected, then the yield distributions would have been artificially altered. Therefore, events with more than one photon surviving the $\pm 3\sigma$ timing cuts were rejected. This cut rejected $\sim$11.0% of the events, which as discussed in Section 7.3 was accounted for in the cross section calculation. Finally, the photon tagger bin cuts detailed in Section 6.2.3 were performed. These cuts were placed after the photon selection cuts to ensure that the cut on the number of surviving photons was not biased.

With the photon cuts in place, the missing momentum of the $\gamma D \rightarrow p\pi^-(p)$ reaction was required to be less than 200 MeV/c. While this cut reduced the background from events with additional particles such as $\gamma D \rightarrow p\pi^-(p\pi^0)$, it was primarily designed to reject events with significant rescattering. π^-'s that rescattered off of the spectator protons traveled in a different direction than when they were produced. These π^-'s also imparted some of their momentum to the spectator protons, sometimes enough that they reached the TOF paddles and were detected. Since this rescattering artificially altered the measured cross section distributions, the missing momentum cut was placed to significantly reduce its effects.

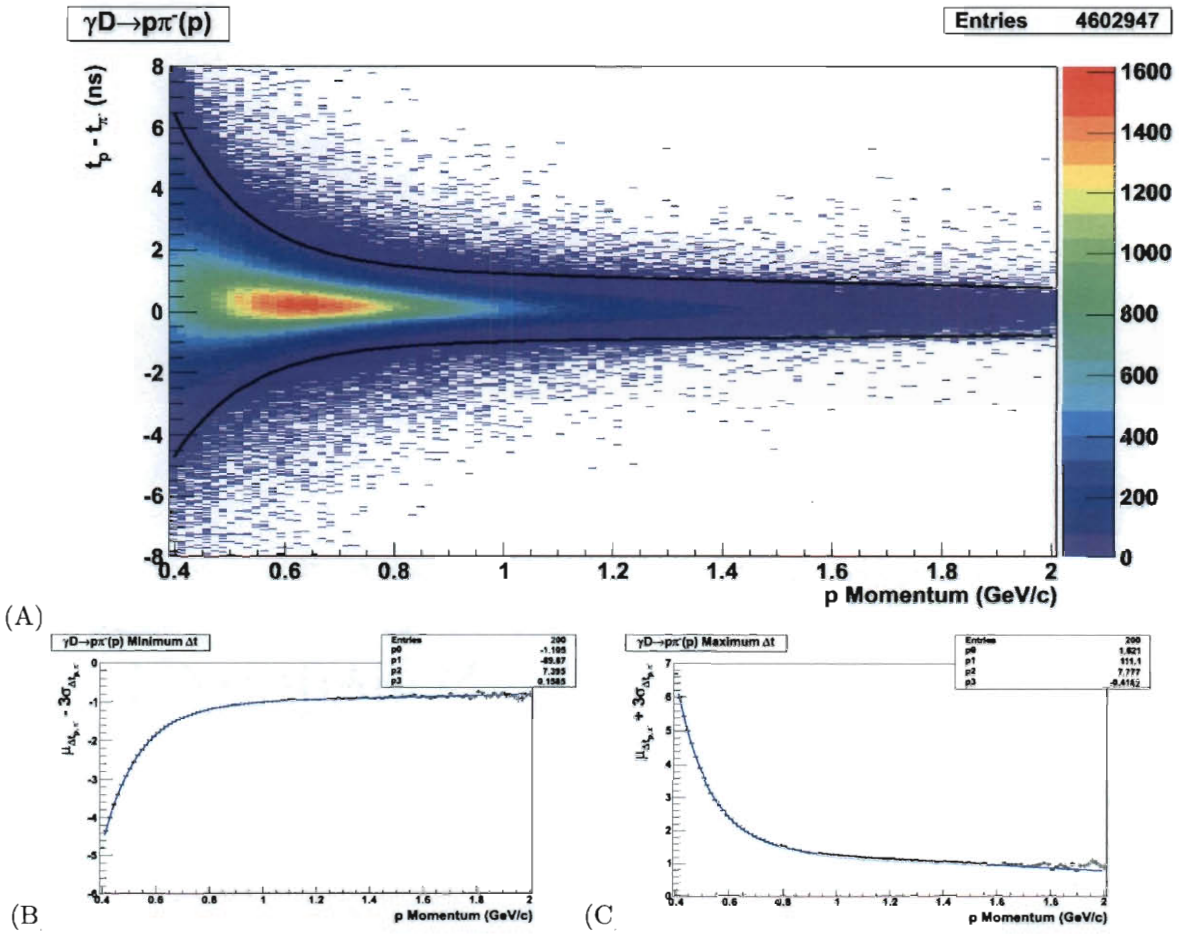

Figure 7.3 : The vertex time difference between the proton and π^- as a function of proton momentum (A), and fits to the minimum (B) and maximum (C) time difference cuts as a function of proton momentum. These cuts were fit as an exponential plus a linear function to the distributions of $\mu_{\Delta t} - 3\sigma_{\Delta t}$ (B) and $\mu_{\Delta t} + 3\sigma_{\Delta t}$ (C) derived from fitting a Gaussian to the time difference in each of the different momentum bins. The divergence of the fit above 1.8 GeV/c was due to issues with the Gaussian fits in the region with low statistics. These $\pm 3\sigma$ cuts on the time difference are illustrated by the black curves in (A). The width of this distribution is much larger at low momentum because the uncertainty in the vertex times increased with σ_β/β.

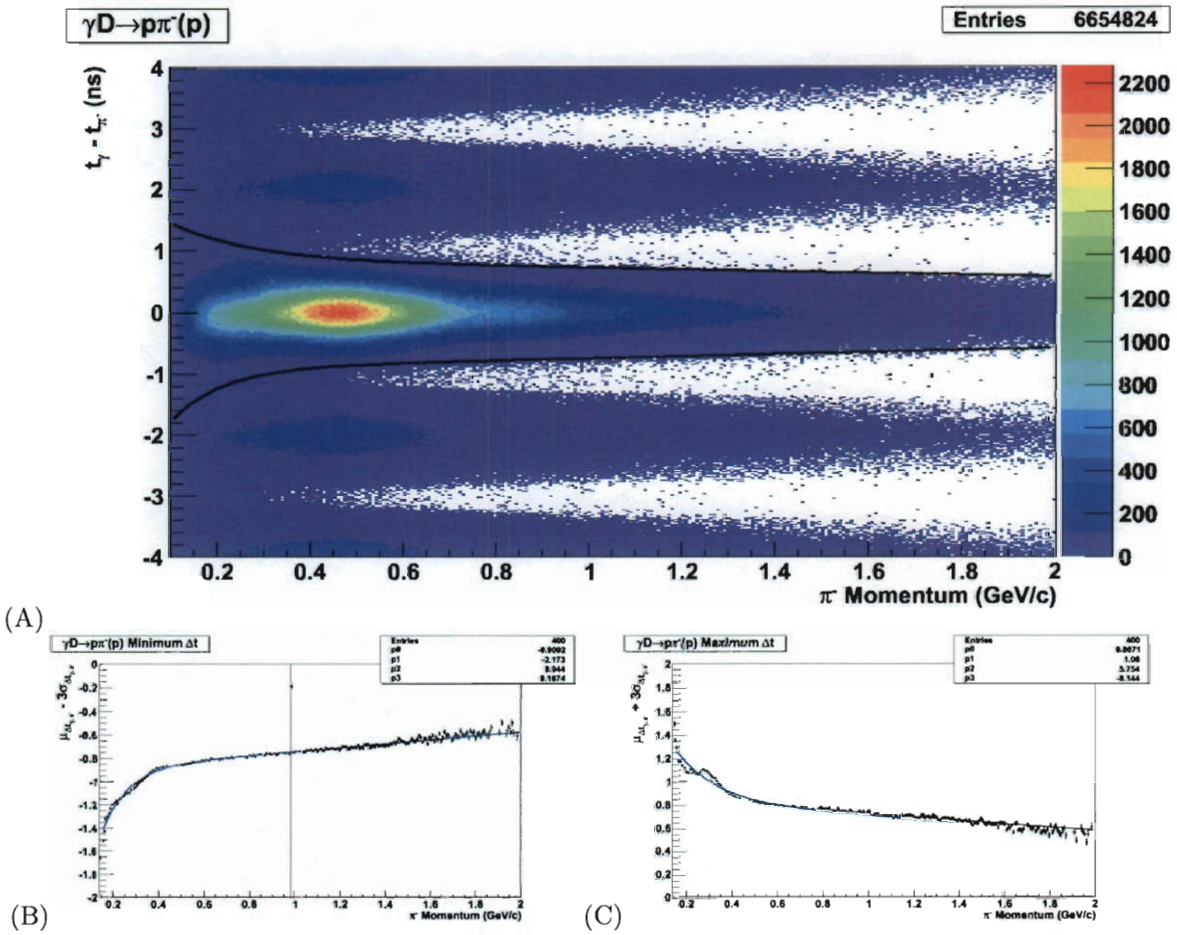

Figure 7.4 :. The vertex time difference between all of the detected photons and the π^- as a function of π^- momentum (A), and fits to the minimum (B) and maximum (C) time difference cuts as a function of π^- momentum. These cuts were fit as an exponential plus a linear function to the distributions of $\mu_{\Delta t} - 3\sigma_{\Delta t}$ (B) and $\mu_{\Delta t} + 3\sigma_{\Delta t}$ (C) derived from fitting a Gaussian to the time difference in each of the different momentum bins. These $\pm 3\sigma$ cuts on the time difference are illustrated by the black curves in (A). The extra bands are either from events with the reaction start time calculated incorrectly, from accidental π^-'s, or from photons originating from other beam bunches. Due to the interference from these bands, the fits were extrapolated below 200 MeV/c.

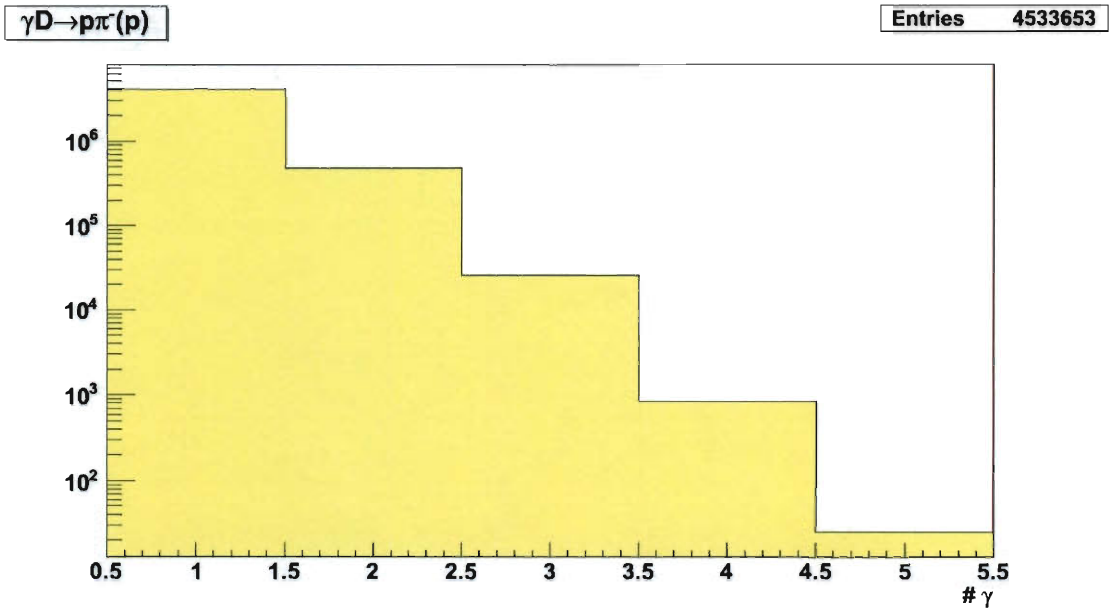

Figure 7.5 : The number of photons per event after 3σ cuts on $\Delta t_{\gamma,\pi^-}$. Events with more than one photon were rejected because it was difficult to determine which photon produced the observed event.

To illustrate the missing momentum distribution of $\gamma D \rightarrow p\pi^-(p)$ events, $\pm 3\sigma$ cuts were temporarily placed around the missing mass peak of the spectator proton. Figure 7.6 shows the missing momentum distributions after this temporary cut. The missing momentum is primarily peaked at low momentum due to Fermi motion, and the high-momentum tail is from rescattering events. Figure 7.6(B) shows that the spectator momentum is relatively uniformly distributed in $\cos(\theta)$, where θ is the angle between the missing momentum and the photon in the laboratory frame. Final cuts on the missing mass of the spectator proton are discussed in more detail in Section 7.1.5.

The cut at 200 MeV/c removed the majority of the events with significant rescattering and a minimal amount of the quasi-free events. However, the rescattering in the events that survived this cut may have had up to a 20% effect on the calculated cross section [109]. These rescattering effects were not not taken into account in this preliminary analysis. However, studies are being performed by Igor Strakovsky at George Washington University in an attempt to model this rescattering [110].

Finally, a cut was placed requiring that only one combination of tracks survived all of the preceding cuts. This was to ensure that no ambiguities remained from events with additional tracks, such as accidental particles that originated from other events. This cut rejected about 0.0026% of

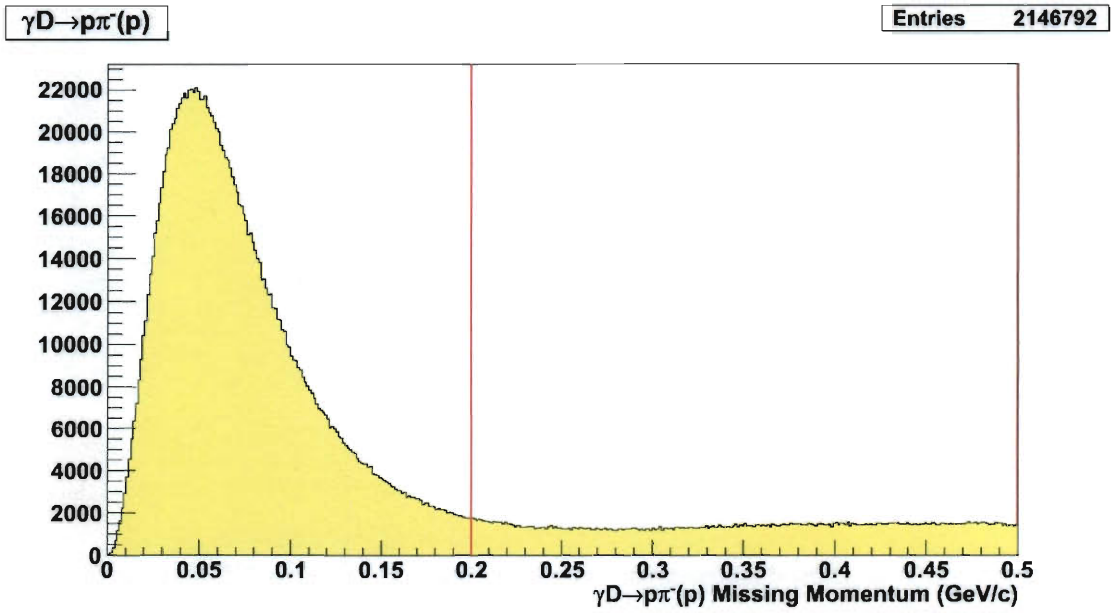

(A)

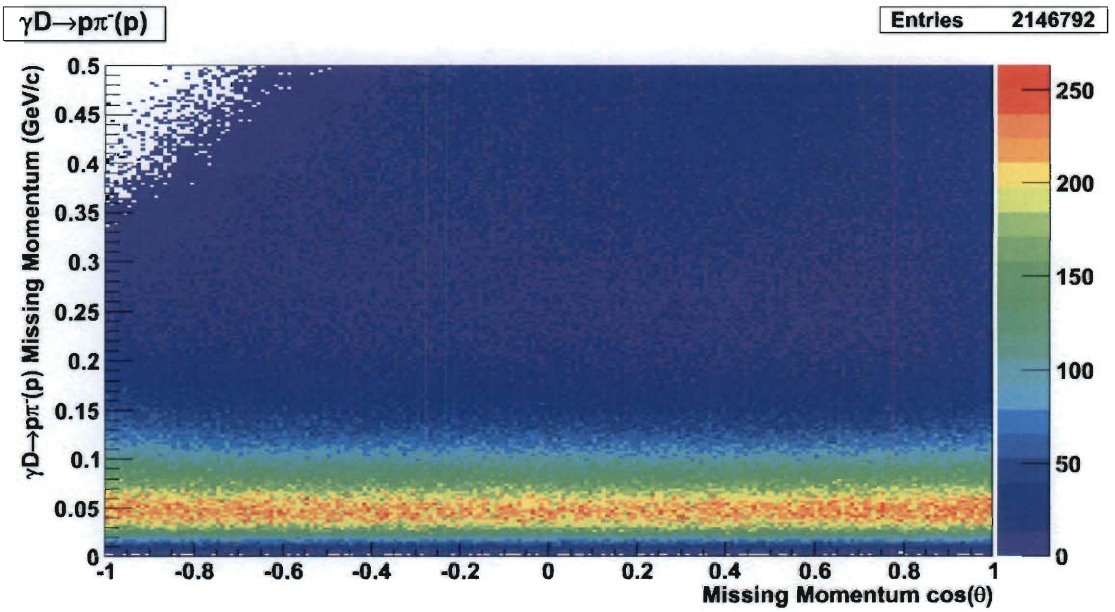

(B)

Figure 7.6 : The missing momentum of the spectator proton (A) shown vs. $\cos(\theta)$ of the missing momentum in the lab frame (B). The low-momentum, quasi-free spectator protons followed the Fermi motion distribution and were relatively uniformly distributed in $\cos(\theta)$. The high-momentum tail of rescattered spectator protons was removed by the 200 MeV/c cut on the missing momentum.

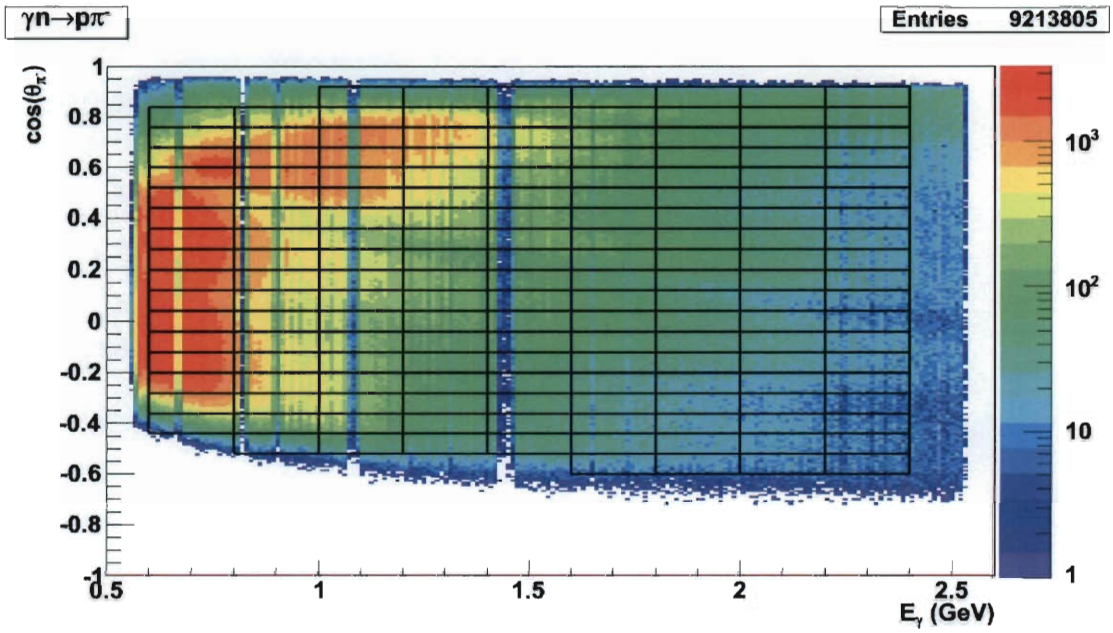

Figure 7.7 : The distribution of the $\gamma n \to p\pi^-$ final-state events from several runs of the g13a experiment as a function of photon energy and $\cos(\theta_{\pi^-})$, where θ_{π^-} is the angle between the π^- and the photon in the center-of-mass frame. The grid overlaid on the distribution illustrates the binning used for extracting the experimental yield of the $\gamma n \to p\pi^-$ reaction.

the events, which as discussed in Section 7.3 was accounted for in the cross section calculation.

7.1.5 Yield Extraction

The distribution of the $\gamma n \to p\pi^-$ final-state events is shown in Figure 7.7 as a function of photon energy and $\cos(\theta_{\pi^-})$, where θ_{π^-} is the angle between the π^- and the photon in the $\gamma n \to p\pi^-$ center-of-mass frame. The holes in the distribution at fixed photon energy are due to bad tagger counters that were removed from this analysis. Overlaid on this distribution is a black grid showing the binning used for yield extraction. These bins were 200 MeV wide in photon energy, and spanned 0.08 in $\cos(\theta_{\pi^-})$. The energy bins were chosen to match those of the g10 analysis, and the $\cos(\theta_{\pi^-})$ bins such that the statistics were large enough for reliable extraction of both the experimental and simulated yields.

For each of these bins, the missing mass of $\gamma D \to p\pi^-(p)$ was fit to a Gaussian over a linear background. Figure 7.8 shows these fits for one $\cos(\theta_{\pi^-})$ bin of each photon energy bin. The red lines indicate the $\pm 3\sigma$ cuts around the spectator proton, and the yield in each bin was calculated

as the number of events above the fit background between these cuts. The secondary peak at about 1.12 GeV/c^2 is from events with an additional π^0 in the final state, which come primarily from either the $\gamma n \rightarrow \pi^-\Delta^+ \rightarrow \pi^- p\pi^0$ or $\gamma n \rightarrow \pi^0\Delta^0 \rightarrow \pi^0 p\pi^-$ reactions. Although small, these events comprise the primary source of background underneath the spectator proton peak. The fits for all of the bins in this analysis are located in Appendix C.1.

Most of the background from accidental tracks was assumed to have been rejected by the $\pm 3\sigma$ timing cuts between the proton and π^-. Also, the non-Gaussian tails of the spectator proton peak arising from the non-Gaussian track measurements were assumed to be modeled in the CLAS detector simulation. The extracted experimental yields are shown in Section 7.2 compared against the yield distributions of the Monte Carlo simulation. Approximately 5.8 million events were present in the experimental yield. These yield events were assumed to be binomially distributed with respect to the background, with statistical uncertainties given by [54]:

$$\sigma_{\text{Stat}} = \sqrt{YP(1-P)}, \tag{7.4}$$

where Y is the yield in the given bin, and P is the fraction of the events within the $\pm 3\sigma$ cuts that were above the background in the given bin. The statistical uncertainties on the yields were less than 1.3% in all bins.

7.2 Simulated Detector Acceptance

Monte Carlo simulation data were analyzed to calculate the CLAS detector acceptance of the $\gamma n \rightarrow p\pi^-$ reaction. As discussed in Section 6.1, *fsgen* [99] was used to generate the Monte Carlo data. The George Washington University SAID [111] cross section predictions, based on the world data of the $\gamma n \rightarrow p\pi^-$ reaction, were used as the input to *fsgen* for generating the particle distributions. At the time these predictions were developed, no data on the $\gamma n \rightarrow p\pi^-$ reaction were available above 2.0 GeV [111]. These cross section predictions were chosen to simulate the distributions of the experimental data to obtain more accurate acceptance corrections. If the simulated distributions differ significantly from the experimental data, then variations of the detector acceptance across the widths of the bins used for yield extraction can cause incorrect modeling of the CLAS acceptance. Approximately 50 million events were generated by *fsgen*.

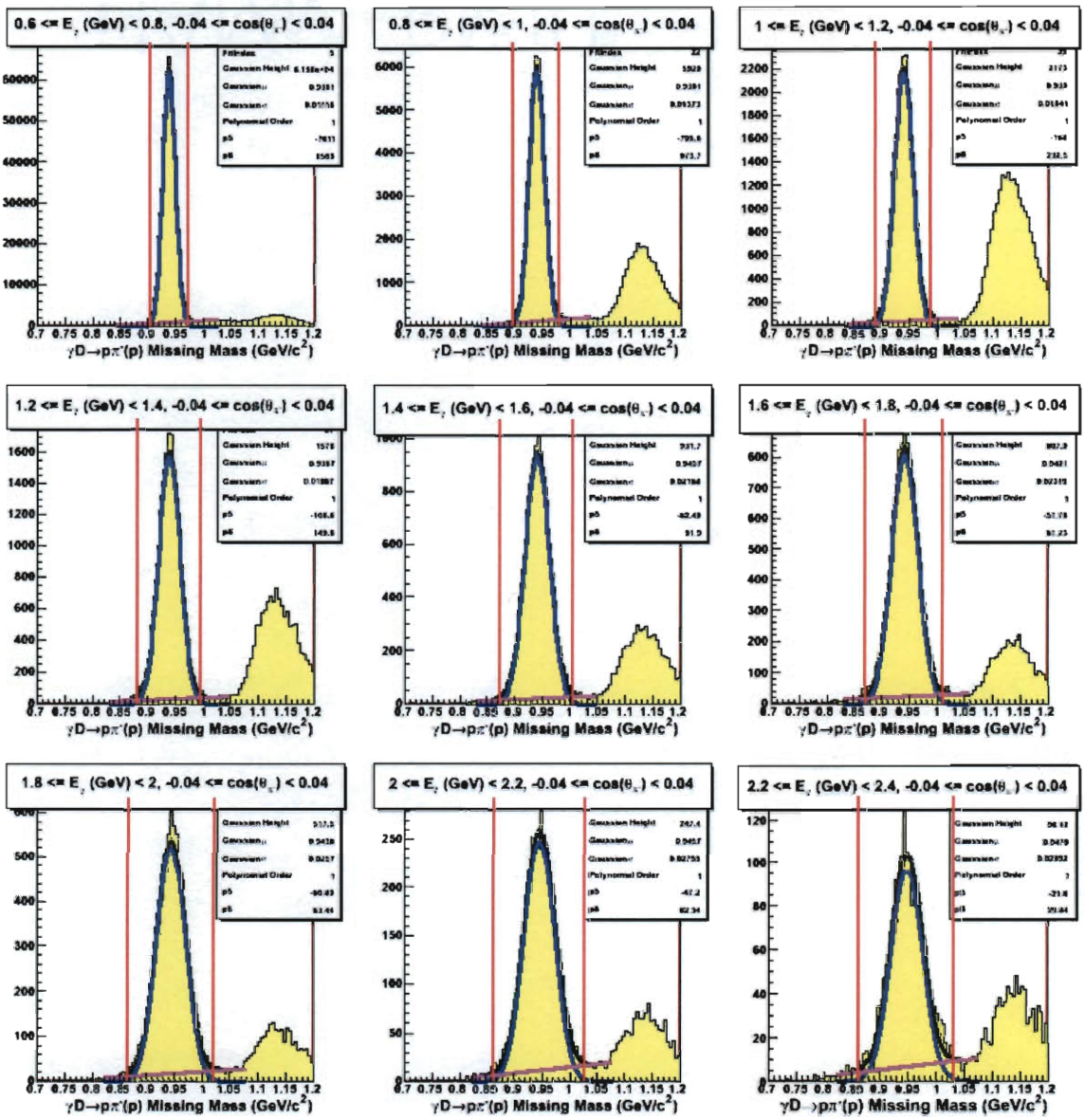

Figure 7.8 : Fits to the missing mass of the spectator proton in the experimental data of the $\gamma D \to p\pi^-(p)$ reaction in the -0.04 $< \cos(\theta_{\pi^-}) <$ 0.04 bins, where θ_{π^-} is the angle between the π^- and the photon in the center-of-mass frame. The signals were fit to a Gaussian over a linear background, and the red lines indicate the $\pm 3\sigma$ cuts used for yield extraction. The blue lineshapes represent the Gaussian fit functions, the magenta lineshapes represent the linear fit functions, and the black lineshapes represent the total fit functions.

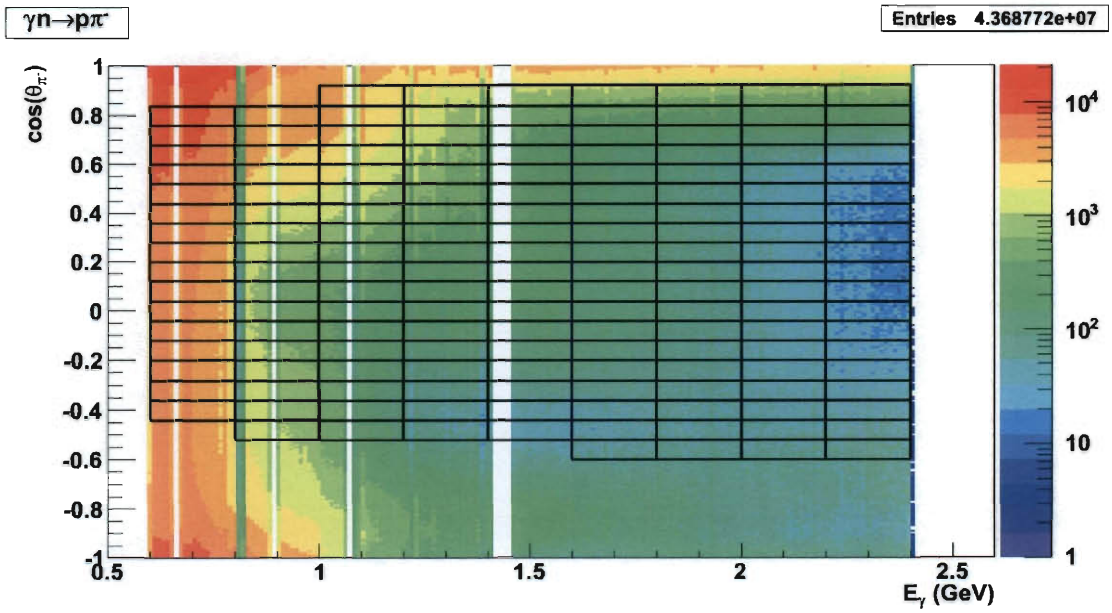

Figure 7.9 : The distribution of the generated Monte Carlo events of the $\gamma n \rightarrow p\pi^-$ reaction after running *gpp* as a function of photon energy and $\cos(\theta_{\pi^-})$, where θ_{π^-} is the angle between the π^- and the photon in the center-of-mass frame. The grid overlaid on the distribution illustrates the binning used for calculating the acceptance of the $\gamma n \rightarrow p\pi^-$ reaction. This distribution was generated using the SAID cross section predictions [111].

The *gsim* and *gpp* software packages [102] were run to simulate the response of the CLAS detector to these events, as discussed in Section 6.1. The distribution of the generated events after *gpp* is shown in Figure 7.9, along with the binning grid from Figure 7.7 that was used for calculating the acceptance corrections. The holes in the distribution are from the rejection of the bad tagger counters by *gpp* as detailed in Section 6.2.3. The generated yields were determined after *gpp* to remove any effects from the photon tagger acceptance. The acceptance of the photon tagger is taken into account in the photon flux determination, as discussed in Section 6.4.

The edges of the photon energy range of the generated distribution were the same as those of the binning. However, since the distribution of the generated events was binned after running *gpp*, the bin edge effects on the calculated acceptance due to photon energy migration are negligible. This distribution is acceptable for comparing the g13 $\gamma n \rightarrow p\pi^-$ cross section to the g10 results, but can be improved slightly by expanding the photon energy range of the generated data.

After track reconstruction of the simulated data with *user_ana* [103], the response of the CLAS trigger was simulated as discussed in Section 6.3.2. The events that failed the simulated trigger were

then rejected from the analysis. The simulated events were evaluated in the same manner as the experimental data, as discussed in Section 7.1.1.

The same analysis cuts used on the experimental data were placed on the simulated data to identify the final state of the $\gamma n \rightarrow p\pi^-$ reaction. This included the minimum momentum, scintillator paddle, drift chamber hole, and fiducial cuts that were detailed in Section 6.2. The skim cuts detailed in Section 7.1.2 on the experimental data were also used for skimming the simulated data. Particle identification cuts, time difference cuts, missing momentum cuts, and a cut on the number of surviving track combinations were then implemented to identify the final state. The cut on the bad tagger counters was performed by *gpp*, and the cut on the number of photons was unnecessary because there was only one simulated photon per event. No events were lost with the cut on the number of track combinations due to the lack of accidental tracks in the simulation.

The $\pm 3\sigma$ cuts on the particle identification, time differences, and missing mass were re-fit for the simulated data. The experimental values were not used for these cuts because the simulated detector resolution did not exactly match the experimental resolution. While Figures 6.2 and 6.3 show that the detector resolution was closely modeled, the $\pm 3\sigma$ cuts were re-fit to ensure that the yield loss due to these cuts would be matched in the simulation.

The distribution of the simulated $\gamma n \rightarrow p\pi^-$ final-state events is shown in Figure 7.10, along with the binning used for the acceptance corrections. The effects of the tagger counters that were rejected from this analysis are shown by the holes in this distribution at fixed photon energies. Figure 7.11 shows the fits to the simulated missing mass of $\gamma D \rightarrow p\pi^-(p)$ for one of the $\cos(\theta_{\pi^-})$ bins in each photon energy bin. These peaks were fit to Gaussian functions and cut at $\pm 3\sigma$, and the $\sim$4.5 million events above the backgrounds between these cuts were the simulated yields.

The extracted experimental and simulated yields of the $\gamma n \rightarrow p\pi^-$ reaction are shown in Figure 7.12 for each of the different photon energy bins. The heights of the distributions of the simulated yields in the histograms were scaled to the experimental yields to better illustrate the comparison. The matching between the experimental and simulated yields was much better at smaller photon energies than at larger photon energies. This was most likely due to differences at large energies between the differential cross sections and the SAID predictions used for generating the Monte Carlo data. These differences were primarily due to the scarcity of published cross section data at these energies, upon which the SAID predictions were based.

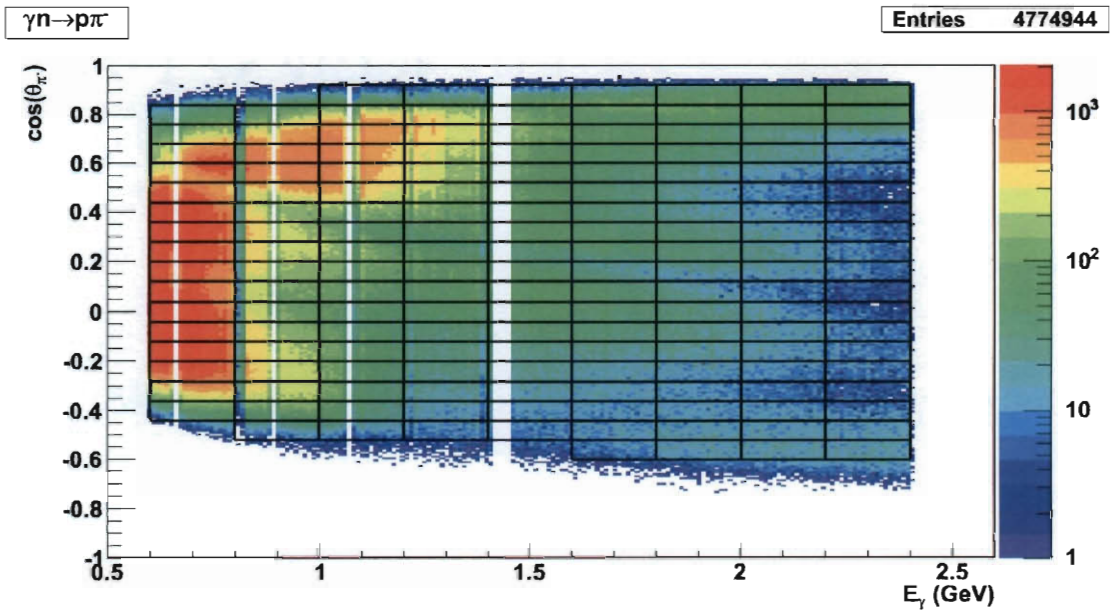

Figure 7.10 : The distribution of the reconstructed final-state Monte Carlo events of the $\gamma n \rightarrow p\pi^-$ reaction as a function of photon energy and $\cos(\theta_{\pi^-})$, where θ_{π^-} is the angle between the π^- and the photon in the center-of-mass frame. The holes in the distribution are due to the cuts placed from the acceptance studies of Chapter 6. The grid overlaid on the distribution illustrates the binning used for calculating the acceptance of the $\gamma n \rightarrow p\pi^-$ reaction.

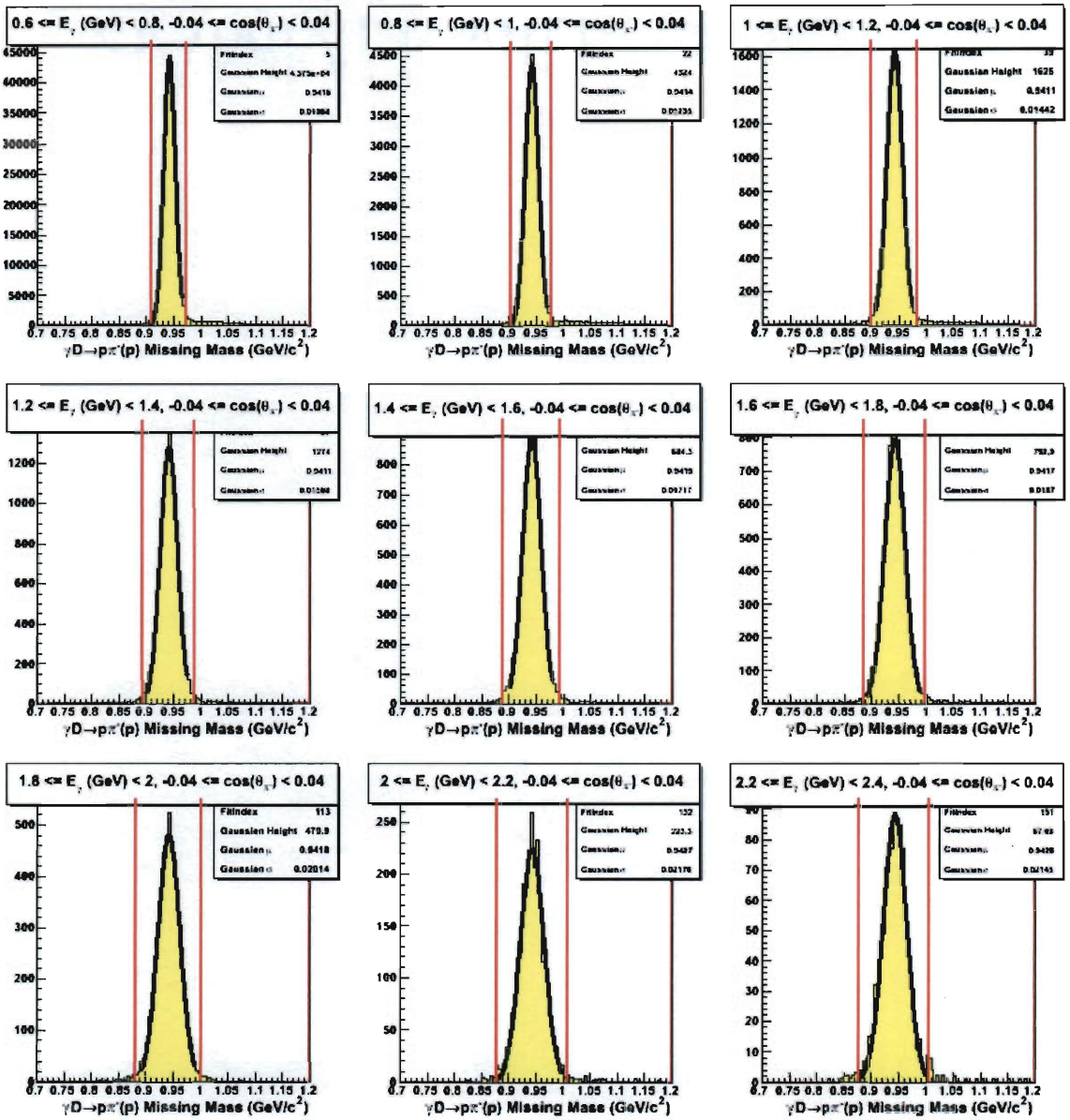

Figure 7.11 : Fits to the missing mass of the spectator proton in the simulated data of the $\gamma D \rightarrow p\pi^-(p)$ reaction in the -0.04 $< \cos(\theta_{\pi^-}) <$ 0.04 bins, where θ_{π^-} is the angle between the π^- and the photon in the center-of-mass frame. The signals were fit to Gaussian functions, and the red lines indicate the $\pm 3\sigma$ cuts used for yield extraction.

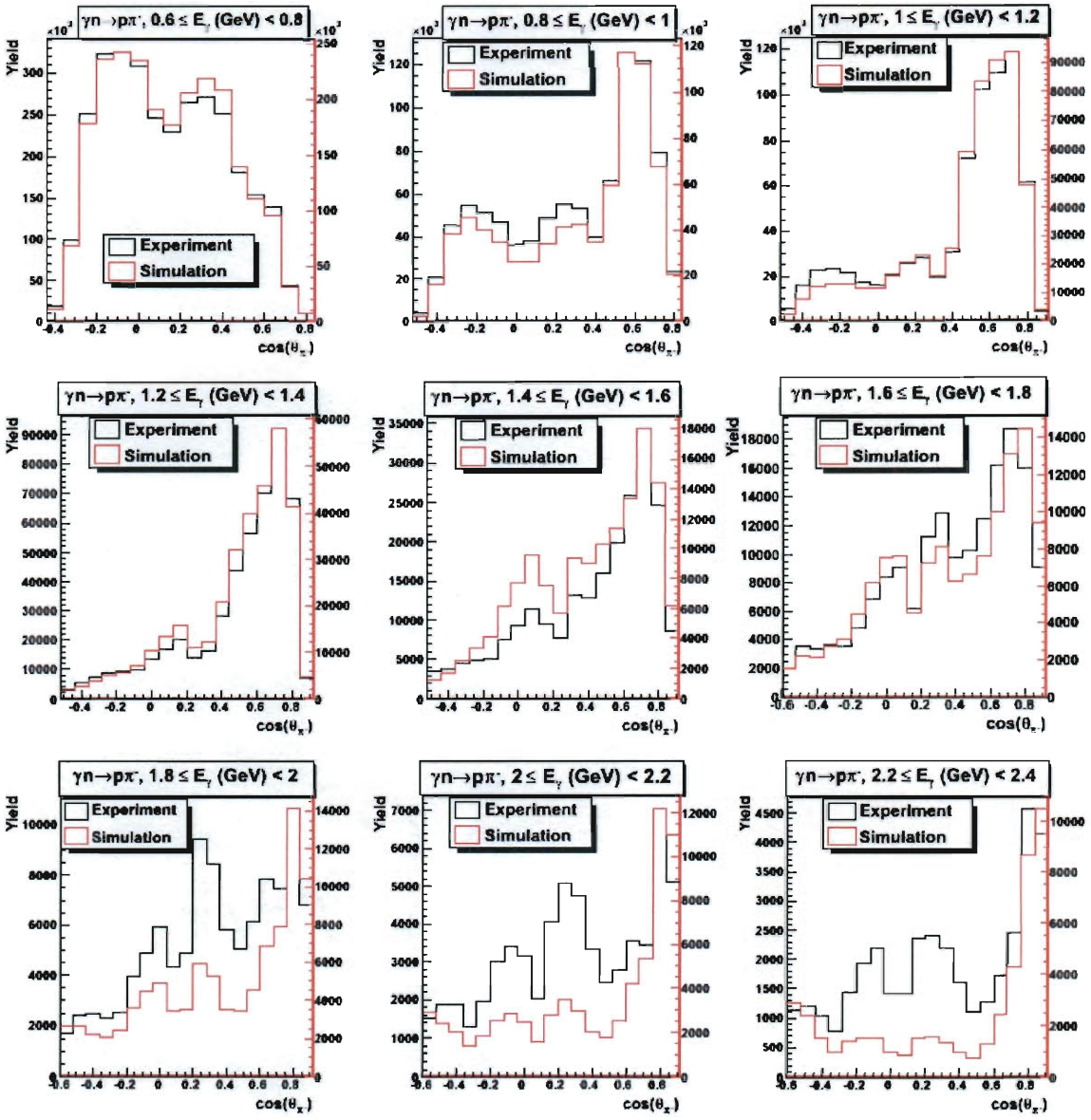

Figure 7.12 : Comparison between the experimental and simulated yields of the $\gamma n \rightarrow p\pi^-$ reaction in different photon energy bins as a function of $\cos(\theta_{\pi^-})$, where θ_{π^-} is the angle between the photon and the π^- in the center-of-mass frame. The axes on the left side of the plots are for the experimental yields, and the axes on the right side of the plots are for the simulated yields. The large differences between the distributions at the higher energies are largely due to differences between the differential cross sections and the SAID predictions.

The simulated acceptance of the $\gamma n \rightarrow p\pi^-$ reaction is shown in Figure 7.13 as a function of $\cos(\theta_{\pi^-})$ in the different photon energy bins. The acceptance was calculated as the fraction of the generated events surviving the tagger counter rejection in *gpp* that were present in the reconstructed yield. The large variations in the acceptance were due to the rejected drift chamber holes, panel overlaps, and scintillator paddles, as well as the simulated triggering inefficiencies. Overall, ~18% of the events generated in these bins were present in the reconstructed yields. The statistical uncertainties on the acceptance were calculated using Equation 7.4, where P was the calculated acceptance of the given bins. The statistical uncertainties on the simulated acceptances were less than 3.3% for all bins.

7.3 Yield Correction Factor and Photon Flux

Before calculating the cross section, the experimental yields were corrected due to event losses that were not modeled in simulation. These included event losses in which the reaction start time was calculated incorrectly, greater than one photon survived the timing cuts, or there was greater than one possible track combination. These yield losses were assumed to be bin-independent, as these effects have a negligible dependence on photon energy or π^- angle.

The yield loss from incorrectly determined start times was calculated by re-analyzing the $\gamma n \rightarrow p\pi^-$ reaction using the inverse of the particle identification and photon-π^- time difference cuts. In other words only events that failed either of these cuts were considered, while most of the final-state identification cuts remained the same. The cut on the number of photons was removed, and instead the missing mass of the spectator proton was calculated for each of the detected photons outside of the timing cuts. Figure 7.14 shows the missing mass of the $\gamma D \rightarrow p\pi^-(p)$ reaction for all of these photons, where the dominant source of the large background is from the photons that did not produce the event.

This missing mass distribution was fit to a Gaussian plus a linear background and cut at $\pm 3\sigma$ to determine the yield. The yield above the background from these inverse cuts was ~5% of the true yield in the experimental data. This same study was performed for the simulated data, where the yield was about 1.2% of the true simulated yield. The losses in simulation were from events on the tails of the $\pm 3\sigma$ Gaussian cuts, including the π^-'s that decayed into μ^-'s and failed the particle identification cuts. The yield losses from the other sources are detailed in Sections 7.1 and 7.2.

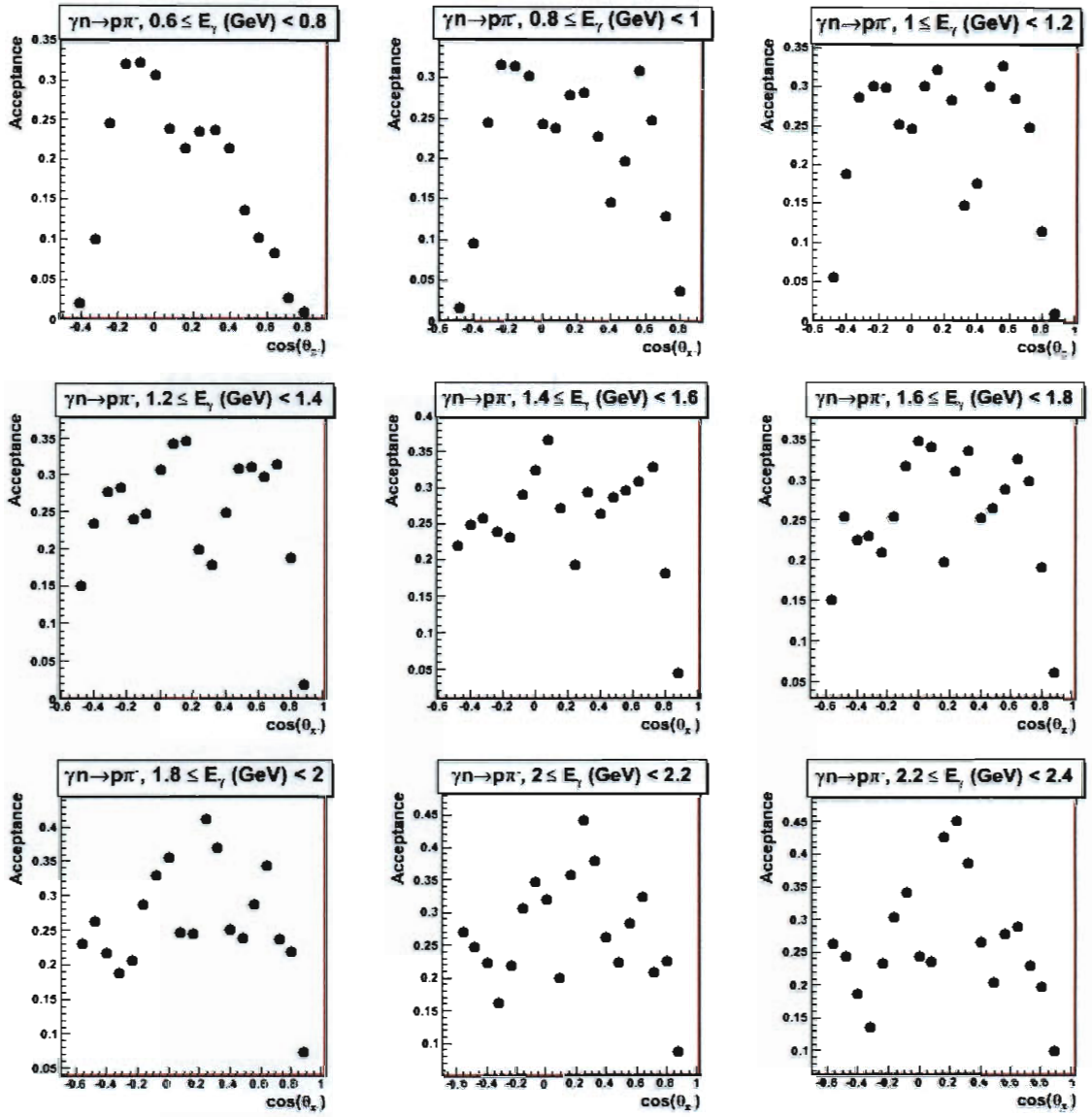

Figure 7.13 : The calculated CLAS acceptance of the $\gamma n \rightarrow p\pi^-$ reaction in different photon energy bins as a function of $\cos(\theta_{\pi^-})$, where θ_{π^-} is the angle between the photon and the π^- in the center-of-mass frame. The error bars for the statistical uncertainties are smaller than the points so are not visible. The large variations in the acceptance were primarily due to inefficient triggering, the TOF panel overlaps, drift chamber holes, and bad scintillator paddles.

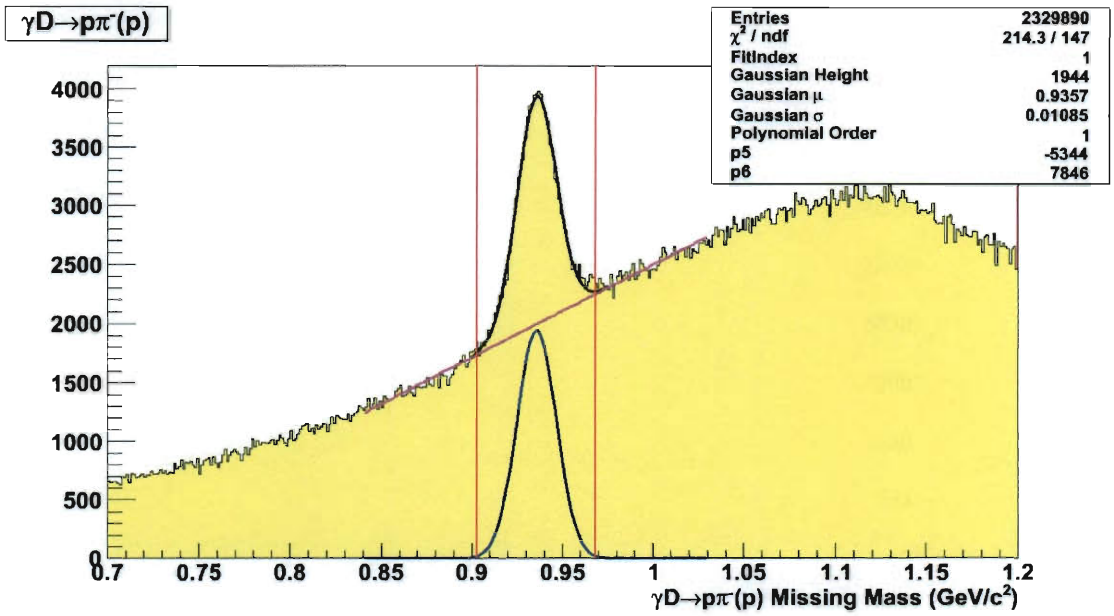

Figure 7.14 : The missing mass of the $\gamma D \to p\pi^-(p)$ reaction for all photons, using inverse photon timing cuts and with the cut on the number of photons removed. The spectator proton peak is fit to a Gaussian plus a linear function, and the $\pm 3\sigma$ cuts are illustrated by the red lines. The blue lineshape represents the Gaussian fit function, the magenta lineshape represents the linear fit function, and the black lineshape represents the total fit function.

The final yield correction factor Y_{CF} was then calculated as:

$$Y_{\mathrm{CF}} = \frac{(1 - \mathrm{Cut\%_{ST\text{-}S}})(1 - \mathrm{Cut\%_{\#TC\text{-}S}})}{(1 - \mathrm{Cut\%_{ST}})(1 - \mathrm{Cut\%_{\#\gamma}})(1 - \mathrm{Cut\%_{\#TC}})}, \tag{7.5}$$

where $\mathrm{Cut\%_{ST}}$ is the fraction of the true yield that was cut due to incorrectly calculated start times in the experimental data, $\mathrm{Cut\%_{ST\text{-}S}}$ is the same but in the simulation, $\mathrm{Cut\%_{\#TC}}$ is the fraction of the true yield cut due to more than one track combination surviving the cuts in the experimental data, $\mathrm{Cut\%_{\#TC\text{-}S}}$ is the same but in the simulation, and $\mathrm{Cut\%_{\#\gamma}}$ is the fraction of the true yield cut from events with greater than one photon. Y_{CF} was calculated to be $\sim$1.17, and its dominant source was the $\sim$11.0% yield cut on the number of photons. The uncertainty on the individual components of the yield correction factor were all less than 0.03%, so the uncertainty on Y_{CF} was ignored for the cross section calculation.

The integrated photon flux from runs 53850 through 53859, excluding run 53853, is shown in Figure 7.15 in the bins used for the cross section calculation. This flux was calculated using the procedure described in Section 6.4. The integrated flux distribution roughly followed the $1/E_\gamma$ bremsstrahlung energy distribution, but deviated primarily due to the inefficient tagger counters. Approximately 1.27 trillion tagged photons were incident on the CLAS target in this analysis. The statistical uncertainties on the integrated photon fluxes were less than 0.0061% for all energy bins.

7.4 Differential Cross Section

The differential cross section of the $\gamma n \rightarrow p\pi^-$ reaction was calculated for each bin of photon energy and $\cos(\theta_{\pi^-})$ as [112]:

$$\frac{d\sigma}{d\Omega}(E_\gamma, \theta_{\pi^-}) = \frac{1}{2\pi(\Delta\cos(\theta_{\pi^-}))} \frac{A_r}{\rho L N_A} \frac{Y(E_\gamma, \theta_{\pi^-}) Y_{\mathrm{CF}}}{\Phi(E_\gamma) A(E_\gamma, \theta_{\pi^-})}, \tag{7.6}$$

where E_γ is the photon energy, $\Delta\cos(\theta_{\pi^-})$ is the width in $\cos(\theta_{\pi^-})$ of the given bin, θ_{π^-} is the angle between the photon and the π^- in the center-of-mass frame, A_r is the atomic weight of the target, ρ is the target density, L is the target length, N_A is Avogadro's number, Φ is the photon flux in the given photon energy bin, Y is the experimental yield in the given bin, A is the simulated acceptance in the given bin, and Y_{CF} is the yield correction factor. The factor of 2π is due to the integration over the azimuthal angle ϕ in the binning used for the cross section calculation. The statistical uncertainty

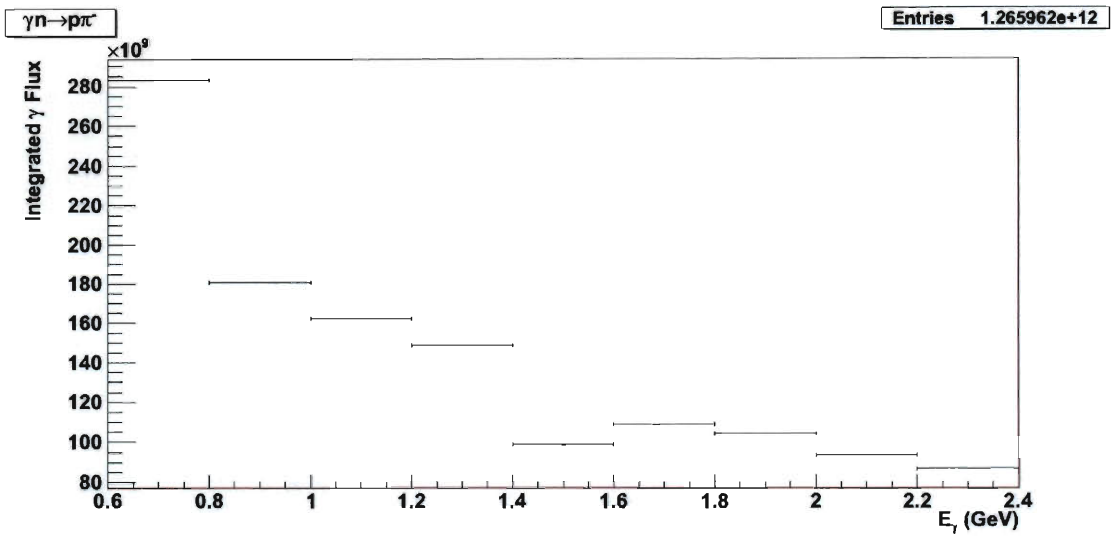

Figure 7.15 : The integrated photon flux from runs 53850 through 53859, excluding run 53853, in the photon energy bins used in the cross section calculation. This distribution deviates from the $1/E_\gamma$ bremsstrahlung energy distribution due to the inefficient tagger counters.

Target Factor	Description	Value and Uncertainty
A_r	Target Atomic Weight	$2.013553212724 \pm 7.8 \times 10^{-11}$ g/mol [113]
ρ	Target Density	$0.1625 \pm 1.79 \times 10^{-4}$ g/cm^3 [82, 112]
L	Target Length	40.00 ± 0.01 cm [92]
N_A	Avogadro's Number	$6.02214179 \times 10^{23} \pm 3.0 \times 10^{16}$ mol^{-1} [114]

Table 7.2 : The liquid-deuterium target factors used in the differential cross section calculation of Equation 7.6. The uncertainties on the atomic weight and Avogadro's number were ignored because they were negligible compared to the other uncertainties.

of the cross section was calculated for each bin by combining the statistical uncertainties of the experimental yield, simulated acceptance, and integrated photon flux in quadrature.

The values and uncertainties of the liquid-deuterium target factors are given in Table 7.2. The uncertainties on the atomic weight of the deuteron and on Avogadro's number were negligible compared to the other uncertainties in the cross section calculation and were thus ignored. The uncertainty of the target density was assigned the same uncertainty percentage of the liquid-hydrogen target density measured for the g1c experiment [112]. This uncertainty is dominated by the statistical uncertainties on the cross section, but can be improved by performing an updated study of the target density using the procedure outlined in Reference [115].

The differential cross sections of the $\gamma n \to p\pi^-$ reaction are shown in Figure 7.16 in the different photon energy bins. These are the average values of the cross section in the given bins, quoted at the

bin centers. Where possible, these cross sections are compared against those from the g10 experiment prior to final-state interaction corrections [109, 110]. For the g13 data both the statistical and total uncertainties are shown, but the statistical uncertainties are typically too small to be visible. The statistical uncertainties were less than 3.3% for all bins, and were dominated by the uncertainties on the acceptance corrections. The systematic uncertainties on the g13 data are discussed later in this section.

Only the statistical uncertainties of the g10 data are shown, as the total uncertainties were unavailable. Although there were some discrepancies between the results, the cross sections matched within the uncertainties for the majority of the data. On average the g13a results were ~6.5% greater than the g10 results, less than the overall systematic uncertainty of ~10.8% discussed below. These differences were largest at the edges of the CLAS acceptance, and in the region of the scintillator panel overlap at photon energies above 1.6 GeV. These differences are most likely due to edge effects in the CLAS acceptance calculations of either the g10 or g13 analyses. The CLAS acceptance calculation can be improved by using these calculated cross sections to generate the simulated event distribution. The strong overall agreement between these results indicates the integrity of the g13a data and the validity of the procedures used for this cross section analysis.

The differential cross section is largest at the forward angles, and decreases with increasing photon energy. This is because the $\gamma n \to p\pi^-$ reaction is dominated by t-channel meson exchange, and at higher energies many more reactions are kinematically available. The rise of the cross section at the backward angles is most likely due to u-channel contributions. The N^* states contribute to these cross sections as well, although their signatures are not readily apparent without a more detailed investigation, such as a partial-wave analysis [116].

A comparison of the cross sections for different π^- sectors was the only systematic uncertainty study performed for this analysis of the $\gamma n \to p\pi^-$ reaction. This study provided a first-order estimation of the systematic uncertainties of the sector-dependent acceptance effects, such as the drift chamber holes, the scintillator paddle inefficiencies, and the triggering inefficiencies. While not a complete measure of the systematic uncertainties of the $\gamma n \to p\pi^-$ analysis, these effects were expected to have the largest contributions to the uncertainty. This was primarily because of the large π^- triggering inefficiencies discussed in Section 6.3.1. Combined with the close matching to the g10 cross section, this study is sufficient for testing the systematics associated with the procedures used

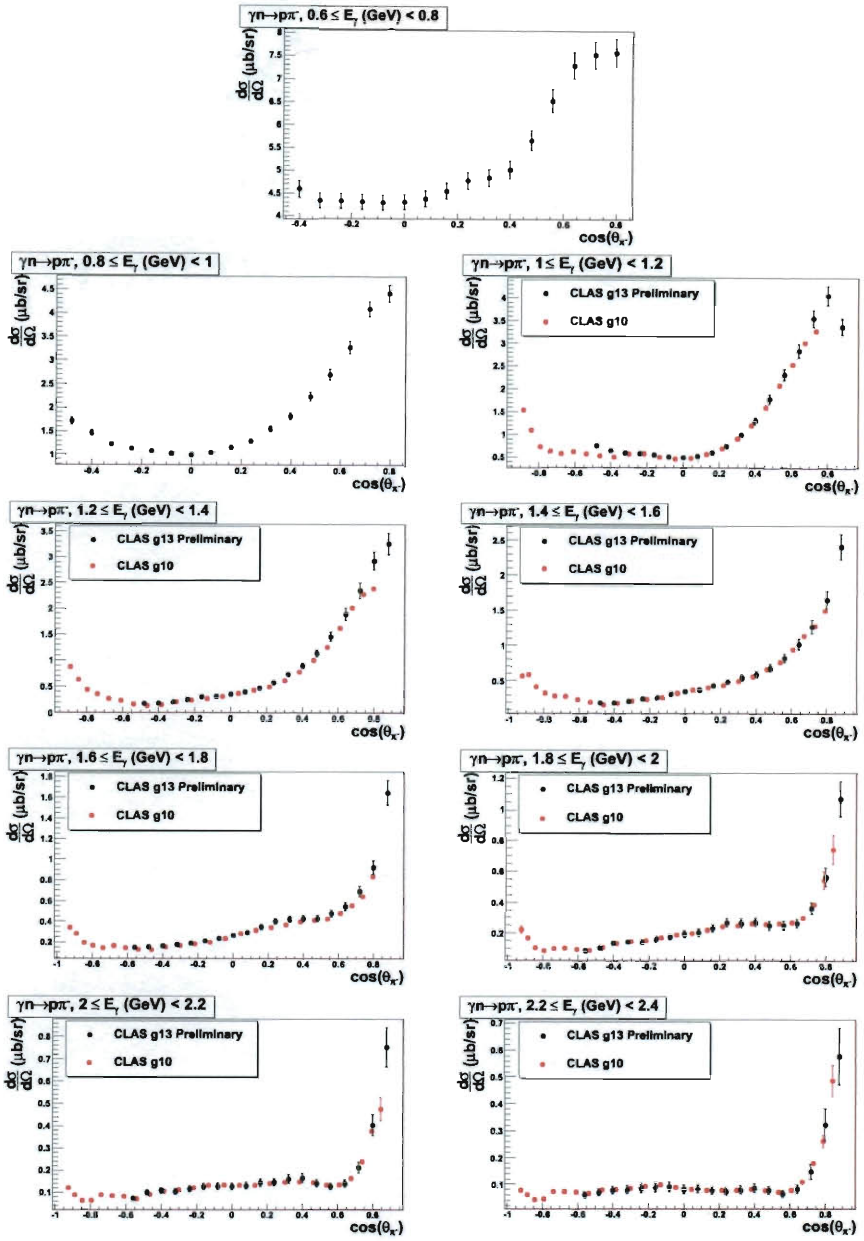

Figure 7.16 : The $\gamma n \rightarrow p\pi^-$ differential cross sections from the g13 experiment as a function of $\cos(\theta_{\pi^-})$, compared against the published results from the CLAS g10 experiment where available. Each plot is of a different photon energy bin, extending from 0.6 GeV to 2.4 GeV. The g13 data are the average values of the cross section for each bin, quoted at the bin centers. These cross sections were not corrected for final-state interactions. For the g13 data two sets of error bars are drawn to illustrate the statistical and total uncertainties, and for the g10 data only the statistical uncertainties are shown. The statistical uncertainties for most bins are too small to be visible. The disagreements are most likely due to edge effects in the CLAS acceptance calculations. The overall strong agreement between the data indicates the validity of the procedures used for this cross section analysis.

in this analysis. Also, the systematic uncertainties on the target density and length measurements were included in the g13 cross section calculation as well.

The differential cross sections of the $\gamma n \rightarrow p\pi^-$ reaction for different π^- sectors is shown in Figure 7.17 for the different photon energy bins. Points with less than 100 events in the signal region were excluded to ensure accurate yield extractions for the systematic uncertainty calculations. The systematic uncertainty percentage for each bin was calculated as the weighted root-mean-square percentage difference of the points:

$$\sigma_{\text{Syst}}\% = 100.0 \sqrt{\frac{\sum_i (\Delta C_i)^2/(C^2\sigma_i^2)}{\sum_i 1/\sigma_i^2}}, \tag{7.7}$$

where the summations are over all of the points in the given bin, C is the full differential cross section of the given bin, ΔC_i is the difference between C and the cross section of the i-th point, and σ_i is the statistical uncertainty on the cross section of the i-th point.

The systematic uncertainty percentages for the π^- sector comparisons are shown in Figure 7.18 as a function of $\cos(\theta_{\pi^-})$ for each photon energy bin. These uncertainty percentages exhibited little $\cos(\theta_{\pi^-})$ dependence, so Equation 7.7 was used to calculate the overall uncertainty percentages for each photon energy bin. These uncertainty percentages are shown in Figure 7.19, and generally increase with photon energy. This was most likely due to edge effects in the CLAS acceptance calculations from the π^- triggering inefficiencies. These edge effects had a larger impact at higher photon energies due to the larger differences between the simulated and experimental event distributions. Using Equation 7.7, the overall sector-based systematic uncertainty was $\sim$10.8%. Although the majority of the overall systematic uncertainties of the photon energy bins were lower than 10.8%, the statistical uncertainties were much smaller for the data in the highest photon energy bin.

The triggering efficiencies calculated in Section 6.3 were extremely low for π^-'s in some regions of the detector. Because g13a used a two-sector trigger and the $\gamma n \rightarrow p\pi^-$ reaction contains two charged particles in the final state, these trigger inefficiencies had a large influence on the cross section calculation. The scale of this effect is illustrated in Figure 7.20, where the differential cross section is compared with and without the trigger simulation. The cross section with the trigger simulation is shown with both the statistical and total uncertainties, while the cross section without the trigger simulation is shown with just the statistical uncertainties. The percentage difference is

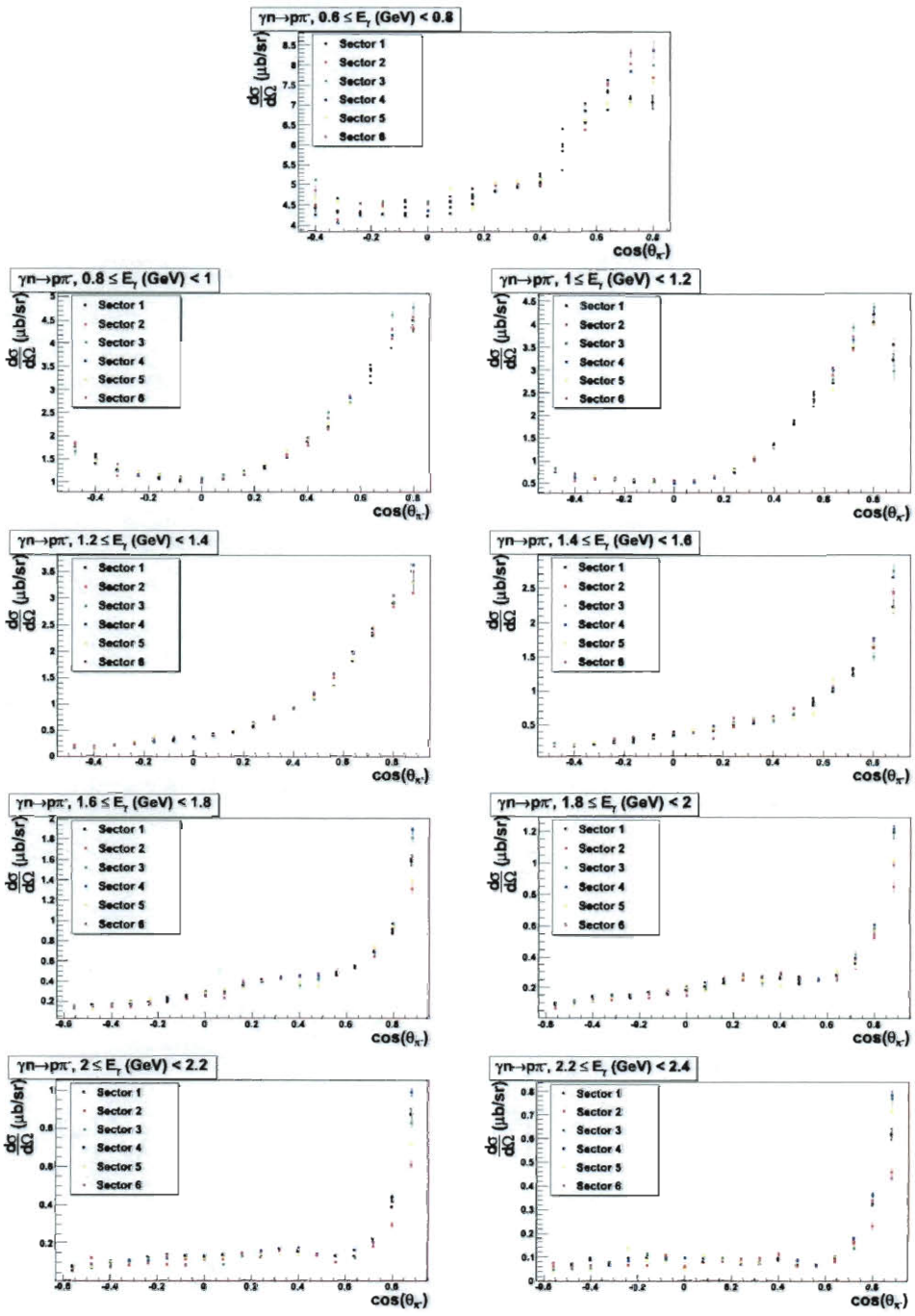

Figure 7.17 : Comparison of the cross sections of the $\gamma n \rightarrow p\pi^-$ reaction for the different sectors in which the π^- was detected. Each plot is of a different photon energy bin, extending from 0.6 GeV to 2.4 GeV. The weighted root-mean-squared percentage difference between these points and the calculated cross sections was used to assign the systematic uncertainty. Points with less than 100 events in the signal region were excluded from the study to ensure accurate yield extraction fits.

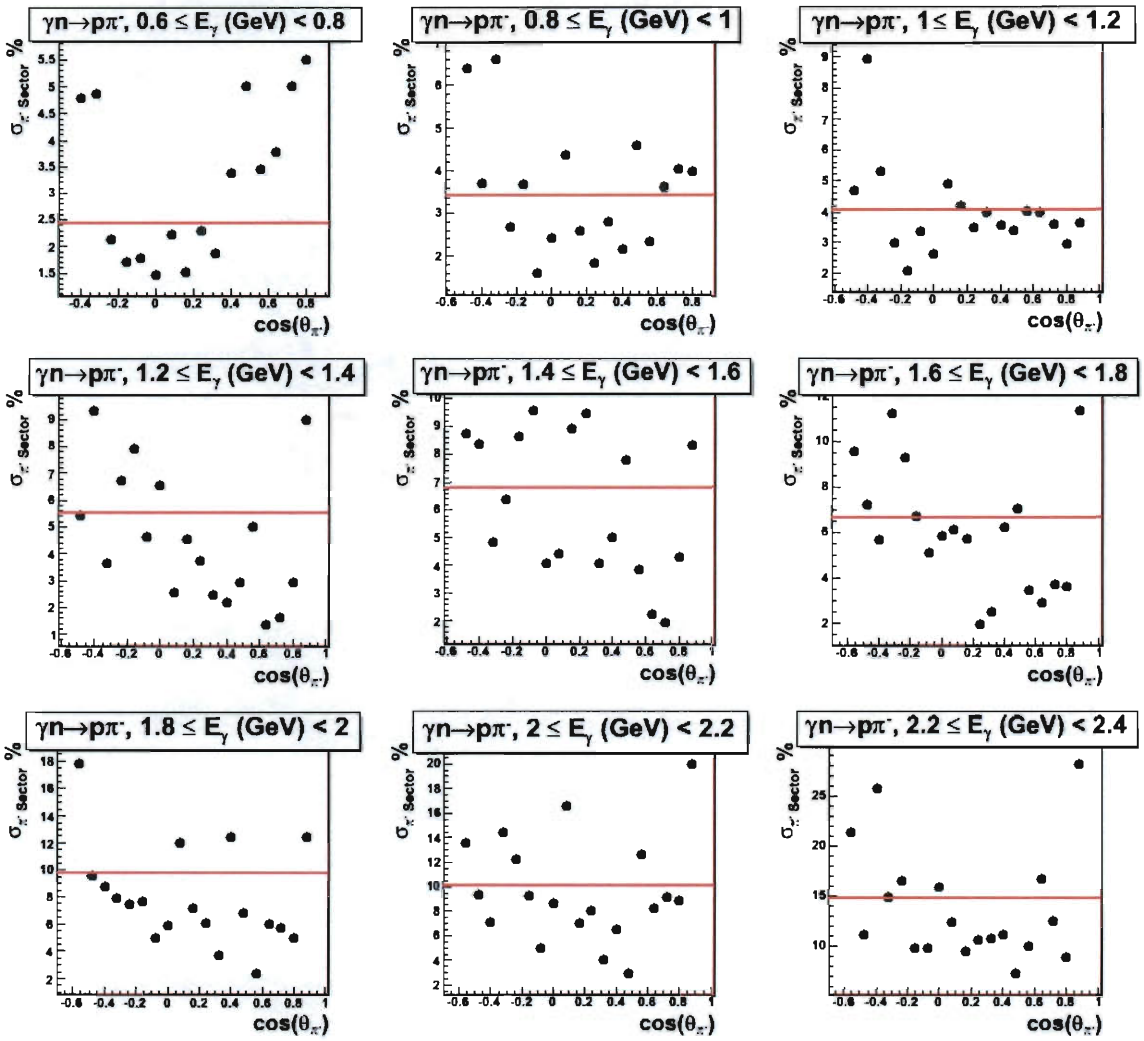

Figure 7.18 : Systematic uncertainty percentages of the comparison of the differential cross section of the $\gamma n \rightarrow p\pi^-$ reaction for the different π^- sectors. These uncertainty percentages are shown as a function of $\cos(\theta_{\pi^-})$ in bins of photon energy, where θ_{π^-} is the angle between the photon and the π^- in the center-of-mass frame. These uncertainties had little angular dependence, so overall uncertainties were calculated for each photon energy bin.

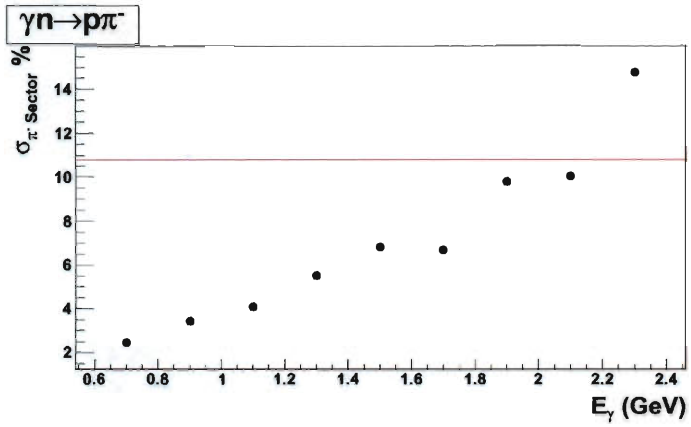

Figure 7.19 : Systematic uncertainty percentages of the comparison of the differential cross section of the $\gamma n \rightarrow p\pi^-$ reaction for the different π^- sectors as a function of photon energy. The increase in uncertainty percentage with photon energy is thought to be primarily due to problems with modeling the CLAS acceptance for higher track momenta.

significantly larger at the backward angles, where the majority of the triggering inefficiencies were located. The excellent matching between these results and those from g10 indicates that these significant event losses due to the triggering inefficiencies were modeled correctly.

The strong agreement with the $\gamma n \rightarrow p\pi^-$ differential cross section results from the g10 experiment illustrates the accuracy of the procedures used in this analysis. The analyses of the $\gamma n \rightarrow K^{*0}\Lambda$ and $\gamma n \rightarrow K^+\Sigma^{*-}$ reactions discussed in Chapter 8 were performed using a similar set of procedures. When finalized, these cross section data will provide a significant increase to the world statistics of the $\gamma n \rightarrow p\pi^-$ reaction. These results can be used to help constrain the N^* couplings to the neutron, and the photo-transition amplitudes to the πN channel. These results can be improved slightly with the recalibration of the photon tagger timing, and an extension of the simulated photon energy range. The statistical uncertainties can be decreased significantly by including the complete g13a dataset instead of the subset of runs that were used for this study. Also, the simulated distribution can be generated to these cross section data to improve the modeling of the CLAS acceptance. Finally, additional studies can be performed to fully quantify the systematic uncertainties.

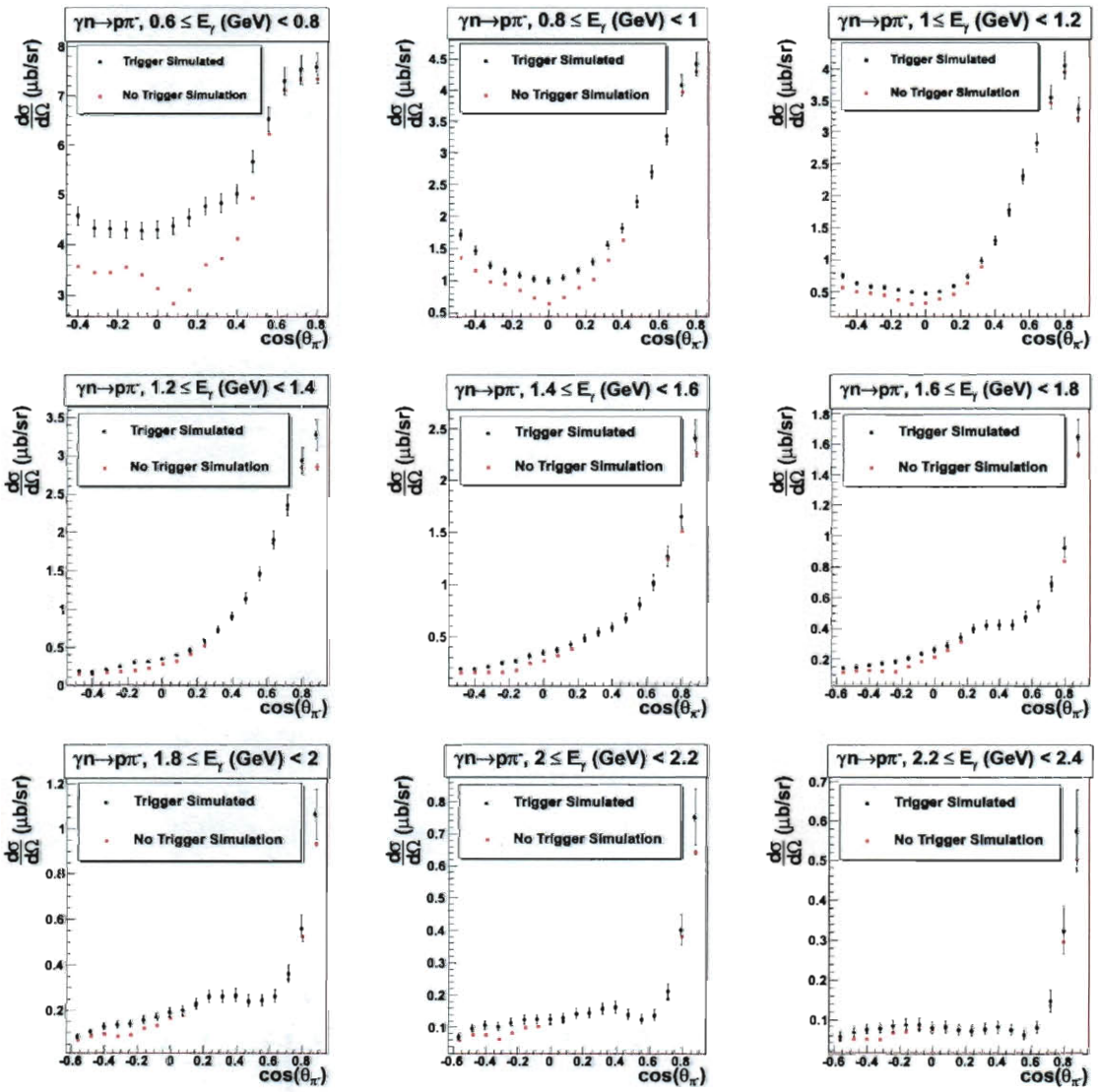

Figure 7.20 : The comparison between the differential cross sections of the $\gamma n \rightarrow p\pi^-$ reaction calculated with and without the trigger simulation. The difference is largest at the backward angles where the majority of the triggering inefficiencies occurred. The strong matching to the g10 results indicates that these large triggering inefficiencies were modeled correctly.

Chapter 8

$\gamma n \to K^{*0}\Lambda$ & $\gamma n \to K^{+}\Sigma^{*-}$ Analyses

The cross section analyses of the $\gamma n \to K^{*0}\Lambda$ and $\gamma n \to K^{+}\Sigma^{*-}$ reactions were performed to contribute to the search for the "missing" N^* resonances, such as those predicted by Capstick and Isgur [34]. As discussed in Section 2.3.2 several of these N^* states are predicted to contribute to these reactions, including the $N\frac{3}{2}^{-}(1960)$, $N\frac{5}{2}^{+}(1980)$, $N\frac{5}{2}^{+}(1995)$, $N\frac{3}{2}^{-}(2055)$, $N\frac{1}{2}^{+}(2065)$, $N\frac{5}{2}^{-}(2080)$, and $N\frac{3}{2}^{-}(2095)$ resonances. However, models of the N^* resonance couplings to these reactions are limited by the sparse cross section data for these hyperon channels.

As discussed in Chapter 3, both the $\gamma n \to K^{*0}\Lambda$ and $\gamma n \to K^{+}\Sigma^{*-}$ reactions were studied through their decays to the $K^{+}\pi^{-}p\pi^{-}$ final-state. Since both of these channels also contained a decaying Λ, much of their analyses were performed simultaneously. The same cuts were used to extract the $\gamma n \to K^{+}\pi^{-}\Lambda$ final-state events of these analyses, which were similar to the cuts performed for the $\gamma n \to p\pi^{-}$ analysis. The majority of the overlapping region between the $\gamma n \to K^{*0}\Lambda$ and $\gamma n \to K^{+}\Sigma^{*-}$ reactions was removed before extracting the experimental yields to minimize the effects of any potential reaction interference. The acceptance corrections, yield correction factors, and integrated photon flux were calculated using the procedures validated by the $\gamma n \to p\pi^{-}$ cross section analysis detailed in Chapter 7. The cross sections of the $\gamma n \to K^{*0}\Lambda$ and $\gamma n \to K^{+}\Sigma^{*-}$ reactions are discussed in Chapter 9.

The majority of the data on these reactions were collected during the 2.655 GeV portion of the g13a experiment. This portion of the dataset had a higher energy range than the 1.990 GeV runs, and also had more data below this energy due to the $1/E_{\gamma}$ bremsstrahlung photon energy distribution.

Also there were a negligible number of $\gamma n \rightarrow K^{*0}\Lambda$ events at photon energies below 1.9 GeV, due to the reaction's ~1.7 GeV production threshold and the minimum momentum cuts. Therefore, only the 2.655 GeV data were used in this cross section analysis. However the $\gamma n \rightarrow K^{+}\Sigma^{*-}$ reaction has a production threshold of ~1.4 GeV, so its cross section was calculated separately for the 1.990 GeV data for comparison. The 1.990 GeV data analysis is discussed in more detail in Section 9.2.

8.1 Experimental $\gamma n \rightarrow K^{+}\pi^{-}\Lambda$ Event Selection

The $\gamma n \rightarrow K^{+}\pi^{-}\Lambda$ final-state events were selected using a method similar to the one used for the $\gamma n \rightarrow p\pi^{-}$ analysis, as detailed in Section 7.1. First the interaction and Λ decay vertices were reconstructed, and the particle timing was calculated at these vertices. Next the invariant masses of the Λ, K^{*0}, and Σ^{*-} particles were reconstructed, as well as the missing mass of the spectator proton. Inefficient regions of the detector were rejected from the analysis, and loose skim cuts were placed to reduce the volume of background events.

Λ events were selected after proton and π^{-} identification, but prior to K^{+} identification. Reconstructing the Λ first significantly reduced the background on the K^{+} identification by selecting events where an $s\bar{s}$ quark-pair was produced. Several more cuts were used to select the final-state events, including cuts on the particle vertex time differences and a cut on the missing momentum of $\gamma D \rightarrow K^{+}\pi^{-}\Lambda(p)$. Table 8.1 shows a summary of the cuts detailed in the following subsections that were used to identify the $\gamma n \rightarrow K^{+}\pi^{-}\Lambda$ final-state events. The cuts used to extract the experimental yields of the $\gamma n \rightarrow K^{*0}\Lambda$ and $\gamma n \rightarrow K^{+}\Sigma^{*-}$ reactions from these final-state events are discussed in Section 8.2.

8.1.1 Physics Evaluation

To test the hypothesis that either the $\gamma n \rightarrow K^{*0}\Lambda$ or $\gamma n \rightarrow K^{+}\Sigma^{*-}$ reaction occurred for a given event, preliminary particle identification was performed. Every positively charged track was labeled as both a proton and K^{+} candidate, and every negatively charged track was labeled a π^{-} candidate. These reactions were then evaluated separately for each possible combination of detected tracks, as discussed in Section 7.1.1 for the $\gamma n \rightarrow p\pi^{-}$ reaction. However since there were two π^{-}'s in the final state, the percentage of the events with multiple track combinations that survived the final-state identification cuts was much larger for these reactions, as discussed in Section 8.2.

Cuts	Details
Data Range Cuts	Cut Junk Runs, Bad Files, Beam Trips
Minimum Momentum Cuts	π^- Momentum $\geq$ 100 MeV/c, p & K^+ Momentum $\geq$ 400 MeV/c
Detector Region Cuts	Cut Inefficient SC Paddles, DC Holes, Fiducial Regions
Loose Skim Cuts	$\#X^+ \geq 2$, $\#X^- \geq 2$, $\lvert\Delta t_{p,\,\pi^-}\rvert \leq 10$ ns
	1.09 $<$ Λ Invariant Mass (GeV/c^2) $<$ 1.14
	$\lvert\Delta t_{K^+,\,\pi^-}\rvert \leq 5$ ns, $\lvert\Delta t_{\gamma,\,\pi^-}\rvert \leq 5$ ns
	0.7 $<$ $\gamma D \rightarrow K^+\pi^-\Lambda(p)$ Missing Mass (GeV/c^2) $<$ 1.2
π^- & p Identification	$\pm 3\sigma$ $\Delta\beta_{\pi^-}$ vs. π^- Momentum, $\pm 3\sigma$ $\Delta\beta_p$ vs. p Momentum
Λ-Vertex Time Difference	$\pm 3\sigma$ $\Delta t_{p,\,\pi^-}$ vs. p Momentum
Λ Reconstruction	$\pm 3\sigma$ Λ Invariant Mass
Photon Selection	$\pm 3\sigma$ $\Delta t_{\gamma,\,\pi^-}$ vs. π^- Momentum
K^+ Identification	$\pm 3\sigma$ $\Delta\beta_{K^+}$ vs. K^+ Momentum
γ-Vertex Time Difference	$\pm 3\sigma$ $\Delta t_{K^+,\,\pi^-}$ vs. K^+ Momentum
Number of Photons	Cut Number of Photons $>$ 1
Photon Tagger Cuts	Cut Bad Tagger Counters
Missing Momentum	$\gamma D \rightarrow K^+\pi^-\Lambda(p)$ Missing Momentum $\leq$ 200 MeV/c

Table 8.1 : Summary of the cuts used to extract the final-state events of the $\gamma n \rightarrow K^{*0}\Lambda$ and $\gamma n \rightarrow K^{+}\Sigma^{*-}$ reactions, in the order that they were performed in this analysis.

The times of the Λ decay products were evaluated at the Λ decay vertex, because with a $c\tau$ of 7.89 cm [8] the Λ's can travel up to several centimeters before they decay. This vertex was determined to be the midpoint of the line bridging the proton and π^- paths at their distance of closest approach. The remaining K^+ and π^- particle times were evaluated at the reaction vertex, which was reconstructed as the midpoint of the line connecting the K^+ and π^- paths at their distance of closest approach. The vertex times of these particles were calculated using Equation 7.1, as used for the $\gamma n \rightarrow p\pi^-$ reaction.

The event photon was selected in the same manner as for the $\gamma n \rightarrow p\pi^-$ reaction, as discussed in Section 7.1.1. Next, the momentum and energy corrections determined in Chapter 5 were applied to the detected particles. The Λ invariant mass was then reconstructed from its $p\pi^-$ decay, and the missing mass of $\gamma D \rightarrow K^+\pi^-\Lambda(p)$ was calculated along with the missing momentum. Finally, the invariant masses of the K^{*0} and Σ^{*-} were reconstructed for each event from their decays to $K^+\pi^-$ and $\Lambda\pi^-$, respectively. Histograms of these calculated quantities are shown in Sections 8.1.4 through 8.2, along with discussions of the cuts used to identify the $\gamma n \rightarrow K^+\pi^-\Lambda$ final-state events and to extract the $\gamma n \rightarrow K^{*0}\Lambda$ and $\gamma n \rightarrow K^+\Sigma^{*-}$ experimental yields.

8.1.2 Initial Cuts

To decrease the volume of the experimental data to a more manageable size for physics analysis, loose cuts were used to remove the vast majority of the background events. First, only events with at least two positively charged tracks and two negatively charged tracks were considered. Also, some of the detector-based data cuts detailed in Section 6.2 were applied, including cuts on the "junk" runs, bad data files, scalar intervals containing beam trips, bad scintillator paddles, the drift chamber holes, and the inefficient fiducial regions. Cuts on events containing additional particles were not employed, as they would have removed signal events containing accidental tracks.

The proton and π^- from the decaying Λ were required to be within 10 ns of each other at the Λ decay vertex. Also, the Λ invariant mass was required to be between 1.09 GeV/c^2 and 1.14 GeV/c^2. Next, the remaining π^- was required to be within 5 ns of both the K^+ and at least one of the tagger photons at the interaction vertex. The missing mass of $\gamma D \rightarrow K^+\pi^-\Lambda(p)$ was then required to be between 0.7 GeV/c^2 and 1.2 GeV/c^2 for at least one of the detected photons. These quantities are studied in more detail in Sections 8.1.4 through 8.2, where tighter cuts are placed. After performing

these cuts, less than 0.01% of the original dataset remained for physics analysis.

8.1.3 Proton and π^- Identification

Particles were identified in the same manner as for the $\gamma n \to p\pi^-$ reaction in Section 7.1.3, by cutting on the $\Delta\beta$ vs. p distributions of the candidates for the given identity hypotheses. However only the protons and π^-'s were identified at this stage, whereas the K^+'s were identified after the Λ events were selected. $\Delta\beta$ is defined by Equation 7.2, and is shown vs. momentum in Figures 8.1(A) and 8.2(A) for protons and π^-'s, respectively. The extra bands of particles in these figures were either due to assigning an incorrect identity hypothesis, accidental tracks, or incorrect selections of the RF electron beam bunch for the reaction start time calculation. However, the background from accidental tracks was significantly reduced due to the loose skim cuts on the timing of the particles and the masses of the Λ and spectator proton.

The $\pm 3\sigma$ cuts on $\Delta\beta$ as a function of momentum were fit by a linear function for π^-'s, and by an exponential plus a linear function for protons. These cuts are shown in Figures 8.1 and 8.2 for protons and π^-'s, respectively. The widths of these cuts varied with momentum as discussed in Section 7.1.3. The functional form of the proton identification cuts was slightly different than for the $\gamma n \to p\pi^-$ reaction, due to the reduced background from accidental tracks. This background was decreased significantly by the numerous skim cuts on the particle times and mass peaks. The yield loss due to cutting events with the start time calculated incorrectly was studied in Section 7.3 for $\gamma n \to p\pi^-$, and was assumed to be reaction independent.

A band of μ^-'s is visible in Figure 8.2(A) from -0.15 $< \Delta\beta <$ -0.03 at momenta less than 400 MeV/c. As discussed in Section 7.1.3, μ^- tracks were acceptable because they were primarily produced from π^- decay, and their inclusion resulted in only a slight widening of the signal peak resolutions. However unlike for $\gamma n \to p\pi^-$, the width of the π^- $\Delta\beta$ distribution was non-linear only up to 400 MeV/c, partially due to the significantly reduced background from accidental tracks. The particle identification cut was extrapolated over momentum less than 400 MeV/c, as fits to the π^- $\Delta\beta$ distribution in this region were complicated by the μ^-'s. The systematic uncertainty on the particle identification is discussed in Section 9.4.3.

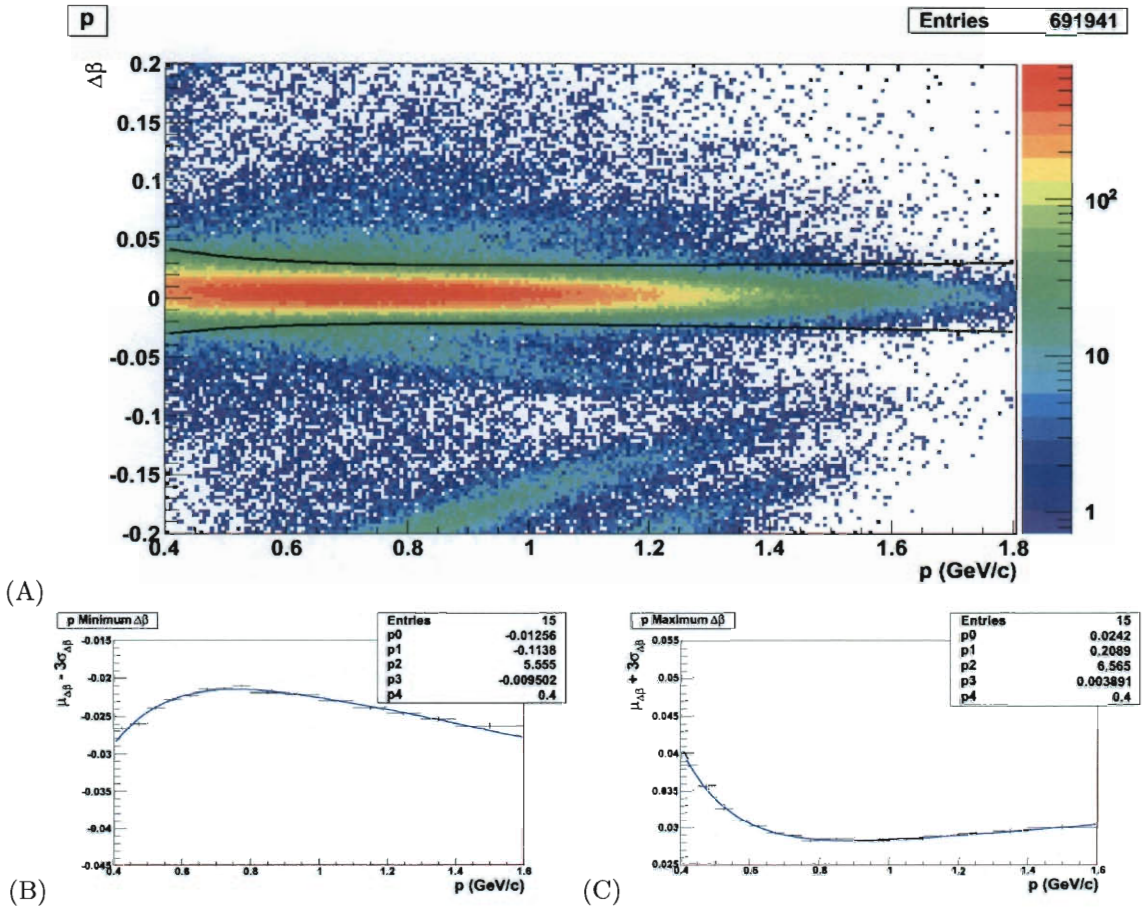

Figure 8.1 : For proton candidates, $\Delta\beta$ vs. p (A), and fits to the minimum (B) and maximum (C) $\Delta\beta$ cuts as a function of track momentum. The $\Delta\beta$ cuts were fit as an exponential plus linear function to the distributions of $\mu_{\Delta\beta} - 3\sigma_{\Delta\beta}$ (B) and $\mu_{\Delta\beta} + 3\sigma_{\Delta\beta}$ (C) derived from fitting a Gaussian to $\Delta\beta$ in each of the different momentum bins. These $\pm 3\sigma$ cuts for proton identification are illustrated by the black curves in (A). The width of $\Delta\beta$ varied with momentum due to the uncertainty in the β calculated from the track momentum. The extra bands of particles are either from accidental tracks, events with the reaction start time calculated incorrectly, or from particles with the incorrect identity hypothesis, such as K^{+}'s.

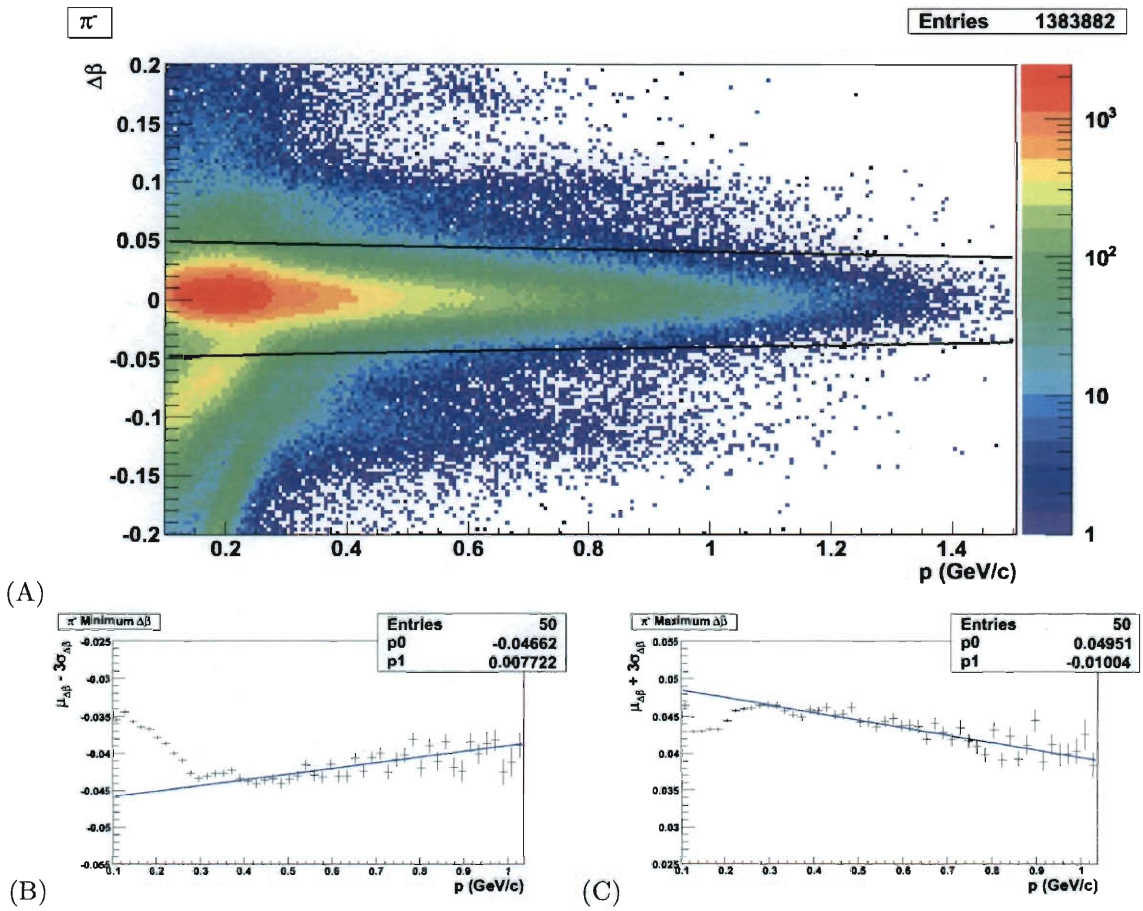

Figure 8.2 : For π^- candidates, $\Delta\beta$ vs. p (A), and fits to the minimum (B) and maximum (C) $\Delta\beta$ cuts as a function of track momentum. The $\Delta\beta$ cuts were fit as a linear function to the distributions of $\mu_{\Delta\beta} - 3\sigma_{\Delta\beta}$ (B) and $\mu_{\Delta\beta} + 3\sigma_{\Delta\beta}$ (C) derived from fitting a Gaussian to $\Delta\beta$ in each of the different momentum bins. These $\pm 3\sigma$ cuts for π^- identification are illustrated by the black lines in (A). The width of $\Delta\beta$ varied with momentum due to the uncertainty in the β calculated from the track momentum. The extra bands of particles are either from accidental tracks, events with the reaction start time calculated incorrectly, or from particles with the incorrect identity hypothesis, such as μ^-'s. π^-'s with momentum less than 400 MeV/c were excluded from the fit due to their decays to μ^-'s.

8.1.4 Selecting Λ Events

With the protons and π^-'s identified, several cuts were used to select Λ events. First the time difference between the proton and the π^- at the Λ decay vertex was cut as a function of proton momentum, as illustrated in Figure 8.3. These cuts were determined by fitting the time difference distribution to a Gaussian in each of the different momentum bins, and then fitting the 3σ distributions to an exponential plus a linear function. This time difference was studied vs. proton momentum because the uncertainty in the vertex times increased with σ_β/β. This relation was derived from Equation 7.1 using the transformation of uncertainties.

The $p\pi^-$ invariant mass is shown in Figure 8.4, and was fit to a Gaussian plus a linear function and cut at $\pm 3\sigma$ to select the Λ events. Because this histogram was filled with every possible track combination, combinations with the wrong π^- were a significant source of background. Also since K^+ identification was not yet performed, reactions with the $\gamma n \to \pi^+\pi^- p\pi^-$ final state contributed to the background, such as N^*, Δ^*, and non-resonant reactions. This fit was adequate for determining $\pm 3\sigma$ cuts, even though it had a large χ^2 per degree of freedom due to the non-Gaussian tails of the Λ peak. The systematic uncertainty associated with the cut on the Λ invariant mass is studied in Section 9.4.3.

8.1.5 Final-State Identification Cuts

Several additional cuts were used to identify the $\gamma n \to p\pi^-\Lambda$ final state. First, the vertex time difference between the photon and π^- was cut as a function of π^- momentum, as shown in Figure 8.5. This cut was performed prior to K^+ identification to reduce the background in the K^+ $\Delta\beta$ distribution as much as possible. Many of these background events, along with the photons originating from the other beam bunches, are manifested by the extra bands of events in the figure.

The $\pm 3\sigma$ cuts on the vertex time difference were determined in the same manner as for the $\gamma n \to p\pi^-$ reaction, as detailed in Section 7.1.4. The time difference was again studied as a function of π^- momentum because the uncertainty in the π^- vertex time increased with σ_β/β. Due to the interference from the extra bands in the Gaussian fits, the $\pm 3\sigma$ cuts were extrapolated below 150 MeV/c. The uncertainty associated with this extrapolation is taken into account by the systematic uncertainty studies on the time difference cuts in Section 9.4.3.

Next, K^+ identification was performed by cutting on the $\Delta\beta$ distribution as a function of K^+

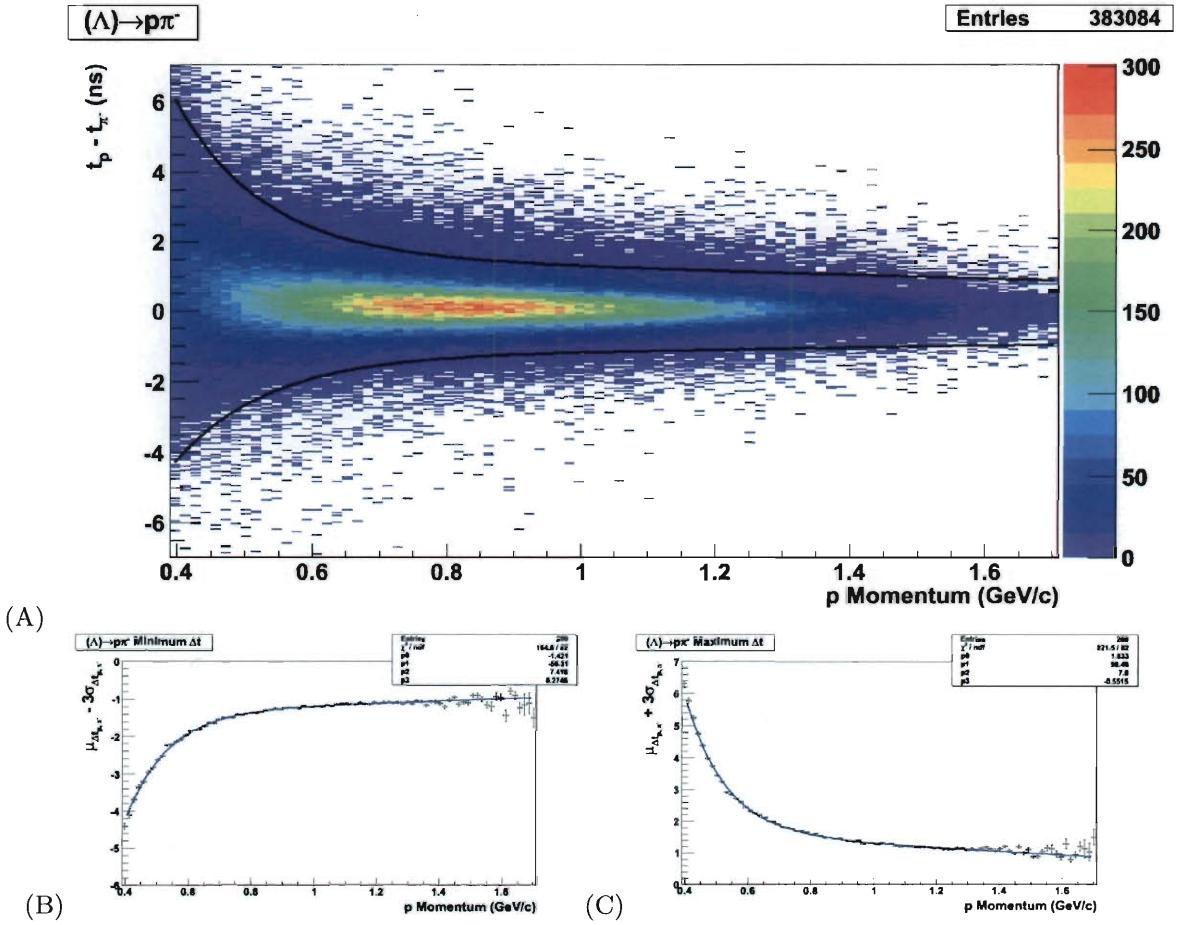

Figure 8.3 : The time difference between the proton and π^- at the Λ decay vertex as a function of proton momentum (A), and fits to the minimum (B) and maximum (C) time difference cuts as a function of proton momentum. These cuts were fit as an exponential plus a linear function to the distributions of $\mu_{\Delta t} - 3\sigma_{\Delta t}$ (B) and $\mu_{\Delta t} + 3\sigma_{\Delta t}$ (C) derived from fitting a Gaussian to the time difference in each of the different momentum bins. These $\pm 3\sigma$ cuts on the time difference are illustrated by the black curves in (A). The width of this distribution is much larger at low momentum because the uncertainty in the vertex times increased with σ_β/β.

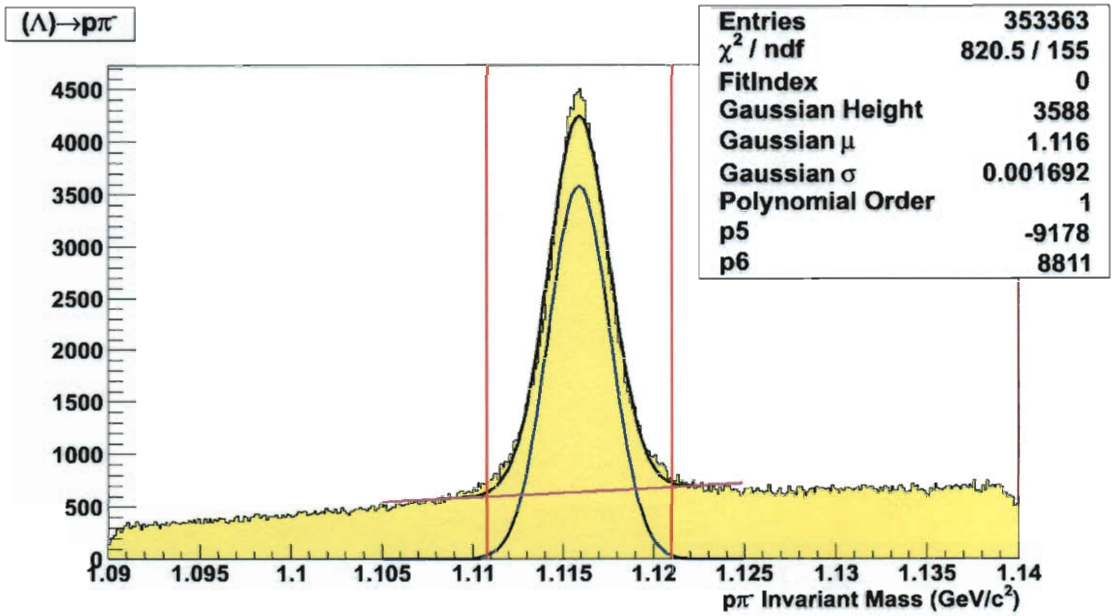

Figure 8.4 : The $p\pi^-$ invariant mass fit to a Gaussian plus a linear function to select Λ events. The blue lineshape represents the Gaussian fit function, the magenta lineshape represents the linear fit function, the black lineshape represents the total fit function, and the red lines indicate the $\pm 3\sigma$ cuts.

momentum, as shown in Figure 8.6(A). In this distribution the K^+ particles are centered around $\Delta\beta = 0$, and the π^+ and proton bands are above and below the K^+'s, respectively. The particle bands are easily distinguishable from one another for the majority of the momentum range, indicating that the background from $\gamma n \to K^0\Lambda \to \pi^+\pi^- p\pi^-$ events due to π^+ misidentification was small. Linear functions were used to fit the $\pm 3\sigma$ cuts, and are also shown in Figure 8.6.

After identifying the K^+'s, the reaction vertex time difference between the K^+ and the remaining π^- was cut as a function of K^+ momentum, as illustrated in Figure 8.7. These cuts were performed to remove some of the additional accidental tracks that were still remaining. Similar to the other time difference cuts, these cuts were determined by fitting the time difference distribution to a Gaussian in each of the different momentum bins, and then fitting the $\pm 3\sigma$ distributions to an exponential plus a linear function. The time difference was studied vs. K^+ momentum because the K^+'s were generally slower than the π^-'s, and the uncertainty in the vertex times increased with σ_β/β.

The distribution of the number of photons surviving these timing cuts per event is shown in Figure 8.8. As in Section 7.1.4 for the $\gamma n \to p\pi^-$ reaction, events with more than one photon that passed the timing cuts were rejected. Approximately 9.2% of the remaining events were removed

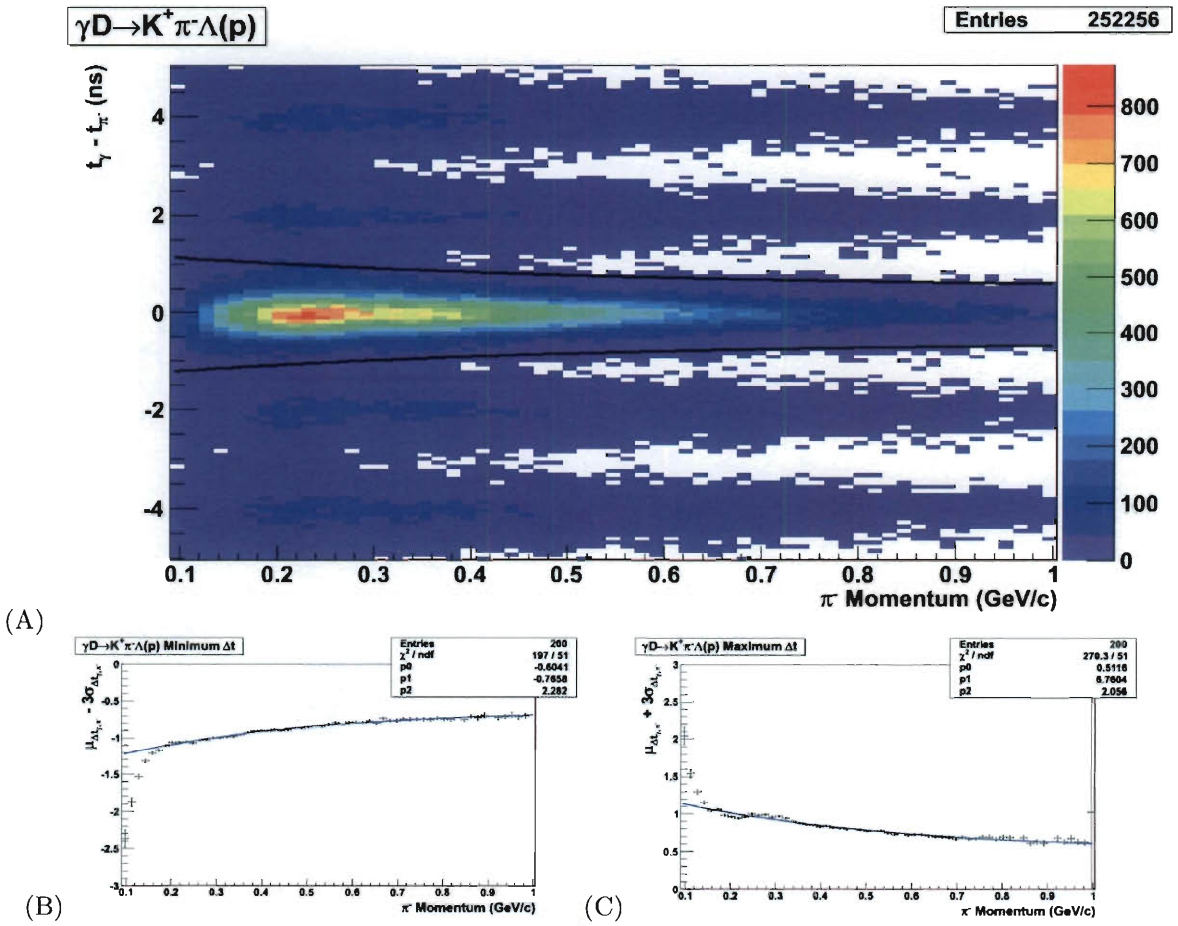

Figure 8.5 : The reaction vertex time difference between all of the detected photons and the π^- as a function of π^- momentum (A), and fits to the minimum (B) and maximum (C) time difference cuts as a function of π^- momentum. These cuts were fit as an exponential function to the distributions of $\mu_{\Delta t} - 3\sigma_{\Delta t}$ (B) and $\mu_{\Delta t} + 3\sigma_{\Delta t}$ (C) derived from fitting a Gaussian to the time difference in each of the different momentum bins. These $\pm 3\sigma$ cuts on the time difference are illustrated by the black curves in (A). The extra bands are either from events with the reaction start time calculated incorrectly, from accidental π^-'s, or from photons originating from other beam bunches. Due to the interference from these bands, the fits were extrapolated below 150 MeV/c.

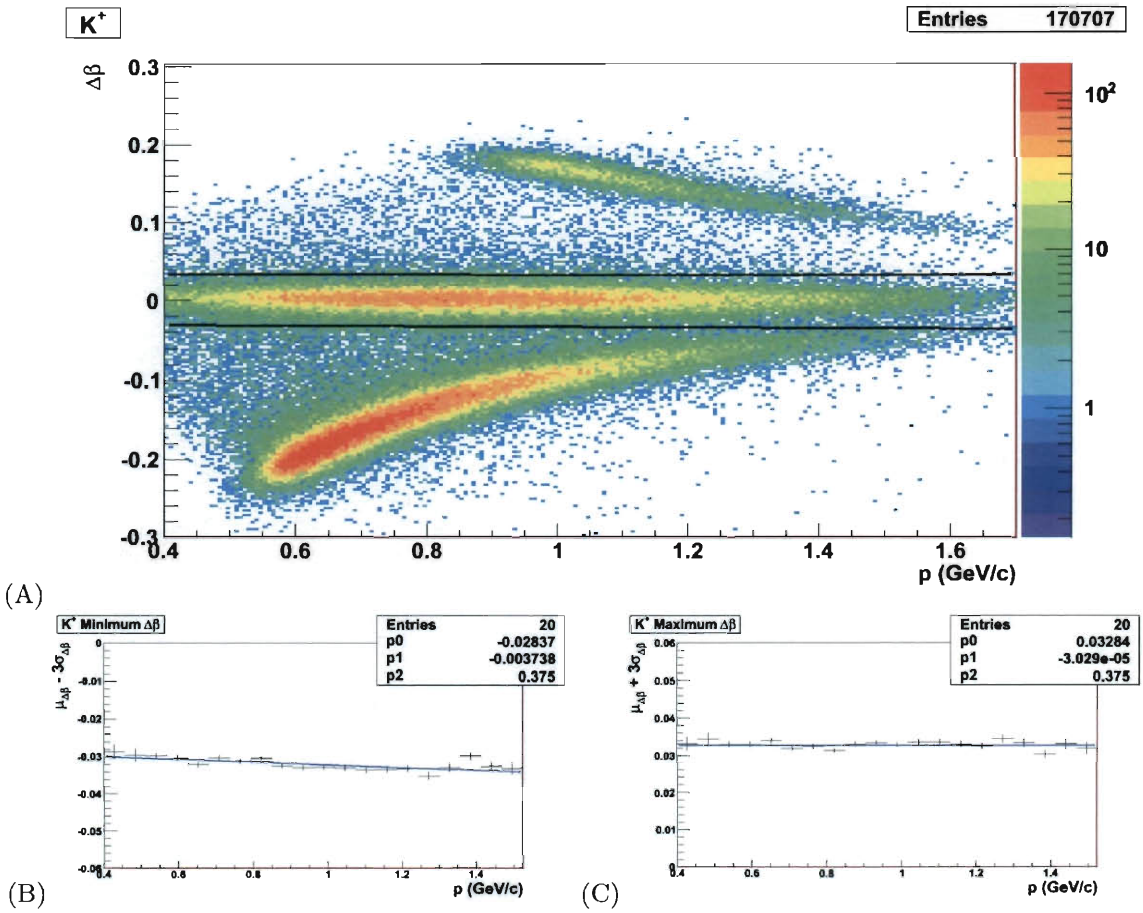

Figure 8.6 : For K^+ candidates, $\Delta\beta$ vs. p (A), and fits to the minimum (B) and maximum (C) $\Delta\beta$ cuts as a function of track momentum. The $\Delta\beta$ cuts were fit as a linear function to the distributions of $\mu_{\Delta\beta} - 3\sigma_{\Delta\beta}$ (B) and $\mu_{\Delta\beta} + 3\sigma_{\Delta\beta}$ (C) derived from fitting a Gaussian to $\Delta\beta$ in each of the different momentum bins. These $\pm 3\sigma$ cuts for K^+ identification are illustrated by the black lines in (A). The width of $\Delta\beta$ varied with momentum due to the uncertainty in the β calculated from the track momentum. Protons and π^+'s are manifested by the bands of particles above and below the K^+'s, respectively.

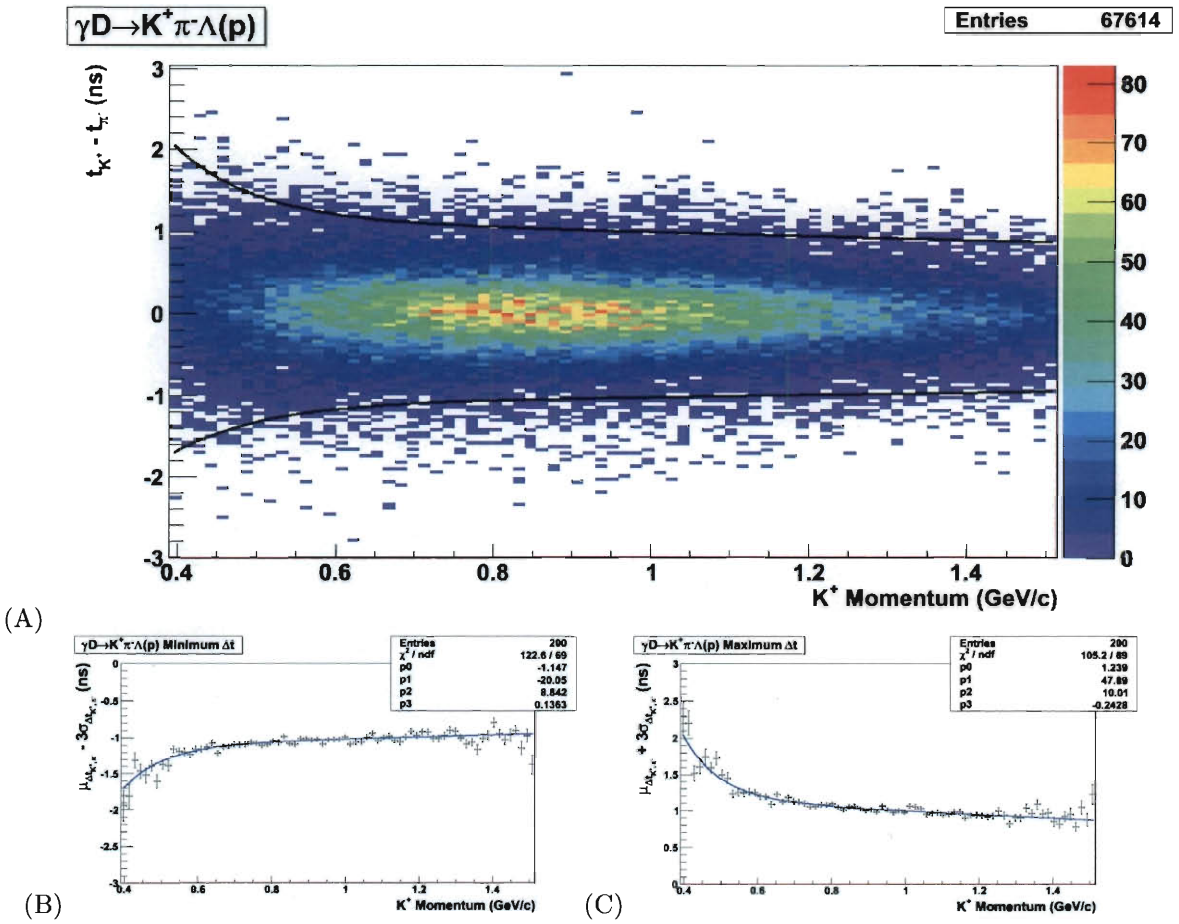

Figure 8.7 : The reaction vertex time difference between the K^+ and π^- as a function of K^+ momentum (A), and fits to the minimum (B) and maximum (C) time difference cuts as a function of K^+ momentum. These cuts were fit as an exponential plus a linear function to the distributions of $\mu_{\Delta t} - 3\sigma_{\Delta t}$ (B) and $\mu_{\Delta t} + 3\sigma_{\Delta t}$ (C) derived from fitting a Gaussian to the time difference in each of the different momentum bins. These $\pm 3\sigma$ cuts on the time difference are illustrated by the black curves in (A). The width of this distribution is larger at low momentum because the uncertainty in the vertex times increased with σ_β/β.

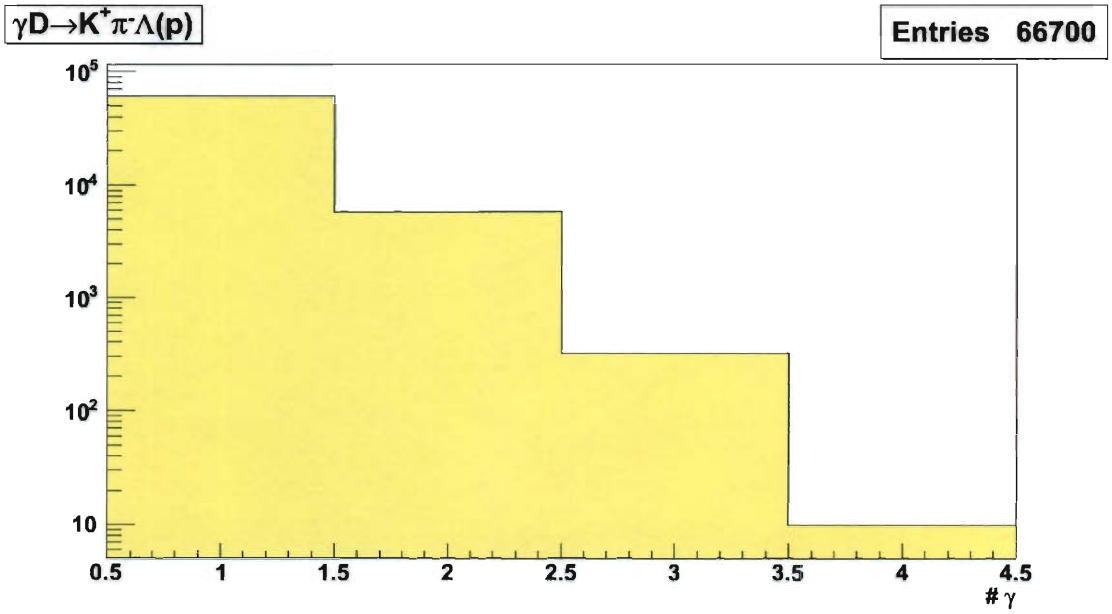

Figure 8.8 : The number of photons per event after $\pm 3\sigma$ cuts on the vertex time differences. Events with more than one photon were rejected because it was difficult to determine which photon produced the observed event.

with this cut, slightly less than the ~11.0% for the $\gamma n \to p\pi^-$ analysis. This difference was primarily due to the increased width of the photon-π^- vertex time difference cut at low π^- momentum for the $\gamma n \to p\pi^-$ reaction. This event loss was accounted for in the cross section calculations, as discussed in Section 8.4. This cut was followed by the photon tagger bin cuts discussed in Section 6.2.3.

Similar to the $\gamma D \to p\pi^-(p)$ reaction in Section 7.1.4, the missing momentum of $\gamma D \to K^+\pi^-\Lambda(p)$ was required to be less than 200 MeV/c to remove the events with the most rescattering. After a temporary $\pm 3\sigma$ cut on the missing mass peak of the spectator proton, the missing momentum distributions are shown in Figure 8.9. The distributions are similar to those from the $\gamma D \to p\pi^-(p)$ reaction shown in Figure 7.6, but for $\gamma D \to K^+\pi^-\Lambda(p)$ the missing momentum was more concentrated at forward angles. The full source of this difference is unknown, although it was partially due to the larger background under the spectator proton peak in this analysis, coming from events such as $\gamma D \to K^{*0}\Sigma^0(p) \to K^+\pi^-\Lambda(p\gamma)$. These rescattering effects were not taken into account in this analysis, but the systematic uncertainty due to the missing momentum cut is studied in Section 9.4.3. The missing mass of the spectator proton is studied in more detail in Section 8.2.

To study the background from $\gamma n \to K^0\Lambda \to \pi^+\pi^- p\pi^-$ events, the K^+ was temporarily assigned

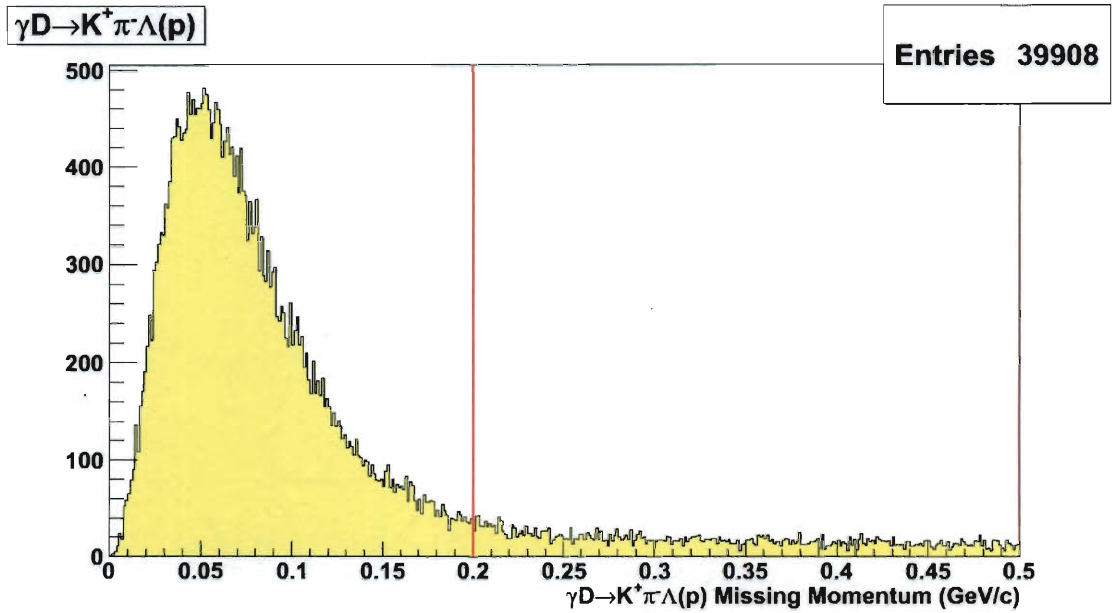

(A)

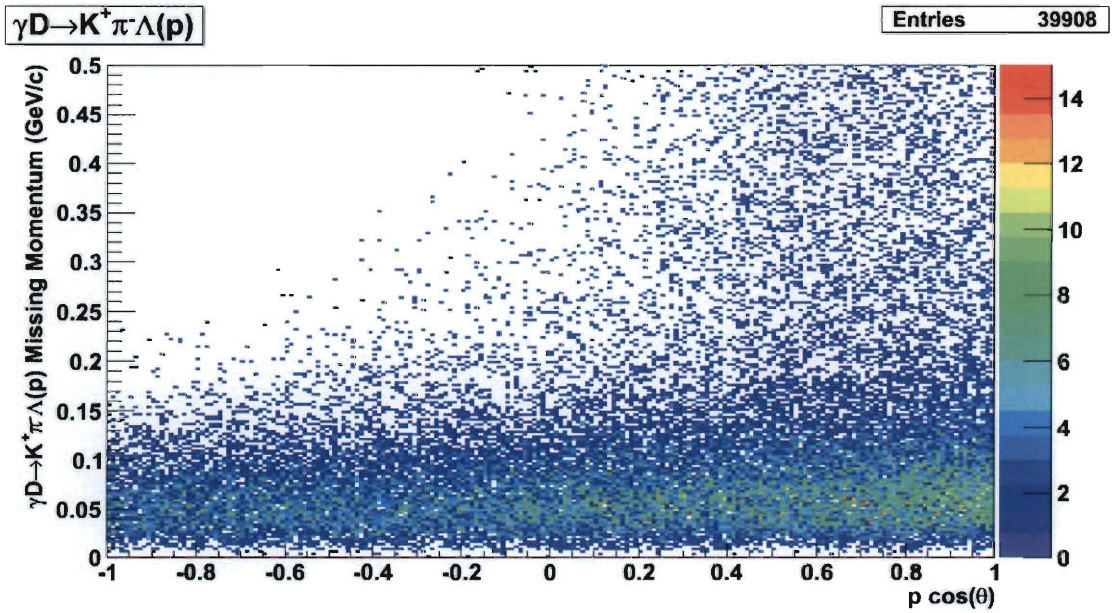

(B)

Figure 8.9 : The missing momentum of the spectator proton (A) shown vs. $\cos(\theta)$ of the missing momentum in the lab frame (B). The increase in low-momentum events at forward angles may have partially been due to background reactions such as $\gamma D \to K^{*0}\Sigma^{0}(p) \to K^{+}\pi^{-}\Lambda(p\gamma)$. The high-momentum tail of rescattered spectator protons was removed by the 200 MeV/c cut on the missing momentum.

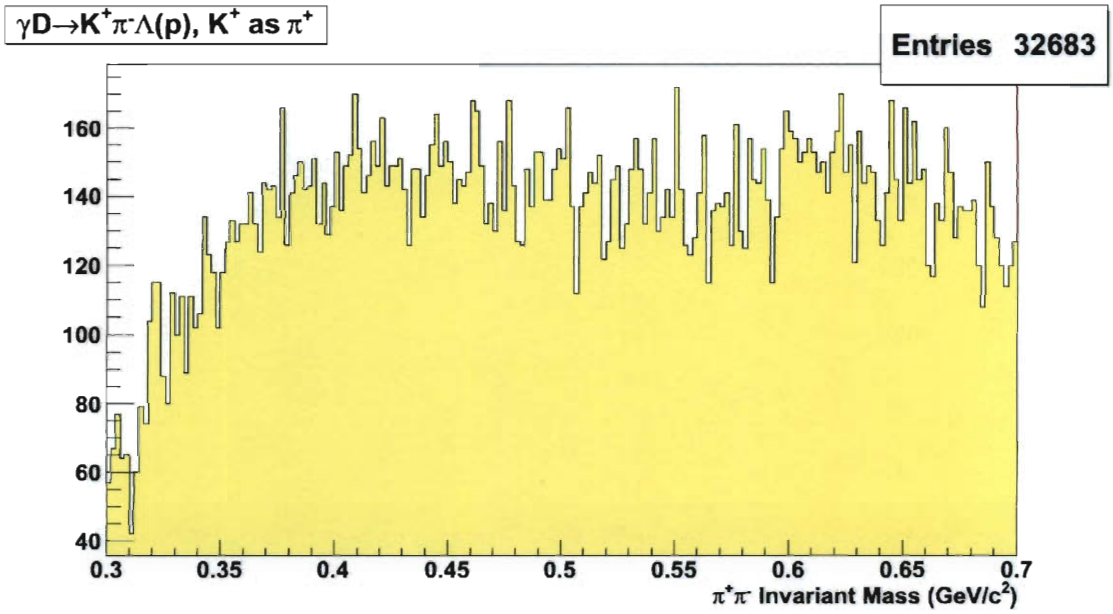

Figure 8.10 : The invariant mass of $\pi^+\pi^-$, where the K^+ was assigned the π^+ mass. No peak is visible near the K^0 mass of 0.498 GeV/c^2, indicating that very few of the K^+'s were misidentified.

the π^+ mass. The invariant mass of $\pi^+\pi^-$ with this assignment is shown in Figure 8.10, where a temporary cut on the missing mass of the spectator proton was used as well. No signal is visible near the K^0 mass of 0.498 GeV/c^2, indicating that very few of the identified K^+'s were actually π^+'s. Therefore, the background from $\gamma n \to K^0\Lambda$ events was assumed to be negligible.

8.2 Experimental Yield Extractions

After the $\gamma n \to K^+\pi^-\Lambda$ final-state events were selected, several additional cuts were performed to extract the yields of the $\gamma n \to K^{*0}\Lambda$ and $\gamma n \to K^+\Sigma^{*-}$ reactions. These include cuts on the missing mass of the spectator proton, the number of remaining track combinations, and the K^{*0} and Σ^{*-} invariant masses. The invariant masses of the K^{*0} and Σ^{*-} were cut on not only to extract the reaction yields, but to remove the majority of the reaction overlap. These cuts are detailed in Tables 8.2 and 8.3 for the $\gamma n \to K^{*0}\Lambda$ and $\gamma n \to K^+\Sigma^{*-}$ reactions, respectively. Despite these cuts some background events remained in the extracted yields, such as $\gamma n \to K^{*0}\Sigma^0 \to K^+\pi^-\Lambda(\gamma)$ and other events with an additional photon or π^0 in the final state. The contributions from these backgrounds are taken into account with scale uncertainties, as detailed in Section 9.4.1.

Cut	Details
Missing Mass	$\pm 3\sigma$ $\gamma D \to K^{+}\pi^{-}\Lambda(p)$ Missing Mass
Σ^{*-} Overlap Cuts	Cut events within $\pm 1\Gamma$ of Σ^{*-} invariant mass.
Track Combinations	Cut Number of Track Combinations > 1
K^{*0} Invariant Mass	$\pm 2\Gamma$ K^{*0} Invariant Mass

Table 8.2 : Summary of the cuts used to extract the experimental yields of the $\gamma n \to K^{*0}\Lambda$ reaction from the $\gamma n \to K^{+}\pi^{-}\Lambda$ final-state events, in the order that they were performed in this analysis.

Cut	Details
Missing Mass	$\pm 3\sigma$ $\gamma D \to K^{+}\pi^{-}\Lambda(p)$ Missing Mass
Temporary Σ^{*-} Cuts	Temporarily cut events within $\pm 1\Gamma$ of Σ^{*-} invariant mass.
K^{*0} Overlap Cuts	Cut events within $\pm 1\Gamma$ of K^{*0} invariant mass.
Track Combinations	Cut Number of Track Combinations > 1
Σ^{*-} Invariant Mass	$\pm 2\Gamma$ Σ^{*-} Invariant Mass

Table 8.3 : Summary of the cuts used to extract the experimental yields of the $\gamma n \to K^{+}\Sigma^{*-}$ reaction from the $\gamma n \to K^{+}\pi^{-}\Lambda$ final-state events, in the order that they were performed in this analysis.

The overlap of the invariant masses of the K^{*0} and Σ^{*-} particles is shown in Figure 8.11 in each of the photon energy bins used for the yield extractions. In the two lowest photon energy bins only Σ^{*-} events are distinguishable, but above 1.9 GeV the K^{*0} events become increasingly prevalent. Although the threshold for the $\gamma n \to K^{*0}\Lambda$ reaction is just below 1.7 GeV, the minimum momentum cuts used in this analysis remove the majority of the events below 1.9 GeV. Therefore the reaction overlap cuts were only performed above 1.9 GeV, and the $\gamma n \to K^{*0}\Lambda$ yields were restricted to this range as well. The cuts used for the yield extractions are detailed in the following subsections.

8.2.1 $\gamma n \to K^{*0}\Lambda$ Experimental Yields

Figure 8.12 shows the distribution of the $\gamma n \to K^{+}\pi^{-}\Lambda$ final-state events as a function of photon energy and $\cos(\theta_{K^{*0}})$, where $\theta_{K^{*0}}$ is the angle between the K^{*0} and the photon in the center-of-mass frame. Overlaid on this distribution is a grid showing the binning used for the $\gamma n \to K^{*0}\Lambda$ yield extractions. As discussed in Section 8.2, almost all of the events below 1.9 GeV were Σ^{*-} events, so no $\gamma n \to K^{*0}\Lambda$ yield extraction was performed in this range. These bins had varying widths in

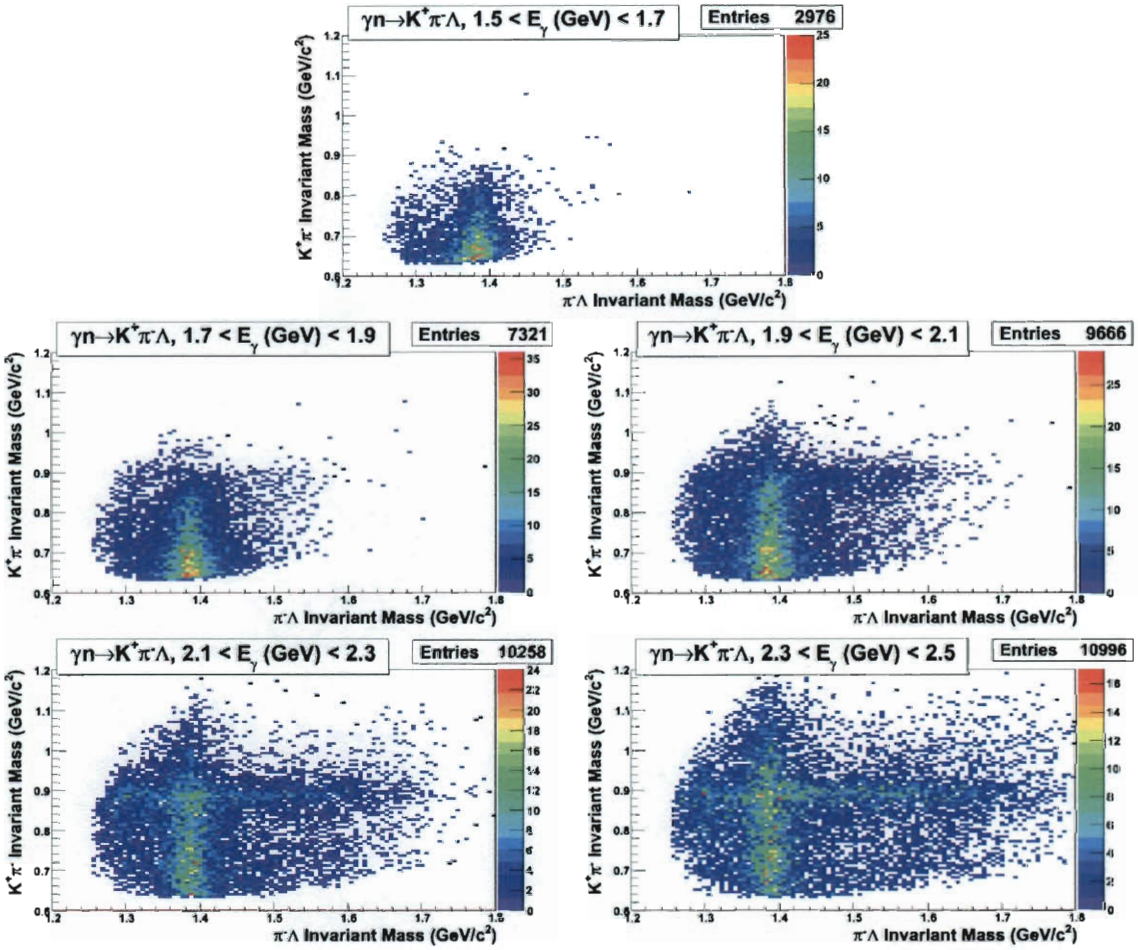

Figure 8.11 : The overlap of the invariant masses of the $K^{*0} \to K^{+}\pi^{-}$ and $\Sigma^{*-} \to \Lambda\pi^{-}$ decays in the photon energy bins used for yield extraction. No K^{*0} events were distinguishable below 1.9 GeV, so the $\gamma n \to K^{*0}\Lambda$ yields were only extracted above this range. Also, the cuts on the invariant masses of these particles to remove the majority of the reaction overlap were only performed above 1.9 GeV.

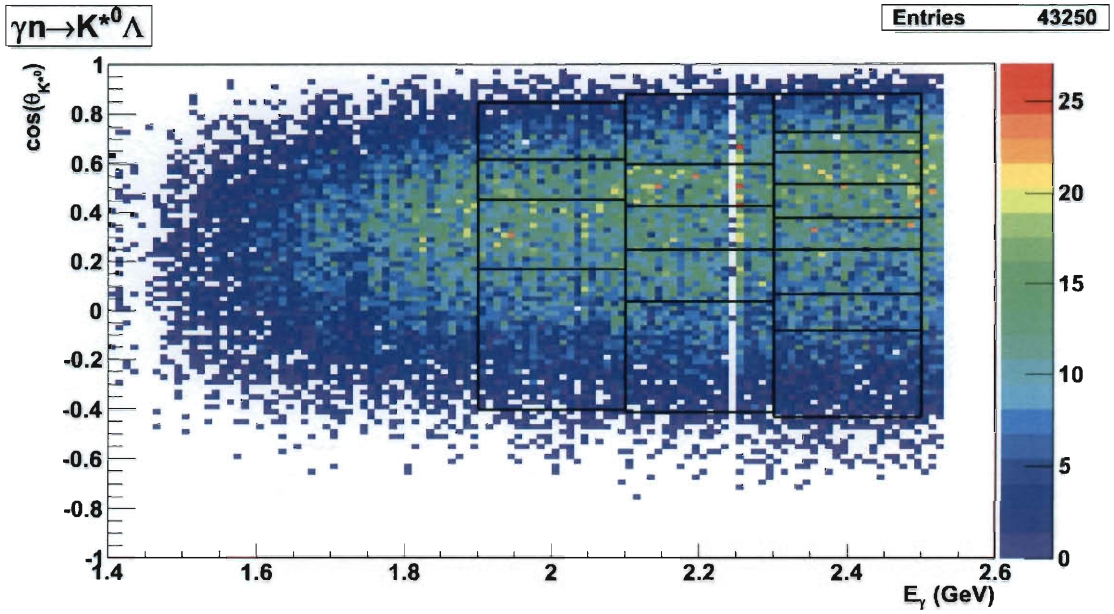

Figure 8.12 : The distribution of the $\gamma n \rightarrow K^{+}\pi^{-}\Lambda$ final-state events from the 2.655 GeV data of the g13a experiment as a function of photon energy and $\cos(\theta_{K^{*0}})$, where $\theta_{K^{*0}}$ is the angle between the K^{*0} and the photon in the center-of-mass frame. The hole in the distribution near $E_{\gamma} = 2.25$ GeV is due to the rejection of the bad photon tagger bins. The grid overlaid on the distribution illustrates the binning used for extracting the experimental yield of the $\gamma n \rightarrow K^{*0}\Lambda$ reaction.

$\cos(\theta_{K^{*0}})$ to ensure that enough statistics were present in each bin to fit the yields.

Within each bin, a $\pm 3\sigma$ cut was placed on the $\gamma D \rightarrow K^{+}\pi^{-}\Lambda(p)$ missing mass to remove the majority of the events with additional missing particles. These cuts on the spectator proton were fit to a Gaussian function over a quadratic background, and are shown in Figure 8.13 for one representative $\cos(\theta_{K^{*0}})$ bin of each photon energy bin. The primary source of background is presumed to be $\gamma n \rightarrow K^{*0}\Sigma^{0} \rightarrow K^{+}\pi^{-}\Lambda(\gamma)$ events, although a detailed study of the background has not yet been performed. The spectator proton fits for all of the bins in this analysis are located in Appendix C.2.

Next, cuts were placed on the invariant mass of $\Lambda\pi^{-}$ to remove the majority of the overlapping $\gamma n \rightarrow K^{+}\Sigma^{*-}$ events. The fits of the Σ^{*-} peak were performed with a Breit-Wigner function over a linear background, and are shown in Figure 8.14 for one $\cos(\theta_{K^{*0}})$ bin of each photon energy bin. These are the same bins that were sampled in Figure 8.13 for the spectator proton fits. The 39.4 MeV/c^2 Σ^{*-} resonance width [8] is the dominant source of the width of the signal peaks, and Gaussian-distributed resolution effects absorbed by the Breit-Wigner function were assumed to not

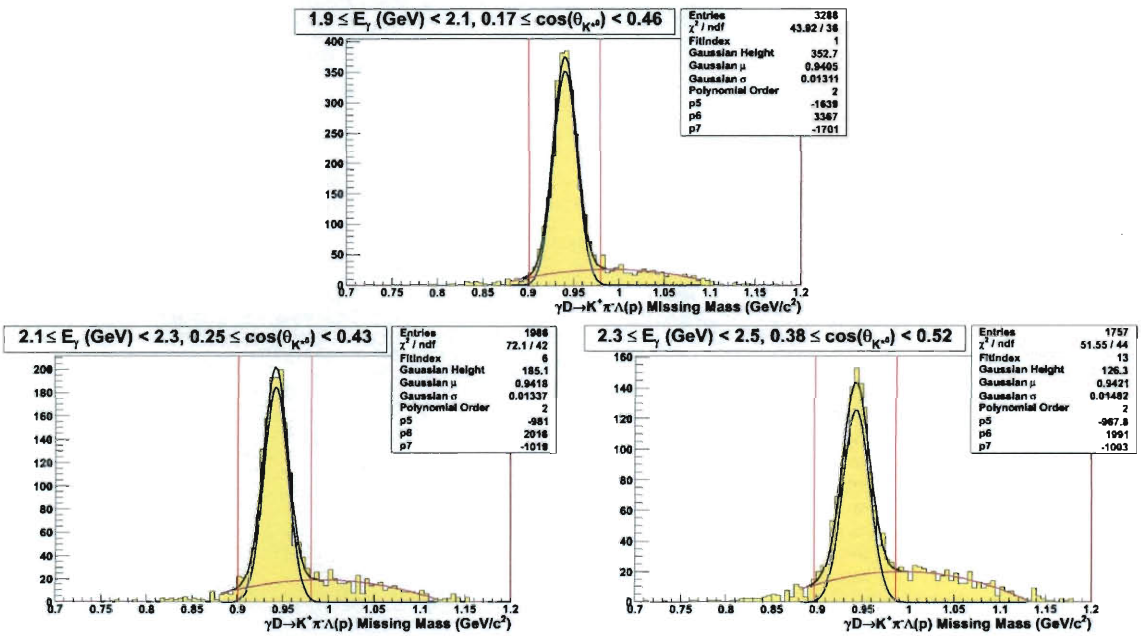

Figure 8.13 : Fits to the missing mass of the spectator proton of the $\gamma D \to K^{+}\pi^{-}\Lambda(p)$ reaction for the extraction of the $\gamma n \to K^{*0}\Lambda$ experimental yields. A fit from one of the $\cos(\theta_{K^{*0}})$ bins is shown for each photon energy bin, where $\theta_{K^{*0}}$ is the angle between the K^{*0} and the photon in the center-of-mass frame. The signals were fit to a Gaussian over a quadratic background, and the red lines indicate the $\pm 3\sigma$ cuts used for yield extraction. The blue lineshapes represent the Gaussian fit functions, the magenta lineshapes represent the quadratic fit functions, and the black lineshapes represent the total fit functions.

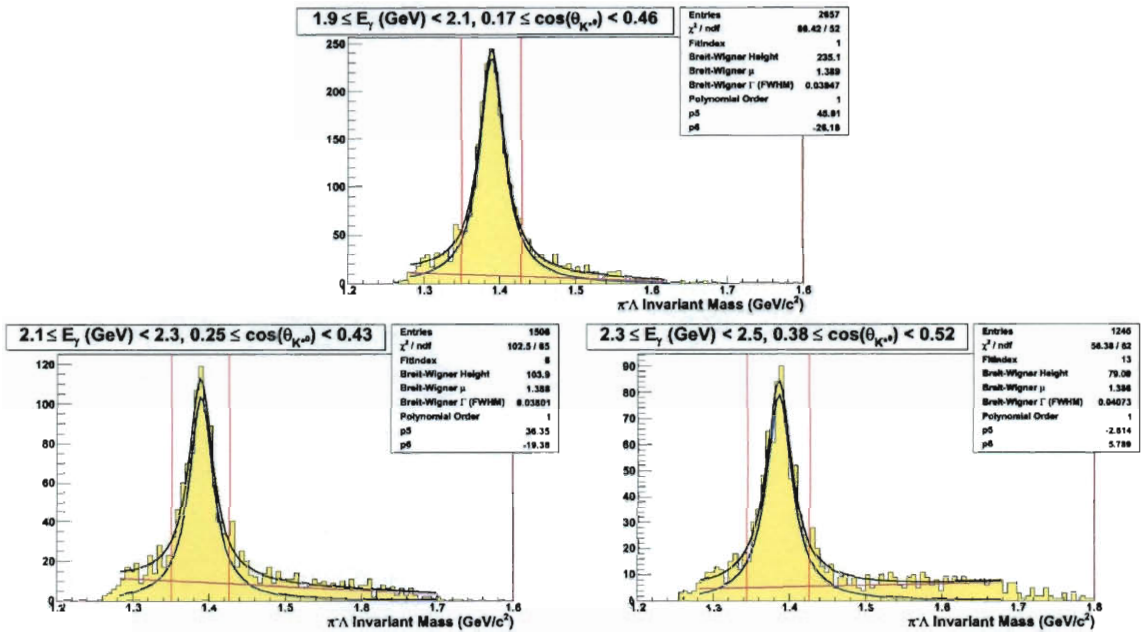

Figure 8.14 : Fits to the invariant mass of the Σ^{*-} in one $\cos(\theta_{K^{*0}})$ bin for each photon energy bin, where $\theta_{K^{*0}}$ is the angle between the K^{*0} and the photon in the center-of-mass frame. These distributions were fit to a Breit-Wigner over a linear function, and events within $\pm 1\Gamma$ were cut to remove the majority of the $\gamma n \to K^{+}\Sigma^{*-}$ events from the $\gamma n \to K^{*0}\Lambda$ analysis. These cuts are illustrated by the red vertical lines, and the blue, magenta, and black lineshapes represent the Breit-Wigner, linear background, and total fit functions, respectively.

significantly distort the fit to the background. Events within $\pm 1\Gamma$ of the signal peaks were cut in each bin, removing events in the central $\sim$70.5% regions of the Breit-Wigner integrals. This cut was chosen to remove the majority of the overlapping $\gamma n \to K^{+}\Sigma^{*-}$ events while retaining a large number of the $\gamma n \to K^{*0}\Lambda$ events. In Sections 9.3 and 9.4.5, the potential reaction interference effects and systematic uncertainties are studied as a function of the width of this cut. Fits of the Σ^{*-} overlap cuts for all bins are located in Appendix C.2.

Before extracting the yields, events with more than one valid track combination were cut from the analysis. This cut removed $\sim$2.6% of the remaining events, significantly more than the $\sim$0.0026% lost from the same cut in the $\gamma n \to p\pi^{-}$ analysis. This event loss was primarily due to the uncertainty on which of the two final-state π^{-}'s originated from the Λ decay. Although the Λ can decay several centimeters away from the production vertex, the vertex reconstruction resolution of the CLAS detector was not precise enough to always fully distinguish the two vertices, especially when the π^{-}'s decayed to μ^{-}'s in the drift chambers. This yield loss is accounted for during the calculation

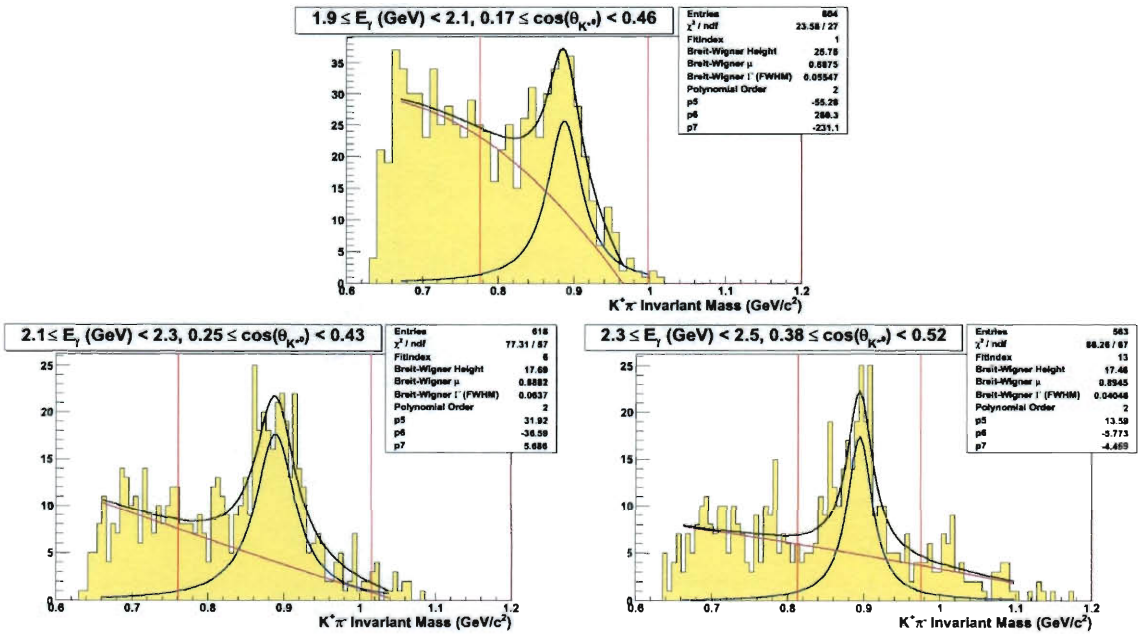

Figure 8.15 : Fits to the invariant mass of the K^{*0} in one $\cos(\theta_{K^{*0}})$ bin for each photon energy bin, where $\theta_{K^{*0}}$ is the angle between the K^{*0} and the photon in the center-of-mass frame. The signals were fit to a Breit-Wigner over a quadratic background, and the red lines indicate the $\pm 2\Gamma$ cuts used for yield extraction. The blue lineshapes represent the Breit-Wigner fit functions, the magenta lineshapes represent the quadratic fit functions, and the black lineshapes represent the total fit functions.

of the cross section, as discussed in Section 8.4.

Finally, fits to the invariant mass of the K^{*0} peak were performed to extract the experimental yields. A fit for one of the $\cos(\theta_{K^{*0}})$ bins in each of the photon energy bins is shown in Figure 8.15, the same bins as shown in Figures 8.13 and 8.14. These distributions were fit to a Breit-Wigner function over a quadratic background, and cut at $\pm 2\Gamma$ to obtain the experimental yields. The K^{*0} fits for all of the bins had an average χ^2 per degree of freedom of $\sim$1.33, and are located in Appendix C.2.

Some of these fits had significantly wider Breit-Wigner functions than the 48.7 MeV/c^2 K^{*0} width [8]. While statistical fluctuations and detector resolutions also contributed to the signal widths, it may be that some of the background fits did not converge properly. The systematic uncertainties of the background fits are studied in Section 9.4.5.

The experimental yields were the number of events above the background within the $\pm 2\Gamma$ cuts. These cuts represent $\sim$84.4% of the Breit-Wigner integrals, and were chosen to accept the majority

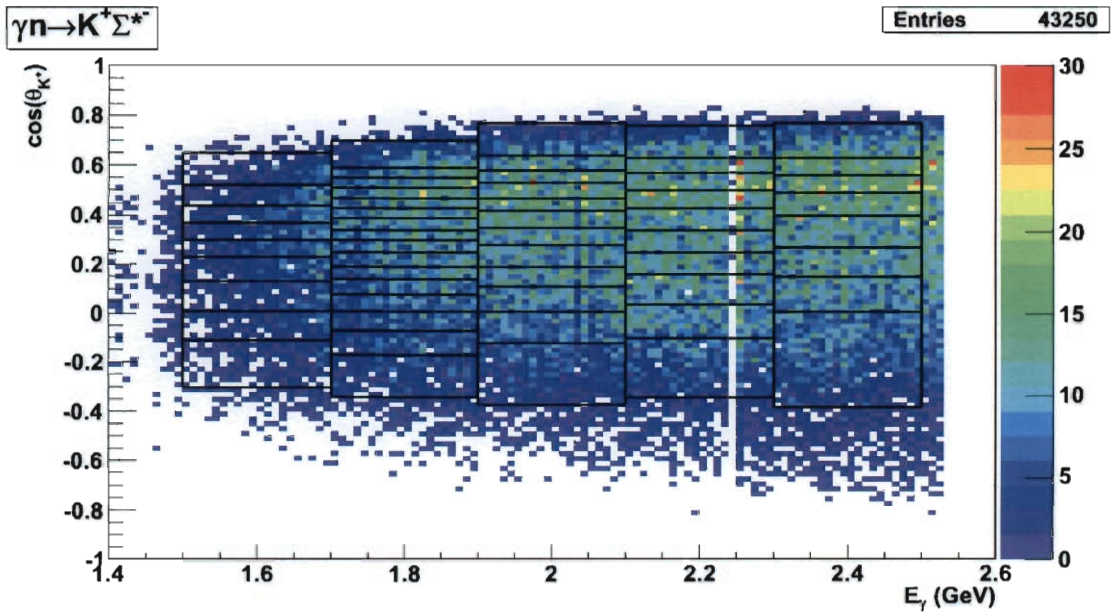

Figure 8.16 : The distribution of the $\gamma n \to K^{+}\pi^{-}\Lambda$ final-state events from the 2.655 GeV data of the g13a experiment as a function of photon energy and $\cos(\theta_{K^+})$, where θ_{K^+} is the angle between the K^+ and the photon in the center-of-mass frame. The hole in the distribution near $E_\gamma = 2.25$ GeV is due to the rejection of the bad photon tagger bins. The grid overlaid on the distribution illustrates the binning used for extracting the experimental yield of the $\gamma n \to K^{+}\Sigma^{*-}$ reaction.

of the K^{*0} signal events while avoiding the edges of the distributions, where the signal-to-background ratios were small. There were approximately 4100 $\gamma n \to K^{*0}\Lambda$ events in the experimental yield, and the yield distributions are shown in Section 8.3 compared to the simulated yields. The statistical uncertainties of the yields were calculated using Equation 7.4, and were less than 6.5% for all bins.

8.2.2 $\gamma n \to K^{+}\Sigma^{*-}$ Experimental Yields

The distribution of the $\gamma n \to K^{+}\pi^{-}\Lambda$ final-state events is shown in Figure 8.16 as a function of photon energy and $\cos(\theta_{K^+})$, where θ_{K^+} is the angle between the K^+ and the photon in the center-of-mass frame. A grid of the binning used for the $\gamma n \to K^{+}\Sigma^{*-}$ yield extraction is also shown. As for the $\gamma n \to K^{*0}\Lambda$ analysis, the bin widths varied to ensure that enough statistics were present in each bin to fit the yields. Since these events were binned differently than in the $\gamma n \to K^{*0}\Lambda$ analysis, the $\gamma n \to K^{+}\Sigma^{*-}$ yield extraction fits were performed separately.

Just as for the $\gamma n \to K^{*0}\Lambda$ analysis, $\pm 3\sigma$ cuts were fit to the $\gamma D \to K^{+}\pi^{-}\Lambda(p)$ missing mass. These distributions were fit to a Gaussian over a flat background in the two lowest energy bins, and

to a Gaussian over a quadratic background above 1.9 GeV. These fits are shown in Figure 8.17 for one representative $\cos(\theta_{K^+})$ bin of each photon energy bin. Again, events with an additional photon or π^0 in the final state comprised the majority of the background. All of the spectator proton fits are shown in Appendix C.3.

Overlap cuts on the K^{*0} invariant mass could not be reliably fit without first temporarily reducing the background in their mass distributions from Σ^{*-} events. However to ensure that enough K^{*0} events were present in each bin for fitting, several adjacent $\cos(\theta_{K^+})$ bins were merged together as shown in Figure 8.18. The overlap cuts obtained for these merged bins were used for each of the component Σ^{*-} bins, as the variations of the width of these distributions due to detector resolution effects were assumed to be small over these ranges. As discussed in Section 8.2, these cuts were only performed above 1.9 GeV.

In these merged bins, fits to the Σ^{*-} invariant mass are shown in Figure 8.19 for one merged $\cos(\theta_{K^+})$ bin of each photon energy bin above 1.9 GeV. These bins contain the same bins as shown in Figure 8.17 for the cuts on the spectator proton. These distributions were fit to a Breit-Wigner function over a linear background, and events within $\pm 1\Gamma$ of the mean were temporarily removed to reduce the background underneath the K^{*0} peak. Fits to the Σ^{*-} invariant mass for all of the merged bins are included in Appendix C.3.

After placing these temporary Σ^{*-} cuts, the fits to the K^{*0} invariant mass peaks are shown in Figure 8.20 for one merged $\cos(\theta_{K^+})$ bin of each photon energy bin above 1.9 GeV, the same bins as in Figure 8.19. These distributions were fit to a Breit-Wigner function over a quadratic background to determine the $\pm 1\Gamma$ $\gamma n \to K^{*0}\Lambda$ reaction overlap cuts. Similar to Section 8.2.1, this cut was chosen to remove the majority of the overlapping $\gamma n \to K^{*0}\Lambda$ events while retaining a large number of the $\gamma n \to K^{+}\Sigma^{*-}$ events. The potential interference effects and systematic uncertainties associated with these cuts are studied in Sections 9.3 and 9.4.4, respectively. Fits to the K^{*0} signal for all of the merged bins are located in Appendix C.3.

After removing the temporary Σ^{*-} cuts and applying the K^{*0} overlap cuts, $\sim$0.83% of the events were rejected because they had more than one valid track combination. This was significantly less than the $\sim$2.6% event loss in the $\gamma n \to K^{*0}\Lambda$ analysis. This difference was partially due to the widths of the K^{*0} fits being significantly larger than those of the Σ^{*-}. When the overlap cuts at $\pm 1\Gamma$ were employed, more of the track combinations were cut from the $\gamma n \to K^{+}\Sigma^{*-}$ analysis than

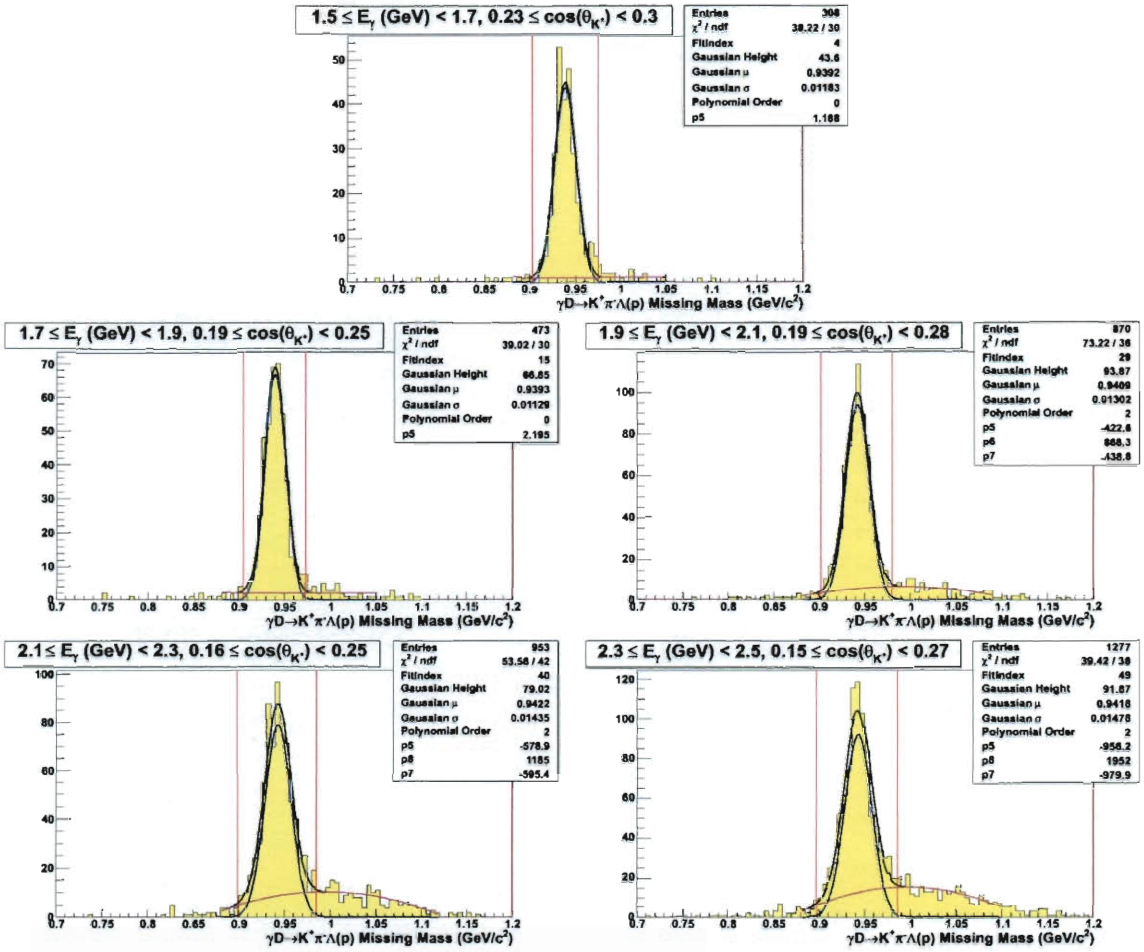

Figure 8.17 : Fits to the missing mass of the spectator proton of the $\gamma D \to K^{+}\pi^{-}\Lambda(p)$ reaction for the extraction of the $\gamma n \to K^{+}\Sigma^{*-}$ experimental yields. A fit from one of the $\cos(\theta_{K^{+}})$ bins is shown for each photon energy bin, where $\theta_{K^{+}}$ is the angle between the K^{+} and the photon in the center-of-mass frame. The signals were fit to a Gaussian over a flat background below 1.9 GeV, and to a Gaussian over a quadratic background above 1.9 GeV. The $\pm 3\sigma$ cuts are illustrated by the red vertical lines, and the blue, magenta, and black lineshapes represent the Gaussian, polynomial background, and total fit functions, respectively.

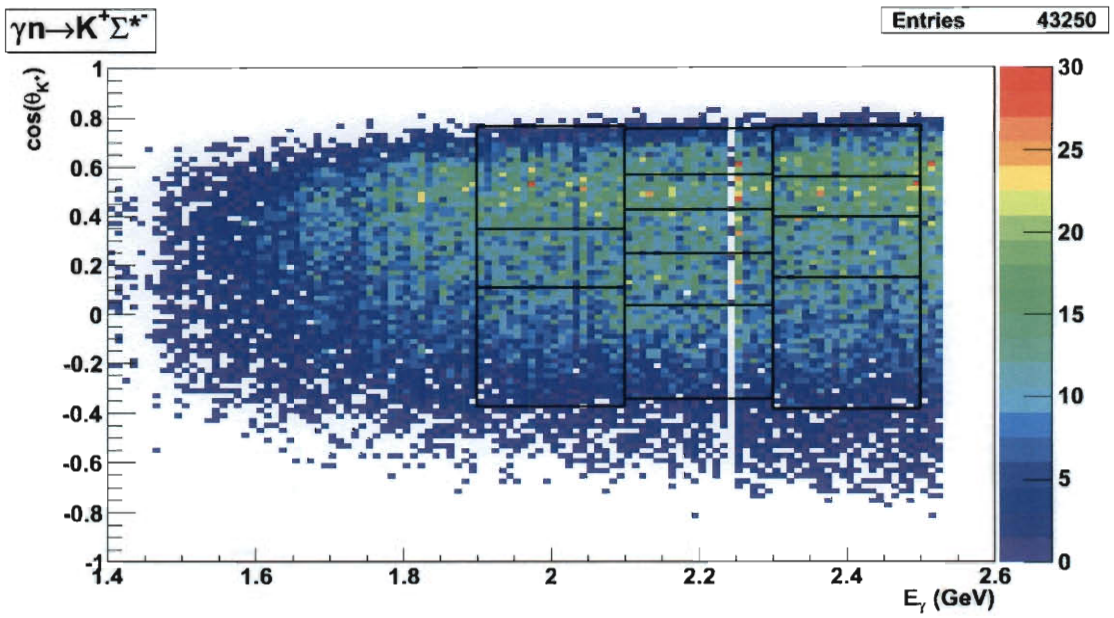

Figure 8.18 : The distribution of the $\gamma n \to K^{+}\pi^{-}\Lambda$ final-state events from the 2.655 GeV data of the g13a experiment as a function of photon energy and $\cos(\theta_{K^+})$, where θ_{K^+} is the angle between the K^+ and the photon in the center-of-mass frame. The hole in the distribution near $E_\gamma = 2.25$ GeV is due to the rejection of the bad photon tagger bins. The grid overlaid on the distribution illustrates the merged binning used to fit the K^{*0} overlap cuts for extraction of the $\gamma n \to K^{+}\Sigma^{*-}$ experimental yields.

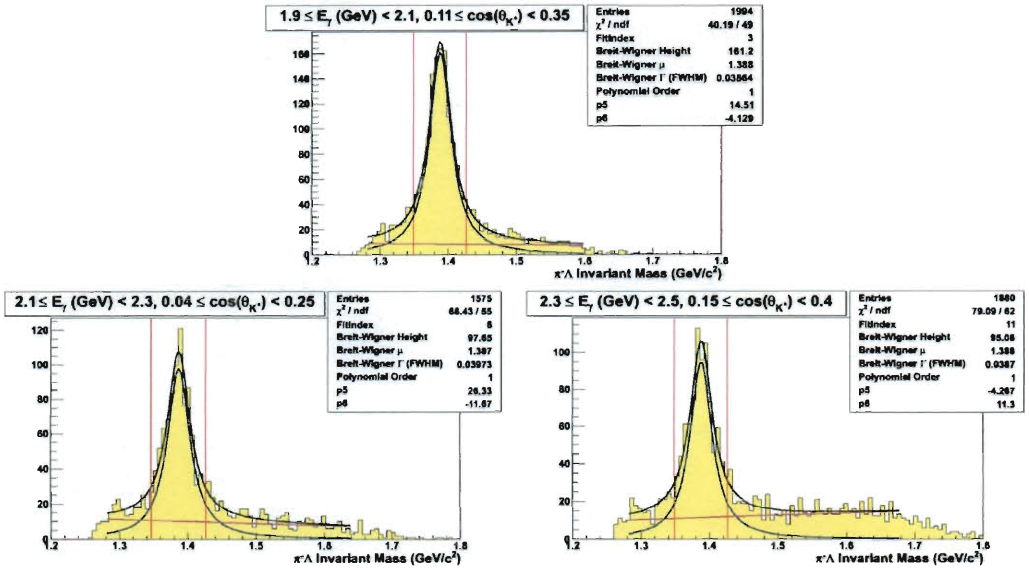

Figure 8.19 : Fits to the invariant mass of the Σ^{*-} in one merged $\cos(\theta_{K^+})$ bin of each photon energy bin above 1.9 GeV, where θ_{K^+} is the angle between the K^+ and the photon in the center-of-mass frame. These distributions were fit to a Breit-Wigner over a linear background, and events within $\pm 1\Gamma$ were cut to remove the majority of the Σ^{*-} events from the K^{*0} distributions for the overlap cut fits. These cuts are illustrated by the red vertical lines, and the blue, magenta, and black lineshapes represent the Breit-Wigner, linear background, and total fit functions, respectively.

from the $\gamma n \to K^{*0}\Lambda$ analysis. The yield correction due to this event loss is discussed in Section 8.4.

Finally, $\pm 2\Gamma$ cuts were placed on the invariant mass of the Σ^{*-} to extract the experimental yields of the $\gamma n \to K^{+}\Sigma^{*-}$ reaction. Fits to one of the $\cos(\theta_{K^+})$ bins in each of the photon energy bins are shown in Figure 8.21, and are the same bins as represented in Figures 8.17 through 8.20. The complete set of Σ^{*-} fits had an average χ^2 per degree of freedom of $\sim$1.37, and are included in Appendix C.3.

The Σ^{*-} signals were fit with a Breit-Wigner function, and the background fits varied with photon energy. In the two lowest photon energy bins background fits were not performed because very few background events appeared to be present. From 1.9 GeV to 2.3 GeV flat backgrounds were fit, and a linear function was used to fit the backgrounds for the highest energy bin. There were approximately 18000 $\gamma n \to K^{+}\Sigma^{*-}$ events above the background within the $\pm 2\Gamma$ cuts, and the distributions of these yields are shown in Section 8.3 compared to the simulated yields.

Since no backgrounds were fit in the two lowest photon energy bins, these sampled yields were

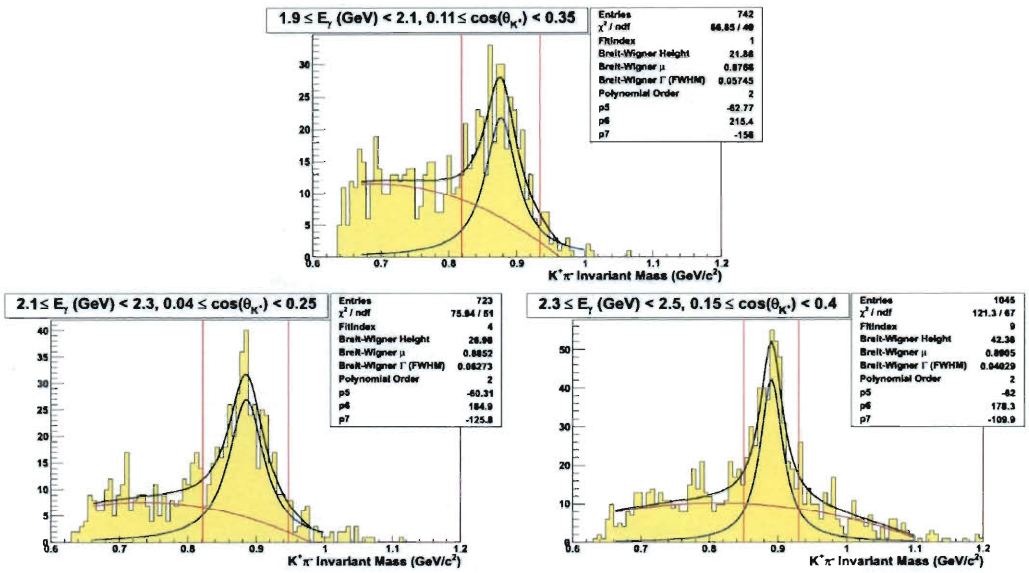

Figure 8.20 : Fits to the invariant mass of the K^{*0} in one merged $\cos(\theta_{K^+})$ bin of each photon energy bin above 1.9 GeV, where θ_{K^+} is the angle between the K^+ and the photon in the center-of-mass frame. These distributions were fit to a Breit-Wigner over a quadratic background, and events within $\pm 1\Gamma$ were cut to remove the majority of the $\gamma n \to K^{*0}\Lambda$ events from the $\gamma n \to K^{+}\Sigma^{*-}$ analysis. These cuts are illustrated by the red vertical lines, and the blue, magenta, and black lineshapes represent the Breit-Wigner, quadratic background, and total fit functions, respectively.

assumed to be Poisson distributed. The statistical uncertainties of these yields were thus calculated as $\sqrt{Y}$, where Y was the sampled yield of the given bin [54]. For the other energy bins, Equation 7.4 was used to calculate the statistical uncertainties of the yields. However a few of these fits resulted in backgrounds that were consistent with zero, so the weighted average uncertainty within the energy bin was assigned to these bins. The statistical uncertainties on the $\gamma n \to K^{+}\Sigma^{*-}$ yields were less than 6.5% for all bins.

8.3 Monte Carlo Simulations

The Monte Carlo simulations used to calculate the acceptance of CLAS for the $\gamma n \to K^{*0}\Lambda$ and $\gamma n \to K^{+}\Sigma^{*-}$ reactions were performed in a similar manner as for the $\gamma n \to p\pi^{-}$ reaction, as discussed in Section 7.2. The *fsgen* software package [99] was used to generate ~150 million events for each reaction. The $\gamma n \to K^{*0}\Lambda$ events were generated using the differential cross section predictions detailed in Section 3.1, and the $\gamma n \to K^{+}\Sigma^{*-}$ events were generated using a t-slope distribution as defined in Equation 6.1. While the $\gamma n \to K^{+}\Sigma^{*-}$ events were also generated using the differential

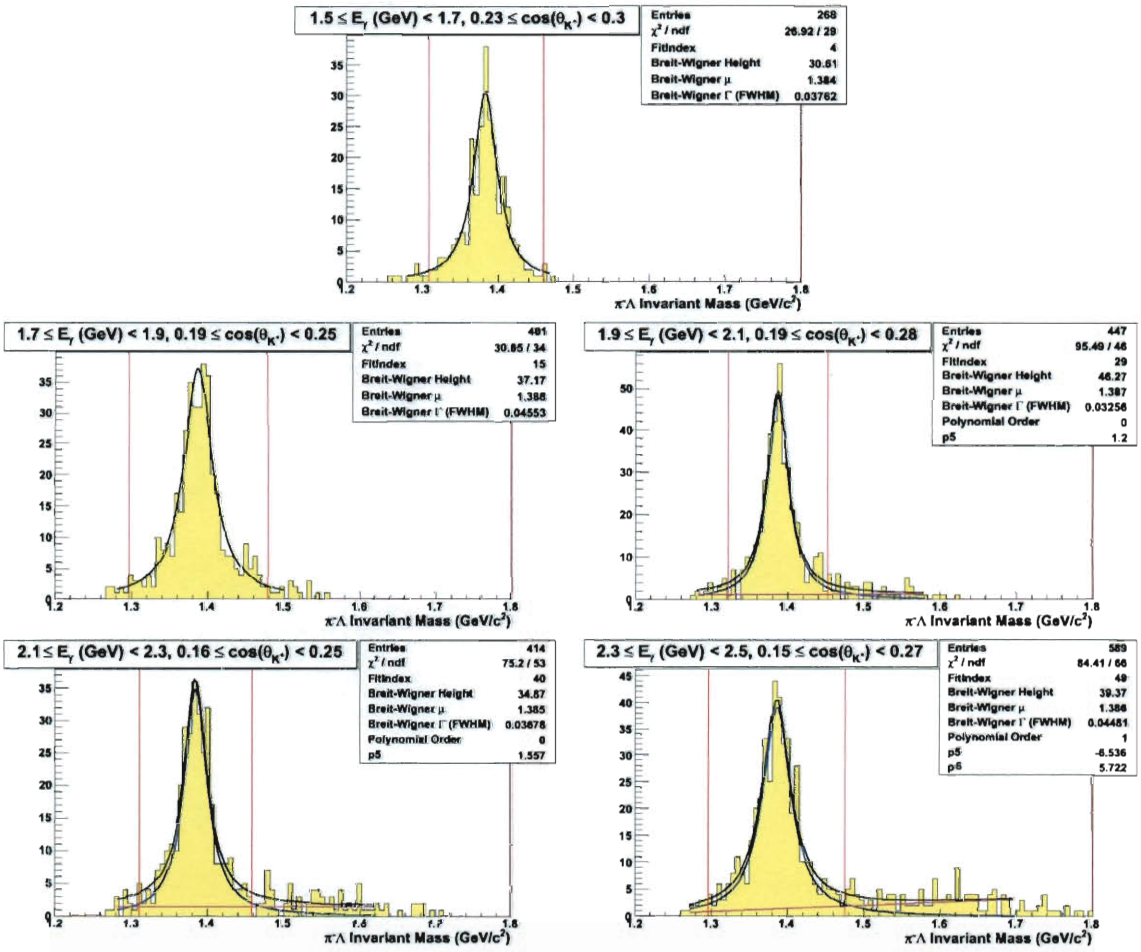

Figure 8.21 : Fits to the invariant mass of the Σ^{*-} in one $\cos(\theta_{K^+})$ bin for each photon energy bin, where θ_{K^+} is the angle between the K^+ and the photon in the center-of-mass frame. The signals were fit to a Breit-Wigner function over a polynomial background that varied with photon energy. From 1.5 GeV to 1.9 GeV no background was fit, from 1.9 GeV to 2.3 GeV a flat background was fit, and from 2.3 GeV to 2.5 GeV a linear background was fit. The red lines indicate the $\pm 2\Gamma$ cuts used for yield extraction, and the blue, magenta, and black lineshapes represent the Breit-Wigner, polynomial background, and total fit functions, respectively.

cross section predictions detailed in Section 3.2, the t-slope distribution with an exponential slope of $b = 3.0$ GeV^{-2} more closely modeled the distributions of the tracks in the final state [117]. For these reactions the $K^{*0} \to K^{+}\pi^{-}$, $\Sigma^{*-} \to \Lambda\pi^{-}$, and $\Lambda \to p\pi^{-}$ decays were simulated by *fsgen*.

After *gsim* and *gpp* [102] were used to simulate the CLAS detector response, the distributions of the generated events of these reactions are shown in Figure 8.22. Again, the generated yields were determined after the bad tagger counters were rejected by *gpp* to remove their effects from the acceptance calculations. After running *gpp* and the track reconstruction software *user_ana* [103], the triggering efficiency was simulated as outlined in Section 6.3.2.

As shown in Figure 8.23 the average detector resolution was closely modeled by the simulations, so the analysis of the simulated data was performed in the same manner as for the experimental data. Although not shown here, the photon-energy-dependence of the detector resolution was matched by both simulations as well. As discussed in Section 7.2 for the $\gamma n \to p\pi^{-}$ analysis, the cut on the number of photons was unnecessary. Also, due to slight resolution differences the $\pm 3\sigma$ cuts on the particle identification and time differences were re-fit for the simulations, as well as the cuts on the mass of the spectator proton and the yield extraction cuts on the Σ^{*-} and K^{*0}. However the overlap cuts were not re-fit, as the fit widths would have been different due to resolution and background modeling effects, causing a different percentage of the signal events to be removed in the simulations than in the experimental data.

The distributions of the simulated $\gamma n \to K^{*0}\Lambda$ and $\gamma n \to K^{+}\Sigma^{*-}$ final-state events are shown in Figure 8.24, along with the binning used for the acceptance corrections. After $\pm 3\sigma$ cuts on the proton missing mass, the reaction overlap cuts determined with the experimental data were applied. Next, $\sim$2.4% and $\sim$0.50% of the events were lost with the cut on the number of track combinations for the $\gamma n \to K^{*0}\Lambda$ and $\gamma n \to K^{+}\Sigma^{*-}$ reactions, respectively. These event losses were less than those for the experimental data, primarily due to the lack of background events. These losses are incorporated into the calculation of the yield correction factor, as discussed in Section 8.4.

Finally, the K^{*0} and Σ^{*-} invariant mass distributions were fit to Breit-Wigner functions for extraction of the simulated yields. One of these fits is shown for each photon energy bin in Figures 8.25 and 8.26 for the $\gamma n \to K^{*0}\Lambda$ and $\gamma n \to K^{+}\Sigma^{*-}$ reactions, respectively. At low photon energies the high-mass edges of the peaks were limited due to phase-space, causing the Breit-Wigner fits to have large χ^2 per degree of freedom. However, these phase-space effects were present in the

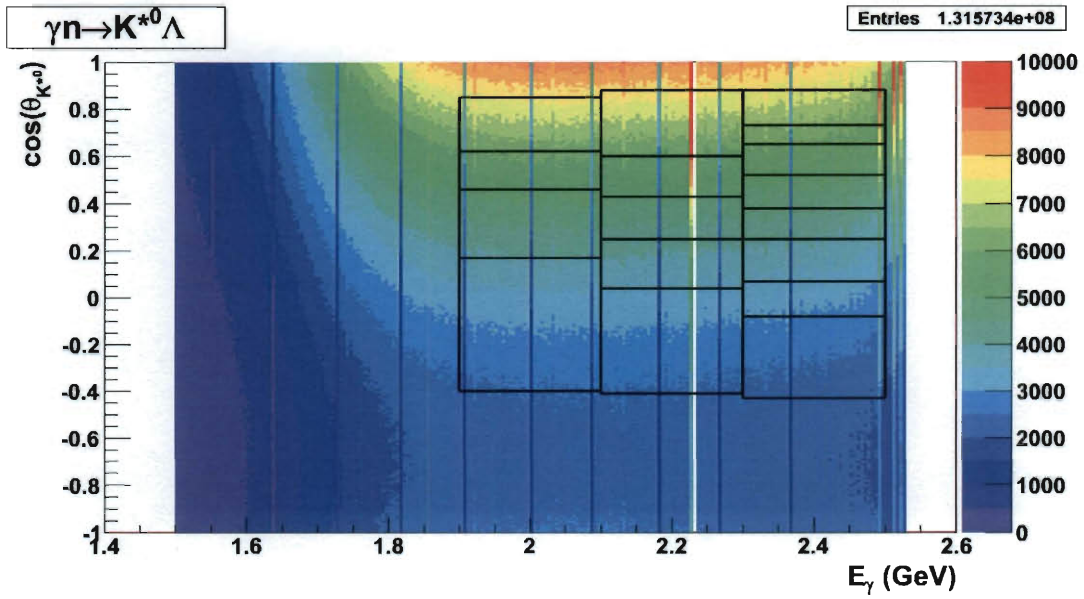

(A)

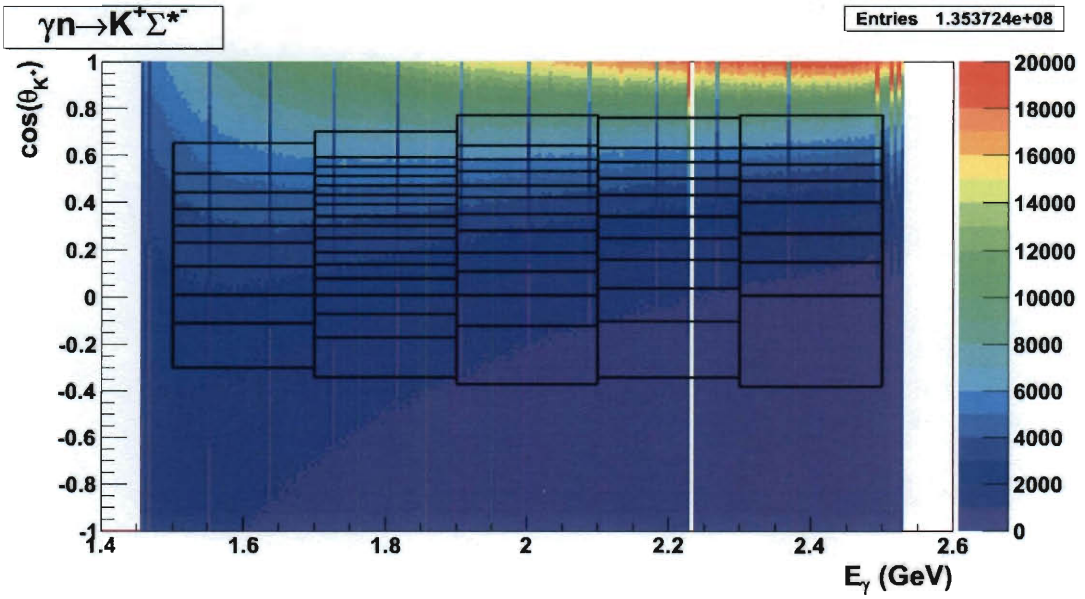

(B)

Figure 8.22 : The distributions of the generated Monte Carlo events of the $\gamma n \to K^{*0}\Lambda$ (A) and $\gamma n \to K^{+}\Sigma^{*-}$ (B) reactions after running *gpp*. These distributions are shown as a function of photon energy and $\cos(\theta)$, where θ is the angle between the meson and the photon in the center-of-mass frame. The grids overlaid on the distributions illustrate the binning used for calculating the acceptances of these reactions. The spikes and holes in the distributions are due to binning effects and the rejection of the tagger counters in *gpp*. The $\gamma n \to K^{*0}\Lambda$ events were generated using the cross section predictions by Oh and Kim [68], and the $\gamma n \to K^{+}\Sigma^{*-}$ events were generated using a t-slope distribution with an exponential slope of $b = 3.0$ GeV^{-2}.

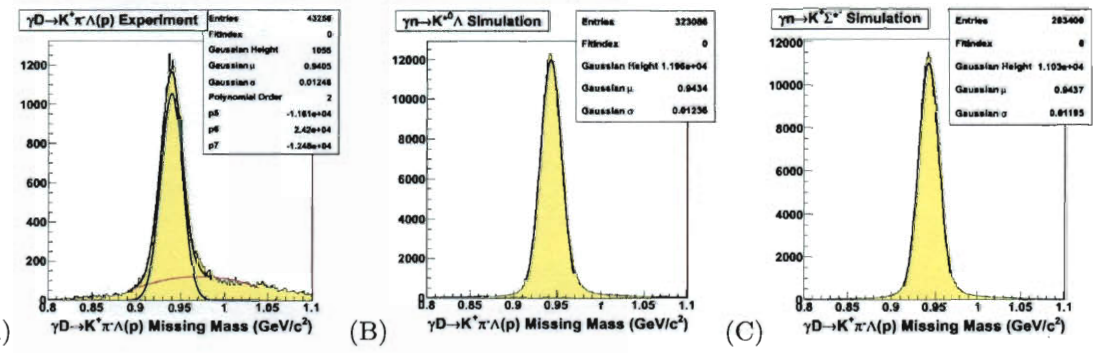

Figure 8.23 : The missing mass of $\gamma D \to K^+\pi^-\Lambda(p)$ in the g13a experiment (A), $\gamma n \to K^{*0}\Lambda$ simulation (B), and $\gamma n \to K^+\Sigma^{*-}$ simulation (C). The simulated distributions have similar resolutions to the experimental data, indicating that the CLAS detector resolution was closely modeled. For (A) the blue lineshape represents the Gaussian fit function, the magenta lineshape represents the polynomial fit functions, and the black lineshape represents the total fit function.

experimental data as well, and the systematic uncertainties associated with the yield extractions are studied in Sections 9.4.4 and 9.4.5. These peaks were cut at $\pm 2\Gamma$, and the ~183,000 and ~185,000 events that survived these cuts were the simulated yields of the $\gamma n \to K^{*0}\Lambda$ and $\gamma n \to K^+\Sigma^{*-}$ reactions, respectively.

The experimental and simulated yields are compared for the $\gamma n \to K^{*0}\Lambda$ and $\gamma n \to K^+\Sigma^{*-}$ reactions in Figures 8.27 and 8.28, respectively. In these plots the heights of the simulated yield distributions were scaled to the experimental yields to better illustrate the comparisons. The large differences between the distributions gave rise to significant systematic uncertainties in the regions where the CLAS acceptance changed rapidly relative to the sizes of the bins used for yield extraction.

These acceptances are shown in Figures 8.29 and 8.30 for the $\gamma n \to K^{*0}\Lambda$ and $\gamma n \to K^+\Sigma^{*-}$ reactions, respectively. The structures visible in the $\gamma n \to K^+\Sigma^{*-}$ acceptances are due primarily to the drift chamber holes and the TOF panel overlaps, but are masked in the $\gamma n \to K^{*0}\Lambda$ acceptances by the coarser binning. The overall acceptance for the $\gamma n \to K^{*0}\Lambda$ reaction was ~0.28%, and was ~0.29% for the $\gamma n \to K^+\Sigma^{*-}$ reaction. Equation 7.4 was used to calculate the statistical uncertainties on the acceptance, where P was the calculated acceptance of the given bins. The statistical uncertainties on the simulated acceptances were less than 1.4% for all bins of the $\gamma n \to K^{*0}\Lambda$ reaction, and were less than 2.6% for all bins of the $\gamma n \to K^+\Sigma^{*-}$ reaction. The systematic uncertainties associated with the generated simulation distributions of the $\gamma n \to K^+\Sigma^{*-}$ and $\gamma n \to K^{*0}\Lambda$ reactions are studied in more detail in Sections 9.4.4 and 9.4.5, respectively.

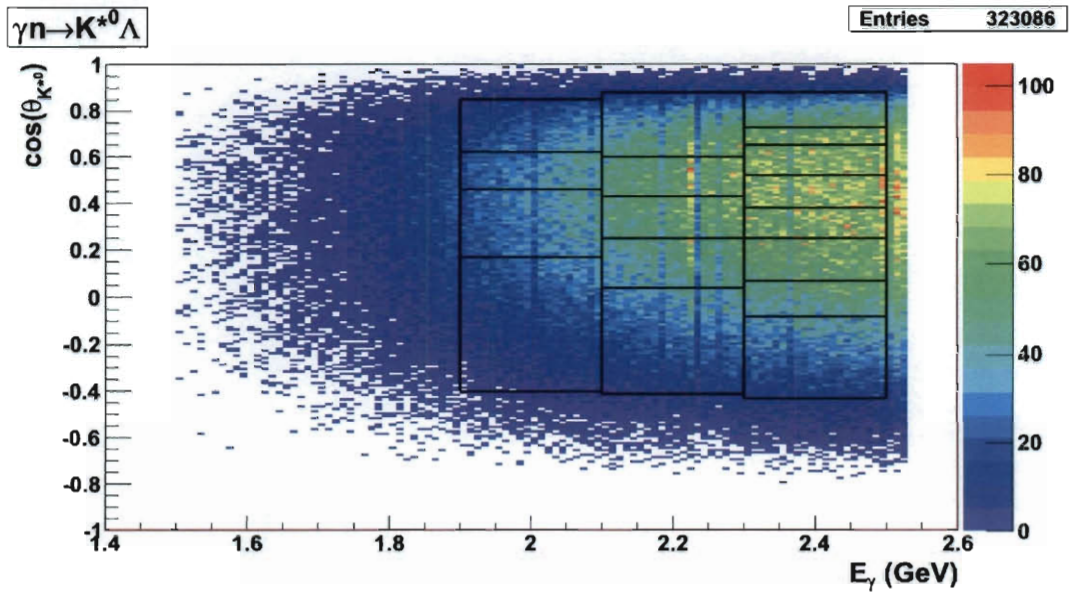

(A)

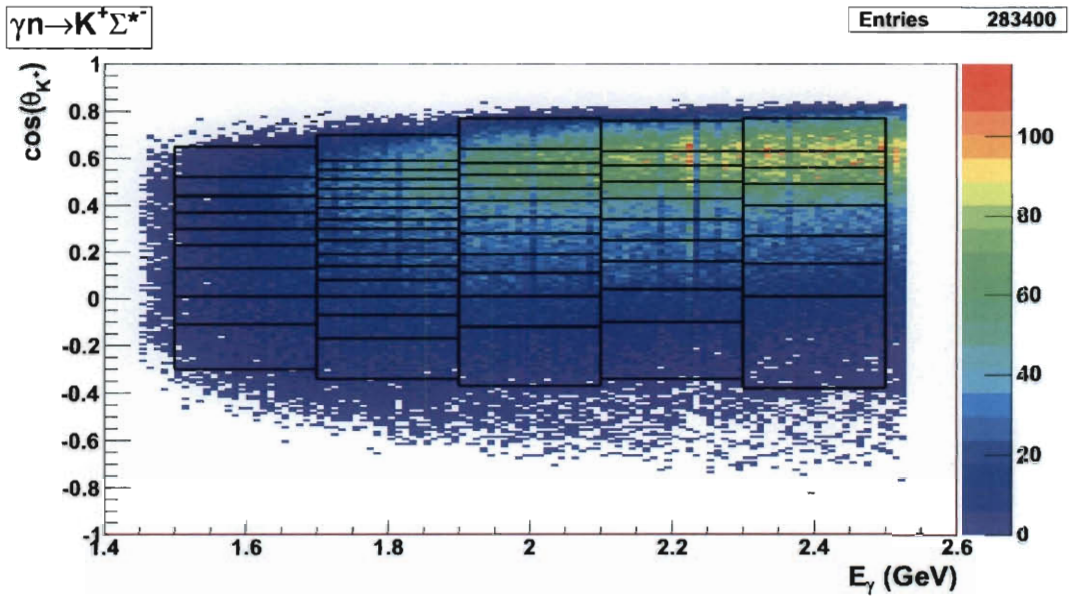

(B)

Figure 8.24 : The distributions of the reconstructed $\gamma n \to K^{+}\pi^{-}\Lambda$ final-state simulation events of the $\gamma n \to K^{*0}\Lambda$ (A) and $\gamma n \to K^{+}\Sigma^{*-}$ (B) reactions as a function of photon energy and $\cos(\theta)$, where θ is the angle between the meson and the photon in the center-of-mass frame. The holes in the distributions are due to binning effects and the rejection of the tagger counters in *gpp*. The grids overlaid on the distributions illustrate the binning used for calculating the acceptance of these reactions.

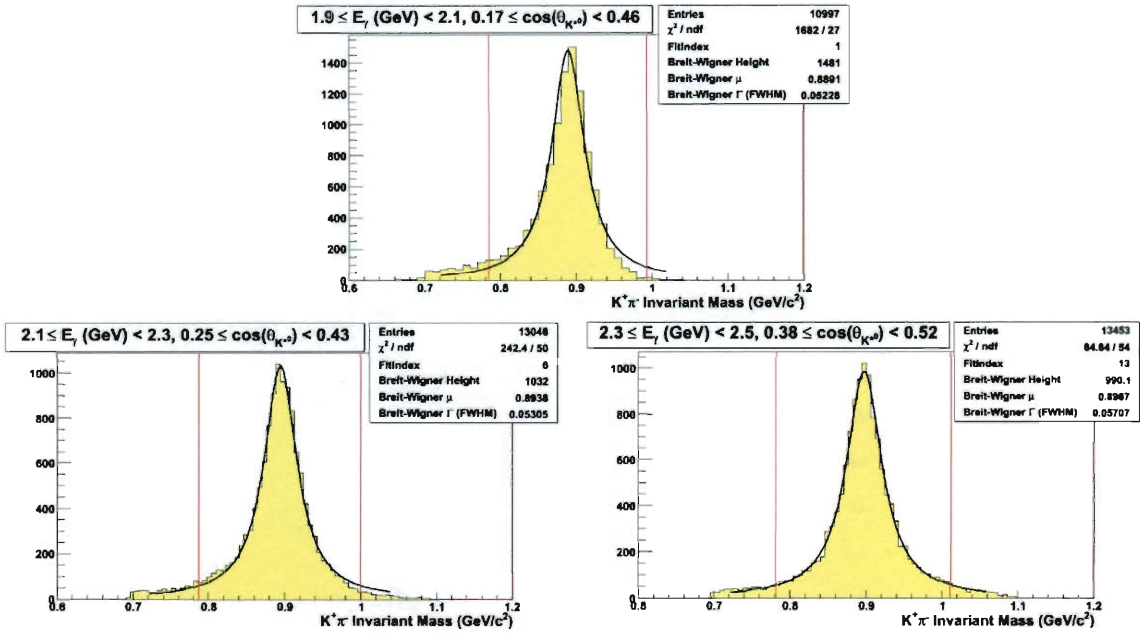

Figure 8.25 : Breit-Wigner fits to the simulated invariant mass distributions of the K^{*0} in one representative $\cos(\theta_{K^{*0}})$ bin for each photon energy bin, where $\theta_{K^{*0}}$ is the angle between the K^{*0} and the photon in the center-of-mass frame. The red lines indicate the $\pm 2\Gamma$ cuts used to extract the $\gamma n \to K^{*0}\Lambda$ simulated yields. The systematic uncertainties associated with the fit deviations due to the edges of phase-space are studied in Section 9.4.5.

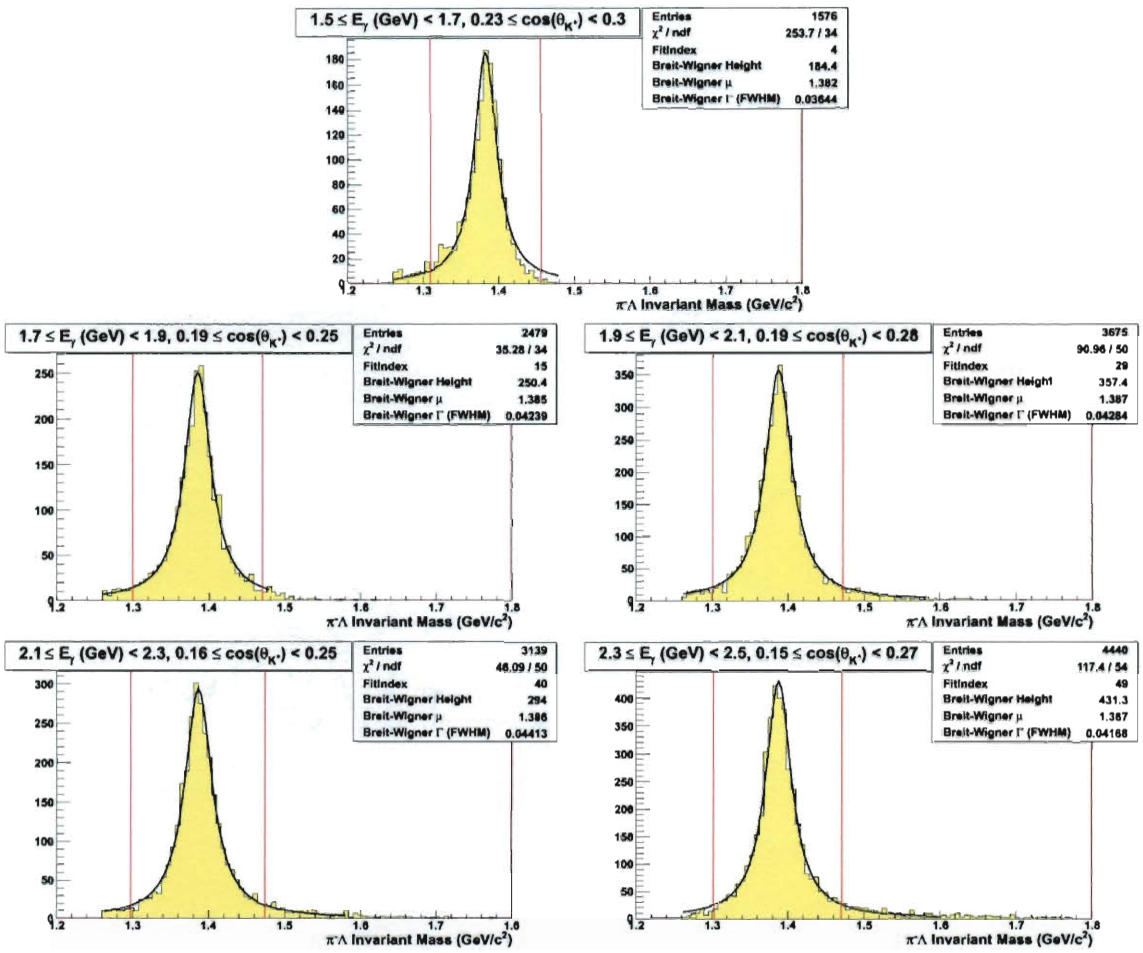

Figure 8.26 : Breit-Wigner fits to the simulated invariant mass distributions of the Σ^{*-} in one representative $\cos(\theta_{K^+})$ bin for each photon energy bin, where θ_{K^+} is the angle between the K^+ and the photon in the center-of-mass frame. The red lines indicate the $\pm 2\Gamma$ cuts used to extract the $\gamma n \to K^{+}\Sigma^{*-}$ simulated yields. The systematic uncertainties associated with the fit deviations due to the edges of phase-space are studied in Section 9.4.4.

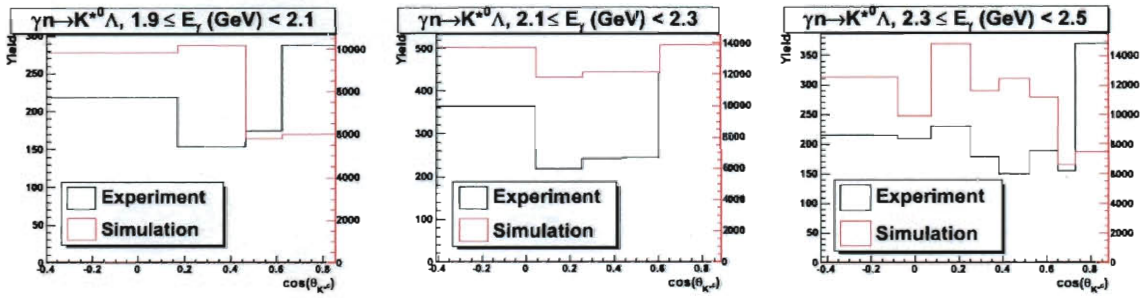

Figure 8.27 : Comparison between the experimental and simulated yields of the $\gamma n \to K^{*0}\Lambda$ reaction in the different photon energy bins as a function of $\cos(\theta_{K^{*0}})$, where $\theta_{K^{*0}}$ is the angle between the K^{*0} and the photon in the center-of-mass frame. The axes on the left side of the plots are for the experimental yields, and the axes on the right side of the plots are for the simulated yields. The systematic uncertainties on the CLAS acceptance associated with the generated simulation distribution are studied in Section 9.4.5.

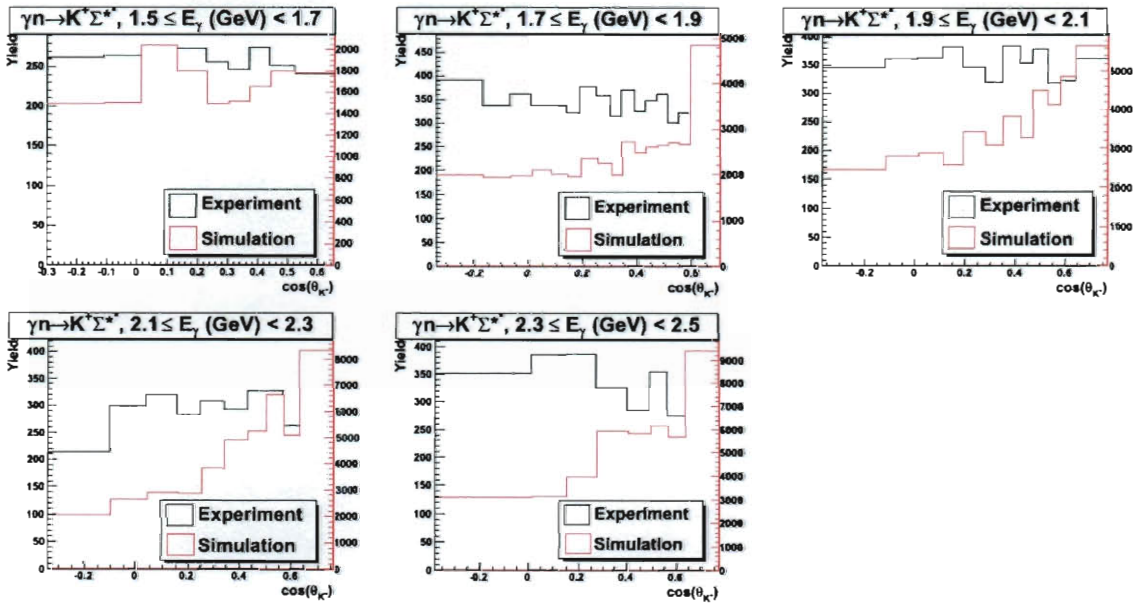

Figure 8.28 : Comparison between the experimental and simulated yields of the $\gamma n \to K^{+}\Sigma^{*-}$ reaction in the different photon energy bins as a function of $\cos(\theta_{K^{+}})$, where $\theta_{K^{+}}$ is the angle between the K^{+} and the photon in the center-of-mass frame. The axes on the left side of the plots are for the experimental yields, and the axes on the right side of the plots are for the simulated yields. The systematic uncertainties on the CLAS acceptance associated with the generated simulation distribution are studied in Section 9.4.4.

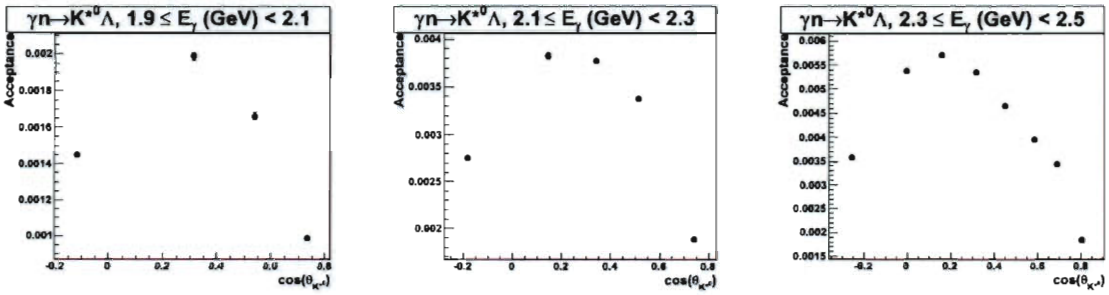

Figure 8.29 : The calculated CLAS acceptance of the $\gamma n \to K^{*0}\Lambda$ reaction in different photon energy bins as a function of $\cos(\theta_{K^{*0}})$, where $\theta_{K^{*0}}$ is the angle between the K^{*0} and the photon in the center-of-mass frame. The structures of the angle-dependent acceptance effects of the drift chamber holes and the TOF panel overlaps were masked by the coarse binning.

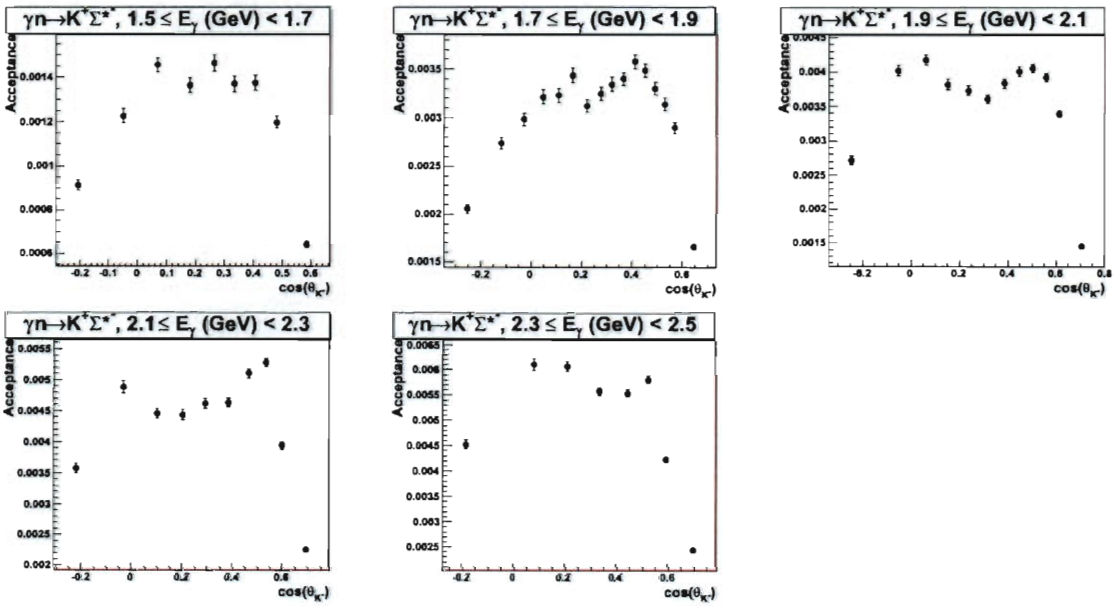

Figure 8.30 : The calculated CLAS acceptance of the $\gamma n \to K^{+}\Sigma^{*-}$ reaction in different photon energy bins as a function of $\cos(\theta_{K^{+}})$, where $\theta_{K^{+}}$ is the angle between the K^{+} and the photon in the center-of-mass frame. The structures in these distributions are primarily due to the drift chamber holes and the TOF panel overlaps.

8.4 Yield Correction Factors and Photon Flux

The yield correction factors of the $\gamma n \to K^{*0}\Lambda$ and $\gamma n \to K^{+}\Sigma^{*-}$ analyses were determined with the same procedure as for the $\gamma n \to p\pi^{-}$ reaction, as discussed in Section 7.3. Equation 7.5 was used to calculate the yield correction factors. The ~5% experimental yield loss due to the cuts that removed events with the start time calculated incorrectly in the $\gamma n \to p\pi^{-}$ analysis was assumed to be reaction independent, along with the ~1.2% yield loss from the same cuts in the $\gamma n \to p\pi^{-}$ simulation.

The yield losses from the cut on the number of photons was discussed in Section 8.1.5, and the yield losses from the cuts on the number of track combinations were discussed in Sections 8.2 and 8.3. The yield correction factors were calculated to be ~1.15 for both reactions, slightly less than the ~1.17 correction for the $\gamma n \to p\pi^{-}$ reaction due to the decrease in the loss of events from the cut on the number of photons. The uncertainties on each of the components of the yield correction factors were less than 0.2%, so these uncertainties were ignored for the cross section calculations.

Shown in Figure 8.31 is the integrated photon flux from the 2.655 GeV data in the bins used for the $\gamma n \to K^{*0}\Lambda$ and $\gamma n \to K^{+}\Sigma^{*-}$ cross section calculations. The *gflux* software package [104] was used to determine the photon flux, as discussed in Section 6.4. Although the integrated photon flux distribution roughly followed the $1/E_{\gamma}$ bremsstrahlung energy distribution, slight deviations were caused by inefficient tagger counters. In this analysis of the 2.655 GeV g13a data, approximately 12.4 trillion tagged photons were incident on the CLAS target. The statistical uncertainties on the integrated photon fluxes were less than 0.0013% for all energy bins. Thus for both the $\gamma n \to K^{*0}\Lambda$ and $\gamma n \to K^{+}\Sigma^{*-}$ analyses, the statistical uncertainties of the experimental yields were significantly larger than the statistical uncertainties on the integrated photon flux or the simulated CLAS acceptances.

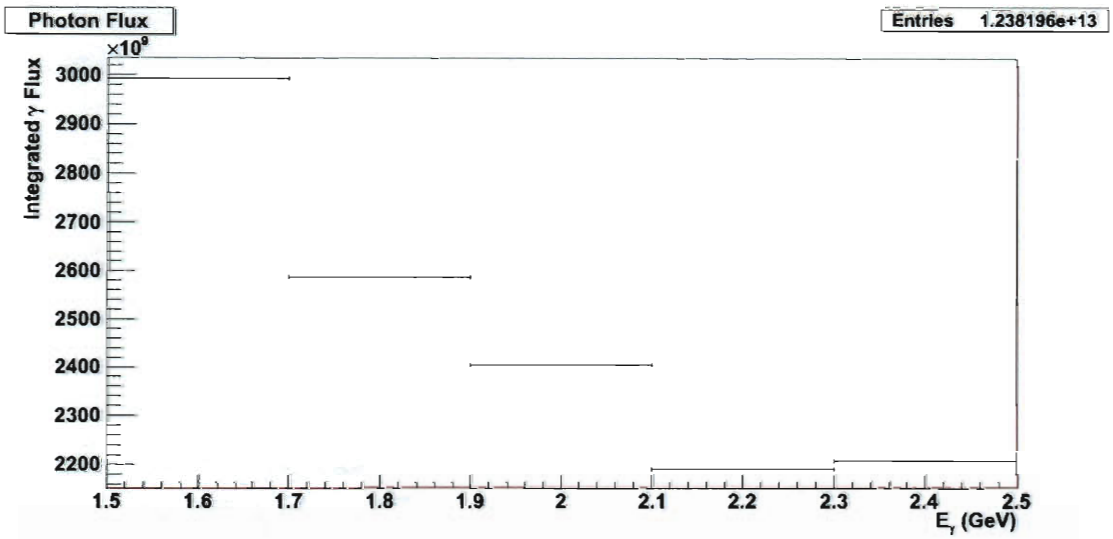

Figure 8.31 : The integrated photon flux from the 2.655 GeV data in the photon energy bins used in the $\gamma n \to K^{*0}\Lambda$ and $\gamma n \to K^{+}\Sigma^{*-}$ cross section calculations. This distribution deviates slightly from the $1/E_\gamma$ bremsstrahlung energy distribution due to the inefficient tagger counters.

Chapter 9

$\gamma n \rightarrow K^{*0}\Lambda$ & $\gamma n \rightarrow K^{+}\Sigma^{*-}$ Cross Sections

As discussed in Section 2.3, the model of the baryon decays by Capstick and Roberts [39] predicts that several of the N^* resonances have non-negligible couplings to the excited K^*Y and KY^* channels. These include the $N\frac{3}{2}^-(1960)$, $N\frac{5}{2}^+(1980)$, $N\frac{5}{2}^+(1995)$, $N\frac{3}{2}^-(2055)$, $N\frac{1}{2}^+(2065)$, $N\frac{5}{2}^-(2080)$, and $N\frac{3}{2}^-(2095)$ resonances, which are predicted to contribute to the $\gamma n \rightarrow K^{*0}\Lambda$ and $\gamma n \rightarrow K^{+}\Sigma^{*-}$ reactions. Measurement of the spectrum of the N^* resonances will help determine the relevant degrees of freedom of the quarks within the nucleon.

The differential cross sections of the $\gamma n \rightarrow K^{*0}\Lambda$ and $\gamma n \rightarrow K^{+}\Sigma^{*-}$ reactions can be used to extract the couplings of the N^* resonances to these channels. These cross sections were calculated using the procedures for determining the experimental yields and the CLAS acceptance discussed in Chapter 8. These differential cross sections were compared against the available experimental data, as well as the theoretical models of these reactions discussed in Chapter 3. The comparison of these data to theoretical models can be used to provide a better understanding of the underlying physical processes in these reactions. These data can be included in coupled-channels analyses to take rescattering effects into account, and to provide simultaneous constraints on the N^* resonance parameters from several different reactions. Also, an analysis of the overlap between the $\gamma n \rightarrow K^{*0}\Lambda$ and $\gamma n \rightarrow K^{+}\Sigma^{*-}$ reactions indicated that if there were any interference effects between these reactions, they were smaller than the systematic uncertainties on the studies. Future studies of the

Branching Ratio	Value
$\Gamma_{K^{*0}\to K^{+}\pi^{-}}/\Gamma_{K^{*0}}$	0.66507 ± 0.00014
$\Gamma_{\Lambda\to p\pi^{-}}/\Gamma_{\Lambda}$	0.639 ± 0.005
$\Gamma_{\Sigma^{*-}\to\Lambda\pi^{-}}/\Gamma_{\Sigma^{*-}}$	0.870 ± 0.015

Table 9.1 : The branching ratios of the K^{*0}, Λ, and Σ^{*-} to the decay channels that were studied in this analysis [8]. The K^{*0} branching ratio was determined as discussed in Section 3.1.

backgrounds and the CLAS acceptance can be performed to significantly reduce the systematic uncertainties on these cross section results, providing tighter constraints on the N^{*} resonance couplings to these channels.

9.1 $\gamma n \to K^{*0}\Lambda$ Differential Cross Section

The $\gamma n \to K^{*0}\Lambda$ differential cross section was calculated for each E_{γ}, $\cos(\theta_{K^{*0}})$ bin as:

$$\frac{d\sigma}{d\cos(\theta_{K^{*0}})}(E_{\gamma},\,\theta_{K^{*0}}) = \frac{1}{\Delta\cos(\theta_{K^{*0}})}\frac{A_r}{\rho L N_A}\frac{Y(E_{\gamma},\,\theta_{K^{*0}})Y_{\mathrm{CF}}}{\Phi(E_{\gamma})A(E_{\gamma},\,\theta_{K^{*0}})}\frac{\Gamma_{K^{*0}}}{\Gamma_{K^{*0}\to K^{+}\pi^{-}}}\frac{\Gamma_{\Lambda}}{\Gamma_{\Lambda\to p\pi^{-}}}, \qquad (9.1)$$

similar to Equation 7.6 for the $\gamma n \to p\pi^{-}$ reaction. E_{γ} is the photon energy, $\theta_{K^{*0}}$ is the angle between the K^{*0} and the photon in the center-of-mass frame, $\Delta\cos(\theta_{K^{*0}})$ is the width in $\cos(\theta_{K^{*0}})$ of the given bin, A_r is the atomic weight of the target, ρ is the target density, L is the target length, N_A is Avogadro's number, Φ is the photon flux in the given photon energy bin, Y is the experimental yield in the given bin, A is the simulated acceptance in the given bin, Y_{CF} is the yield correction factor, and the Γ fractions are the ratios of the total widths of the K^{*0} and Λ particles to the widths of the decay channels that were studied in this analysis. The inverses of these fractions are the branching ratios, and their values are given in Table 9.1. The values of the target factors are given in Table 7.2. Also, the substitution $d\Omega = 2\,\pi(d\cos(\theta_{K^{*0}}))$ was performed to yield the standard convention of published cross section results of the strangeness channels. The statistical uncertainty of the cross section was calculated for each bin by combining the statistical uncertainties of the experimental yield, simulated acceptance, and integrated photon flux in quadrature. The systematic uncertainties are discussed in Section 9.4, and the cross section results are tabulated in Appendix D.

The differential cross section of the $\gamma n \to K^{*0}\Lambda$ reaction from this analysis is shown in Figure 9.1

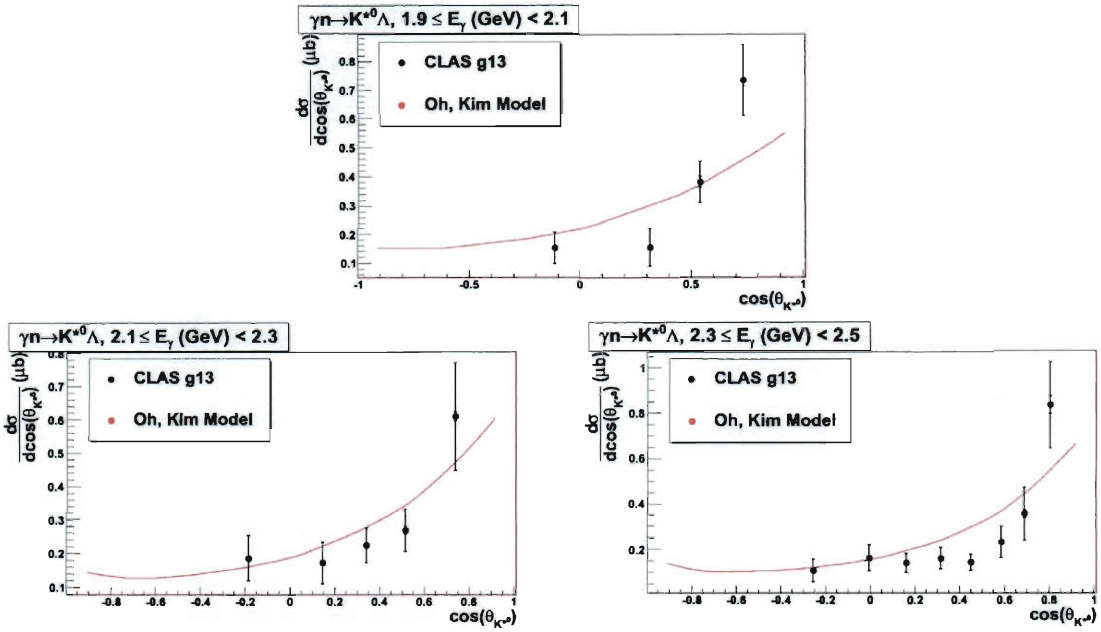

Figure 9.1 : The $\gamma n \to K^{*0}\Lambda$ differential cross section from the g13 experiment in different photon energy bins as a function of $\cos(\theta_{K^{*0}})$, where $\theta_{K^{*0}}$ is the angle between the K^{*0} and the photon in the center-of-mass frame. Also shown are the model predictions by Oh and Kim [68], linearly interpolated to the centers of these energy bins. The values of the g13 cross sections were averaged over the widths of their bins, are quoted at their bin centers, and do not include final-state interaction corrections. The backgrounds from events with an additional photon or π^0 in the final state were not subtracted, and had overall scale uncertainties of ~5.4%, ~15.0%, and ~18.0% for the different photon energy bins, listed in order of increasing photon energy. These uncertainties were added in quadrature with the other uncertainties. The statistical and total uncertainties of the g13 data are shown, but in some bins the statistical uncertainties are too small to be visible. Overall the model predictions were ~12.1% less than the g13 results, well within the g13 total uncertainties. However, these predictions were partially constrained by CLAS preliminary $\gamma p \to K^{*+}\Lambda$ total cross section data [75] that were too low by a factor of 1.5 [79, 78].

compared to the Oh and Kim model predictions detailed in Section 3.1 [68]. As mentioned in Section 3.1, there are no published cross section data for this reaction. The g13 results are the average cross section values within the given bins, quoted at the bin centers. These data are forward peaked and decrease rapidly with $\cos(\theta_{K^{*0}})$ until the mid-range angles, indicating that t-channel meson exchange is the dominant interaction process in this reaction. The cross section also decreases slightly with increasing photon energy, although the change is small compared to the uncertainties on the data.

Both the statistical and total uncertainties on the g13 cross section data are shown in Figure 9.1, but there were no quoted uncertainties on the predictions by Oh and Kim. The g13 results were not corrected for final-state interactions, or for background events with an additional photon or π^0

in the final state. The overall scale uncertainties for these backgrounds were ~5.4%, ~15.0%, and ~18.0% for the different photon energy bins, listed by increasing photon energy. These uncertainties are discussed in Section 9.4.1, and were combined into the systematic uncertainties by adding them in quadrature.

The statistical, systematic, and total uncertainty percentages of the g13 cross sections are shown in Figure 9.2. The statistical uncertainties varied from ~2.2% to ~6.5%, and as discussed in Section 8.4, the experimental yields were their largest source. The g13 systematic uncertainties ranged from ~16.6% to ~45.5%, and were typically greatest at large angles. There were several large sources of systematic uncertainty, including the background fits to the K^{*0} invariant mass peaks, the distribution of the simulated events for the acceptance calculations, and the Σ^{*-} overlap cuts. The total uncertainties were between ~16.9% and ~45.6%, and were dominated by the systematic uncertainties. The systematic uncertainties are discussed in more detail in Section 9.4, and should decrease significantly with future studies.

As discussed in Section 3.1, the cross section predictions of the Oh and Kim model were constrained by a preliminary total cross section measurement of the $\gamma p \to K^{*+}\Lambda$ reaction from CLAS [75]. These data were too low by a factor of 1.5 due to a scale error, so the cross section predictions of the $\gamma n \to K^{*0}\Lambda$ reaction are expected to increase when the model is updated. However, the scale and angular dependence of this increase are unknown.

The g13 results are consistent with the current model predictions within the uncertainties. The model predictions are on average ~25.2% less than the g13 results in the lowest photon energy bin, ~0.71% greater than g13 results in the middle photon energy bin, and ~2.0% less than the g13 results in the highest photon energy bin. Overall the model predictions are ~12.1% below the g13 data, within the ~16.9% and ~45.6% total uncertainties.

Both the g13 results and the model predictions increase slightly with photon energy. However, in each energy bin the g13 cross section changes more rapidly at forward angles than the model predictions. Although this may be due to a discrepancy with the predicted K^0 and κ t-channel contributions, the large uncertainties and coarse binning of the g13 data make this source difficult to determine. Also, the backgrounds from events with an additional photon or π^0 in the final state were not subtracted. These backgrounds were assigned as overall scale uncertainties, but they may have had a large angular dependence. These backgrounds are expected to be primarily $\gamma n \to K^{*0}\Sigma^0$

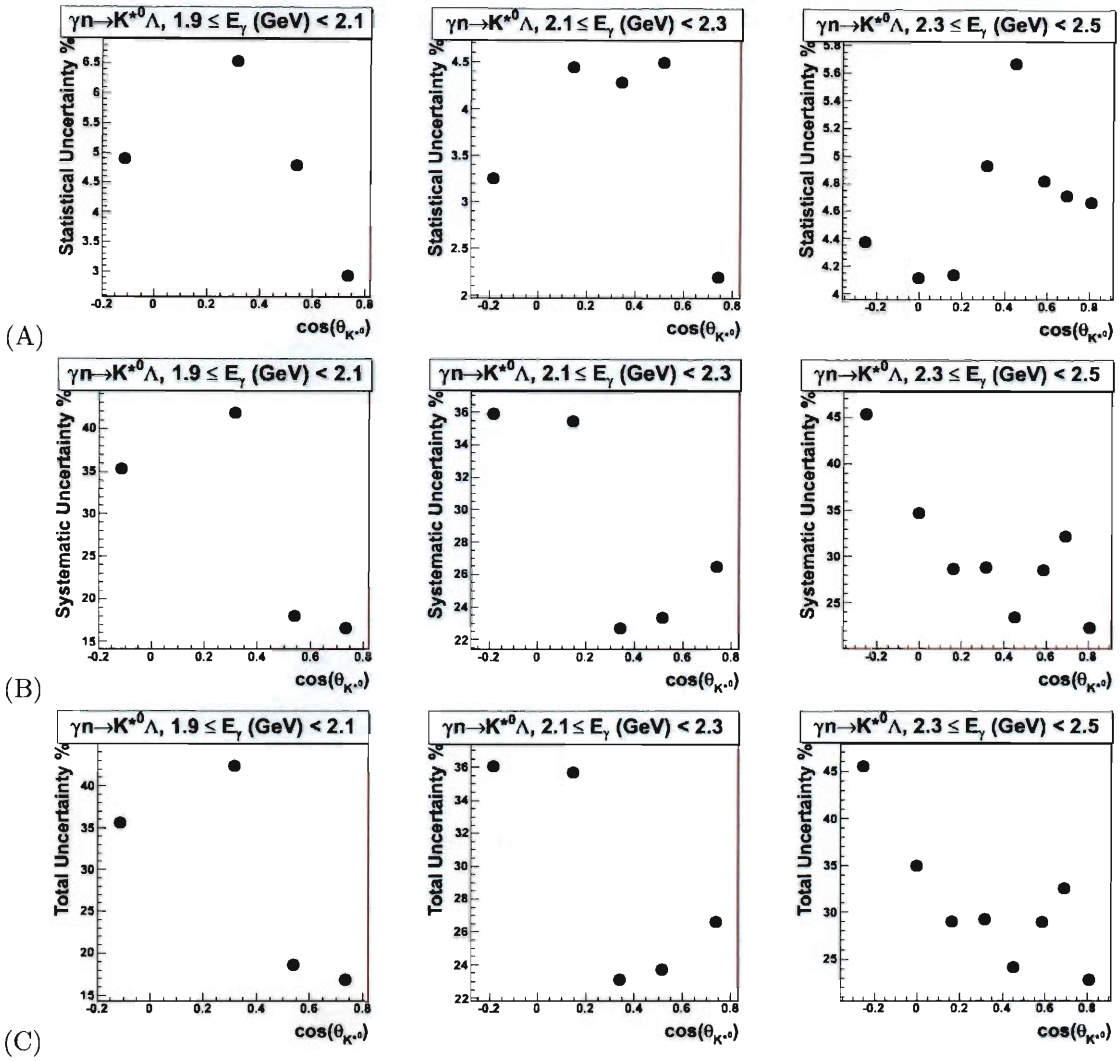

Figure 9.2 : The statistical (A), systematic (B), and total (C) uncertainties of the $\gamma n \to K^{*0}\Lambda$ differential cross section from the g13 experiment. The total uncertainties were dominated by the systematic uncertainties, which were greatest at large angles. The experimental yields were the largest source of the statistical uncertainties. The statistical uncertainties are discussed in more detail in Chapter 8, and the systematic uncertainties are discussed in Section 9.4.

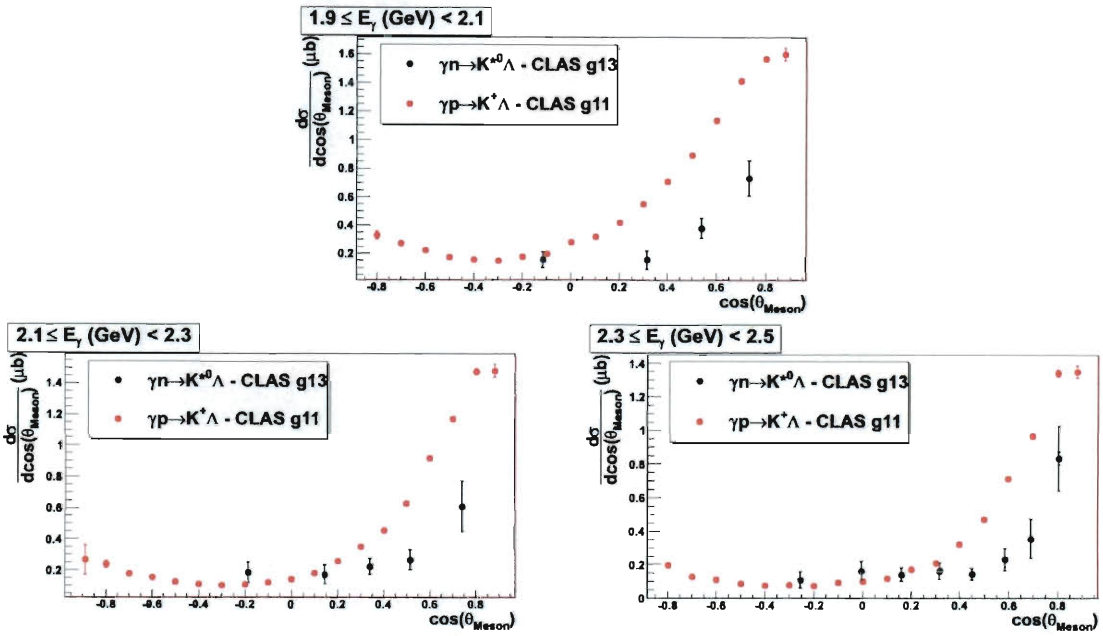

Figure 9.3 : A comparison of the g13 $\gamma n \to K^{*0}\Lambda$ cross section results with the published $\gamma p \to K^{+}\Lambda$ cross section data from the CLAS g11 experiment [118]. The $\gamma p \to K^{+}\Lambda$ cross section data were linearly interpolated to these photon energy bins. Both the statistical and total uncertainties are shown for the g13 data, and the total uncertainties are shown for the g11 data. Many of these uncertainties are too small to be visible. These results are shown as function of $\cos(\theta_{\text{Meson}})$, where θ_{Meson} is the angle between the meson and the photon in the center-of-mass frame. The similarity between these cross sections suggests that the $\gamma n \to K^{*0}\Lambda$ reaction needs to be included in coupled-channels analyses to extract the N^{*} resonances, which take rescattering effects into account.

events, but their angular distributions are unknown. There are no known differential cross section data or predictions of the $\gamma n \to K^{*0}\Sigma^{0}$ reaction.

To study the relative scale of the $\gamma n \to K^{*0}\Lambda$ cross section to that of the ground state $K\Lambda$ channel, the g13 data are compared against the $\gamma p \to K^{+}\Lambda$ cross section data from the CLAS g11 experiment [118] in Figure 9.3. The $\gamma p \to K^{+}\Lambda$ cross section data were linearly interpolated to the $\gamma n \to K^{*0}\Lambda$ photon energy bins. These cross sections are shown as a function of $\cos(\theta_{\text{Meson}})$, where θ_{Meson} is the angle between the meson and the photon in the center-of-mass frame. Although the mesons are different for the two reactions, this study is only meant to provide an approximate scale comparison of the cross sections. This reaction was chosen for comparison because there are no published cross section data on the $\gamma n \to K^{0}\Lambda$ reaction. An analysis of this cross section is currently being performed by Charles Taylor of Idaho State University on the g13 data.

In each photon energy bin, at $\cos(\theta_{\text{Meson}}) > 0.5$ the $\gamma p \to K^{+}\Lambda$ cross sections are 54% - 58%

greater than the $\gamma n \to K^{*0}\Lambda$ cross sections. At large angles these cross sections are more similar, and at $\cos(\theta_{\text{Meson}}) < 0.0$ the g13 $\gamma n \to K^{*0}\Lambda$ cross section data are larger in the two highest photon energy bins. However, the $\gamma n \to K^{*0}\Lambda$ scale uncertainties due to background events containing an additional photon or π^0 were large for these energy bins, so the exact difference between these cross sections is difficult to determine.

Although at the mid-range angles these cross sections are relatively similar, there is not enough information to determine whether the scale of the s-channel contributions from N^* resonances are similar at these energies. However as discussed in Section 2.4, hadronic rescattering can have a large effect on the measurements of the $\gamma N \to KY$ cross sections. The scale difference between the $\gamma p \to K^+\Lambda$ and $\gamma n \to K^{*0}\Lambda$ cross sections, especially at the mid-range angles, suggests that the $\gamma n \to K^{*0}\Lambda$ reaction needs to be included in the coupled-channels analyses used for the extraction of the N^* resonance parameters.

These $\gamma n \to K^{*0}\Lambda$ results are the first cross section measurements of this reaction, and can be analyzed to provide information on the N^* resonances. Future studies, such as background modeling and additional CLAS acceptance studies, will significantly reduce the systematic uncertainties on these data. As discussed in Section 9.4, the total uncertainties may decrease to about 10% to 20%. Updated model predictions of this reaction can be used to study the possible contributions of the N^* resonances to this reaction. The similarity of the scales of the $\gamma n \to K^{*0}\Lambda$ and $\gamma p \to K^+\Lambda$ cross sections suggest that rescattering to the K^*Y channels may be significant. These cross section data can be used in coupled-channels analyses to determine whether the predicted $N\frac{3}{2}^-(1960)$, $N\frac{1}{2}^+(2065)$, and $N\frac{5}{2}^-(2080)$ resonances contribute to the $\gamma n \to K^{*0}\Lambda$ reaction.

9.2 $\gamma n \to K^+\Sigma^{*-}$ Differential Cross Section

The differential cross section of the $\gamma n \to K^+\Sigma^{*-}$ reaction was calculated for each E_γ, $\cos(\theta_{K^+})$ bin as:

$$\frac{d\sigma}{d\cos(\theta_{K^+})}(E_\gamma, \theta_{K^+}) = \frac{1}{\Delta\cos(\theta_{K^+})} \frac{A_r}{\rho L N_A} \frac{Y(E_\gamma, \theta_{K^+}) Y_{\text{CF}}}{\Phi(E_\gamma) A(E_\gamma, \theta_{K^+})} \frac{\Gamma_{\Sigma^{*-}}}{\Gamma_{\Sigma^{*-}\to\Lambda\pi^-}} \frac{\Gamma_\Lambda}{\Gamma_{\Lambda\to p\pi^-}}, \tag{9.2}$$

similar to Equation 9.1 for the $\gamma n \to K^{*0}\Lambda$ reaction. θ_{K^+} is the angle between the K^+ and the

photon in the center-of-mass frame, and the values of the branching ratios are given in Table 9.1. The statistical uncertainties were calculated by combining the statistical uncertainties of the experimental yield, simulated acceptance, and integrated photon flux in quadrature. The systematic uncertainties are detailed in Section 9.4, and the cross section results are tabulated in Appendix D.

The differential cross section of the $\gamma n \to K^{+}\Sigma^{*-}$ reaction from this analysis is shown in Figure 9.4 compared with the LEPS results [74], the Oh, Ko, and Nakayama model predictions [69, 78], and the preliminary results from the CLAS eg3 experiment [117, 119]. Both statistical and total uncertainties are shown for the g13 data. No uncertainties were quoted for the model predictions, and the systematic uncertainties of the eg3 results have not yet been determined. As mentioned in Section 3.2, the LEPS results are the only published cross section data for this reaction.

All of the experimental cross section results are the average values of the cross section in their given bins, shown at their bin centers. The LEPS, eg3, and predicted cross sections were quoted in different energy bins, so their values were linearly interpolated to the centers of these energy bins. However, the 1.8 GeV eg3 data were linearly extrapolated by 75 MeV, and the 2.4 GeV LEPS data were linearly extrapolated by 50 MeV. These cross sections are largest at forward angles, and decrease gradually at large angles and with increasing photon energy. None of the experimental results were corrected for final-state interactions, and the g13 data still contain some background events with an additional photon or π^0 in the final state. The overall scale uncertainties for these backgrounds were ~4.8%, ~6.8%, ~4.0%, ~4.2%, and ~5.4% for the different photon energy bins, in the order of increasing photon energy. These backgrounds are discussed in Section 9.4.1, and these scale uncertainties were grouped into the systematic uncertainties by adding them in quadrature.

Figure 9.5 shows the statistical and systematic uncertainties of the g13 $\gamma n \to K^{+}\Sigma^{*-}$ cross section data. The statistical uncertainties of the g13 results varied from ~1.6% to ~6.9%, and were largest for the lowest two photon energy bins. As discussed in Section 8.4, the statistical uncertainties of the experimental yields were larger than the statistical uncertainties on the simulated acceptance and the integrated photon flux. The g13 systematic uncertainties ranged from ~16.3% to ~31.3%, and were greatest at large angles. The largest sources of the systematic uncertainties were the simulated CLAS acceptance and the Σ^{*-} background fits, and are discussed in more detail in Section 9.4. Figure 9.6 shows the total uncertainties of the g13 cross section, which were between ~16.4% and ~32.0% and were dominated by the systematic uncertainties.

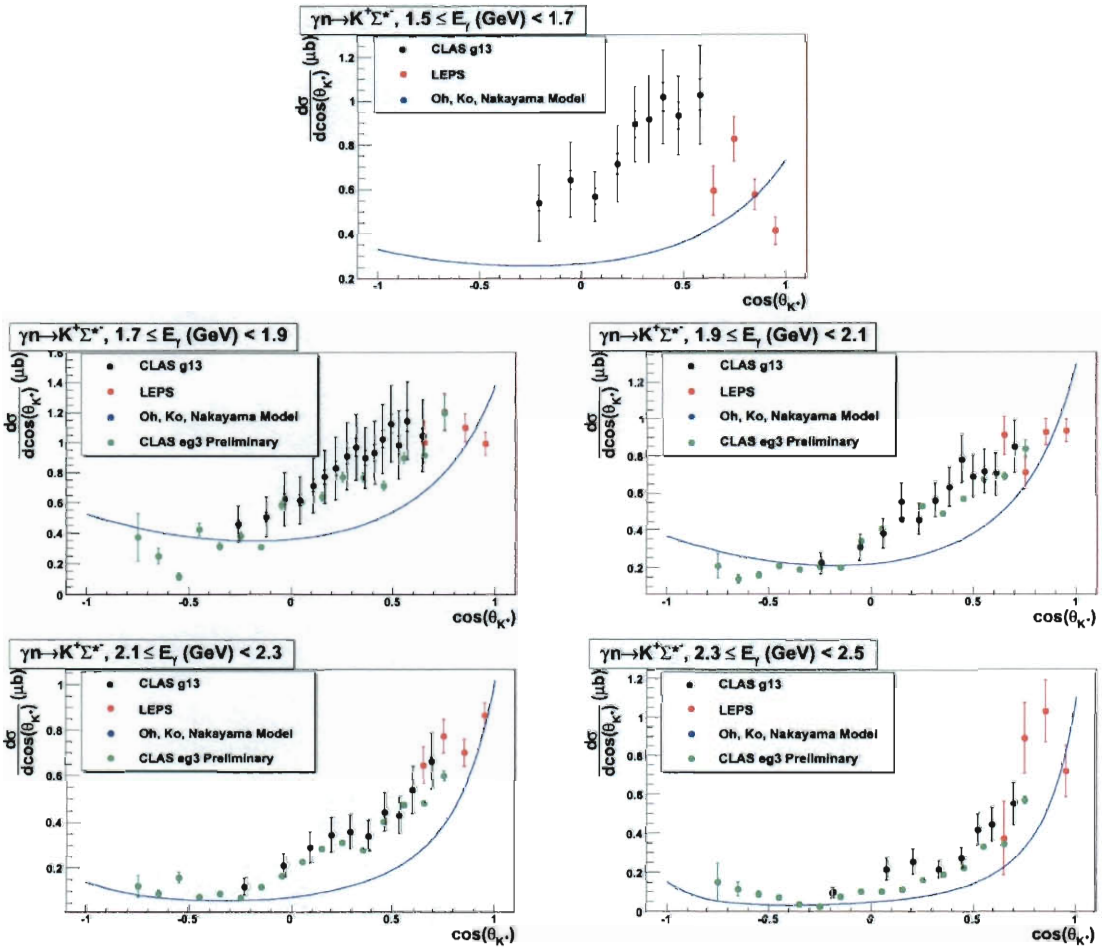

Figure 9.4 : The $\gamma n \to K^{+}\Sigma^{*-}$ differential cross section from the g13 experiment in different photon energy bins as a function of $\cos(\theta_{K^+})$, where θ_{K^+} is the angle between the K^+ and the photon in the center-of-mass frame. Also shown are the published LEPS data [74], the Oh, Ko, and Nakayama model predictions [69, 78], and the preliminary CLAS eg3 results [117, 119]. Each plot is of a different photon energy bin, extending from 1.5 GeV to 2.5 GeV. The values of the experimental cross sections were averaged over the widths of their bins, were quoted at their bin centers, and do not include final-state interaction corrections. The backgrounds from events with an additional photon or π^0 in the final state were not subtracted from the g13 data, and have overall scale uncertainties of ~4.8%, ~6.8%, ~4.0%, ~4.2%, and ~5.4% for the different photon energy bins, in order of increasing photon energy. The values of the LEPS, eg3, and the predicted cross sections were either linearly interpolated or extrapolated to the centers of these energy bins. For the g13 data the statistical and total uncertainties are shown, for the eg3 data only the statistical uncertainties are shown, and no uncertainties on the model predictions were quoted. In some bins, the statistical uncertainties on these data are too small to be visible.

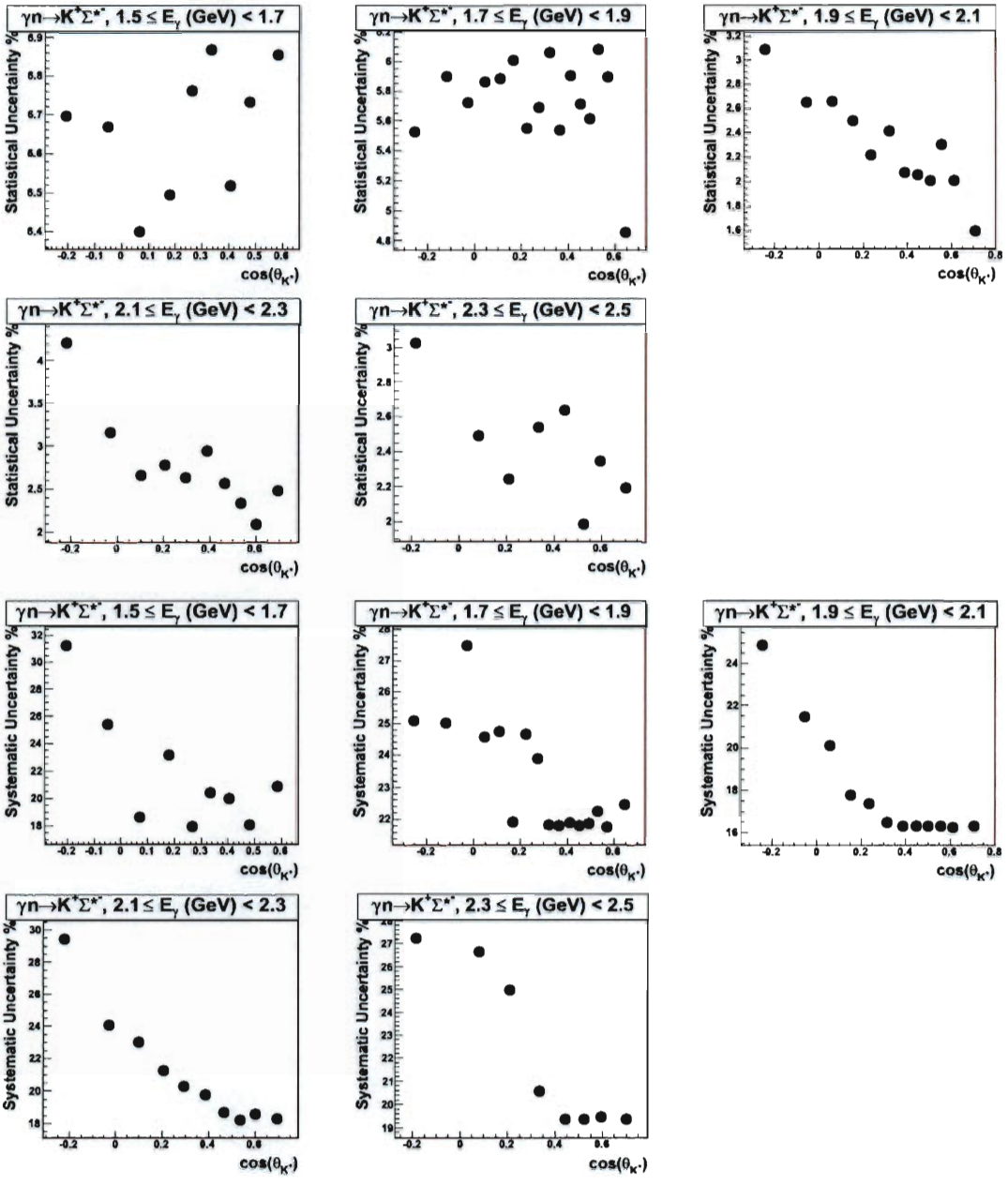

Figure 9.5 : The statistical (A) and systematic (B) uncertainties of the $\gamma n \to K^{+}\Sigma^{*-}$ differential cross section from the g13 experiment. The experimental yields were the largest source of the statistical uncertainties, and the simulated CLAS acceptance and the Σ^{*-} background fits were the largest sources of the systematic uncertainties. The systematic uncertainties were typically greatest at large angles, and are discussed in more detail in Section 9.4.

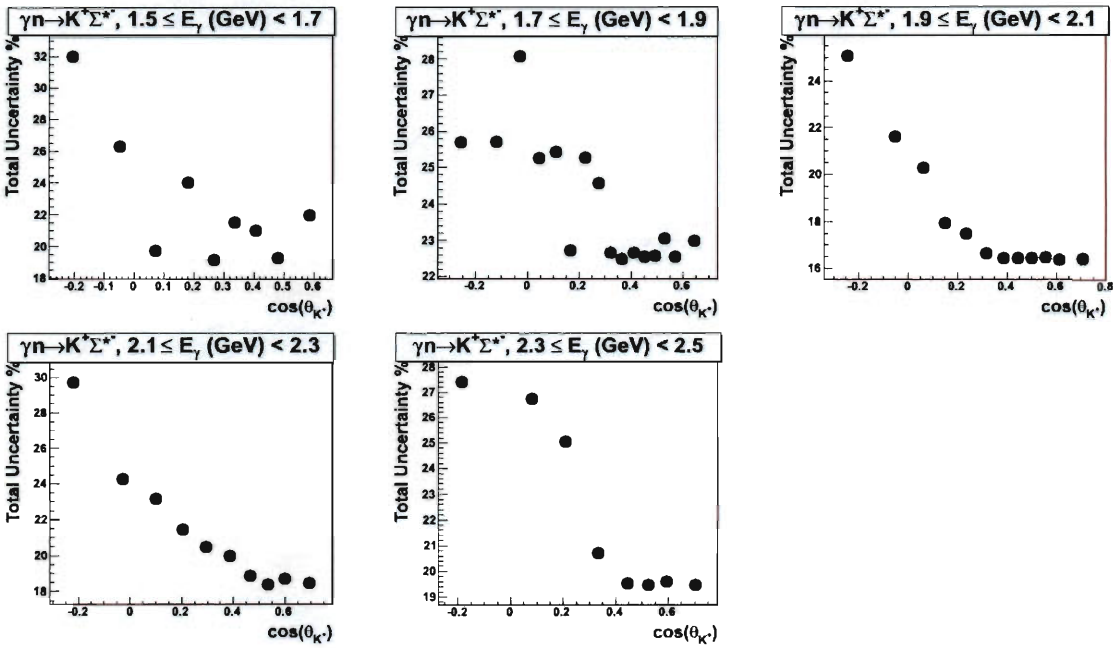

Figure 9.6 : The total uncertainties of the $\gamma n \to K^{+}\Sigma^{*-}$ differential cross section from the g13 experiment. The total uncertainties were dominated by the systematic uncertainties, but should decrease significantly with future studies of the backgrounds and the CLAS acceptance.

For the majority of their overlap, the g13 and preliminary eg3 results show very good agreement. The eg3 data are on average ~18.4% less than the g13 results, but are ~32.2% less in the 2.3 GeV to 2.5 GeV photon energy bin. These differences are much larger than the ~5% scaling uncertainties due to the backgrounds from events containing an additional photon or π^0 in the final state. The sources of these differences are still being investigated, but the results are consistent within their uncertainties for the majority of the data. The differences between the g13 and preliminary eg3 data will be more fully understood when the systematic uncertainties on the eg3 results have been determined. Also, the eg3 data extend further back in $\cos(\theta_{K^+})$ than the g13 data due to the rejection of the back-angle, multiplexed scintillator paddles in the g13 analysis, as discussed in Section 6.2.5. Because the eg3 experiment ran several years prior to g13, the TOF PMTs did not exhibit aging inefficiencies as strongly as in the g13 experiment.

Except for the 1.5 GeV to 1.7 GeV photon energy bin, the g13 data matches the LEPS results within their uncertainties. At $\cos(\theta_{K^+}) = 0.65$ in this photon energy bin, the linearly extrapolated g13 cross section is ~80.8% larger than the LEPS cross section. Although the source of this difference is unknown, the differences between the cross sections at $\cos(\theta_{K^+}) = 0.65$ in the other photon

energy bins are small compared to their uncertainties. The differences between the LEPS and the preliminary eg3 results are largest in the two highest photon energy bins, but cannot be fully qualified without the systematic uncertainties on the eg3 data.

There are significant differences between the cross section predictions by Oh, Ko, and Nakayama and the experimental results. The model predictions are on average ~56.5% less than the g13 cross sections, and are well outside of the uncertainties of the g13 data at all photon energies for the majority of the angular range. Only at the back-most angles are some of the differences within the g13 uncertainties, although no uncertainties on the model predictions were quoted. The eg3 preliminary cross sections are significantly larger than the predictions back to around $\cos(\theta_{K^+}) = -0.15$, although without the systematic uncertainties the significance of these differences is difficult to determine. Even though final-state interaction corrections were not performed on the experimental data, they are expected to be small relative to the size of the uncertainties [120].

As discussed in Section 3.2, these phenomenological predictions were primarily constrained by a preliminary total cross section measurement of the $\gamma p \rightarrow K^{+}\Sigma^{*0}$ reaction [75] and SU(3) flavor symmetry transformations of the interaction vertex coupling constants. Without differential cross section data it is more difficult to predict the amplitudes of the different s-, t-, and u-channel interaction contributions to the $\gamma n \rightarrow K^{+}\Sigma^{*-}$ reaction. Also, while the inclusion of several of the predicted N^* and Δ^* resonances allowed the predictions to largely reproduce the preliminary $\gamma p \rightarrow K^{+}\Sigma^{*0}$ total cross section measurement, the $K\Sigma^*$ couplings may be different for the excited states of the proton and the neutron.

Additional analyses are needed to quantify the source of the disagreements between the experimental results and the predictions. A partial-wave analysis is necessary to determine which N^* and Δ^* resonances may have contributed to these results. However, the large differences at the forward angles are likely due to incorrect modeling of the t-channel meson exchange, rather than the contribution of any additional resonances.

As discussed in Section 2.4, rescattering effects can have a substantial effect on the measured cross sections. For comparison, the published cross sections of the $\gamma n \rightarrow K^{+}\Sigma^{-}$ reaction from the CLAS g10 experiment [121] are shown with the g13 and LEPS $\gamma n \rightarrow K^{+}\Sigma^{*-}$ cross section measurements in Figure 9.7. To perform the comparison, the $\gamma n \rightarrow K^{+}\Sigma^{-}$ cross section data were linearly interpolated to the $\gamma n \rightarrow K^{+}\Sigma^{*-}$ photon energy bins. The cross sections shown in this figure are similar in scale,

except the $\gamma n \to K^+\Sigma^-$ cross section is significantly larger than the $\gamma n \to K^+\Sigma^{*-}$ cross section at the forward angles of the two highest photon energy bins. At $\cos(\theta_{K^+}) > 0.4$ for the 2.1 GeV to 2.3 GeV and 2.3 GeV to 2.5 GeV photon energy bins, the $\gamma n \to K^+\Sigma^-$ cross section is ~61.8% and ~80.4% larger than the g13 cross section, respectively, and ~48.3% and ~25.6% larger than the LEPS cross section, respectively.

However at $\cos(\theta_{K^+}) < 0.4$, the $\gamma n \to K^+\Sigma^-$ cross section data are overall ~13.2% less than the g13 $\gamma n \to K^+\Sigma^{*-}$ results. This difference is largest in the 1.7 GeV to 1.9 GeV photon energy bin, where the $\gamma n \to K^+\Sigma^-$ results are ~28.4% less than the g13 data. As discussed in Section 9.1 for the $\gamma n \to K^{*0}\Lambda$ analysis, the similarities between the scale of these results indicates that the $\gamma n \to K^+\Sigma^{*-}$ data cannot be excluded from full-coupled-channels analyses used for extracting the N^* resonance parameters.

Also, these $\gamma n \to K^+\Sigma^{*-}$ cross section results from the 2.655 GeV portion of g13a are compared against those from the 1.990 GeV data in Figure 9.8. These 1.990 GeV data were not included in the analysis due to their low statistics. As discussed in Chapter 6, the 1.990 GeV data were split up into two separate run ranges due to run-dependence of the acceptance of the scintillator paddles and tagger counters. Cross sections were only available below 1.9 GeV for these runs because the photon tagger was only capable of tagging photons with energies up to ~95% of the electron beam energy, which for these data was ~1.89 GeV. These cross sections were calculated using the same analysis cuts as the 2.655 GeV data. Only the statistical uncertainties were determined for the 1.990 GeV data, but their cross sections are well within the total uncertainties of the 2.655 GeV data. This agreement indicated that the run-dependent aspects of this analysis, such as the integrated photon flux and the CLAS acceptance, were determined consistently within the uncertainties.

The g13 $\gamma n \to K^+\Sigma^{*-}$ cross sections from this analysis, along with the preliminary results from the CLAS eg3 experiment, are the first data on this reaction with large angular coverage. The large difference between these data and the model predictions of Oh, Ko, and Nakayama indicate that these data can be used to provide a better understanding of the production mechanisms of these interactions. The similar scale of the $\gamma n \to K^+\Sigma^{*-}$ and $\gamma n \to K^+\Sigma^-$ cross sections indicates that rescattering to the KY^* channels may have a significant effect. These rescattering effects can be taken into account with a coupled-channels analysis, which can be used to study the couplings of the N^* and Δ^* resonances to the $\gamma n \to K^+\Sigma^-$ cross section.

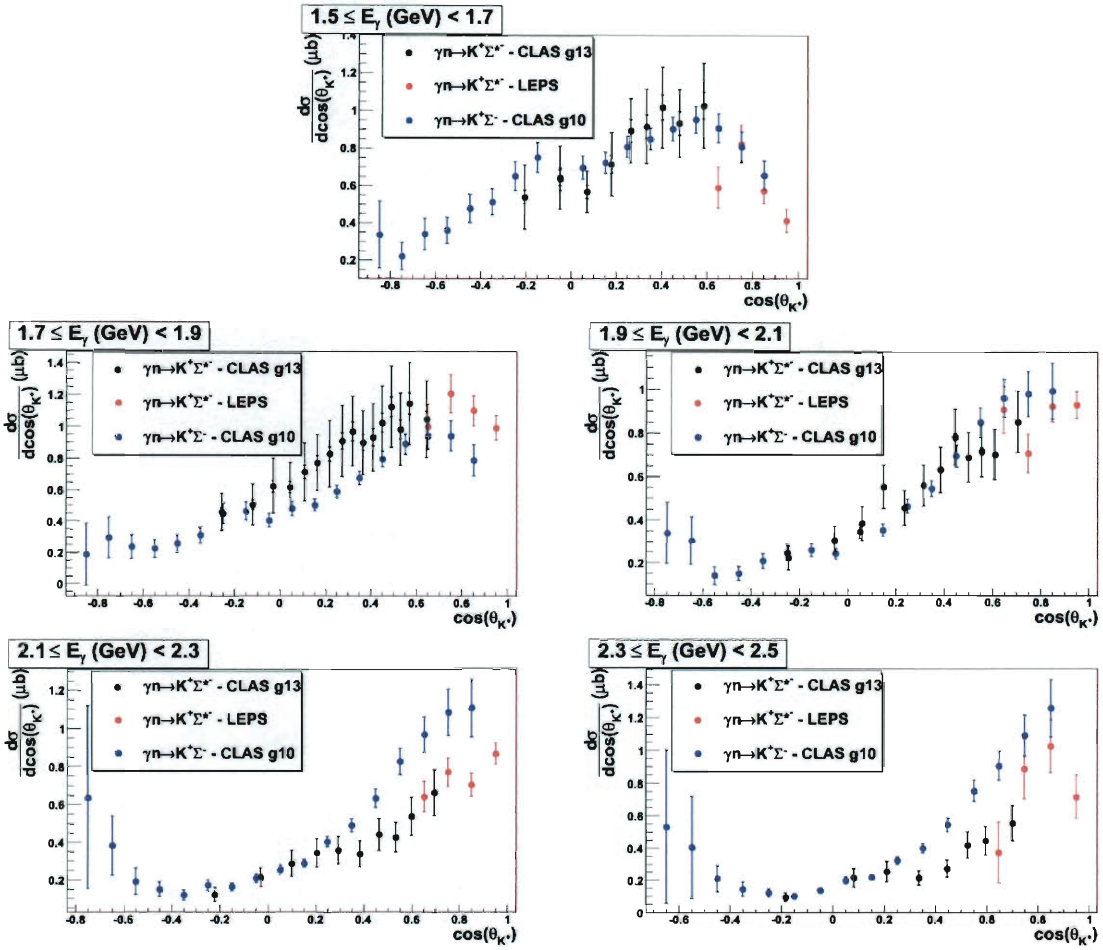

Figure 9.7 : A comparison of the g13 and LEPS [74] $\gamma n \to K^+\Sigma^{*-}$ cross section results with the published $\gamma n \to K^+\Sigma^-$ cross section data from the CLAS g10 experiment [121]. The LEPS and g10 cross section data were linearly interpolated or extrapolated to these photon energy bins. Both the statistical and total uncertainties are shown for the g13 data, but some of the statistical uncertainties are too small to be visible. These results are shown as a function of $\cos(\theta_{K^+})$, where θ_{K^+} is the angle between the K^+ and the photon in the center-of-mass frame. The similarity between these cross sections suggests that the $\gamma n \to K^+\Sigma^{*-}$ reaction needs to be included in the coupled-channels analyses used to extract the N^* resonances, which take rescattering effects into account.

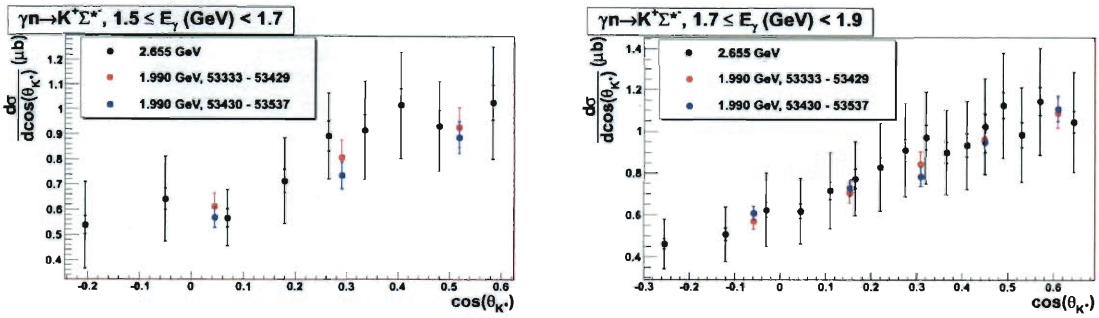

Figure 9.8 : Comparison of the $\gamma n \to K^{+}\Sigma^{*-}$ cross sections from the different portions of the g13a dataset. The 2.655 GeV data were used for this analysis, and the cross sections of the 1.990 GeV data were calculated to study the run-dependence of these cross section results. Both the statistical and total uncertainties are shown for the 2.655 GeV data, but only the statistical uncertainties are shown for the 1.990 GeV data. The agreement between these cross sections indicates that the run-dependent effects of this analysis were determined consistently within the uncertainties.

9.3 Reaction Overlap Studies

As discussed in Chapter 3, because the $\gamma n \to K^{*0}\Lambda$ and $\gamma n \to K^{+}\Sigma^{*-}$ reactions have the same particles in the final state, there may be an amplitude-level interference between these reactions. As discussed in Section 8.2, events within $\pm 1\Gamma$ of the K^{*0} and Σ^{*-} invariant masses were cut to remove the majority of the overlap between the $\gamma n \to K^{*0}\Lambda$ and $\gamma n \to K^{+}\Sigma^{*-}$ reactions. To study the degree of potential interference between these reactions, the $\gamma n \to K^{*0}\Lambda$ and $\gamma n \to K^{+}\Sigma^{*-}$ cross sections were calculated with different sets of overlap cuts.

Figure 9.9 shows the $\gamma n \to K^{*0}\Lambda$ cross section with the nominal $\pm 1\Gamma$ Σ^{*-} overlap cuts, compared to the cross sections calculated with $\pm 0.5\Gamma$ and $\pm 1.5\Gamma$ Σ^{*-} overlap cuts. These cuts removed the central ~70.5%, 50.0%, and ~79.5% regions of the fit Σ^{*-} Breit-Wigner functions, respectively. In the figure the nominal, $\pm 1\Gamma$ overlap cut data are shown with both the statistical and total uncertainties, but some of the statistical uncertainties are too small to be visible. The other cross sections are offset by 0.01 in $\cos(\theta_{K^{*0}})$ for clarity, and are shown with only their statistical uncertainties. The average percentage differences between these cross sections in each photon energy bin are listed in Table 9.2.

Except for the 1.9 GeV to 2.1 GeV photon energy bin, the average percentage differences between these cross sections are all less than 7%. In this photon energy bin, the $\pm 0.5\Gamma$ Σ^{*-} overlap cut cross sections are on average ~15.6% and ~17.9% greater than the $\pm 1\Gamma$ and $\pm 1.5\Gamma$ Σ^{*-} overlap cut cross sections, respectively. However as shown in Section 9.4.5, there were large systematic uncertainties

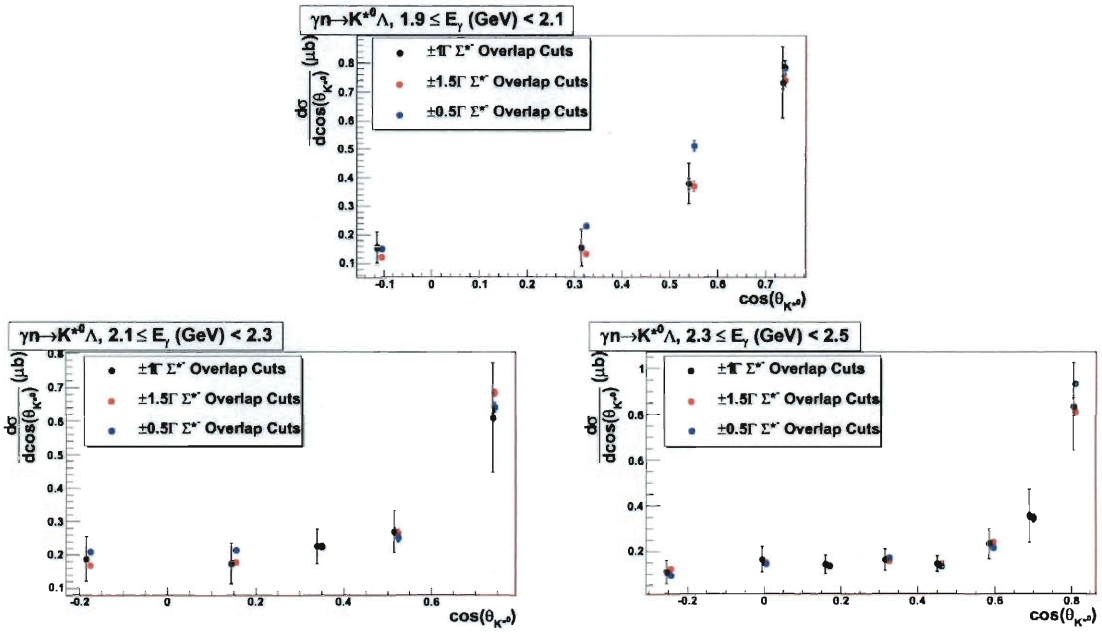

Figure 9.9 : Comparison between the $\gamma n \to K^{*0}\Lambda$ cross sections calculated with different Σ^{*-} overlap cuts. The nominal, $\pm 1\Gamma$ Σ^{*-} overlap cut data are shown with both statistical and total uncertainties, and the other cross sections are shown with only their statistical uncertainties. These other cross sections are shown offset by 0.01 in $\cos(\theta_{K^{*0}})$, and some of the statistical uncertainties are smaller than the data points. The average differences between these cross sections were on average less than the combined average systematic uncertainties on the analysis steps that were performed separately for these cross sections.

E_γ (GeV)	$\pm 0.5\Gamma$ vs. $\pm 1\Gamma$ Σ^{*-} Cuts	$\pm 1.5\Gamma$ vs. $\pm 1\Gamma$ Σ^{*-} Cuts	$\pm 0.5\Gamma$ vs. $\pm 1.5\Gamma$ Σ^{*-} Cuts
1.9 - 2.1	$C_{\pm 0.5\Gamma} \approx 15.6\% > C_{\pm 1\Gamma}$	$C_{\pm 1.5\Gamma} \approx 4.65\% < C_{\pm 1\Gamma}$	$C_{\pm 0.5\Gamma} \approx 17.9\% > C_{\pm 1.5\Gamma}$
2.1 - 2.3	$C_{\pm 0.5\Gamma} \approx 2.02\% > C_{\pm 1\Gamma}$	$C_{\pm 1.5\Gamma} \approx 0.22\% < C_{\pm 1\Gamma}$	$C_{\pm 0.5\Gamma} \approx 0.17\% > C_{\pm 1.5\Gamma}$
2.3 - 2.5	$C_{\pm 0.5\Gamma} \approx 2.71\% < C_{\pm 1\Gamma}$	$C_{\pm 1.5\Gamma} \approx 2.27\% < C_{\pm 1\Gamma}$	$C_{\pm 0.5\Gamma} \approx 6.31\% > C_{\pm 1.5\Gamma}$

Table 9.2 : The average differences between the $\gamma n \to K^{*0}\Lambda$ cross sections with different Σ^{*-} overlap cuts, where C is the cross section. These differences were all less than the combined average systematic uncertainties on the analysis steps that were performed separately for these cross sections.

on both the background fits and yield cuts of the K^{*0} invariant mass distributions. Other than the Σ^{*-} overlap cuts, these were the only steps of the analysis that were performed separately for these cross sections. For the nominal cross sections, the combined average uncertainties on these analysis steps were ~22.1%, ~14.0%, and ~13.9% for the different photon energy bins, listed in order of increasing photon energy. The average differences between these cross sections are well within the average of these systematic uncertainties. Therefore, no interference effects between the $\gamma n \to K^{*0}\Lambda$ and $\gamma n \to K^{+}\Sigma^{*-}$ reactions on the $\gamma n \to K^{*0}\Lambda$ cross section were observed beyond these uncertainties.

The $\gamma n \to K^{+}\Sigma^{*-}$ cross sections shown in Figure 9.10 were calculated with $\pm 1\Gamma$ and $\pm 2\Gamma$ K^{*0} overlap cuts, as well as with the K^{*0} overlap cuts removed. As discussed in Section 8.2, the K^{*0} overlap cuts were only performed at photon energies greater than 1.9 GeV. The $\pm 2\Gamma$ K^{*0} overlap cut removed the central ~84.4% region of the fit K^{*0} Breit-Wigner functions. The significantly larger statistics of the $\gamma n \to K^{+}\Sigma^{*-}$ allowed reliable fits to the invariant mass distributions for a broader range of overlap cuts than were possible for the $\gamma n \to K^{*0}\Lambda$ analysis. The nominal, $\pm 1\Gamma$ K^{*0} overlap cut cross section is shown with both the statistical and total uncertainties. The other cross sections are shown with only their statistical uncertainties, and are offset by 0.01 in $\cos(\theta_{K^+})$ for clarity.

Table 9.3 shows the average percentage differences between the $\gamma n \to K^{+}\Sigma^{*-}$ cross sections with different K^{*0} overlap cuts for each photon energy bin. These average differences are all less than 4%, within the combined average systematic uncertainties of the background fits and yield cuts of the Σ^{*-} invariant mass distributions. The combination of these uncertainties ranged between ~4.0% and ~12.7%, and these uncertainties are discussed in more detail in Section 9.4.4. These uncertainties represent the only analysis steps that were performed separately for these cross sections, other than K^{*0} overlap cuts. If there were any interference effects between the $\gamma n \to K^{*0}\Lambda$ and $\gamma n \to K^{+}\Sigma^{*-}$ reactions on the $\gamma n \to K^{+}\Sigma^{*-}$ cross section, they were on average less than these systematic uncertainties.

9.4 Systematic Uncertainty Studies

Many different studies were performed to determine the systematic uncertainties associated with these measurements of the $\gamma n \to K^{*0}\Lambda$ and $\gamma n \to K^{+}\Sigma^{*-}$ cross sections. These studies were

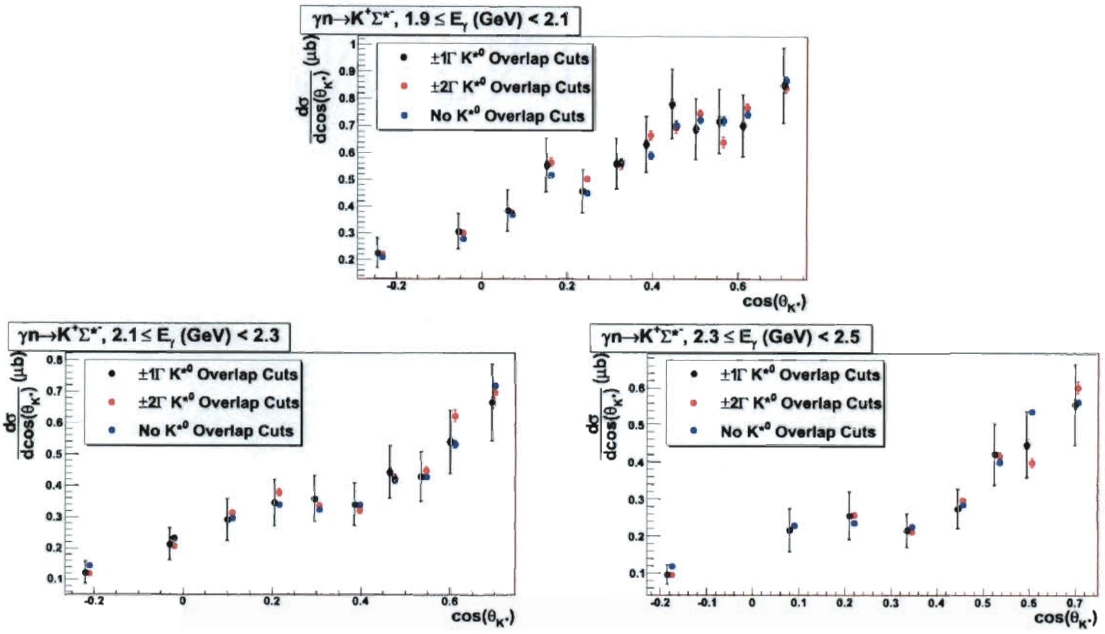

Figure 9.10 : Comparison between the $\gamma n \to K^{+}\Sigma^{*-}$ cross sections calculated with different K^{*0} overlap cuts. The nominal, $\pm 1\Gamma$ K^{*0} overlap cut data are shown with both statistical and total uncertainties, and the other cross sections are shown with only their statistical uncertainties. The other cross sections are shown offset by 0.01 in $\cos(\theta_{K^{+}})$, and some of the statistical uncertainties are smaller than the data points. The average differences between these cross sections were on average less than the combined average systematic uncertainties on the analysis steps that were performed separately for these cross sections.

E_γ (GeV)	None vs. $\pm 1\Gamma$ K^{*0} Cuts	$\pm 2\Gamma$ vs. $\pm 1\Gamma$ K^{*0} Cuts	None vs. 2Γ K^{*0} Cuts
1.9 - 2.1	$C_{\text{None}} \approx 2.34\% < C_{\pm 1\Gamma}$	$C_{\pm 2\Gamma} \approx 0.39\% < C_{\pm 1\Gamma}$	$C_{\text{None}} \approx 3.11\% < C_{\pm 2\Gamma}$
2.1 - 2.3	$C_{\text{None}} \approx 0.11\% > C_{\pm 1\Gamma}$	$C_{\pm 2\Gamma} \approx 1.65\% > C_{\pm 1\Gamma}$	$C_{\text{None}} \approx 2.63\% < C_{\pm 2\Gamma}$
2.3 - 2.5	$C_{\text{None}} \approx 3.54\% > C_{\pm 1\Gamma}$	$C_{\pm 2\Gamma} \approx 0.37\% < C_{\pm 1\Gamma}$	$C_{\text{None}} \approx 1.63\% > C_{\pm 2\Gamma}$

Table 9.3 : The average differences between the $\gamma n \to K^{+}\Sigma^{*-}$ cross sections with different K^{*0} overlap cuts, where C is the cross section. These differences were all less than the combined average systematic uncertainties on the analysis steps that were performed separately for these cross sections.

categorized as either CLAS acceptance studies, final-state identification studies, or yield extraction studies. These studies are detailed in the following subsections, and are summarized in Tables 9.4 and 9.5 for the $\gamma n \to K^{+}\Sigma^{*-}$ and $\gamma n \to K^{*0}\Lambda$ analyses, respectively. Also shown in these tables are the systematic uncertainties on the branching ratios, target factors, and photon flux, as well as a summary of the overall statistical, systematic, and total uncertainties. The systematic uncertainty percentages of the photon flux and target density were not determined for the g13 experiment. Instead, the uncertainties from the studies of the CLAS g1c experiment [112] were used as representative values until these studies are performed for g13.

For each systematic uncertainty study, the uncertainties were determined by first calculating the cross sections with either different procedures or with tighter cuts. The systematic uncertainties were then calculated for each study by comparing these cross sections to the cross sections calculated with the nominal cuts and procedures, using Equation 7.7. For the $\gamma n \to K^{+}\Sigma^{*-}$ studies that did not exhibit a systematic angular dependence, the overall uncertainties of each photon energy bin were assigned to each of the individual angular bins. These overall uncertainties were again calculated using Equation 7.7, but with the sums over all of the points in the given photon energy bin. This assumed that the source of the systematic uncertainties was θ-independent, and that the uncertainties of the individual points were Gaussian distributed about their true uncertainties. However, individual points that caused a greater than 50% change in the overall uncertainty percentage of their energy bin were not included in these overall percentages, and were instead assigned their individual uncertainties. The only $\gamma n \to K^{+}\Sigma^{*-}$ systematic uncertainty study with a large angular dependence was the generated simulation distribution study, which is discussed in Section 9.4.2.

Due to the similarities between the cross section analyses, many of the studies of the $\gamma n \to K^{+}\Sigma^{*-}$ systematic uncertainties were used to set the $\gamma n \to K^{*0}\Lambda$ systematic uncertainties. These included all of the CLAS acceptance studies except for the simulation distribution study, all of the final-state identification studies, and the spectator proton missing mass cut study. These steps of the analyses were performed similarly for both reactions, so within each photon energy bin it was assumed that the overall systematic uncertainties were the same for both cross sections. These uncertainty assignments can be cross-checked by performing these studies separately for the $\gamma n \to K^{*0}\Lambda$ analysis. In the $\gamma n \to K^{*0}\Lambda$ analysis-specific uncertainty studies, each point was assigned its individual uncertainty percentage due to the small number of bins, rather than the average

Category	Source	Study	$\sim\sigma$ Range
CLAS Acceptance	π^- Momentum Cut	100 vs. 150 (MeV/c)	3.2% - 5.4%
	p & K^+ Momentum Cuts	400 vs. 450 (MeV/c)	0.33% - 0.53%
	Fiducial Cuts	0.02 rad Tighter	1.7% - 6.2%
	Trigger Simulation	K^+, No Simulation	2.3% - 3.4%
	Simulation Distribution	t-slope vs. Model [69]	θ: 0.19% - 23.1%
Final-State Identification	Particle Identification Cuts	$\pm3\sigma$ vs. $\pm2\sigma$	3.6% - 7.4%
	Time Difference Cuts	$\pm3\sigma$ vs. $\pm2\sigma$	5.0% - 9.3%
	Λ Invariant Mass Cuts	$\pm3\sigma$ vs. $\pm2\sigma$	4.4% - 6.6%
	Missing Momentum Cut	200 vs. 150 (MeV/c)	2.0% - 3.6%
Yield Extraction	p Missing Mass Cuts	$\pm3\sigma$ vs. $\pm2\sigma$	2.7% - 6.5%
	K^{*0} Overlap Cuts	$\pm1\Gamma$ vs. $\pm2\Gamma$	3.8% - 5.6%
	Σ^{*-} Background Fits	Function Type	3.3% - 15.4%
	Σ^{*-} Invariant Mass Cuts	$\pm2\Gamma$ vs. $\pm1\Gamma$	1.4% - 2.8%
	γ, π^0 Background	Sideband Yield	4.0% - 6.8%
Miscellaneous	Photon Flux	Reference [112]	1.8%
	Target Length	Reference [92]	0.025%
	Target Density	Reference [112]	0.11%
	$\Gamma_{\Sigma^{*-}\to\Lambda\pi^-}/\Gamma_{\Sigma^{*-}}$	Reference [8]	1.72%
	$\Gamma_{\Lambda\to p\pi^-}/\Gamma_{\Lambda}$	Reference [8]	0.78%
Overall	Statistics	NA	θ: 1.60% - 6.87%
	Systematics	NA	θ: 16.3% - 31.3%
	Total	NA	θ: 16.4% - 32.0%

Table 9.4 : Summary of the systematic uncertainties on the measurement of the $\gamma n \to K^{+}\Sigma^{*-}$ cross section. The specifics of these studies are discussed in Sections 9.4.1 through 9.4.4. The uncertainty ranges are the ranges of the θ-independent, overall uncertainties of the photon energy bins, except where the θ-dependence is indicated by the "θ :." The uncertainties of the outlier points not included in the calculation of the overall uncertainties are not listed in this table. The θ-dependent ranges of the overall statistical, systematic, and total uncertainties are shown as well.

Category	Source	Study	$\sim\sigma$ Range
CLAS Acceptance	π^- Momentum Cut	From $\gamma n \to K^{+}\Sigma^{*-}$	3.2% - 5.1%
	p & K^+ Momentum Cuts	From $\gamma n \to K^{+}\Sigma^{*-}$	0.38% - 0.53%
	Fiducial Cuts	From $\gamma n \to K^{+}\Sigma^{*-}$	1.7% - 6.2%
	Trigger Simulation	From $\gamma n \to K^{+}\Sigma^{*-}$	3.3% - 3.4%
	Simulation Distribution	Model [68] vs. t-slope	θ: 0.036% - 32.2%
Final-State Identification	Particle Identification Cuts	From $\gamma n \to K^{+}\Sigma^{*-}$	3.6% - 5.5%
	Time Difference Cuts	From $\gamma n \to K^{+}\Sigma^{*-}$	5.0% - 9.3%
	Λ Invariant Mass Cuts	From $\gamma n \to K^{+}\Sigma^{*-}$	5.1% - 6.6%
	Missing Momentum Cut	From $\gamma n \to K^{+}\Sigma^{*-}$	2.4% - 3.6%
Yield Extraction	p Missing Mass Cuts	From $\gamma n \to K^{+}\Sigma^{*-}$	5.1% - 6.5%
	Σ^{*-} Overlap Cuts	$\pm 1\Gamma$ vs. $\pm 1.5\Gamma$	θ: 0.067% - 20.3%
	K^{*0} Background Fits	Function Type	θ: 0.19% - 31.6%
	K^{*0} Invariant Mass Cuts	$\pm 2\Gamma$ vs. $\pm 1\Gamma$	θ: 1.5% - 16.5%
	γ, π^0 Background	Sideband Yield	5.4% - 18.0%
Miscellaneous	Photon Flux	Reference [112]	1.8%
	Target Length	Reference [92]	0.025%
	Target Density	Reference [112]	0.11%
	$\Gamma_{K^{*0}\to K^{+}\pi^{-}}/\Gamma_{K^{*0}}$	Reference [8]	0.021%
	$\Gamma_{\Lambda\to p\pi^{-}}/\Gamma_{\Lambda}$	Reference [8]	0.78%
Overall	Statistics	NA	θ: 2.20% - 6.53%
	Systematics	NA	θ: 16.6% - 45.4%
	Total	NA	θ: 16.9% - 45.6%

Table 9.5 : Summary of the systematic uncertainties on the measurement of the $\gamma n \to K^{*0}\Lambda$ cross section. The specifics of these studies are discussed in Sections 9.4.1 through 9.4.5. The uncertainty ranges are the ranges of the θ-independent, overall uncertainties of the photon energy bins, except where the θ-dependence is indicated by the "θ :." The uncertainties of the outlier points not included in the calculation of the overall uncertainties are not listed in this table. Due to the similarity of their analyses, many of these systematic uncertainties were taken from the study of the $\gamma n \to K^{+}\Sigma^{*-}$ cross section. The θ-dependent ranges of the overall statistical, systematic, and total uncertainties are shown as well.

uncertainty percentage of the given photon energy bin.

The systematic uncertainties of the $\gamma n \rightarrow K^{*0}\Lambda$ cross section varied between $\sim$16.6% and $\sim$45.4%, and the systematic uncertainties of the $\gamma n \rightarrow K^{+}\Sigma^{*-}$ cross section varied between $\sim$16.3% and $\sim$31.3%. For the $\gamma n \rightarrow K^{*0}\Lambda$ analysis, the primary sources of these uncertainties were the simulation distribution, the backgrounds from events with an additional photon or π^0 in the final state, and fits to the K^{*0} invariant mass distributions. For the $\gamma n \rightarrow K^{+}\Sigma^{*-}$ analysis, the primary sources of the systematic uncertainties were the simulation distribution and the background fit functions of the Σ^{*-} invariant mass distributions. Also, the large uncertainties on the K^{*0} and Σ^{*-} invariant mass fits may have contributed to the systematic uncertainty assignments from the other studies. Although these effects could not be disentangled, they can be decreased with additional studies of these distributions.

With future studies of these backgrounds and the CLAS acceptance, the total uncertainties can be reduced to around 10% to 20%. This range was estimated by assuming a $\sim$50% reduction of the systematic uncertainties associated with these studies. The procedures for reducing these systematic uncertainties are still under development.

9.4.1 γ & π^0 Background Scale Uncertainties

Due to low statistics, a θ-independent study of the backgrounds from events containing an additional photon or π^0 in the final state was conducted. The overall percentage of these backgrounds was determined for each photon energy bin of the $\gamma n \rightarrow K^{*0}\Lambda$ and $\gamma n \rightarrow K^{+}\Sigma^{*-}$ analyses, and was assigned as a scale uncertainty. These scale uncertainties were added in quadrature with the results from the systematic uncertainty studies. With future studies, the angular dependence of these backgrounds can be determined and subtracted from the $\gamma n \rightarrow K^{*0}\Lambda$ and $\gamma n \rightarrow K^{+}\Sigma^{*-}$ cross sections, resulting in a smaller systematic uncertainty assignment from this source.

The scale uncertainties due to these backgrounds, such as $\gamma n \rightarrow K^{+}\Sigma^{*-}(\pi^0)$ and $\gamma n \rightarrow K^{*0}\Sigma^0 \rightarrow K^{*0}\Lambda(\gamma)$ events, were calculated by studying the high-mass sidebands of the $\gamma D \rightarrow K^{+}\pi^{-}\Lambda(p)$ missing mass distributions. Samples of these distributions are shown in Figures 8.13 and 8.17 for the $\gamma n \rightarrow K^{*0}\Lambda$ and $\gamma n \rightarrow K^{+}\Sigma^{*-}$ analyses, respectively. The high-mass sidebands were the regions of these distributions that started from the $+3\sigma$ cuts and spanned 6σ in the direction of increasing missing mass. After the final-state identification cuts, the Σ^{*-} and K^{*0} overlap cuts determined in

Section 8.2 were placed on the data in these sideband regions of the $\gamma n \to K^{*0}\Lambda$ and $\gamma n \to K^{+}\Sigma^{*-}$ analyses, respectively. Cuts were then placed on the number of remaining track combinations, which rejected ~3.1% and ~2.1% of the events in the $\gamma n \to K^{*0}\Lambda$ and $\gamma n \to K^{+}\Sigma^{*-}$ analyses, respectively.

After these cuts the statistics were too low in the E_γ, $\cos(\theta)$ bins of both reactions to obtain reliable fits, so within each photon energy bin all of the data were merged together. The K^{*0} and Σ^{*-} invariant mass distributions of these data are shown in Figures 9.11 and 9.12 for the $\gamma n \to K^{*0}\Lambda$ and $\gamma n \to K^{+}\Sigma^{*-}$ analyses, respectively. These distributions were fit to Breit-Wigner functions over various polynomial backgrounds, where present. The K^{*0} backgrounds were still primarily comprised of Σ^{*-} events, so their distributions remained quadratic. The two lowest Σ^{*-} photon energy bins appeared to contain negligible backgrounds, so were only fit to Breit-Wigner functions. The backgrounds of the other Σ^{*-} photon energy bins contained significantly larger backgrounds, most likely from $\gamma n \to K^{*0}\Sigma^{0}$ events. Due to the lack of statistics and the size of the backgrounds, the Σ^{*-} invariant mass peaks in the 1.5 GeV to 1.7 GeV and 1.9 GeV to 2.1 GeV photon energy bins were fit with the Breit-Wigner function widths fixed to 45 MeV/c^2. This was necessary to obtain stable fits for these bins, as these fits failed to converge to physical resonance widths without these restrictions. The fixed 45 MeV/c^2 width was chosen to be slightly wider than the 39.4 MeV/c^2 Σ^{*-} resonance width to take into account Gaussian resolution effects. As seen in Figure 9.12 these fits had reasonable values of χ^2 per degree of freedom, and were thus acceptable for this study.

These distributions were cut at $\pm 2\Gamma$, and the yields within the sidebands were the number of events above the backgrounds within these cuts. For the $\gamma n \to K^{*0}\Lambda$ analysis, the number of K^{*0} events within the sidebands were ~9.2%, ~20.6%, and ~24.9% of the total number of K^{*0} events within the spectator proton signal regions of the different photon energy bins, listed in order of increasing energy. For the $\gamma n \to K^{+}\Sigma^{*-}$ analysis, the Σ^{*-} event percentages were ~6.6%, ~8.9%, ~6.9%, ~7.4%, and ~8.7%, listed in order of increasing energy. These sideband percentages $S\%$ are listed in Table 9.6 and were calculated as:

$$S\% = \frac{100.0 Y_{\text{Sideband}}(1 - \text{Cut}\%_{\#\text{TC-Sideband}})}{Y(1 - \text{Cut}\%_{\#\text{TC}})}, \tag{9.3}$$

where Y and Y_{Sideband} are the yields within the signal and sideband regions of the $\gamma D \to K^{+}\pi^{-}\Lambda(p)$ missing mass distributions, respectively, and $\text{Cut}\%_{\#\text{TC}}$ and $\text{Cut}\%_{\#\text{TC-Sideband}}$ are the fractions of the true yields cut due to more than one track combination surviving the cuts in the signal and

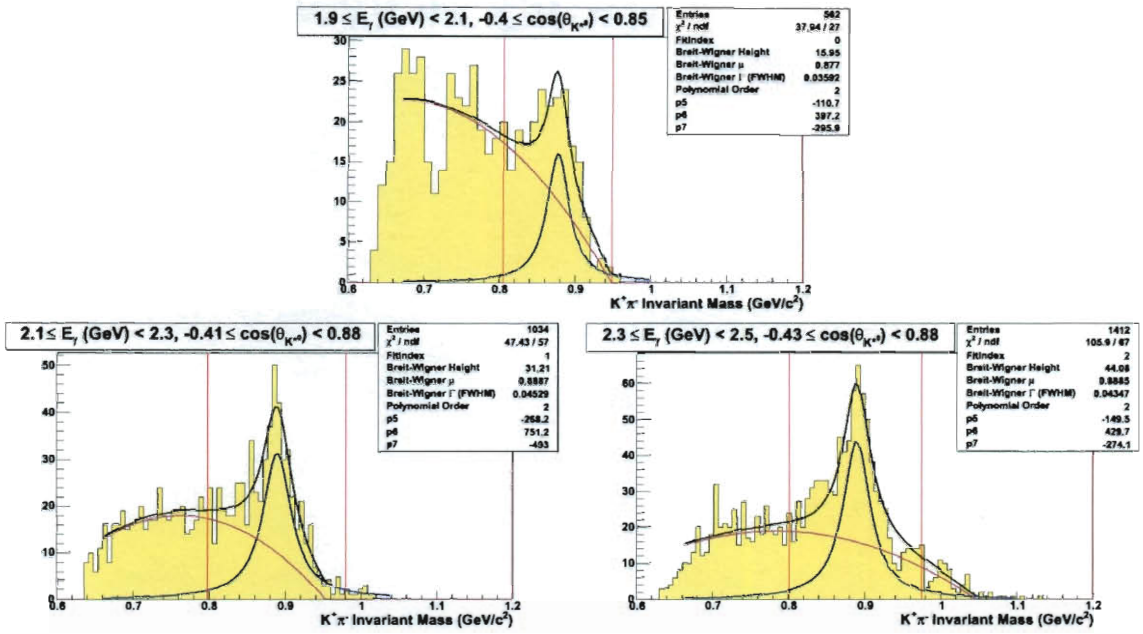

Figure 9.11 : Fits to the invariant mass of the K^{*0} in the high-mass sidebands of the $\gamma D \to K^{+}\pi^{-}\Lambda(p)$ missing mass distributions for each photon energy bin of the $\gamma n \to K^{*0}\Lambda$ analysis. The signals were fit to a Breit-Wigner function over a quadratic background, and the red lines indicate the $\pm 2\Gamma$ cuts used for yield extraction. The blue lineshapes represent the Breit-Wigner fit functions, the magenta lineshapes represent the quadratic fit functions, and the black lineshapes represent the total fit functions. The number of K^{*0} events within the sidebands were ~9.2%, ~20.6%, and ~24.9% of the total number of K^{*0} events within the spectator proton signal regions of the different photon energy bins, listed in order of increasing energy.

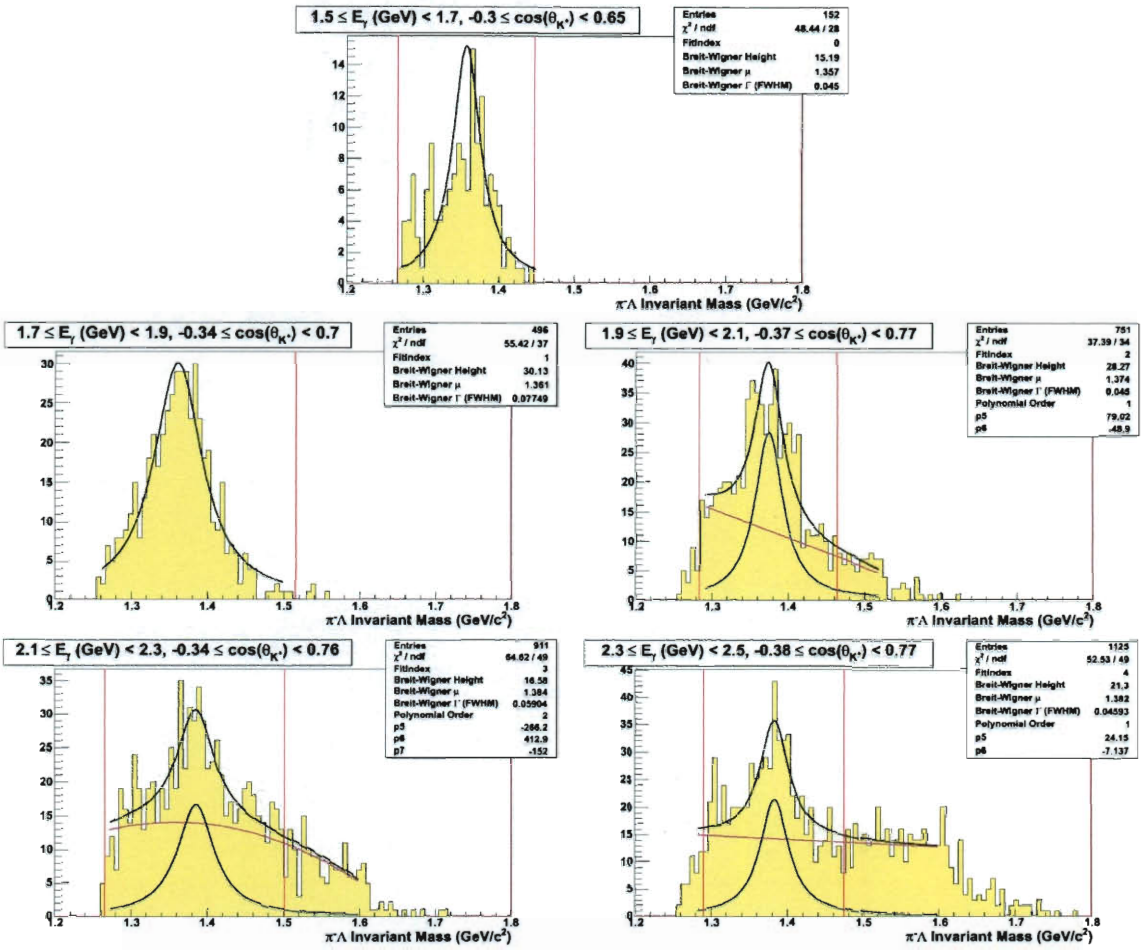

Figure 9.12 : Fits to the invariant mass of the Σ^{*-} in the high-mass sidebands of the $\gamma D \to K^{+}\pi^{-}\Lambda(p)$ missing mass distributions for each photon energy bin of the $\gamma n \to K^{+}\Sigma^{*-}$ analysis. The signals were fit to a Breit-Wigner function over a polynomial background that varied with photon energy. From 1.5 GeV to 1.9 GeV no background was fit, in the 1.9 GeV to 2.1 GeV and 2.3 GeV to 2.5 GeV bins a linear background was fit, and in the 2.1 GeV to 2.3 GeV bin a quadratic background was fit. The red lines indicate the $\pm 2\Gamma$ cuts used for yield extraction, and the blue, magenta, and black lineshapes represent the Breit-Wigner, polynomial background, and total fit functions, respectively. The number of Σ^{*-} events within the sidebands were ~6.6%, ~8.9%, ~6.9%, ~7.4%, and ~8.7% of the total number of Σ^{*-} events within the spectator proton signal regions of the different photon energy bins, listed in order of increasing energy.

Signal, E_γ Bin (GeV)	Experiment Sideband %	Simulation Sideband %	Experiment Sideband Yield %	Background Integral Ratio	Background %
K^{*0}, 1.9 - 2.1	~9.2%	~3.1%	~6.1%	~0.86	~5.4%
K^{*0}, 2.1 - 2.3	~20.6%	~3.2%	~17.4%	~0.84	~15.0%
K^{*0}, 2.3 - 2.5	~24.9%	~3.2%	~21.6%	~0.81	~18.0%
Σ^{*-}, 1.5 - 1.7	~6.6%	~1.8%	~4.8%	1.0	~4.8%
Σ^{*-}, 1.7 - 1.9	~8.9%	~2.1%	~6.8%	1.0	~6.8%
Σ^{*-}, 1.9 - 2.1	~6.9%	~2.4%	~4.5%	~0.89	~4.0%
Σ^{*-}, 2.1 - 2.3	~7.4%	~2.5%	~4.9%	~0.86	~4.2%
Σ^{*-}, 2.3 - 2.5	~8.7%	~2.8%	~5.9%	~0.92	~5.4%

Table 9.6 : Results from the studies used to determine the cross section scale uncertainties due to background events containing an additional photon or π^0 in the final state. The sideband percentages were the amounts of K^{*0} or Σ^{*-} events in the sideband regions with respect to the signal regions of the spectator proton. The experimental sideband yield percentages were the experimental sideband percentages subtracted by the simulated sideband percentages, which removed the effects of the non-Gaussian tails of the signals that were in the sideband regions. The background integral ratios were the ratios of the integrals of the background fit functions of the $\gamma D \to K^{+}\pi^{-}\Lambda(p)$ missing mass distributions in the signal and sideband regions. The background percentages were the percentages of the $\gamma n \to K^{*0}\Lambda$ and $\gamma n \to K^{+}\Sigma^{*-}$ true yields that were background events, and were assigned as scale uncertainties.

sideband regions, respectively. The fractions of the true yields cut in the signal regions are discussed in Sections 8.2.1 and 8.2.2 for the $\gamma n \to K^{*0}\Lambda$ and $\gamma n \to K^{+}\Sigma^{*-}$ reactions, respectively.

However, due to non-Gaussian resolution effects some of the events within the sideband yields were actually $\gamma n \to K^{*0}\Lambda$ and $\gamma n \to K^{+}\Sigma^{*-}$ events. To determine the size of these backgrounds in the sideband yields, the same sideband study was performed on the simulated data. The Σ^{*-} and K^{*0} overlap cuts were applied to the 6σ-wide high-mass sidebands of the simulated $\gamma D \to K^{+}\pi^{-}\Lambda(p)$ distributions for the $\gamma n \to K^{*0}\Lambda$ and $\gamma n \to K^{+}\Sigma^{*-}$ analyses, respectively. Cuts on the number of remaining track combinations in the simulated data rejected ~1.6% and ~0.56% of the events in the $\gamma n \to K^{*0}\Lambda$ and $\gamma n \to K^{+}\Sigma^{*-}$ analyses, respectively. Figures 9.13 and 9.14 show Breit-Wigner fits to the simulated K^{*0} and Σ^{*-} invariant mass distributions of the $\gamma n \to K^{*0}\Lambda$ and $\gamma n \to K^{+}\Sigma^{*-}$ simulated data, respectively.

The yields within the simulated sidebands were the number of events within the $\pm 2\Gamma$ cuts on these distributions. Using Equation 9.3, the percentages of K^{*0} events in the simulated sidebands

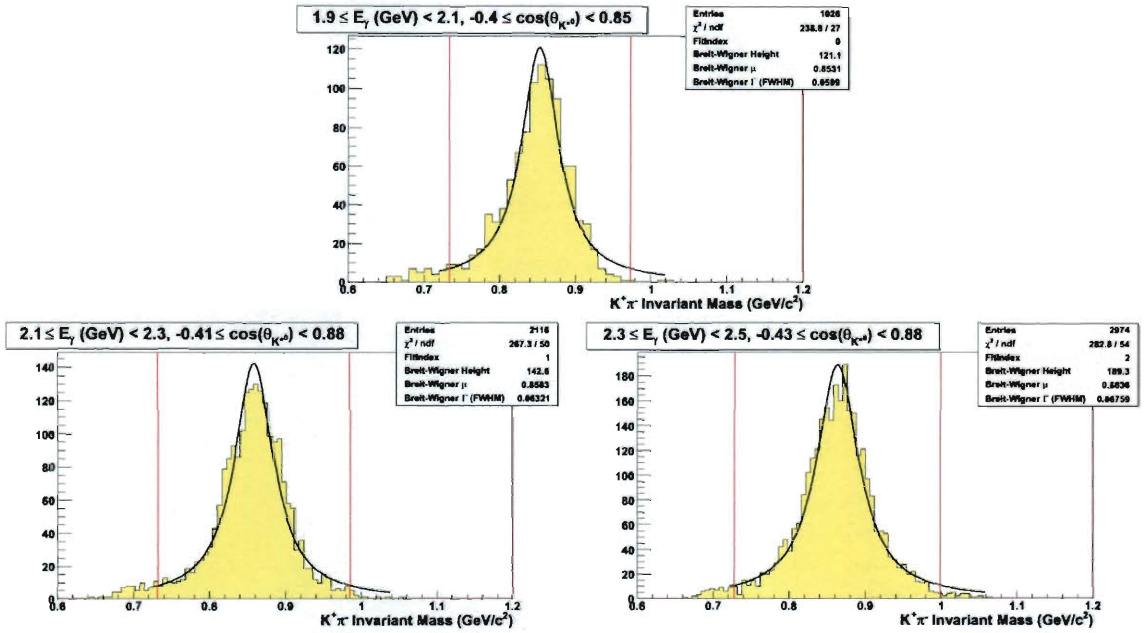

Figure 9.13 : Fits to the invariant mass of the K^{*0} in the high-mass sidebands of the simulated $\gamma D \to K^{+}\pi^{-}\Lambda(p)$ missing mass distributions for each photon energy bin of the $\gamma n \to K^{*0}\Lambda$ analysis. The signals were fit to a Breit-Wigner function, and the red lines indicate the $\pm 2\Gamma$ cuts used for yield extraction. The number of K^{*0} events within the simulated sidebands were ~3.1%, ~3.2%, and ~3.2% of the total number of simulated K^{*0} events within the spectator proton signal regions of the different photon energy bins, listed in order of increasing energy.

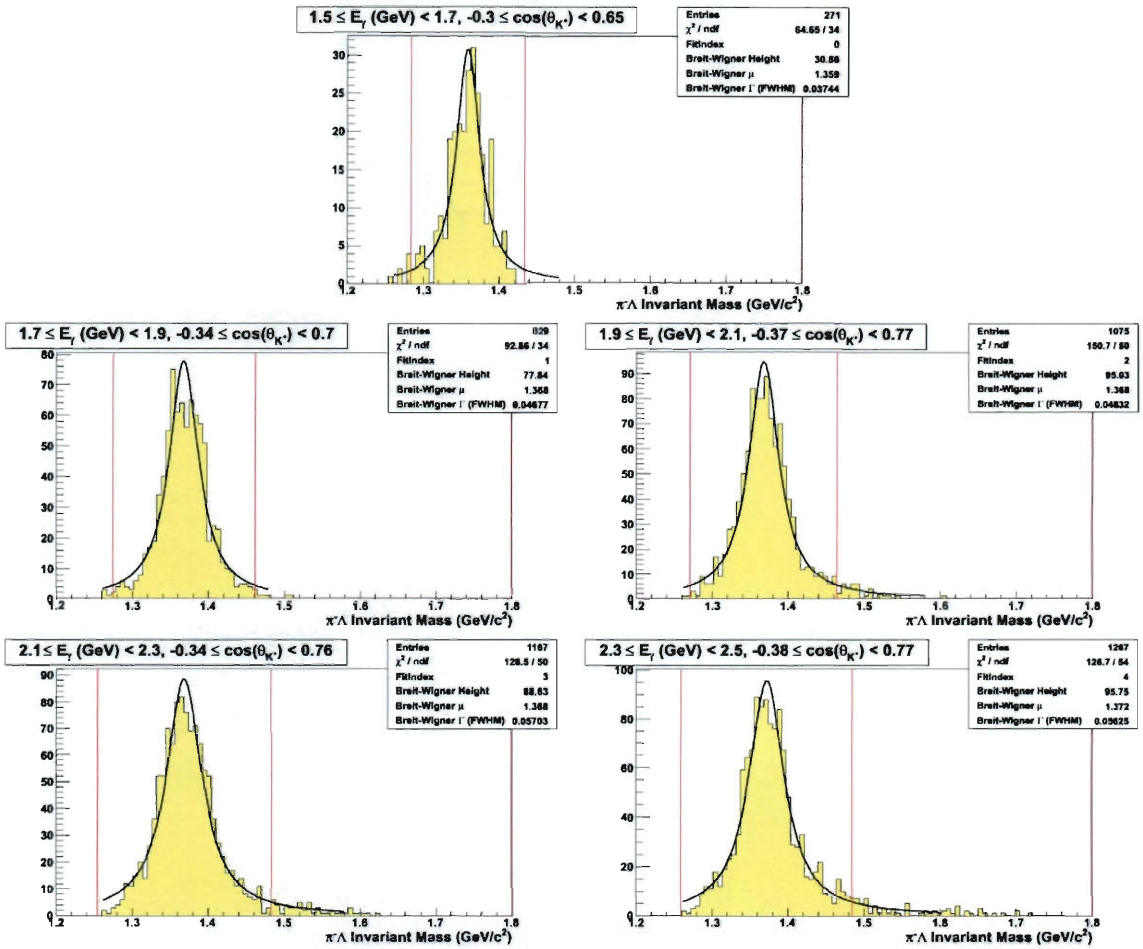

Figure 9.14 : Fits to the invariant mass of the Σ^{*-} in the high-mass sidebands of the simulated $\gamma D \to K^{+}\pi^{-}\Lambda(p)$ missing mass distributions for each photon energy bin of the $\gamma n \to K^{+}\Sigma^{*-}$ analysis. The signals were fit to a Breit-Wigner function, and the red lines indicate the $\pm 2\Gamma$ cuts used for yield extraction. The number of Σ^{*-} events within the simulated sidebands were ~1.8%, ~2.1%, ~2.4%, ~2.5%, and ~2.8% of the total number of simulated Σ^{*-} events within the spectator proton signal regions of the different photon energy bins, listed in order of increasing energy.

were ~3.1%, ~3.2%, and ~3.2% of the K^{*0} events within the simulated spectator proton signal regions of the different photon energy bins, listed in order of increasing energy. Similarly, the Σ^{*-} simulated event percentages were ~1.8%, ~2.1%, ~2.4%, ~2.5%, and ~2.8%, listed in order of increasing energy. These simulated sideband percentages are listed in Table 9.6. Due to the similarity between the experimental and simulated detector resolutions, these percentages were used to approximate the number of non-Gaussian distributed signal events in the sideband regions of the $\gamma D \to K^{+}\pi^{-}\Lambda(p)$ missing mass distributions. These simulated sideband percentages were subtracted from the experimental sideband percentages to remove these events, and the resulting sideband yield percentages are listed in Table 9.6.

To determine the size of these backgrounds in the signal regions, the integrals of the $\gamma D \to K^{+}\pi^{-}\Lambda(p)$ background fit functions were calculated in both the spectator proton sideband and signal regions of each energy bin. To fit these background functions for the $\gamma n \to K^{*0}\Lambda$ and $\gamma n \to K^{+}\Sigma^{*-}$ analyses, first the Σ^{*-} and K^{*0} overlap cuts were performed on the $\gamma n \to K^{+}\pi^{-}\Lambda$ final-state events, respectively. These cuts were necessary to produce the correct background distributions for these analyses, as both the experimental yields and sideband yield percentages were determined with these cuts in place.

Figures 9.15 and 9.16 show the fits to the $\gamma D \to K^{+}\pi^{-}\Lambda(p)$ distributions after performing the Σ^{*-} and K^{*0} overlap cuts for the $\gamma n \to K^{*0}\Lambda$ and $\gamma n \to K^{+}\Sigma^{*-}$ analyses, respectively. These distributions were fit to Breit-Wigner functions over various polynomial background functions, as detailed in the figures. The red lines indicate the average $\pm 3\sigma$ cuts used for the experimental yield extractions of the $\gamma n \to K^{*0}\Lambda$ and $\gamma n \to K^{+}\Sigma^{*-}$ reactions within the photon energy bins. These average cuts were determined by merging all of the $\cos(\theta)$ bins of these analyses after the final-state identification cuts, and fitting the $\gamma D \to K^{+}\pi^{-}\Lambda(p)$ distributions of each photon energy bin. The ratios of the integrals of these fit backgrounds between the sideband and signal regions are listed in Table 9.6.

The sideband yield percentages were multiplied by these background integral ratios to obtain the percentages of the experimental yields that were background events. This assumed that the backgrounds from events that contained an additional photon or π^0 in the final state were distributed as the background fits of the $\gamma D \to K^{+}\pi^{-}\Lambda(p)$ distributions. These percentages were ~5.4%, ~15.0%, and ~18.0% for the $\gamma n \to K^{*0}\Lambda$ analysis, and were ~4.8%, ~6.8%, ~4.0%, ~4.2%, and

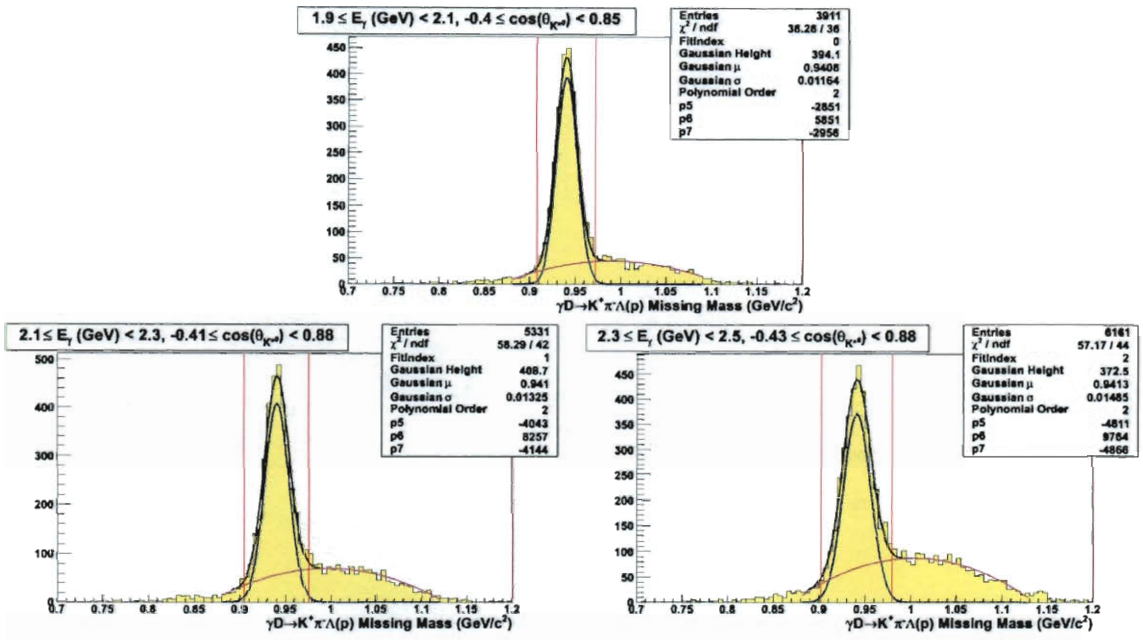

Figure 9.15 : Fits to the $\gamma D \to K^{+}\pi^{-}\Lambda(p)$ missing mass distributions of the $\gamma n \to K^{*0}\Lambda$ analysis to determine the ratios of the backgrounds in the signal and sideband regions. The signals were fit to a Gaussian function over a quadratic background. The $\pm 3\sigma$ signal regions are illustrated by the red vertical lines, and the blue, magenta, and black lineshapes represent the Gaussian, quadratic background, and total fit functions, respectively. The background ratios were determined as the ratios of the integrals of the background fit functions in the signal and sideband regions, and are listed in Table 9.6.

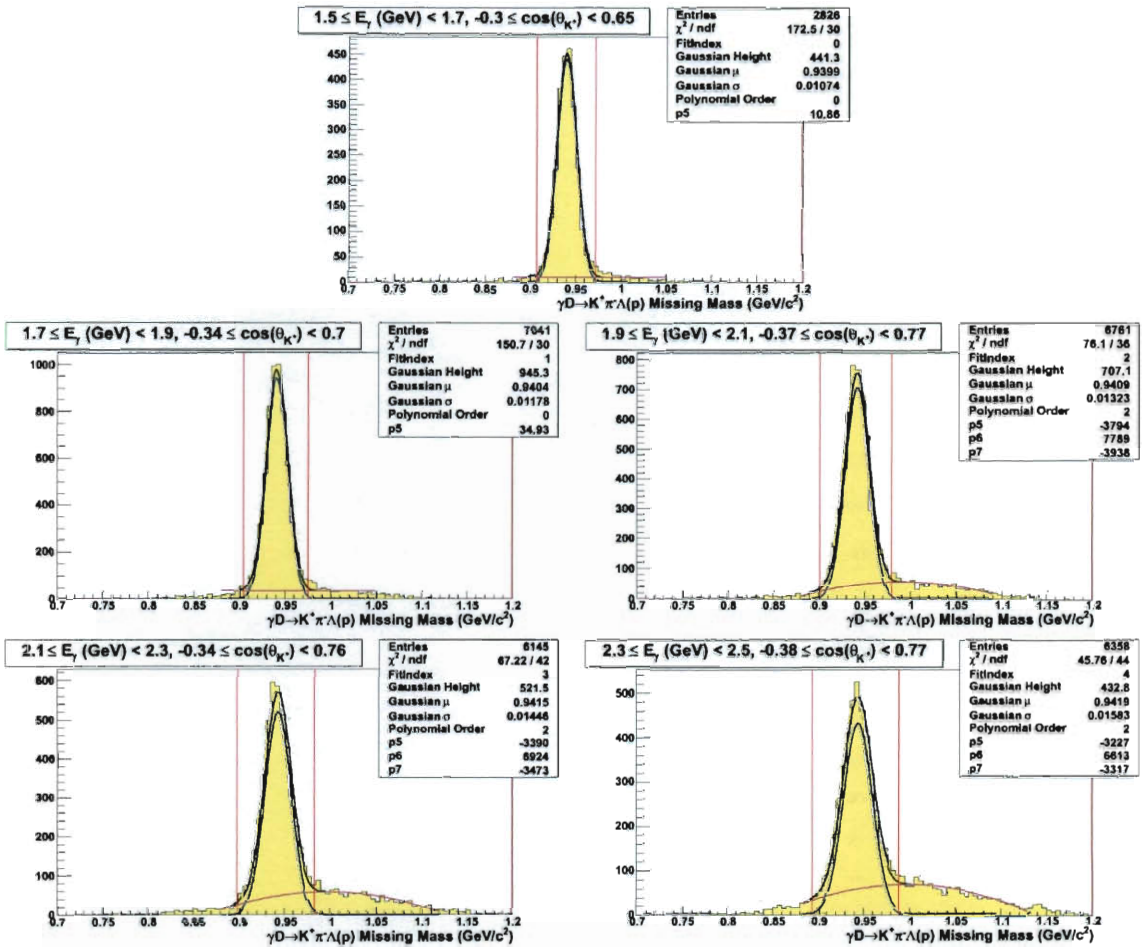

Figure 9.16 : Fits to the $\gamma D \to K^{+}\pi^{-}\Lambda(p)$ missing mass distributions of the $\gamma n \to K^{+}\Sigma^{*-}$ analysis to determine the ratios of the backgrounds in the signal and sideband regions. The signals were fit to a Gaussian over a flat background below 1.9 GeV, and to a Gaussian over a quadratic background above 1.9 GeV. The $\pm 3\sigma$ signal regions are illustrated by the red vertical lines, and the blue, magenta, and black lineshapes represent the Gaussian, polynomial background, and total fit functions, respectively. The background ratios were determined as the ratios of the integrals of the background fit functions in the signal and sideband regions, and are listed in Table 9.6.

~5.4% for the $\gamma n \rightarrow K^{+}\Sigma^{*-}$ analysis. These percentages are for the different photon energy bins, listed in order of increasing photon energy. These backgrounds were largest for the $\gamma n \rightarrow K^{*0}\Lambda$ analysis at photon energies above 2.1 GeV, which indicated that the majority of these backgrounds were most likely $\gamma n \rightarrow K^{*0}\Sigma^{0}$ events. The other sources of these backgrounds were most likely $\gamma n \rightarrow K^{*0}\Lambda(\gamma)$ or $\gamma n \rightarrow K^{+}\Sigma^{*-}(\gamma)$ events, although some events with π^{0}'s may have been included as well. These percentages were assigned as scale uncertainties on the $\gamma n \rightarrow K^{*0}\Lambda$ and $\gamma n \rightarrow K^{+}\Sigma^{*-}$ cross section calculations.

9.4.2 $\gamma n \rightarrow K^{+}\Sigma^{*-}$ CLAS Acceptance Studies

Several studies were performed to determine the systematic uncertainties of the CLAS acceptance for the $\gamma n \rightarrow K^{+}\Sigma^{*-}$ reaction. These included studies of the π^{-} minimum momentum cut, the proton and K^{+} minimum momentum cuts, the fiducial cuts, the trigger simulation, and the simulation event distribution. These systematic uncertainty studies are shown in Figures 9.17 through 9.22, and are summarized in Table 9.4. The average uncertainties of the three highest photon energy bins were assigned to the $\gamma n \rightarrow K^{*0}\Lambda$ cross section as well, except for the uncertainties from the simulation event distribution study. These uncertainties were calculated as discussed in Section 9.4.

With the exception of the outliers, the systematic uncertainties on the minimum momentum cuts were significantly larger for the π^{-} cut shown in Figure 9.17 than for the proton and K^{+} cuts shown in Figure 9.18. This was primarily because there were significantly fewer low-momentum protons and K^{+}'s than there were low-momentum π^{-}'s. The 150 MeV/c cut on the π^{-} momentum reduced the experimental yield by ~20.8%, while the simultaneous 450 MeV/c cuts on the proton and K^{+} momentum only reduced the experimental yield by ~0.83%. Also, the 100 MeV/c momentum cut on the π^{-}'s is near the edge of CLAS acceptance, while the edges of the CLAS acceptance for protons and K^{+}'s are closer to 300 MeV/c. The outliers in the proton and K^{+} minimum cut study at the large angles were primarily due to the large size of their bins, and their locations near the edges of the data distributions where the CLAS acceptance changes rapidly.

The overall systematic uncertainties of the fiducial cuts shown in Figure 9.19 were concentrated near 3%, except the overall uncertainty of the 2.3 GeV to 2.5 GeV photon energy bin was ~6.2%. The source of this deviation is unknown, although it may be that the fiducial cuts were not tight enough at high momentum to remove all of the inefficient regions at the edges of CLAS. However,

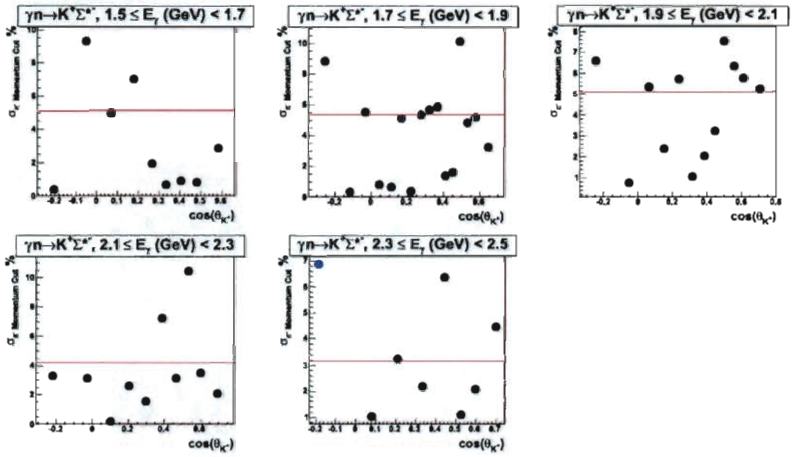

Figure 9.17 : The black points indicate the systematic uncertainty percentages on the $\gamma n \to K^{+}\Sigma^{*-}$ cross section from changing the π^{-} minimum momentum cut from 100 MeV/c to 150 MeV/c. The uncertainties did not have a systematic angular dependence, so for each energy bin the overall systematic uncertainty percentage indicated by the red lines was assigned for every point. The blue point had a $> 50\%$ effect on the overall uncertainty percentage of its energy bin, so it was excluded from the calculation and was assigned its individual uncertainty. The overall uncertainties of the three highest photon energy bins were assigned to the $\gamma n \to K^{*0}\Lambda$ cross section for the same photon energy ranges. These uncertainties were larger than those for the proton and K^{+} momentum cuts, partially due to the larger number of low-momentum π^{-}'s.

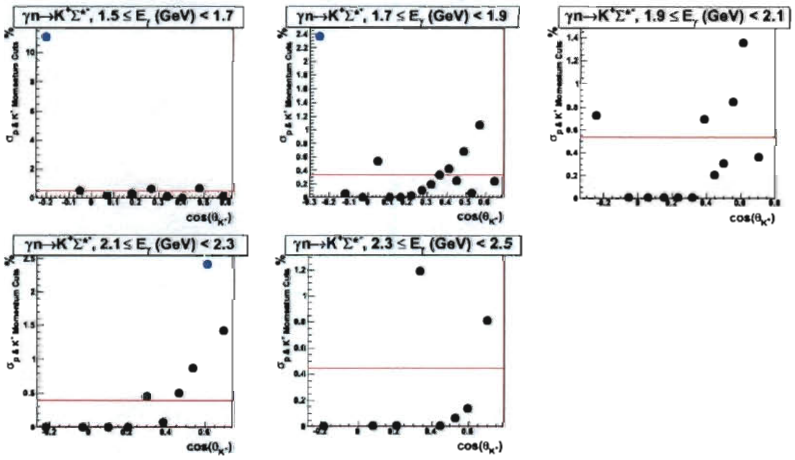

Figure 9.18 : The black points indicate the systematic uncertainty percentages on the $\gamma n \to K^{+}\Sigma^{*-}$ cross section from simultaneously changing the proton and K^{+} minimum momentum cuts from 400 MeV/c to 450 MeV/c. The uncertainties did not have a strong systematic angular dependence, so for each energy bin the overall systematic uncertainty percentage indicated by the red lines was assigned for every point. The blue points had a $> 50\%$ effect on the overall uncertainty percentage of their energy bins, so they were excluded from the calculation and were assigned their individual uncertainties. The overall uncertainties of the three highest photon energy bins were assigned to the $\gamma n \to K^{*0}\Lambda$ cross section for the same photon energy ranges. Except for the outliers these uncertainties were smaller than those for the π^{-} momentum cuts, partially due to the smaller number of low-momentum protons and K^{+}'s.

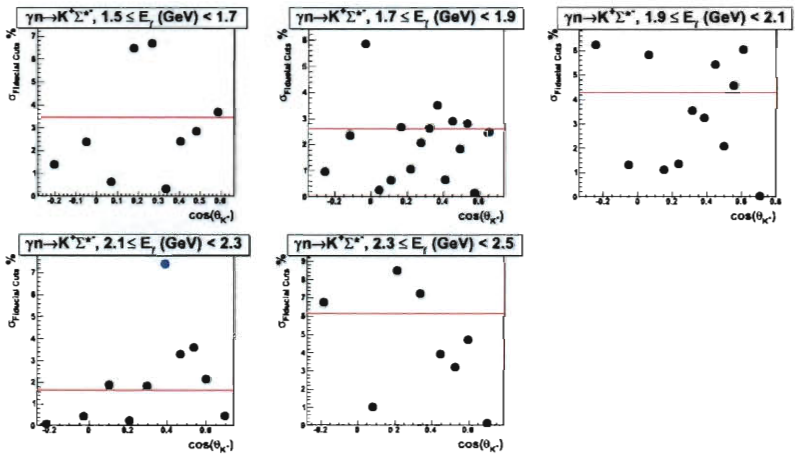

Figure 9.19 : The black points indicate the systematic uncertainty percentages on the $\gamma n \to K^{+}\Sigma^{*-}$ cross section from tightening the fiducial cuts by 0.02 radians on all sides. The uncertainties did not have a systematic angular dependence, so for each energy bin the overall systematic uncertainty percentage indicated by the red lines was assigned for every point. The blue point had a $> 50\%$ effect on the overall uncertainty percentage of its energy bin, so it was excluded from the calculation and was assigned its individual uncertainty. The overall uncertainties of the three highest photon energy bins were assigned to the $\gamma n \to K^{*0}\Lambda$ cross section for the same photon energy ranges.

these uncertainties are significantly smaller than those of the Σ^{*-} background fits and the simulated distribution, and thus have a small impact on the total uncertainties.

The systematic uncertainties on the triggering efficiency simulation shown in Figure 9.20 were determined by comparing the nominal $\gamma n \to K^{+}\Sigma^{*-}$ cross section, where the proton triggering efficiencies were assigned to the K^{+}, to the cross section calculated with the π^{-} triggering efficiencies assigned to the K^{+}, and to the cross section calculated with the triggering simulation removed. With the π^{-} triggering efficiencies assigned to the K^{+} the total simulated yields only decreased by $\sim$0.33%, while with the trigger simulation removed the total simulated yields increased by $\sim$4.41%. The triggering inefficiencies played a much smaller role in the $\gamma n \to K^{+}\Sigma^{*-}$ analysis than in the $\gamma n \to p\pi^{-}$ analysis due to the larger number of charged particles in the final state.

The simulation event distribution systematic uncertainties were calculated by changing the simulation distribution from the t-slope distribution discussed in Section 8.3 to the Oh, Ko, and Nakayama model predictions [69, 78]. The experimental yields are shown in Figure 9.21 compared against the simulated yields of both simulation distributions. In these plots, the simulated yields were vertically scaled so that their maximum values were the same as those of the experimental yields in each photon energy bin. The yields of the generated t-slope distribution were generally larger at the

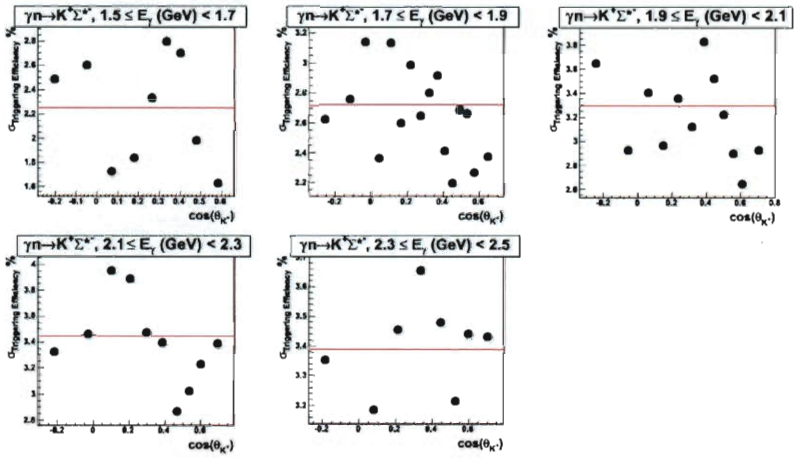

Figure 9.20 : The black points indicate the systematic uncertainty percentages on the $\gamma n \to K^{+}\Sigma^{*-}$ cross section from the triggering efficiencies. These uncertainties were determined by comparing the results with the K^{+} assigned the proton triggering efficiency to the results with the K^{+} assigned the π^{-} triggering efficiency, and to the results without the trigger simulation. The uncertainties did not have a systematic angular dependence, so for each energy bin the overall systematic uncertainty percentage indicated by the red lines was assigned for every point. None of the individual points had a $> 50\%$ effect on the overall uncertainty percentage. The overall uncertainties of the three highest photon energy bins were assigned to the $\gamma n \to K^{*0}\Lambda$ cross section for the same photon energy ranges. The triggering inefficiencies had a much smaller effect on the $\gamma n \to K^{+}\Sigma^{*-}$ cross section than the $\gamma n \to p\pi^{-}$ cross section due to the larger number of charged particles in the final state.

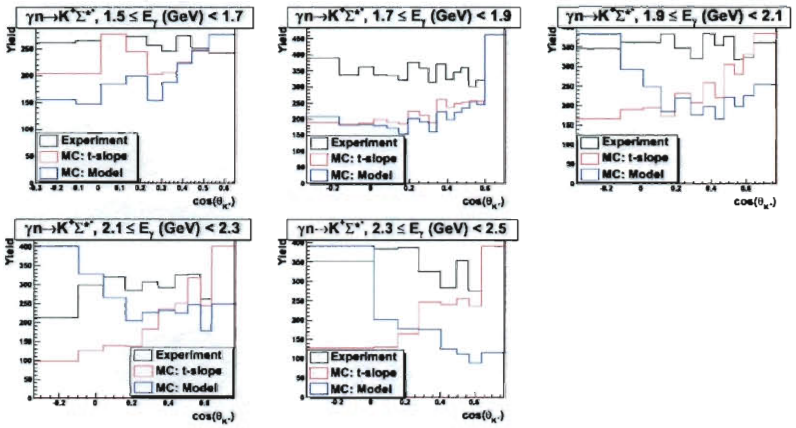

Figure 9.21 : For the $\gamma n \to K^{+}\Sigma^{*-}$ reaction, a comparison of the experimental yields to those from the different simulation distributions. The simulated yields were scaled such that their maximum values were the same as those of the experimental yields in each photon energy bin. The nominal $\gamma n \to K^{+}\Sigma^{*-}$ cross section was calculated using a t-slope simulation distribution with an exponential slope of $b = 3.0$ GeV^{-2}, and for comparison was also calculated using the Oh, Ko, and Nakayama model predictions [69, 78]. The differences between the simulated yields resulted in systematic uncertainties of up to ~23.1% at the large angles, where the bins were generally widest.

forward angles than those of the model predictions, and the yields of the generated model prediction distribution were generally greater at the large angles.

The systematic uncertainties from the simulation event distribution study are shown in Figure 9.22. These uncertainties exhibited a large angular dependence, increasing from below 5% at the forward angles of most of the photon energy bins to between ~11% and ~23% at large angles. Although the simulation distributions had significant differences throughout the angular range, the uncertainties were greatest at the large angles because their bin widths were generally larger. Large variations in the CLAS acceptance across the widths of the bins caused large differences between the calculated acceptances of the different simulation distributions. To reduce these uncertainties, in future studies the calculated cross section distribution will be used to generate the simulation events for the acceptance calculations. This distribution will improve the matching between the experimental and simulated event distributions, improving the accuracy of the acceptance corrections used for the $\gamma n \to K^{+}\Sigma^{*-}$ cross section calculation. Additionally, the exponential slope of the t-slope simulation distribution will be tuned to better match the experimental data.

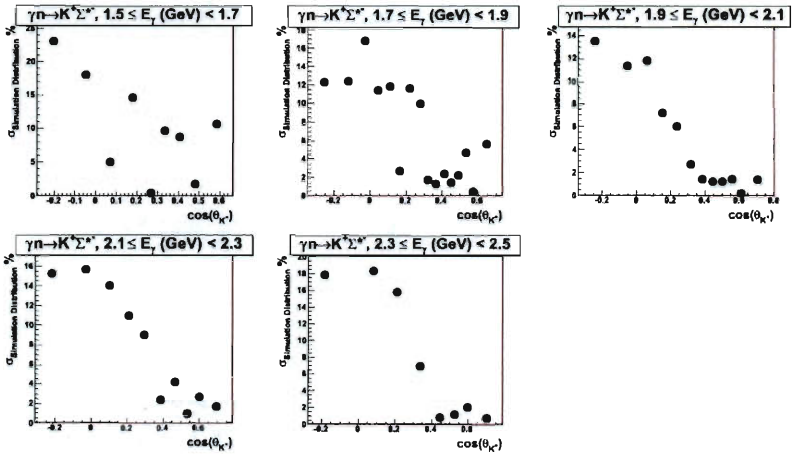

Figure 9.22 : The systematic uncertainty percentages on the $\gamma n \rightarrow K^{+}\Sigma^{*-}$ cross section from changing the simulation distribution used for calculating the CLAS acceptance from a t-slope distribution with an exponential slope of $b = 3.0$ GeV^{-2} to the Oh, Ko, and Nakayama predictions [69, 78]. The uncertainties were significantly greater at the large angles due to the increased bin widths, so the systematic uncertainties were assigned for each point individually.

9.4.3 $\gamma n \rightarrow K^{+}\Sigma^{*-}$ Final-State Identification Studies

For the final-state identification cuts, the systematic uncertainties on the $\gamma n \rightarrow K^{+}\Sigma^{*-}$ cross section were studied by varying the particle identification cuts, the time difference cuts, the Λ invariant mass cut, and the missing momentum cut. The results of these systematic uncertainty studies are shown in Figures 9.23 through 9.26, respectively, and are summarized in Table 9.4. Because the same final-state identification cuts were performed for the $\gamma n \rightarrow K^{+}\Sigma^{*-}$ and $\gamma n \rightarrow K^{*0}\Lambda$ analyses, the average uncertainties of the three highest photon energy bins were assigned to the $\gamma n \rightarrow K^{*0}\Lambda$ cross section as well. The method used to calculate these uncertainties is discussed in Section 9.4.

The overall uncertainties assigned to the photon energy bins of the particle identification study and the Λ invariant mass study were all between 3.6% and 7.4%. The systematic uncertainties on the missing momentum cuts were lower, ranging between 2.0% and 3.6%. However, the uncertainties on the time difference cuts were larger, varying between 5.0% and 9.3%. There were several large outliers in the time difference uncertainty distributions shown in Figure 9.24 that were not excluded from the overall uncertainty calculations. These points had less than a 50% effect on the overall uncertainty percentages, but their inclusion may have caused the overall uncertainties of these photon energy bins to be slightly overestimated. However these uncertainties did not have a large effect on the total uncertainties, as they were much smaller than the uncertainties on the simulated event

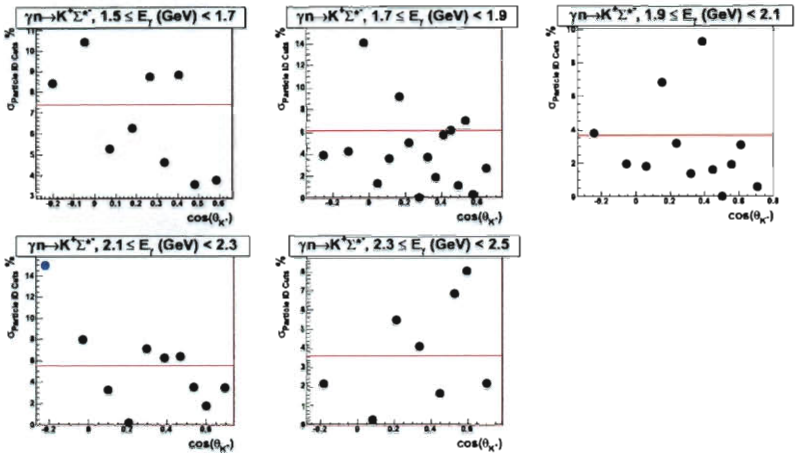

Figure 9.23 : The black points indicate the systematic uncertainty percentages on the $\gamma n \to K^{+}\Sigma^{*-}$ cross section from simultaneously tightening the proton, π^{-}, and K^{+} particle identification cuts from $\pm 3\sigma$ to $\pm 2\sigma$. The uncertainties did not have a systematic angular dependence, so for each energy bin the overall systematic uncertainty percentage indicated by the red lines was assigned for every point. The blue point had a $> 50\%$ effect on the overall uncertainty percentage of its energy bin, so it was excluded from the calculation and was assigned its individual uncertainty. The overall uncertainties of the three highest photon energy bins were assigned to the $\gamma n \to K^{*0}\Lambda$ cross section for the same photon energy ranges.

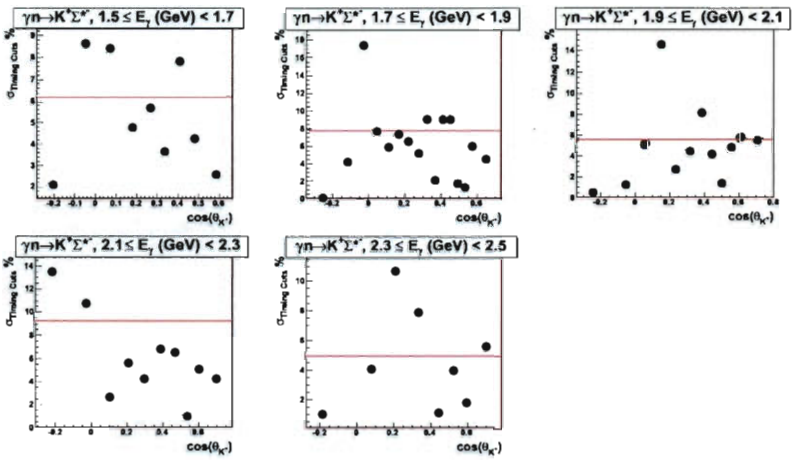

Figure 9.24 : The black points indicate the systematic uncertainty percentages on the $\gamma n \to K^{+}\Sigma^{*-}$ cross section from simultaneously tightening the $\Delta t_{p,\,\pi^-}$, $\Delta t_{\gamma,\,\pi^-}$, $\Delta t_{K^+,\,\pi^-}$ timing cuts from $\pm 3\sigma$ to $\pm 2\sigma$. The uncertainties did not have a systematic angular dependence, so for each energy bin the overall systematic uncertainty percentage indicated by the red lines was assigned for every point. None of the individual points had a $> 50\%$ effect on the overall uncertainty percentage, although several of the points with large uncertainties may have caused the overall uncertainties to be slightly overestimated. The overall uncertainties of the three highest photon energy bins were assigned to the $\gamma n \to K^{*0}\Lambda$ cross section for the same photon energy ranges.

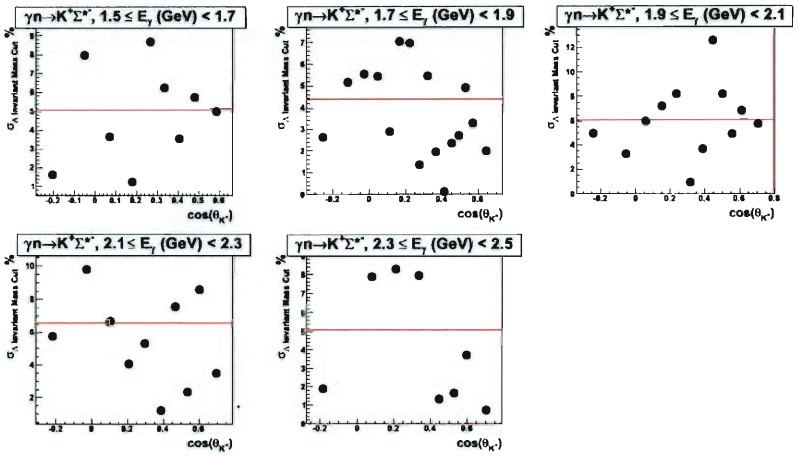

Figure 9.25 : The black points indicate the systematic uncertainty percentages on the $\gamma n \to K^{+}\Sigma^{*-}$ cross section from tightening the Λ invariant mass cut from $\pm 3\sigma$ to $\pm 2\sigma$. The uncertainties did not have a systematic angular dependence, so for each energy bin the overall systematic uncertainty percentage indicated by the red lines was assigned for every point. None of the individual points had a $> 50\%$ effect on the overall uncertainty percentage. The overall uncertainties of the three highest photon energy bins were assigned to the $\gamma n \to K^{*0}\Lambda$ cross section for the same photon energy ranges.

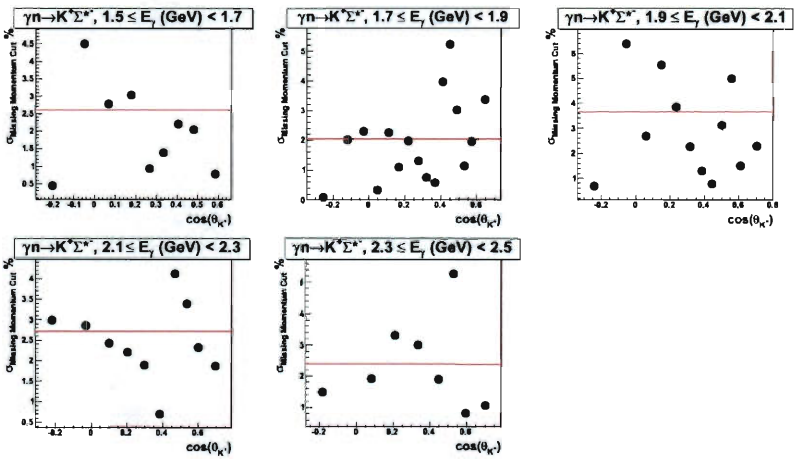

Figure 9.26 : The black points indicate the systematic uncertainty percentages on the $\gamma n \to K^{+}\Sigma^{*-}$ cross section from changing the missing minimum cut from 200 MeV/c to 150 MeV/c. The uncertainties did not have a systematic angular dependence, so for each energy bin the overall systematic uncertainty percentage indicated by the red lines was assigned for every point. None of the individual points had a $> 50\%$ effect on the overall uncertainty percentage. The overall uncertainties of the three highest photon energy bins were assigned to the $\gamma n \to K^{*0}\Lambda$ cross section for the same photon energy ranges.

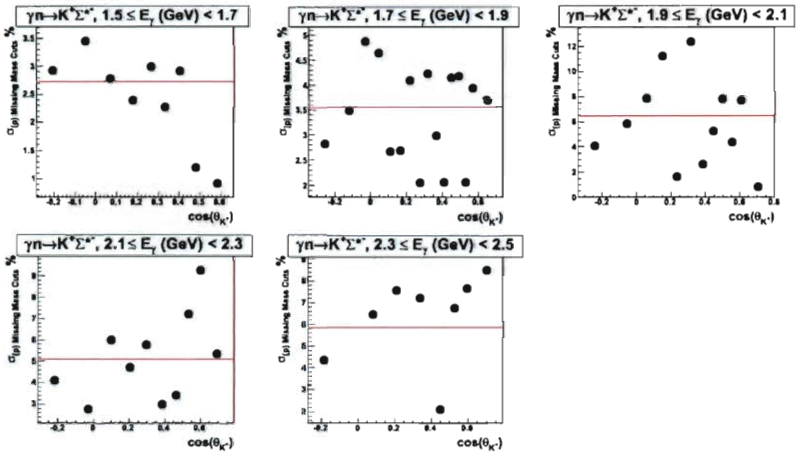

Figure 9.27 : The black points indicate the systematic uncertainty percentages on the $\gamma n \to K^{+}\Sigma^{*-}$ cross section from tightening the spectator proton missing mass cut from $\pm 3\sigma$ to $\pm 2\sigma$. The uncertainties did not have a systematic angular dependence, so for each energy bin the overall systematic uncertainty percentage indicated by the red lines was assigned for every point. None of the individual points had a $> 50\%$ effect on the overall uncertainty percentage. The overall uncertainties of the three highest photon energy bins were assigned to the $\gamma n \to K^{*0}\Lambda$ cross section for the same photon energy ranges.

distributions and the Σ^{*-} background fits. These systematic uncertainties are discussed in Sections 9.4.2 and 9.4.4, respectively.

9.4.4 $\gamma n \to K^{+}\Sigma^{*-}$ Yield Extraction Studies

The systematic uncertainties on the $\gamma n \to K^{+}\Sigma^{*-}$ yield extraction were determined by studying the missing mass cuts on the spectator proton, the overlap cuts on the K^{*0}, and the background fits and invariant mass cuts on the Σ^{*-} distributions. These systematic uncertainty studies are shown in Figures 9.27 through 9.31, and are summarized in Table 9.4. The scaling uncertainties due to the background events that contained an additional photon or π^0 in the final state are discussed in Section 9.4.1. The systematic uncertainties from these studies were all less than 7%, except for the study of the Σ^{*-} background fits.

The systematic uncertainties of the Σ^{*-} background fits were determined by fitting the Σ^{*-} invariant mass distributions using different background functions. Fits to one Σ^{*-} invariant mass distribution for each photon energy bin are shown in Figure 9.29, the same distributions as shown in Figure 8.21 for the nominal extraction of the $\gamma n \to K^{+}\Sigma^{*-}$ experimental yields. For the systematic uncertainty study, the background functions for the different photon energy bins were changed from

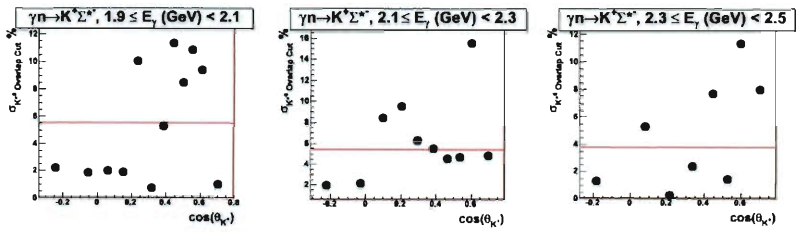

Figure 9.28 : The black points indicate the systematic uncertainty percentages on the $\gamma n \to K^{+}\Sigma^{*-}$ cross section from changing the K^{*0} invariant mass overlap cuts from $\pm 1\Gamma$ to $\pm 2\Gamma$. The uncertainties did not have a systematic angular dependence, so for each energy bin the overall systematic uncertainty percentage indicated by the red lines was assigned for every point. None of the individual points had a $> 50\%$ effect on the overall uncertainty percentage.

no, no, flat, flat, and linear functions to flat, flat, linear, linear, and flat functions, in order of increasing energy. However, if the background fits in a given bin were consistent with zero for both functions, then for the systematic study the height of the background was forced to be the average number of events on the low-mass side of the Σ^{*-} invariant mass peak, from 1.265 GeV/c^2 to 1.3 GeV/c^2. This assignment ensured that the systematic uncertainties were not underestimated from identical fit results. All of the Σ^{*-} fits in this study had a χ^2 per degree of freedom less than 3.0, indicating that these fits were a viable alternative to the nominal background fits.

The systematic uncertainties of this study are shown in Figure 9.30. The overall uncertainties of the highest photon energy bin and the two lowest photon energy bins were all larger than 10%. With future studies of the distributions of these backgrounds, these systematic uncertainties can likely be reduced.

9.4.5 $\gamma n \to K^{*0}\Lambda$ Systematic Uncertainty Studies

As discussed in Section 9.4, many of the results from the $\gamma n \to K^{+}\Sigma^{*-}$ systematic uncertainty studies were assigned to the $\gamma n \to K^{*0}\Lambda$ analysis. Studies of the simulation distribution, the Σ^{*-} overlap cuts, and the background fits and invariant mass cuts of the K^{*0} invariant mass distributions were performed separately for the $\gamma n \to K^{*0}\Lambda$ analysis. These studies are shown in Figures 9.32 through 9.37, and are summarized in Table 9.5. The study of the backgrounds due to events that contained an additional photon or π^0 were performed separately, and are discussed in Section 9.4.1. Due to the small number of bins, the individual uncertainties of each point were assigned for these studies instead of the average uncertainties of the photon energy bins. These uncertainties were

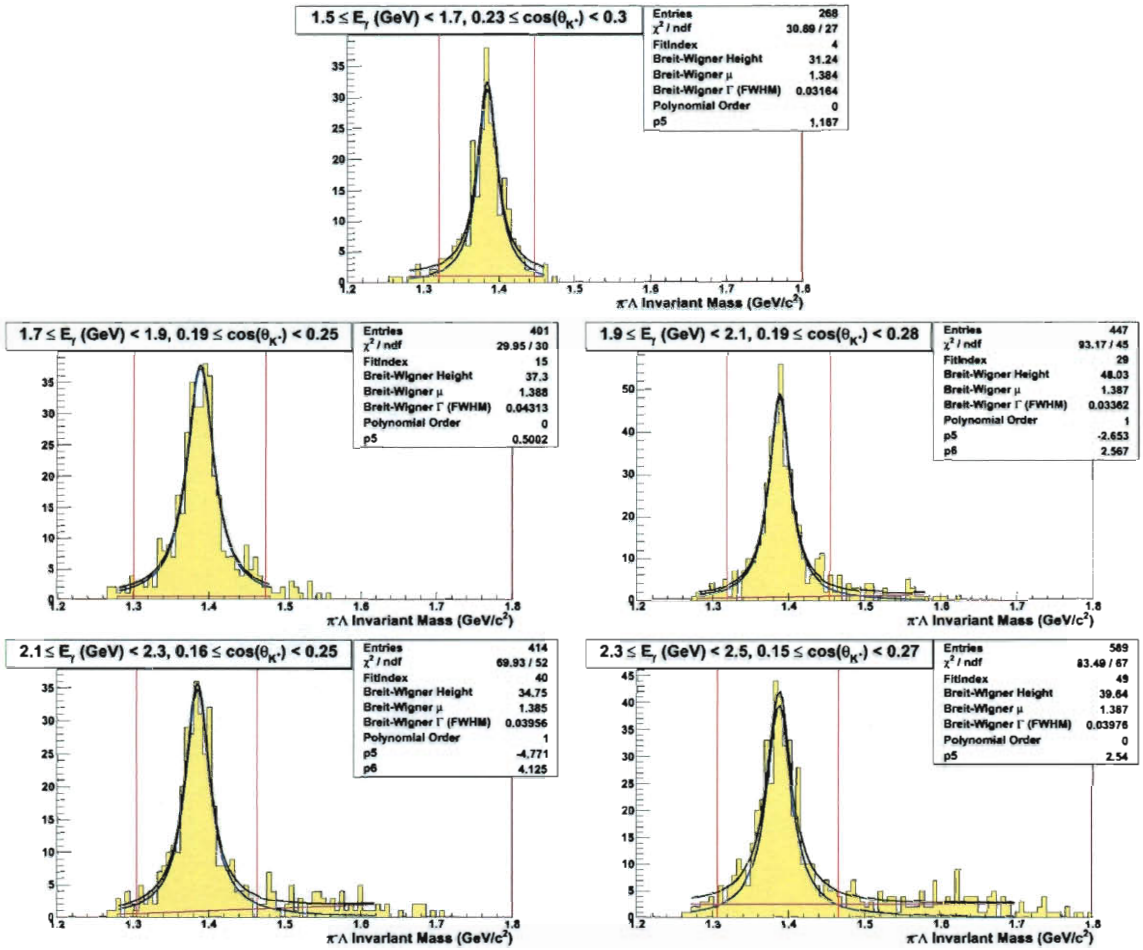

Figure 9.29 : Fits to the invariant mass of the Σ^{*-} for the study of the systematic uncertainties of the background fits. These fits are shown for one $\cos(\theta_{K^+})$ bin of each photon energy bin, where θ_{K^+} is the angle between the K^+ and the photon in the center-of-mass frame. The signals were fit to a Breit-Wigner function over a polynomial background that varied with photon energy. From 1.5 GeV to 1.9 GeV flat backgrounds were fit, from 1.9 GeV to 2.3 GeV linear backgrounds were fit, and from 2.3 GeV to 2.5 GeV flat backgrounds were fit. The red lines indicate the $\pm 2\Gamma$ cuts used for yield extraction, and the blue, magenta, and black lineshapes represent the Breit-Wigner, polynomial background, and total fit functions, respectively. All of the Σ^{*-} fits in this study had a χ^2 per degree of freedom of less than 3.0.

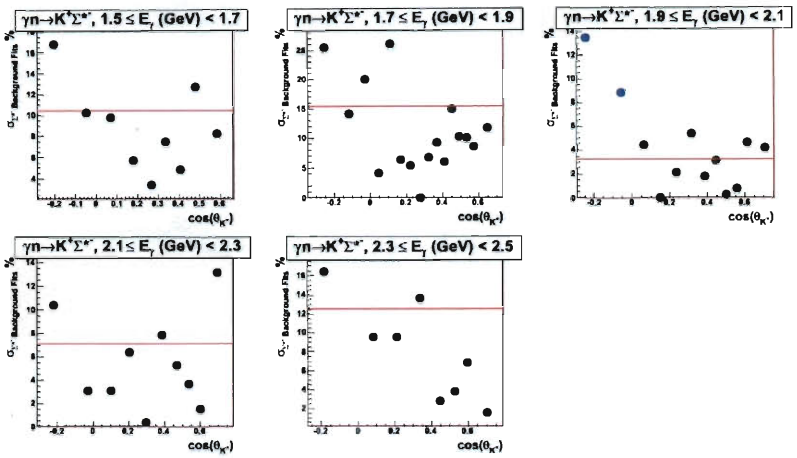

Figure 9.30 : The black points indicate the systematic uncertainty percentages on the $\gamma n \to K^{+}\Sigma^{*-}$ cross section from the Σ^{*-} background fits. These uncertainties were determined by changing the Σ^{*-} background fit functions for the different photon energy bins from no, no, flat, flat, and linear backgrounds to flat, flat, linear, linear, and flat backgrounds, listed in order of increasing photon energy. The uncertainties did not have a systematic angular dependence, so for each energy bin the overall systematic uncertainty percentage indicated by the red lines was assigned for every point. The blue points had a $> 50\%$ effect on the overall uncertainty percentage of their energy bins, so they were excluded from the calculation and were assigned their individual uncertainties.

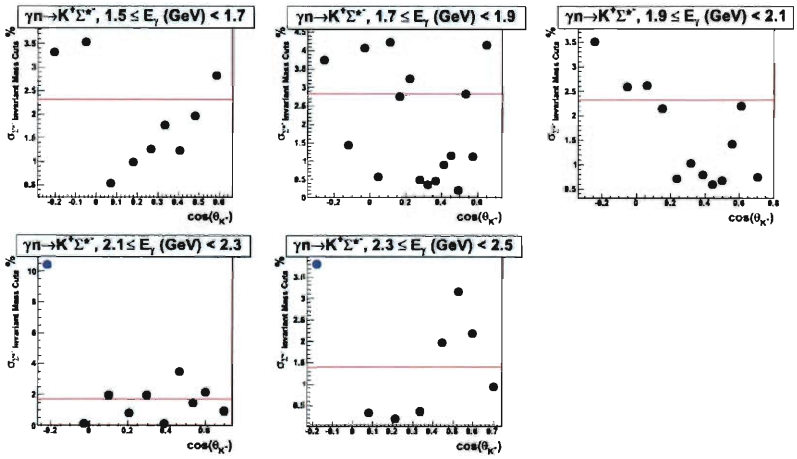

Figure 9.31 : The black points indicate the systematic uncertainty percentages on the $\gamma n \to K^{+}\Sigma^{*-}$ cross section from tightening the Σ^{*-} invariant mass cuts from $\pm 2\Gamma$ to $\pm 1\Gamma$. The uncertainties did not have a systematic angular dependence, so for each energy bin the overall systematic uncertainty percentage indicated by the red lines was assigned for every point. The blue points had a $> 50\%$ effect on the overall uncertainty percentage of their energy bins, so they were excluded from the calculation and were assigned their individual uncertainties.

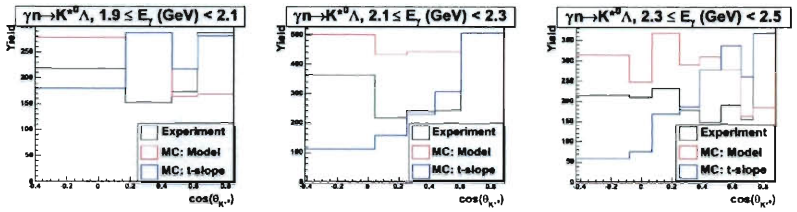

Figure 9.32 : For the $\gamma n \to K^{*0}\Lambda$ reaction, a comparison of the experimental yields to those from the different simulation distributions. The simulated yields were scaled such that their maximum values were the same as those of the experimental yields in each photon energy bin. The nominal $\gamma n \to K^{*0}\Lambda$ cross section was calculated using the Oh and Kim model predictions [68] for the simulation distribution, and for comparison was also calculated using a t-slope simulation distribution with an exponential slope of $b = 3.0$ GeV^{-2}. The differences between the simulated yields resulted in systematic uncertainties of up to ~32.2% at the large angles, where the bins were generally widest.

significantly larger than those for the $\gamma n \to K^{+}\Sigma^{*-}$ analysis, primarily due to either coarser binning or the fits to the K^{*0} invariant mass distributions.

The systematic uncertainties of the simulation distribution were determined by changing the distribution from the Oh and Kim model predictions [68] to a t-slope distribution with an exponential slope of $b = 3.0$ GeV^{-2}. This exponential slope was chosen to be the same as the one for the $\gamma n \to K^{+}\Sigma^{*-}$ analysis. In Figure 9.32, the experimental yields are shown compared against the simulated yields from both of these distributions. The simulated yields were vertically scaled for comparison, such that their maximum values were the same as those of the experimental yields in each photon energy bin. At large angles the relative simulated yields of the model prediction were much larger than those of the t-slope distribution. The systematic uncertainties from this study are shown in Figure 9.33. As for the $\gamma n \to K^{+}\Sigma^{*-}$ analysis discussed in Section 9.4.2, the simulated uncertainties were much greater at large angles due to the increased size of the bin widths. These uncertainties can be reduced by using the $\gamma n \to K^{*0}\Lambda$ cross sections from this analysis to generate the simulation distributions. Additionally, the exponential slope of the t-slope simulation distribution can be tuned to more closely match the experimental data.

The systematic uncertainties due to the Σ^{*-} overlap cuts are shown in Figure 9.34. As discussed in Section 9.3, while some of the differences between these cross sections may be due to interference effects, on average these systematic uncertainties are less than those on the K^{*0} invariant mass fits. It may be that a significant source of these uncertainties were the yield extraction fits of the K^{*0} invariant mass distributions, which were performed separately for each study.

As discussed in Section 8.2.1, there was a large bin-to-bin variation in the fit widths of the K^{*0}

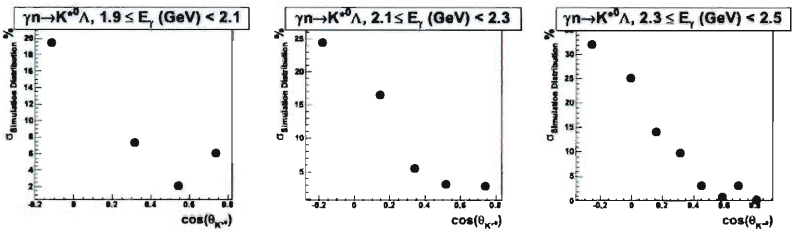

Figure 9.33 : The systematic uncertainty percentages on the $\gamma n \to K^{*0}\Lambda$ cross section from changing the simulation distribution used for calculating the CLAS acceptance from the Oh and Kim model predictions [68] to a t-slope distribution with an exponential slope of $b = 3.0$ GeV^{-2}. Due to the small number of bins and the large angular dependence, the uncertainties were assigned for each point individually.

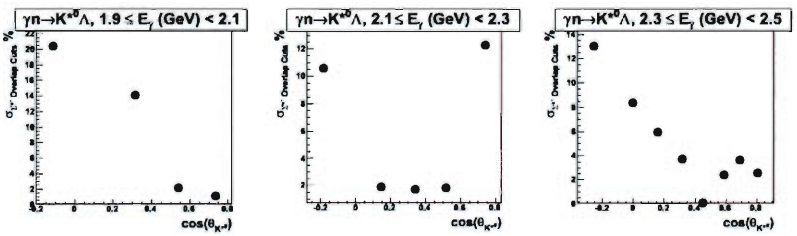

Figure 9.34 : The systematic uncertainty percentages on the $\gamma n \to K^{*0}\Lambda$ cross section from changing the Σ^{*-} invariant mass overlap cuts from $\pm 1\Gamma$ to $\pm 1.5\Gamma$. Due to the small number of bins, the uncertainties were assigned for the cross section points individually. A significant portion of these uncertainties may be due to the fits of the K^{*0} invariant mass distributions for yield extraction, which were performed separately for each study.

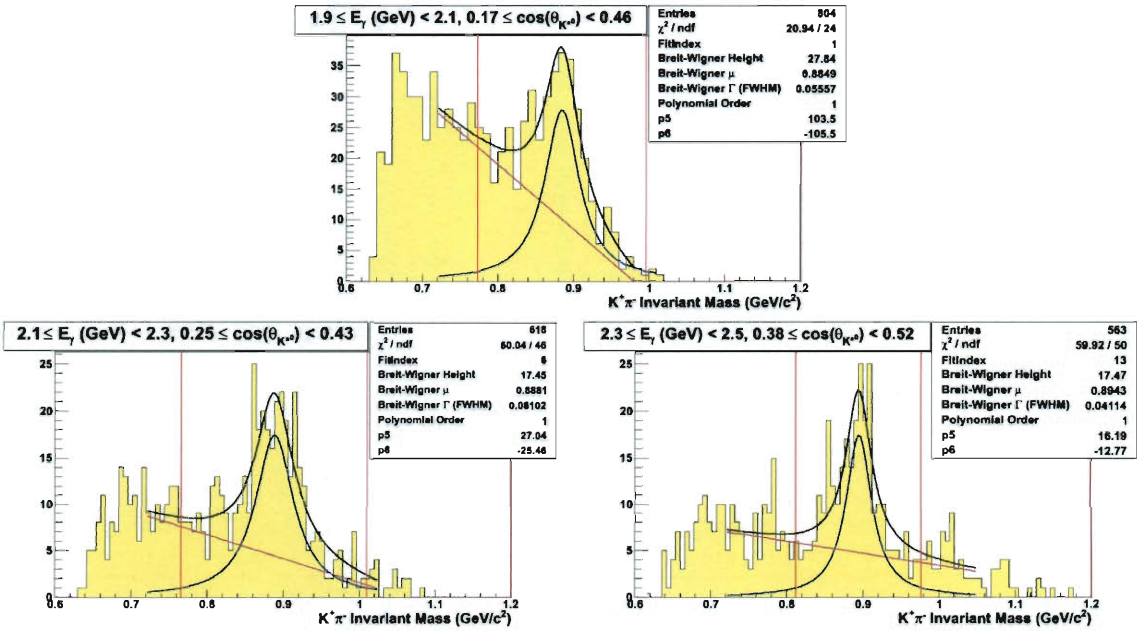

Figure 9.35 : Fits to the invariant mass of the K^{*0} for the study of the systematic uncertainties of the background fits. These fits are shown for one $\cos(\theta_{K^{*0}})$ bin of each photon energy bin, where $\theta_{K^{*0}}$ is the angle between the K^{*0} and the photon in the center-of-mass frame. The signals were fit to a Breit-Wigner function over a linear background, and the red lines indicate the $\pm 2\Gamma$ cuts used for yield extraction. The blue lineshapes represent the Breit-Wigner fit functions, the magenta lineshapes represent the quadratic fit functions, and the black lineshapes represent the total fit functions. All of the K^{*0} fits in this study had a χ^2 per degree of freedom of less than 2.5.

invariant mass distributions. The systematic uncertainties on these fits were determined by fitting linear functions to the backgrounds instead of quadratic functions, and by cutting at $\pm 1\Gamma$ to extract the $\gamma n \to K^{*0}\Lambda$ yields instead of at $\pm 2\Gamma$. Sample fits to K^{*0} invariant mass distributions with linear background functions are shown in Figure 9.35, the same bins as shown in Figure 8.15 for the nominal fits. All of the K^{*0} fits using linear background functions had a χ^2 per degree of freedom of less than 2.5, indicating that these background functions also produced viable results.

The systematic uncertainties from this background study are shown in Figure 9.36. There was a large variation of the uncertainties between the different bins, which ranged from ~0.2% to ~31.6%. Since both the quadratic and linear background functions yielded a low χ^2 per degree of freedom for the fits, background modeling will be necessary to reduce these large uncertainties. Due to the uncertainties in the K^{*0} invariant mass fits, the systematic uncertainties from tightening the width of the K^{*0} invariant mass cuts shown in Figure 9.37 varied between ~1.5% and ~16.5%.

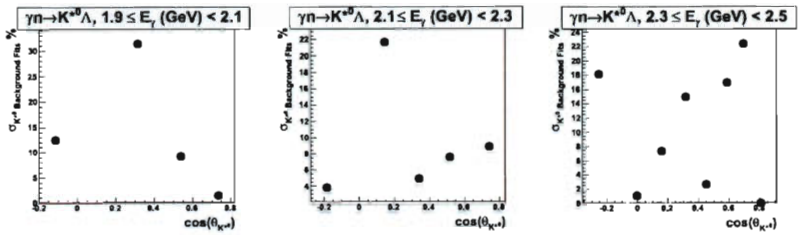

Figure 9.36 : The systematic uncertainty percentages on the $\gamma n \to K^{*0}\Lambda$ cross section from changing the K^{*0} background fits from quadratic to linear functions. Due to the small number of bins, the uncertainties were assigned for the cross section points individually. Due to the low χ^2 per degree of freedom for both sets of fits, background modeling will be necessary to reduce these large uncertainties.

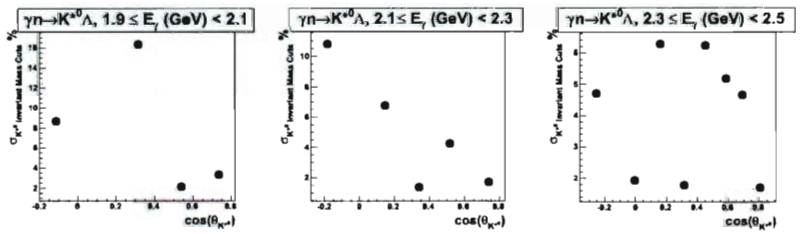

Figure 9.37 : The systematic uncertainty percentages on the $\gamma n \to K^{*0}\Lambda$ cross section from tightening the K^{*0} invariant mass cuts from $\pm 2\Gamma$ to $\pm 1\Gamma$. Due to the small number of bins, the uncertainties were assigned for the cross section points individually. These uncertainties can be attributed to ambiguities in fitting the experimental K^{*0} invariant mass distributions, and should be significantly reduced in future studies with background modeling.

9.5 Summary

The structure of hadronic matter is one of the major incompletely understood properties of the universe. Diquark models predict that if the quarks within the nucleons form a correlated quark-pair, then the spectrum of the N^* states will be significantly reduced [38]. Models of the baryons with uncorrelated quarks predict a much larger number of N^* resonances, but many of these states have not yet been observed. Some of these "missing" states are predicted to have non-negligible couplings to strangeness channels, and their observation would significantly limit the possible role of diquarks within hadrons.

In this analysis, the differential cross sections of the $\gamma n \to K^{*0}\Lambda$ and $\gamma n \to K^{+}\Sigma^{*-}$ reactions were measured using data from the CLAS g13 experiment performed in Hall B at Jefferson Lab. No previous measurements have been published on the $\gamma n \to K^{*0}\Lambda$ cross section, and the only published results on the $\gamma n \to K^{+}\Sigma^{*-}$ reaction are limited to forward angles. Several of the "missing" N^* resonances are predicted to have sizable couplings to these reactions, including the $N\frac{3}{2}^{-}(1960)$, $N\frac{5}{2}^{+}(1980)$, $N\frac{5}{2}^{+}(1995)$, $N\frac{3}{2}^{-}(2055)$, $N\frac{1}{2}^{+}(2065)$, $N\frac{5}{2}^{-}(2080)$, and $N\frac{3}{2}^{-}(2095)$ resonances. A partial-wave analysis of these cross sections can be used to study whether any of these predicted resonances contributed to these reactions.

The $\gamma n \to K^{+}\Sigma^{*-}$ cross section was significantly larger than the model predictions by Oh, Ko, and Nakayama [69, 78] at forward angles, but was closer in scale at large angles. Within the uncertainties, the $\gamma n \to K^{*0}\Lambda$ cross section was similar to the model predictions by Oh and Kim [68], but these predictions were partially constrained by a preliminary total cross section measurement that contained a scaling error. The comparison between these cross section measurements and the phenomenological models can be used to study the interactions that give rise to these distributions.

The cross sections of these reactions are sizable compared to those of the ground state KY channels, indicating that rescattering into the excited K^*Y and KY^* channels may be significant. Therefore, the $\gamma n \to K^{*0}\Lambda$ and $\gamma n \to K^{+}\Sigma^{*-}$ reactions need to be included in coupled-channels analyses used to extract the N^* resonance parameters. Also, no interference between these reactions was observed on a scale larger than the systematic uncertainties.

Several additional studies can be performed to improve these cross section results. With the recalibration of the photon tagger timing, the photon energy and timing will be known to greater accuracy. Also, the CLAS acceptance calculation can be improved by generating the simulation

distributions to these cross section measurements. This will also significantly reduce the systematic uncertainties associated with these distributions. Studies of the target density and integrated photon flux can be performed to update the systematic uncertainties used from previous experiments.

In addition to acceptance studies, the large systematic uncertainties on the $\gamma n \rightarrow K^{*0}\Lambda$ and $\gamma n \rightarrow K^{+}\Sigma^{*-}$ cross sections can be reduced with future analyses of the backgrounds. Background modeling can be used to subtract the backgrounds from events that contained an additional photon or π^0 in the final state. It can also be used to improve the yield extraction fits to the K^{*0} and Σ^{*-} invariant mass distributions. These improvements will also reduce the effects of the yield extraction uncertainties on the other systematic uncertainty studies. Also, the systematic uncertainty studies that were used for both analyses can be calculated separately for the $\gamma n \rightarrow K^{*0}\Lambda$ analysis, and would provide a cross-check of its systematic uncertainties. These total uncertainties may decrease to around 10% to 20% from these additional studies.

The matching between the $\gamma n \rightarrow p\pi^-$ cross section and the published world data verified the quality of the g13 data, as well as the procedures used in this analysis. When these $\gamma n \rightarrow p\pi^-$ cross section data are published they will provide tighter constraints on the couplings of the N^* states to the neutron, and additional information on the photo-transition amplitudes of the γN interaction. The $\gamma n \rightarrow p\pi^-$ cross section statistical uncertainties can be reduced by including the complete g13a dataset, and additional studies can be performed to fully determine the systematic uncertainties. Also, the accuracy of the acceptance corrections can be improved by extending the range of the simulated photon energy.

The analysis procedures that can be used to reduce the systematic uncertainties on these data are still under development. When finalized, these results can provide better resolution of the potential reaction interference effects, and tighter constraints on the N^* resonance couplings to the $\gamma n \rightarrow K^{*0}\Lambda$ and $\gamma n \rightarrow K^{+}\Sigma^{*-}$ reactions. The N^* resonance couplings to these reactions can then be studied by including these measurements in partial-wave coupled-channels analyses. The extraction of the spectrum of the N^* resonances will provide information on the relevant degrees of freedom of the quarks within the nucleon.

Bibliography

[1] W.S.C. Williams, *Nuclear and Particle Physics*, Oxford University Press Inc., New York (1991).

[2] M. E. Peskin and D. V. Schroeder, An Introduction to Quantum Field Theory, Westview Press (1995).

[3] S. Fukuda *et al.* (The Super-Kamiokande Collaboration), Phys. Lett. B **539**, 179 (2002).

[4] Q. R. Ahmad *et al.* (The SNO Collaboration), Phys. Rev. Lett. **89**, 011301 (2002).

[5] T. Araki *et al.* (The KamLAND Collaboration), Phys. Rev. Lett. **94**, 081801 (2004).

[6] T. Kajita, New J. Phys. **6**, 194 (2004).

[7] M. H. Ahn *et al.* (The K2K collaboration), Phys. Rev. Lett. **90**, 041801 (2003).

[8] K. Nakamura *et al.* (The Particle Data Group), J. Phys. G **37**, 075021 (2010).

[9] M. Fukugita and T. Yanagida, Phys. Lett. B **174**, 45 (1986).

[10] Fermilab, *What is the world made of?*, `http://www.fnal.gov/pub/inquiring/matter/madeof/index.html` (2004).

[11] J. W. F. Valle, arXiv:0608101 [hep-ph] (2006).

[12] S. L. Glashow, Nucl. Phys. **22**, 579 (1961).

[13] S. Weinberg, Phys. Rev. Lett. **19**, 1264 (1967).

[14] A. Salam, *Weak and Electromagnetic Interactions*, in *Elementary Particle Theory: Relativistic Groups and Analysticity (Nobel Symposium No. 8)*, edited by N. Svartholm, (Almqvist & Wiksell, Stockholm), 367 (1968).

[15] G. 't Hooft, Nucl. Phys. B **35** 167 (1971).

[16] F. Englert and R. Brout, Phys. Rev. Lett. **13,** 321 (1964).

[17] P. W. Higgs, Phys. Rev. Lett. **13**, 508 (1964).

[18] P. W. Higgs, Phys. Lett. **12,** 132 (1964).

[19] G. S. Guralnik, C. R. Hagen, and T. W. B. Kibble, Phys. Rev. Lett. **13,** 585 (1964).

[20] The TEVNPH Working Group (The CDF and D0 Collaborations), Fermilab Note FERMILAB-CONF-11-044-E (2011).

[21] European Organization for Nuclear Research (CERN), *Missing Higgs*, `http://public.web.cern.ch/public/en/Science/Higgs-en.html` (2008).

[22] T. W. B. Kibble, *Englert-Brout-Higgs-Guralnik-Hagen-Kibble mechanism*, Scholarpedia, 4(1):6441 (2009).

[23] J. D. Walecka, *Theoretical Nuclear and Subnuclear Physics*, Oxford University Press, Inc., New York, New York (1995).

[24] M. Gell-Mann, Phys. Rev. **125**, 1067 (1962).

[25] The Particle Adventure, *Quark Confinement*, `http://www.particleadventure.org/quark_confinement.html` (2009).

[26] D. J. Gross and F. Wilczek, Phys. Rev. D **8**, 3633 (1973).

[27] D. J. Gross and F. Wilczek, Phys. Rev. Lett. **30**, 1343 (1973).

[28] H. D. Politzer, Phys. Rev. Lett. **30**, 1346 (1973).

[29] H. D. Politzer, Phys. Rep. **14**, 129 (1974).

[30] Wikimedia Commons, *Particle physics*, `http://commons.wikimedia.org/wiki/Particle_physics` (2010).

[31] F. Halzen and A. D. Martin, *Quarks & Leptons: An Introductory Course in Modern Particle Physics,* John Wiley & Sons, New York, New York (1984).

[32] Wikimedia Commons, *File:Meson-octet-small.svg*, `http://commons.wikimedia.org/wiki/File:Meson-octet-small.svg` (2007).

[33] Wikipedia, *Baryon*, `http://en.wikipedia.org/wiki/Baryon` (2011).

[34] S. Capstick and N. Isgur, Phys. Rev. D **34**, 2809 (1986).

[35] A. Thomas, *Meson-Nucleon Physics: An Overview,* 12th International Conference on Meson-Nucleon Physics and the Structure of the Nucleon, College of William and Mary (2010).

[36] Nanowerk News, *High-energy proton collisions help solve the puzzle of what determines the proton's spin,* `http://www.nanowerk.com/news/newsid=13284.php` (2009).

[37] University of Bonn, *Physics at Crystal-Barrel@ELSA*, `http://www1.cb.uni-bonn.de/index.php?id=3&L=1`.

[38] E. Santopinto, Phys. Rev. C **72**, 022201(R) (2005).

[39] S. Capstick and W. Roberts, Phys. Rev. D **47**, 1994 (1993).

[40] S. Capstick and W. Roberts, Phys. Rev. D **58**, 074011 (1998).

[41] N. Isgur and G. Karl, Phys. Lett. **72B**, 109 (1977).

[42] W. Roberts, *Hadron Physics*, `http://www.physics.fsu.edu/users/roberts/roberts_hadrons.html`.

[43] V. A. Nikonov *et al.*, Phys. Lett. B **662**, 245 (2008).

[44] D. S. Carman *et al.* (The CLAS Collaboration), Phys. Rev. C **79**, 065205 (2009).

[45] E. S. Ackleh, T. Barnes, and E. S. Swanson, Phys. Rev. D **54**, 6811 (1996).

[46] N. Isgur and J. Paton, Phys. Lett. **124B** 124B, 247 (1983); Phys. Rev. D **31**, 2910 (1985).

[47] R. Kokoski and N. Isgur, Phys. Rev. D **35**, 907 (1987).

[48] S. Kumano and V. R. Pandharipande, Phys. Rev. D **38**, 146 (1988).

[49] Fl. Stancu and P. Stassart, Phys. Rev. D **38**, 233 (1988); **39**, 343 (1989); **41**, 916 (1990); **42**, 1521 (1990).

[50] H. Dosch and D. Gromes, Phys. Rev. D **33**, 1378 (1986).

[51] J. W. Alcock, M. J. Burfitt, and W. N. Cottingham, Z. Phys. C **25**, 161 (1984).

[52] R. Koniuk and N. Isgur, Phys. Rev. D **21**, 1868 (1980).

[53] W. Roberts and B. Silvestre-Brac, Few Body Syst. **11**, 171 (1992).

[54] L. Lyons, Statistics for Nuclear and Particle Physicists, Cambridge University Press, Cambridge, England (1986).

[55] S. Capstick, Phys. Rev. D **46**, 2864 (1992).

[56] S. Capstick, Phys. Rev. D **46**, 1965 (1992).

[57] I. S. Barker, A. Donnachie, and J.K. Storrow, Nucl. Phys. **B95**, 347 (1975).

[58] R. Schumacher, *Electromagnetic Strangeness Production*, MENU 2010 Conference Presentation (2010).

[59] A. Sandorfi, S. Hoblit, H. Kamano, and T.-S. H. Lee, arXiv:1010.4555 [nucl-th].

[60] R. Bradford *et al.* (The CLAS Collaboration), Phys. Rev. C **75**, 035205 (2007).

[61] W-T. Chiang and F. Tabakin, Phys. Rev. C **55**, 2054 (1997).

[62] M. Pichowski, C. Savkli, and F. Tabakin, Phys. Rev. C **53**, 593 (1996).

[63] W-T. Chiang, F. Tabakin, T.-S. H. Lee, and B. Saghai, Phys. Lett. B **517**, 101 (2001).

[64] A. Usov and O. Scholten, Phys. Rev. C **72**, 025205 (2005).

[65] P. Nadel-Turonski *et al.*, Jefferson Lab PAC30 Proposal: PR-06-103, `http://www.jlab.org/exp_prog/proposals/06/PR-06-103.pdf` (2006).

[66] B. Julia-Diaz, B. Saghai, T.-S. H. Lee, and F. Tabakin, Phys. Rev. C **73**, 055204 (2006).

[67] V. Shklyar, H. Lenske, and U. Mosel, Phys. Rev. C **72**, 015210 (2005).

[68] Y. Oh, H. Kim, Phys. Rev. C **73**, 065202 (2006).

[69] Y. Oh, C. M. Ko, K. Nakayama, Phys. Rev. C **77**, 045204 (2008).

[70] J.W.C. McNabb *et al.* (The CLAS Collaboration), Phys. Rev. C **69**, 042201(R) (2004).

[71] R. Bradford *et al.* (The CLAS Collaboration), Phys. Rev. C **73**, 035202 (2006).

[72] A. Lleres *et al.*, Eur. Phys. J. A **31**, 79 (2007).

[73] K. Ardashev *et al.* (The CLAS Collaboration), Jefferson Lab PAC30 Proposal: PR-06-101, `http://www.jlab.org/exp_prog/proposals/06/PR-06-101.pdf` (2006).

[74] K. Hicks *et al.* (The LEPS Collaboration), arXiv:0812.0771 [nucl-ex] (2008).

[75] L. Guo and D. P. Weygand (The CLAS Collaboration), arXiv:0601010 [hep-ex] (2006).

[76] I. Hleiqawi *et al.* (The CLAS Collaboration), Phys. Rev. C **75**, 042201(R) (2007).

[77] I. Hleiqawi *et al.* (The CLAS Collaboration), Phys. Rev. C **76**, 039905(E) (2007).

[78] Y. Oh, KyungPook National University, Private Communication (2009).

[79] L. Guo, Florida International University, Private Communication (2011).

[80] C. W. Leemann, D.R. Douglas, G.A. Krafft, Annu. Rev. Nucl. Part. Sci. **51**, 413 (2001).

[81] B. A. Mecking *et al.* (The CLAS Collaboration), Nucl. Instr. and Meth. A **503**, 513 (2003).

[82] P. Nadel-Turonski *et al.*, Few Body Syst. **43**, 227 (2008).

[83] R. Fersch, *Measurement of Inclusive Proton Double-Spin Asymmetries and Polarized Structure Functions*, Ph.D. Thesis, The College of William and Mary, `http://www.jlab.org/Hall-B/general/thesis/Fersch_thesis.pdf` (2008).

[84] D. I. Sober *et al.* (The CLAS Collaboration), Nucl. Instr. and Meth. A **440**, 263 (2000).

[85] S. K. Matthews, H. Crannell, J. T. O'Brien, D.I. Sober, Nucl. Instr. and Meth. A **421**, 23 (1999).

[86] M. D. Mestayer *et al.* (The CLAS Collaboration), Nucl. Instr. and Meth. A **449**, 81 (2000).

[87] Y. G. Sharabian *et al.* (The CLAS Collaboration), Nucl. Instr. and Meth. A **556**, 246 (2006).

[88] H. Olsen and L. C. Maximom, Phys. Rev. **114**, 887 (1959).

[89] K. Livingston, Nucl. Instr. and Meth. A **603**, 205 (2009).

[90] U. Timm, Fortschr. Phys. **17**, 765 (1969).

[91] F. A. Natter et al., Nucl. Instr. and Meth. B **211**, 465 (2003).

[92] S. Christo, `http://www.jlab.org/~christo/g11a%20target.html` (2004).

[93] S. Boyarinov and V. Kubarovsky, Jefferson Lab, Private Communication (2009 - 2010).

[94] E. Pasyuk, Jefferson Lab CLAS-Note 2007-106 (2007).

[95] M. Williams, D. Applegate, and C.A. Meyer, Jefferson Lab CLAS-Note 2004-017 (2004).

[96] M. Williams and C. A. Meyer, Jefferson Lab CLAS-Note 2003-017 (2003).

[97] P. Mattione, *Kinematic Fitting of Detached Vertices,* M.S. Thesis, Rice University, `http://www1.jlab.org/Ul/Publications/view_pub.cfm?pub_id=7379` (2007).

[98] K. Y. Kim, H. Denizli, J. A. Mueller, and S. A. Dytman, Jefferson Lab CLAS-Note 2001-018 (2001).

[99] S. Stepanyan, Jefferson Lab CVS Repository, /group/clas/clas_cvs/packages/fsgen/ (2006).

[100] M. Lacombe *et al.*, Phys. Lett. **101B**, 139 (1981).

[101] CERN Application Software Group, *GEANT - Detector Description and Simulation Tool*, `http://wwwinfo.cern.ch/asdoc/pdfdir/geant.pdf` (1993).

[102] M. Holtrop, *CLAS GEANT Simulation*, `http://www.physics.unh.edu/maurik/gsim_info.shtml`.

[103] Jefferson Lab Hall B, *Recsis*, `http://clasweb.jlab.org/wiki/index.php/Recsis` (2007).

[104] J. Ball and E. Pasyuk, Jefferson Lab CLAS-Note 2005-002 (2005).

[105] P. Mattione, *TripFixer*, `http://clasweb.jlab.org/rungroups/g13/wiki/index.php/TripFixer`.

[106] E. Pasyuk, Jefferson Lab, Private Communication (2010).

[107] D. Applegate, M. Bellis, Z. Krahn, C. A. Meyer, and M. Williams, Jefferson Lab CLAS-Note 2006-017 (2006).

[108] R. Schumacher, Jefferson Lab CLAS-Note 2001-010 (2001).

[109] W. Chen *et al.* (The CLAS Collaboration), Phys. Rev. Lett. **103**, 012301 (2009).

[110] I. Strakovsky, George Washington University, Private Communication (2010).

[111] R. A. Arndt, W. J. Briscoe, R. L. Workman, and I. I. Strakovsky, GWU CNS DAC SAID Database `http://gwdac.phys.gwu.edu/analysis/pr_analysis.html`.

[112] M. Williams, *Measurement of Differential Cross Sections and Spin Density Matrix Elements along with a Partial Wave Analysis for $\gamma p \to p\omega$ using CLAS at Jefferson Lab*, Ph.D. Thesis, Carnegie Mellon University, `http://www.jlab.org/Hall-B/general/clas_thesis.html` (2007).

[113] NIST CODATA, *deuteron mass in u*, `http://physics.nist.gov/cgi-bin/cuu/Value?mdu` (2006).

[114] NIST CODATA, *Avogadro constant*, `http://physics.nist.gov/cgi-bin/cuu/Value?na` (2006).

[115] R. Bradford and R. Schumacher, Jefferson Lab CLAS-Note 2002-003 (2002).

[116] M. Dugger *et al.* (The CLAS Collaboration), Phys. Rev. C **76**, 025211 (2007).

[117] H. Lu, Carnegie Mellon University, Private Communication (2010).

[118] M. E. McCracken *et al.* (The CLAS Collaboration), Phys. Rev. C **81**, 025201 (2010).

[119] H. Lu, *Exclusive Photo-Production Measurement of $K^+\Sigma^{*-}$ off Quasi-Free Neutrons in Deuterium*, Ph.D. Thesis, University of South Carolina, `http://www.jlab.org/Hall-B/general/thesis/HLu_thesis.pdf` (2010).

[120] Q. Zhao, Institute of High Energy Physics, Private Communication (2010).

[121] S. Anefalos Pereira *et al.* (The CLAS Collaboration), Phys. Lett. B **688**, 289 (2010).

Appendix A

Momentum Correction Plots

A.1 Prior to Kinematic Fitting

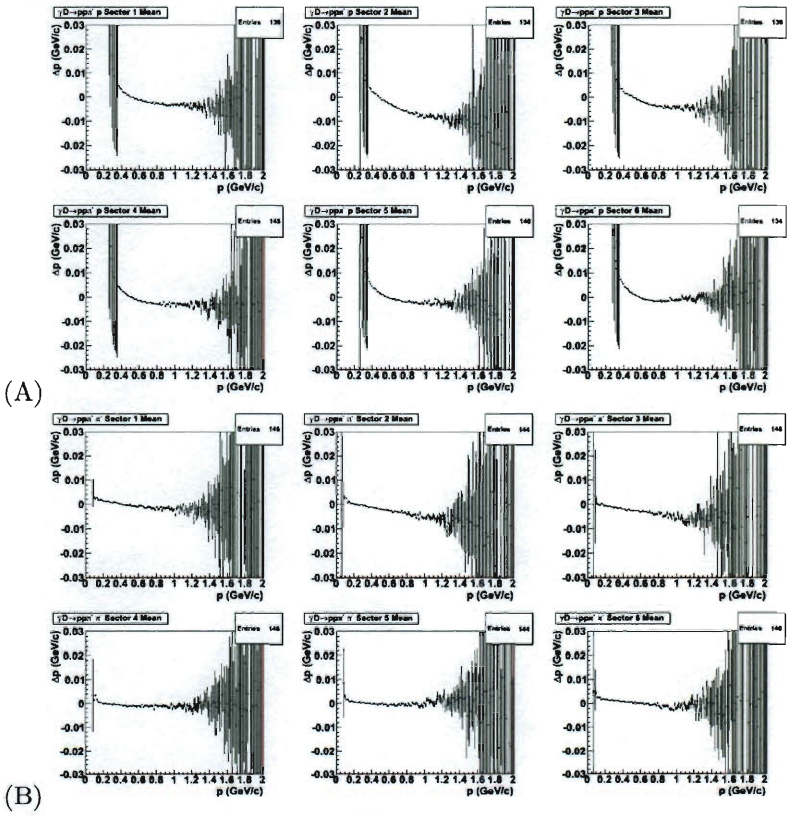

Figure A.1 : The average difference between the fit and detected momentum after *eloss* corrections as a function of p in the six sectors of CLAS for the (A) proton and (B) π^-.

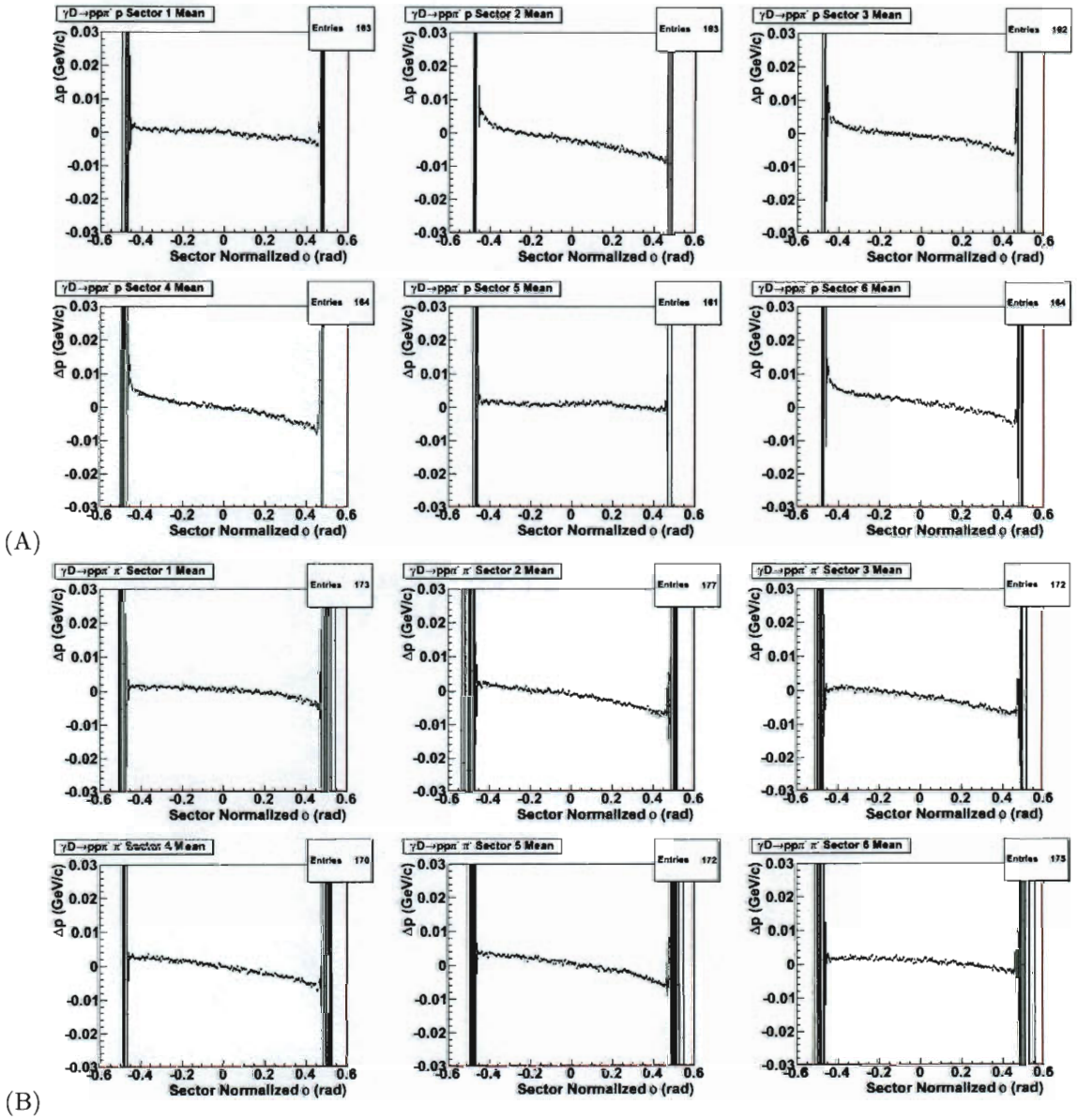

Figure A.2 : The average difference between the fit and detected momentum after *eloss* corrections as a function of the sector-normalized ϕ in the six sectors of CLAS for the (A) proton and (B) π^-.

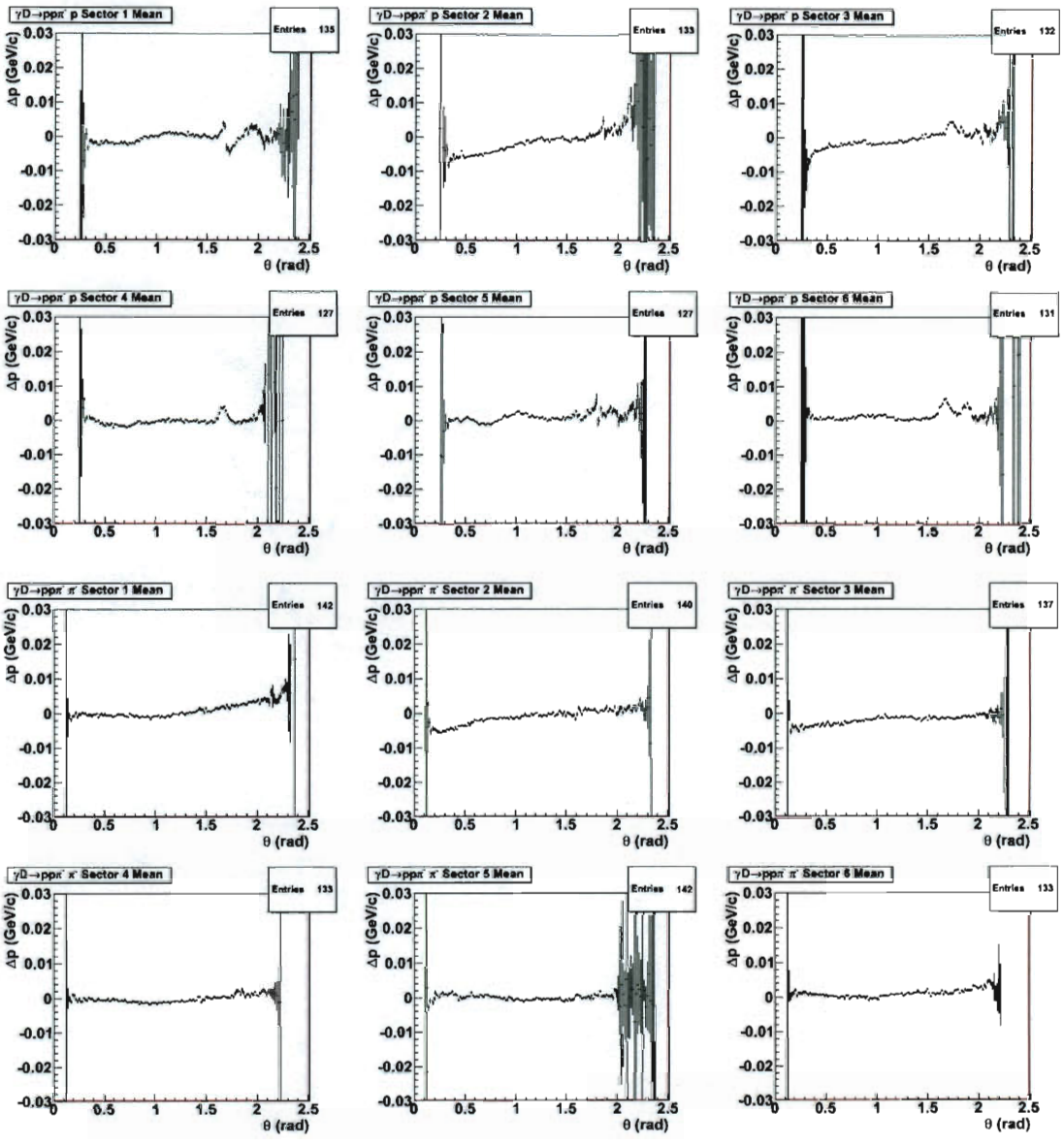

(A)

(B)

Figure A.3 : The average difference between the fit and detected momentum after *eloss* corrections as a function of θ in the six sectors of CLAS for the (A) proton and (B) π^-.

A.2 Momentum Correction Fits

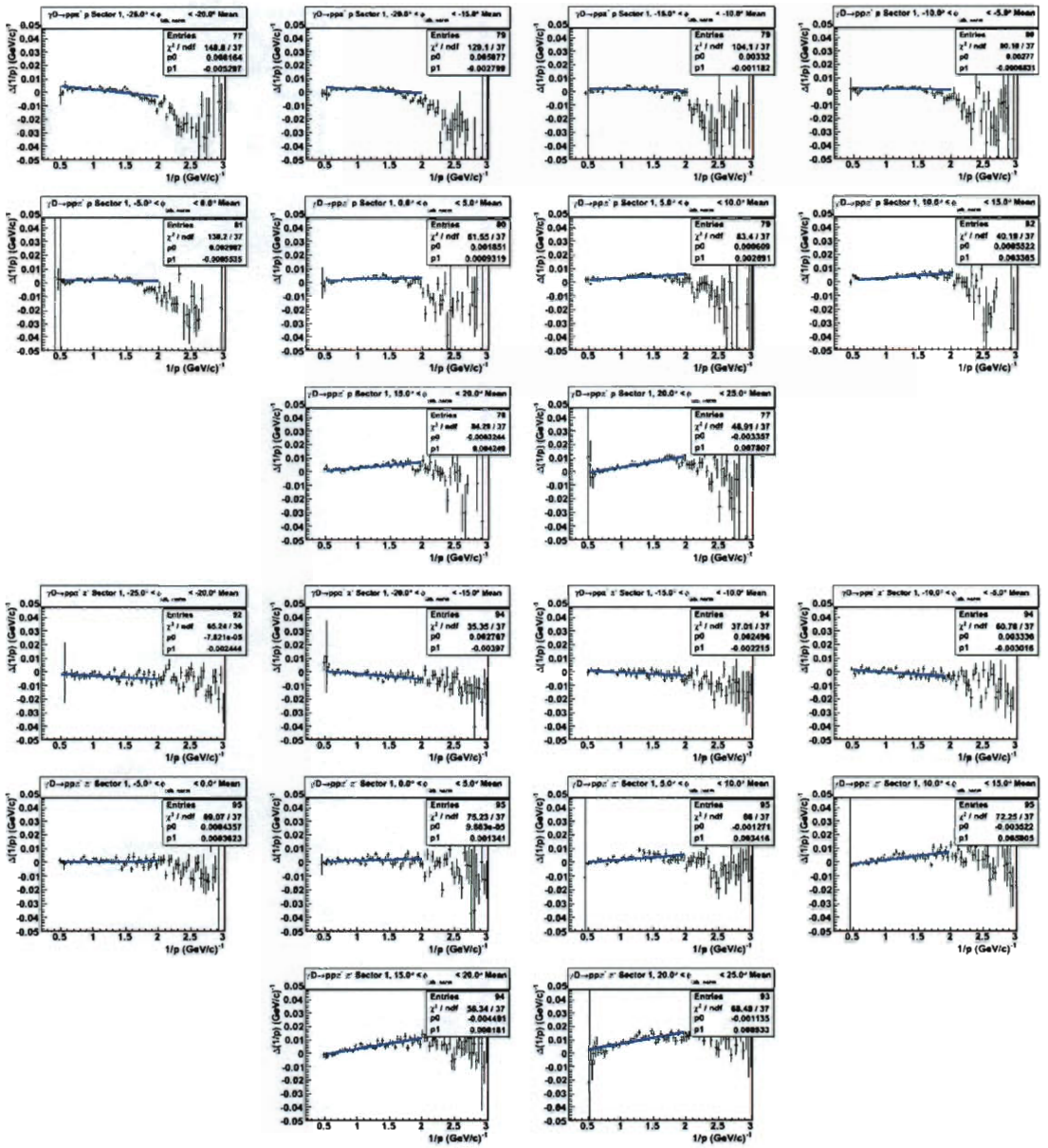

(A)

(B)

Figure A.4 : The fit to the mean $\Delta(1/p)$ vs. $1/p$ for the 10 ϕ bins in Sector 1 for the (A) protons and the (B) π^-. These errors are due to the ϕ-dependent drift chamber misalignments and differences between the actual magnetic field and the calculated map used for track reconstruction.

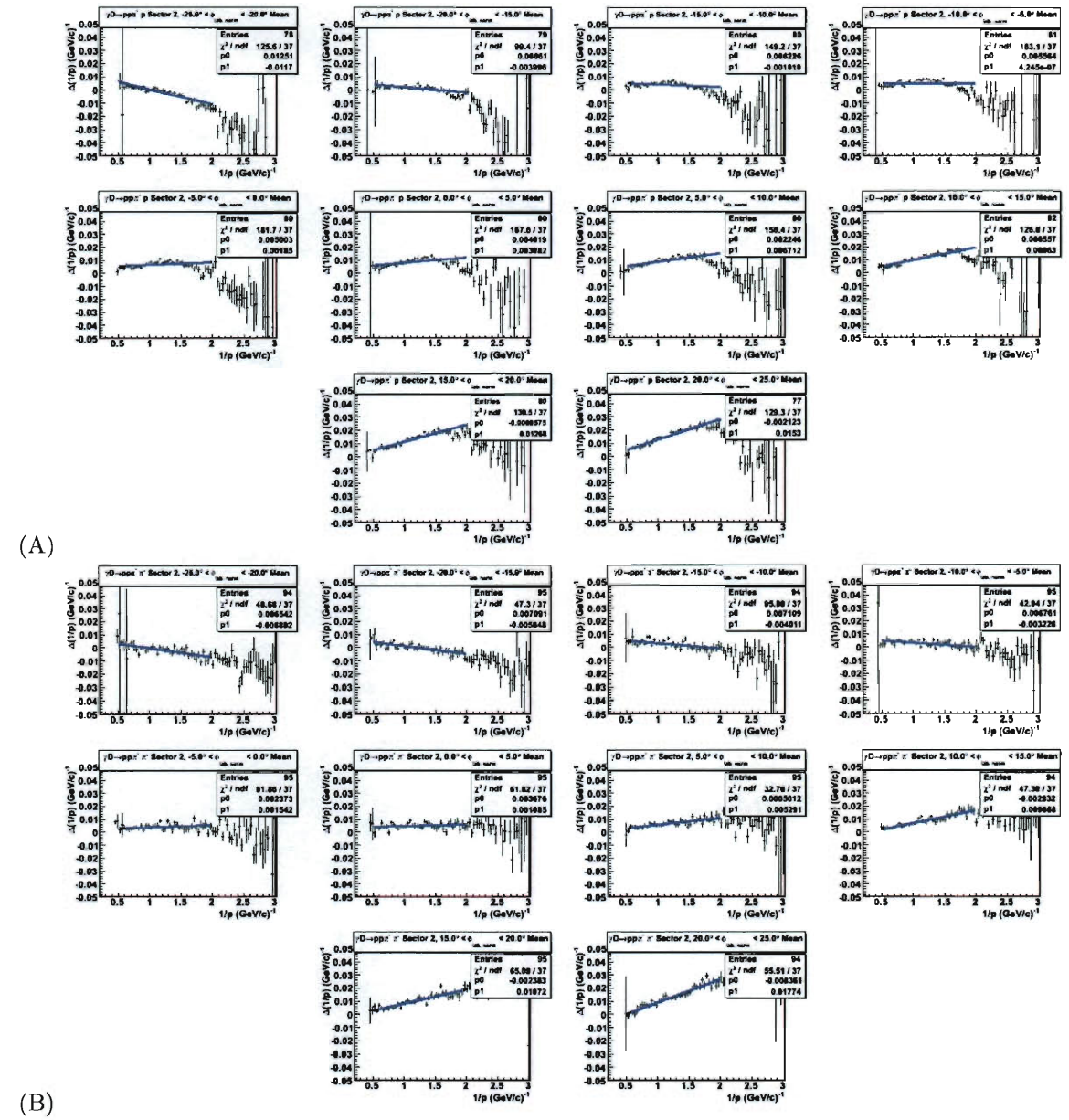

(A)

(B)

Figure A.5 : The fit to the mean $\Delta(1/p)$ vs. $1/p$ for the 10 ϕ bins in Sector 2 for the (A) protons and the (B) π^-. These errors are due to the ϕ-dependent drift chamber misalignments and differences between the actual magnetic field and the calculated map used for track reconstruction.

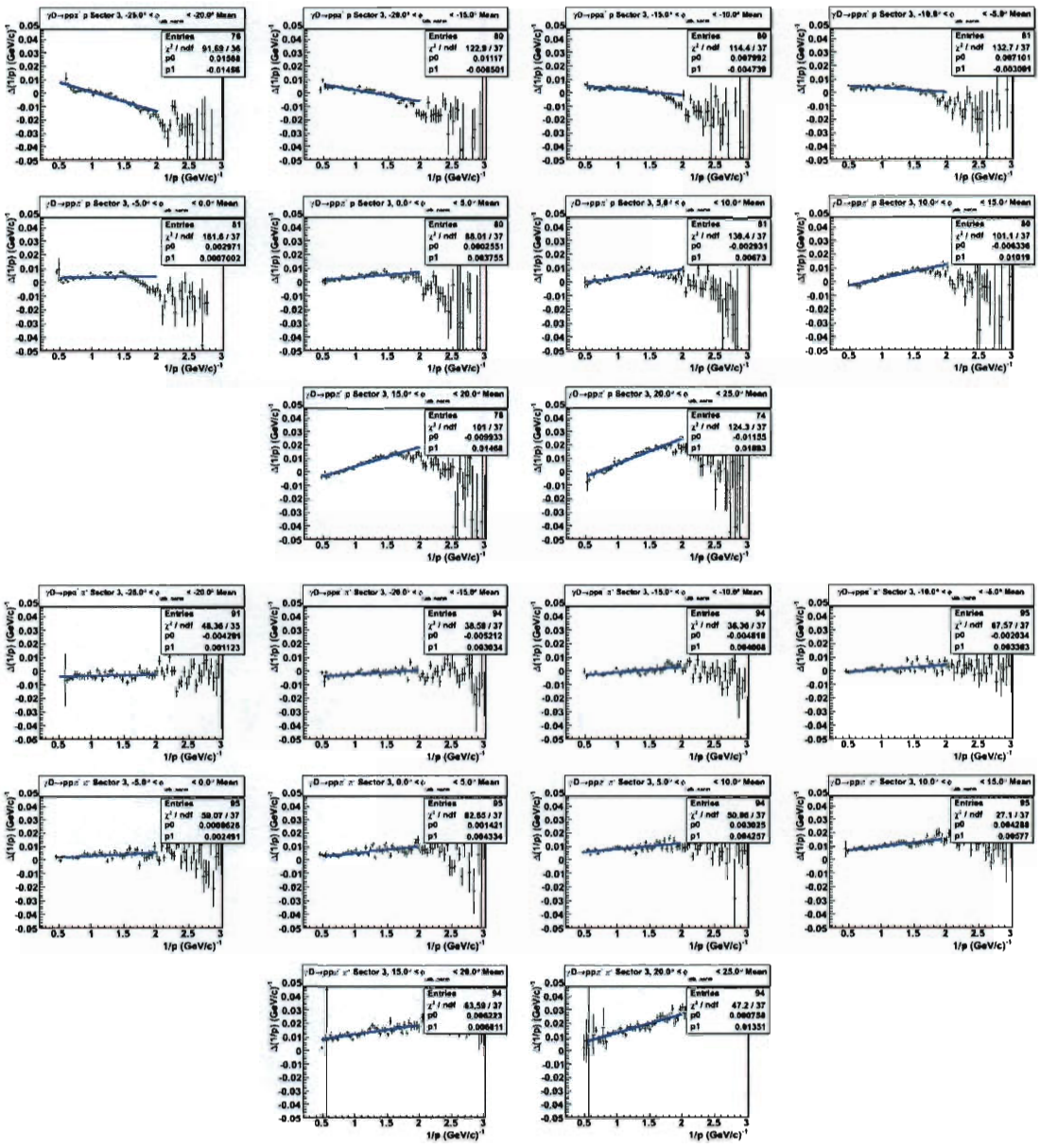

(A)

(B)

Figure A.6 : The fit to the mean $\Delta(1/p)$ vs. $1/p$ for the 10 ϕ bins in Sector 3 for the (A) protons and the (B) π^-. These errors are due to the ϕ-dependent drift chamber misalignments and differences between the actual magnetic field and the calculated map used for track reconstruction.

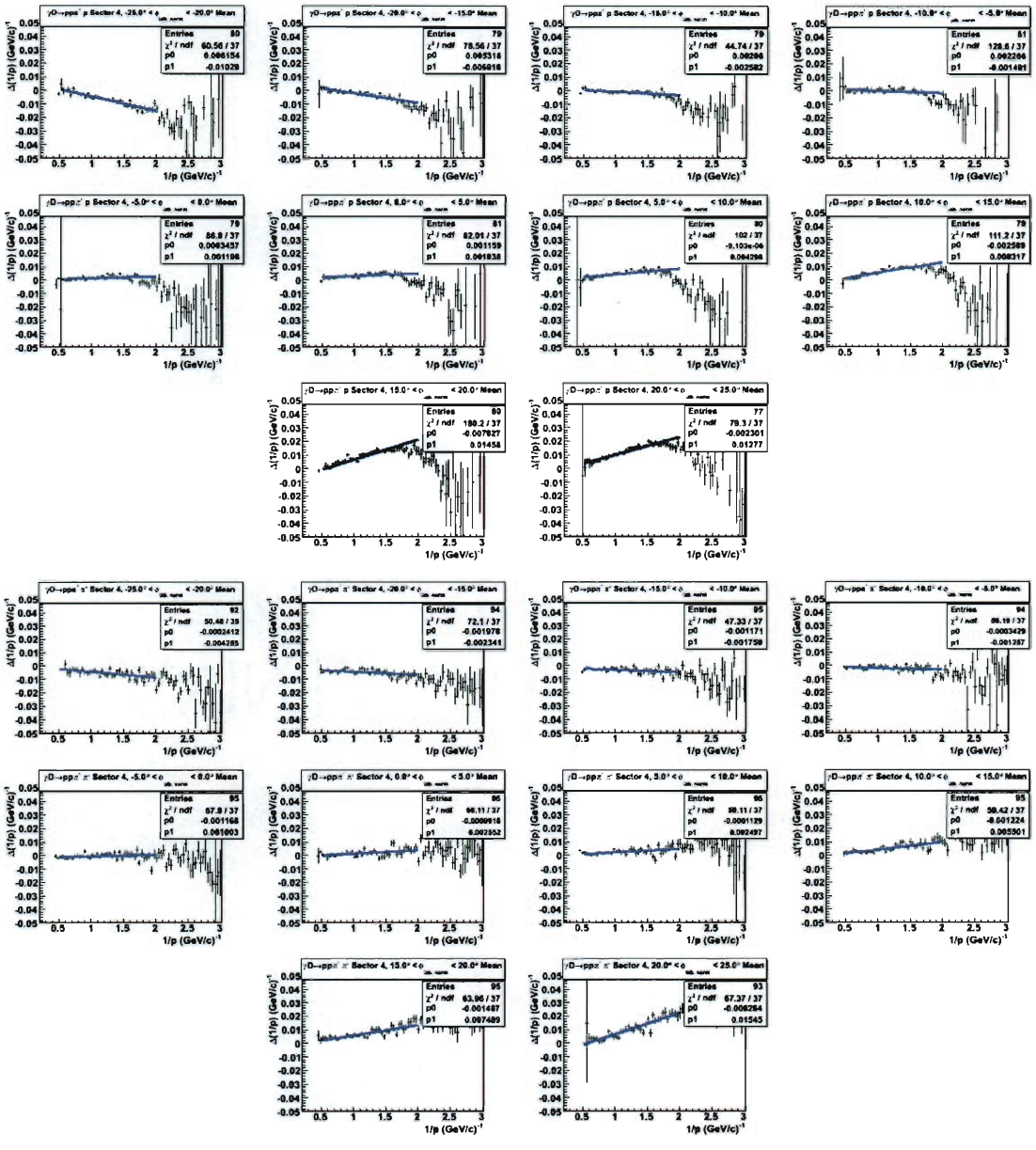

Figure A.7 : The fit to the mean $\Delta(1/p)$ vs. $1/p$ for the 10 ϕ bins in Sector 4 for the (A) protons and the (B) π^-. These errors are due to the ϕ-dependent drift chamber misalignments and differences between the actual magnetic field and the calculated map used for track reconstruction.

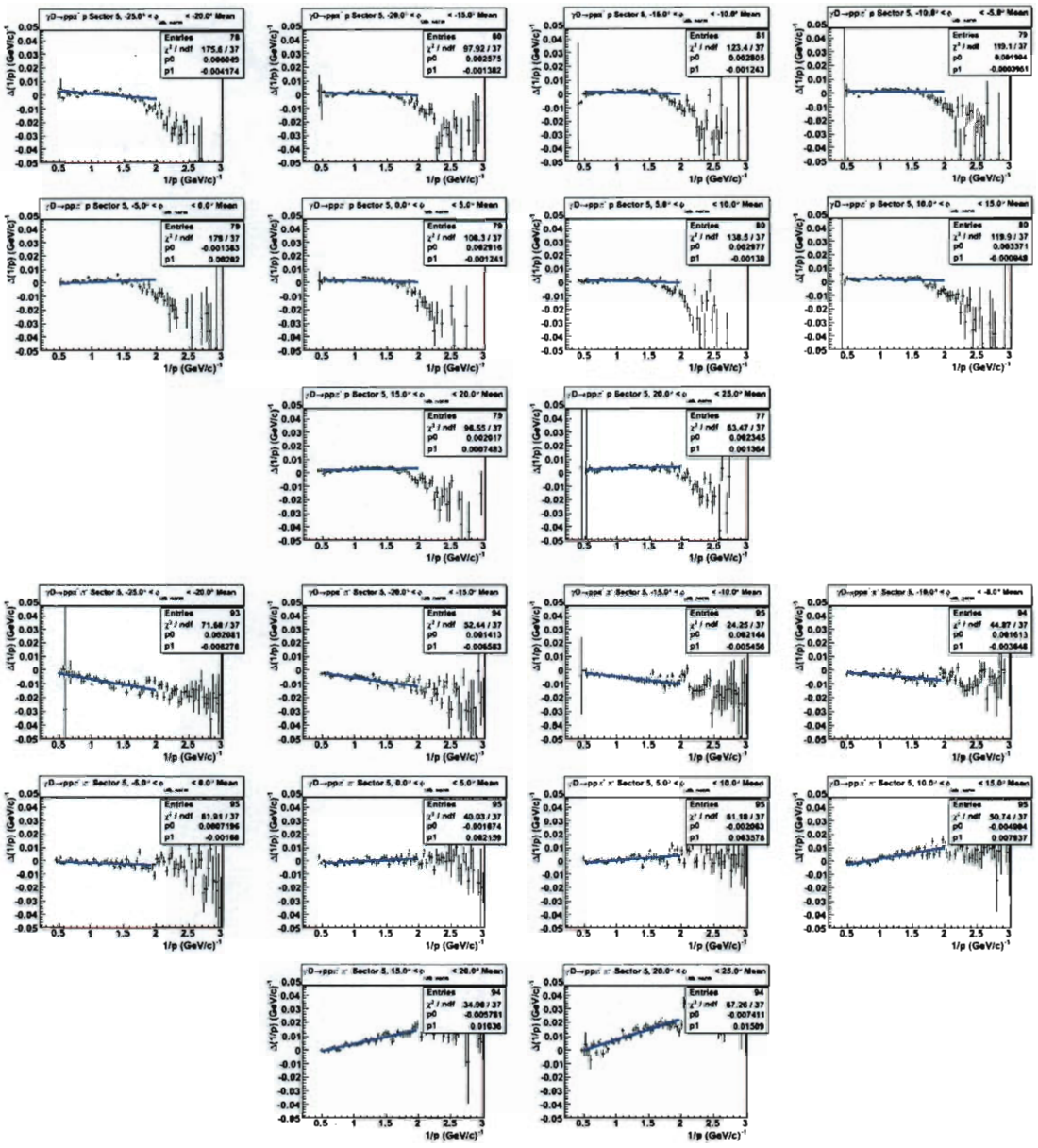

(A)

(B)

Figure A.8 : The fit to the mean $\Delta(1/p)$ vs. $1/p$ for the 10 ϕ bins in Sector 5 for the (A) protons and the (B) π^-. These errors are due to the ϕ-dependent drift chamber misalignments and differences between the actual magnetic field and the calculated map used for track reconstruction.

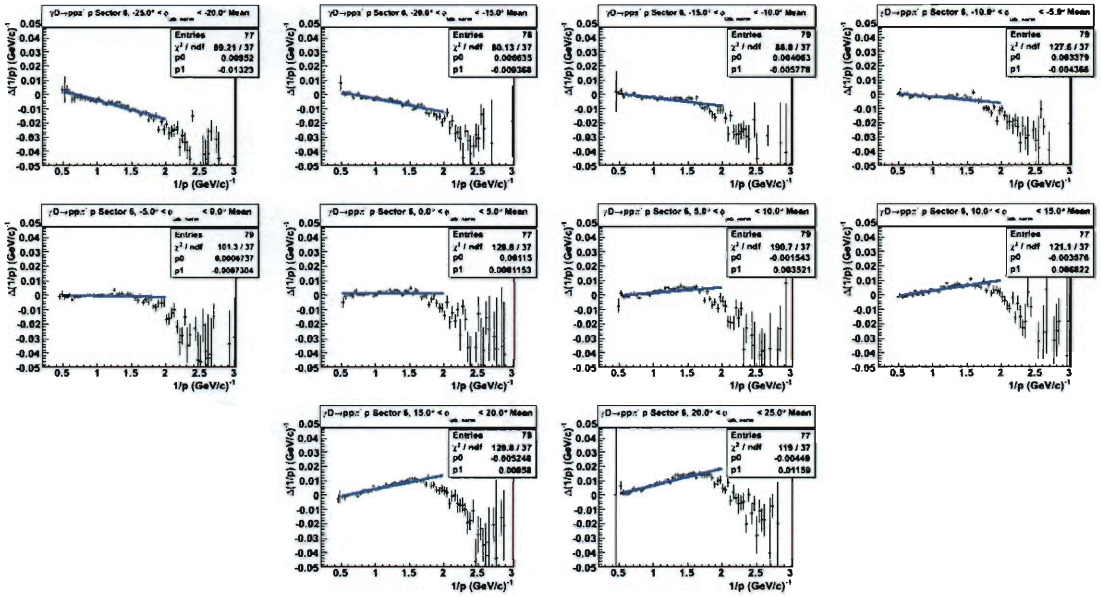

(A)

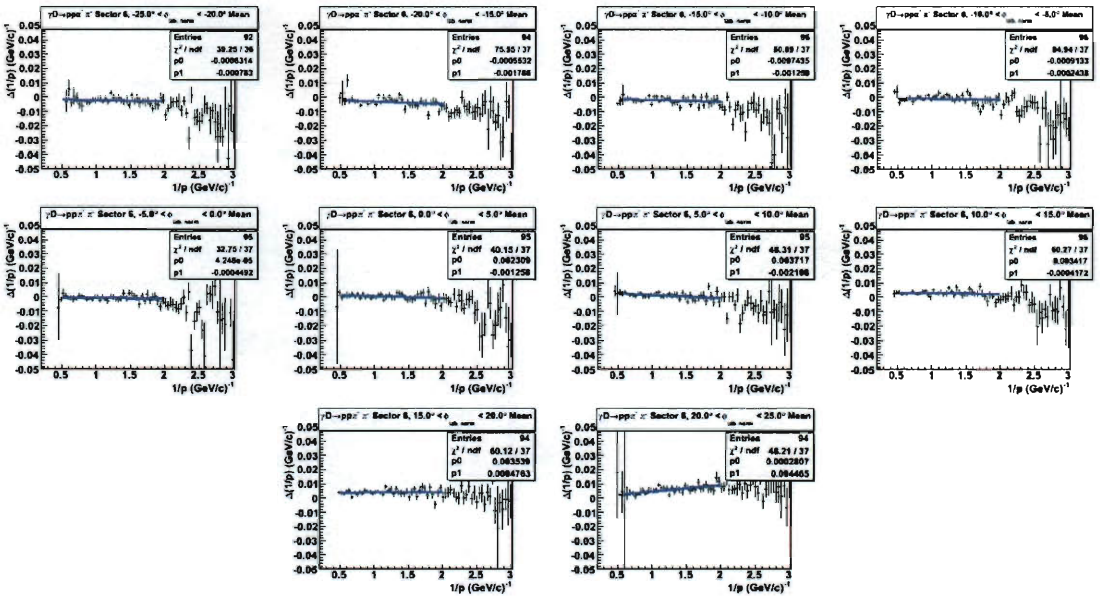

(B)

Figure A.9 : The fit to the mean $\Delta(1/p)$ vs. $1/p$ for the 10 ϕ bins in Sector 6 for the (A) protons and the (B) π^-. These errors are due to the ϕ-dependent drift chamber misalignments and differences between the actual magnetic field and the calculated map used for track reconstruction

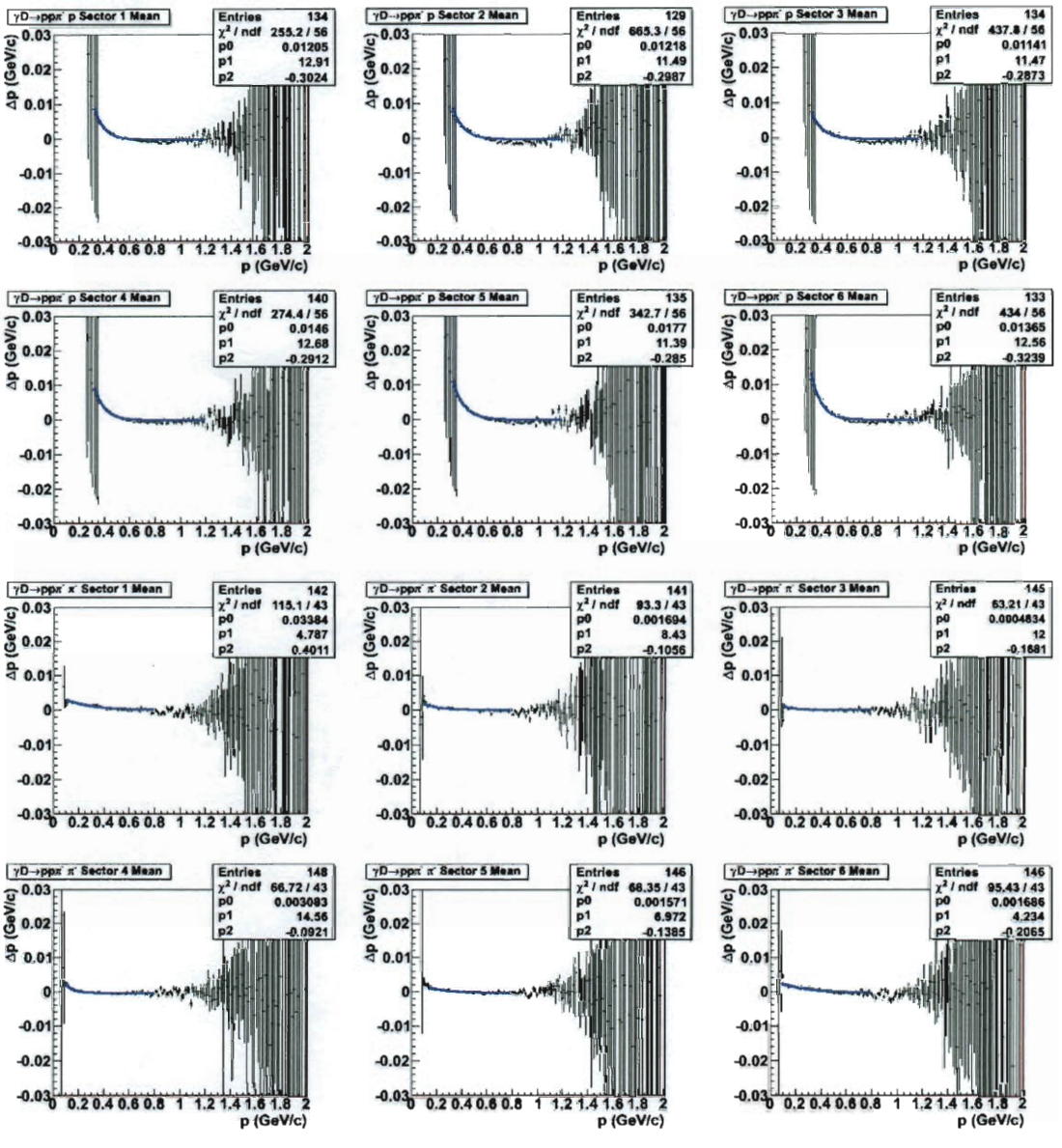

Figure A.10 : The mean Δp vs. p, updated with the ϕ-dependent corrections, in the six sectors of CLAS for the (A) proton and (B) π^-. These errors are due to the energy losses of the track not taken into account by the *eloss* software package, such as those in the drift chambers.

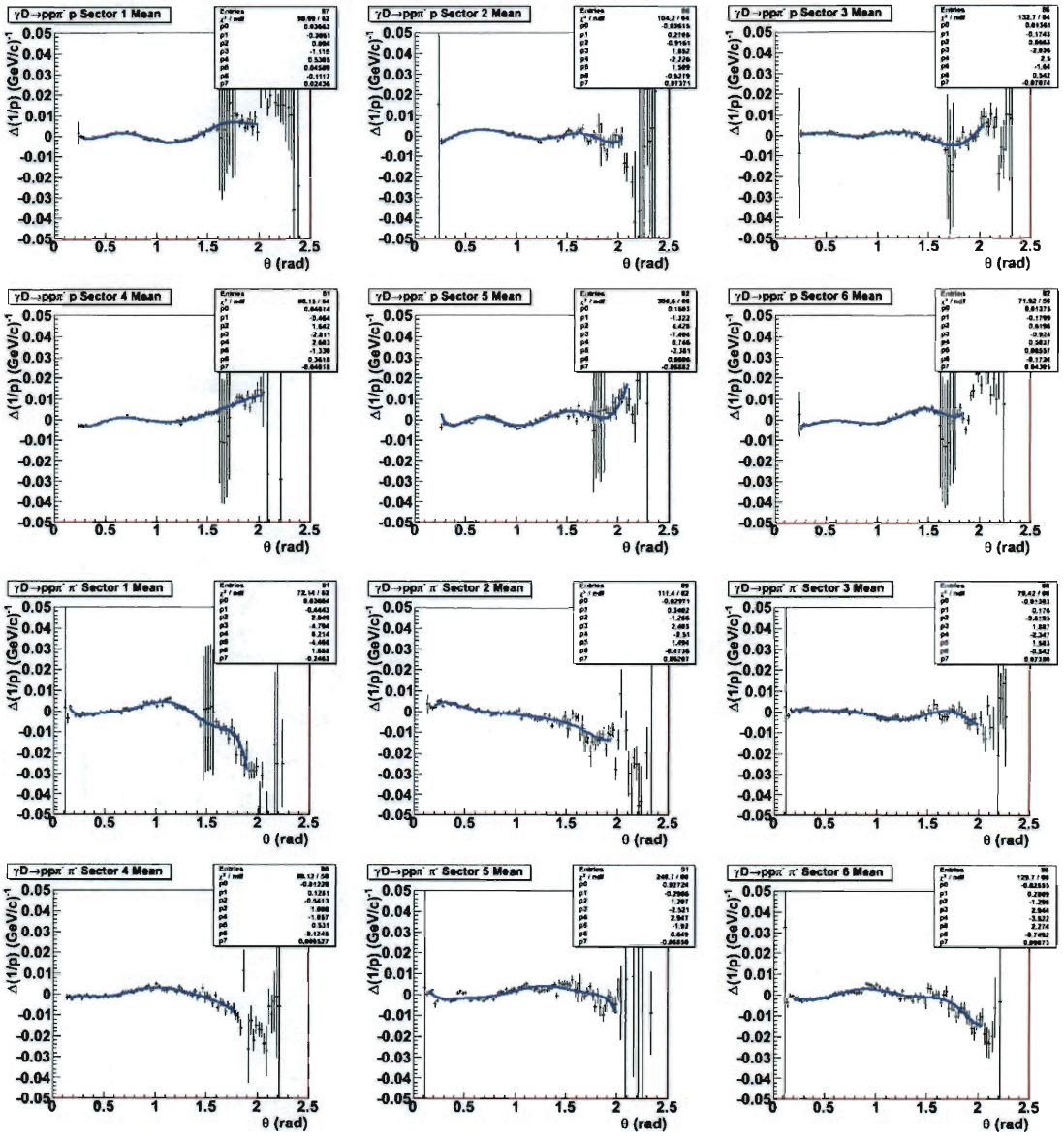

(A)

(B)

Figure A.11 : The fit to the mean $\Delta(1/p)$ in $(\mathrm{GeV/c})^{-1}$ as a function of θ in the six sectors of CLAS for the (A) proton and (B) π^-. These corrections are not fit to the tracks that traverse the back-most angles of the detector as the data is too sparse in these regions to be confident of the mean $\Delta(1/p)$.

A.3 After Kinematic Fitting

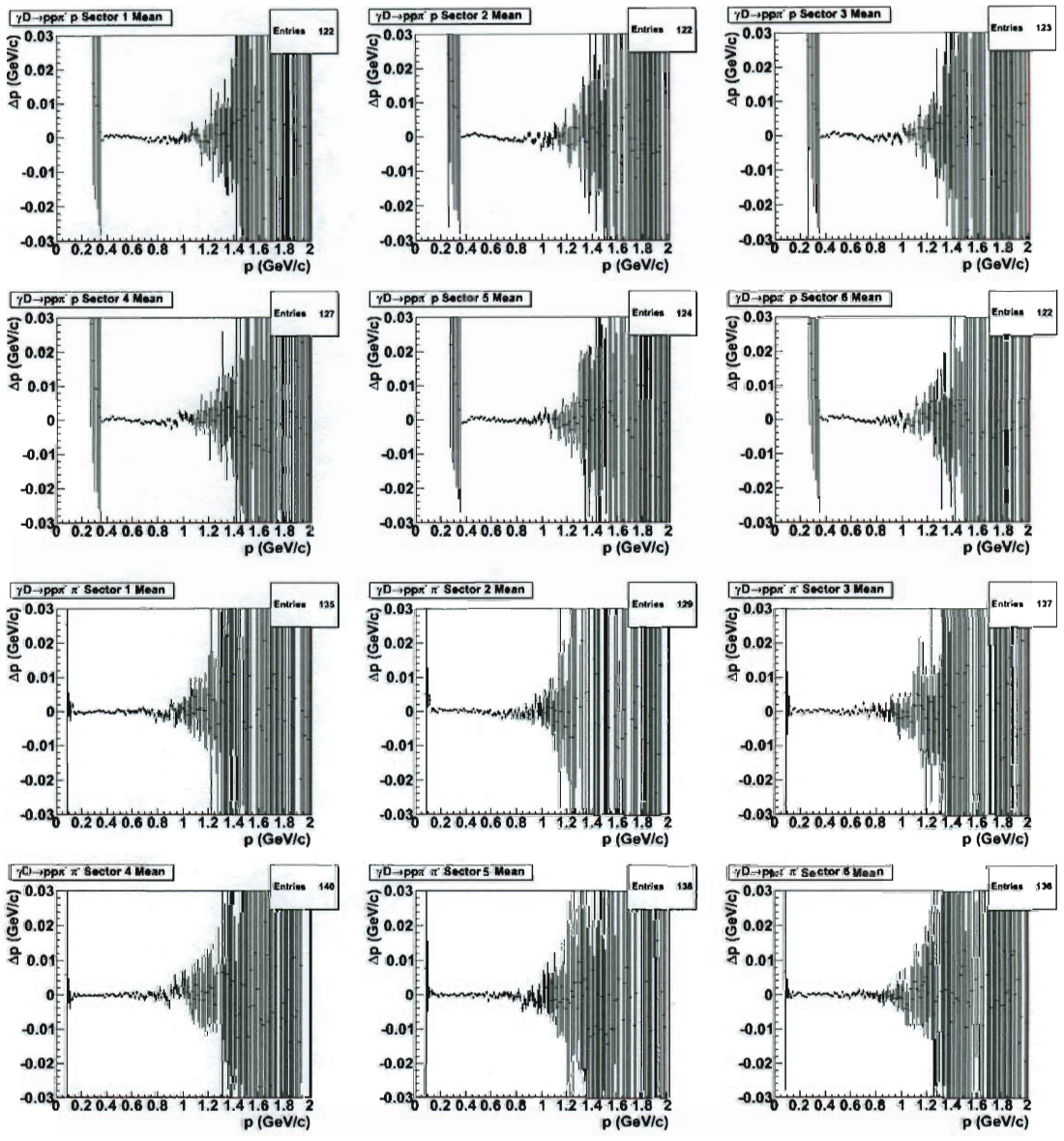

(A)

(B)

Figure A.12 : The average difference between the fit and corrected momentum as a function of p in the six sectors of CLAS for the (A) proton and (B) π^-.

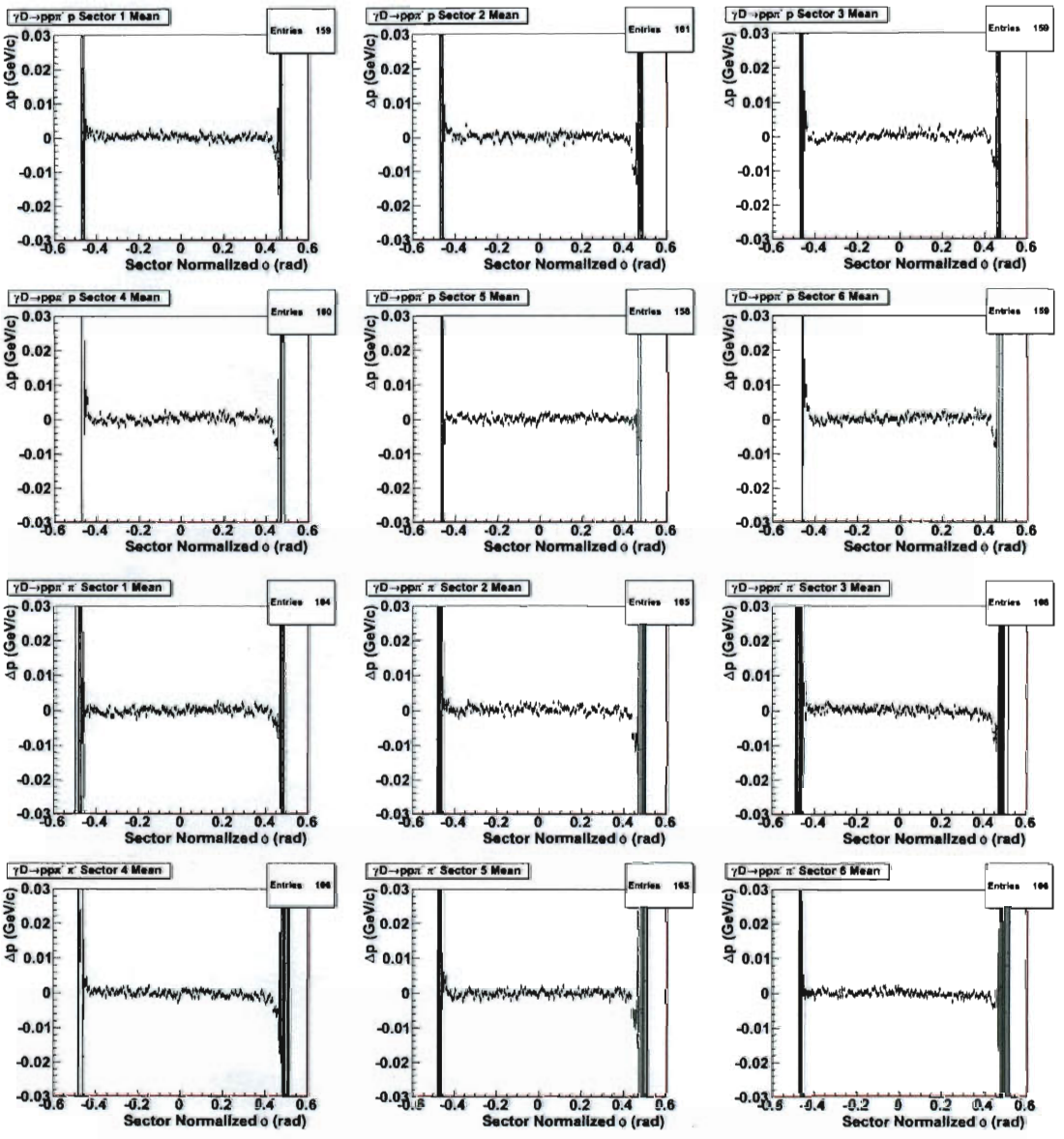

Figure A.13 : The average difference between the fit and corrected momentum as a function of the sector-normalized ϕ in the six sectors of CLAS for the (A) proton and (B) π^-.

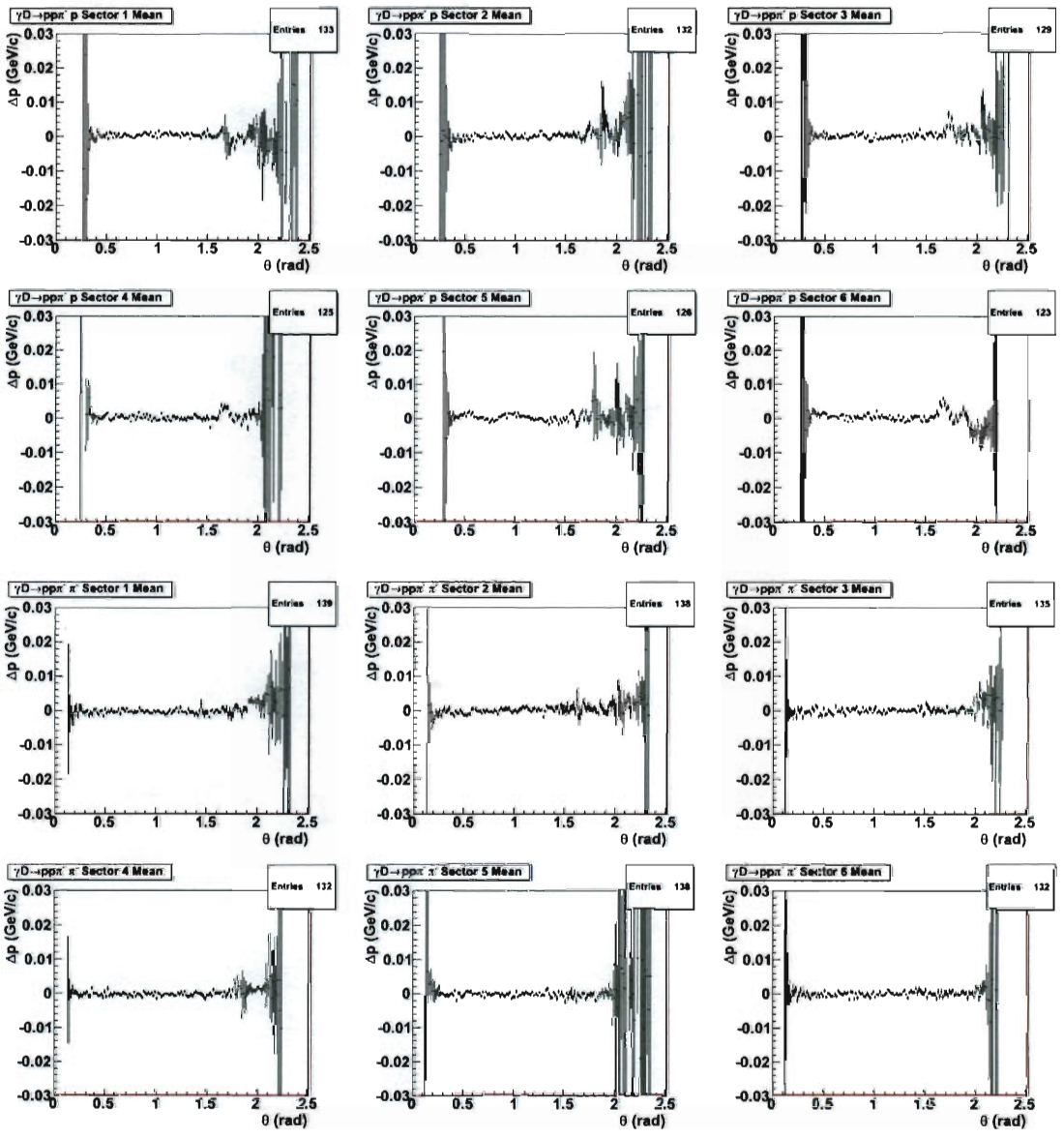

(A)

(B)

Figure A.14 : The average difference between the fit and corrected momentum as a function of θ in the six sectors of CLAS for the (A) proton and (B) π^-.

Appendix B

Acceptance Study Plots

B.1 Fiducial Cuts

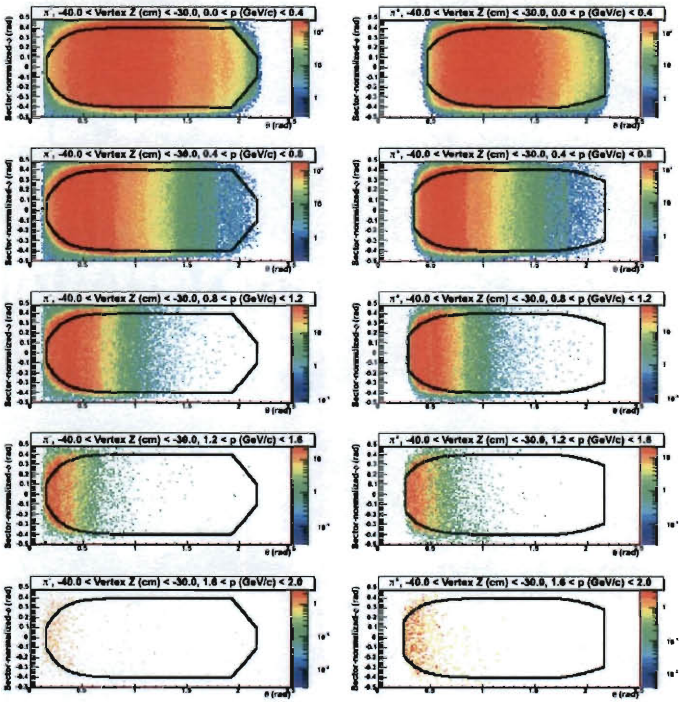

Figure B.1 : Log-scale distributions of reconstructed π^-'s in all sectors of CLAS as a function of θ and sector-normalized-ϕ. The two columns represent the vertex-z bins from -40 cm to -30 cm and from -30 cm to -20 cm. The different rows represent 400 MeV wide momentum bins from 0 GeV/c to 2 GeV/c. The fiducial cuts are drawn in black.

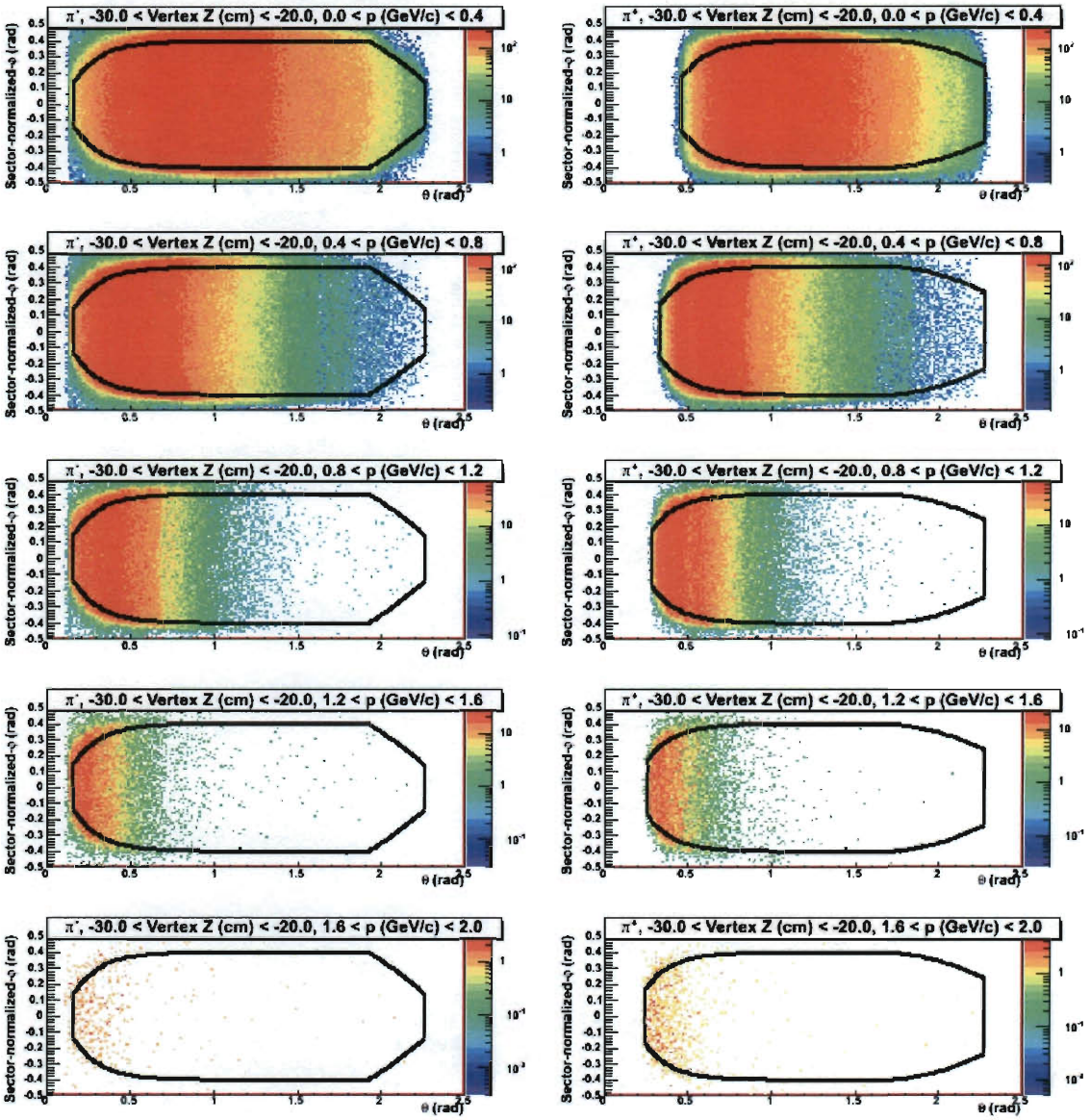

Figure B.2 : Log-scale distributions of reconstructed π^-'s in all sectors of CLAS as a function of θ and sector-normalized-ϕ. The two columns represent the vertex-z bins from -20 cm to -10 cm and from -10 cm to 0 cm. The different rows represent 400 MeV wide momentum bins from 0 GeV/c to 2 GeV/c. The fiducial cuts are drawn in black.

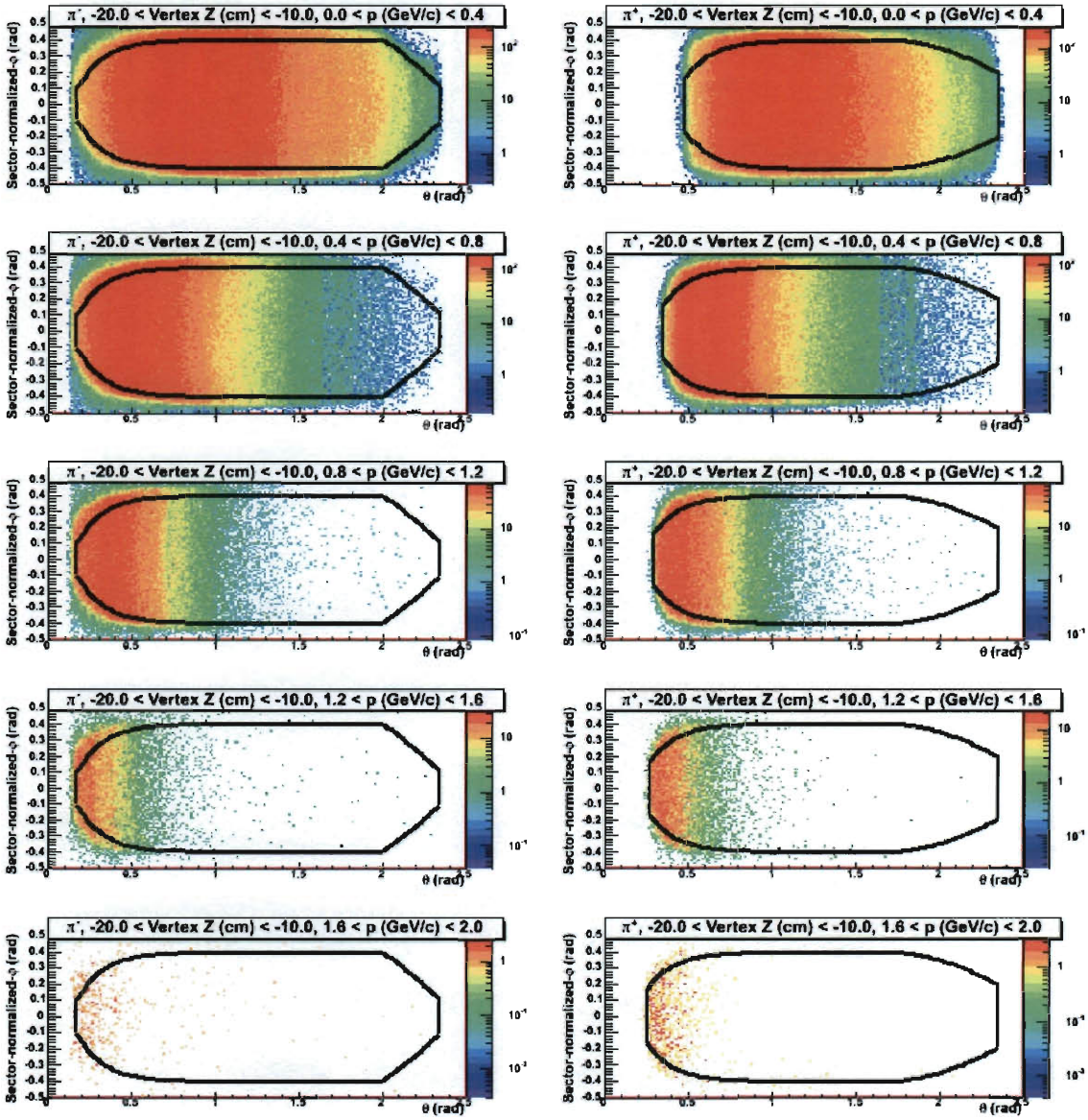

Figure B.3 : Log-scale distributions of reconstructed π^+'s in all sectors of CLAS as a function of θ and sector-normalized-ϕ. The two columns represent the vertex-z bins from -40 cm to -30 cm and from -30 cm to -20 cm. The different rows represent 400 MeV wide momentum bins from 0 GeV/c to 2 GeV/c. The fiducial cuts are drawn in black.

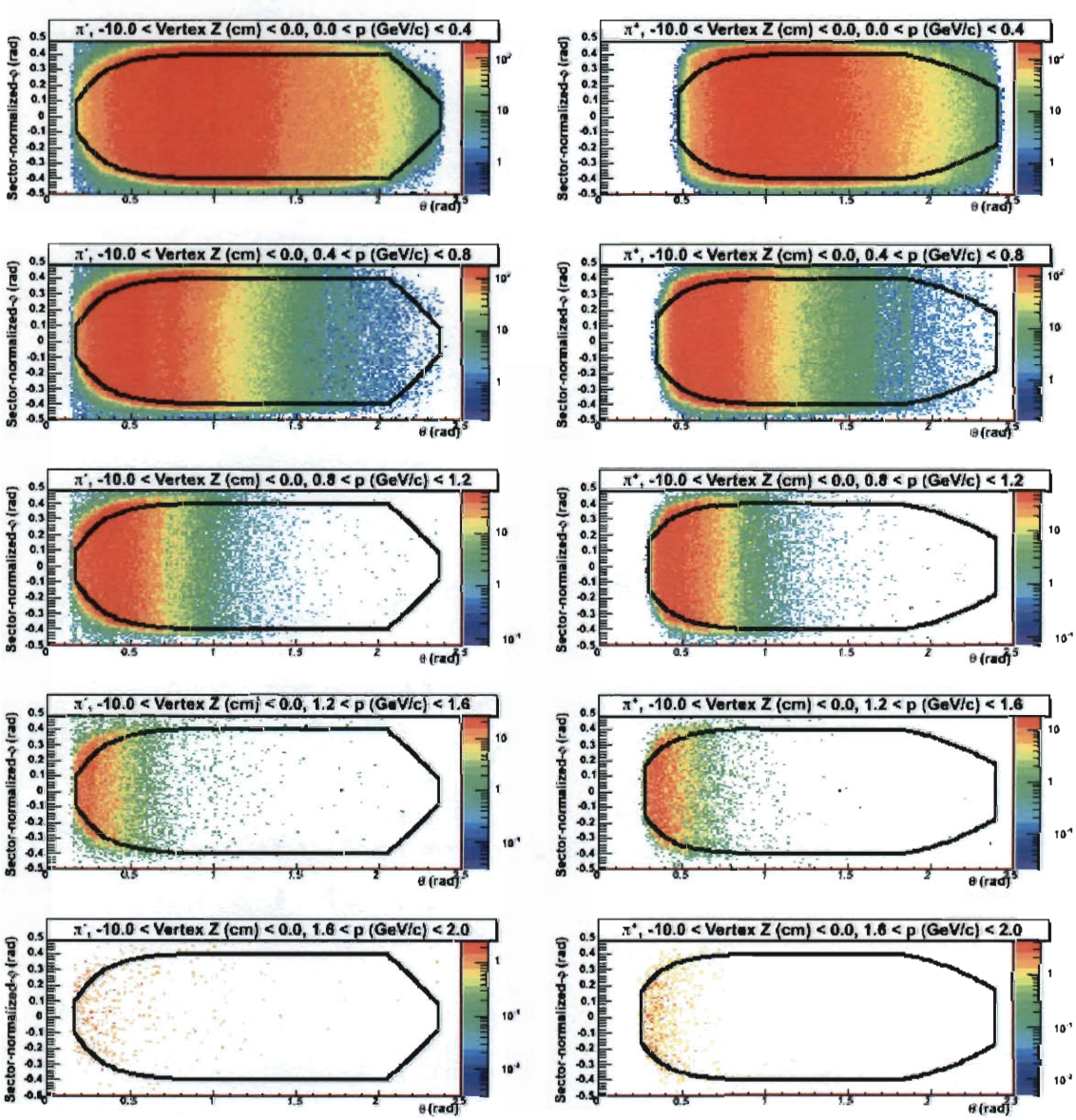

Figure B.4 : Log-scale distributions of reconstructed π^+'s in all sectors of CLAS as a function of θ and sector-normalized-ϕ. The two columns represent the vertex-z bins from -20 cm to -10 cm and from -10 cm to 0 cm. The different rows represent 400 MeV wide momentum bins from 0 GeV/c to 2 GeV/c. The fiducial cuts are drawn in black.

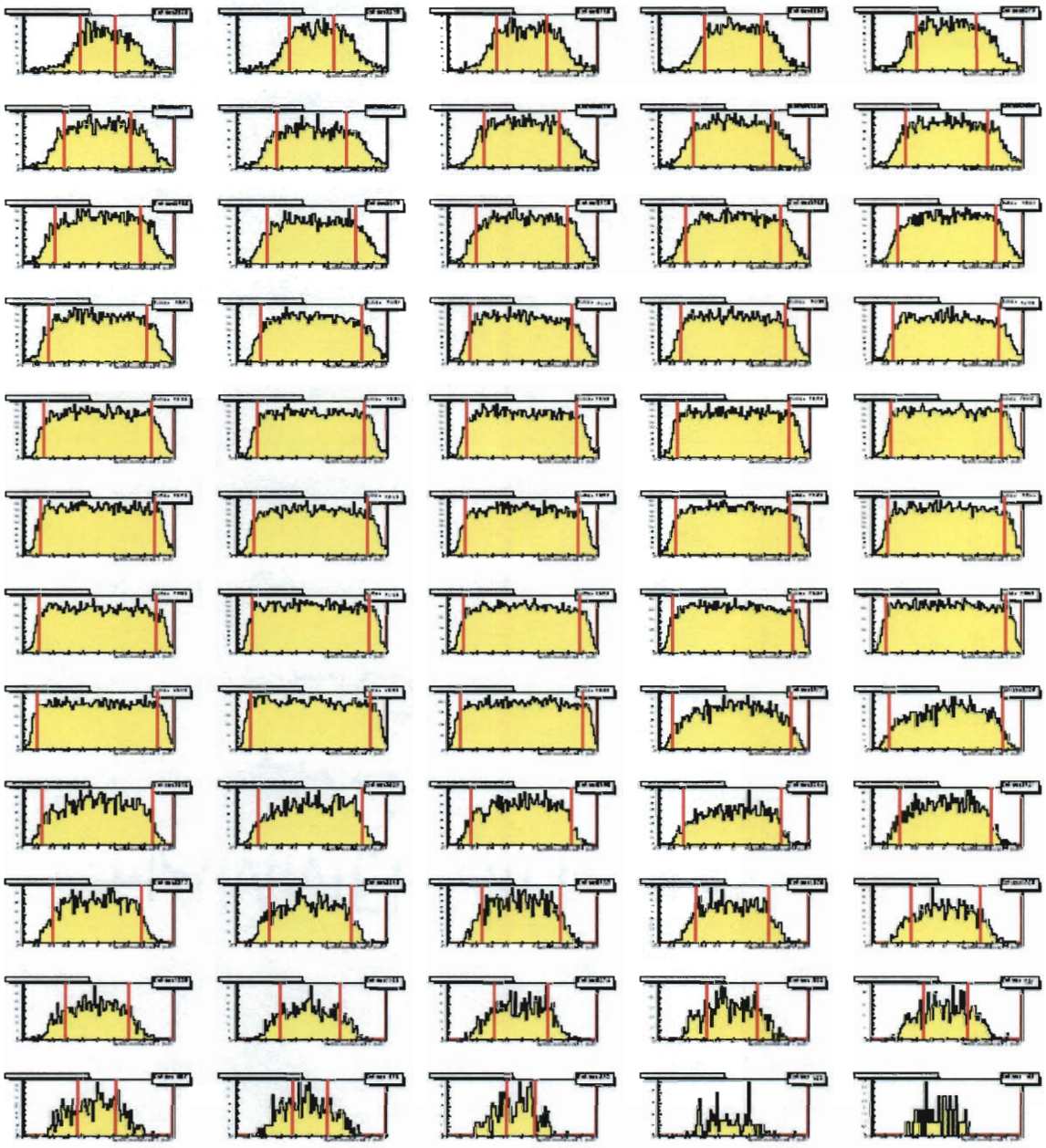

Figure B.5 : For π^-'s with -40 cm < vertex-z < -30 cm and momentum < 400 MeV/c, the distribution of reconstructed tracks for all sectors in bins of θ as a function of sector-normalized-ϕ. The θ-bins are from the front to the back of CLAS, excluding the middle θ-bins where the cuts were relatively constant. The red lines indicate the location of the fiducial cuts.

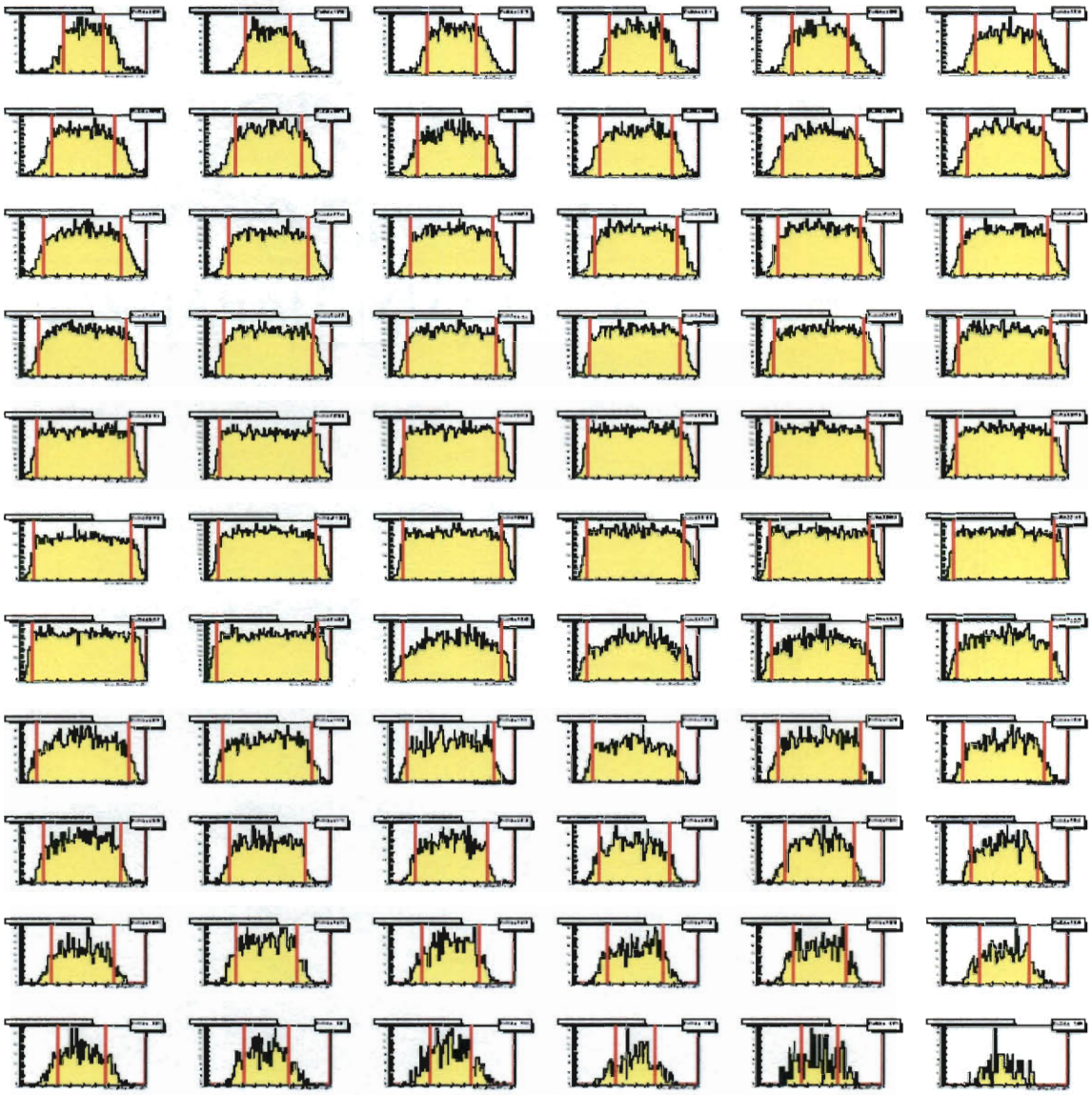

Figure B.6 : For π^-'s with -30 cm < vertex-z < -20 cm and momentum < 400 MeV/c, the distribution of reconstructed tracks for all sectors in bins of θ as a function of sector-normalized-ϕ. The θ-bins are from the front to the back of CLAS, excluding the middle θ-bins where the cuts were relatively constant. The red lines indicate the location of the fiducial cuts.

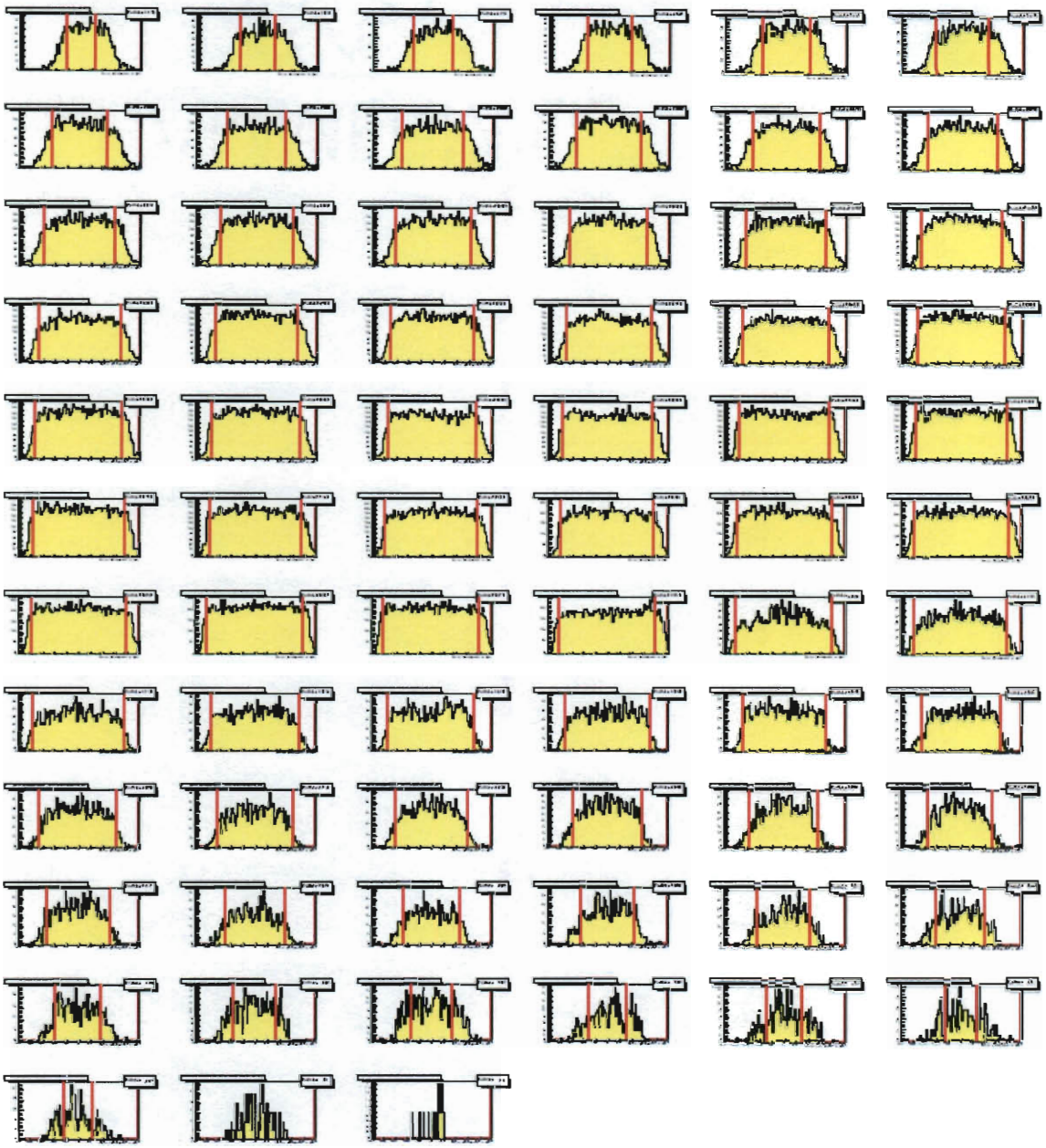

Figure B.7 : For π^-'s with -20 cm < vertex-z < -10 cm and momentum < 400 MeV/c, the distribution of reconstructed tracks for all sectors in bins of θ as a function of sector-normalized-ϕ. The θ-bins are from the front to the back of CLAS, excluding the middle θ-bins where the cuts were relatively constant. The red lines indicate the location of the fiducial cuts.

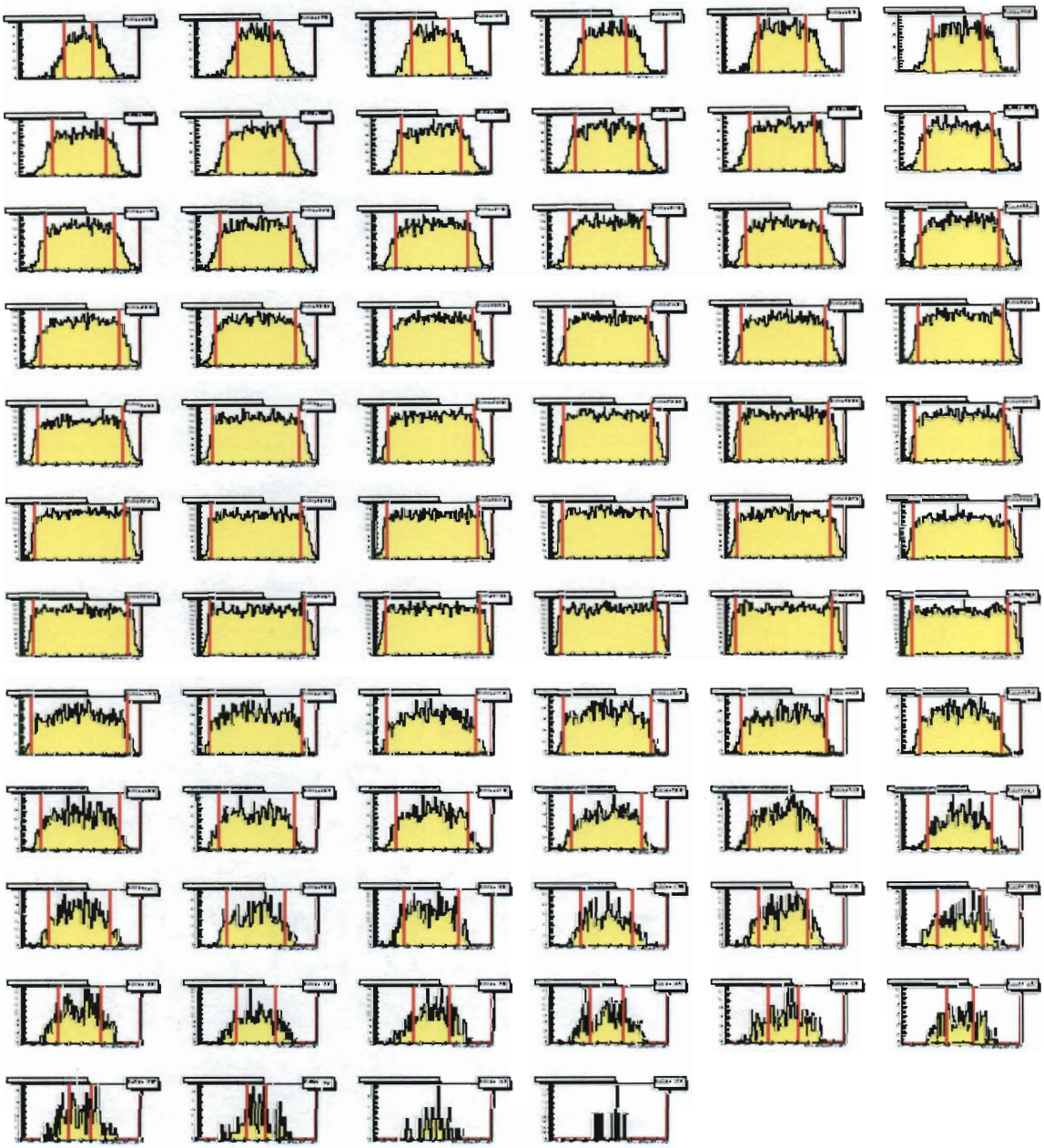

Figure B.8 : For π^-'s with -10 cm < vertex-z < 0 cm and momentum < 400 MeV/c, the distribution of reconstructed tracks for all sectors in bins of θ as a function of sector-normalized-ϕ. The θ-bins are from the front to the back of CLAS, excluding the middle θ-bins where the cuts were relatively constant. The red lines indicate the location of the fiducial cuts.

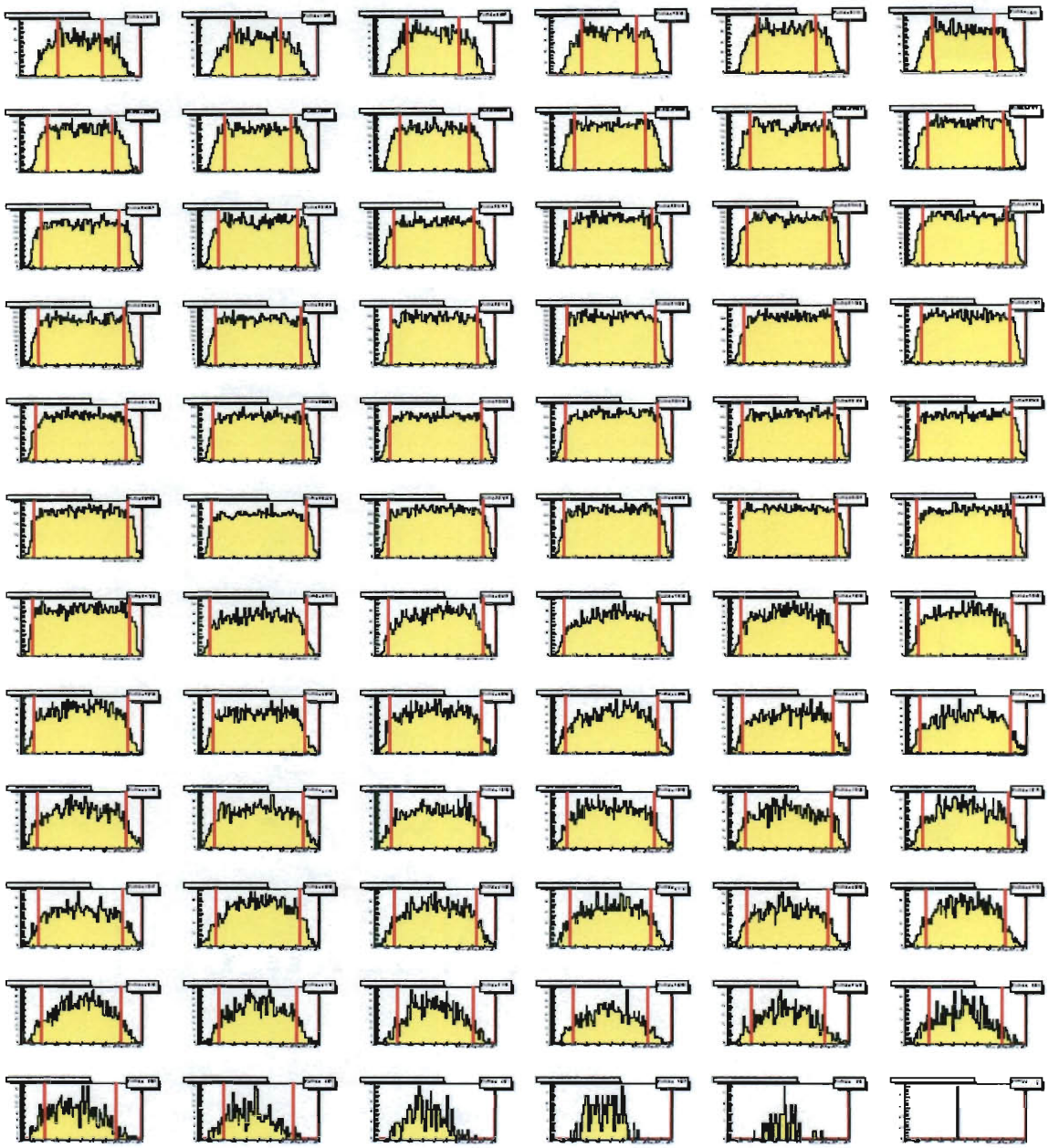

Figure B.9 : For π^+'s with -40 cm < vertex-z < -30 cm and momentum < 400 MeV/c, the distribution of reconstructed tracks for all sectors in bins of θ as a function of sector-normalized-ϕ. The θ-bins are from the front to the back of CLAS, excluding the middle θ-bins where the cuts were relatively constant. The red lines indicate the location of the fiducial cuts.

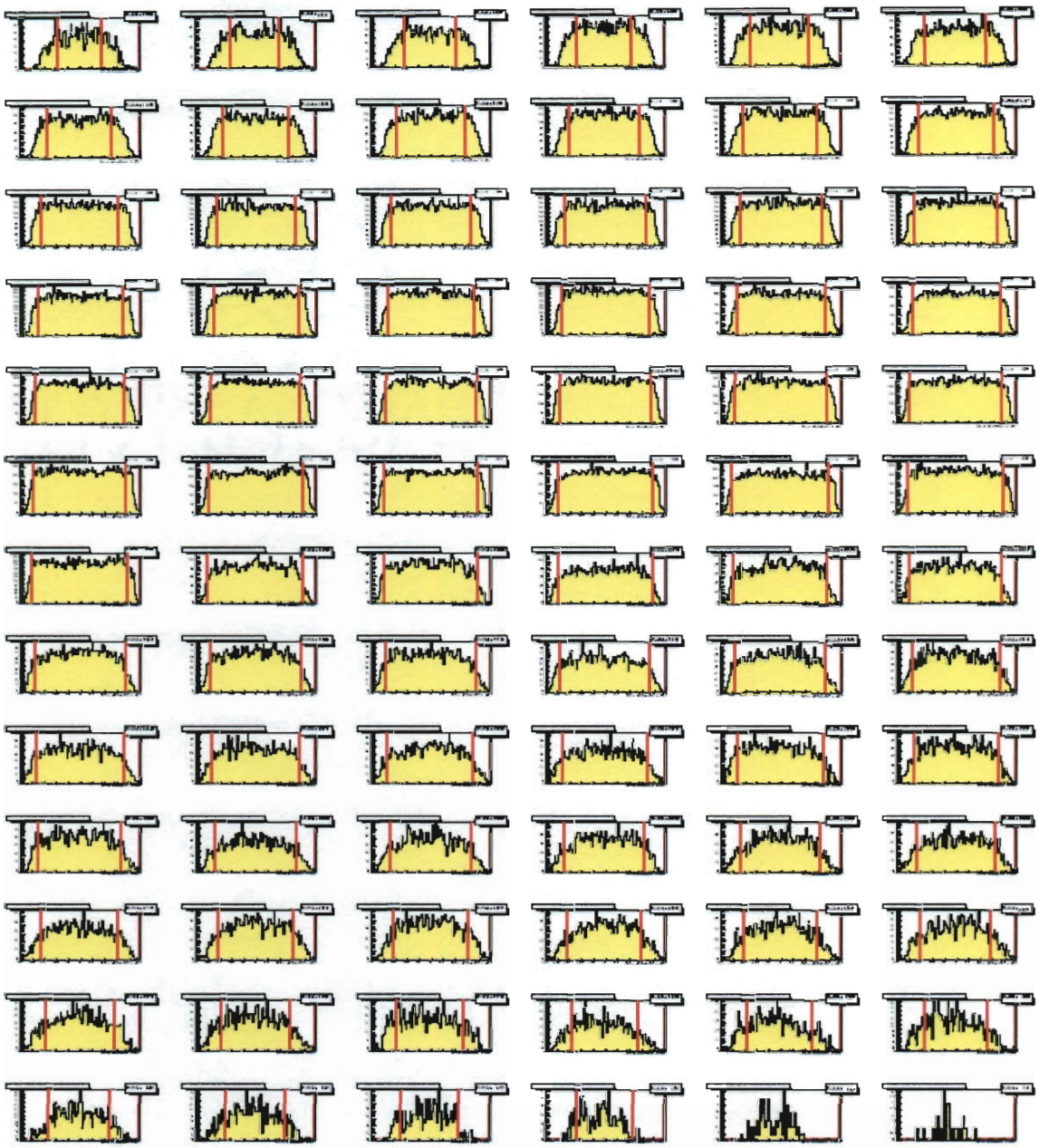

Figure B.10 : For π^+'s with -30 cm < vertex-z < -20 cm and momentum < 400 MeV/c, the distribution of reconstructed tracks for all sectors in bins of θ as a function of sector-normalized-ϕ. The θ-bins are from the front to the back of CLAS, excluding the middle θ-bins where the cuts were relatively constant. The red lines indicate the location of the fiducial cuts.

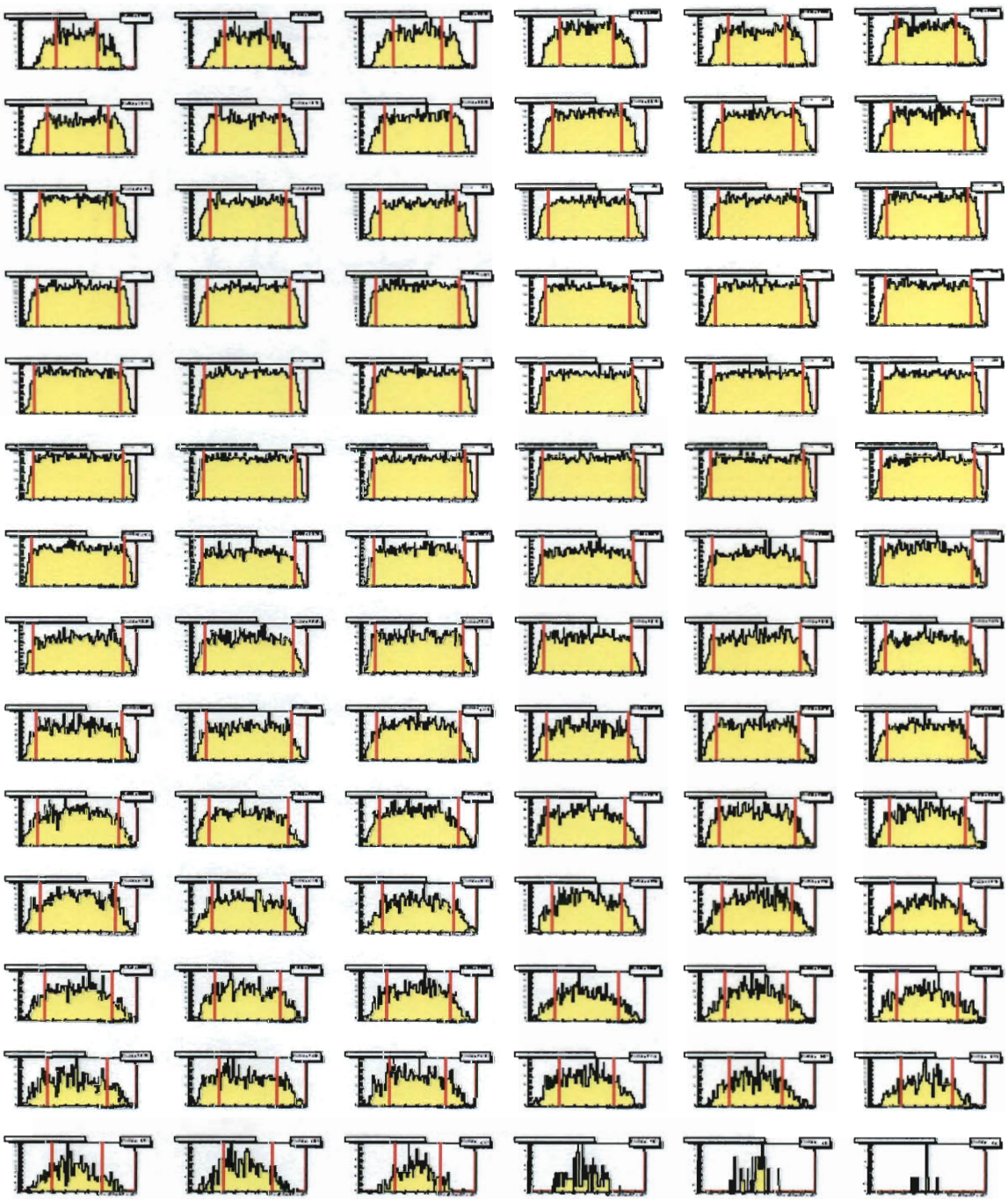

Figure B.11 : For π^+'s with -20 cm < vertex-z < -10 cm and momentum < 400 MeV/c, the distribution of reconstructed tracks for all sectors in bins of θ as a function of sector-normalized-ϕ. The θ-bins are from the front to the back of CLAS, excluding the middle θ-bins where the cuts were relatively constant. The red lines indicate the location of the fiducial cuts.

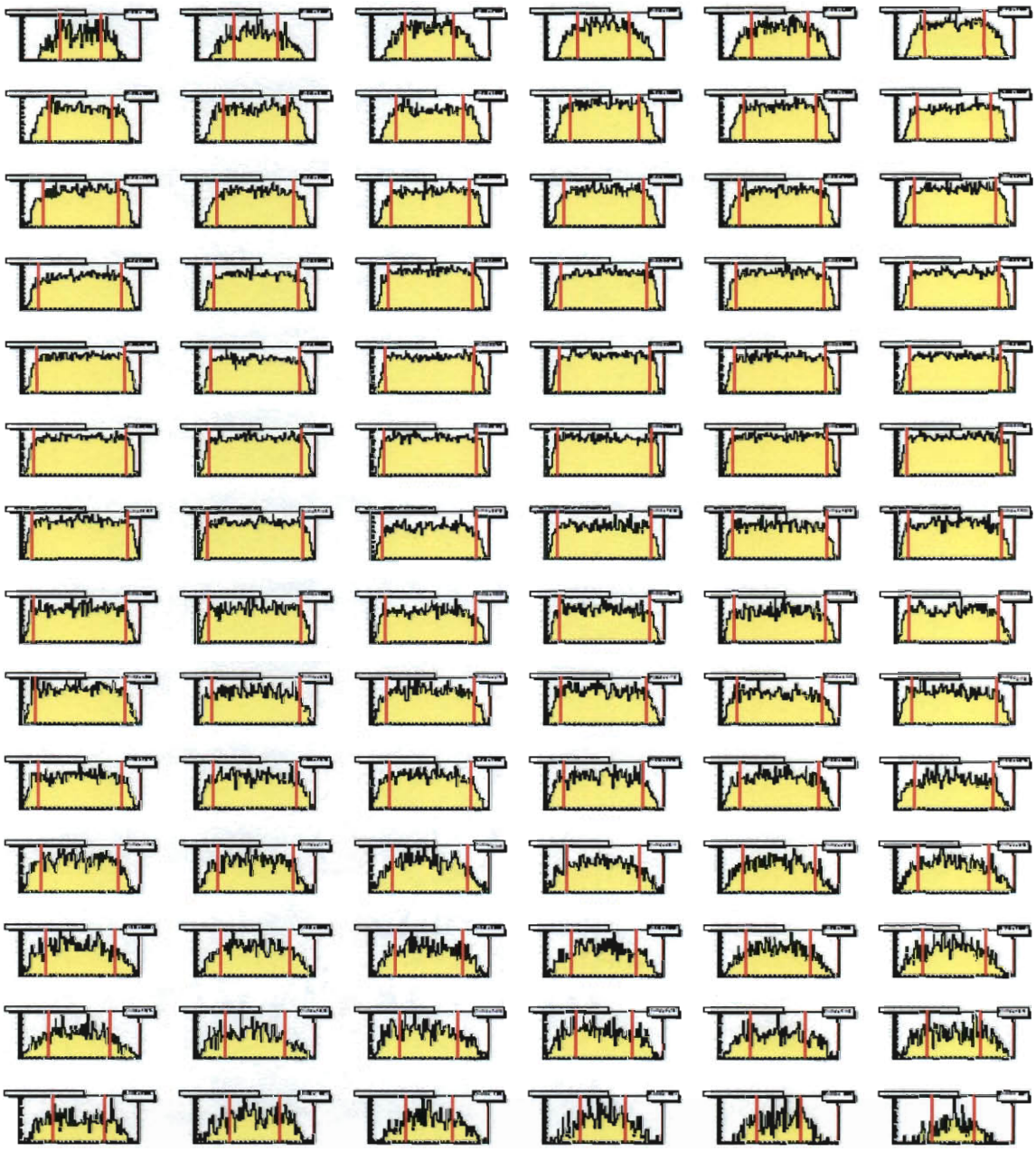

Figure B.12 : For π^+'s with -10 cm < vertex-z < 0 cm and momentum < 400 MeV/c, the distribution of reconstructed tracks for all sectors in bins of θ as a function of sector-normalized-ϕ. The θ-bins are from the front to the back of CLAS, excluding the middle θ-bins where the cuts were relatively constant. The red lines indicate the location of the fiducial cuts.

B.2 Drift Chamber Hole Cuts

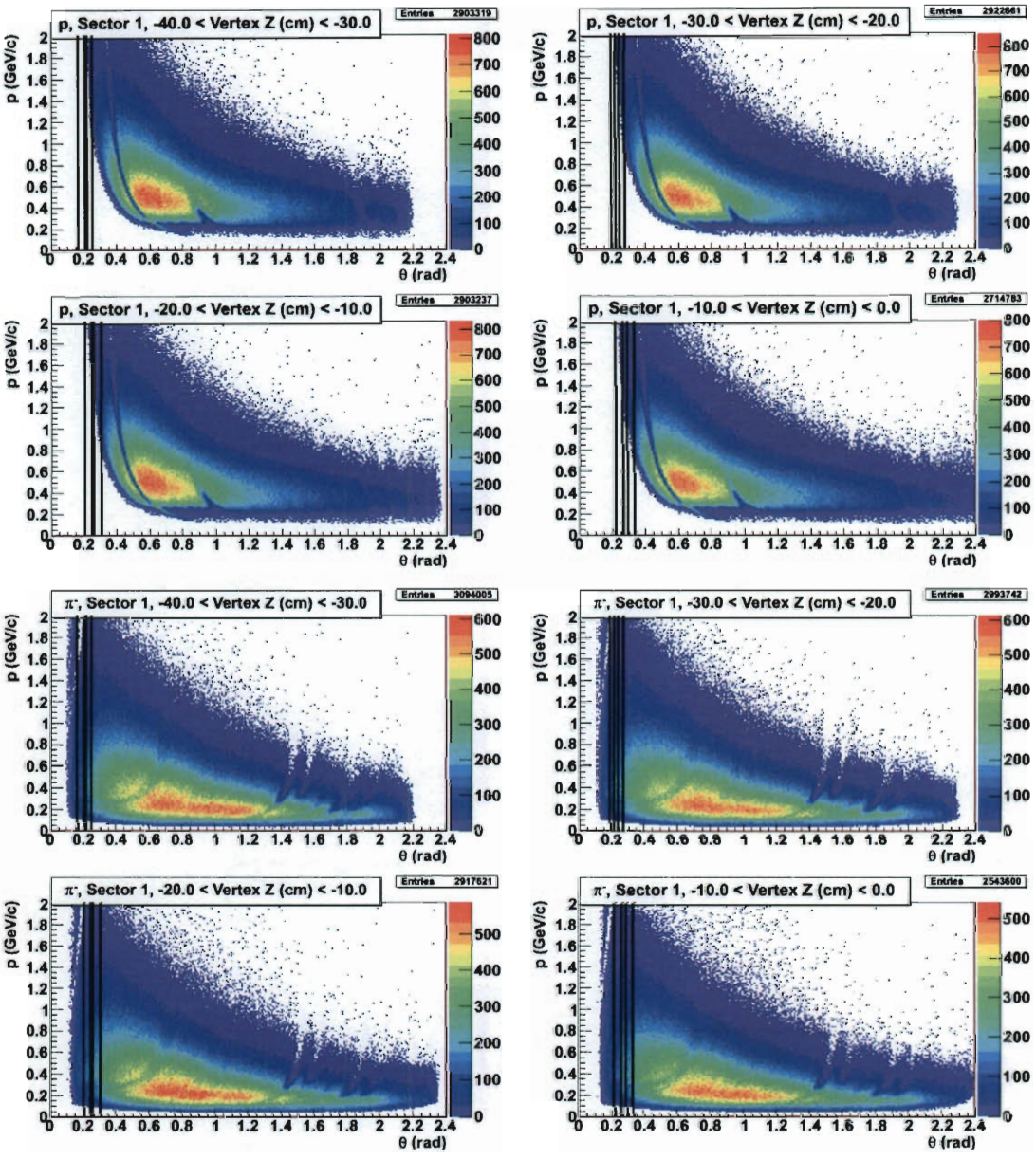

Figure B.13 : Track distributions of the protons (A) and π^-'s (B) in different vertex-z bins in Sector 1. The black lines indicate the borders of the regions cut out of the analysis in both data and in simulation due to holes in the drift chambers. The holes in the distributions without associated cuts correspond to either the panel overlap regions, or dead or inefficient scintillator paddles.

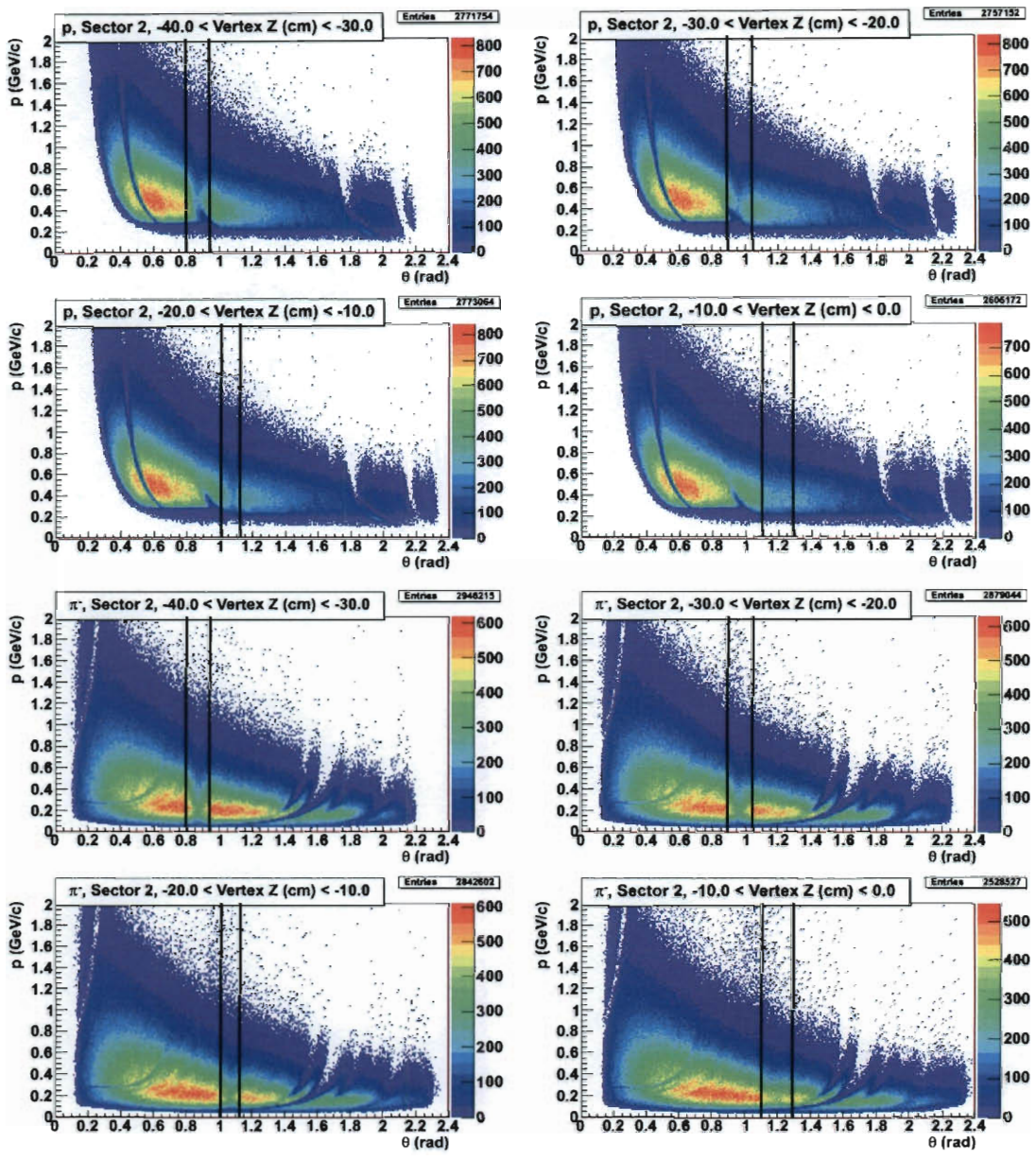

Figure B.14 : Track distributions of the protons (A) and π^-'s (B) in different vertex-z bins in Sector 2. The black lines indicate the borders of the regions cut out of the analysis in both data and in simulation due to holes in the drift chambers. The holes in the distributions without associated cuts correspond to either the panel overlap regions, or dead or inefficient scintillator paddles.

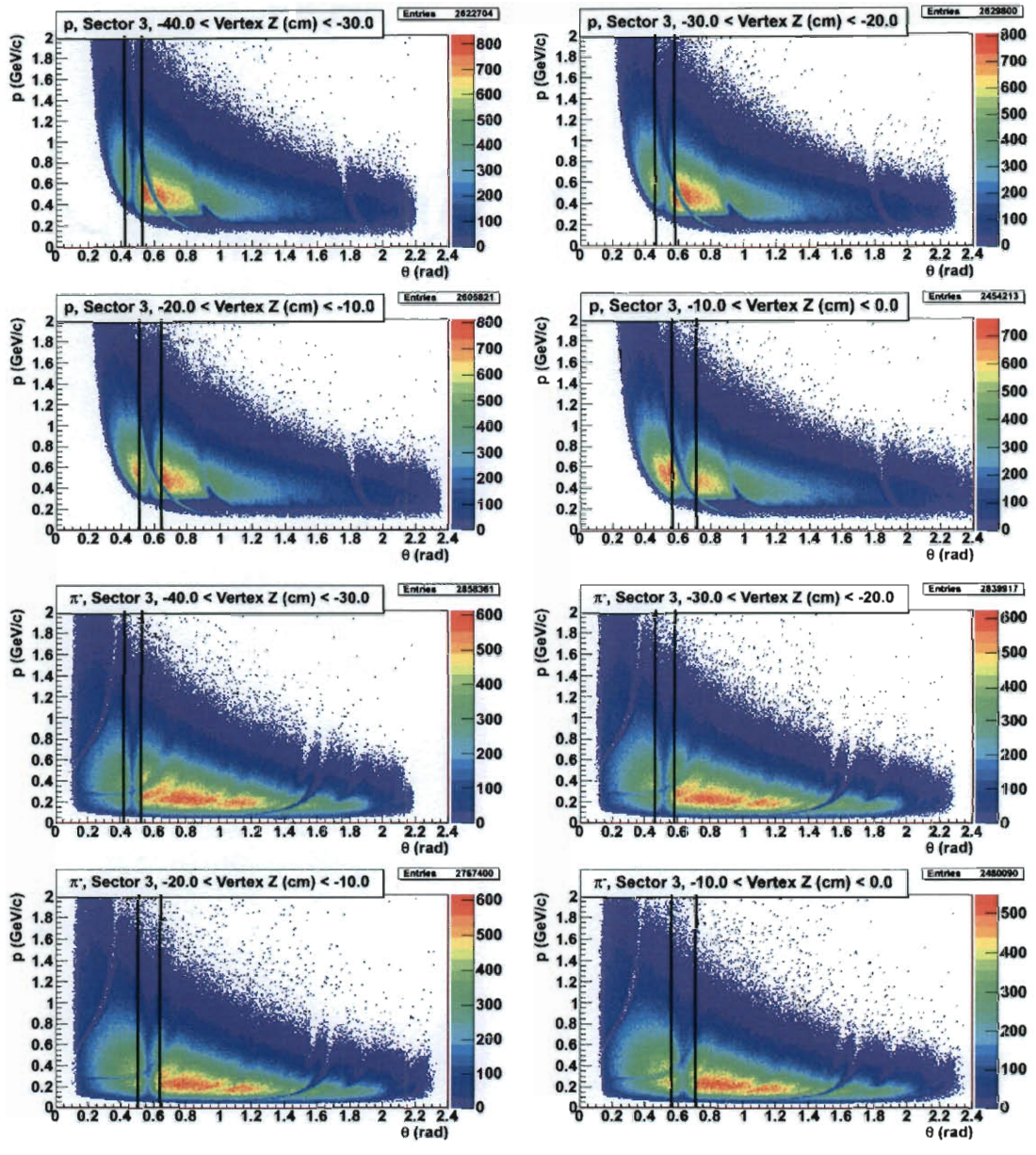

Figure B.15 : Track distributions of the protons (A) and π^-'s (B) in different vertex-z bins in Sector 3. The black lines indicate the borders of the regions cut out of the analysis in both data and in simulation due to holes in the drift chambers. The holes in the distributions without associated cuts correspond to either the panel overlap regions, or dead or inefficient scintillator paddles.

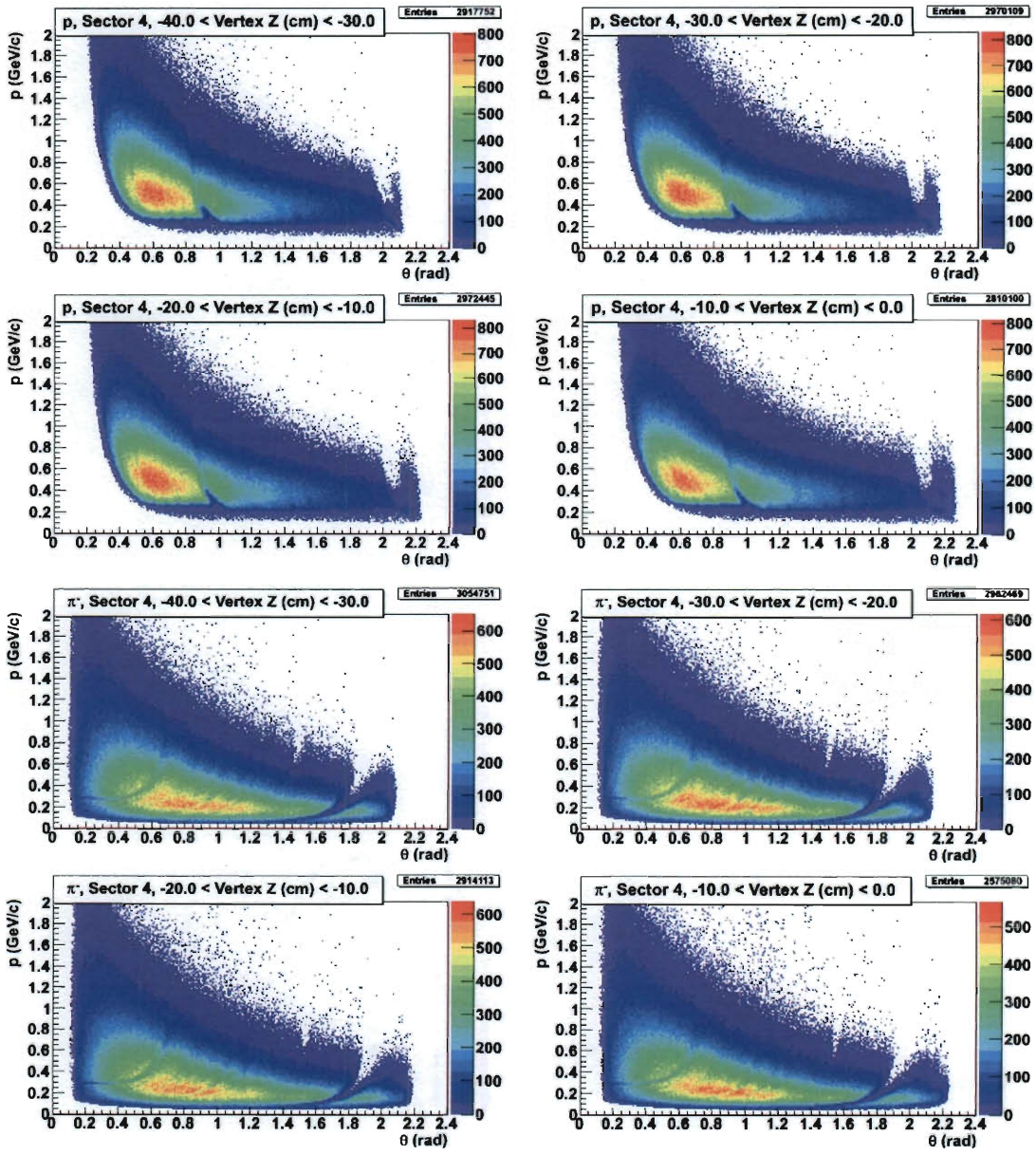

Figure B.16 : Track distributions of the protons (A) and π^-'s (B) in different vertex-z bins in Sector 4. The black lines indicate the borders of the regions cut out of the analysis in both data and in simulation due to holes in the drift chambers. The holes in the distributions without associated cuts correspond to either the panel overlap regions, or dead or inefficient scintillator paddles.

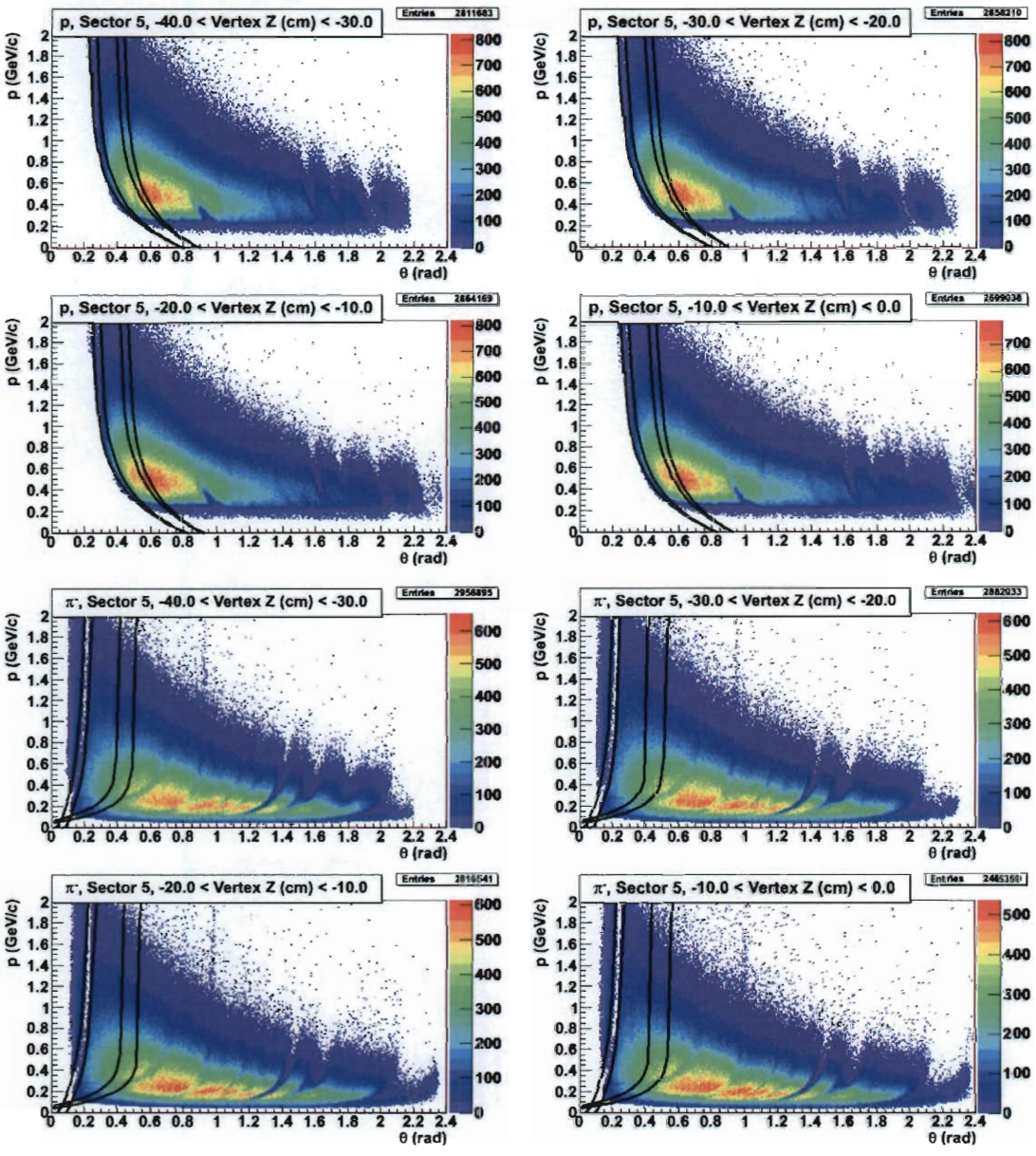

Figure B.17 : Track distributions of the protons (A) and π^-'s (B) in different vertex-z bins in Sector 5. The black lines indicate the borders of the regions cut out of the analysis in both data and in simulation due to holes in the drift chambers. The holes in the distributions without associated cuts correspond to either the panel overlap regions, or dead or inefficient scintillator paddles.

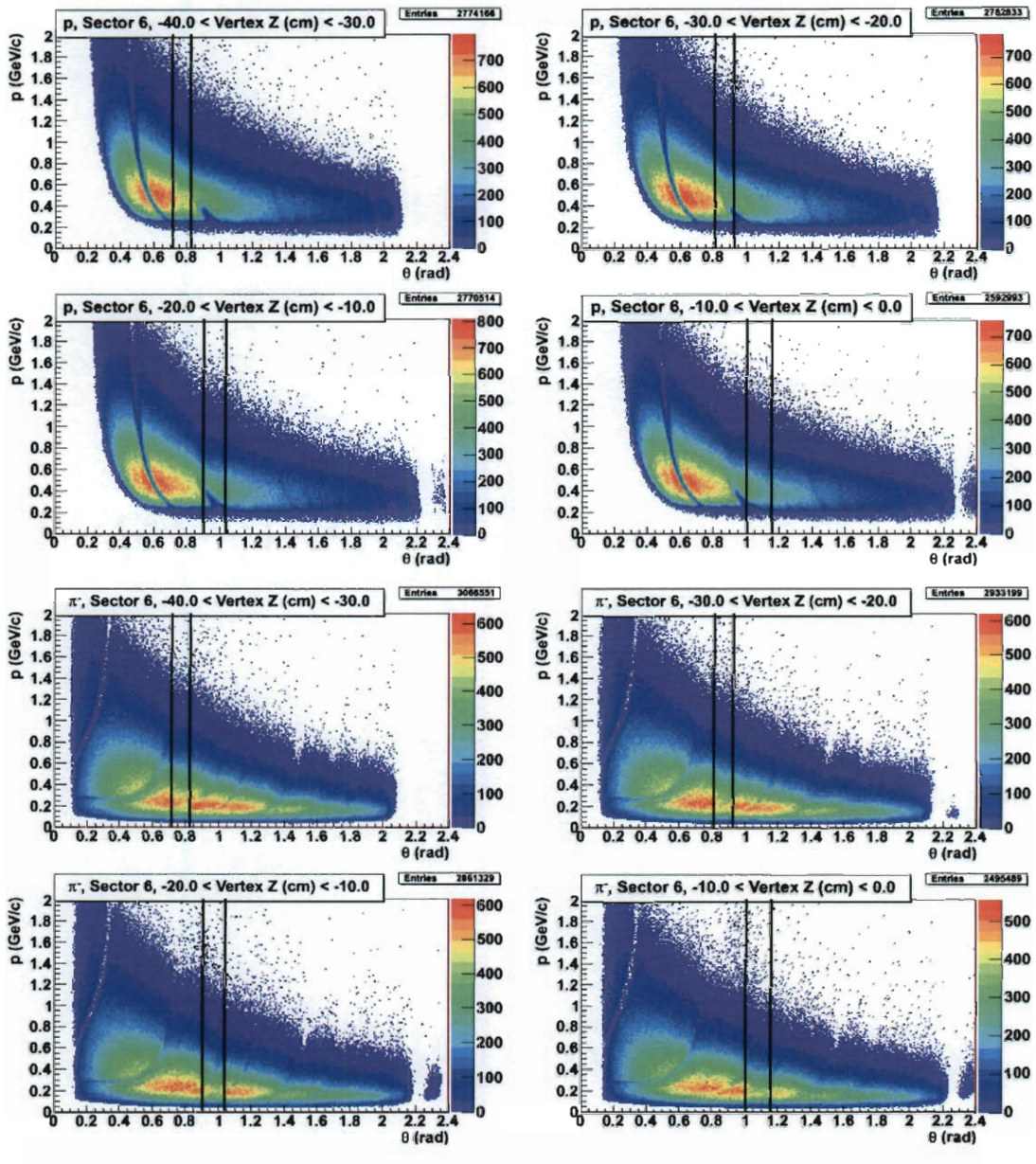

Figure B.18 : Track distributions of the protons (A) and π^-'s (B) in different vertex-z bins in Sector 6. The black lines indicate the borders of the regions cut out of the analysis in both data and in simulation due to holes in the drift chambers. The holes in the distributions without associated cuts correspond to either the panel overlap regions, or dead or inefficient scintillator paddles.

Appendix C

Yield Extraction Signal Fits

C.1 $\gamma n \to p\pi^-$ Fits

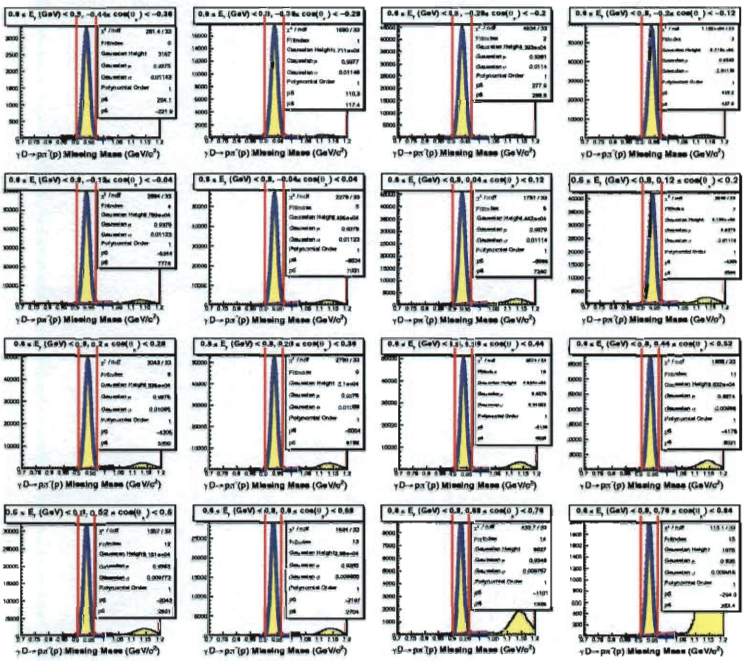

Figure C.1 : Fits to the missing mass of the spectator proton in the experimental data of the $\gamma D \to p\pi^-(p)$ reaction in the 0.6 GeV $< E_\gamma <$ 0.8 GeV bin. Each plot represents a different bin of $\cos(\theta_{\pi^-})$, where θ_{π^-} is the angle between the π^- and the photon in the center-of-mass frame. The signals were fit to a Gaussian over a linear background, and the red lines indicate the $\pm 3\sigma$ cuts used for yield extraction. The blue lineshapes represent the Gaussian fit functions, the magenta lineshapes represent the linear fit functions, and the black lineshapes represent the total fit functions.

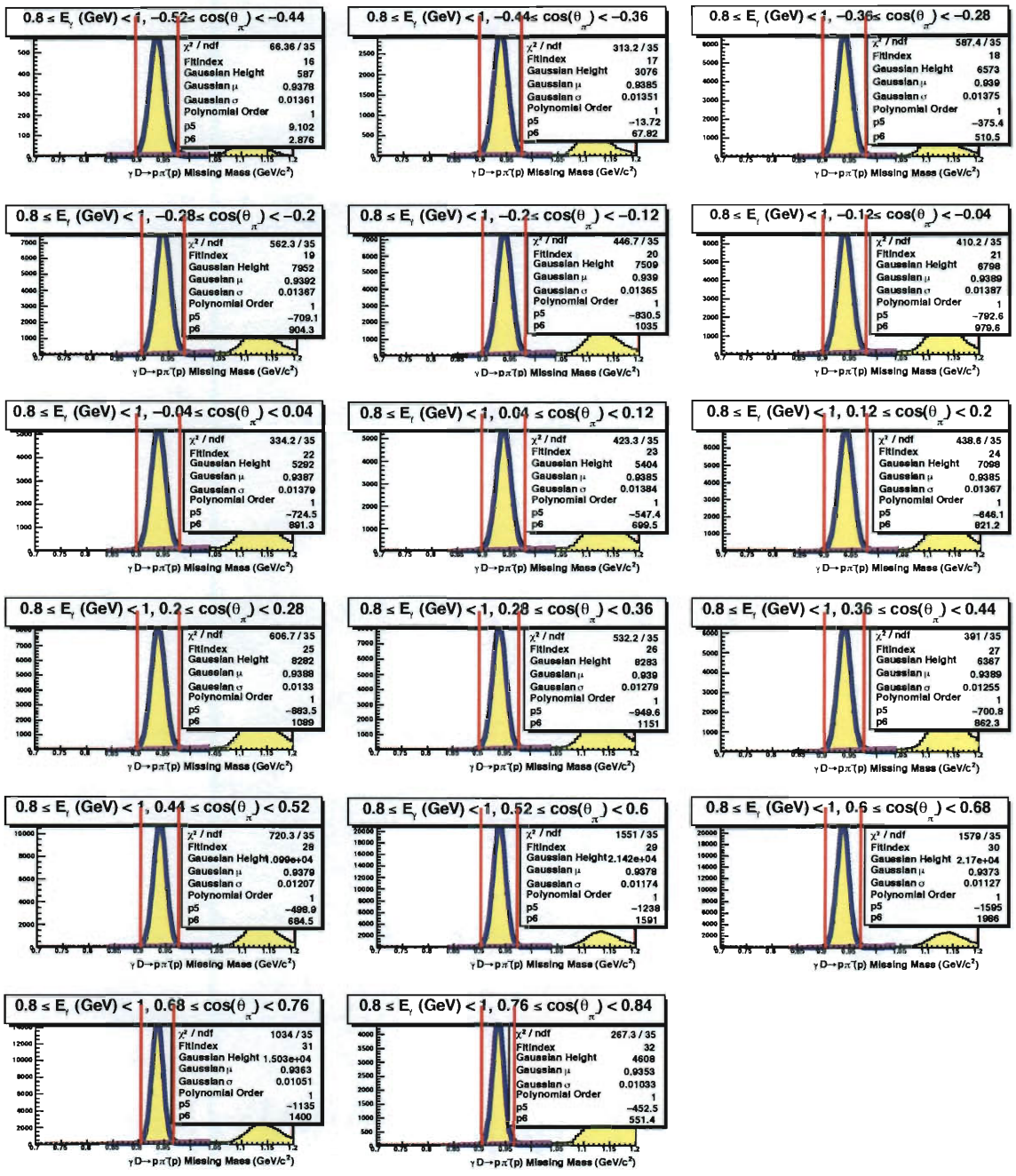

Figure C.2 : Fits to the missing mass of the spectator proton in the experimental data of the $\gamma D \rightarrow p\pi^-(p)$ reaction in the 0.8 GeV $< E_\gamma <$ 1.0 GeV bin. Each plot represents a different bin of $\cos(\theta_{\pi^-})$, where θ_{π^-} is the angle between the π^- and the photon in the center-of-mass frame. The signals were fit to a Gaussian over a linear background, and the red lines indicate the $\pm 3\sigma$ cuts used for yield extraction. The blue lineshapes represent the Gaussian fit functions, the magenta lineshapes represent the linear fit functions, and the black lineshapes represent the total fit functions.

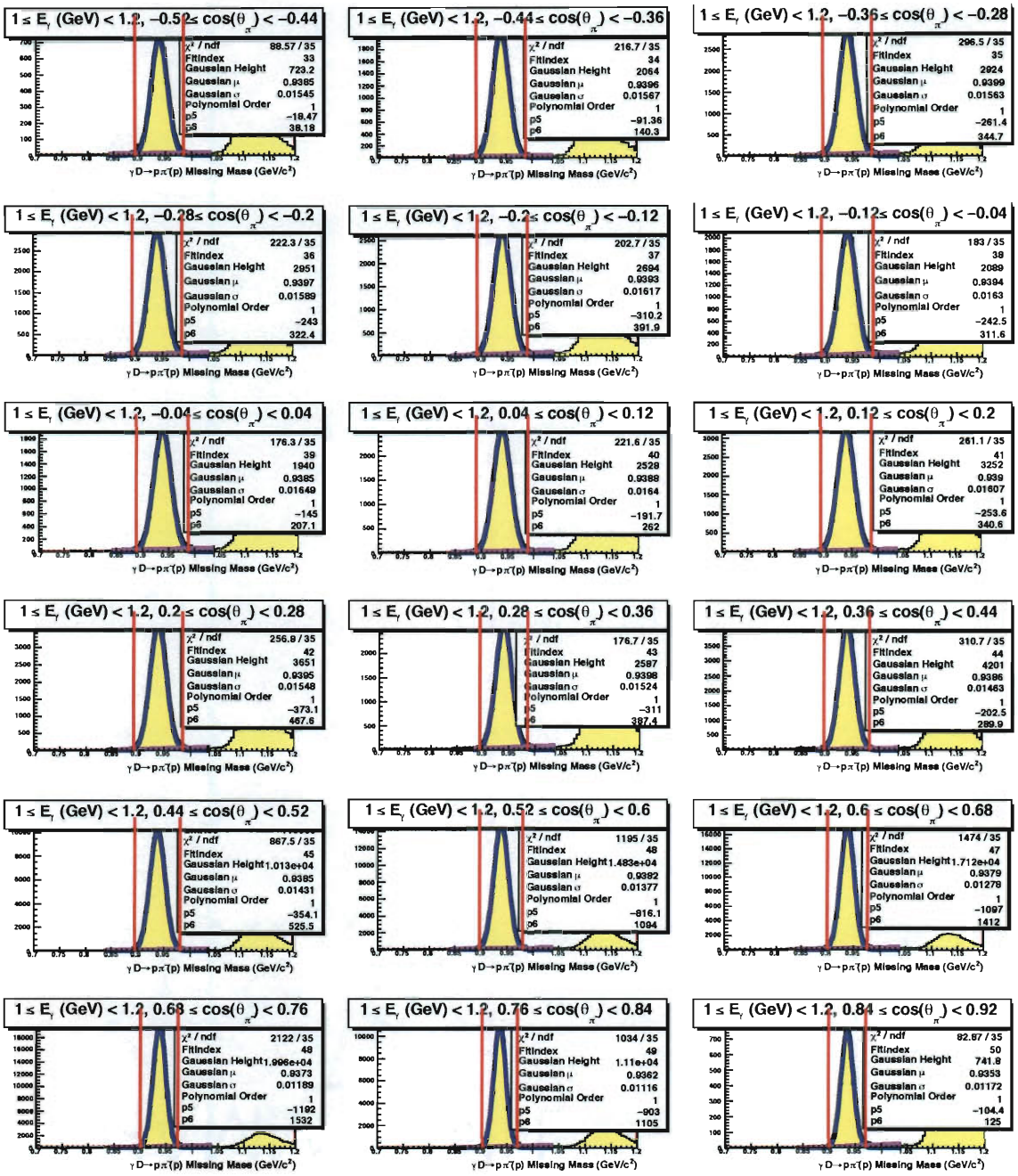

Figure C.3 : Fits to the missing mass of the spectator proton in the experimental data of the $\gamma D \rightarrow p\pi^-(p)$ reaction in the 1.0 GeV $< E_\gamma <$ 1.2 GeV bin. Each plot represents a different bin of $\cos(\theta_{\pi^-})$, where θ_{π^-} is the angle between the π^- and the photon in the center-of-mass frame. The signals were fit to a Gaussian over a linear background, and the red lines indicate the $\pm 3\sigma$ cuts used for yield extraction. The blue lineshapes represent the Gaussian fit functions, the magenta lineshapes represent the linear fit functions, and the black lineshapes represent the total fit functions.

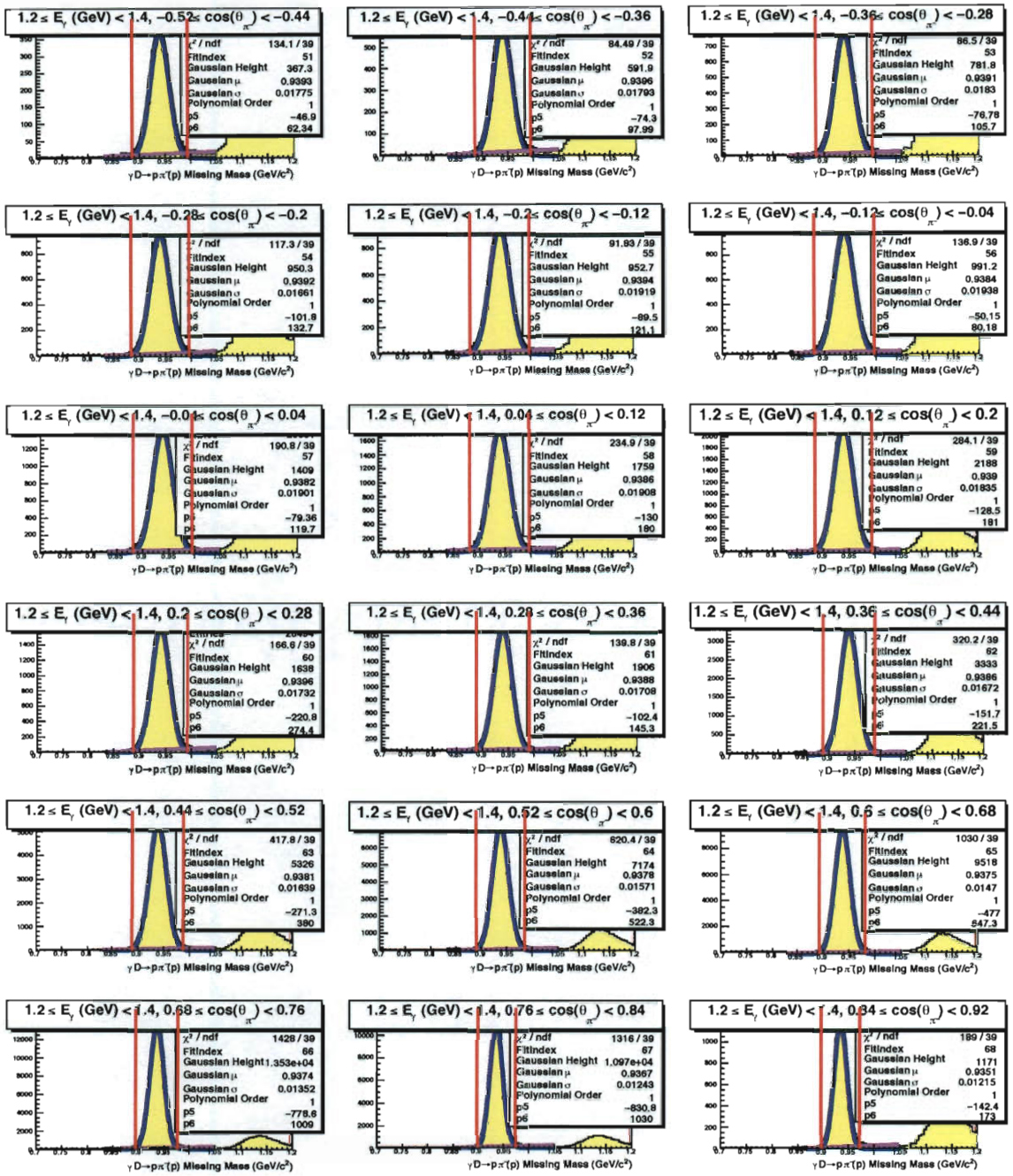

Figure C.4 : Fits to the missing mass of the spectator proton in the experimental data of the $\gamma D \to p\pi^-(p)$ reaction in the 1.2 GeV $< E_\gamma <$ 1.4 GeV bin. Each plot represents a different bin of $\cos(\theta_{\pi^-})$, where θ_{π^-} is the angle between the π^- and the photon in the center-of-mass frame. The signals were fit to a Gaussian over a linear background, and the red lines indicate the $\pm 3\sigma$ cuts used for yield extraction. The blue lineshapes represent the Gaussian fit functions, the magenta lineshapes represent the linear fit functions, and the black lineshapes represent the total fit functions.

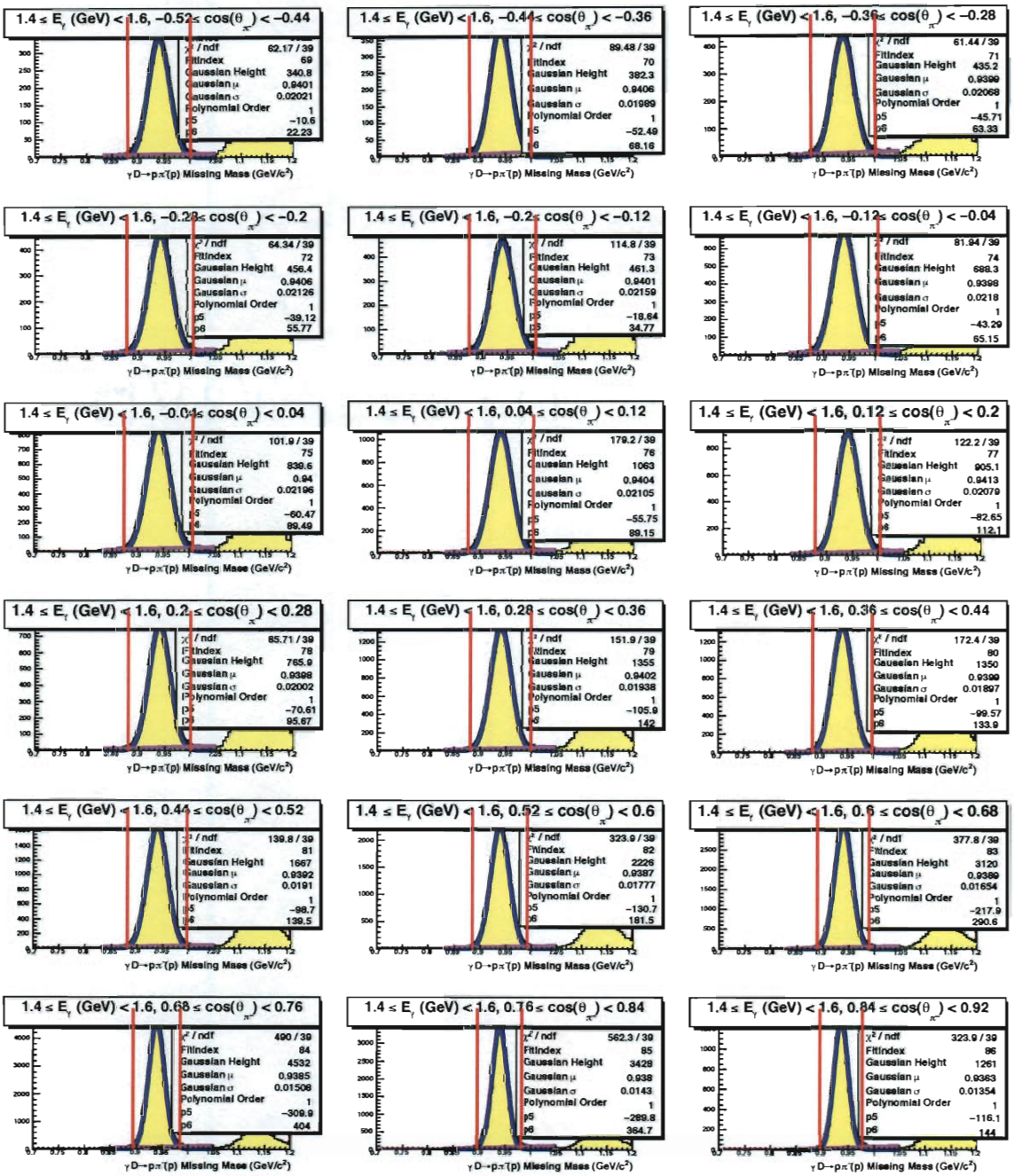

Figure C.5 : Fits to the missing mass of the spectator proton in the experimental data of the $\gamma D \rightarrow p\pi^-(p)$ reaction in the 1.4 GeV $< E_\gamma <$ 1.6 GeV bin. Each plot represents a different bin of $\cos(\theta_{\pi^-})$, where θ_{π^-} is the angle between the π^- and the photon in the center-of-mass frame. The signals were fit to a Gaussian over a linear background, and the red lines indicate the $\pm 3\sigma$ cuts used for yield extraction. The blue lineshapes represent the Gaussian fit functions, the magenta lineshapes represent the linear fit functions, and the black lineshapes represent the total fit functions.

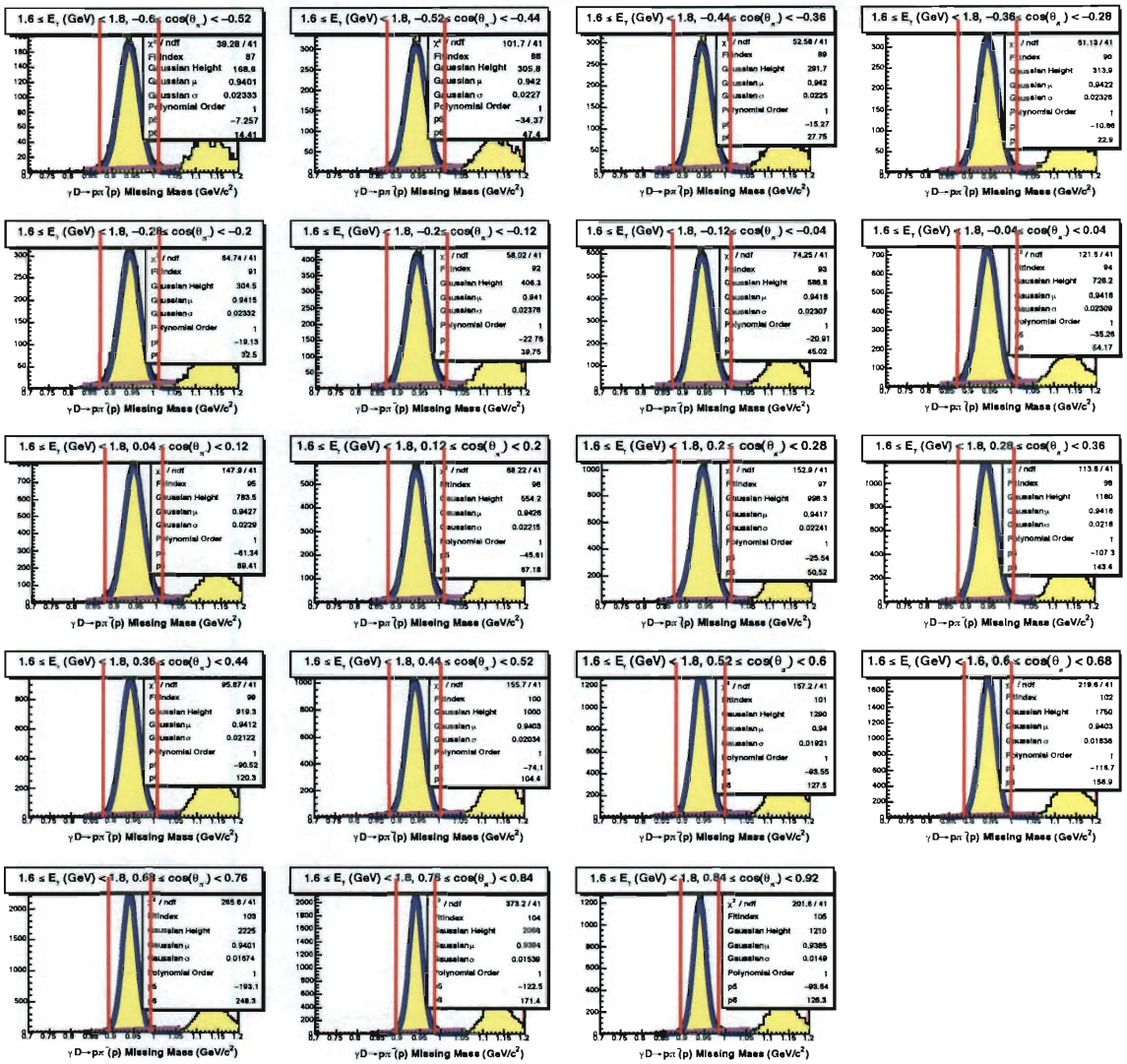

Figure C.6 : Fits to the missing mass of the spectator proton in the experimental data of the $\gamma D \rightarrow p\pi^-(p)$ reaction in the 1.6 GeV $< E_\gamma <$ 1.8 GeV bin. Each plot represents a different bin of $\cos(\theta_{\pi^-})$, where θ_{π^-} is the angle between the π^- and the photon in the center-of-mass frame. The signals were fit to a Gaussian over a linear background, and the red lines indicate the $\pm 3\sigma$ cuts used for yield extraction. The blue lineshapes represent the Gaussian fit functions, the magenta lineshapes represent the linear fit functions, and the black lineshapes represent the total fit functions.

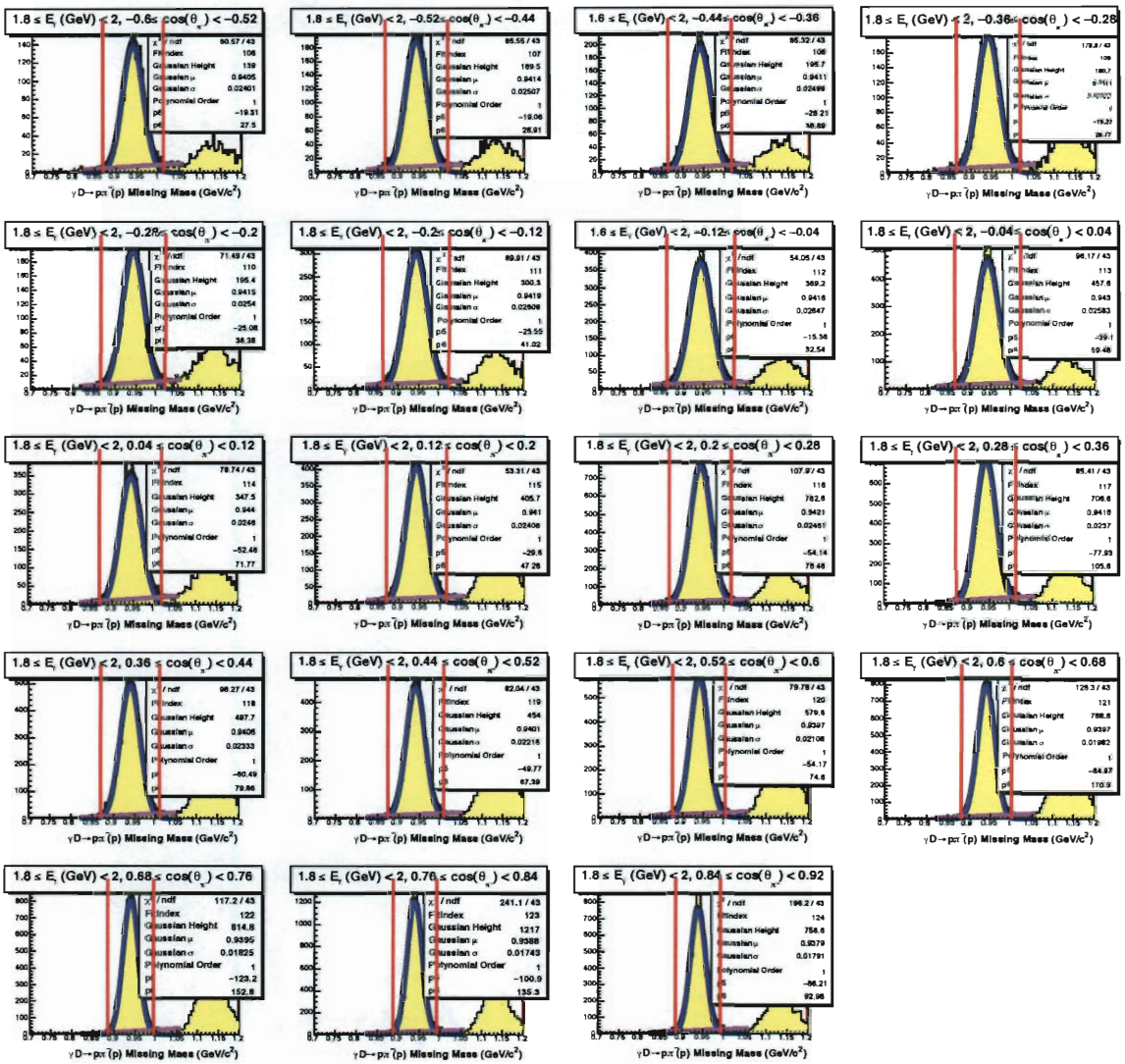

Figure C.7 : Fits to the missing mass of the spectator proton in the experimental data of the $\gamma D \to p\pi^-(p)$ reaction in the 1.8 GeV $< E_\gamma <$ 2.0 GeV bin. Each plot represents a different bin of $\cos(\theta_{\pi^-})$, where θ_{π^-} is the angle between the π^- and the photon in the center-of-mass frame. The signals were fit to a Gaussian over a linear background, and the red lines indicate the $\pm 3\sigma$ cuts used for yield extraction. The blue lineshapes represent the Gaussian fit functions, the magenta lineshapes represent the linear fit functions, and the black lineshapes represent the total fit functions.

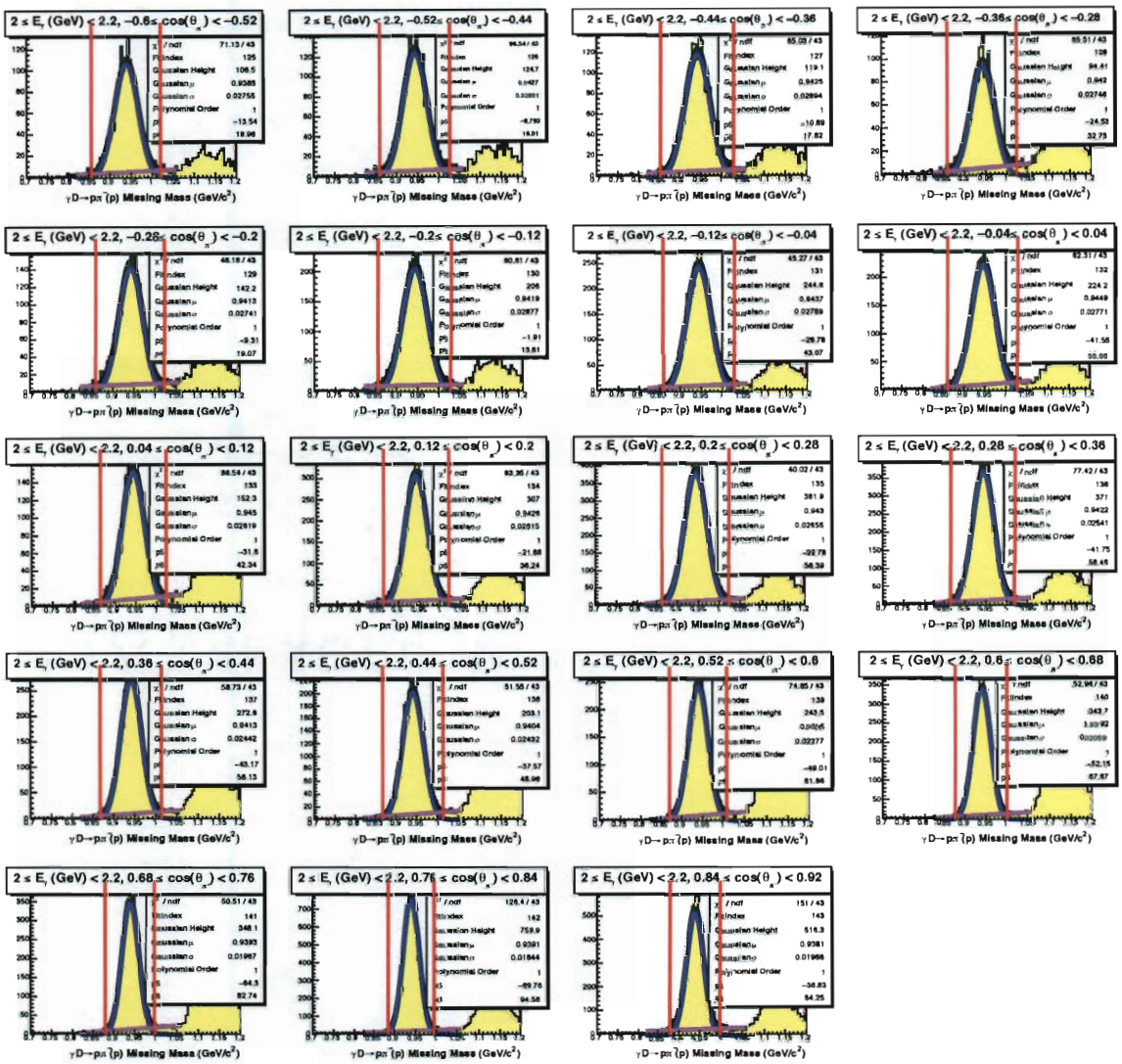

Figure C.8 : Fits to the missing mass of the spectator proton in the experimental data of the $\gamma D \rightarrow p\pi^-(p)$ reaction in the 2.0 GeV $< E_\gamma <$ 2.2 GeV bin. Each plot represents a different bin of $\cos(\theta_{\pi^-})$, where θ_{π^-} is the angle between the π^- and the photon in the center-of-mass frame. The signals were fit to a Gaussian over a linear background, and the red lines indicate the $\pm 3\sigma$ cuts used for yield extraction. The blue lineshapes represent the Gaussian fit functions, the magenta lineshapes represent the linear fit functions, and the black lineshapes represent the total fit functions.

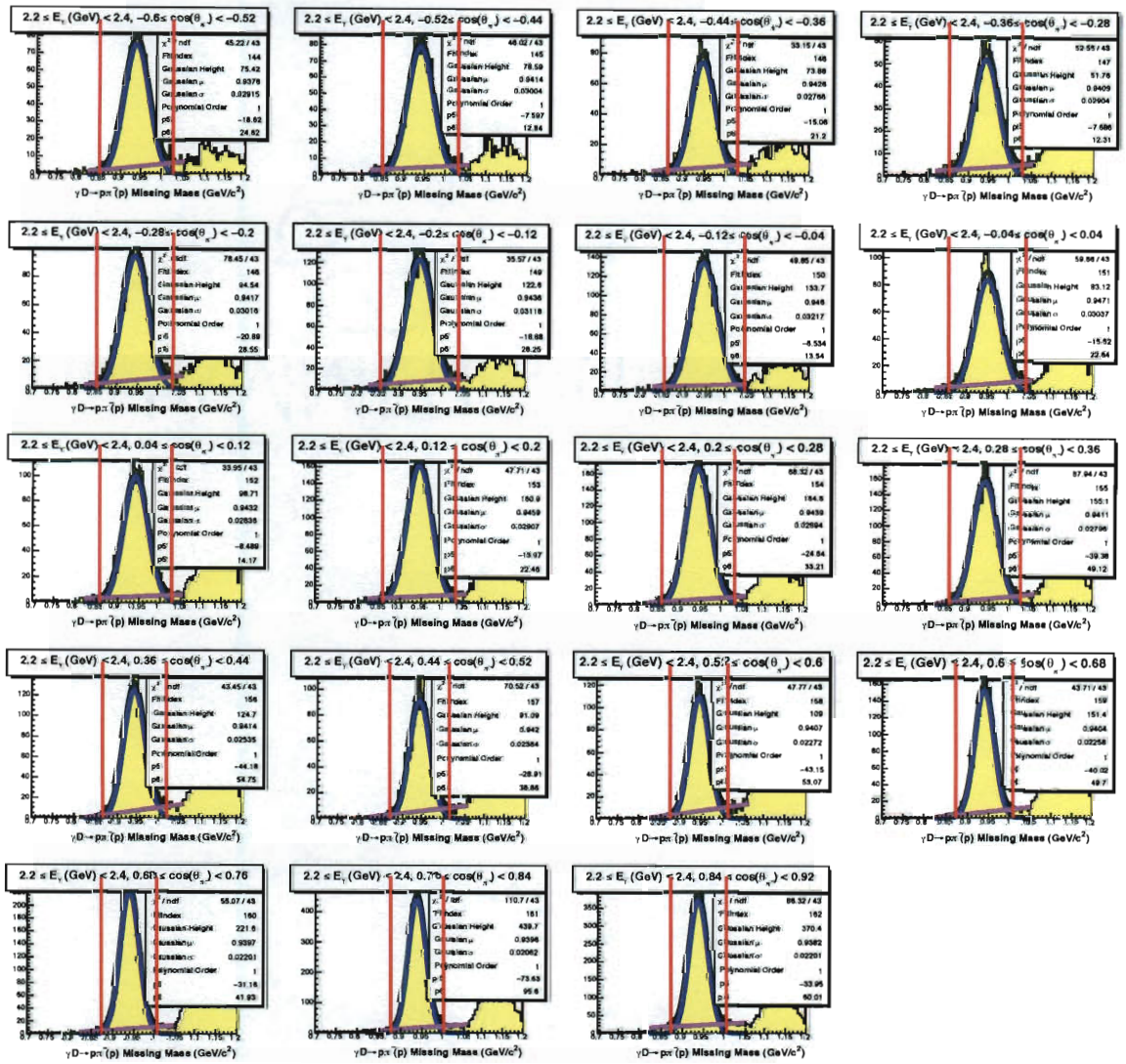

Figure C.9 : Fits to the missing mass of the spectator proton in the experimental data of the $\gamma D \rightarrow p\pi^-(p)$ reaction in the 2.2 GeV $< E_\gamma <$ 2.4 GeV bin. Each plot represents a different bin of $\cos(\theta_{\pi^-})$, where θ_{π^-} is the angle between the π^- and the photon in the center-of-mass frame. The signals were fit to a Gaussian over a linear background, and the red lines indicate the $\pm 3\sigma$ cuts used for yield extraction. The blue lineshapes represent the Gaussian fit functions, the magenta lineshapes represent the linear fit functions, and the black lineshapes represent the total fit functions.

C.2 $\gamma n \rightarrow K^{*0}\Lambda$ Fits

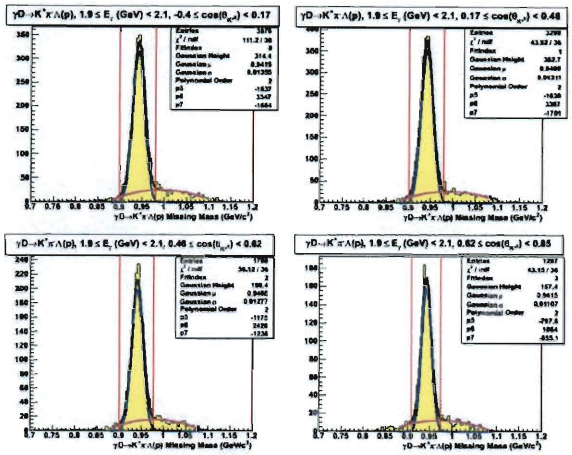

Figure C.10 : Fits to the missing mass of the spectator proton of the $\gamma D \rightarrow K^{+}\pi^{-}\Lambda(p)$ reaction for the $\gamma n \rightarrow K^{*0}\Lambda$ analysis in the 1.9 GeV to 2.1 GeV photon energy bin. Each plot represents a different bin of $\cos(\theta_{K^{*0}})$, where $\theta_{K^{*0}}$ is the angle between the K^{*0} and the photon in the center-of-mass frame. The signals were fit to a Gaussian over a quadratic background, and the red lines indicate the $\pm 3\sigma$ cuts. The blue lineshapes represent the Gaussian fit functions, the magenta lineshapes represent the quadratic fit functions, and the black lineshapes represents the total fit functions.

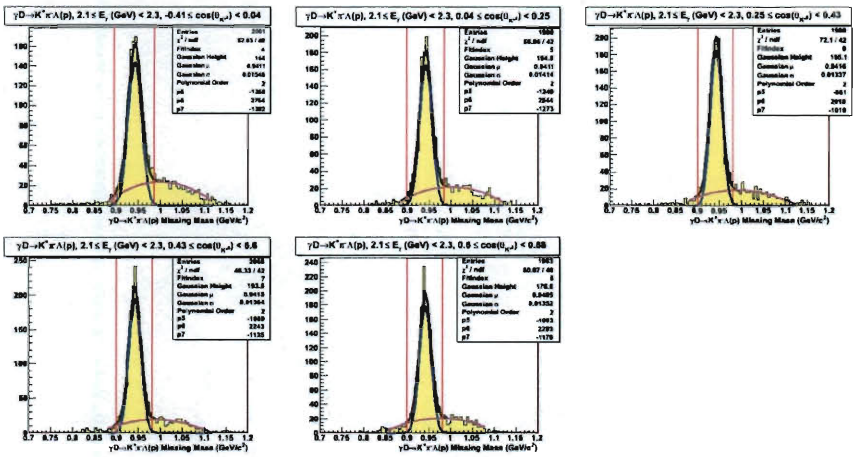

Figure C.11 : Fits to the missing mass of the spectator proton of the $\gamma D \rightarrow K^{+}\pi^{-}\Lambda(p)$ reaction for the $\gamma n \rightarrow K^{*0}\Lambda$ analysis in the 2.1 GeV to 2.3 GeV photon energy bin. Each plot represents a different bin of $\cos(\theta_{K^{*0}})$, where $\theta_{K^{*0}}$ is the angle between the K^{*0} and the photon in the center-of-mass frame. The signals were fit to a Gaussian over a quadratic background, and the red lines indicate the $\pm 3\sigma$ cuts. The blue lineshapes represent the Gaussian fit functions, the magenta lineshapes represent the quadratic fit functions, and the black lineshapes represents the total fit functions.

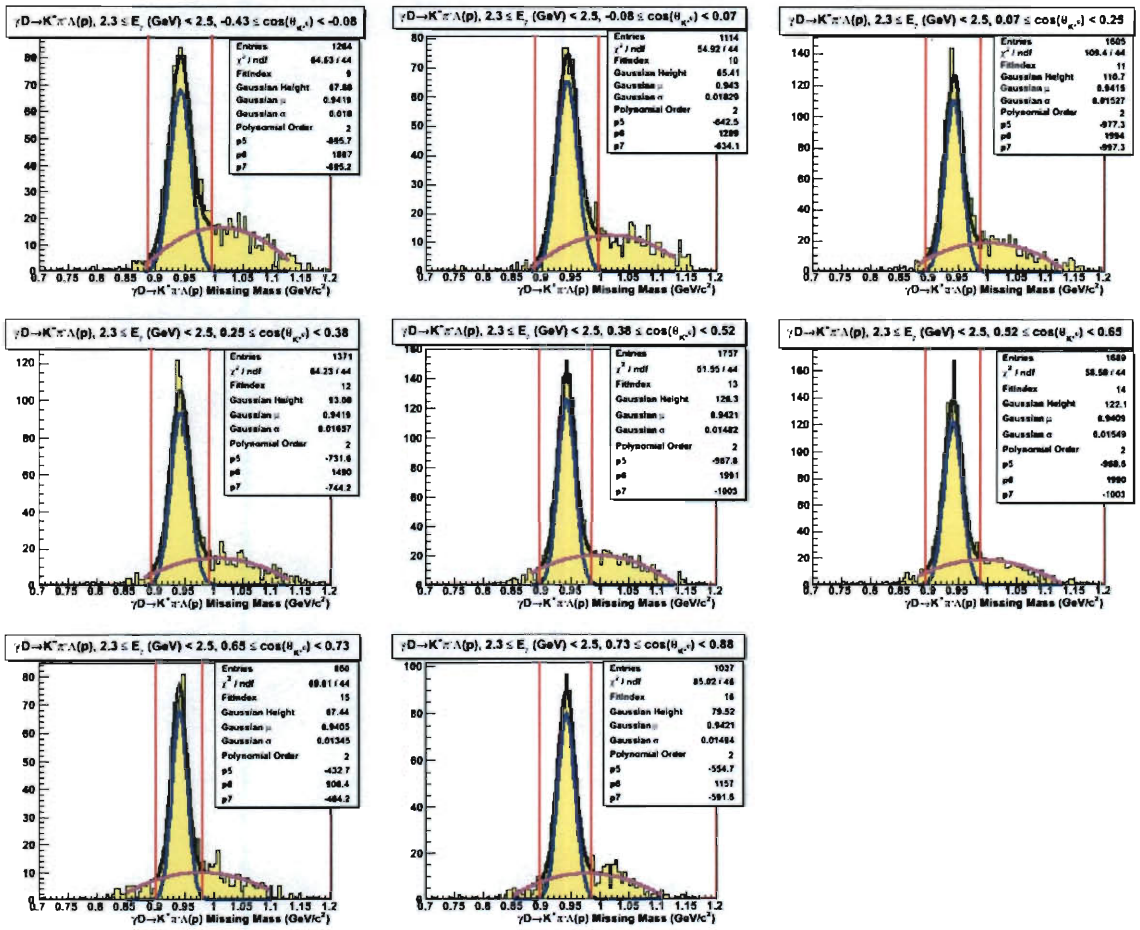

Figure C.12 : Fits to the missing mass of the spectator proton of the $\gamma D \to K^+\pi^-\Lambda(p)$ reaction for the $\gamma n \to K^{*0}\Lambda$ analysis in the 2.3 GeV to 2.5 GeV photon energy bin. Each plot represents a different bin of $\cos(\theta_{K^{*0}})$, where $\theta_{K^{*0}}$ is the angle between the K^{*0} and the photon in the center-of-mass frame. The signals were fit to a Gaussian over a quadratic background, and the red lines indicate the $\pm 3\sigma$ cuts. The blue lineshapes represent the Gaussian fit functions, the magenta lineshapes represent the quadratic fit functions, and the black lineshapes represents the total fit functions.

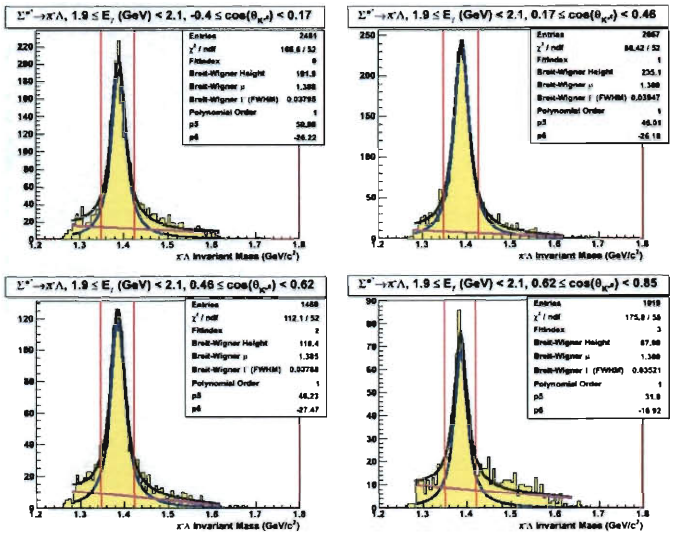

Figure C.13 : Fits to the invariant mass of the Σ^{*-} for the $\gamma n \to K^{*0}\Lambda$ analysis in the 1.9 GeV to 2.1 GeV photon energy bin. Each plot represents a different bin of $\cos(\theta_{K^{*0}})$, where $\theta_{K^{*0}}$ is the angle between the K^{*0} and the photon in the center-of-mass frame. These distributions were fit to a Breit-Wigner over a linear background, and events within $\pm 1\Gamma$ were cut to remove the majority of the $\gamma n \to K^{+}\Sigma^{*-}$ events. These cuts are illustrated by the red vertical lines, and the blue, magenta, and black lineshapes represent the Breit-Wigner, linear background, and total fit functions, respectively.

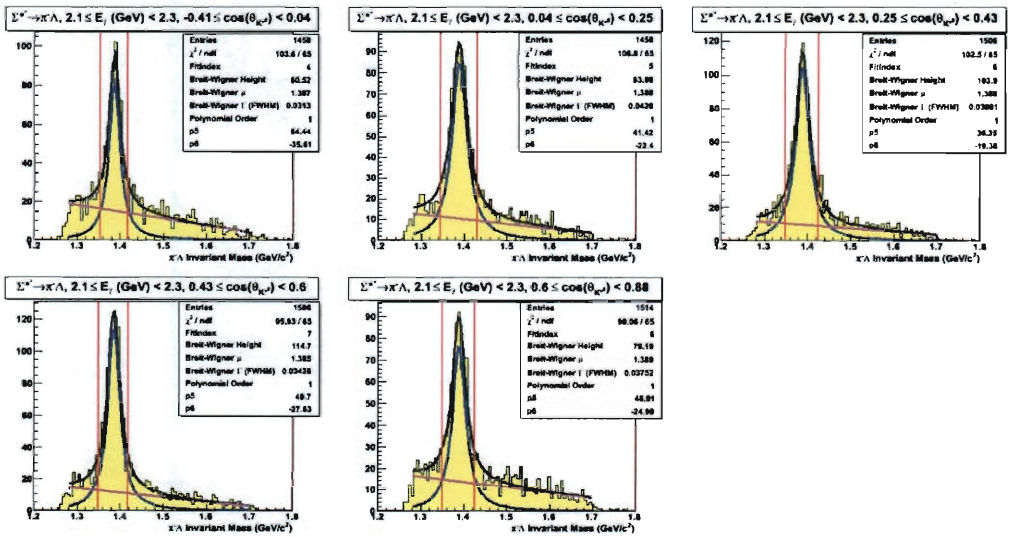

Figure C.14 : Fits to the invariant mass of the Σ^{*-} for the $\gamma n \to K^{*0}\Lambda$ analysis in the 2.1 GeV to 2.3 GeV photon energy bin. Each plot represents a different bin of $\cos(\theta_{K^{*0}})$, where $\theta_{K^{*0}}$ is the angle between the K^{*0} and the photon in the center-of-mass frame. These distributions were fit to a Breit-Wigner over a linear background, and events within $\pm 1\Gamma$ were cut to remove the majority of the $\gamma n \to K^{+}\Sigma^{*-}$ events. These cuts are illustrated by the red vertical lines, and the blue, magenta, and black lineshapes represent the Breit-Wigner, linear background, and total fit functions, respectively.

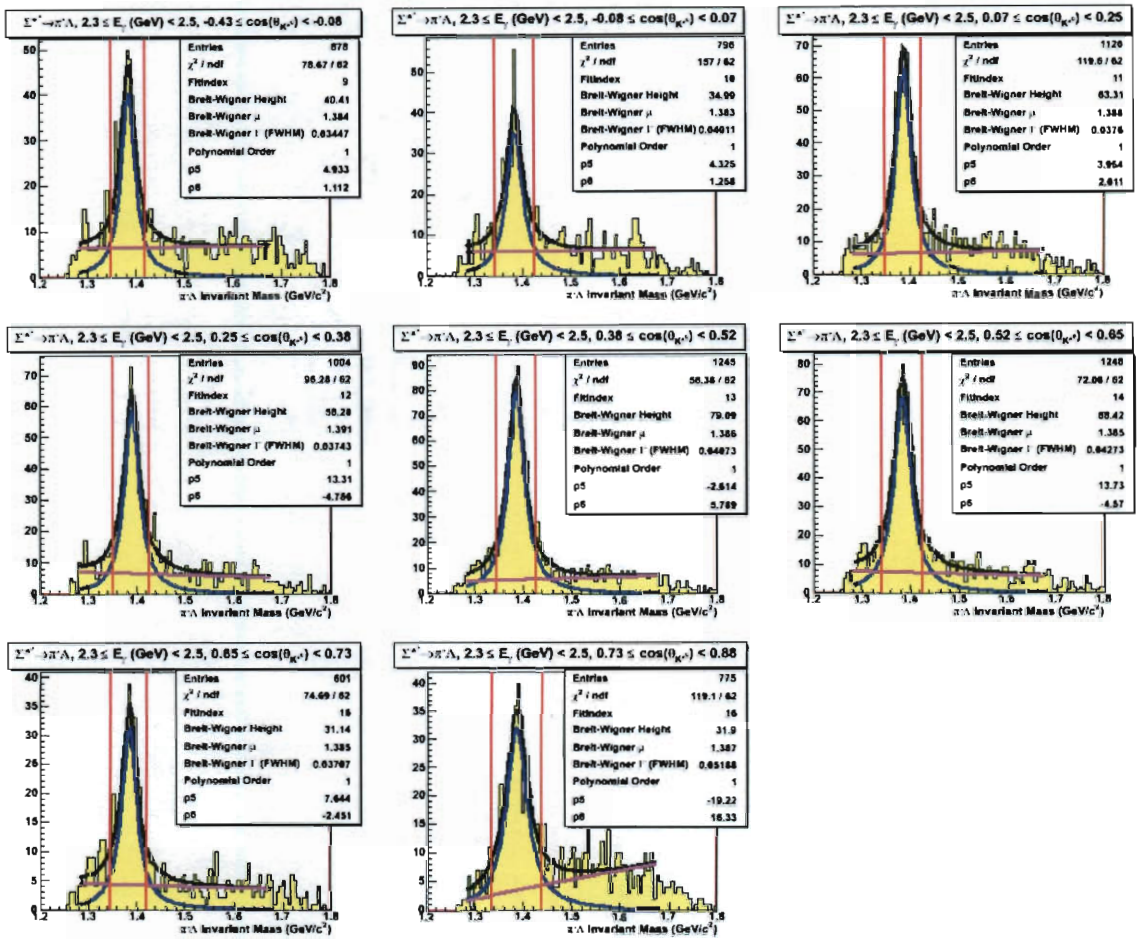

Figure C.15 : Fits to the invariant mass of the Σ^{*-} for the $\gamma n \to K^{*0}\Lambda$ analysis in the 2.3 GeV to 2.5 GeV photon energy bin. Each plot represents a different bin of $\cos(\theta_{K^{*0}})$, where $\theta_{K^{*0}}$ is the angle between the K^{*0} and the photon in the center-of-mass frame. These distributions were fit to a Breit-Wigner over a linear background, and events within $\pm 1\Gamma$ were cut to remove the majority of the $\gamma n \to K^{+}\Sigma^{*-}$ events. These cuts are illustrated by the red vertical lines, and the blue, magenta, and black lineshapes represent the Breit-Wigner, linear background, and total fit functions, respectively.

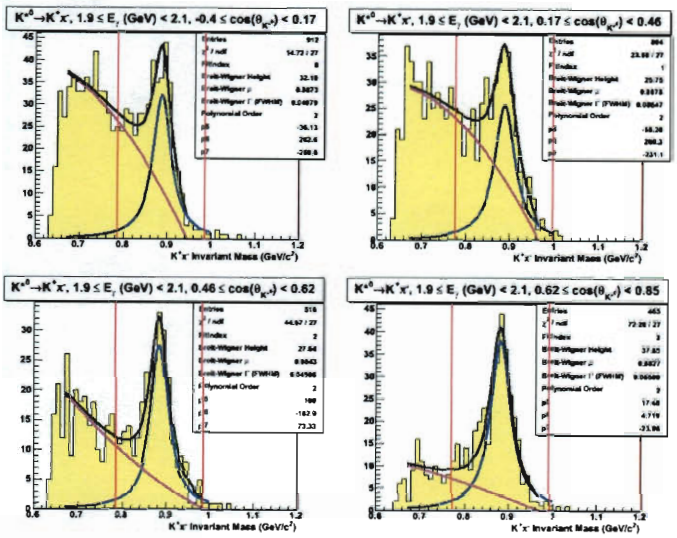

Figure C.16 : Fits to the invariant mass of the K^{*0} for the $\gamma n \rightarrow K^{*0}\Lambda$ analysis in the 1.9 GeV to 2.1 GeV photon energy bin. Each plot represents a different bin of $\cos(\theta_{K^{*0}})$, where $\theta_{K^{*0}}$ is the angle between the K^{*0} and the photon in the center-of-mass frame. These distributions were fit to a Breit-Wigner over a quadratic background, and the red lines indicate the $\pm 2\Gamma$ cuts used for yield extraction. The blue lineshapes represent the Gaussian fit functions, the magenta lineshapes represent the quadratic fit functions, and the black lineshapes represents the total fit functions.

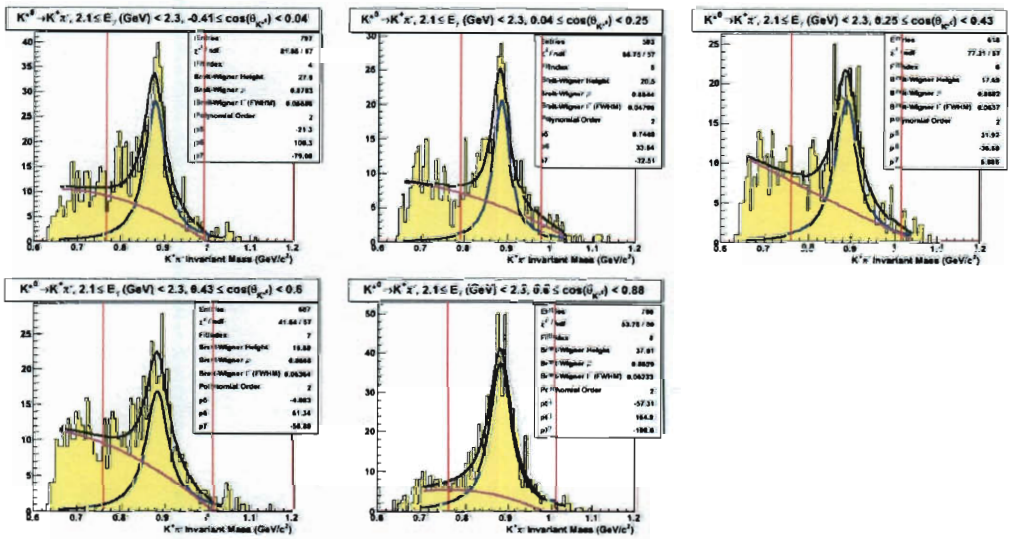

Figure C.17 : Fits to the invariant mass of the K^{*0} for the $\gamma n \rightarrow K^{*0}\Lambda$ analysis in the 2.1 GeV to 2.3 GeV photon energy bin. Each plot represents a different bin of $\cos(\theta_{K^{*0}})$, where $\theta_{K^{*0}}$ is the angle between the K^{*0} and the photon in the center-of-mass frame. These distributions were fit to a Breit-Wigner over a quadratic background, and the red lines indicate the $\pm 2\Gamma$ cuts used for yield extraction. The blue lineshapes represent the Gaussian fit functions, the magenta lineshapes represent the quadratic fit functions, and the black lineshapes represents the total fit functions.

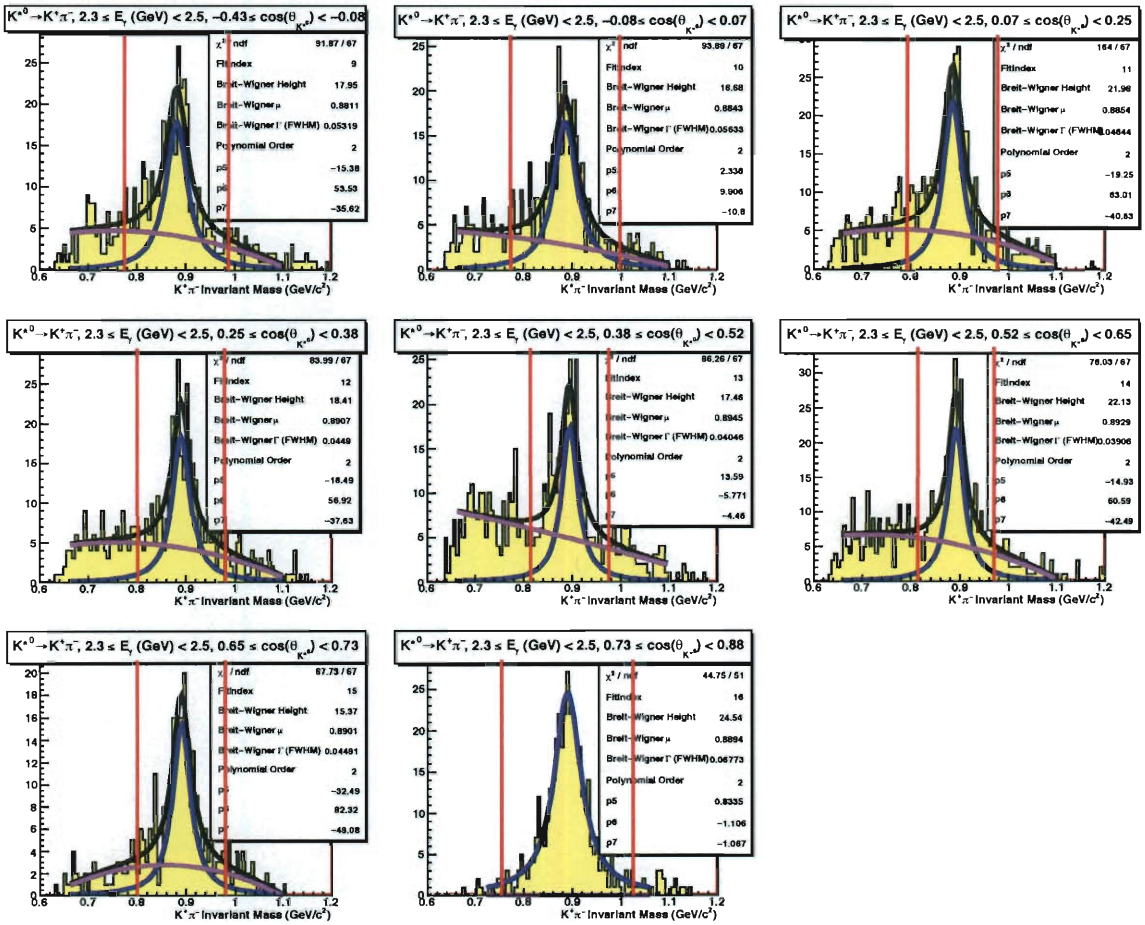

Figure C.18 : Fits to the invariant mass of the K^{*0} for the $\gamma n \rightarrow K^{*0}\Lambda$ analysis in the 2.3 GeV to 2.5 GeV photon energy bin. Each plot represents a different bin of $\cos(\theta_{K^{*0}})$, where $\theta_{K^{*0}}$ is the angle between the K^{*0} and the photon in the center-of-mass frame. These distributions were fit to a Breit-Wigner over a quadratic background, and the red lines indicate the $\pm 2\Gamma$ cuts used for yield extraction. The blue lineshapes represent the Gaussian fit functions, the magenta lineshapes represent the quadratic fit functions, and the black lineshapes represents the total fit functions.

C.3 $\gamma n \to K^+\Sigma^{*-}$ Fits

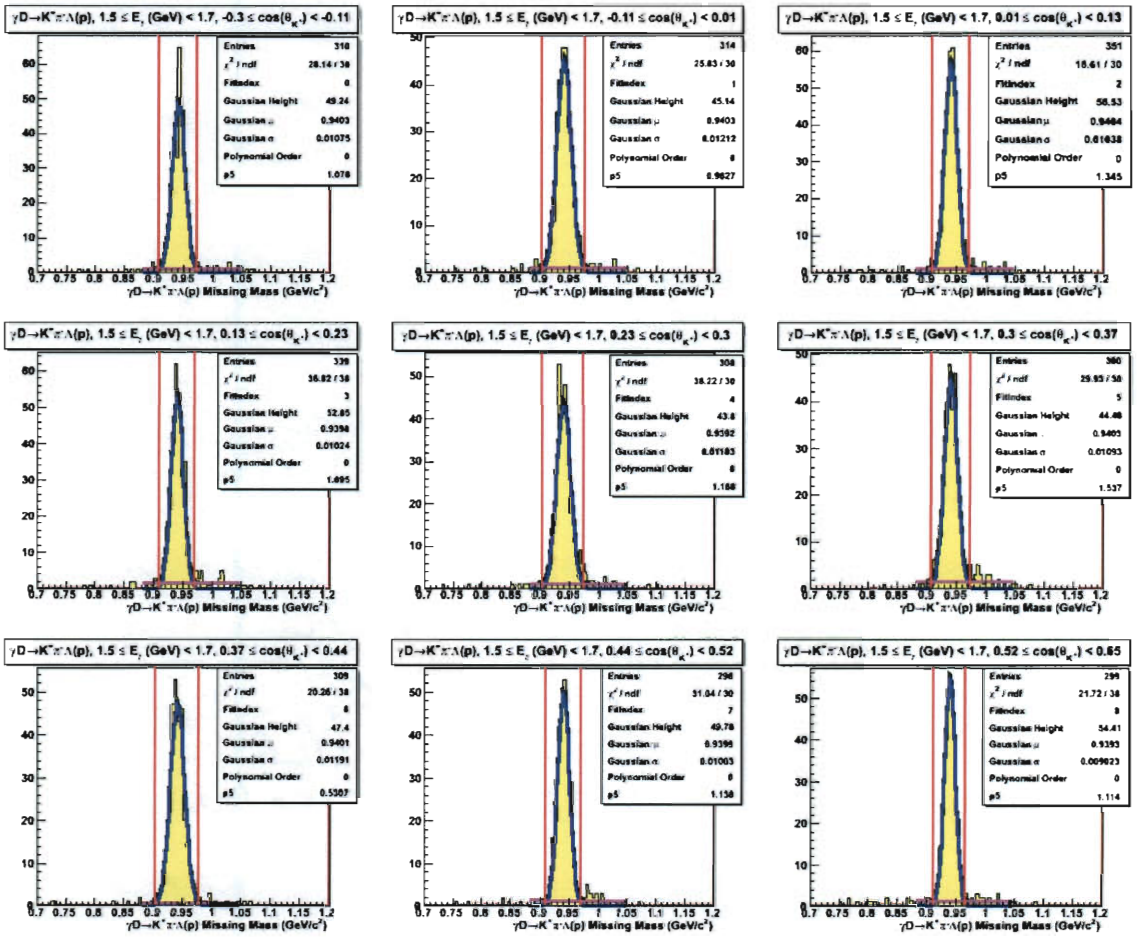

Figure C.19 : Fits to the missing mass of the spectator proton of the $\gamma D \to K^+\pi^-\Lambda(p)$ reaction for the $\gamma n \to K^+\Sigma^{*-}$ analysis in the 1.5 GeV to 1.7 GeV photon energy bin. Each plot represents a different bin of $\cos(\theta_{K^+})$, where θ_{K^+} is the angle between the K^+ and the photon in the center-of-mass frame. The signals were fit to a Gaussian over a flat background, and the red lines indicate the $\pm 3\sigma$ cuts. The blue lineshapes represent the Gaussian fit functions, the magenta lineshapes represent the flat fit functions, and the black lineshapes represent the total fit functions.

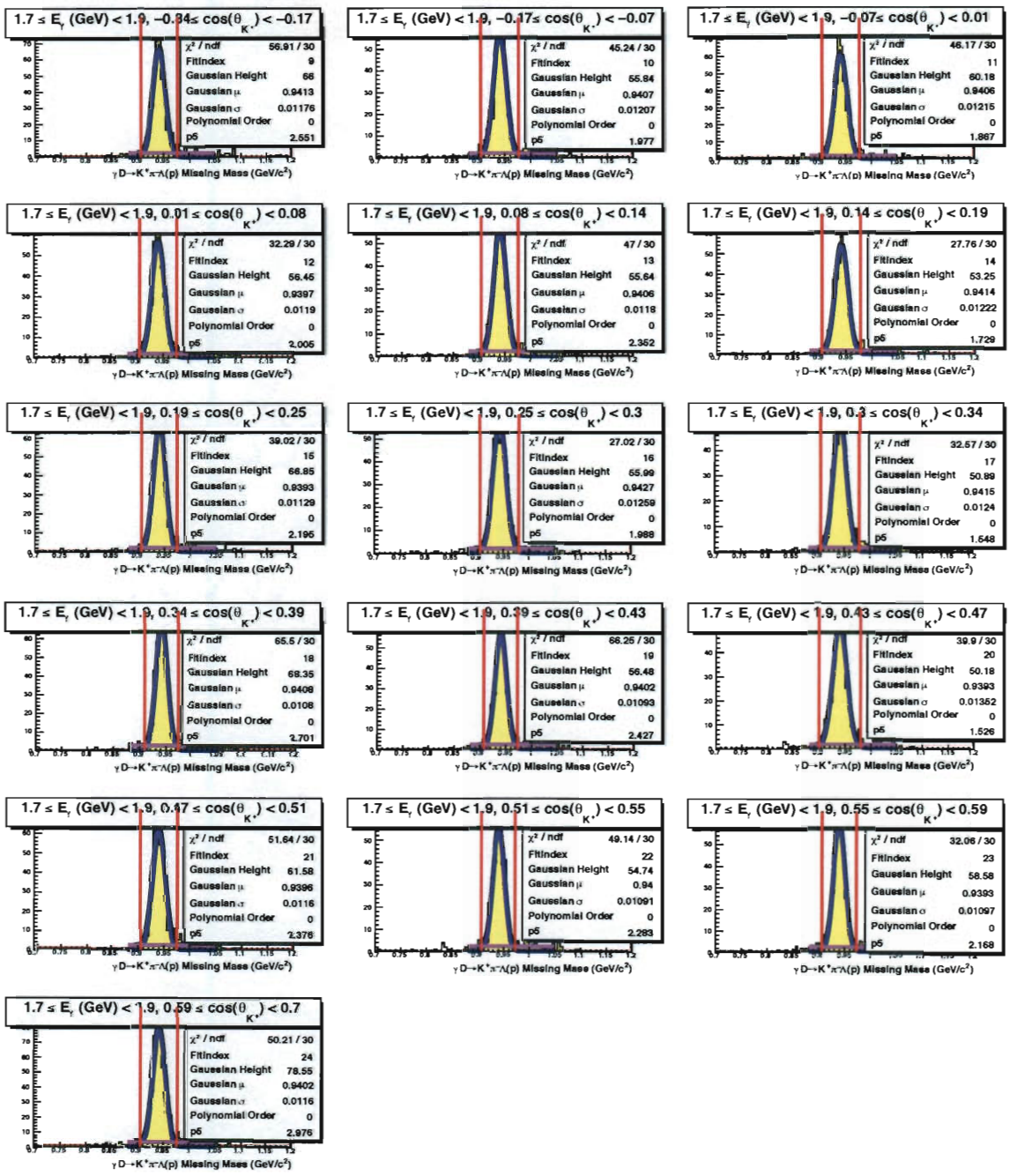

Figure C.20 : Fits to the missing mass of the spectator proton of the $\gamma D \to K^+\pi^-\Lambda(p)$ reaction for the $\gamma n \to K^+\Sigma^{*-}$ analysis in the 1.7 GeV to 1.9 GeV photon energy bin. Each plot represents a different bin of $\cos(\theta_{K^+})$, where θ_{K^+} is the angle between the K^+ and the photon in the center-of-mass frame. The signals were fit to a Gaussian over a flat background, and the red lines indicate the $\pm 3\sigma$ cuts. The blue lineshapes represent the Gaussian fit functions, the magenta lineshapes represent the flat fit functions, and the black lineshapes represent the total fit functions.

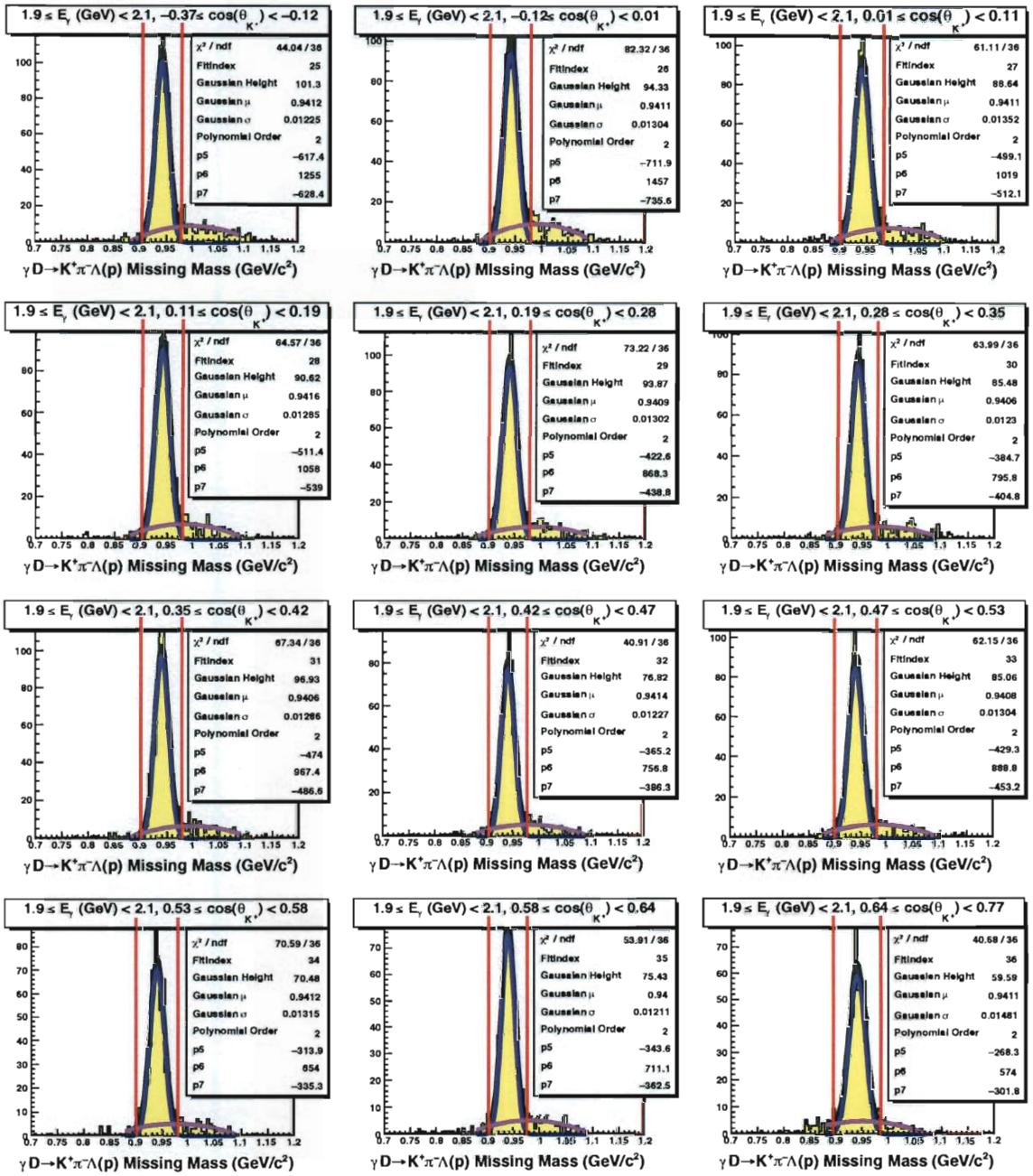

Figure C.21 : Fits to the missing mass of the spectator proton of the $\gamma D \to K^+\pi^-\Lambda(p)$ reaction for the $\gamma n \to K^+\Sigma^{*-}$ analysis in the 1.9 GeV to 2.1 GeV photon energy bin. Each plot represents a different bin of $\cos(\theta_{K^+})$, where θ_{K^+} is the angle between the K^+ and the photon in the center-of-mass frame. The signals were fit to a Gaussian over a quadratic background, and the red lines indicate the $\pm 3\sigma$ cuts. The blue lineshapes represent the Gaussian fit functions, the magenta lineshapes represent the quadratic fit functions, and the black lineshapes represent the total fit functions.

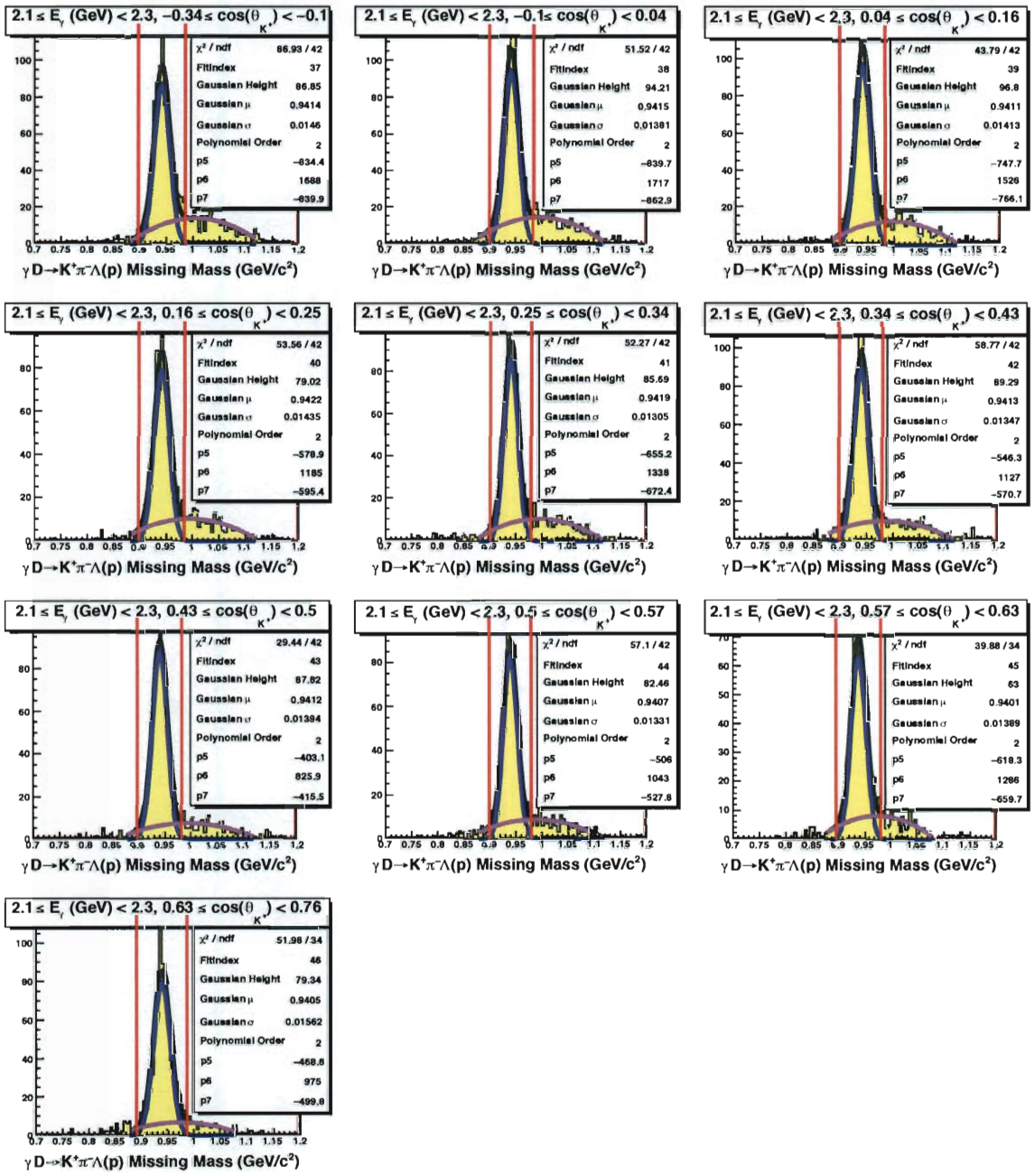

Figure C.22 : Fits to the missing mass of the spectator proton of the $\gamma D \to K^+\pi^-\Lambda(p)$ reaction for the $\gamma n \to K^+\Sigma^{*-}$ analysis in the 2.1 GeV to 2.3 GeV photon energy bin. Each plot represents a different bin of $\cos(\theta_{K^+})$, where θ_{K^+} is the angle between the K^+ and the photon in the center-of-mass frame. The signals were fit to a Gaussian over a quadratic background, and the red lines indicate the $\pm 3\sigma$ cuts. The blue lineshapes represent the Gaussian fit functions, the magenta lineshapes represent the quadratic fit functions, and the black lineshapes represent the total fit functions.

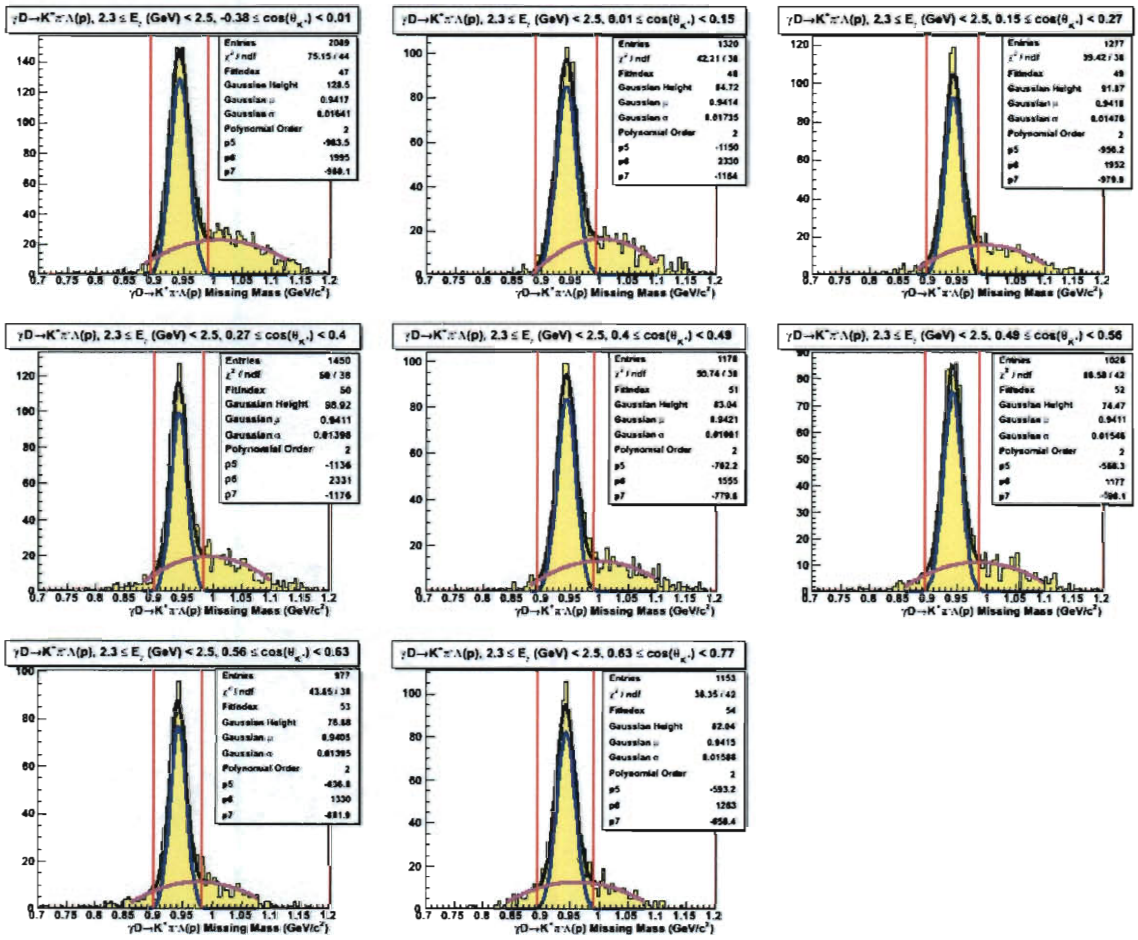

Figure C.23 : Fits to the missing mass of the spectator proton of the $\gamma D \to K^+\pi^-\Lambda(p)$ reaction for the $\gamma n \to K^+\Sigma^{*-}$ analysis in the 2.3 GeV to 2.5 GeV photon energy bin. Each plot represents a different bin of $\cos(\theta_{K^+})$, where θ_{K^+} is the angle between the K^+ and the photon in the center-of-mass frame. The signals were fit to a Gaussian over a quadratic background, and the red lines indicate the $\pm 3\sigma$ cuts. The blue lineshapes represent the Gaussian fit functions, the magenta lineshapes represent the quadratic fit functions, and the black lineshapes represent the total fit functions.

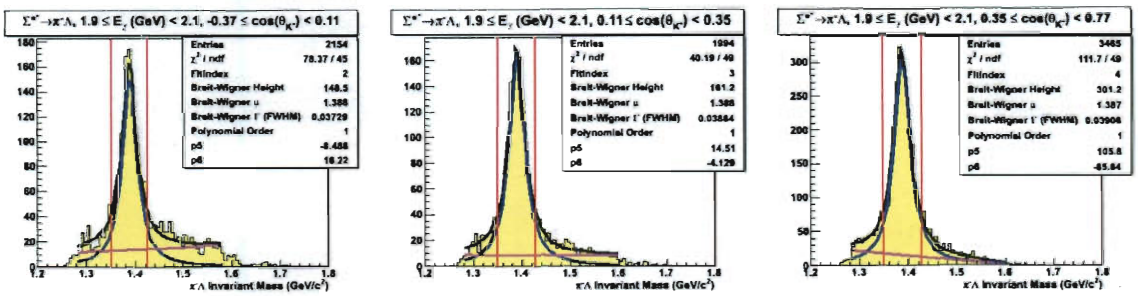

Figure C.24 : Fits to the invariant mass of the Σ^{*-} for the $\gamma n \to K^+\Sigma^{*-}$ analysis in the 1.9 GeV to 2.1 GeV photon energy bin. Each plot represents a different merged bin of $\cos(\theta_{K^+})$, where θ_{K^+} is the angle between the K^+ and the photon in the center-of-mass frame. These distributions were fit to a Breit-Wigner over a linear background, and events within $\pm 1\Gamma$ were cut to remove the majority of the Σ^{*-} events from the K^{*0} distributions for the overlap cut fits. These cuts are illustrated by the red vertical lines, and the blue, magenta, and black lineshapes represent the Breit-Wigner, linear background, and total fit functions, respectively.

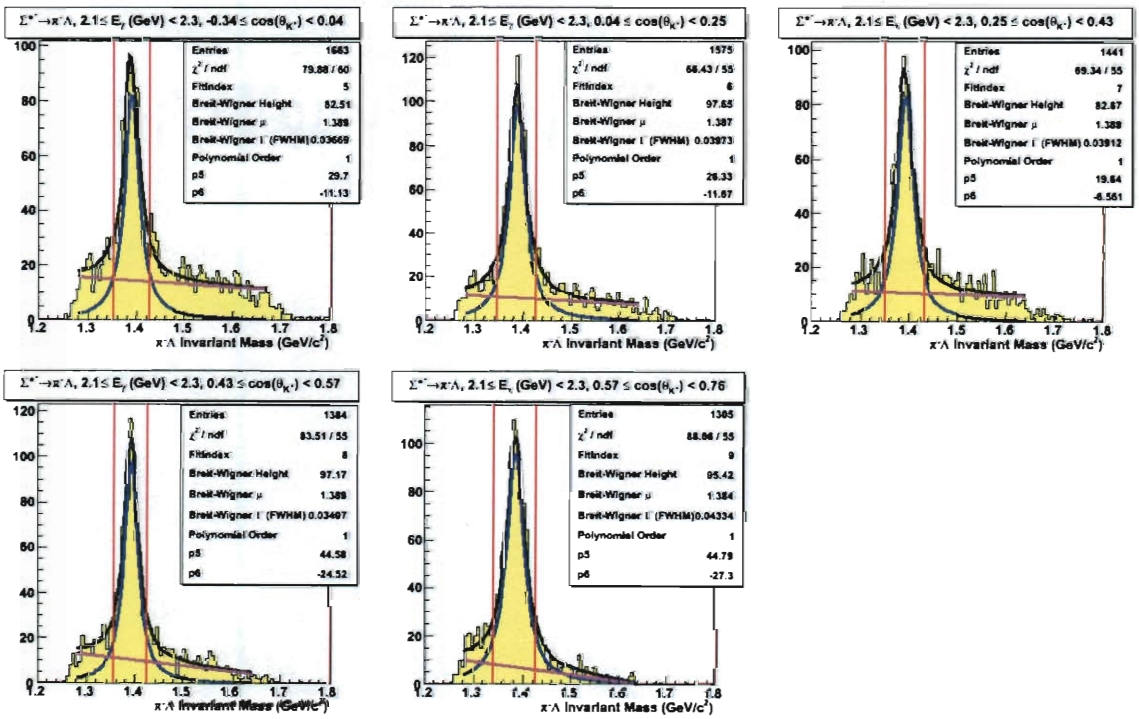

Figure C.25 : Fits to the invariant mass of the Σ^{*-} for the $\gamma n \to K^+\Sigma^{*-}$ analysis in the 2.1 GeV to 2.3 GeV photon energy bin. Each plot represents a different merged bin of $\cos(\theta_{K^+})$, where θ_{K^+} is the angle between the K^+ and the photon in the center-of-mass frame. These distributions were fit to a Breit-Wigner over a linear background, and events within $\pm 1\Gamma$ were cut to remove the majority of the Σ^{*-} events from the K^{*0} distributions for the overlap cut fits. These cuts are illustrated by the red vertical lines, and the blue, magenta, and black lineshapes represent the Breit-Wigner, linear background, and total fit functions, respectively.

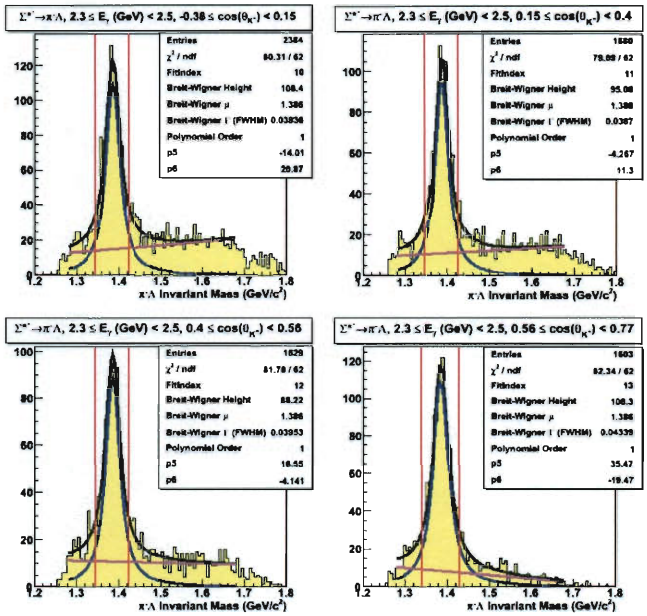

Figure C.26 : Fits to the invariant mass of the Σ^{*-} for the $\gamma n \to K^+\Sigma^{*-}$ analysis in the 2.3 GeV to 2.5 GeV photon energy bin. Each plot represents a different merged bin of $\cos(\theta_{K^+})$, where θ_{K^+} is the angle between the K^+ and the photon in the center-of-mass frame. These distributions were fit to a Breit-Wigner over a linear background, and events within $\pm 1\Gamma$ were cut to remove the majority of the Σ^{*-} events from the K^{*0} distributions for the overlap cut fits. These cuts are illustrated by the red vertical lines, and the blue, magenta, and black lineshapes represent the Breit-Wigner, linear background, and total fit functions, respectively.

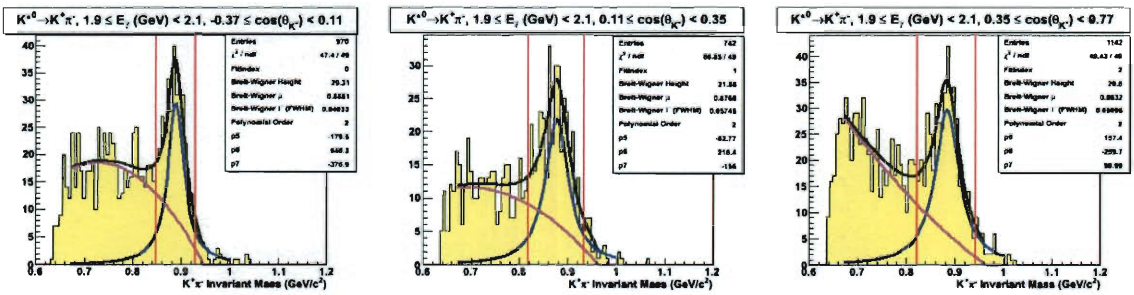

Figure C.27 : Fits to the invariant mass of the K^{*0} for the $\gamma n \to K^+\Sigma^{*-}$ analysis in the 1.9 GeV to 2.1 GeV photon energy bin. Each plot represents a different merged bin of $\cos(\theta_{K^+})$, where θ_{K^+} is the angle between the K^+ and the photon in the center-of-mass frame. These distributions were fit to a Breit-Wigner over a quadratic background, and events within $\pm 1\Gamma$ were cut to remove the majority of the $\gamma n \to K^{*0}\Lambda$ events from the $\gamma n \to K^+\Sigma^{*-}$ analysis. These cuts are illustrated by the red vertical lines, and the blue, magenta, and black lineshapes represent the Breit-Wigner, quadratic background, and total fit functions, respectively.

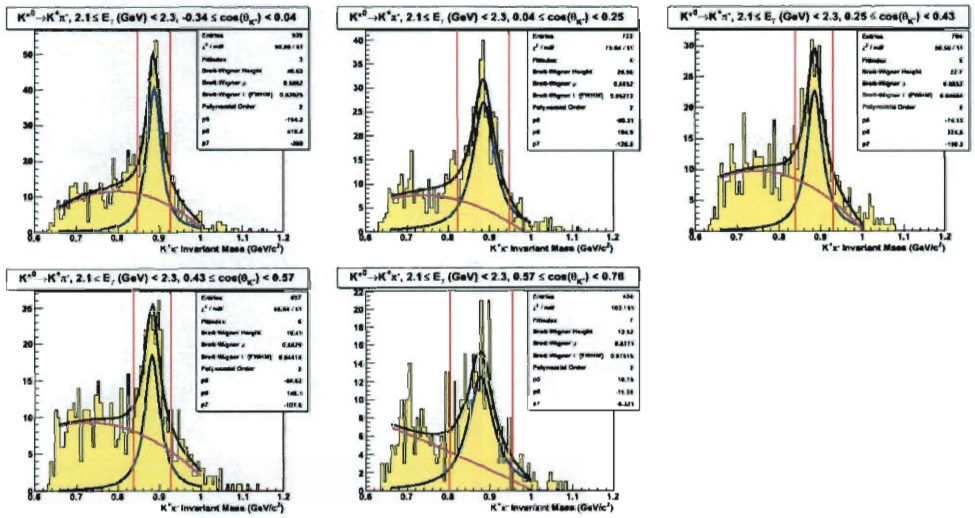

Figure C.28 : Fits to the invariant mass of the K^{*0} for the $\gamma n \to K^+\Sigma^{*-}$ analysis in the 2.1 GeV to 2.3 GeV photon energy bin. Each plot represents a different merged bin of $\cos(\theta_{K^+})$, where θ_{K^+} is the angle between the K^+ and the photon in the center-of-mass frame. These distributions were fit to a Breit-Wigner over a quadratic background, and events within $\pm 1\Gamma$ were cut to remove the majority of the $\gamma n \to K^{*0}\Lambda$ events from the $\gamma n \to K^+\Sigma^{*-}$ analysis. These cuts are illustrated by the red vertical lines, and the blue, magenta, and black lineshapes represent the Breit-Wigner, quadratic background, and total fit functions, respectively.

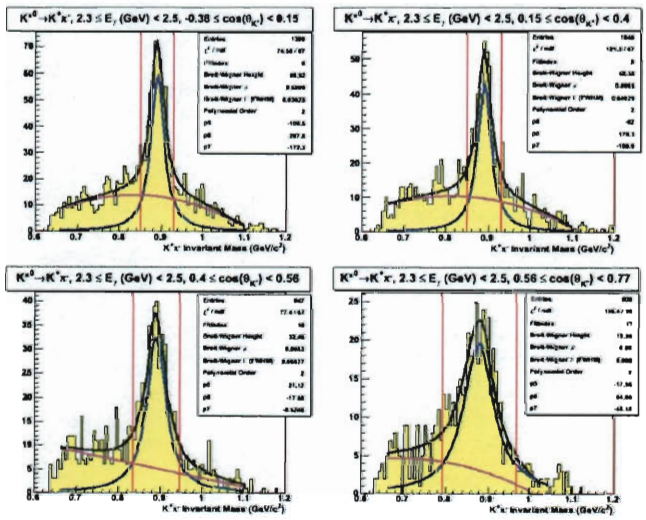

Figure C.29 : Fits to the invariant mass of the K^{*0} for the $\gamma n \to K^+\Sigma^{*-}$ analysis in the 2.3 GeV to 2.5 GeV photon energy bin. Each plot represents a different merged bin of $\cos(\theta_{K^+})$, where θ_{K^+} is the angle between the K^+ and the photon in the center-of-mass frame. These distributions were fit to a Breit-Wigner over a quadratic background, and events within $\pm 1\Gamma$ were cut to remove the majority of the $\gamma n \to K^{*0}\Lambda$ events from the $\gamma n \to K^+\Sigma^{*-}$ analysis. These cuts are illustrated by the red vertical lines, and the blue, magenta, and black lineshapes represent the Breit-Wigner, quadratic background, and total fit functions, respectively.

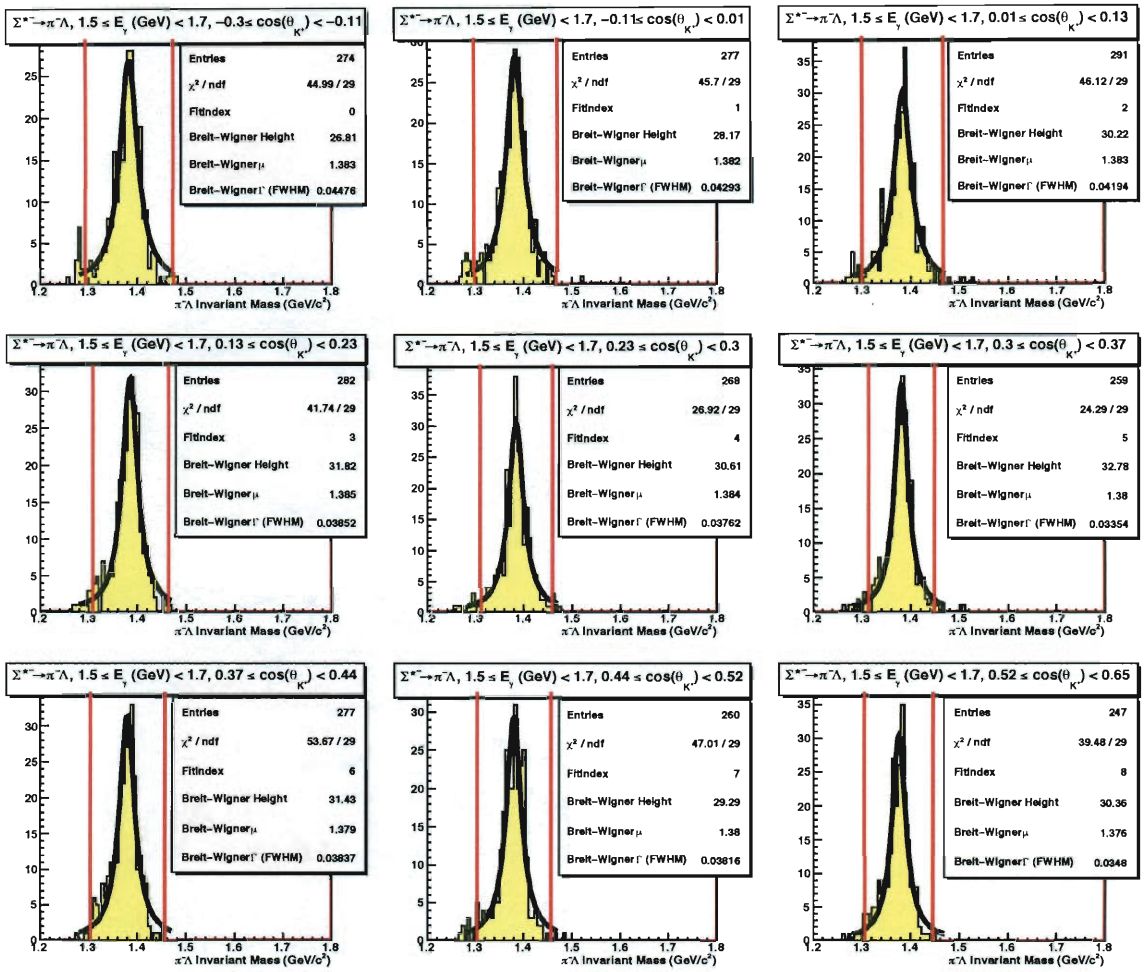

Figure C.30 : Fits to the invariant mass of the Σ^{*-} for the $\gamma n \to K^+\Sigma^{*-}$ analysis in the 1.5 GeV to 1.7 GeV photon energy bin. Each plot represents a different bin of $\cos(\theta_{K^+})$, where θ_{K^+} is the angle between the K^+ and the photon in the center-of-mass frame. These distributions were fit to a Breit-Wigner function, and the red lines indicate the $\pm 2\Gamma$ cuts used for yield extraction.

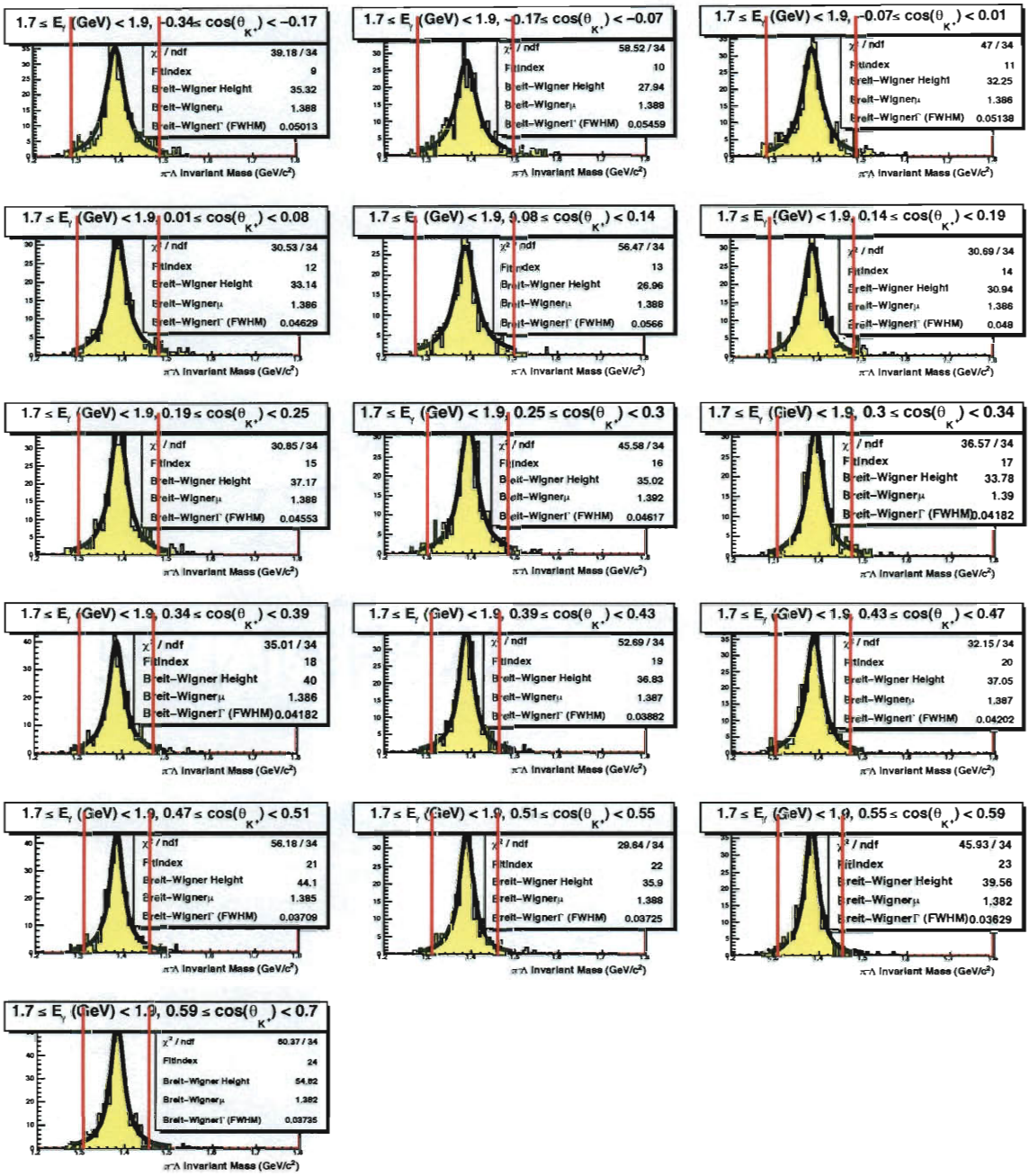

Figure C.31 : Fits to the invariant mass of the Σ^{*-} for the $\gamma n \to K^+\Sigma^{*-}$ analysis in the 1.7 GeV to 1.9 GeV photon energy bin. Each plot represents a different bin of $\cos(\theta_{K^+})$, where θ_{K^+} is the angle between the K^+ and the photon in the center-of-mass frame. These distributions were fit to a Breit-Wigner function, and the red lines indicate the $\pm 2\Gamma$ cuts used for yield extraction.

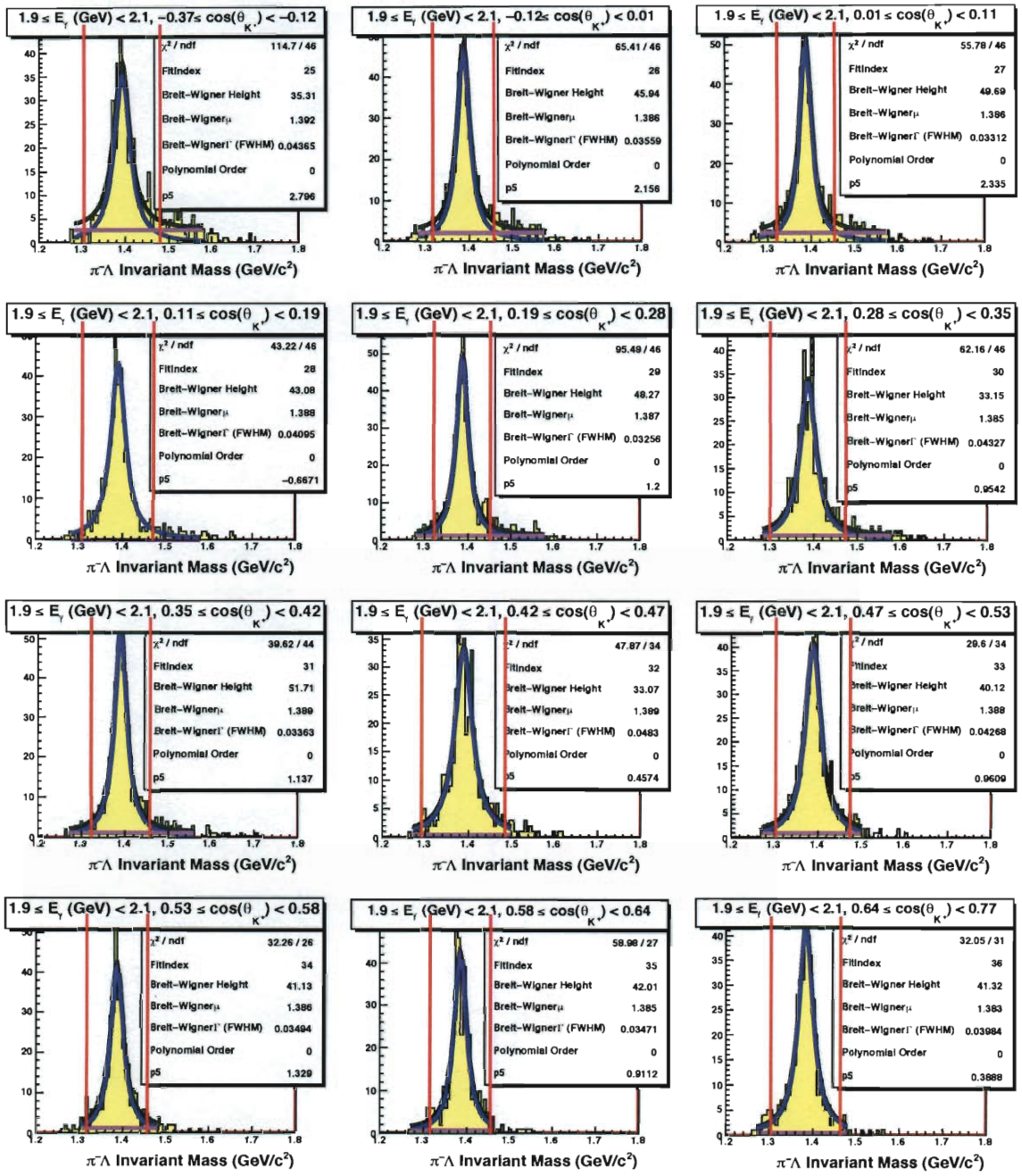

Figure C.32 : Fits to the invariant mass of the Σ^{*-} for the $\gamma n \to K^+\Sigma^{*-}$ analysis in the 1.9 GeV to 2.1 GeV photon energy bin. Each plot represents a different bin of $\cos(\theta_{K^+})$, where θ_{K^+} is the angle between the K^+ and the photon in the center-of-mass frame. These distributions were fit to a Breit-Wigner over a flat background, and the red lines indicate the $\pm 2\Gamma$ cuts used for yield extraction. The blue lineshapes represent the Breit-Wigner fit functions, the magenta lineshapes represent the flat fit functions, and the black lineshapes represent the total fit functions.

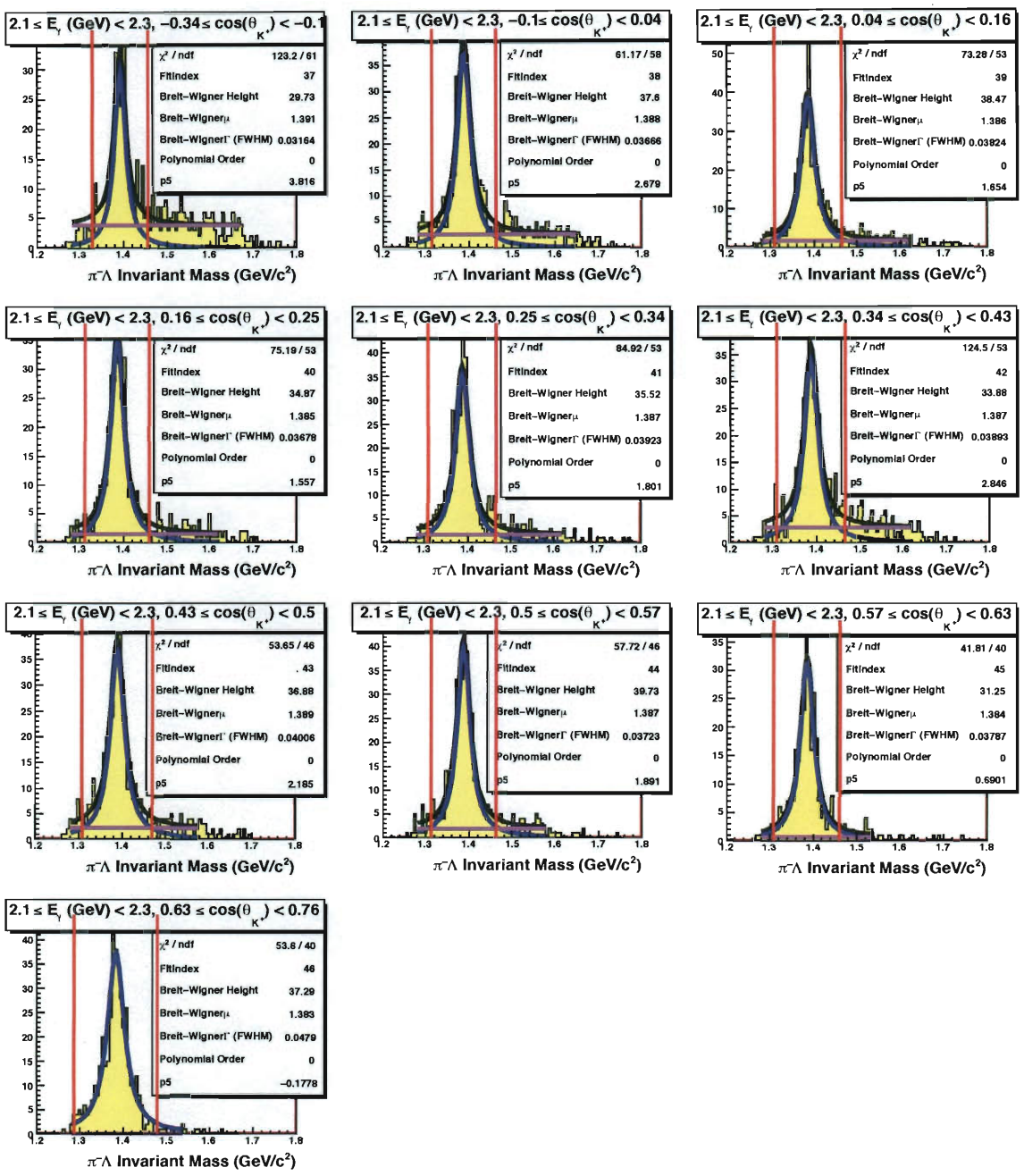

Figure C.33 : Fits to the invariant mass of the Σ^{*-} for the $\gamma n \to K^+\Sigma^{*-}$ analysis in the 2.1 GeV to 2.3 GeV photon energy bin. Each plot represents a different bin of $\cos(\theta_{K^+})$, where θ_{K^+} is the angle between the K^+ and the photon in the center-of-mass frame. These distributions were fit to a Breit-Wigner over a flat background, and the red lines indicate the $\pm 2\Gamma$ cuts used for yield extraction. The blue lineshape represents the Breit-Wigner fit function, the magenta lineshape represents the flat fit function, and the black lineshape represents the total fit function.

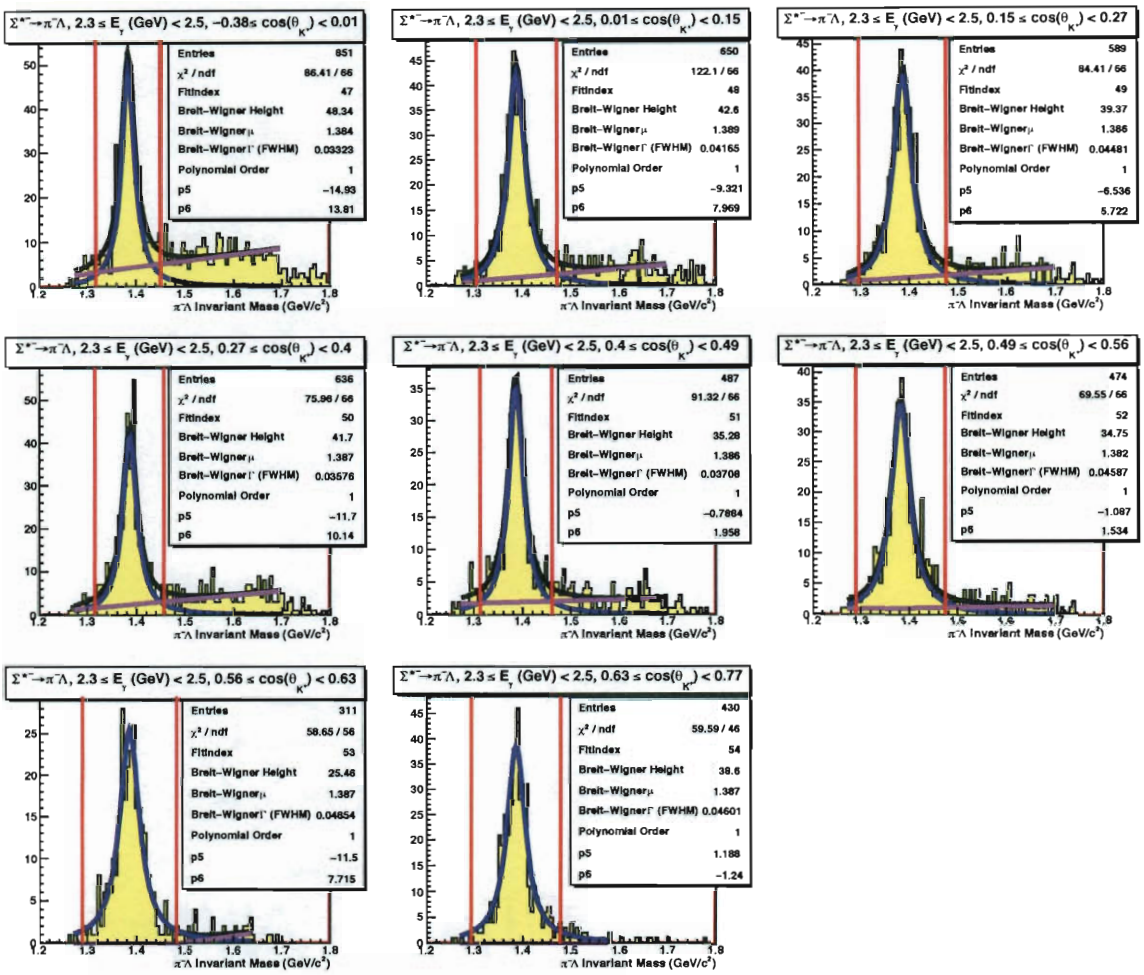

Figure C.34 : Fits to the invariant mass of the Σ^{*-} for the $\gamma n \to K^+\Sigma^{*-}$ analysis in the 2.3 GeV to 2.5 GeV photon energy bin. Each plot represents a different bin of $\cos(\theta_{K^+})$, where θ_{K^+} is the angle between the K^+ and the photon in the center-of-mass frame. These distributions were fit to a Breit-Wigner over a linear background, and the red lines indicate the $\pm 2\Gamma$ cuts used for yield extraction. The blue lineshapes represent the Breit-Wigner fit functions, the magenta lineshapes represent the linear fit functions, and the black lineshapes represent the total fit functions.

Appendix D

Cross Section Tables

E_γ (GeV)	$\cos(\theta_{K^{*0}})$	$\frac{d\sigma}{d\cos(\theta_{K^{*0}})}$ (μb)	$\sigma_{\text{Statistical}}$ (μb)	$\sigma_{\text{Systematic}}$ (μb)	σ_{Total} (μb)
1.9 - 2.1	-0.4 - 0.17	0.153	0.00749	0.0541	0.0546
1.9 - 2.1	0.17 - 0.46	0.153	0.01	0.0639	0.0647
1.9 - 2.1	0.46 - 0.62	0.379	0.0181	0.0685	0.0709
1.9 - 2.1	0.62 - 0.85	0.732	0.0215	0.122	0.124
2.1 - 2.3	-0.41 - 0.04	0.186	0.00606	0.0668	0.0671
2.1 - 2.3	0.04 - 0.25	0.172	0.00767	0.0608	0.0613
2.1 - 2.3	0.25 - 0.43	0.225	0.00962	0.0509	0.0518
2.1 - 2.3	0.43 - 0.6	0.269	0.0121	0.0625	0.0637
2.1 - 2.3	0.6 - 0.88	0.61	0.0134	0.16	0.161
2.3 - 2.5	-0.43 - -0.08	0.108	0.00472	0.0487	0.0489
2.3 - 2.5	-0.08 - 0.07	0.163	0.0067	0.0564	0.0568
2.3 - 2.5	0.07 - 0.25	0.141	0.00582	0.0404	0.0408
2.3 - 2.5	0.25 - 0.38	0.161	0.00795	0.0464	0.0471
2.3 - 2.5	0.38 - 0.52	0.144	0.00816	0.0337	0.0347
2.3 - 2.5	0.52 - 0.65	0.232	0.0112	0.0659	0.0668
2.3 - 2.5	0.65 - 0.73	0.355	0.0167	0.114	0.115
2.3 - 2.5	0.73 - 0.88	0.834	0.0388	0.187	0.191

Table D.1 : Cross section of the $\gamma n \rightarrow K^*(892)^0\Lambda$ reaction measured using the 2.655 GeV data from the CLAS g13a experiment.

E_γ (GeV)	$\cos(\theta_{K^+})$	$\frac{d\sigma}{d\cos(\theta_{K^+})}$ (μb)	$\sigma_{\text{Statistical}}$ (μb)	$\sigma_{\text{Systematic}}$ (μb)	σ_{Total} (μb)
1.5 - 1.7	-0.3 - -0.11	0.53	0.0357	0.166	0.17
1.5 - 1.7	-0.11 - 0.01	0.641	0.0428	0.163	0.168
1.5 - 1.7	0.01 - 0.13	0.564	0.0362	0.105	0.111
1.5 - 1.7	0.13 - 0.23	0.705	0.0461	0.163	0.169
1.5 - 1.7	0.23 - 0.3	0.886	0.0601	0.159	0.17
1.5 - 1.7	0.3 - 0.37	0.913	0.0628	0.186	0.196
1.5 - 1.7	0.37 - 0.44	1.01	0.0661	0.202	0.213
1.5 - 1.7	0.44 - 0.52	0.927	0.0626	0.167	0.178
1.5 - 1.7	0.52 - 0.65	1.01	0.0699	0.212	0.223
1.7 - 1.9	-0.34 - -0.17	0.461	0.0255	0.116	0.118
1.7 - 1.9	-0.17 - -0.07	0.506	0.0299	0.127	0.13
1.7 - 1.9	-0.07 - 0.01	0.632	0.036	0.174	0.177
1.7 - 1.9	0.01 - 0.08	0.619	0.0362	0.152	0.156
1.7 - 1.9	0.08 - 0.14	0.714	0.042	0.177	0.182
1.7 - 1.9	0.14 - 0.19	0.776	0.0465	0.17	0.176
1.7 - 1.9	0.19 - 0.25	0.826	0.0459	0.204	0.209
1.7 - 1.9	0.25 - 0.3	0.908	0.0516	0.217	0.223
1.7 - 1.9	0.3 - 0.34	0.969	0.0587	0.211	0.219
1.7 - 1.9	0.34 - 0.39	0.897	0.0496	0.196	0.202
1.7 - 1.9	0.39 - 0.43	0.929	0.0549	0.203	0.211
1.7 - 1.9	0.43 - 0.47	1.02	0.0584	0.223	0.23
1.7 - 1.9	0.47 - 0.51	1.13	0.0632	0.247	0.254
1.7 - 1.9	0.51 - 0.55	0.978	0.0596	0.218	0.226
1.7 - 1.9	0.55 - 0.59	1.14	0.0674	0.249	0.258
1.7 - 1.9	0.59 - 0.7	1.04	0.0507	0.234	0.24

Table D.2 : Cross section of the $\gamma n \rightarrow K^+\Sigma^*(1385)^-$ reaction from 1.5 GeV to 1.9 GeV in photon energy, measured using the 2.655 GeV data from the CLAS g13a experiment.

E_γ (GeV)	$\cos(\theta_{K^+})$	$\frac{d\sigma}{d\cos(\theta_{K^+})}$ (μb)	$\sigma_{\text{Statistical}}$ (μb)	$\sigma_{\text{Systematic}}$ (μb)	σ_{Total} (μb)
1.9 - 2.1	-0.37 - -0.12	0.225	0.00695	0.056	0.0564
1.9 - 2.1	-0.12 - 0.01	0.306	0.0081	0.0656	0.0661
1.9 - 2.1	0.01 - 0.11	0.384	0.0102	0.0772	0.0779
1.9 - 2.1	0.11 - 0.19	0.554	0.0138	0.0984	0.0994
1.9 - 2.1	0.19 - 0.28	0.457	0.0101	0.0792	0.0799
1.9 - 2.1	0.28 - 0.35	0.56	0.0135	0.0923	0.0932
1.9 - 2.1	0.35 - 0.42	0.632	0.0131	0.103	0.104
1.9 - 2.1	0.42 - 0.47	0.782	0.016	0.127	0.128
1.9 - 2.1	0.47 - 0.53	0.688	0.0138	0.112	0.113
1.9 - 2.1	0.53 - 0.58	0.717	0.0165	0.117	0.118
1.9 - 2.1	0.58 - 0.64	0.702	0.0141	0.114	0.115
1.9 - 2.1	0.64 - 0.77	0.851	0.0136	0.139	0.139
2.1 - 2.3	-0.34 - -0.1	0.121	0.0051	0.0356	0.036
2.1 - 2.3	-0.1 - 0.04	0.212	0.00667	0.0509	0.0514
2.1 - 2.3	0.04 - 0.16	0.291	0.00773	0.0668	0.0672
2.1 - 2.3	0.16 - 0.25	0.346	0.0096	0.0735	0.0741
2.1 - 2.3	0.25 - 0.34	0.359	0.00945	0.0729	0.0735
2.1 - 2.3	0.34 - 0.43	0.34	0.01	0.0672	0.068
2.1 - 2.3	0.43 - 0.5	0.444	0.0114	0.0829	0.0837
2.1 - 2.3	0.5 - 0.57	0.429	0.0101	0.0782	0.0789
2.1 - 2.3	0.57 - 0.63	0.54	0.0113	0.1	0.101
2.1 - 2.3	0.63 - 0.76	0.666	0.0165	0.122	0.123
2.3 - 2.5	-0.38 - 0.01	0.0959	0.0029	0.0261	0.0263
2.3 - 2.5	0.01 - 0.15	0.217	0.0054	0.0577	0.058
2.3 - 2.5	0.15 - 0.27	0.256	0.00573	0.0638	0.0641
2.3 - 2.5	0.27 - 0.4	0.216	0.00548	0.0444	0.0447
2.3 - 2.5	0.4 - 0.49	0.275	0.00725	0.0532	0.0537
2.3 - 2.5	0.49 - 0.56	0.421	0.00836	0.0815	0.0819
2.3 - 2.5	0.56 - 0.63	0.448	0.0105	0.0871	0.0877
2.3 - 2.5	0.63 - 0.77	0.555	0.0122	0.107	0.108

Table D.3 : Cross section of the $\gamma n \to K^+\Sigma^*(1385)^-$ reaction from 1.9 GeV to 2.5 GeV in photon energy, measured using the 2.655 GeV data from the CLAS g13a experiment.